STUDY ON THE PERFORMANCE ENHANCEMENT OF BIOMEDICAL IMPLANTS: *IN VITRO* TEST UNDER UV IRRADIATION OF TITANIUM ANODISED IN MIXED ELECTROLYTE

SALEH S SALEH ELFALLAH

A thesis submitted in
fulfillment of the requirement for the award of the
Doctor of Philosophy

Faculty of Mechanical and Manufacturing Engineering
Universiti Tun Hussein Onn Malaysia

APRIL 2018

ACKNOWLEDGEMENTS

The author would like to express his sincere appreciation to his supervisor, Associate Professor Dr. Hasan Zuhudi Bin Abdullah for the support given throughout the duration for this research. Also the Co-supervisor, Dr. Mohamed Radzi Bin Mohamed Yunus.

The cooperation given by the Ministry of Higher Education, Malaysia for the financial support provided for the research through Research Grant Scheme, FRGS vot 1212 and to Universiti Tun Hussein Onn Malaysia for the financial support Geran Insentif Penyelidik Siswazah (GIPS) vot 1251 are also highly appreciated. Appreciation also goes to everyone involved directly or indirectly towards the compilation of this thesis.

ABSTRACT

Titanium (Ti) recently has widely been used in the biomedical applications due to its high performance. Therefore, surface modifications of titanium have attracted a lot of interest to provide better osseointegration. Ti was subjected to anodic oxidation process and *in vitro* testing to assess the bioactivity of titanium oxide (TiO_2) coating. TiO_2 coating has been anodised at room temperature in different electrolyte; in sulphuric acid (H_2SO_4); phosphoric acid (H_3PO_4); and a mixture of H_2SO_4 and H_3PO_4 acids. The parameters used in anodization were: concentration of the electrolytes, applied voltage and current density. The coated surface is then evaluated using different testing techniques; the microstructure using scanning electron microscope (SEM); the elemental analysis using Energy-dispersive x-ray spectroscopy (EDX); mineralogical and crystal structure using x-ray diffraction (XRD); absorption analysis using Fourier transform infrared spectroscopy (FT-IR); and the hydrophilicity using water contact angle (WCA). TiO_2 was then subjected *in vitro* testing to assess the bioactivity of TiO_2 surface; that is the apatite formation ability. The apatite formation of the TiO_2 coating was precipitated by using simulated body fluid (SBF) in the dark and under the ultraviolet (UV) irradiation to mimic the reactions that may occur with the human bone-like cells layer. The testing was done to evaluate the apatite's microstructure, mineralogy, elements and absorption. From the results it was found that higher apatite was obtained with the increased of the immersion time; higher apatite formation and crystallization was found at earlier time of immersion for the TiO_2 that was immersed in SBF under the UV; higher apatite was obtained on the TiO_2 coatings that were anodised in H_2SO_4, H_3PO_4 and mixture electrolyte at lower electrolyte concentration. The increased apatite on these coatings can be related to the strong $Ti\text{-}O^-$ functional groups on the coating surface. The highest apatite was obtained on the TiO_2 coating that was anodised in a mixture electrolyte that has obtained Ti-OH functional group. The UV has resulted in the increased $Ti\text{-}O^-$ and Ti-OH groups, thus higher apatite precipitation ability.

ABSTRAK

Kebelakangan ini Ti telah banyak digunakan dalam aplikasi bioperubatan disebabkan oleh prestasinya yang sangat baik. Oleh yang demikian, ubah suai permukaan Ti telah menarik minat ramai untuk menghasilkan sifat biologinya yang lebih baik. Ti adalah telah dilakukan kepada proses pengoksidaan anodik dan ujian *in vitro* untuk menilai bioaktiviti salutan TiO_2. Salutan TiO_2 telah dioksidakan pada suhu bilik di dalam larutan elektrolit yang berbeza iaitu; H_2SO_4, H_3PO_4 dan campuran asid H_2SO_4 dan asid H_3PO_4. Pemboleh ubah yang digunakan dalam pengoksidaan anodik adalah: kepekatan elektrolit, voltan dan ketumpatan arus. Permukaan salutan kemudiannya di analisis menggunakan teknik pengujian yang berbeza; analisis mikrostruktur menggunakan SEM, analisis kandungan elemen menggunakan EDX, struktur hablur dan mineralogi menggunakan XRD, analisis penyerapan menggunakan FT-IR dan hidrofilik menggunakan WCA. Seterusnya ujian *in vitro* dilakukan untuk menilai aktiviti biologi permukaan salutan TiO_2. Penilaian aktiviti biologi pada permukaan TiO_2 dilakukan dengan menggunakan SBF yang dilakukan di dalam keadaan gelap dan di bawah UV untuk menyerupai tindak balas yang mungkin terjadi terhadap lapisan sel seperti tulang manusia. Ujian ini dilakukan untuk menilai mikrostruktur apatit, mineralogi, elemen dan penyerapan. Daripada keputusan ujian tersebut dapat disimpulkan bahawa banyak apatit dan tumpat mendap pada lapisan TiO_2 yang direndam di dalam SBF di bawah sinar UV berbanding salutan yang direndam di dalam SBF dalam keadaan gelap terutamanya pada permulaan eksperimen. Penyinaran UV juga telah mempercepatkan penghabluran apatit. Semua salutan memperolehi nisbah Ca/P apatit tulang dalam julat di antara 1.02 dan 1.57. Didapati juga fungsi bumpulan Ti-O menyumbang kepada peningkatan pembentukan apatit dan penghabluran untuk salutan oksida dalam larutan elektrolit H_2SO_4 dan H_3PO_4. Manakala fungsi kumpulan Ti-OH dan campuran ion S dan P dalam salutan telah menyumbang pembentukan apatit dan penghabluran yang lebih tinggi.

CONTENTS

LIST OF TABLES

LIST OF FIGURES

REFERENCES

Abdullah, H. Z. (2010). *Titanium Surface Modification by Oxidation for Biomedical Application*. University of New South Wales: Ph.D. Thesis.

Abdullah, H. Z., & Sorrell, C. C. (2007). Preparation and characterisation of TiO_2 thick Films fabricated by anodic oxidation. in materials science forum. *Trans Tech Publications*, 561, pp. 2159-2162.

Abdullah, H. Z., & Sorrell, C. C. (2007). TiO_2 thick films by anodic oxidation. *Journal of the Australasian Ceramic Society*, 43(2), pp. 125-130.

Abdullah, H. Z., & Sorrell, C. C. (2012). Gel oxidation of titanium and effect of UV irradiation on precipitation of hydroxyapatite from simulated body fluid. in Advanced Materials Research. *Trans Tech Publications*, 488, pp. 1229-1237.

Åberg, J., Eriksson, O., Spens, E., Nordblom, J., Mattsson, P., Sjödahl, J & Engqvist, H. (2012). Calcium sulfate spinal cord scaffold: a study on degradation and fibroblast growth factor 1 loading and release. *Journal of Biomaterials Applications*, 26(6), pp. 667-685.

Acero, J., Calderon, J., Salmeron, J. I., Verdaguer, J. J., Concejo, C., & Somacarrera, M. L. (1999). The behaviour of titanium as a biomaterial: microscopy study of plates and surrounding tissues in facial osteosynthesis. *Journal of cranio-maxillo-facial surgery*, 27(2), pp. 117-123.

Afshar, A., & Vaezi, M. R. (2004). Evaluation of electrical breakdown of anodic films on titanium in phosphate-base solutions. *Surface and Coatings Technology*, 186(3), pp. 398-404.

Agrawal, C. M. (1998). Reconstructing the human body using biomaterials. *Jom*, 50(1), pp. 31-35.

Allouni, Z. E., Cimpan, M. R., Høl, P. J., Skodvin, T., & Gjerdet, N. R. (2009). Agglomeration and sedimentation of TiO_2 nanoparticles in cell culture medium. *Colloids and Surfaces B: Biointerfaces*, 68(1), pp. 83-87.

Ambrosio, L. (Ed.). (2017). *Biomedical Composites*. 2nd ed UK: Woodhead Publishing.

Ambrosio, L., De Santis, R., & Nicolais, L. (1998). Composite hydrogels for implants. Proceedings of the Institution of Mechanical Engineers, *Part H: Journal of Engineering in Medicine*, 212(2), pp. 93-99.

American Society for Testing and Materials (ASTM). (2013a). *Standard Specification for Unalloyed Titanium for Surgical Implant Applications*. Philadelphia, PA: F67-13.

American Society for Testing and Materials (ASTM). (2013b). *Standard Specification for Wrought Titanium-6 Aluminium-4 Vanadium ELI (Extra Low Interstitial) Alloy for Surgical Implant Applications*. Philadelphia, PA: F136 - 08.

Angelova, N., & Hunkeler, D. (1999). Rationalizing the design of polymeric biomaterials. *Trends in Biotechnology*, 17(10), pp. 409-421.

AnthonyáSpackman, R. (1996). Photoelectrochemical study of titanium dioxide films prepared by anodisation of titanium metal in sulfuric acid. *Journal of the Chemical Society, Faraday Transactions*, 92(20), pp. 4049-4052.

Artursson, P., Palm, K., & Luthman, K. (2012). Caco-2 monolayers in experimental and theoretical predictions of drug transport. *Advanced Drug Delivery Reviews*, 64, pp. 280-289.

Augustynski, J. (1993). The role of the surface intermediates in the photoelectrochemical behaviour of anatase and rutile TiO_2. *Electrochimica Acta*, 38(1), pp. 43-46.

Balamurugan, A., Michel, J., Faure, J., Benhayoune, H., Wortham, L., Sockalingum, G., & Balossier, G. (2006). Synthesis and structural analysis of sol gel derived stoichiometric monophasic hydroxyapatite. *Ceramics-Silikaty*, 50(1), pp. 27-31.

Banerjee, S., Dionysiou, D. D., & Pillai, S. C. (2015). Self-cleaning applications of TiO_2 by photo-induced hydrophilicity and photocatalysis. *Applied Catalysis B: Environmental*, 176, pp. 396-428.

Banfield, J. (1998). Thermodynamic analysis of phase stability of nanocrystalline titania. *Journal of Materials Chemistry*, 8(9), pp. 2073-2076.

Bard, A. J. (1980). Photoelectrochemistry. *Science*, 207(4427), pp. 139-144.

Batzill, M., Morales, E. H., & Diebold, U. (2006). Influence of nitrogen doping on the defect formation and surface properties of TiO_2 rutile and anatase. *Physical Review Letters*, 96(2), pp. 026103.

Beltran, A., Gracia, L., & Andres, J. (2006). Density functional theory study of the brookite surfaces and phase transitions between natural titania polymorphs. *The Journal of Physical Chemistry B*, 110(46), pp. 23417 - 23423.

Ben-Nissan, B., Choi, A. H., Roest, R., Latella, B. A., & Bendavid, A. (2015). Adhesion of Hydroxyapatite on Titanium Medical Implants. in *Hydroxyapatite (Hap) for Biomedical Applications*. pp. 21-51.

Bergallo, C. (2000). Friction and wear of medical implants and prosthetic devices. *Revista Chilena de Infectología*, 17, 97-91.

Berger-Keller, N., Bertrand, G., Filiatre, C., Meunier, C., & Coddet, C. (2003). Microstructure of plasma-sprayed titania coatings deposited from spray-dried powder. *Surface and Coatings Technology*, 168(2-3), pp. 281-290.

Bickley, R. I., Gonzalez-Carreno, T., Lees, J. S., Palmisano, L., & Tilley, R. J. (1991). A structural investigation of titanium dioxide photocatalysts. *Journal of Solid State Chemistry*, 92(1), pp. 178 - 190.

Bigelow, P. (2010). How to Make Standard Solutions for Chemistry.

Binnig, G., Quate, C. F., & Gerber, C. (1986). Atomic force microscope. Physical Review Letters, pp, 56(9). 930.

Black, J. (2005). *Biological Performance of Materials: Fundamentals of Biocompatibility*. Roca Raton, FL: CRC Press.

Bogya, E. S., Károly, Z., & Barabás, R. (2015). Atmospheric plasma sprayed silica-hydroxyapatite coatings on magnesium alloy substrates. *Ceramics International*, 41(4), pp. 6005-6012.

Bohner, M., & Lemaitre, J. (2009). Can bioactivity be tested *in vitro* with SBF solution?. *Biomaterials*, 30(12), pp. 2175-2179.

BomBač, D., Brojan, M., Fajfar, P., Kosel, F., & Turk, R. (2007). Review of materials in medical applications pregled materialov v medicinskih aplikacijah. *RMZ-Materials and Geoenvironment*, 54(4), pp. 471-499.

Bonfield, W., Grynpas, M. D., Tully, A. E., Bowman, J., & Abram, J. (1981). Hydroxyapatite reinforced polyethylene-a mechanically compatible implant material for bone replacement. *Biomaterials*, 2(3), pp. 185-186.

Bos, R. R., Boering, G., Rozema, F. R., & Leenslag, J. W. (1987). Resorbable poly (L-lactide) plates and screws for the fixation of zygomatic fractures. *Journal of Oral and Maxillofacial Surgery*, 45(9), pp. 751-753.

Bragg, W. L. (2014). The diffraction of X-rays by crystals. *Zeitschrift Für Physikalische Chemie*, 228(10-12), pp. 957-968.

Brunella, M. F., Diamanti, M. V., Pedeferri, M. P., Di Fonzo, F., Casari, C. S., & Bassi, A. L. (2007). Photocatalytic behavior of different titanium dioxide layers. *Thin Solid Films*, 515(16), pp. 6309 - 6313.

Brunette, D. M., Tengvall, P., Textor, M., & Thomsen, P. (Eds.). (2012). Titanium in Medicine: Material Science, Surface Science, Engineering, Biological Responses and Medical Applications. Berlin: Springer Science and Business Media.

Brzezińska-Miecznik, J., Haberko, K., Sitarz, M., Bućko, M. M., & Macherzyńska, B. (2015). Hydroxyapatite from animal bones-extraction and properties. *Ceramics International*, 41(3), pp. 4841-4846.

Burnside, S. D., Shklover, V., Barbé, C., Comte, P., Arendse, F., Brooks, K., & Grätzel, M. (1998). Self-organization of TiO_2 nanoparticles in thin films. *Chemistry of Materials*, 10(9), pp. 2419-2425.

Busby, F., Hughes, K. R., & Hyun, K. S. (1999). Colour Measurement Techniques for Rapid Determination of Residence Time Distributions. in *ANTEC 99, Society of Plastics Engineers Annual Technical Papers*. New York City: ANTEC. (1). pp. 230-234.

Capek, D., Gigandet, M. P., Masmoudi, M., Wery, M., & Banakh, O. (2008). Long-time anodisation of titanium in sulphuric acid. *Surface and Coatings Technology*, 202(8), pp. 1379-1384.

Carp, O., Huisman, C. L., & Reller, A. (2004). Photoinduced reactivity of titanium dioxide. *Progress in solid state chemistry*, 32(1-2), pp. 33-177.

Cerruti, M. G. (2004). Characterisation of bioactive glasses. Effect of the immersion in solutions that simulate body fluids. *International Journal of Innovative Research in Science and Engineering*.

Cervantes, B., López-Huerta, F., Vega, R., Hernández-Torres, J., García-González, L., Salceda, E., & Soto, E. (2016). Cytotoxicity evaluation of anatase and rutile TiO_2 thin films on CHO-K1 cells *in vitro*. *Materials*, 9(8), pp. 619.

Chang-Ha, K., Su-Il, P., & Eung-Jo, L. (1991). Donor distribution over anodically passivating crystalline and amorphous TiO_2 films. *Materials Letters*, 10(7-8), pp. 387-391.

Chen, X., & Mao, S. S. (2007). Titanium dioxide nanomaterials: synthesis, properties, modifications, and applications. *Chemical Reviews*, 107(7), pp. 2891-2959.

Cheng, Y., & Hu, C. (1999). *MOSFET Modeling and BSIM3 User's Guide*. US: Springer Science and Business Media.

Chien, C. S., Chiao, C. L., Hong, T. F., Han, T. J., & Kuo, T. Y. (2009). Synthesis and Characterisation of TiO_2 + HA Coatings on Ti-6Al-4V Substrates by Nd-YAG Laser Cladding. in *13th International Conference on Biomedical Engineering*. Berlin, Heidelberg: Springer. pp. 1401-1404.

Chiesa, R., Sandrini, E., Santin, M., Rondelli, G., & Cigada, A. (2003). Osteointegration of titanium and its alloys by anodic spark deposition and other electrochemical techniques: a review. *Journal of Applied Biomaterials and Biomechanics*, 1(2), pp. 91-107.

Choi, J., Wehrpohn, R. B., Lee, J., & Gösele, U. (2004). Anodization of nanoimprinted titanium: a comparison with formation of porous alumina. *Electrochimica Acta*, 49(16), pp. 2645-2652.

Chu, P. K. (2013). Surface engineering and modification of biomaterials. *Thin Solid Films*, 528, pp. 93-105.

Commandeur, S., Van Beusekom, H. M., & Van Der Giessen, W. J. (2006). Polymers, Drug Release, and Drug-Eluting Stents. *Journal of Interventional Cardiology*, 19(6), pp. 500-506.

Coolibar (2014). *It's all in the Fabric-Coolibar SUNTECT*. 2011. Retrieved 23 May 2014 from http://blog.coolibar.com/coolibar-suntect/

Criado, J., & Real, C. (1983). Mechanism of the inhibiting effect of phosphate on the anatase→ rutile transformation induced by thermal and mechanical treatment of TiO_2. *Journal of the Chemical Society, Faraday Transactions 1: Physical Chemistry in Condensed Phases*, 79(12), pp. 2765-2771.

Cui, X., Kim, H. M., Kawashita, M., Wang, L., Xiong, T., Kokubo, T., & Nakamura, T. (2009). Preparation of bioactive titania films on titanium metal via anodic oxidation. *Dental Materials*, 25(1), pp. 80-86.

Currey, J. D. (1998). Mechanical properties of vertebrate hard tissues. *Proceedings of the Institution of Mechanical Engineers, Part H: Journal of Engineering in Medicine*, 212(6), pp. 399-411.

Dai, Y., Liu, H., Liu, B., Wang, Z., Li, Y., & Zhou, G. (2015). Porous β-Ca_2SiO_4 ceramic scaffolds for bone tissue engineering: *In vitro* and *in vivo* characterisation. *Ceramics International*, 41(4), pp. 5894-5902.

Damore, A., Pompo, A., Netti, P., Masi, E., & Nicolais, L. (1993). Non-linear viscoelastic behavior of poly-ether-ether-ketone (PEEK) and PEEK-based composites. *Journal of Reinforced Plastics and Composites*, 12(3), pp. 327-340.

Das, K., Bose, S., & Bandyopadhyay, A. (2007). Surface modifications and cell–materials interactions with anodised Ti. Acta Biomaterialia, 3(4), pp. 573-585.

Dash, S. R., Sarkar, R., & Bhattacharyya, S. (2015). Gel casting of hydroxyapatite with naphthalene as pore former. *Ceramics International*, 41(3), pp. 3775-3790.

Davidson, J. A., & Georgette, F. S. (1987). State of the art materials for orthopedic prosthetic devices. *Society of Manufacturing Engineers*, pp. 87-122.

Davidson, J. A., Mishra, A. K., Kovacs, P., & Poggie, R. A. (1994). New surface-hardened, low-modulus, corrosion-resistant Ti-13Nb-13Zr alloy for total hip arthroplasty. *Bio-medical materials and engineering*, 4(3), pp. 231-243.

Davis, E. A., & Mott, N. (1970). Conduction in non-crystalline systems V. Conductivity, optical absorption and photoconductivity in amorphous semiconductors. *Philosophical Magazine*, 22(179), pp. 0903 - 0922.

Davis, J. R. (Ed.). (2006). *Handbook of Materials for Medical Devices*. Materials Park, OH: ASM international.

De Clercq, E. (2005). Recent highlights in the development of new antiviral drugs. *Current Opinion in Microbiology*, 8(5), pp. 552-560.

de Mussy, J. P. G., Langelaan, G., Decerf, J., & Delplancke, J. L. (2003). TEM and X-ray diffraction investigation of the structural characteristics of the microporous oxide film formed on polycrystalline Ti. *Scripta Materialia*, 48(1), pp. 23-29.

de Oliveira, P. T., & Nanci, A. (2004). Nanotexturing of titanium-based surfaces upregulates expression of bone sialoprotein and osteopontin by cultured osteogenic cells. *Biomaterials*, 25(3), pp. 403-413.

De Sena, L. A., Rocha, N. C. C., Andrade, M. C., & Soares, G. A. (2003). Bioactivity assessment of titanium sheets electrochemically coated with thick oxide film. *Surface and Coatings Technology*, 166(2-3), pp. 254-258.

Deer, W. A., Howie, R. A., & Zussman, J. (1992). *An Introduction to the Rock-Forming Minerals*. Hong Kong: Longman Scientific and Technical. 696.

Del Pino, A. P., Fernández-Pradas, J. M., Serra, P., & Morenza, J. L. (2004). Coloring of titanium through laser oxidation: comparative study with anodizing. *Surface and Coatings Technology*, 187(1), pp. 106-112.

Deligianni, D. D., Katsala, N., Ladas, S., Sotiropoulou, D., Amedee, J., & Missirlis, Y. F. (2001). Effect of surface roughness of the titanium alloy Ti-6Al-4V on human bone marrow cell response and on protein adsorption. *Biomaterials*, 22(11), pp. 1241-1251.

Delplancke, J. L., Degrez, M., Fontana, A., & Winand, R. (1982). Self-colour anodizing of titanium. *Surface Technology*, 16(2), pp. 153-162.

Deng, X., Yue, Y., & Gao, Z. (2002). Gas-phase photo-oxidation of organic compounds over nanosized TiO_2 photocatalysts by various preparations. *Applied Catalysis B: Environmental*, 39(2), pp. 135-147.

Diamanti, M. V., & Pedeferri, M. P. (2007). Effect of anodic oxidation parameters on the titanium oxides formation. *Corrosion Science*, 49(2), pp. 939-948.

Diamanti, M. V., Del Curto, B., & Pedeferri, M. (2008). Interference colors of thin oxide layers on titanium. *Color Research and Application*, 33(3), 221-228.

Diamanti, M. V., Ormellese, M., Marin, E., Lanzutti, A., Mele, A., & Pedeferri, M. P. (2011). Anodic titanium oxide as immobilized photocatalyst in UV or visible light devices. *Journal of Hazardous Materials*, 186(2-3), pp. 2103-2109.

Diamanti, M. V., Spreafico, F. C., & Pedeferri, M. P. (2013). Production of anodic TiO_2 nanofilms and their characterisation. *Physics Procedia*, 40, pp. 30-37.

Diebold, U. (2003). The surface science of titanium dioxide. *Surface Science Reports*, 48(5-8), pp. 53-229.

Ding, X. Z., Liu, X. H., & He, Y. Z. (1996). Grain size dependence of anatase-to-rutile structural transformation in gel-derived nanocrystalline titania powders. *Journal of Materials Science Letters*, 15(20), pp. 1789-1791.

Dubrovinsky, L. S., Dubrovinskaia, N. A., Swamy, V., Muscat, J., Harrison, N. M., Ahuja, R., & Johansson, B. (2001). Materials science: The hardest known oxide. *Nature*, 410(6829), pp. 653.

Duta, L., Oktar, F. N., Stan, G. E., Popescu-Pelin, G., Serban, N., Luculescu, C., & Mihailescu, I. N. (2013). Novel doped hydroxyapatite thin films obtained by pulsed laser deposition. *Applied Surface Science*, 265, pp. 41-49.

Dynamics, L. (2013). *Types of UV and Visible Light*. Retrieved 23 May 2014. From http://blog.coolibar.com/coolibar-suntect/

El Kader, J. A., El Wahab, F. A., El Shayeb, H. A., & Khedr, M. G. A. (1981). Oxide film thickening on titanium in aqueous solutions in relation to anion type and concentration. *British Corrosion Journal*, 16(2), pp. 111-114.

Elias, C. N., Lima, J. H. C., Valiev, R., & Meyers, M. A. (2008). Biomedical applications of titanium and its alloys. *Jom*, 60(3), pp. 46-49.

Fahmi, A., Minot, C., Silvi, B., & Causa, M. (1993). Theoretical analysis of the structures of titanium dioxide crystals. *Physical Review B*, 47(18), pp. 11717.

Feenstra, L. (2018). Medical Use of Calcium Phosphate Ceramics. in *Bioceramics Calcium Phosphate*. CRC Press. pp. 131-141.

Feng, B., Chen, J. Y., Qi, S. K., He, L., Zhao, J. Z., & Zhang, X. D. (2002). Characterisation of surface oxide films on titanium and bioactivity. *Journal of materials science: Materials in Medicine*, 13(5), pp. 457-464.

Fernandez, A., Lassaletta, G., Jimenez, V. M., Justo, A., Gonzalez-Elipe, A. R., Herrmann, J. M., & Ait-Ichou, Y. (1995). Preparation and characterisation of TiO_2 photocatalysts supported on various rigid supports (glass, quartz and stainless steel). Comparative studies of photocatalytic activity in water purification. *Applied Catalysis B: Environmental*, 7(1-2), pp. 49-63.

Finklea, H. O. (1988). *Semiconductor Electrodes*. Netherlands: International Nuclear Information System. (21)10.

Förch, R., Schönherr, H., & Jenkins, A. T. A. (Eds.). (2009). Surface Design: Applications in *Bioscience and Nanotechnology*. John Wiley & Sons.

Ford, W. E., & Dana, E. S. (1991). A textbook of Mineralogy. 4nd ed. US: John Whiley & Sons.

Frauchiger, V. M., Schlottig, F., Gasser, B., & Textor, M. (2004). Anodic plasma-chemical treatment of CP titanium surfaces for biomedical applications. *Biomaterials*, 25(4), pp. 593-606.

Fujishima, A. Kohayakawa, K and Honda, K. Hydrogen production under sunlight with an electrochemical photocell. *Journal of the Electrochemical Society*. 1975. 122(11): 1487.

Fujishima, A. Zhang, X and Tryk, D. (2008). TiO_2 photocatalysis and related surface phenomena. *Surface Science Reports*, 63(12), pp. 515.

Fujishima, A., & Honda, K. (1972). Electrochemical photolysis of water at a semiconductor electrode. *Nature*, 238(5358), pp. 37.

Fujishima, A., Rao, T. N., & Tryk, D. A. (2000). Titanium dioxide photocatalysis. *Journal of Photochemistry and Photobiology C: Photochemistry Reviews*, 1(1), pp. 1-21.

Gamble, J. L. (1947). *Chemical Anatomy, Physiology and Pathology of Extracellular Fluid: A Lecture Syllabus*. UK: Harvard University Press.

Gao, Y., Masuda, Y., Peng, Z., Yonezawa, T., & Koumoto, K. (2003). Room temperature deposition of a TiO_2 thin film from aqueous peroxotitanate solution. *Journal of Materials Chemistry*, 13(3), pp. 608-613.

Gargas, M. L., Burgess, R. J., Voisard, D. E., Cason, G. H., & Andersen, M. E. (1989). Partition coefficients of low-molecular-weight volatile chemicals in various liquids and tissues. *Toxicology and Applied Pharmacology*, 98(1), pp. 87-99.

Gaul, E. (1993). Coloring titanium and related metals by electrochemical oxidation. *Journal of Chemical Education*, 70(3), pp. 176.

Ge, R., Fu, W., Yang, H., Zhang, Y., Zhao, W., Liu, Z., & Zou, G. (2008). Fabrication and characterisation of highly-ordered titania nanotubes via electrochemical anodization. *Materials Letters*, 62(17-18), pp. 2688-2691.

Geetha, M., Singh, A. K., Asokamani, R., & Gogia, A. K. (2009). Ti based biomaterials, the ultimate choice for orthopaedic implants–a review. *Progress in Materials Science*, 54(3), pp. 397-425.

Gheisari, H., Karamian, E., & Abdellahi, M. (2015). A novel hydroxyapatite–hardystonite nanocomposite ceramic. *Ceramics International*, 41(4), pp. 5967-5975.

Ghosh, T. B., Dhabal, S., & Datta, A. K. (2003). On crystallite size dependence of phase stability of nanocrystalline TiO_2. *Journal of Applied Physics*, 94(7), pp. 4577-4582.

Giordano, C., Saino, E., Rimondini, L., Pedeferri, M. P., Visai, L., Cigada, A., & Chiesa, R. (2011). Electrochemically induced anatase inhibits bacterial colonization on Titanium Grade 2 and Ti6Al4V alloy for dental and orthopedic devices. *Colloids and Surfaces B: Biointerfaces*, 88(2), pp. 648-655.

Goldstein, J. I., Newbury, D. E., Michael, J. R., Ritchie, N. W., Scott, J. H. J., & Joy, D. C. (2017). *Scanning Electron Microscopy and X-Ray Microanalysis*. 3rd ed. Springer.

Goossens, A., Maloney, E. L., & Schoonman, J. (1998). Gas-Phase synthesis of nanostructured anatase TiO_2. *Chemical Vapor Deposition*, 4(3), pp. 109-114.

Greenwood, N. N., & Earnshaw, A. (2012). *Chemistry of the Elements*. 2nd ed. Elsevier.

Grujić-Brojčin, M., Šćepanović, M., Dohčević-Mitrović, Z., & Popović, Z. V. (2006). Infrared study of nonstoichiometric anatase TiO_2 nanopowders. *Science of Sintering*, 38(2), pp. 183-189.

Guillemot, F., Prima, F., Bareille, R., Gordin, D., Gloriant, T., Porté-Durrieu, M. C., & Baquey, C. (2004). Design of new titanium alloys for orthopaedic applications. *Medical and Biological Engineering and Computing*, 42(1), pp, 137-141.

Guo, Y. P., Tang, H. X., Zhou, Y., Jia, D. C., Ning, C. Q., & Guo, Y. J. (2010). Effects of mesoporous structure and UV irradiation on *in vitro* bioactivity of titania coatings. *Applied Surface Science*, 256(16), 4945-4952.

Ha, H. S., Kim, C. W., Lim, Y. J., & Kim, M. J. (2006). Surface characteristics of anodic oxidized titanium according to the pore size. *Journal of Korean Academic Prosthodontics*, 44(3), pp. 200.

Hamilton, R. F., Wu, N., Porter, D., Buford, M., Wolfarth, M., & Holian, A. (2009). Particle length-dependent titanium dioxide nanomaterials toxicity and bioactivity. *Particle and Fibre Toxicology*, 6(1), pp. 35.

Han, Y., Chen, D., Sun, J., Zhang, Y., & Xu, K. (2008). UV-enhanced bioactivity and cell response of micro-arc oxidized titania coatings. *Acta Biomaterialia*, 4(5), pp. 1518-1529.

Hanaor, D. (2007). PhD Thesis. UNSW: School of Materials Science and Engineering.

Hanaor, D. A., & Sorrell, C. C. (2011). Review of the anatase to rutile phase transformation. *Journal of Materials Science*, 46(4), 855-874.

Harold, R. M. (2001). An introduction to appearance analysis. *Gatfworld*, 13(3), pp. 5-12.

Hayashi, K., Matsuguchi, N., Uenoyama, K., Kanemaru, T., & Sugioka, Y. (1989). Evaluation of metal implants coated with several types of ceramics as

biomaterials. *Journal of Biomedical Materials Research Part A*, 23(11), pp. 1247-1259.

Hayashi, K., Matsuguchi, N., Uenoyama, K., Kanemaru, T., & Sugioka, Y. (1989). Evaluation of metal implants coated with several types of ceramics as biomaterials. *Journal of Biomedical Materials Research Part A*, 23(11), pp. 1247-1259.

He, Q. J., Huang, Z. L., Cheng, X. K., & Yu, J. (2008). Thermal stability of porous A-type carbonated hydroxyapatite spheres. *Materials Letters*, 62(3), pp. 539-542.

Hench, L. L. (1991a). Bioceramics: from concept to clinic. *Journal of the American Ceramic Society*, 74(7), pp. 1487-1510.

Hench, L. L. (1991b). Molecular design of bioactive glasses and ceramics for implants. *Ceramics: Towards the 21st Century Ceram Soc of Japan*, pp. 519-34.

Hench, L. L. (Ed.). (2013). *An Introduction to Bioceramics*. Singapore: World Scientific Publishing Company.

Hench, L. L., Splinter, R. J., Allen, W. C., & Greenlee, T. K. (1971). Bonding mechanisms at the interface of ceramic prosthetic materials. *Journal of Biomedical Materials Research Part A*, 5(6), pp. 117-141.

Heness, G. L., & Ben-Nissan, B. (2004). Innovative bioceramics. *Materials Forum*, 27, pp. 104-114.

Hengerer, R., Bolliger, B., Erbudak, M., & Grätzel, M. (2000). Structure and stability of the anatase TiO_2 (101) and (001) surfaces. *Surface Science*, 460(1-3), pp. 162-169.

Herman, H. (1988). Plasma spray deposition processes. *MRS Bulletin*, 13(12), pp. 60-67.

Herrmann, J.-M. (1999). Heterogeneous photocatalysis: fundamentals and applications to the removal of various types of aqueous pollutants. *Catalysis Today*, 53(1): pp. 115.

Hoffmann, M. R., Martin, S. T., Choi, W., & Bahnemann, D. W. (1995). Environmental applications of semiconductor photocatalysis. *Chemical Reviews*, 95(1), pp. 69-96.

Hollinger, J. O. (Ed.). (2011). *An Introduction to Biomaterials*. Boca Raton, FL: CRC press.

Howard, C. J., Sabine, T. M., & Dickson, F. (1991). Structural and thermal parameters for rutile and anatase. *Acta Crystallographica Section B: Structural Science*, 47(4), pp. 462-468.

Huang, H., Winchester, K. J., Suvorova, A., Lawn, B. R., Liu, Y., Hu, X. Z., & Faraone, L. (2006). Effect of deposition conditions on mechanical properties of low-temperature PECVD silicon nitride films. *Materials Science and Engineering: A*, 435, pp. 453-459.

Iida, Y., & Ozaki, S. (1961). Grain growth and phase transformation of titanium oxide during calcination. *Journal of the American Ceramic Society*, 44(3), pp. 120-127.

Ikonopisov, S. (1977). Theory of electrical breakdown during formation of barrier anodic films. *Electrochimica Acta*, 22(10), pp. 1077-1082.

Imam, M. A., Fraker, A. C., Harris, J. S., & Gilmore, C. M. (1983). Influence of heat treatment on the fatigue lives of Ti-6Al-4V and Ti-4.5 Al-5Mo-1.5 CR. in Titanium Alloys in Surgical Implants, ASTM International.

Ishizawa, H., & Ogino, M. (1995). Characterisation of thin hydroxyapatite layers formed on anodic titanium oxide films containing Ca and P by hydrothermal treatment. Journal of Biomedical Materials Research Part A, 29(9), pp. 1071-1079.

Iwasa, F., Hori, N., Ueno, T., Minamikawa, H., Yamada, M., & Ogawa, T. (2010). Enhancement of osteoblast adhesion to UV-photofunctionalized titanium via an electrostatic mechanism. Biomaterials, 31(10), pp. 2717-2727.

Izman, S., Abdul-Kadir, M. R., Anwar, M., Nazim, E. M., Rosliza, R., Shah, A., & Hassan, M. A. (2012). Surface modification techniques for biomedical grade of titanium alloys: oxidation, carburization and ion implantation processes. in *Titanium Alloys-Towards Achieving Enhanced Properties for Diversified Applications*, London: InTech. 9, pp. 201-228.

Jackson, M. J., & Ahmed, W. (Eds.). (2007). *Surface Engineered Surgical Tools and Medical Devices*. US: Springer Science and Business Media.

Jaeggi, C., Kern, P., Michler, J., Patscheider, J., Tharian, J., & Munnik, F. (2006). Film formation and characterisation of anodic oxides on titanium for biomedical applications. *Surface and Interface Analysis*, 38(4), pp. 182-185.

Jaeggi, C., Kern, P., Michler, J., Zehnder, T., & Siegenthaler, H. (2005). Anodic thin films on titanium used as masks for surface micropatterning of biomedical devices. *Surface and Coatings Technology*, 200(5-6), pp. 1913-1919.

Jahromi, M. T., Yao, G., & Cerruti, M. (2013). The importance of amino acid interactions in the crystallization of hydroxyapatite. *Journal of the Royal Society Interface*, 10(80), pp. 20120906.

Jamieson, J. C., & Olinger, B. (1969). Pressure-temperature studies of anatase, brookite, and TiO_2: a discussion. *American Mineralogist*, 54(9-10), pp. 1477.

Jimmy, C. Y., Yu, J., Tang, H. Y., & Zhang, L. (2002). Effect of surface microstructure on the photoinduced hydrophilicity of porous TiO_2 thin films. *Journal of Materials Chemistry*, 12(1), pp. 81-85.

Johansson, C. B. (1991). *On Tissue Reactions to Metal Implants*. University of Göteborg. Dental Implants.

Jokanović, V., Izvonar, D., Dramićanin, M. D., Jokanović, B., Živojinović, V., Marković, D., & Dačić, B. (2006). Hydrothermal synthesis and nanostructure of carbonated calcium hydroxyapatite. *Journal of Materials Science: Materials in Medicine*, 17(6), pp. 539-546.

Jones, J. R. (2015). Reprint of: Review of bioactive glass: From Hench to hybrids. *Acta Biomaterialia*, 23, pp. S53-S82.

Jordan, D. R., Brownstein, S., Gilberg, S., Coupal, D., Kim, S., & Mawn, L. (2002). Hydroxyapatite and calcium phophate coatings on aluminium oxide orbital implants. *Canadian Journal of Ophthalmology*, 37(1), pp. 7-13.

Kaito, T., Myoui, A., Takaoka, K., Saito, N., Nishikawa, M., Tamai, N., & Yoshikawa, H. (2005). Potentiation of the activity of bone morphogenetic protein-2 in bone regeneration by a PLA–PEG/hydroxyapatite composite. *Biomaterials*, 26(1), pp. 73-79.

Kalita, S. J., Bhardwaj, A., & Bhatt, H. A. (2007). Nanocrystalline calcium phosphate ceramics in biomedical engineering. *Materials Science and Engineering: C*, 27(3), 441-449.

Kamei, M., & Mitsuhashi, T. (2000). Hydrophobic drawings on hydrophilic surfaces of single crystalline titanium dioxide: surface wettability control by mechanochemical treatment. *Surface Science*, 463(1), pp. L609-L612.

Kannan, S., Lemos, A. F., & Ferreira, J. M. F. (2006). Synthesis and mechanical performance of biological-like hydroxyapatites. *Chemistry of Materials*, 18(8), pp. 2181-2186.

Karambakhsh, A., Afshar, A., & Malekinejad, P. (2012). Corrosion resistance and color properties of anodised Ti-6Al-4V. *Journal of Materials Engineering and Performance*, 21(1), pp. 121-127.

Kasuga, T., Kondo, H., & Nogami, M. (2002). Apatite formation on TiO_2 in simulated body fluid. *Journal of Crystal Growth*, 235(1-4), pp. 235-240.

Katsumata, K. I., Nakajima, A., Shiota, T., Yoshida, N., Watanabe, T., Kameshima, Y., & Okada, K. (2006). Photoinduced surface roughness variation in polycrystalline TiO_2 thin films. *Journal of Photochemistry and Photobiology A: Chemistry*, 180(1-2), pp. 75-79.

Kavan, L., Grätzel, M., Gilbert, S. E., Klemenz, C., & Scheel, H. J. (1996). Electrochemical and photoelectrochemical investigation of single-crystal anatase. *Journal of the American Chemical Society*, 118(28), pp. 6716-6723.

Kern, P., Michler, J., & Jäggi, C. H. (2005). Anodic titanium oxides grown in sulphuric and phosphoric acid electrolytes. *European Cells and Materials*. 5(10): pp. STE5.

Keshmiri, M., & Troczynski, T. (2003). Apatite formation on TiO_2 anatase microspheres. *Journal of Non-Crystalline Solids*, 324(3), pp. 289-294.

Khan, W., Kapoor, M., & Kumar, N. (2007). Covalent attachment of proteins to functionalized polypyrrole-coated metallic surfaces for improved biocompatibility. *Acta Biomaterialia*, 3(4), pp. 541-549.

Kim, H. M. (2003). Ceramic bioactivity and related biomimetic strategy. *Current Opinion in Solid State and Materials Science*, 7(4-5), pp. 289-299.

Kim, H. M., Miyaji, F., Kokubo, T., & Nakamura, T. (1996). Preparation of bioactive Ti and its alloys via simple chemical surface treatment. *Journal of Biomedical Materials Research: An Official Journal of the Society for Biomaterials and the Japanese Society for Biomaterials*, 32(3), pp. 409-417.

Kim, H. M., Miyaji, F., Kokubo, T., & Nakamura, T. (1997). Effect of heat treatment on apatite-forming ability of Ti metal induced by alkali treatment. *Journal of Materials Science: Materials in Medicine*, 8(6), pp. 341-347.

Kim, H. M., Miyaji, F., Kokubo, T., Nishiguchi, S., & Nakamura, T. (1999). Graded surface structure of bioactive titanium prepared by chemical treatment.

Journal of Biomedical Materials Research: An Official Journal of The Society for Biomaterials, *The Japanese Society for Biomaterials, and The Australian Society for Biomaterials*, 45(2), pp. 100-107.

Kinnings, S. L., Liu, N., Buchmeier, N., Tonge, P. J., Xie, L., & Bourne, P. E. (2009). Drug discovery using chemical systems biology: repositioning the safe medicine Comtan to treat multi-drug and extensively drug resistant tuberculosis. *PLoS Computational Biology*, 5(7), pp. e1000423.

Kobayakawa, K., Sato, C., Sato, Y., & Fujishima, A. (1998). Continuous-flow photoreactor packed with titanium dioxide immobilized on large silica gel beads to decompose oxalic acid in excess water. *Journal of Photochemistry and Photobiology A: Chemistry*, 118(1), pp. 65-69.

Kokubo, T. (1990). Surface chemistry of bioactive glass-ceramics. *Journal of Non-Crystalline Solids*, 120(1-3), pp. 138-151.

Kokubo, T. (1991). Recent progress in glass-based materials for biomedical applications. *Journal of the Ceramic Society of Japan*, 99(1154), pp. 965-973.

Kokubo, T. (2014). *Implants for Surgery-In Vitro Evaluation for Apatite-Forming Ability of Implant Materials*. ISO 23317.

Kokubo, T., & Takadama, H. (2006). How useful is SBF in predicting *in vivo* bone bioactivity?. *Biomaterials*, 27(15), pp. 2907-2915.

Kokubo, T., & Yamaguchi, S. (2009). Novel bioactive titanate layers formed on Ti metal and its alloys by chemical treatments. *Materials*, 3(1), pp. 48-63.

Kokubo, T., Kim, H. M., & Kawashita, M. (2003). Novel bioactive materials with different mechanical properties. *Biomaterials*, 24(13), pp. 2161-2175.

Kokubo, T., Kushitani, H., Sakka, S., Kitsugi, T., & Yamamuro, T. (1990). Solutions able to reproduce *in vivo* surface-structure changes in bioactive glass-ceramic A-W3. *Journal of Biomedical Materials Research Part A*, 24(6), pp. 721-734.

Kraft, L., & Hermansson, L. (2003). *Dimension Stable Binding Agent Systems for Dental. Application*. U.S. Patent 6,620,232.

Kumar, R., Prakash, K. H., Cheang, P., & Khor, K. A. (2004). Temperature driven morphological changes of chemically precipitated hydroxyapatite nanoparticles. *Langmuir*, 20(13), pp. 5196-5200.

Kumar, S., Narayanan, T. S., Raman, S. G. S., & Seshadri, S. K. (2010). Thermal oxidation of Ti6Al4V alloy: Microstructural and electrochemical characterisation. *Materials Chemistry and Physics*, 119(1-2), pp. 337-346.

Kuriakose, T. A., Kalkura, S. N., Palanichamy, M., Arivuoli, D., Dierks, K., Bocelli, G., & Betzel, C. (2004). Synthesis of stoichiometric nano crystalline hydroxyapatite by ethanol-based sol–gel technique at low temperature. *Journal of Crystal Growth*, 263(1-4), pp. 517-523.

Kuromoto, N. K., Simão, R. A., & Soares, G. A. (2007). Titanium oxide films produced on commercially pure titanium by anodic oxidation with different voltages. *Materials Characterisation*, 58(2), pp. 114-121.

Kutz, M. (2003). Standard handbook of biomedical engineering and design. McGraw-Hill.

Langer, R., & Peppas, N. A. (2003). Advances in biomaterials, drug delivery, and bionanotechnology. *AIChE Journal*, 49(12), pp. 2990-3006.

Lausmaa, J., & Linder, L. (1988). Surface spectroscopic characterisation of titanium implants after separation from plastic-embedded tissue. Biomaterials, 9(3), pp. 277-280.

Leach, J. S. L., & Pearson, B. R. (1988). Crystallization in anodic oxide films. *Corrosion Science*, 28(1), pp. 43-56.

Leconte, J., Markovits, A., Skalli, M. K., Minot, C., & Belmajdoub, A. (2002). Periodic ab initio study of the hydrogenated rutile TiO_2 (1 1 0) surface. *Surface Science*, 497(1-3), pp. 194-204.

Lee, H. B. (1989). Application of Synthetic Polymers in Implants. in Seagusa, L., Higashimura, T., & Abe, A. (Eds.). *Frontiers of Macromolecular Sciences.* Oxford: Blackwell Scientific Publications. pp. 579-584.

LeGeros, R. Z. (1988). Calcium phosphate materials in restorative dentistry: a review. *Advances in Dental Research*, 2(1), pp. 164-180.

Li, G., Li, L., Boerio-Goates, J., & Woodfield, B. F. (2005). High purity anatase TiO_2 nanocrystals: near room-temperature synthesis, grain growth kinetics, and surface hydration chemistry. *Journal of the American Chemical Society*, 127(24), pp. 8659-8666.

Li, L. H., Kong, Y. M., Kim, H. W., Kim, Y. W., Kim, H. E., Heo, S. J., & Koak, J. Y. (2004). Improved biological performance of Ti implants due to surface modification by micro-arc oxidation. *Biomaterials*, 25(14), pp. 2867-2875.

Li, P., & Ducheyne, P. (1998). Quasi-biological apatite film induced by titanium in a simulated body fluid. *Journal of Biomedical Materials Research: An Official Journal of The Society for Biomaterials, The Japanese Society for*

Biomaterials, and the Australian Society for Biomaterials, 41(3), pp. 341-348.

Li, P., Kangasniemi, I., Groot, K., & Kokubo, T. (1994). Bonelike Hydroxyapatite Induction by a Gel-Derived Titania on a Titanium Substrate. *Journal of the American Ceramic Society*, 77(5), pp. 1307-1312.

Li, P., Kangasniemi, I., Groot, K., & Kokubo, T. (1994). Bonelike Hydroxyapatite Induction by a Gel-Derived Titania on a Titanium Substrate. *Journal of the American Ceramic Society*, 77(5), pp. 1307-1312.

Li, W., Guo, T., Meng, T., Huang, Y., Li, X., Yan, W., & Li, X. (2013). Enhanced reversible wettability conversion of micro-nano hierarchical TiO_2/SiO_2 composite films under UV irradiation. *Applied Surface Science*, 283, pp. 12-18.

Liang, B., Fujibayashi, S., Tamura, J., Neo, M., Kim, H. M., Uchida, M., & Nakamura, T. (2003). Bone-bonding ability of anodic oxidized titanium. in Key Engineering Materials. *Trans Tech Publications*. 240, pp. 923-926.

Liang, Q., Chen, Y., Fan, Y., Hu, Y., Wu, Y., Zhao, Z., & Meng, Q. (2012). Tailoring the wettability of nanocrystalline TiO_2 films. *Applied Surface Science*, 258(7), pp. 2266-2269.

Lin, C. M., & Yen, S. K. (2006). Biomimetic growth of apatite on electrolytic TiO_2 coatings in simulated body fluid. *Materials Science and Engineering: C*, 26(1), pp. 54-64.

Lindberg, F., Heinrichs, J., Ericson, F., Thomsen, P., & Engqvist, H. (2008). Hydroxylapatite growth on single-crystal rutile substrates. *Biomaterials*, 29(23), pp. 3317-3323.

Linsebigler, A. L., Lu, G., & Yates Jr, J. T. (1995). Photocatalysis on TiO_2 surfaces: principles, mechanisms, and selected results. *Chemical reviews*, 95(3), pp. 735-758.

Liu, J., Ye, X., Wang, H., Zhu, M., Wang, B., & Yan, H. (2003). The influence of pH and temperature on the morphology of hydroxyapatite synthesized by hydrothermal method. *Ceramics International*, 29(6), pp. 629-633.

Liu, Q., Matinlinna, J. P., Chen, Z., Ning, C., Ni, G., Pan, H., & Darvell, B. W. (2015). Effect of thermal treatment on carbonated hydroxyapatite: Morphology, composition, crystal characteristics and solubility. *Ceramics International*, 41(5), pp. 6149-6157.

Liu, S., Li, B., Liang, C., Wang, H., & Qiao, Z. (2016). Formation mechanism and adhesive strength of a hydroxyapatite/TiO_2 composite coating on a titanium surface prepared by micro-arc oxidation. *Applied Surface Science*, 362, pp. 109-114.

Liu, X. Y., Zhao, X. B., Ding, C. X., & Chu, P. K. (2006). Light-induced Bioactive TiO_2 Surface. *Applied Physics Letters*. 2006. (88): 13905.

Liu, X., Chu, P. K., & Ding, C. (2004). Surface modification of titanium, titanium alloys, and related materials for biomedical applications. *Materials Science and Engineering: R: Reports*, 47(3-4), 49-121.

Liu, X., Zhao, X., Li, B., Cao, C., Dong, Y., Ding, C., & Chu, P. K. (2008). UV-irradiation-induced bioactivity on TiO_2 coatings with nanostructural surface. *Acta Biomaterialia*, 4(3), 544-552.

Long, M., & Rack, H. J. (1998). Titanium alloys in total joint replacement-a materials science perspective. *Biomaterials*, 19(18), 1621-1639.

Ma, J., Ge, X., Pelate, N., & Lei, S. (2015). Numerical investigation of two-dimensional thermally assisted ductile regime milling of nanocrystalline hydroxyapatite bioceramic material. *Ceramics International*, 41(3), pp. 3409-3419.

Ma, M. G. (2012). Hierarchically nanostructured hydroxyapatite: hydrothermal synthesis, morphology control, growth mechanism, and biological activity. *International Journal of Nanomedicine*, 7, pp. 1781.

Mann, S., Archibald, D. D., Didymus, J. M., Douglas, T., Heywood, B. R., Meldrum, F. C., & Reeves, N. J. (1993). Crystallization at inorganic-organic interfaces: biominerals and biomimetic synthesis. *Science*, 261(5126), pp. 1286-1292.

Mao, C., Li, H., Cui, F., Ma, C., & Feng, Q. (1999). Oriented growth of phosphates on polycrystalline titanium in a process mimicking biomineralization. *Journal of Crystal Growth*, 206(4), pp. 308-321.

Marchenoir, J. C., Loup, J. P., & Masson, J. (1980). Étude des couches poreuses formées par oxydation anodique du titane sous fortes tensions. *Thin Solid Films*, 66(3), pp. 357-369.

Mary, I. R., Sonia, S., Viji, S., Mangalaraj, D., Viswanathan, C., & Ponpandian, N. (2016). Novel multiform morphologies of hydroxyapatite: Synthesis and growth mechanism. *Applied Surface Science*, 361, pp. 25-32.

Masahashi, N., Semboshi, S., Ohtsu, N., & Oku, M. (2008). Microstructure and superhydrophilicity of anodic TiO_2 films on pure titanium. *Thin Solid Films*, 516(21), pp. 7488-7496.

Matthews, A. (1976). The crystallization of anatase and rutile from amorphous titanium dioxide under hydrothermal conditions. *American Mineralogist*, 61(5-6), pp. 419-424.

Mattie, D. R., & Bajpai, P. K. (1988). Analysis of the biocompatibility of ALCAP ceramics in rat femurs. *Journal of Biomedical Materials Research Part A*, 22(12), pp. 1101-1126.

Meagher, E. P., & Lager, G. A. (1979). Polyhedral thermal expansion in the TiO_2 polymorphs; refinement of the crystal structures of rutile and brookite at high temperature. *The Canadian Mineralogist*, 17(1), pp. 77-85.

Mehta, R. (2015). Powder metallurgy processing for low-cost titanium. Materials World Magazine. IOM^3. Retrieved June 5, 2018, from http://www.iom3.org/materials-world-magazine/news/2008/jul/01/powder-metallurgy-processing-lowcost-titanium

Messer, R. L., Lockwood, P. E., Wataha, J. C., Lewis, J. B., Norris, S., & Bouillaguet, S. (2003). *In vitro* cytotoxicity of traditional versus contemporary dental ceramics. *Journal of Prosthetic Dentistry*, 90(5), pp. 452-458.

Metzger, A. (1976). Polyethylene terephthalate and the pillar™ palatal implant: its historical usage and durability in medical applications. *Biomedical Engineering*, 11(9), pp. 301-306.

Mihov, D., & Katerska, B. (2010). Some biocompatible materials used in medical practice. *Trakia Journal of Sciences*, 8(2), pp. 119-125.

Mikula, M., Blecha, J., & Čeppan, M. (1992). Photoelectrochemical properties of anodic TiO_2 layers prepared by various current densities. *Journal of the Electrochemical Society*, 139(12), pp. 3470-3474.

Milella, E., Cosentino, F., Licciulli, A., & Massaro, C. (2001). Preparation and characterisation of titania/hydroxyapatite composite coatings obtained by sol-gel process. *Biomaterials*, 22(11), pp. 1425-1431.

Mills, A., & Le Hunte, S. (1997). An overview of semiconductor photocatalysis. *Journal of photochemistry and photobiology A: Chemistry*, 108(1), pp. 1-35.

Mills, A., Lee, S. K., & Lepre, A. (2003). Photodecomposition of ozone sensitised by a film of titanium dioxide on glass. *Journal of Photochemistry and Photobiology A: Chemistry*, 155(1-3), pp. 199-205.

Milošev, I., Blejan, D., Varvara, S., & Muresan, L. M. (2013). Effect of anodic oxidation on the corrosion behavior of Ti-based materials in simulated physiological solution. *Journal of Applied Electrochemistry*, 43(7), pp.645-658.

Miyata, T., Tsukada, S., & Minami, T. (2006). Preparation of anatase TiO_2 thin films by vacuum arc plasma evaporation. *Thin Solid Films*, 496(1), pp. 136-140.

Miyauchi, M., Kieda, N., Hishita, S., Mitsuhashi, T., Nakajima, A., Watanabe, T., & Hashimoto, K. (2002). Reversible wettability control of TiO_2 surface by light irradiation. *Surface Science*, 511(1-3), pp. 401-407.

Miyauchi, T., Yamada, M., Yamamoto, A., Iwasa, F., Suzawa, T., Kamijo, R., & Ogawa, T. (2010). The enhanced characteristics of osteoblast adhesion to photofunctionalized nanoscale TiO_2 layers on biomaterials surfaces. *Biomaterials*, 31(14), pp. 3827-3839.

Mor, G. K., Varghese, O. K., Paulose, M., Shankar, K., & Grimes, C. A. (2006). A review on highly ordered, vertically oriented TiO_2 nanotube arrays: Fabrication, material properties, and solar energy applications. Solar Energy *Materials and Solar Cells*, 90(14), pp. 2011-2075.

Morejón-Alonso, L., Santos, L. A., & García Carrodeguas, R. (2009). Influence of mixing liquid on the properties of calcium aluminate cement. in Key Engineering Materials. *Trans Tech Publications*. 396. pp. 241-244.

Murmson (2017). *Use of Sulfuric Acid and Phosphoric Acid in Titration*. Retrieved June 29, 2017, from http://sciencing.com/use-sulfuric-acid-phosphoric-acid-titration-9632.html

Murray, J. L. (1987). Phase diagrams of binary titanium alloys. *ASM international*, 340-345.

Nan, H., Ping, Y., Xuan, C., Yongxang, L., Xiaolan, Z., Guangjun, C., & Tingfei, X. (1998). Blood compatibility of amorphous titanium oxide films synthesized by ion beam enhanced deposition. *Biomaterials*, 19(7-9), 771-776.

Narayan, R. (Ed.). (2009). *Biomedical Materials*. US: Springer Science and Business Media.

Narayanan, T. S., Park, I. S., & Lee, M. H. (2014). Strategies to improve the corrosion resistance of microarc oxidation (MAO) coated magnesium alloys for degradable implants: prospects and challenges. *Progress in Materials Science*, 60, pp. 1-71.

Negishi, N., Iyoda, T., Hashimoto, K., & Fujishima, A. (1995). Preparation of transparent TiO_2 thin film photocatalyst and its photocatalytic activity. *Chemistry letters*, 24(9), pp. 841-842.

Niinomi, M. (2003). Recent research and development in titanium alloys for biomedical applications and healthcare goods. *Science and Technology of Advanced Materials*, 4(5), pp. 445.

Niinomi, M. (2008a). Mechanical biocompatibilities of titanium alloys for biomedical applications. *Journal of the Mechanical Behavior of Biomedical Materials*, 1(1), pp. 30-42.

Niinomi, M. (2008b). Biologically and mechanically biocompatible titanium alloys. *Materials Transactions*, 49(10), pp. 2170-2178.

Niinomi, M., Hanawa, T., & Narushima, T. (2005). Japanese research and development on metallic biomedical, dental, and healthcare materials. *JOM*, 57(4), pp. 18-24.

Nishiguchi, S., Fujibayashi, S., Kim, H. M., Kokubo, T., & Nakamura, T. (2003). Biology of alkali-and heat-treated titanium implants. *Journal of Biomedical Materials Research Part A*, 67(1), pp. 26-35.

Nishiguchi, S., Nakamura, T., Kobayashi, M., Kim, H. M., Miyaji, F., & Kokubo, T. (1999). The effect of heat treatment on bone-bonding ability of alkali-treated titanium. *Biomaterials*, 20(5), pp. 491-500.

Nordström, E. G., & Sánchez Muñoz, O. L. (2001). Physics of bone bonding mechanism of different surface bioactive ceramic materials *in vitro* and *in vivo*. *Bio-medical Materials and Engineering*, 11(3), pp. 221-231.

Oh, H. J., Lee, J. H., Jeong, Y., Kim, Y. J., & Chi, C. S. (2005). Microstructural characterisation of biomedical titanium oxide film fabricated by electrochemical method. *Surface and Coatings Technology*, 198(1-3), pp. 247-252.

Oh, H. J., Lee, J. H., Kim, Y. J., Suh, S. J., Lee, J. H., & Chi, C. S. (2008). Surface characteristics of porous anodic TiO_2 layer for biomedical applications. *Materials Chemistry and Physics*, 109(1), pp. 10-14.

Ohno, T., Sarukawa, K., Tokieda, K., & Matsumura, M. (2001). Morphology of a TiO_2 photocatalyst (Degussa, P-25) consisting of anatase and rutile crystalline phases. *Journal of Catalysis*, 203(1), pp. 82-86.

Ohno, T., Tokieda, K., Higashida, S., & Matsumura, M. (2003). Synergism between rutile and anatase TiO_2 particles in photocatalytic oxidation of naphthalene. *Applied Catalysis A: General*, 244(2), pp. 383-391.

OIV (2006). *Determination of chromatic characteristics according to CIELab. Compendium of International Methods of Analysis of Wines and Musts*. Retrieved June 5, 2018, from http://www.oiv.int/oiv/info/enmethodesinternationalesvin

Oldani, C., & Dominguez, A. (2012). Titanium as a Biomaterial for Implants. in *Recent Advances in Arthroplasty*. London: InTech, 9, pp. 149-162.

Oliva, A., Salerno, A., Locardi, B., Riccio, V., Della Ragione, F., Iardino, P., & Zappia, V. (1998). Behaviour of human osteoblasts cultured on bioactive glass coatings. *Biomaterials*, 19(11-12), pp. 1019-1025.

Oshida, Y., & Farzin-Nia, F. (2009). Response of Ti–Ni Alloys for Dental Biomaterials to Conditions in The Mouth. in *Shape Memory Alloys for Biomedical Applications*, pp. 101-149.

Palache, C., Berman, H., & Frondel, C. (1952). Dana's System of Mineralogy. *Geologiska Föreningen i Stockholm Förhandlingar*, 74(2), pp. 218-219.

Pan, H., & Darvell, B. W. (2010). Effect of carbonate on hydroxyapatite solubility. *Crystal Growth & Design*, 10(2), pp. 845-850.

Panda, R. N., Hsieh, M. F., Chung, R. J., & Chin, T. S. (2003). FTIR, XRD, SEM and solid state NMR investigations of carbonate-containing hydroxyapatite nano-particles synthesized by hydroxide-gel technique. *Journal of Physics and Chemistry of Solids*, 64(2), pp. 193-199.

Park, J. W., Jang, J. H., Lee, C. S., & Hanawa, T. (2009). Osteoconductivity of hydrophilic microstructured titanium implants with phosphate ion chemistry. *Acta Biomaterialia*, 5(6), pp. 2311-2321.

Park, J., & Lakes, R. S. (2007). Biomaterials: An Introduction. US: Springer Science & Business Media.

Park, S. J. (2008). Chemical observation of anodic TiO_2 for biomaterial application. *Metals and Materials International*, 14(4), pp. 449.

Park, T. E., Choe, H. C., & Brantley, W. A. (2013). Bioactivity evaluation of porous TiO_2 surface formed on titanium in mixed electrolyte by spark anodization. *Surface and Coatings Technology*, 235, pp. 706-713.

Pelkonen, O., & Turpeinen, M. (2007). *In vitro-in vivo* extrapolation of hepatic clearance: biological tools, scaling factors, model assumptions and correct concentrations. *Xenobiotica*, 37(10-11), pp. 1066-1089.

Pereira, B. L., Tummler, P., Marino, C. E., Soares, P. C., & Kuromoto, N. K. (2014). Titanium bioactivity surfaces obtained by chemical/electrochemical treatments. Matéria (Rio de Janeiro), 19(1), pp. 16-23.

Pham, H. H., & Wang, L. W. (2015). Oxygen vacancy and hole conduction in amorphous TiO_2. *Physical Chemistry Chemical Physics*, 17(1), pp. 541-550.

Pookmanee, P., & Phanichphant, S. (2009). Titanium dioxide powder prepared by a sol-gel method. *Journal of Ceramic Processing Research*, 10(2), pp. 167-170.

Prodana, M., Duta, M., Ionita, D., Bojin, D., Stan, M. S., Dinischiotu, A., & Demetrescu, I. (2015). A new complex ceramic coating with carbon nanotubes, hydroxyapatite and TiO_2 nanotubes on Ti surface for biomedical applications. *Ceramics International*, 41(5), pp. 6318-6325.

Qi, S., Huang, Y., Lin, Q., Cheng, H., & Seo, H. J. (2015). A bioactive Ca2SiB2O7 ceramics and *in vitro* hydroxyapatite mineralization ability in SBF. *Ceramics International*, 41(9), pp. 12011-12019.

Rack, H. J., & Qazi, J. I. (2006). Titanium alloys for biomedical applications. *Materials Science and Engineering: C*, 26(8), pp. 1269-1277.

Ramakrishna, S., Mayer, J., Wintermantel, E., & Leong, K. W. (2001). Biomedical applications of polymer-composite materials: a review. *Composites Science and Technology*, 61(9), pp. 1189-1224.

Ramamoorthy, M., Vanderbilt, D., & King-Smith, R. D. (1994). First-principles calculations of the energetics of stoichiometric TiO_2 surfaces. *Physical Review B*, 49(23), pp. 16721.

Ramesh, S., Tan, C. Y., Hamdi, M., Sopyan, I., & Teng, W. D. (2007). The influence of Ca/P ratio on the properties of hydroxyapatite bioceramics. in *International Conference on Smart Materials and Nanotechnology in Engineering. International Society for Optics and Photonics*. 6423, pp. 64233A.

Randorn, C., Kanta, A., Yaemsunthorn, K., & Rujijanakul, G. (2015). Fabrication of dense biocompatible hydroxyapatite ceramics with high hardness using a

peroxide-based route: a potential process for scaling up. *Ceramics International*, 41(4), pp. 5594-5599.

Rao, C. N. R., Turner, A., & Honig, J. M. (1959). Some observations concerning the effect of impurities on the anatase-rutile transition. *Journal of Physics and Chemistry of Solids*, 11(1-2), pp. 173-175.

Rao, S., Ushida, T., Tateishi, T., Okazaki, Y., & Asao, S. (1996). Effect of Ti, Al, and V ions on the relative growth rate of fibroblasts (L929) and osteoblasts (MC3T3-E1) cells. *Bio-medical materials and engineering*, 6(2), pp. 79-86.

Ratner, B. D. (2001). A Perspective on Titanium Biocompatibility. in *Titanium in Medicine*. Berlin, Heidelberg: Springer. pp. 1-12.

Ravaglioli, A., & Krajewski, A. (2012). *Bioceramics: Materials Properties·Applications*. US: Springer Science and Business Media.

Relman, D. A. (1998). Detection and identification of previously unrecognized microbial pathogens. *Emerging Infectious Diseases*, 4(3), pp. 382.

Rey, C., Collins, B., Goehl, T., Dickson, I. R., & Glimcher, M. J. (1989). The carbonate environment in bone mineral: a resolution-enhanced Fourier transform infrared spectroscopy study. *Calcified Tissue International*, 45(3), pp. 157-164.

Rothman, S. S. (2002). *Lessons from the Living Cell: The Culture Of Science And The Limits Of Reductionism*, New York: McGraw-Hill.

Rupp, F., Scheideler, L., Olshanska, N., De Wild, M., Wieland, M., & Geis-Gerstorfer, J. (2006). Enhancing surface free energy and hydrophilicity through chemical modification of microstructured titanium implant surfaces. *Journal of Biomedical Materials Research Part A*, 76(2), pp. 323-334.

Sakai, H., Baba, R., Hashimoto, K., Kubota, Y., & Fujishima, A. (1995). Selective killing of a single cancerous T24 cell with TiO_2 semiconducting microelectrode under irradiation. *Chemistry Letters*, 24(3), 185-186.

Saleh, S. S., & Abdullah, H. Z. (2015). Optimization and Characterisation of Anatase Formed on Anodised Titanium in Sulfuric Acid. in Advanced Materials Research. *Trans Tech Publications*. 1125, pp. 479-483.

Saleh, S. S., & Abdullah, H. Z. (2016). Optimization and Characterisation of Anatase Formed on Anodised Titanium in Phosphoric Acid. in Materials Science Forum. *Trans Tech Publications*. 840, pp. 240-244.

Samsonov, G. V. (2013). *The Oxide Handbook*. US: Springer Science and Business Media.

Samuneva, B., Kozhukharov, V., Trapalis, C., & Kranold, R. (1993). Sol-gel processing of titanium-containing thin coatings. *Journal of Materials Science*, 28(9), pp. 2353-2360.

Sarmiento, A. U. G. U. S. T. O., Zych, G. A., Latta, L. L., & Tarr, R. R. (1979). Clinical experiences with a titanium alloy total hip prosthesis: a posterior approach. *Clinical Orthopaedics and Related Research*, (144), pp. 166-173.

Sato, N. (1971). A theory for breakdown of anodic oxide films on metals. *Electrochimica Acta*, 16(10), pp. 1683-1692.

Sava, L., Pillai, S., More, U., & Sontakke, A. (2005). Serum calcium measurement: total versus free (ionized) calcium. *Indian Journal of Clinical Biochemistry*, 20(2), pp. 158-161.

Šćepanović, M., Dohčević-Mitrović, Z., Hinić, I., Grujić-Brojčin, M., Stanišić, G., & Popović, Z. V. (2005). Photoluminescence of laser-synthesized anatase titanium dioxide nanopowders. in *Materials Science Forum*. Trans Tech Publications. 494, pp. 265-270.

Scholz, M. S., Blanchfield, J. P., Bloom, L. D., Coburn, B. H., Elkington, M., Fuller, J. D., & Trevarthen, J. A. (2011). The use of composite materials in modern orthopaedic medicine and prosthetic devices: A review. *Composites Science and Technology*, 71(16), pp. 1791-1803.

Schreckenbach, J. P., Marx, G., Schlottig, F. E. A., Textor, M., & Spencer, N. D. (1999). Characterisation of anodic spark-converted titanium surfaces for biomedical applications. *Journal of Materials Science: Materials in Medicine*, 10(8), pp. 453-457.

Schwartz, Z., Kieswetter, K., Dean, D. D., & Boyan, B. D. (1997). Underlying mechanisms at the bone-surface interface during regeneration. *Journal of Periodontal Research*, 32(1), pp. 166-171.

Sclafani, A., & Herrmann, J. M. (1996). Comparison of the photoelectronic and photocatalytic activities of various anatase and rutile forms of titania in pure liquid organic phases and in aqueous solutions. *The Journal of Physical Chemistry*, 100(32), pp. 13655-13661.

Segneanu, A. E., Gozescu, I., Dabici, A., Sfirloaga, P., & Szabadai, Z. (2012). Organic Compounds FT-IR Spectroscopy. in *Macro To Nano Spectroscopy*. London: InTech.

Setiawati, E., & Kawano, K. (2008). Stabilization of anatase phase in the rare earth; Eu and Sm ion doped nanoparticle TiO_2. *Journal of Alloys and Compounds*, 451(1-2), pp. 293-296.

Setiawati, E., Kawano, K., Tsuboi, T., & Seo, H. J. (2008). Studies on thermal migration of Eu ion doped into TiO_2 nanoparticles. *Japanese Journal of Applied Physics*, 47(6R), pp. 4651.

Shannon, R. D., & Pask, J. A. (1965). Kinetics of the Anatase-Rutile Transformation. *Journal of the American Ceramic Society*, 48(8), pp. 391-398.

Shin, H., Jung, H. S., Hong, K. S., & Lee, J. K. (2005). Crystal phase evolution of TiO_2 nanoparticles with reaction time in acidic solutions studied via freeze-drying method. *Journal of Solid State Chemistry*, 178(1), pp. 15-21.

Silver, F. H., & Christiansen, D. L. (1999). Introduction to Structure and Properties of Polymers, Metals, and Ceramics. in *Biomaterials Science and Biocompatibility*. Springer: New York, NY. pp. 87-120.

Smith, S. J., Stevens, R., Liu, S., Li, G., Navrotsky, A., Boerio-Goates, J., & Woodfield, B. F. (2009). Heat capacities and thermodynamic functions of TiO_2 anatase and rutile: Analysis of phase stability. *American Mineralogist*, 94(2-3), pp. 236-243.

Song, H. J., Park, S. H., Jeong, S. H., & Park, Y. J. (2009). Surface characteristics and bioactivity of oxide films formed by anodic spark oxidation on titanium in different electrolytes. *Journal of Materials Processing Technology*, 209(2), pp. 864-870.

Spivak, J. M., Ricci, J. L., Blumenthal, N. C., & Alexander, H. (1990). A new canine model to evaluate the biological response of intramedullary bone to implant materials and surfaces. *Journal of Biomedical Materials Research Part A*, 24(9), pp. 1121-1149.

Spurr, R. A., & Myers, H. (1957). Quantitative analysis of anatase-rutile mixtures with an X-ray diffractometer. *Analytical Chemistry*, 29(5), pp. 760-762.

Steinemann, S. G. (1980). Corrosion of surgical implants *in vivo* and *in vitro* tests in evaluation of biomaterials. *Advances in Biomaterials*, 1, pp. 1-34.

Stepien, M., Saarinen, J. J., Teisala, H., Tuominen, M., Aromaa, M., Kuusipalo, J., & Toivakka, M. (2012). Surface chemical analysis of photocatalytic wettability conversion of TiO_2 nanoparticle coating. *Surface and Coatings Technology*, 208, pp. 73-79.

Sul, Y. T., Johansson, C. B., Jeong, Y., & Albrektsson, T. (2001). The electrochemical oxide growth behaviour on titanium in acid and alkaline electrolytes. *Medical Engineering and Physics*, 23(5), pp. 329-346.

Sul, Y. T., Johansson, C. B., Jeong, Y., Wennerberg, A., & Albrektsson, T. (2002b). Resonance frequency and removal torque analysis of implants with turned and anodised surface oxides. *Clinical Oral Implants Research*, 13(3), pp. 252-259.

Sul, Y. T., Johansson, C. B., Kang, Y., Jeon, D. G., & Albrektsson, T. (2002d). Bone reactions to oxidized titanium implants with electrochemical anion sulphuric acid and phosphoric acid incorporation. *Clinical implant dentistry and related research*, 4(2), pp. 78-87.

Sul, Y. T., Johansson, C. B., Petronis, S., Krozer, A., Jeong, Y., Wennerberg, A., & Albrektsson, T. (2002a). Characteristics of the surface oxides on turned and electrochemically oxidized pure titanium implants up to dielectric breakdown: the oxide thickness, micropore configurations, surface roughness, crystal structure and chemical composition. *Biomaterials*, 23(2), pp. 491-501.

Sul, Y. T., Johansson, C. B., Röser, K., & Albrektsson, T. (2002c). Qualitative and quantitative observations of bone tissue reactions to anodised implants. *Biomaterials*, 23(8), pp. 1809-1817.

Sumita, T., Yamaki, T., Yamamoto, S., & Miyashita, A. (2002). Photo-induced surface charge separation of highly oriented TiO_2 anatase and rutile thin films. *Applied Surface Science*, 200(1-4), pp. 21-26.

Sutherland, B. (1997). Ultraviolet Radiation Hazards to Humans. in Hardy, K. Meltz, M and Glickman, R (Eds.). *Nonionizing Radiation: An Overview of the Physics and Biology*. Madison: Medical Physics Publishing.

Svetina, M., Ciacchi, L. C., Sbaizero, O., Meriani, S., & De Vita, A. (2001). Deposition of calcium ions on rutile (110): a first-principles investigation. *Acta Materialia*, 49(12), pp. 2169-2177.

Takami, K., Adachi, T., Nakajima, A., Hashimoto, K., & Watanabe, T. (2002). Inorganic-organic functionally-graded films: The role of intermediate layers between TiO_2 coatings and polymer substrates. *Surface Coatings International Part B: Coatings Transactions*, 85(2), pp. 155-158.

Tanaka, K., Capule, M. F., & Hisanaga, T. (1991). Effect of crystallinity of TiO_2 on its photocatalytic action. *Chemical Physics Letters*, 187(1-2), pp. 73-76.

Teh, T. H., Berkani, A., Mato, S., Skeldon, P., Thompson, G. E., Habazaki, H., & Shimizu, K. (2003). Initial stages of plasma electrolytic oxidation of titanium. *Corrosion Science*, 45(12), pp. 2757-2768.

Thamaraiselvi, T., & Rajeswari, S. (2004). Biological evaluation of bioceramic materials-a review. *Carbon*, 24(31), pp. 172.

Thomas, M. V., & Puleo, D. A. (2009). Calcium sulfate: properties and clinical applications. *Journal of Biomedical Materials Research Part B: Applied Biomaterials*, 88(2), pp. 597-610.

Thomsen, P., Eriksson, A. S., & Olsson, R. (1986). Morphological Studies on Titanium Implants Inserted in Rabbit Knee-Joints. *Biomaterials and Clinical Applications*, pp. 87-92.

Tian, H., Tang, Z., Zhuang, X., Chen, X., & Jing, X. (2012). Biodegradable synthetic polymers: preparation, functionalization and biomedical application. *Progress in Polymer Science*, 37(2), pp. 237-280.

Tümmler, P., Pereira, B. L., Lepienski, C. M., Kuromoto, N. K., de Souza, P. R., & Soares, P. (2011). Bioactive films on titanium surface obtained by anodic oxidation in sulphuric and phosphuric Acid. in: *21st Brazilian Congress of Mechanical Engineering*. Natal, RN: Brazil. pp. 24-28.

Uchida, M., Kim, H. M., Kokubo, T., & Nakamura, T. (2001). Apatite-Forming Ability of Sodium-Containing Titania Gels in a Simulated Body Fluid. *Journal of the American Ceramic Society*, 84(12), pp. 2969-2974.

Uchida, M., Kim, H. M., Kokubo, T., Fujibayashi, S., & Nakamura, T. (2002). Effect of water treatment on the apatite-forming ability of NaOH-treated titanium metal. *Journal of Biomedical Materials Research Part A*, 63(5), pp. 522-530.

Uchida, M., Kim, H. M., Kokubo, T., Fujibayashi, S., & Nakamura, T. (2003). Structural dependence of apatite formation on titania gels in a simulated body fluid. *Journal of Biomedical Materials Research Part A*, 64(1), pp. 164-170.

Ueda, M., Kinoshita, T., Ikeda, M., & Ogawa, M. (2009). Photo-induced formation of hydroxyapatite on TiO_2 synthesized by a chemical-hydrothermal treatment. *Materials Science and Engineering: C*, 29(7), pp. 2246-2249.

Ueda, M., Sai, H., Ikeda, M., & Ogawa, M. (2010). Formation of hydroxyapatite on titanium oxides in simulated body fluid under UV irradiation. in Materials Science Forum. *Trans Tech Publications*. 654, pp. 2257-2260.

Uetsuki, K., Kaneda, H., Shirosaki, Y., Hayakawa, S., & Osaka, A. (2010). Effects of UV-irradiation on *in vitro* apatite-forming ability of TiO_2 layers. *Materials Science and Engineering: B*, 173(1-3), pp. 213-215.

Vallet-Regí, M. (2001). Ceramics for medical applications. Journal of the Chemical Society, *Dalton Transactions*, (2), pp. 97-108.

Van Gils, S., Mast, P., Stijns, E., & Terryn, H. (2004). Colour properties of barrier anodic oxide films on aluminium and titanium studied with total reflectance and spectroscopic ellipsometry. *Surface and Coatings Technology*, 185(2-3), pp. 303-310.

Van Noort, R. (1987). Titanium: the implant material of today. *Journal of Materials Science*, 22(11), pp. 3801-3811.

Venkatraman, S., Boey, F., & Lao, L. L. (2008). Implanted cardiovascular polymers: Natural, synthetic and bio-inspired. *Progress in Polymer Science*, 33(9), pp. 853-874.

Vergaro, V., Carlucci, C., Cascione, M., Lorusso, C., Conciauro, F., Scremin, B. F., & Ciccarella, G. (2015). Interaction between human serum albumin and different anatase TiO_2 nanoparticles: A nano-bio interface study. *Nanomaterials and Nanotechnology*, 5, 30.

Viceconti, M., Muccini, R., Bernakiewicz, M., Baleani, M., & Cristofolini, L. (2000). Large-sliding contact elements accurately predict levels of bone–implant micromotion relevant to osseointegration. *Journal of biomechanics*, 33(12), pp. 1611-1618.

Vignais, P. V., & Vignais, P. M. (2010). Discovering Life, Manufacturing Life: How The Experimental Method Shaped Life Sciences. US: Springer Science and Business Media.

von Laue, M. (1915). *Concerning the Detection of X-Ray Interferences*. Nobel lecture, 13.

von Recum, A. F. (1994). Biomaterials: Educational Goals. in *Annual Biomaterials Society Meeting*.

Vuvlsteker, P. (2004) *Colour Topics in Computer Graphics. Visible Spectrum*. Retrieved 6 June 2014, from http://escience.anu.edu.au/lecture/cg/ Colour/ HSV_HLS.en.html

Wang, H., Wang, T., & Xu, P. (1998). Effects of substrate temperature on the microstructure and photocatalytic reactivity of TiO_2 films. *Journal of Materials Science: Materials in Electronics*, 9(5), pp. 327-330.

Wang, M. C., Chen, H. T., Shih, W. J., Chang, H. F., Hon, M. H., & Hung, I. M. (2015). Crystalline size, microstructure and biocompatibility of hydroxyapatite nanopowders by hydrolysis of calcium hydrogen phosphate dehydrate (DCPD). *Ceramics International*, 41(2), pp. 2999-3008.

Wang, R., Hashimoto, K., Fujishima, A., Chikuni, M., Kojima, E., Kitamura, A., & Watanabe, T. (1998). Photogeneration of highly amphiphilic TiO_2 surfaces. *Advanced Materials*, 10(2), pp. 135-138.

Wang, R., Hashimoto, K., Fujishima, A., Chikuni, M., Kojima, E., Kitamura, A., & Watanabe, T. (1997). Light-induced amphiphilic surfaces. *Nature*, 388(6641), pp. 431.

Wang, Y., Yu, H., Chen, C., & Zhao, Z. (2015). Review of the biocompatibility of micro-arc oxidation coated titanium alloys. *Materials and Design*, 85, pp. 640-652.

Watanabe, T., Nakajima, A., Wang, R., Minabe, M., Koizumi, S., Fujishima, A., & Hashimoto, K. (1999). Photocatalytic activity and photoinduced hydrophilicity of titanium dioxide coated glass. *Thin solid films*, 351(1-2), pp. 260-263.

Wei, W., Jie, T., Tao, W., & Ling, W. A. N. G. (2007). Photocatalytic activity of porous TiO_2 films prepared by anodic oxidation. *Rare Metals*, 26(2), pp. 136-141.

Weir, A., Westerhoff, P., Fabricius, L., Hristovski, K., & Von Goetz, N. (2012). Titanium dioxide nanoparticles in food and personal care products. Environmental Science and Technology, 46(4), pp. 2242-2250.

Weller, M. T. (1994). *Inorganic Materials Chemistry*. UK: Oxford University Press.

Wells, A. F. (2012). *Structural Inorganic Chemistry*. UK: Oxford university press.

Williams, D. (1990). An introduction to medical and dental materials. Concise Encyclopedia of Medical and Dental Materials. In: W. D (Ed.). *Pergamon Press and The MIT Press*.

Williams, D. F. (2008). On the mechanisms of biocompatibility. *Biomaterials*, 29(20), pp. 2941-2953.

Wong, J. Y., & Bronzino, J. D. (2007). *Biomaterials*. Boca Raton, FL: CRC Press.

Wong, J. Y., Bronzino, J. D., & Peterson, D. R. (2013). *Biomaterials: Principles and Practices*. Boca Raton, FL: CRC Press.

Wu, C., & Chang, J. (2013). A review of bioactive silicate ceramics. *Biomedical materials*, 8(3), pp. 032001.

Wu, H., Lu, X., Long, B., Wang, X., Wang, J., & Jin, Z. (2005). The effects of cathodic and anodic voltages on the characteristics of porous nanocrystalline titania coatings fabricated by microarc oxidation. *Materials Letters*, 59(2-3), pp. 370-375.

Wu, K. R., Ting, C. H., Liu, W. C., Lin, C. H., & Wu, J. K. (2006). Successive deposition of layered titanium oxide/indium tin oxide films on unheated substrates by twin direct current magnetron sputtering. *Thin Solid Films*, 500(1-2), pp. 110-116.

Xia, W., Lindahl, C., Lausmaa, J., & Engqvist, H. (2011). Biomimetic hydroxyapatite deposition on titanium oxide surfaces for biomedical application. in *Advances in Biomimetics*. InTech. 20, pp. 429-452.

Xia, W., Lindahl, C., Lausmaa, J., Borchardt, P., Ballo, A., Thomsen, P., & Engqvist, H. (2010). Biomineralized strontium-substituted apatite/titanium dioxide coating on titanium surfaces. *Acta Biomaterialia*, 6(4), pp. 1591-1600.

Xiao, F., Tsuru, K., Hayakawa, S., & Osaka, A. (2003). *In vitro* apatite deposition on titania film derived from chemical treatment of Ti substrates with an oxysulfate solution containing hydrogen peroxide at low temperature. *Thin Solid Films*, 441(1-2), pp. 271-276.

Xie, L., Yin, G., Yan, D., Liao, X., Huang, Z., Yao, Y., & Liu, Y. (2010). Structure, morphology and fibroblasts adhesion of surface-porous titanium via anodic oxidation. *Journal of Materials Science: Materials in Medicine*, 21(1), pp. 259-266.

Xiong, T. Y., Cui, X. Y., Kim, H. M., Masakazu, K., Kokubo, T., Wu, J., & Nakamura, T. (2004). Effect of surface morphology and crystal structure on bioactivity

of titania films formed on titanium metal via anodic oxidation in sulfuric acid solution. in Key Engineering Materials. *Trans Tech Publications*. 254, pp. 375-378.

Yahalom, J. (1972). The role of the film/electrolyte interface in anodic breakdown. *Journal of The Electrochemical Society*, 119(8), pp. C231.

Yamamoto, A., Honma, R., Sumita, M., & Hanawa, T. (2004). Cytotoxicity evaluation of ceramic particles of different sizes and shapes. *Journal of Biomedical Materials Research Part A*, 68(2), 244-256.

Yamamoto, D., Iida, T., Arii, K., Kuroda, K., Ichino, R., Okido, M., & Seki, A. (2012b). Surface hydrophilicity and osteoconductivity of anodised Ti in aqueous solutions with various solute ions. *Materials Transactions*, 53(11), pp. 1956-1961.

Yamamoto, D., Kawai, I., Kuroda, K., Ichino, R., Okido, M., & Seki, A. (2011). Osteoconductivity of anodised titanium with controlled micron-level surface roughness. *Materials Transactions*, 52(8), 1650-1654.

Yamamoto, D., Kawai, I., Kuroda, K., Ichino, R., Okido, M., & Seki, A. (2012a). Osteoconductivity and hydrophilicity of TiO_2 coatings on Ti substrates prepared by different oxidizing processes. *Bioinorganic chemistry and applications*. pp. 1-7.

Yamamuro, T. (1989). Patterns of osteogenesis in relation to various biomaterials. Journal of Japanese Society for Biomaterials, 7, pp. 19-23.

Yang, B. C., Gan, L., Li, Z. S., Huang, Y., Qu, Y., & Zhang, X. D. (2007). Preparation of bioactive tantalum metal via anodic oxidation treatment. *Key Engineering Materials*. 330, pp. 637-640.

Yang, B., Uchida, M., Kim, H. M., Zhang, X., & Kokubo, T. (2004a). Preparation of bioactive titanium metal via anodic oxidation treatment. *Biomaterials*, 25(6), pp. 1003-1010.

Yang, C. L., Chen, F. L., & Chen, S. W. (2006). Anodization of the dental arch wires. Materials Chemistry and Physics, 100(2-3), pp. 268-274.

Yang, M. C., Yang, T. S., & Wong, M. S. (2004). Nitrogen-doped titanium oxide films as visible light photocatalyst by vapor deposition. *Thin Solid Films*, 469, pp. 1-5.

Yang, Y., & Ong, J. L. (2003). Bond strength, compositional, and structural properties of hydroxyapatite coating on Ti, ZrO_2-coated Ti, and TPS-coated Ti substrate. *Journal of Biomedical Materials Research Part A*, 64(3), pp. 509-516.

Yerokhin, A. L., Nie, X., Leyland, A., Matthews, A., & Dowey, S. J. (1999). Plasma electrolysis for surface engineering. *Surface and Coatings Technology*, 122(2-3), pp. 73-93.

Yin, Z. F., Wu, L., Yang, H. G., & Su, Y. H. (2013). Recent progress in biomedical applications of titanium dioxide. *Physical Chemistry Chemical Physics*, 15(14), pp. 4844-4858.

Yoruç, A. B. H., & Şener, B. C. (2012). Biomaterials. In: Kara, S (Ed.). *A Roadmap of Biomedical Engineers and Milestones*. London: InTech, pp. 67-114.

Youn, H. Y., McCanna, D. J., Sivak, J. G., & Jones, L. W. (2011). *In vitro* ultraviolet-induced damage in human corneal, lens, and retinal pigment epithelial cells. *Molecular Vision*, 17, 237.

Young, C. (2009). Solar ultraviolet radiation and skin cancer. *Occupational Medicine*, 59(2), pp. 82-88.

Young, T. (1832). An essay on the cohesion of fluids. In Abstracts of the Papers Printed in the Philosophical Transactions of the Royal Society of London, *The Royal Society*, 1, pp. 171-172.

Yu, J., & Zhao, X. (2001). Effect of surface microstructure on the super-hydrophilic property of the sol-gel derived porous TiO_2 thin films. *Journal of Materials Science Letters*, 20(7), pp. 671-673.

Yu, J., Zhao, X., Zhao, Q., & Wang, G. (2001). Preparation and characterisation of super-hydrophilic porous TiO_2 coating films. *Materials Chemistry and Physics*, 68(1-3), pp. 253-259.

Zadpoor, A. A. (2014). Relationship between in vitro apatite-forming ability measured using simulated body fluid and *in vivo* bioactivity of biomaterials. *Materials Science and Engineering: C*, 35, pp. 134-143.

Zeman, P., & Takabayashi, S. (2002). Self-cleaning and antifogging effects of TiO_2 films prepared by radio frequency magnetron sputtering. Journal of Vacuum Science & Technology A: Vacuum, *Surfaces, and Films*, 20(2), pp. 388-393.

Zhang, J., Xu, Q., Feng, Z., Li, M., & Li, C. (2008). Importance of the relationship between surface phases and photocatalytic activity of TiO_2. *Angewandte Chemie International Edition*, 47(9), pp. 1766-1769.

Zhang, M., & Matinlinna, J. P. (2012). E-glass fiber reinforced composites in dental applications. *Silicon*, 4(1), pp. 73-78.

Zhang, Y. H., & Reller, A. (2002). Phase transformation and grain growth of doped nanosized titania. *Materials Science and Engineering: C*, 19(1-2), pp. 323-326.

Zhao, J., Wang, X., Chen, R., & Li, L. (2005). Fabrication of titanium oxide nanotube arrays by anodic oxidation. *Solid State Communications*, 134(10), pp. 705-710.

Zhao, M., Li, J., Li, Y., Wang, J., Zuo, Y., Jiang, J., & Wang, H. (2014). Gradient control of the adhesive force between Ti/TiO_2 nanotubular arrays fabricated by anodization. *Scientific Reports*, 4, pp. 7178.

Zhao, W., Lemaître, J., & Bowen, P. (2017). A comparative study of simulated body fluids in the presence of proteins. *Acta Biomaterialia*, 53, pp. 506-514.

Zhou, M., Yu, J., & Cheng, B. (2006). Effects of Fe-doping on the photocatalytic activity of mesoporous TiO_2 powders prepared by an ultrasonic method. *Journal of Hazardous Materials*, 137(3), pp. 1838-1847.

Zhu, X., Kim, K., Ong, J. L., & Jeong, Y. (2002). Surface analysis of anodic oxide films containing phosphorus on titanium. *International Journal of Oral and Maxillofacial Implants*, 17(3).

Zinger, O., Chauvy, P. F., & Landolt, D. (2003). Scale-resolved electrochemical surface structuring of titanium for biological applications. *Journal of The Electrochemical Society*, 150(11), pp. B495-B503.

Zisman, W. A. (1964). Relation of the equilibrium contact angle to liquid and solid constitution. In: Fowkes, F. M (Ed.). *Contact Angle, Wettability, and Adhesion*. Washington D.C: American Chemical society. pp. 43.

Zuldesmi, M., Waki, A., Kuroda, K., & Okido, M. (2013). High osteoconductive surface of pure titanium by hydrothermal treatment. *Journal of Biomaterials and Nanobiotechnology*, 4(03), pp. 284.

Zyman, Z. Z., Rokhmistrov, D. V., & Loza, K. I. (2013). Determination of the Ca/P ratio in calcium phosphates during the precipitation of hydroxyapatite using X-ray diffractometry. *Processing and Application of Ceramics*, 7(2), pp. 93-95.

UNIVERSITI TUN HUSSEIN ONN MALAYSIA

STATUS CONFIRMATION FOR DOCTORAL THESIS

ENHANCED PERFORMANCE OF BIOMEDICAL IMPLANTS: IN VITRO TEST ON ANODISED TITANIUM IN SIMULATION BODY FLUID UNDER UV IRRADIATION

ACADEMIC SESSION: 2017/2018

I, **SALEH S SALEH ELFALLAH,** agree to allow this Doctoral Thesis to be kept at the Library under the following terms:

1. This Doctoral Thesis is the property of the Tun Hussein Onn University Malaysia.
2. The library has the right to make copies for educational purposes only.
3. The library is allowed to make copies of this report for educational exchange between higher educational institutions.
4. ** Please Mark (√)

☐	CONFIDENTIAL	(Contains information of high security or of great importance to Malaysia as STIPULATED under the OFFICIAL SECRET ACT 1972)
☐	RESTRICTED	(Contains restricted information as determined by the Organization/institution where research was conducted)
☑	FREE ACCESS	

Approved by,

(WRITER'S SIGNITURE)

(SUPERVISOR'S SIGNATURE)

Permanent Address:

16 A, JALAN LIMAU 9, TAMAN BINTANG,

86400 PARIT RAJA BATU

PAHAT, JOHOR

DR. HASAN ZUHUDI BIN ABDULLAH
Profesor Madya
Jabatan Kejuruteraan Bahan dan Rekabentuk
Fakulti Kejuruteraan Mekanikal dan Pembuatan
Universiti Tun Hussein Onn Malaysia

Date : 6/6/2018

Date : 6/6/2018

NOTE:

** If this Doctoral Thesis is classified as CONFIDENTIAL or RESTRICTED, please attach the letter from the relevant authority/organization stating reasons and duration for such classifications.

This thesis has been examined on date 3 APRIL 2018
and is sufficient in fulfilling the scope and quality for the purpose of awarding the Degree of Doctor of Philosophy.

Chairperson:

PROF. DR. YUSRI BIN YUSOF
Faculty of Mechanical and Manufacturing Engineering
Universiti Tun Hussein Onn Malaysia

Examiners:

PROF. DR. HANAFI ISMAIL
School of Materials and Mineral Resources Engineering
Universiti Sains Malaysia

PROF. MADYA DR. MOHAMAD ZAKY NOH
Faculty of Applied Science and Technology
Universiti Tun Hussein Onn Malaysia

STUDY ON THE PERFORMANCE ENHANCEMENT OF BIOMEDICAL IMPLANTS: *IN VITRO* TEST UNDER UV IRRADIATION OF TITANIUM ANODISED IN MIXED ELECTROLYTE

SALEH S SALEH ELFALLAH

A thesis submitted in
fulfillment of the requirement for the award of the
Doctor of Philosophy

Faculty of Mechanical and Manufacturing Engineering
Universiti Tun Hussein Onn Malaysia

APRIL 2018

I hereby declare that the work in this thesis is my own except for quotations and summaries which have been duly acknowledged

Student : .....

SALEH S SALEH ELFALLAH

Date : 6 / June / 2018

Supervisor : .....

ASSOCIATE PROFESSOR DR. HASAN ZUHUDI BIN ABDULLAH

Co Supervisor : .....

DR. MOHAMED RADZI BIN MOHAMED YUNUS

To my beloved mother who has supported me all way and in the hard times. To my beloved sister and family. To the supervisor and the co-supervisor. To my friends and relatives. Thank you for your support and encouragement.

ACKNOWLEDGEMENTS

The author would like to express his sincere appreciation to his supervisor, Associate Professor Dr. Hasan Zuhudi Bin Abdullah for the support given throughout the duration for this research. Also the Co-supervisor, Dr. Mohamed Radzi Bin Mohamed Yunus.

The cooperation given by the Ministry of Higher Education, Malaysia for the financial support provided for the research through Research Grant Scheme, FRGS vot 1212 and to Universiti Tun Hussein Onn Malaysia for the financial support Geran Insentif Penyelidik Siswazah (GIPS) vot 1251 are also highly appreciated. Appreciation also goes to everyone involved directly or indirectly towards the compilation of this thesis.

ABSTRACT

Titanium (Ti) recently has widely been used in the biomedical applications due to its high performance. Therefore, surface modifications of titanium have attracted a lot of interest to provide better osseointegration. Ti was subjected to anodic oxidation process and *in vitro* testing to assess the bioactivity of titanium oxide (TiO_2) coating. TiO_2 coating has been anodised at room temperature in different electrolyte; in sulphuric acid (H_2SO_4); phosphoric acid (H_3PO_4); and a mixture of H_2SO_4 and H_3PO_4 acids. The parameters used in anodization were: concentration of the electrolytes, applied voltage and current density. The coated surface is then evaluated using different testing techniques; the microstructure using scanning electron microscope (SEM); the elemental analysis using Energy-dispersive x-ray spectroscopy (EDX); mineralogical and crystal structure using x-ray diffraction (XRD); absorption analysis using Fourier transform infrared spectroscopy (FT-IR); and the hydrophilicity using water contact angle (WCA). TiO_2 was then subjected *in vitro* testing to assess the bioactivity of TiO_2 surface; that is the apatite formation ability. The apatite formation of the TiO_2 coating was precipitated by using simulated body fluid (SBF) in the dark and under the ultraviolet (UV) irradiation to mimic the reactions that may occur with the human bone-like cells layer. The testing was done to evaluate the apatite's microstructure, mineralogy, elements and absorption. From the results it was found that higher apatite was obtained with the increased of the immersion time; higher apatite formation and crystallization was found at earlier time of immersion for the TiO_2 that was immersed in SBF under the UV; higher apatite was obtained on the TiO_2 coatings that were anodised in H_2SO_4, H_3PO_4 and mixture electrolyte at lower electrolyte concentration. The increased apatite on these coatings can be related to the strong $Ti\text{-}O^-$ functional groups on the coating surface. The highest apatite was obtained on the TiO_2 coating that was anodised in a mixture electrolyte that has obtained Ti-OH functional group. The UV has resulted in the increased $Ti\text{-}O^-$ and Ti-OH groups, thus higher apatite precipitation ability.

ABSTRAK

Kebelakangan ini Ti telah banyak digunakan dalam aplikasi bioperubatan disebabkan oleh prestasinya yang sangat baik. Oleh yang demikian, ubah suai permukaan Ti telah menarik minat ramai untuk menghasilkan sifat biologinya yang lebih baik. Ti adalah telah dilakukan kepada proses pengoksidaan anodik dan ujian *in vitro* untuk menilai bioaktiviti salutan TiO_2. Salutan TiO_2 telah dioksidakan pada suhu bilik di dalam larutan elektrolit yang berbeza iaitu; H_2SO_4, H_3PO_4 dan campuran asid H_2SO_4 dan asid H_3PO_4. Pemboleh ubah yang digunakan dalam pengoksidaan anodik adalah: kepekatan elektrolit, voltan dan ketumpatan arus. Permukaan salutan kemudiannya di analisis menggunakan teknik pengujian yang berbeza; analisis mikrostruktur menggunakan SEM, analisis kandungan elemen menggunakan EDX, struktur hablur dan mineralogi menggunakan XRD, analisis penyerapan menggunakan FT-IR dan hidrofilik menggunakan WCA. Seterusnya ujian *in vitro* dilakukan untuk menilai aktiviti biologi permukaan salutan TiO_2. Penilaian aktiviti biologi pada permukaan TiO_2 dilakukan dengan menggunakan SBF yang dilakukan di dalam keadaan gelap dan di bawah UV untuk menyerupai tindak balas yang mungkin terjadi terhadap lapisan sel seperti tulang manusia. Ujian ini dilakukan untuk menilai mikrostruktur apatit, mineralogi, elemen dan penyerapan. Daripada keputusan ujian tersebut dapat disimpulkan bahawa banyak apatit dan tumpat mendap pada lapisan TiO_2 yang direndam di dalam SBF di bawah sinar UV berbanding salutan yang direndam di dalam SBF dalam keadaan gelap terutamanya pada permulaan eksperimen. Penyinaran UV juga telah mempercepatkan penghabluran apatit. Semua salutan memperolehi nisbah Ca/P apatit tulang dalam julat di antara 1.02 dan 1.57. Didapati juga fungsi bumpulan Ti-O menyumbang kepada peningkatan pembentukan apatit dan penghabluran untuk salutan oksida dalam larutan elektrolit H_2SO_4 dan H_3PO_4. Manakala fungsi kumpulan Ti-OH dan campuran ion S dan P dalam salutan telah menyumbang pembentukan apatit dan penghabluran yang lebih tinggi.

CONTENTS

LIST OF TABLES

LIST OF FIGURES

LIST OF SYMBOLS AND ABBREVIATIONS

%	-	Percentage
Å	-	10^{-10} metre
ASTM	-	American Standard Test Method
µm	-	Micrometre
CO_2	-	Carbone dioxide
Cp-Ti	-	Commercially pure titanium
CH_3COOH	-	Acetic acid
cm	-	Centimentre
cm^{-1}	-	Wavenumber unit
C_p^o	-	Heat capacity
EDX	-	Energy-dispersive x-ray spectroscopy
e^-	-	Electron
eV	-	Electron volt
FT-IR	-	Fourier transform infrared spectroscopy
GPa	-	Giga Pascal
g	-	Gram
h	-	Plank constant
h^+	-	Electron hole
H_2SO_4	-	Sulphuric acid
H_3PO_4	-	Phosphuric acid
H_2O	-	Water
HA	-	Hydroxylapatite
hr	-	Hours
Kcal		Kilo calorie
Kv	-	Kilo volt
L	-	Litre
M	-	Mole

MAO		
min	-	
m	-	Micro arc oxidation
mm	-	Minutes
MPa	-	Metre
N	-	Milimetre
nm	-	Mega Pascal
^{o}C	-	Newton
^{o}K	-	Nanometre
pH	-	Degree Celsius
Ra	-	Degree Kelvin
SBF	-	Potential of hydrogen
SEM	-	Roughness average
TiO_2	-	Simulation body fluid
Ti	-	Scanning electron microscope
US	-	Titanium oxide
UV	-	Titanium
WCA	-	United States
XRD	-	Ultra violet
V	-	Water contact angle
ν	-	X-ray diffraction
W	-	Volt
Wt	-	Frequency
α	-	Watt
β	-	Weight
θ	-	Alpha
λ	-	Beta
ξ	-	Theta
	-	Wavelength
		Zeta

LIST OF APPENDICES

CHAPTER 1

INTRODUCTION

The increasing demand for the implants nowadays has come vital due to the increased population. However, failure of implants is a common occurrence that requires expensive and problematic revision surgery. Hence, there is a widespread effort to improve the quality and performance of such implants. Titanium (Ti) and its alloys are widely used in biomedical implants especially in dental and hip prostheses because of their excellent biocompatibility, superior mechanical properties, and corrosion resistance. A new technique to generate a bioactive surface layer, which is hydroxyapatite (HA) layer under ultraviolet irradiation (UV) on titanium oxide (TiO_2) coating in simulated body fluid (SBF) liquid. Therefore, HA is chemically bonded and strongly attached to the Ti implant. Moreover, the microstructure of this Ti/TiO_2/HA can be controlled to facilitate bone ingrowth and, therefore, create better adhesion of implant with the surrounding bone in the human body.

1.1 Background

Biomaterials as a biomedical engineering field have become a vital area of research, as these materials can enhance the quality and longevity of human life and have led to a multi-million dollar business (Geetha *et al.*, 2009). Biomaterials as natural or artificial materials are used to form structures or implants to replace the lost or diseased biological structure for restoration and other function. Thus, biomaterials may help in improving the quality of life and longevity of human being. The field of biomaterials has shown rapid growth to keep up with the demands of an aging population. Biomaterials are used in different parts of the human body as artificial valves in the

heart, stents in blood vessels, replacement implants in shoulders, knees, hips, elbows, ears and dental structures (Ramakrishna *et al.,* 2001).

A growing of the aging population in the US had required an increasing need of materials for biomedical devices application (Rack and Qazi, 2006). Degeneration and deterioration of weight-bearing joints often require surgery to reduce pain and increase mobility (Bergallo, 2000). That led to an increasing need for artificial joints namely total joint replacement specifically total hip replacement and total knee replacement. Due to their complex behavior and the population needs, they have been the focus of that field of study (AAOS, 1995). Revision surgeries often take place due to the failure of total joint replacement implants, *e.g.* in the year 2000 revision surgeries of have counted about 12.8% of total total hip replacement implants (Rack and Qazi, 2006). Various metallic materials have been used for total joint replacement for hips, knee, and shoulders and other applications include trauma, spinal fixation devices cardiovascular and recently spinal discs. The materials used include stainless steel, Co-Cr-Mo alloys, Ti alloys and other more specialized alloys, *e.g.* Au-Pd.

Ti and Ti-based alloys are widely used as biomedical constructing materials, especially as a hard tissue replacement and cardiovascular application due to their desirable properties, such as relatively low modulus, good fatigue strength, formability, machinability, corrosion resistance, and biocompatibility, compared to more conventional stainless steels and cobalt-based alloys (Liu *et al.,* 2004; Long and Rack, 1998).

TiO_2 is a native oxide film that forms spontaneously on Ti is believed to be the reason for the advantageous interactions between the tissue and Ti implant (Hazan *et al.,* 1993). However, the poor induction of apatite due to the bio-inertness of Ti and TiO_2 has led to further biocompatibility improvement through the development of apatite coating on TiO_2 interface (Hayashi *et al.,* 1989; Kim *et al.,* 1997; Oliva *et al.,* 1998). Studies found that the bonding between the implant and living bones can be achieved by the formation of bone-like apatite HA (Keshmiri and Troczynski, 2003). Apatite, due to its excellent biocompatibility, relatively slow biodegradation, and tissue bioactivity properties (Spivak *et al.,* 1990), has been considered as a successful biomaterial coating promoting osteoconductive bonding of metallic implants. Many techniques can introduce apatite particularly HA on the TiO_2 surface, such as sputtering, plasma spraying, sol-gel processing and biomimetic, as well as the development of the composites of these two materials (Milella *et al.,* 2001).

Biomimetics is a deposition technique that is used to prepare surfaces that provide a favorable bone tissue response, thus enhancing the fixation of bone and implants. Via mimicking bone mineralization on crystalline TiO_2 (Xia *et al.,* 2010), apatite formation on certain substrates (such as alumina and Bioglass®) could be observed *in vitro* when immersed in SBF under the controlled physiological condition (Kokubo *et al.,* 1990). Since the formed apatite has characteristics similar to bone tissue apatite, it is believed that the kinetics of this process (i.e. the rate of apatite nucleation and growth) indicates the bioactive behavior of the substrate *in vivo*. It is also known that the tissue response could be considerably affected by the morphology and chemistry of the implant surface, as well as its design and topography (Nordström and Muñoz, 2001).

The resultant sample is to be characterised with scanning electron microscopy (SEM) to illustrate the surface image, to investigate the formed anodised TiO_2 and the precipitated HA on the Ti surface. The chemical elements of the Ti samples can be detected by energy-dispersive x-ray spectroscopy (EDX) (Goldstein *et al.*, 2017). The hydrophilicity of the Ti surface is to be tested using water contact angle (WCA) method (Förch *et al.*, 2009; Zisman, 1964). The sample was also characterised using x-ray diffraction (XRD) to identify the atomic planes of a crystal(s) (crystal structure analysis) in the crystalline TiO_2 and HA (Bragg, 2014; Dana and Ford, 1991; Laue, 1915). As for the chemical bonds and compounds, it is identified using fourier transform infrared spectroscopy (FT-IR).

1.2 Problem Statement

Spinal, hip and knee replacements as biomaterials are the most replacements in the human body (Ramakrishna *et al.*, 2001). Bone is made naturally made of HA, which is considered ceramics. The synthetic ceramics can form bioactive bonding with the bone surface by forming apatite layers such as HA and glass-ceramic (A-W). However, they can’t be used as bulk replacements due to the lack of fracture resistance (Hench, 1991a; Kokubo, 1991). The current materials used for biomaterials applications such as 316 L stainless steel, Co-Cr alloys, and Ti-based alloys exhibit high fracture toughness compared to ceramics bioactive materials (Hench, 1991a; Ratner, 2001; Thomsen *et al.,* 1987). However, it tends to fail after long-term use, where problems

such as having high modulus compared to bone, low wear and corrosion resistance and lack of biocompatibility may occur (Geetha *et al.,* 2009). The main problem of the current implants lies in the chemical and physical bonding between the implant surface and bone surface interface. Therefore an improvement is needed to enhance the implant / bone interface.

Researchers found that Ti metal and its alloys by subject to several treatments can form a bioactive layer on its surface and integrate with the bone (Kim *et al.,* 1999; Kokubo *et al.,* 2001; Yang *et al.,* 2004a). Because Ti is a bioinert material; it can't connect to bone tissue directly due to the weak passive layer (TiO_2) that forms spontaneously on Ti surface. Thus it can't induces bone growth apatite on it surface. Therefore, the various surface modifications have been developed to improve the bioactivity of Ti implant surface (Deligianni *et al.,* 2001; Liu *et al.,* 2004; Schwartz *et al.,* 1997).

Studies have contributed to the bioactivity of Ti toward achieving favorable bone healing of implant, that is, better cell attachment, proliferation, and osseointegration. It is found that these parameters depend on a combination of physical and chemical characteristics: microtopography, chemical composition and wettability of the implant surface (Das *et al.,* 2007; Park *et al.,* 2009; Yamamoto *et al.,* 2013). However, the effects of the surface characteristics on the bioactivity of Ti implants are not completely understood.

TiO_2 has naturally formed on Ti surface with approximated layer thickness from 1.5 nm to 10 nm after exposing to atmosphere. This surface oxide plays an important part in the biocompatibility of Ti. TiO_2 exist in three crystal forms: anatase, rutile, and brookite (Ding *et al.,* 1996; Ghosh *et al.,* 2003; Smith *et al.,* 2009). Studies to increase the oxide layer has been applied to increase the Ti bioactivity such as thermal annealing (Feng *et al.,* 2002), chemical synthesis (Samuneva *et al.,* 1993), physical vapour deposition (Wu *et al.,* 2006) and anodic oxidation (de Sena *et al.,* 2003; Sul *et al.,* 2002a; Yang *et al.,* 2004a).

Anodization is simple techniques that are useful at low temperature (Xiao *et al.,* 2003). It is an electrochemical treatment that traditionally has been a surface modification method that recently has become an attractive method to produce a bioactive oxide layer on metals especially Ti (Sul *et al.,* 2001; Giordano *et al.,* 2011; Park *et al.,* 2013). Studies by Cui et al. (2009), Giordano et al. (2011) and Park et al.

(2013) have proven that TiO_2 films prepared by anodization have increased apatite formation HA *in vitro* treatment in SBF.

TiO_2 that is formed by anodization is mainly anatase and/or rutile (Song *et al.,* 2009). Anatase obtains superior photocatalytic performance to that of rutile. This is due to higher density of localized states and consequent surface-adsorbed hydroxyl radicals and slower charge carrier recombination in anatase compared to rutile (Sclafani and Herrmann, 1996; Setiawati *et al.,* 2008; Sumita *et al.,* 2002).

As an effort to increase the bioactivity enhancement of TiO_2 coatings, UV irradiation was found to induce TiO_2 by means of both *in vitro* and *in vivo* evaluation. Also, the ability of apatite formation on TiO_2 was increased with the increase of UV irradiation duration (Guo *et al.,* 2010; Miyauchi *et al.,* 2010; Uetsuki *et al.,* 2010; Abdullah and Sorrell, 2012).

Previous studies have reported the exposure of TiO_2 to UV prior to *in vitro* test conducted using SBF (Guo *et al.,* 2010; Uetsuki *et al.,* 2010; Miyauchi *et al.,* 2010; Iwasa *et al.,* 2010). Also, UV was exposed to TiO_2 during the *in vitro* test in SBF (Ueda *et al.,* 2009; Abdullah and Sorrell, 2012). However, the TiO_2 in these studies have created using different modification techniques, such as dip-coating, chemical treatment, sputtering deposition, chemical treatment and gel oxidation. In this study a new approach was proposed to generate HA in SBF upon exposure to UV on TiO_2 that is been formed using anodic oxidation technique using sulfuric acid (H_2SO_4), phosphoric acid (H_3PO_4) and the mixture of both acids. UV irradiation was used to activate the photocatalytic effect of TiO_2, which it's believed to increase the apatite formation on TiO_2 surface. Therefore, mimicking the reaction between the implant and human bone, nonetheless, the microstructure of this Ti / TiO_2 / HA can be controlled to facilitate bone ingrowth and therefore creating better adhesion of implant with the surrounding bone in the human body.

1.3 Objectives

This project proposed a new approach to generate HA in SBF upon exposure to UV on TiO_2 that is been formed using anodic oxidation technique using different electrolytes, i.e., individual and mixture electrloytes. This approach has proposed a

better bioactive Ti implant surface that can provide better chemical bonding with the bone and therefore create a strong attachment.

The objectives of this research are summarized as follows:

i. To determine and analyse the growth of TiO_2 on Ti that is formed by anodic oxidation in H_2SO_4, H_3PO_4 and mixed of (H_2SO_4+H_3PO_4) electrloyte.

ii. To analyse and discuss the effect of applied voltage, electrolyte composition and breakdown voltage on the morphology and mineralogy of the TiO_2 oxide layer.

iii. To measure and analyse the growth of HA on TiO_2 layer in SBF (*in vitro* assessment).

iv. To evaluate and analyse of HA on TiO_2 layer in SBF under UV irradiation (*in vitro* assessment).

1.4 Significance of Study

The main aim of this research was to provide thicker TiO_2 by anodzing Ti in H_2SO_4, H_3PO_4, and a mixture of (H_2SO_4+H_3PO_4) electrolyte provide significant information on the characterisation of HA/TiO_2/Ti composite that is fabricated by a new technique of *in vitro* test using SBF under UV irradiation on anodised Ti. This new approach was to provide a strong chemical bonding attachment between Ti implant and the bone.

1.5 Scope of Study

The research was conducted within the following boundaries:

i. Sample preparation of commercially pure titanium (Cp-Ti grade 2) for anodic oxidation.

ii. Fabrication of photocatalytic (TiO_2) surface layers of controlled thickness and pore size on Ti by anodizing in H_2SO_4, H_3PO_4 and mixed electrolyte (H_2SO_4 + H_3PO_4).

iii. Parameters for anodic oxidation used are:

   a. At voltages (100,150 and 180 V),

   b. At current density (60 and 100 $mA.cm^{-2}$)

   c. Time (10 min)

d. Electrolyte concentration of (0.1, 0.3 and 2 M) for H_2SO_4 (S) and H_3PO_4 (P) and, (0.1 S + 0.1 P, 0.1 S + 0.3 P, 0.3 S + 0.1 P, 0.1 S + 2.0 P and 2.0 S +0.1 P).

e. Characterisation of fabricated TiO_2 by using SEM, EDX, AFM, WCA, XRD and FT-IR testing.

f. Preparing of simulated body fluid (SBF).

g. Precipitation of HA on the TiO_2 using SBF.

h. Precipitation of HA under UV irradiation on the TiO_2 using SBF.

i. Characterizing the formed HA using SEM, EDX, XRD, and FT-IR

CHAPTER 2

LITERATURE REVIEW

2.1 Introduction

Ti recently has widely been used in clinical biomedical application due to its high performance especially in total knee replacement and total hip replacement in the human body. However, great efforts are been made by researchers to enhance the performance titanium implants *in vivo*. Therefore surface modifications of titanium have attracted a lot of interest. Many techniques have been used to deal with the surface of titanium implants to provide better biological outcomes. One of the techniques is to generate bioactive surface layer hydroxyapatite (HA) on titanium oxide (that is formed via anodization of titanium) through precipitation into SBF under UV light. This chapter has also covered related researches in the same area of study.

2.2 Biomaterials

Biomaterials are materials of nature of man-made origin, which are distinguished from any other materials by its ability to co-exist in contact with body's tissues without causing an unacceptable degree of harm to the body. It is used to replace and/or restore form and function of traumatized or degenerated tissues or organs, and to improve the quality and longitively of the life of the human being (Geetha *et al.*, 2009; Williams, 2008; Ramakrishna *et al.*, 2001). Examples of multiple field applications that contribute to the development of biomaterials in medicine and dentistry are observed in (Table 2.1).

Table 2.1: Fields of knowledge to develop biomaterials (Von Recum, 1994)

Discipline	Applications
Science and engineering	Structure-property relationship of synthetic and biological materials, including metals, ceramics, polymers, composites, tissues (blood and connective tissues)
Biology and physiology	Cell and molecular biology, anatomy, animal and human physiology
Clinical science	Dentistry, maxillofacial, neurosurgery, plastic and reconstructive surgery

2.3 Biomaterials Properties

Biomaterials are expected to work in aggressive natured body's environment without any considerable amount of harm. Over the past 40 years, there have been efforts which led to considerable progress in understanding the interactions between the materials and tissues (Ramakrishna *et al.*, 2001). The performance and applications of biomaterials in biological systems are of critical importance for the development of biomedical implants and tissue engineering (Niinomi, 2008a).

Metals and their alloys, polymers, ceramics, and composites are common biomaterials used in medical applications. These materials have a different atomic arrangement, which gives unique diversity in their structural, physical, chemical and mechanical properties, and these different properties offer alternative applications in the human body.

Polymers exhibit flexibility, low mechanical strength, and stiffness. They are attractive materials in various soft tissue replacement and proliferation such as cardiovascular devices. They are also used in drug delivery systems, diagnostic supports and as a reconstructive material for tissue engineering (Yoruç and Şener, 2012). Synthetic and natural polymers are different types of materials that can be used as biomaterials in biomedical implants.

Ceramics are desirable biomaterials due to their biocompatibility properties, such as bioactive, bioinert and biodegradable properties. However, ceramics exhibit significant disadvantages such as high brittleness and low strength. Known ceramics used as biomaterials such as aluminium oxide (Al_2O_3) and zirconia (ZrO_2) (Mihov and Katerska, 2010).

Composites are materials composed of two or more of a different or same material. A composite is a material comprised of two or more metal, polymer or ceramic structures which are separated by an interface. For example, a composite try

to combine the features of a stiff ceramics and flexible polymers to get superior properties from both materials. Composite materials have long been used in innovative technological applications due to their superior mechanical properties.

Metals and their alloys exhibit high strength, elastic modulus, and fatigue properties, which make them attractive materials for load bearing applications (Yoruç and Şener, 2012). Metals used as biomaterials such as stainless steel, cobalt (Co)-chromium (Cr) and Ti and Ti-based alloys are currently used as structural materials in hard tissue replacements (Niinomi, 2008a). Among bio-metals, Ti and Ti-based alloys are considered the most attractive biomatels in biomedical applications due to their good combination of superior biocompatibility and good strength (Elias *et al.,* 2008; Izman *et al.,* 2012; Niinomi, 2008b). Due to these properties Ti and Ti-based alloys have demonstrated success in the biomedical implants and devices (Elias *et al.,* 2008).

2.3.1 Mechanical Properties of Biomaterials

Generally, biomaterials must exhibit the following properties and characteristics that may refer as (mechanically biocompatible):

i. High strength for long fatigue life (fatigue resistance).
ii. A low Young's modulus equivalent to that of the cortical bone in order to inhibit bone absorption.
iii. Various characteristics such as super-elasticity and shape memory.
iv. High wear and fretting (corrosion resulted from wear) fatigue resistance.

The Young's modulus and tensile strength, ductility, fatigue life, fretting fatigue life, wear properties and functionalities should be controlled so that their levels are suitable for structural biomaterials used in implants that replace hard tissue (Niinomi, 2008b).

Metals, ceramics, and polymers have to exhibit structural and mechanical compatibility with tissues. The mechanical and chemical advantages and disadvantages of most biomaterials are listed in Table 2.2. In general, tissues are grouped into soft tissues and hard tissues. Soft tissues (e.g. skin, blood vessels, cartilage, and ligaments) exhibit low mechanical and structural properties which are preferred to be replaced with polymers biomaterials. Hard tissues like bone and tooth have higher elastic modulus and stronger tensile strength than the soft tissues, which

are preferred to be replaced with metals and ceramics. However, metals and ceramics have elastic modulus of 10-20 times greater than the values of hard tissues. This difference is a major problem in orthopaedic implantation due to the variation in stress distribution between the implant and bone under load (Ramakrishna *et al.*, 2001).

Table 2.2: The mechanical and chemical advantages and disadvantages of biomaterials

Biomaterial	Advantages	Disadvantages	References
Metals	Strength, ductility, wear resistance	low biocompatibility corrosion, stiffness, density, metal ion releasing on body system	(Ramakrishna *et al.*, 2001)
Ceramics	Biocompatibility, corrosion resistance, compressive resistance	Brittleness, low fracture strength, production difficulties	
Polymers	Flexibility	Low strength, low stiffness	(Yoruç and Şener, 2012)

Ceramics are brittle and hard materials due to their strong ionic and covalent bonding of their structure (Yoruç and Şener, 2012) which has restricted their field of application in biomedics (Vallet-Regi, 2001). The poor tensile strength and brittleness properties of ceramics and glasses are their main disadvantages. They also fail at low stress under tension and bending loads, however, they have an exceptional compressive strength (Yoruç and Şener, 2012). Alumina (Al_2O_3) and zirconia (ZrO_2) have the highest mechanical properties among bioceramics, which made them be used in load bearing applications in (Vallet-Regi, 2001). The mechanical properties of these bioceramics and bone are listed in Table 2.3. From the table, it can be seen that alumina has desirable mechanical characteristics such as high hardness, good abrasion resistance, excellent wear and fraction behavior (Thamaraiselvi and Rajeswari, 2004). Phosphates are bioactive bioceramics that have a similar mineral component to bone (Vallet-Regi, 2001). The mechanical properties of phosphates make them unsuitable for load bearing applications (Yoruç and Şener, 2012). A member of phosphate family, that is, HA (Ca_{10} $(PO_4)_6$ OH). HA is weak and brittle material, however, it has excellent biocompatibility, which makes it used widely as an interfacial of many orthopaedic and dental implants with the biological system (Oldani and Dominguez, 2012). Mechanical properties of HA are shown in Table 2.3.

Table 2.3: Mechanical properties of some bioceramics and bone (Thamaraiselvi and Rajeswari, 2004)

Material	Young's modulus (GPa)	Compressive strength (MPa)	Bond strength (GPa)	Hardness (HV)	Density (g/cc)	K_{Ic} (MPa $m^{1/2}$)
Al_2O_3 (Inert)	380	4000	300-400	2000-3000	>3.9	5.0-6.0
ZrO_2 (PS)	150-200	2000	200-500	1000-3000	~ 6.0	4.0-12.0
Bioactive HA	73-117	600	120	350	3.1	<1
Bone	3-30	130-180	60-160	NA	NA	NA

PS: Partially stabilized, NA: Not available.

Biocomposite materials have been developed in order to combine the bioactivity of ceramics and mechanical properties of metals (Oldani and Dominguez, 2012), also combined with the stiffness of ceramics and the flexibility of polymers (Yoruç and Şener, 2012). These properties are considered when combining biomaterials as composites. Biomedical composites which show continuous progression are very attractive and promising engineering materials made from two or more constituents with different physical properties (Scholz *et al.*, 2011).

Biometals such as stainless steel (grade 316L) and Co-based alloys have been used as implants due to their good biocompatibility, but physically and mechanically they have encountered problems such as heavyweight and stress shield effect in load bearing applications (Kumar *et al.*, 2010). This group of biometals has gradually been replaced by another lighter biometal such as Ti-based alloys. Table 2.4 list some mechanical properties of common biometals used in medical applications. Ti and Ti-based alloys exhibit great tensile strength, good overall strength (Williams, 2008) and low Young´s modulus (Ratner, 2001). These properties made them be considered as the most convincing materials in medical applications nowadays when compared to stainless steels and Co-based alloys (Izman *et al.*, 2012). Table 2.4 observe a relative scale of mechanical characteristics of biometals alloys. The most widely used Ti-based alloy is grade 5 and grade 2 for unalloyed Ti, according to ASTM F67 and ASTM F136 respectively.

It's important to mention about the mismatch of Young's modulus between the Ti implant (103-120 GPa) as seen in Table 2.4 and bone (10-30 GPa), which is unfavourable for bone healing and remodeling. However, there is a contradiction between elastic modulus and other mechanical properties such as contradiction between elastic modulus and strength (Elias *et al.*, 2008). Wear debris generated from

these articulation joints can induce inflammation problem and toxic effect to the human body.

Many new Ti alloys have been developed to overcome such problem. For example, alloys such as Ti-Nb and Ti-Zn based alloys. These alloys have a high strength to weight ratio but they suffer from poor tribological properties especially when applied to joint movements (Izman *et al.,* 2012).

Table 2.4: Properties and characteristics of common used biometal alloys

	Stainless steels	Co-base alloys	Ti and Ti-based alloys	References
Grade	Stainless steel	Co-Cr alloy	α and α-β alloy	(Davis, 2006; Silver and Christiansen, 1999)
Type	F55, F138, F745	F75, F90, F562, F563	F67, F136	
Ultimate tensile strength (MPa)	480-860	655-1586	240-896	
Yield strength (MPa)	170-690	276-1586	170-827	(Silver and Christiansen, 1999)
Ultimate stain (%)	12-40	8-50	10-24	
Young's modulus (GPa)	193	210 (F90) 232 (F562)	103-107 (F67) 114-120 (F136)	(Davis, 2006)
Stiffness	High	Medium	Low	(BomBac *et al.,* 2007)
Strength	Medium	Medium	High	
Corrosion Resistance	Low	Medium	High	
Biocompatibility	Low	Medium	High	

2.3.2 Biocompatibility Properties of Biomaterials

Biocompatibility is the ability of a foreign object to live inside the human body with a minimum of rejection or inflammatory response with the surrounding tissue (Geetha *et al.,* 2009; Hollinger, 2011; Williams, 2008).

According to the biocompatibility of biomaterials, the interaction between the human body tissue and the implant can undergo different reactions, and any reaction between the human body tissue and implants depend on the tissue response to that implant. These reactions can classify the materials into bioactive, bioresorbable and bioinert materials (Table 2.5) (Langer and Peppas, 2003; Hench 1991b; LeGeros, 1988).

Bioinert materials refer to materials with minimal interaction with the surrounding tissue, for that a fibrous capsule might form around the implant. Bioactive refers to a material that interacts with the surrounding tissue with the bone tissue

through kinetic modification, where an ion-exchange reaction takes place and results in a formation of carbonate apatite between the implant and the surrounding body fluids. Bioresorbable materials have the ability to get dissolved upon interacting with the human body and being replaced by advanced tissue (Heness and Ben-Nissan, 2004).

Table 2.5: Classification of biomaterials based on its interaction with its surrounding tissue

Classification	Response	Example material	Effect	References
Bioinert (biotolerant) materials	Formation of thin connective tissue capsules (0.1-10 µm) and the capsule does not adhere to the implant surface	Poly tetra fluorethylene (PTFE), polymethylmethaacralyte (PMMA), Ti, Co-Cr, Stainless steel, Al_2O_3, ZrO_2, Ultra high molecular weight polyethylene (UHMWP)	Rejection of the implant leading to failure of the implant	(Geetha *et al.*, 2009) (Heness and Ben-Nissan, 2004)
Bioactive materials	Formation of bony tissue around the implant material and strongly integrates with the implant surface	Bioglass, synthetic calcium phosphate, hydroxylapatite (HA), carbonate apatite CHA, class ceramic A-W	Acceptance of the implant leading to success of implantation	(Geetha *et al.*, 2009) (Heness and Ben-Nissan, 2004)
Bioresorbable materials	Replaced by the autologous tissue	Polylactic and polyglycolic acid copolymers and processed bone grafts, composites of all tissue extracts or proteins and structural support system, tricalcium phosphate ($Ca_3(PO_4)_2$), calcium oxide, calcium carbonate and gypsum	Acceptance of the implant leading to success of implantation	(Geetha *et al.*, 2009) (Heness and Ben-Nissan, 2004)

The ability of an implant to integrate with the adjacent bone and the soft tissues depend on the implant material surface conditions (Viceconti *et al.*, 2000). Studies have demonstrated that material's surface topography, surface chemistry and surface energy influence the cell material interaction and biological response, where a good surface conditions lead to rapid and strong bone integration between the bone and the implant, and therefore their osseointegration (Das *et al.*, 2007; Geetha *et al.*, 2009; Park *et al.*, 2009).

Synthetic polymers lack biocompatibility and often cause inflammatory reactions, i.e., swelling. Therefore, researches recently focused on the possibility of

usage of natural polymers such as chitosan, carrageenan, and alginate (Yoruç and Şener, 2012).

Ceramics are desirable materials due to their biocompatible properties (Yoruç and Şener, 2012). Bioceramics observe three types of biocompatibility: bioinert ceramics, bioactive ceramics which form direct chemical bonding with bone and/or soft tissues in biological system, bioresorbable ceramics that actively participate in the metabolic activities in organism (Messer *et al.*, 2003; Thamaraiselvi and Rajeswari, 2004; Yamamoto *et al.*, 2004). Most researches have been focused on the interfacial reactions of HA with the biological system. HA has an excellent biocompatibility and is bioactive, due to their chemical structure very similar to the mineral phase of bone. It's a popular surface coating material for stainless steel, Ti and Ti-based alloys implants (Yoruç and Şener, 2012). Examples of Ceramics used in medical applications are listed in Table 2.6.

Table 2.6: Ceramics used in medical applications (Yoruç and Şener, 2012)

Bioeramic	Biocompatibility
Alumina (Al_2O_3)	Bioinert
Zirconia (ZrO_2)	
Pyrolytic carbon	
Bioglass ($Na_2OCaOP_2O_3$-SiO)	Bioactive
Hydroxyapatite ($Ca_{10}(PO_4)_6(OH)_2$	Biodegradable
Tricalcium phosphate ($Ca_3(PO_4)_2$	

Biocomposites try to improve the biocompatibility of implants by combining two or more biomaterials (Kurtz, 2003). An example of biocomposites is metal-ceramic composite, where ceramics used as coating materials to improve the biocompatibility of metals. HA/Ti composite is considered one of the promising ceramic-metal biocomposites used to develop the bioactivity and to increase the lifetime of implants (Oldani and Dominguez, 2012).

Biometals such as stainless steel and Co-based alloys have been used for 50 years in medical applications due to their good biocompatibility. These materials gradually have been replaced with a more biocompatible biometal that *is* Ti and Ti-based alloys. Table 2.4 list a relative scale of biological characteristics of common biometals alloys. Because of their superior biocompatibility and tissue acceptance, Ti and Ti-based alloys did acquire a huge interest in medical applications (Elias *et al.*, 2008; Niinomi, 2008b; Williams, 2008).

The main physical properties of Ti responsible for the biocompatibility are:

i. Low level of electronic conductivity,
ii. High corrosion resistance,
iii. Thermodynamic state at physiological pH values,
iv. The low ion-formation tendency in aqueous environments, and an isoelectric point of the oxide of 5-6.
v. The passive film covered surface is slightly negatively charged at physiological pH, titanium has a dielectric constant comparable to that of water with the consequence that the Coulomb interaction of charged species is similar to that in water (Niinomi, 2008b).

Ti-6Al-4V (grade 5) and Cp-Ti (grade 2) are the most used Ti grades in orthopaedic and dentistry implantation, respectively (Elias *et al.,* 2008). However, for permanent implant applications, Ti-6Al-4V has a possible toxic effect result from released vanadium (V) and aluminium (Al). For this reason, V and Al free-Ti alloys have been introduced for implant applications, such as Ti-Nb and Ti-Zr based alloys (Elias *et al.,* 2008; Izman *et al.,* 2012). Cp-Ti is considered to have the most biocompatibility among biometals because its surface properties result in the spontaneous build-up of a stable and inert oxide layer (Elias *et al.,* 2008).

Post-implantation is a very critical stage where the interaction between the implant and the human body tissue is evaluated. The possibility of toxication to the host body is an issue in either the short or long run. Hence, the materials of the implant have the major role to the responses of the biological environment and therefore surface modification is often required to improve the biological and tribological properties of the implants (Huang *et al.,* 2006; Kumar *et al.,* 2010). Ti is classified as a bioinert metal (Yamamuro, 1989), therefore researches have been made to develop a bioactive ceramic surface modification on Ti and Ti-based alloys surface (Niinomi *et al.,* 2005).

2.4 Types of Biomaterials

In general, most of the materials used in medical and/or dental applications can be categorized as follows:

i. Metallic biomaterials

ii. Ceramic biomaterials

iii. Polymeric biomaterials

iv. Composite biomaterials

Metallic materials include pure metals and alloys, ceramics include glasses, glass-ceramics, and carbons, and the polymers include thermosets, thermoplastics, elastomers and textiles (Williams, 2008).

2.4.1 Metallic Biomaterials

Biometals used in implants due to their excellent electricity and thermal conductivity and mechanical properties (Black, 2005). Biometals are most widely used for load-bearing implants. In addition to orthopaedics, they are also used in maxillofacial surgery, cardiovascular surgery and dental implants (Khan *et al.*, 2007). Table 2.7 list some known biometals used in medical and dental applications. They were used to manufacture implants due to their tolerance in the human body in the minute amount. This is natural since the red blood cells have essential metallic elements such as Fe and/or Co for vitamin B_{12} synthesis (Black, 2005).

Table 2.7: Examples of biometals used in medical and dental applications

Biometals	Principle application	References
316L stainless steel	Fracture fixation, stents, surgical instruments	(Williams, 1990)
Ti and Ti-based alloys	Bone and joint replacement, fracture fixation, dental implants, pacemaker encapsulation	
Co-Cr based alloys	Bone and joint replacement, dental implants, dental restorations, heart valves	
Ni-Ti	Bone plates, stents, orthodontic wires	
Gold alloys Dental	Restorations	
Silver products	Antibacterial agents	
Platinum and Pt-Ir	Electrodes	
Hg-Ag-Sn amalgam	Dental restorations	
Cp-Ta	Nerve anastomoses, clips for ligation of vessels and staples for abdominal surgery and as pliable sheets and plates for cranioplasty and reconstructive surgery	(BomBac *et al.*, 2007)

The most commonly used biometals in medical and dental applications are stainless steels (Khan *et al.*, 2007), Co base alloys, Cp-Ti and Ti-based alloys and some other biometals (Agrawal, 1998). The advantages and disadvantages of these biometals are listed in Table 2.8.

Table 2.8: Properties and characteristics of some most common used biometal alloys

	Stainless steels	Co-base alloys	Ti and Ti-base alloys	References
Grade	Stainless steel	Co-Cr alloy	α and α-β alloy	(Davis, 2006; Silver and Christiansen, 1999)
Type	F55, F138, F745	F75, F90, F562, F563	F67, F136	
Advantages	Cost, availability, processing	Wear resistance, corrosion resistance, fatigue strength	Biocompatibility, corrosion, minimum modulus, fatigue strength	
Disadvantages	Long-term behaviour, high modulus	High modulus, biocompatibility	Lower wear resistance, low shear strength	

2.4.2 Ceramic Biomaterials

Ceramics are used as biomaterials because:

i. Relativity inert to the body fluids.

ii. High compressive strength.

iii. The aesthetically pleasing appearance which led to being used in dentistry as a dental crown.

iv. High specific strength, which makes it used as reinforcement for composites and for tensile loading applications (Park and Lakes, 2007).

One of the primary restrictions on the clinical use of bioceramics is the uncertain lifetime under the complex stress states, slow crack growth, and cyclic fatigue that arise in many clinical applications. Bioceramics can be single crystals; (sapphire), polycrystalline; (alumina or hydroxyapatite (HA)), glass (Bioglass®), glass-ceramics (Ceravital® or A/W glass-ceramic), or composites (stainless-steel-fiber-reinforced Bioglass® or polyethylene-hydroxyapatite (PE-HA) (Hench and Ethridge, 1982).

Table 2.9 summarizes and classifies the mechanism of bioceramics-tissue attachment, with examples. There are three types of bioceramics according to human body response, bioinert, bioresorbable and bioactive ceramics.

2.4.2.1 Bioinert Ceramics

Bioinert ceramics refer to bioceramics that maintain their physical and mechanical properties while in the host body (Wong *et al.,* 2013). Examples of bioinert ceramics

are listed in Table 2.10. Bioinert ceramics are typically used as structural-support implants. Some of these are bone plates, bone screws, and femoral heads. Examples of nonstructural support uses are ventilation tubes, sterilization devices (Feenstra, 2018) and drug delivery devices (Wong *et al.,* 2013).

Table 2.9: Types of bioceramics-tissue attachment and bioceramic classification (Hench, 1991a)

Type of bioceramics	Type of attachment example	Examples
1	Dense, nonporous, nearly inert growth into surface irregularities by cementing the device into the tissues, or by press fitting into a defect (termed morphological fixation).	Al_2O_3 (single crystal and ceramics attach by bone polycrystalline)
2	For porous inert implants bone in-growth occurs, which mechanically metals attaches the bone to the material (termed biological fixation).	Al_2O_3 (porous polycrystalline) Hydroxyapatite-coated porous
3	Dense, nonporous, surface-reactive ceramics, glasses, and glass-ceramics attach directly by chemical bonding with the bone (termed bioactive fixation).	Bioactive glasses Bioactive glass-ceramics Hydroxyapatite
4	Dense, nonporous (or porous), resorbable ceramics are designed to be slowly replaced by bone.	Calcium sulfate (plaster of Paris) Tricalcium phosphate Calcium phosphate salts

Table 2.10: Examples of relatively bioinert bioceramics

Bioinert Ceramics	Applications	References
Pyrolitic carbon coated devices	Percutaneous access devices Artificial heart valve	(Hench, 2013)
Zirconia (ZiO_2)	Orthopaedic load bearing application	
Alumina (Al_2O_3)	Otolaryngological implants, maxillofacial reconstruction, dental implants, alveolar ridge augmentation, orthopaedic load bearing application Ossicular (middle ear) bone substitutes Coatings for tissue ingrowth	(Hench, 2013) (Cerruti, 2004) (Hench, 1991a)
Calcium aluminates (CA)	Dental restorative material Load-bearing application, filler, strengthening material, eg; vertebroplasty Bone repairing and substituting material in dental and orthopedic application	(Kraft and Hermansson, 2003) (Morejón-Alonso *et al.*, 2009) (LeGeros, 1988)
Titania (TiO_2)	Coatings for hard tissue replacements implants	(Chu, 2013)

2.4.2.2 Bioresorbable Ceramics

Resorbable ceramics tend to degrade upon implantation in the host and replaced with tissues. The rate of degradation varies from material to material (Wong *et al.,* 2013). Examples of resorbable ceramics are listed in Table 2.11.

Table 2.11: Examples of biodegradable bioceramics (Wong *et al.,* 2013)

Biodegradable or Resorbable Ceramics	Applications	References
Aluminium-calcium-phosphorous oxide (ALCAP)	Femur bone replacement	(Mattie and Bajpai, 1988)
Glass fibers and their composites (FGC)	Dentistry, bone plates, implants and prostheses	(Zhang and Matinlinna, 2011)
Calcium sulfates, including Plaster of Paris	Fill bone defects and periodontal defect repair Degradable spinal cord scaffolds.	(Thomas and Puleo, 2009) (Åberg *et al.,* 2012)
Dense HA	Otolaryngological implants, Bone graft substitutes	(Hench, 2013) (Jordan *et al.,* 2002)
Tricalcium phosphate (TCP)	Alveolar ridge augmentation, periodontal pocket obliteration, bone space fillers	(Hench, 2013)
Calcium phosphate salts	Periodontal pocket obliteration, bone space fillers. Bone repair and augmentation, drug delivery device Coatings for metal implants	(Hench, 2013) (Kalita, Bhardwaj and Bhatt 2007) (Vallet-Regi, 2001)

2.4.2.3 Bioactive Ceramics

These materials tend to form a strong bond with adjacent tissue. Examples of surface reactive ceramics listed in Table 2.12. They are used as a coating to the metal implants and prostheses due to the stronger bonding they provide to the adjacent tissues. Among these materials porous HA coating used for chemical bonding (orthopaedic, dental, and maxillofacial prosthetics) (Hench, 1991a).

2.4.3 Polymeric Biomaterials

Polymeric biomaterials are advantageous over metal or ceramic materials because of:

Table 2.12: Examples of active bioceramics

Surface reactive bioceramics	Applications	References
(Ceravital™) Glass-ceramics	Implant in middle-ear surgery to replace ossicles	(Hench, 1991)
Porous hydroxapatite	Coating for chemical bonding (orthopaedic, dental, and maxillofacial prosthetics), dental implants	
Bioglasses	Cranial repair, otolaryngological implants, maxillofacial, dental implants, alveolar ridge augmentation, periodontal pocket obliteration, percutaneous access devices	(Hench, 2013)
Glass-ceramics	Otolaryngological implants, percutaneous access devices, spinal surgery, iliac crest repair Coating for chemical bonding (orthopaedic, dental, and maxillofacial prosthetics), dental implants	(Hench, 2013) (Hench, 1991a)

i. The ease of manufacturability to produce various shapes (latex, film, sheet, fibres).
ii. Ease of secondary processability.
iii. Reasonable cost.
iv. Availability with desired mechanical and physical properties.

Polymers are generally classified into three categories depending on their source:

i. Natural polymers: These are obtained from natural sources (plants and animal origin). However, they suffer from various disadvantages such as the possibility of antigenicity; the possibility of microbial contamination and source-to-source variability of properties (Venkatraman *et al.,* 2008). Natural polymers used in biomedical applications such as tissue regeneration and drug delivery systems (Yoruç and Şener, 2012).
ii. Synthetic polymers: They are based on totally synthetic sources. Natural polymers have been replaced with synthetic polymers due to their ease of production, availability, and versatility of properties (Venkatraman *et al.,* 2008). Hence, Synthetic polymeric materials have been widely used in medical applications (Lee, 1989). However, only 10 to 20 synthetic polymer type used in fabrications from disposable to long-term implants out of hundreds of types used in the medical device (Wong *et al.,* 2013). The main disadvantage of synthetic polymers is the general lack of biocompatibility in the majority of cases, often associated with inflammatory reactions. Therefore, recent researches have focused on the usage possibilities of natural origin polymers such as chitosan, carrageenan, and alginate. Examples of the synthetic polymer

is Poly(methylmethacrylate) that is used in dental implants and bone replacements (Yoruç and Şener, 2012). Examples of polymers used for total joint replacements and dental implants are listed in Table 2.13.

Table 2.13: Some polymers used for total joint replacements and dental implants (Angelova and Hunkeler, 1999)

Polymer	Applications
Low and high density polyethylene	Knee, hip, shoulder joints
Polymethylmethacrylate (PMMA)	Dental restorations, intraocular lenses, joint replacement, e.g. bone cements

Polymers can be categorized into two types regarding tissue attachment reaction to:

i. Non-biodegradable polymers: Polymers that maintain their physical and mechanical properties while they are in the host body. Table 2.14 list properties and medical applications of some non-biodegradable polymers.

ii. Biodegradable polymers: Polymers that can react with the surrounding tissue to restore the later function over time after having benefited from the degraded polymer. The degradable nature of this material allows for its temporospatial clearance from the body (Commandeur *et al.*, 2006). Table 2.15 list potential applications of some biodegradable polymers.

Table 2.14: Examples of non-biodegradable polymers

Non-biodegradable polymer	Applications	References
Ultrahigh molecular weight polyethylene (UHMWPE)	Bearing materials in total joint replacements	(BomBac *et al.*, 2007)
Polymethylmethacrylate (PMMA)	Bone cement total joint replacement stem, replacement of intraocular lenses, injections to reduce wrinkles and scars	(Agrawal, 1998)
Polyetheretherketone	Trauma, orthopaedic and spinal implant.	
Polyethylene terephthalate (PET)	Sutures, surgical mesh, cascular grafts, sewing cuffs for heart valves and components for percutaneous access devices	(Metzger, 1976)

2.4.1 Composites Biomaterials

The use of composites in biomedical application is due to the following reasons:

Table 2.15: The potential applications of biodegradable synthetic biopolymers (Tian *et al.,* 2012)

Biodegradable polymer	Applications
Polyanhydrides	Bone
Polyurethane Vascular,	Bone
Polyelectroactive materials	Nerve
Polyphosphoester	Bone
Poly(propylene fumarate)	Bone
Polyesterurethane	Genitourinary

i. To closely match or exceed the mechanical properties of the natural tissue that is replaced for soft tissue, e.g. tendons and the intervertebral disc (Ambrosio *et al.,* 1998), and hard tissues, e.g. with bone replacement and augmentation.

ii. Optimizing the biological response of the implant to the surrounding tissue and body, therefore a strong biological interface can be produced by the body to surround and integrate the implant by tailoring the biological properties of the composites (Bonfield *et al.,* 1981).

iii. The third rationale relates solely to degradable composites, which as the implants degrade, allows the degradual transfer of load from the implant into the natural tissue (Bos *et al.,* 1987).

The bone itself is a composite, comprise of an organic phase and a ceramic phase. This ceramic phase is predominantly calcium hydroxyapatite with a Ca/P ratio of 1.67. Thus, synthetic calcium HA is a good candidate for a successful biomaterial. Several dental and orthopaedic metal implants are coated with HA to ensure long-term fixation in bone (Agrawal, 1998). Table 2.16 lists some composites biomaterials used in medical applications.

2.5 Titanium (Ti)

Ti and Ti-based alloys are fast emerging as the first choice for the majority of biomedical implant applications. There are various aspects of Ti that make this material an ideal choice for bio-applications (Geetha *et al.,* 2009). According to Van Noort (1987), Ti was found to be the only biometal to osseointegrate (Van Noort, 1987). Li et al. (1994) assumed the possibility of bioactivity behavior of Ti that leads to incorporate of calcium and phosphorous (Li *et al.,* 1994).

Table 2.16: Composite biomaterials (biocomposties)

Biocomposites	Applications	References
HA / high density polyethylene (HDPE) composite	Bone repair	(Ambrosio, 2017)
Poly(methylmethacrylate) (PMMA)	Injectable composites for bone repair: Injectable bone cement in orthopaedics to enhance wound healing and bone in-growth	
	Joint replacement: Bone cement for anchoring joint prosthesis	
Carbon-fibre-reinforced poly(ether ether ketone) (PEEK) and Kevlar fibre reinforced polyethylene	Hip joint replacement: Composite acetabular cup	(D'amore *et al.*, 1993)
HA/Ti, HA/Stainless steel composites	Total joint replacements	(Agrawal, 1998)

2.5.1 Application of Titanium Alloys in Biomedical Applications

An attempt to use Ti as an implant dates back to 1930s; it was found that Ti was well tolerated in cat femurs (Niinomi, 2003). Ti and Ti-based alloys have been used increasingly since the late 1960s in the manufacturing of orthopedic implant for joint replacement and fracture fixation (Narayan, 2009).

The range of applications of Ti and Ti-based alloys in biomedical implantation is wide, it comprises:

i. Dental implants.
ii. Joint replacement; hip, knee, shoulder, spine, and elbow.
iii. Bone fixation; nails, screws, nuts, and plates.
iv. Housing device for pacemakers and artificial heart valves.
v. Surgical instruments and components in high-speed blood centrifuge (Machara *et al.*, 2002).

Due to its excellent biocompatibility and non-allergic nature, Ti and Ti-based implants can also be used in healthcare goods such as wheelchairs, artificial limbs and artificial legs (Niinomi, 2003).

2.5.2 Properties of Titanium

Ti and Ti-based alloys have advantageous properties that make it an attractive candidate for biomedical applications.

2.5.2.1 Mechanical Properties

The mechanical properties of Ti and Ti-based alloys can be discussed as follows:

i. High specific strength: Ti and Ti-based alloys have high strength compared to weight ratio (high specific strength) (Oldani and Dominguez, 2012). High strength compared to weight ratio

ii. Poor shear and wear resistance: Ti obtains poor shear strength, and due to that they are less desirable for bone screws, plates, and similar applications. Ti tends to slide contact with itself or another metal (Miller *et al.,* 1958). Also, the low wear resistance is another problem of Ti. For example, Ti6Al4V alloy cause wears problems in articulation surface when used as an implant (Oldani and Dominguez, 2012).

iii. Stress shield effect of the implant with the bone: Stress shielding occurs because there is a mismatch between the implant and bone. The Young's modulus of bone (3-30 GPa) according to (Thamaraiselvi and Rajeswari, 2004) and (7-25 GPa) according to Currey (1998), which is considered much lower than the Young's modulus of Ti and Ti-based alloys (Currey, 1998). Although Ti and Ti-based alloys have much lower modulus compared to stainless steel and Co-based alloys (Dadvinson and Gergette, 1986). Various methods to solve this problem have been considered, including:

    a. Changing the shape or size of the joint replacement implants, to reduce the effect of the structural stiffness of the implant.

    b. Proposing Cp-Ti and a developed metastable β-Ti alloys with low Young's modulus ranging (55-85 GPa) as listed in Table 2.17 are to replace steel alloys (Guillemot *et al.,* 2004; Sarmento *et al.,* 1979). These alloys are expected to be more proximal to the bone modulus, however, they are still greater than the cortical bone (Oldani and Dominguez, 2012).

2.5.2.2 Chemical Properties

The chemical properties of Ti and Ti-based alloys will be discussed as follows:

Table 2.17: Mechanical properties of biomedical titanium alloys (Geetha *et al.*, 2009)

Material	Standard	Modulus (GPa)	Tensile strength	Alloy type
First generation biomaterials (1950-1990)				
(Cp Ti grade 1-4)	ASTM F67	103-107	240-550	α
Ti-6Al-4V ELI wrought	ASTM F136	116	860-896	α+β
Ti-6Al-4V ELI standard grade	ASTM F1472	112	895-930	α+β
Ti-6Al-7Nb Wrought	ASTM F1295	110	900-1050	α+β
Ti-5Al-2.5Fe	ISO 5832	110	1020	α+β
Second generation biomaterials (1990-present)				
Ti-13Nb-13Zr Wrought	ASTM 1713	79-84	973-1037	Metastable β
Ti-12Mo-6Zr-2Fe	ASTM 1813	74-85	1060-1100	β
Ti-35Nb-5Zr-5Ta		55	596	β
Ti-29Nb-13Ta-4.6Zr	ASTM F1813	65	911	β
Ti-35Nb-5Ta-7Zr-0.40		66	1010	β
Ti-15Mo-5Zr-3Al		82		β
Ti-Mo	ASTM F2066			β
Bone		30 max		

i. Biocompatibility of Ti: The excellent biocompatibility of Ti comes from the formation of TiO_2 oxide which provides corrosion resistance to Ti. Cp-Ti has a high superficial energy and *in vivo* results have proven that provides favorable body reaction that leads to direct apposition of minerals on the bone-Ti interface and Ti Osseointegration (Acreo *et al.*, 1999).

ii. Cytotoxicity of additives: The additives in the Ti-based alloys can cause potential toxicity. Table 2.18 List the potential toxic additives that may cause diseases to the human body system and their replacements (Oldani and Dominguez, 2012).

Table 2.18: Potential toxic additives and their replacement additives

Toxic additives	Tolerance	Potential disease	Replaced additives	References
V, Cu, Sn	Should be avoided	V can cause adverse tissue reaction	Nb, Fe, Mo for V	(Mehta, 2008; Steinemann, 1980)
Co, Ni, Al	Minimal amounts	Al can cause long-term Alzheimer diseases	Ta, Hf, Zr for Al	(Mehta, 2008; Rao *et al.*, 1996)

2.5.2.3 Physical Properties

Ti is very light with a density of 4.5 g/cm^3 (Oldani and Dominguez, 2012) and when comparing the strength by specific strength (strength per density) the Ti and Ti-based alloys exceed any other implant materials as shown in Table 2.19 (Wong *et al.*, 2013).

The Ti-CP (Grade 2) is 99.305 % Ti, O, C and N are the main trace elements influence significantly the Ti yield, tensile and fatigue strengths (Table 2.19). Interstitial elements such as (C and N) strengthen the metal through interstitial solid solution strengthening mechanism, with N having approximately twice the hardening effect (per atom) of either C or O (Oldani and Dominguez, 2012).

Table 2.19: Specific gravities of some metallic implant alloys (Wong *et al.*, 2013)

Alloys	Density (g/cm^3)
Ti and Ti-based alloys	4.5
316 L Stainless steel	7.9
CoCrMo	8.3
CoNiCrMo	9.2
NiTi	6.7

Pure Ti is an allotropic metal have hexagonal closed packed (HCP) crystal structure (Alpha (α)) phase below 882 ºC and transforming to a body centre cubic (BCC) structure (Beta (β)) phase over that temperature. As its typical microstructure is a single alpha phase α-phase, cold work is also an applied strengthening mechanism.

The addition of alloying elements to titanium in Ti6Al4V alloy enables it to have a wide range of properties because Al tends to stabilize the α-phase and V tends to stabilize the β-phase, lowering the temperature of the transformation from α to β. The α-phase promotes good weldability, excellent strength characteristics and oxidation resistance. The addition of controlled amounts of V as a β-stabilizer causes the higher strength of β-phase to persist below the transformation temperature which results in a two-phase system. The β-phase can precipitate by an ageing heat treatment. This microstructure produces local strain fields capable of absorbing deformation energy. Cracks are arrested or deterred at the particles (Oldani and Dominguez, 2012).

Metastable β-Ti alloys were developed for this purpose, with low elastic modulus (Table 2.17) (Guillemot *et al.*, 2004). Low modulus alloys are nowadays desired because the moduli of alloys are required to be much more similar to that of bone to minimizing the stress shielding phenomena. However, they are still greater than that of cortical bone (Oldani and Dominguez, 2012).

2.5.3 Commercial Purity Ti Alloys

Unalloyed Ti, commercially pure titanium (Cp-Ti) is very common Ti-based implants. Cp-Ti can be defined as follows:

i. Cp-Ti has α-alloy phase structure. The α-alloy has a single phase microstructure (Figure 2.1), which promotes good wettability (Davidson *et al.*, 1994).

ii. There are four grades of unalloyed commercially pure titanium (Cp-Ti) (Imam *et al.*, 1983). The mechanical properties of the Cp-Ti grades and Ti6Al4V (ASTM, 2013a, 2013b) are given in Table 2.20 and their impurity composition is observed in Table 2.21. From Table 2.20 and Table 2.21 it can see that the higher impurity content of the Cp-Ti leads to higher strength and reduced ductility. Grade 1 has the lowest O content and yield strength with the highest ductility among all grades. Grade 4 has the highest O content and strength with the ductility (Narayan, 2009).

iii. Cp-Ti can contain a small amount of interstitial elements including O, N, and H with small quantities. These elements affect the mechanical properties through interstitial solid solution strengthening (Davis, 2006).

iv. Cp-Ti, in general, is used in endosseous dental implant due to its characteristic of promoting rapid osseointegration. Grades (3 and 4) in particular are used for fabricating implants for use in osteosynthesis (fracture repair and spinal fusion), however, it has a low mechanical strength (low fatigue strength in particular).

v. Cp-Ti is particularly attractive material, due to its characteristics promoting rapid osseointegration. This is believed to be due to OH^- ions incorporation within the passive TiO_2 layer and their reaction with bone mineral phase constituents (Ca^{2+}) and (PO_4^{-3}) (Narayan, 2009).

Cp-Ti and extra low interstitial Ti-6Al-4V (ELI) are the two most common Ti implant (Oldani and Dominguez, 2012). Table 2.22 compare between Cp-Ti (Grade 2) and Ti-6Al-4V (ELI) (Grade 5) in terms of characteristics and properties.

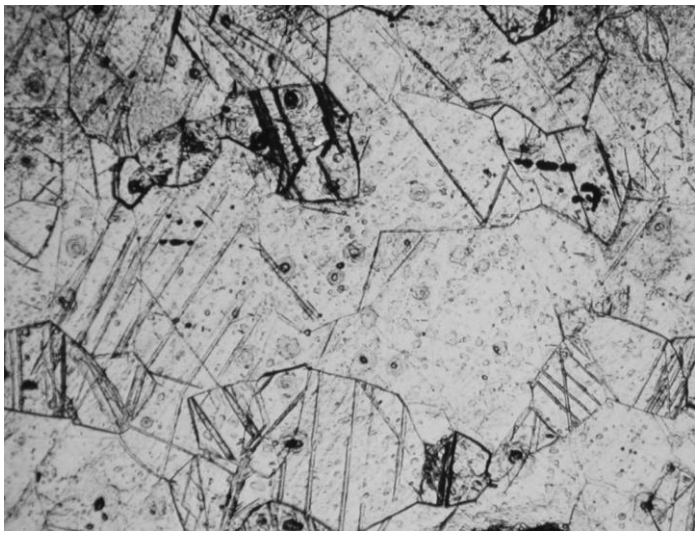

Figure 2.1: SEM of Cp-Ti with α-alloy phase structure (Narayan, 2009)

Table 2.20: Mechanical properties of Ti and Ti alloys (ASTM, 2013a, 2013b)

Properties	Grade 1	Grade 2	Grade 3	Grade 4	Ti6Al4V[a]
Tensile Strength (MPa)	240	345	450	550	860
Yield strength (MPa)	170	275	380	485	795
Ultimate strain (%)	24	20	18	15	10
Young's modulus (GPa)	30	30	30	25	25

Table 2.21: Chemical composition of titanium and its alloy (ASTM, 2013a, 2013b)

Element	Grade 1	Grade 2	Grade 3	Grade 4	Ti6Al4V[a]
Nitrogen	0.03	0.03	0.05	0.05	0.05
Carbon	0.10	0.10	0.10	0.10	0.08
Hydrogen	0.015	0.015	0.015	0.015	0.0125
Iron	0.2	0.3	0.3	0.5	0.25
Oxygen	0.18	0.25	0.35	0.4	0.13
Titanium	Balance				

[a]Aluminium 6.00% (5.50-6.50), vanadium 4.00% (3.50-4.50), and other elements 0.1% total. All the maximum allowable weight percent (ASTM, 2013)

2.6 Titanium Oxide (TiO_2)

TiO_2 is the most investigated single-crystalline system in the surface science of metal oxides due to its wide range of applications. TiO_2 is a preferred system for experimental because it is well-suited for many experimental techniques (Diebold, 2003). Table 2.23 summarizes the bulk properties of TiO_2.

Table 2.22: Comparison between grade 2 and grade 5 characteristics and properties

Ti Type	Grade 2: commercially pure Ti (Cp-Ti)	Grade 5: (Ti-6Al-4V)	References
Chemical composition	N = 0.03, C = 0.1, H = 0.015, Fe = 0.3, O = 0.25, Ti = Balance	N = 0.05, C = 0.08, H = 0.0125, Fe = 0.25, O = 0.13, Ti = Balance	ASTM F 67 ASTM F136
Applications	Dental implants	Total joint replacements, dental implants, surgical wire, plates, screws, IM nails	(Elias *et al.*, 2008) (Wong and Bronzino, 2007) (Herman, 1988)
Advantages	Mechanical properties: has higher Ti purity, higher ductility Physical and chemical properties: high corrosion resistance, excellent biocompatibility and osseointegration	Mechanical properties: higher strength due to the additives in the alloy. Physical and chemical properties: Biocompatible due to the advantage of the Ti, excellent bone contact	
Disadvantages	Mechanical properties: lower strength (unavailability of usage in load bearing applications).	Mechanical properties: high elastic modulus (4 to 6 times higher than cortical bone), it is used in an annealed state and present low shear and low wear resistance when used as orthopedic implant. Physical and chemical properties: Toxic effect resulting from released V and Al.	(Elias *et al.*, 2008; Rao *et al.*, 1996; Steinemann, 1980) (Wong and Bronzino, 2007) (Park and Lakes, 2007)
Mechanical properties	Tensile strength (MPa): 345 Yield strength (MPa): 275 Ultimate strain (%): 20 Young's modulus (GPa): 103-107	Tensile strength (MPa): 860 Yield strength (MPa): 795 Elongation (%): 10 Young's modulus (GPa): 114-120	(Silver and Christiansen, 1999), ASTM F67, ASTM F136
	It provides a favourable body reaction that leads to direct apposition of minerals on the bone-titanium interface	Higher removal torque when used as screws and significantly higher bone contact	(Johansson, 1991) (Acero *et al.*, 1999)

Table 2.23: Bulk properties of titanium dioxide (Samsonov, 2013)

Property	Value
Atomic radius (nm)	
O	0.066 (covalent)
Ti	0.146 (metallic)
Ionic radius (nm)	
O(-2)	0.14
Ti(+4)	0.064

2.6.1 Applications of TiO_2 in Various Fields

TiO_2 can be prepared in the form of powder, crystals, or thin films. While powders are frequently utilized, thin films can be prepared by different methods. Both powders and films can have a crystalline structure ranging from few to hundreds of nanometers (Allouni *et al.*, 2009).

Table 2.24 lists the uses of TiO_2 in different fields. Continued researches have been conducted in the past decades on the nano activities of TiO_2. This is due to the very stable, nontoxic, and cheap TiO_2 nano-materials. The applications of TiO_2 can also be seen in Table 2.24.

Table 2.24: Applications of TiO_2

Type	Application	References
Thin film	Heterogeneous catalysis as a photocatalyst	(Diebold, 2003)
	Solar cells for production of hydrogen and electric energy	
Deposition	Gas sensor	
Powder	White pigment for paints and cosmetic products	
Thin film	Corrosion protective coating	
	Optical coating	
Bulk	Ceramics	
Thin film, deposition	Electric devices as a varistors	
Thin film	Earth science by reducing global worming; photocatalytic activity breaks down nitrous oxides from automobile exhaust and turns them into harmless gases	
Thin film, deposition	Bone implants due to its biocompatibility	
Deposition	Gate insulator for the new generation of MOSFET	(Cheng and Hu, 1999)
additives	Food and Personal Care Products	(Weir *et al.*, 2012)
Nano-materials		
Thin film	Paint	(Chen and Mao, 2007)
Additives	Toothpaste	
Thin film	UV protection	
Thin film, deposition	photovoltaics	
Thin film, deposition	Sensors for various gases and humidity due to the electrical or optical properties which change upon adsorption	
Thin film, deposition	Electrochromics and photochromics	

2.6.2 Photocatalysis of TiO_2

TiO_2 has presented a photocatalytic property. A study by Fujishima and Honda (1972) has discovered that water can photolysis on TiO_2 without an external bias (Fujishima and Honda, 1972). It is believed that the surface defect states may play a role in the decomposition of water into H_2 and O_2. This phenomenon has stimulated much of the early work on TiO_2 (Finklea, 1988).

As a semiconductor, TiO_2 has a photo-assisted ability for degradation of organic molecules (Sakai *et al.,* 1995). The electron-hole pair that is created upon irradiation with sunlight may separate and the resulting charge carriers might migrate to the surface where they react with adsorbed water and oxygen to produce radical species. These species attack any adsorbed organic molecule and can, ultimately, lead to complete decomposition into CO_2 and H_2O. It was shown that subcutaneous injection of TiO_2 slurry in rats, and subsequent near-UV illumination, could slow or halt the development of tumor cells (Sakai *et al.,* 1995). The applications of this process are listed in Table 2.25.

2.6.3 Application of TiO_2 in Biomedical

TiO_2 has been widely used for many years. TiO_2 have strongly been interested in multiple studies, owing to its unique photocatalytic properties, excellent biocompatibility, high chemical stability, and low toxicity. Recent studies have suggested that nano-scale TiO_2 can solve and improve some of the current problems of life science (Yin *et al.,* 2013). Some recent advances in the biomedical applications of TiO_2 are shown in Table 2.26.

2.6.3.1 TiO_2 in Biomedical Implantation

The better interaction between the tissues and Ti implants is believed to be linked to TiO_2, which gives Ti priority over other conventional biometal implants (Hazn *et al.,* 1993). TiO_2 has been attributed to biomedical implantation due to:

Table 2.25: Applications of TiO_2 photocatalysis (Fujishima et al., 2000)

Property	Gregory	Applications
Self-cleaning	Materials for residential and office buildings	Exterior tiles, kitchen and bathroom components, interior furnishings. plastic surfaces, aluminium siding, building stone and curtains, paper window blinds
	Indoor and outdoor lamps and related systems	Translucent paper for indoor lamp covers, coatings on fluorescent lamps and highway tunnel lamp cover glass
	Materials for roads	Tunnel wall. Sound proofed wall. traffic VMS and reflectors
	Others	Tent material, cloth for hospital garments and uniforms and spray coatings for cars
Air cleaning	Indoor air cleaners	Room air cleaner, photocatalyst-equipped air conditioners and interior air cleaner for factories
	Outdoor air purifiers	Concrete for highways, roadways and footpaths, tunnel walls, soundproof walls and building walls
Water purification	Drinking water	River water, ground water. lakes and water-storage tanks
	Others	Fish feeding tanks, drainage water and industrial wastewater
Antitumor activity	Cancer therapy	Endoscopx-like insauments
	Hospital	Tiles to cover the Poor and walls of operating rooms, silicone rubber for medical catheters and hospital garments and uniforms
	Others	Public rest rooms, bathrooms and rat breeding rooms

Table 2.26: Preparation of TiO_2 active surface layers

Application	References
Photodynamic therapy for cancer treatment	(Yin *et al.,* 2013)
Drug delivery systems	
Cell imaging	
Biosensors for biological assay	
Genetic engineering	
Biomedical Implantation: Orthopaedic/dental implants	(Chien *et al.,* 2009)

i. The superior biocompatibility of Ti is due to the thin layer oxide of 1.5-10 nm thick that forms naturally upon exposure to air at room temperature (Sul *et al.,* 2001).

ii. TiO_2 is in direct contact with bone tissue upon implantation. This explains the good biocompatibility of Ti implants (Sul *et al.*, 2002a; Sul *et al.,* 2002d).

iii. TiO_2 provides corrosion resistance and contribute to the biological performance of Ti at molecular and tissue level (Lausmaa and Linder, 1988).

Surface properties of TiO_2 are very important to understand the osseointegration between the implant and bone tissue (Sul *et al.,* 2002a; Sul *et al.,* 2002d). Due to that, many studies of tissue reactions to implant surfaces have been directed at modifying the roughness of TiO_2 (Sul *et al.,* 2002d). Table 2.27 shows the TiO_2 deposition and formation techniques.

Further biocompatibility improvement of Ti-based implants for orthopedic and dental applications has been attempted through the development of apatite coating on the TiO_2 interface (Hayashi *et al.,* 1989; Oliva *et al.,* 1998).

Table 2.27: Biomedical applications of TiO_2

No	Method	Year	References
1	Thermal oxidation	1975	(Fujishima *et al.,* 1975)
2	Sol-gel	1995	(Negishi *et al.,* 1995)
3	Electrophoretic deposition	1995	(Fernández *et al.,* 1995)
4	Silica gel substrate	1998	(Kobayakawa *et al.,* 1998)
5	CVD	1998	(Goossens *et al.,* 1998)
6	Spray-pyrolysis	1998	(Wang *et al.,* 1998a)
7	RF Magnetron sputtering	2002	(Zeman and Takabayashi, 2002)
8	Inorganic-organic graded film	2002	(Takami *et al.,* 2002)
9	Chemical bath deposition	2003	(Gao *et al.,* 2003)
10	Plasma spray	2003	(Berger-Keller *et al.,* 2003)
11	Electron-beam evaporation	2004	(Yang *et al.,* 2004b)
12	Vacuum evaporation	2006	(Miyata *et al.,* 2006)
13	Anodic oxidation	2006	(Mor *et al.,* 2006)

2.6.3.2 TiO_2 crystalline Bioactivity (*In Vitro* Test)

Extensive research on TiO_2 shows that the morphology, surface chemistry, roughness, crystalline phases significantly influences the apatite-inducing ability (Pereira *et al.,* 2014). The crystalline phases of TiO_2, anatase, and rutile, have good ability to induce HA formation on the surface. However, Ti dental implants with native amorphous surface oxide have obtained good osseointegration and clinically were successful (Xia *et al.,* 2011).

Uchida *et al.* 2003 have reported that the epitaxy of apatite crystals were facilitated by the crystalline planar arrangement structure (Uchida *et al.,* 2003). It is believed that Ti-OH groups give rise to the apatite formation in SBF (Leconte *et al.,* 2002). However, certain types of Ti-OH groups in a specific structural arrangement are effective in inducing apatite nucleation. This indicates that a specific structure of

TiO_2 is effective in inducing apatite formation in a body environment (Uchida *et al.*, 2003). The question is how well the interface between the organised hydroxylated surface (Ti-OH) and HA nuclei is structurally matched along with surface charge.

When comparing anatase and/or rutile bioactivity with HA. Anatase is speculated to have a higher bioactivity than rutile, due to a better lattice match with HA and a higher acidity, as well as lower surface ζ-potential, caused by a larger number of hydroxyl groups on the surface. The degree of surface acidity at a given pH is the value of the surface ζ-potential. The surface ζ-potential is lower for a more acidic surface. It has been shown that deposition of HA on anatase, at pH 7.4, is faster than on rutile at the same pH, while a less negative ζ-potential will inhibit the HA nucleation (Svetina *et al.*, 2001). Furthermore, a rise in temperature and ion concentration increases the growth rate of HA (Kim, 2003).

Hydroxylated 110 (anatase) and 0001 (HA) as obtained in Figure .2.2 (a,b) are suggested to have three matching parts between their interface:

i. Hydrogen bond interaction; Ti-OH groups can form hydrogen bonds with OPO_3^{-3} on the HA (0001) surface, and also with OH on the HA (0001).

ii. Crystal lattice matching, i.e. how the Ti-OH groups are arranged on the anatase (110) surface matching the HA (0001)

iii. Stereochemical matching, which is the anatase OH^- arrangement surrounded a Ca^{2+} ion along the c-axis of HA, resulted in oriented nucleation (Mao *et al.*, 1999). The nucleation of the crystallized species and their orientation tend to be determined more by stereochemical matching than lattice matching (Lindberg *et al.*, 2008).

The rutile (101) surface has also a lattice match with HA (0001) (Uchida *et al.*, 2003) as shown in Figure 2.2 (c). However, researches have reported contradictory results. Some reported the preference of anatase over rutile and others reported the contrary in SBF and some others reported preference of anatase with rutile phase as shown in Table 2.28. Abdullah and Sorrell have reported when depositing HA on TiO_2 gel in SBF the superiority reactivity of the anatase phase to be more advantageous for biomaterials applications (Abdullah and Sorrell, 2007a).

Anatase is reported that can effectively attract protein molecules and reduce the formation of connective tissue after implantation (Hamilton *et al.*, 2009; Nan *et al.*, 1998). Anatase has also been reported to have relatively lower strength than

anatase (Li and Ducheyne, 1998). However, regarding TiO_2 produced using anodic oxidation and then incubated in SBF; results obtained a progression of apatite deposition and growth with rutile phase and pore size increased (Yang *et al.*, 2004a). Cui *et al.* (2009) have reported that anatase and rutile phase increase apatite deposition more that anatase or amorphous structure also with an increased pore size (Cui *et al.*, 2009).

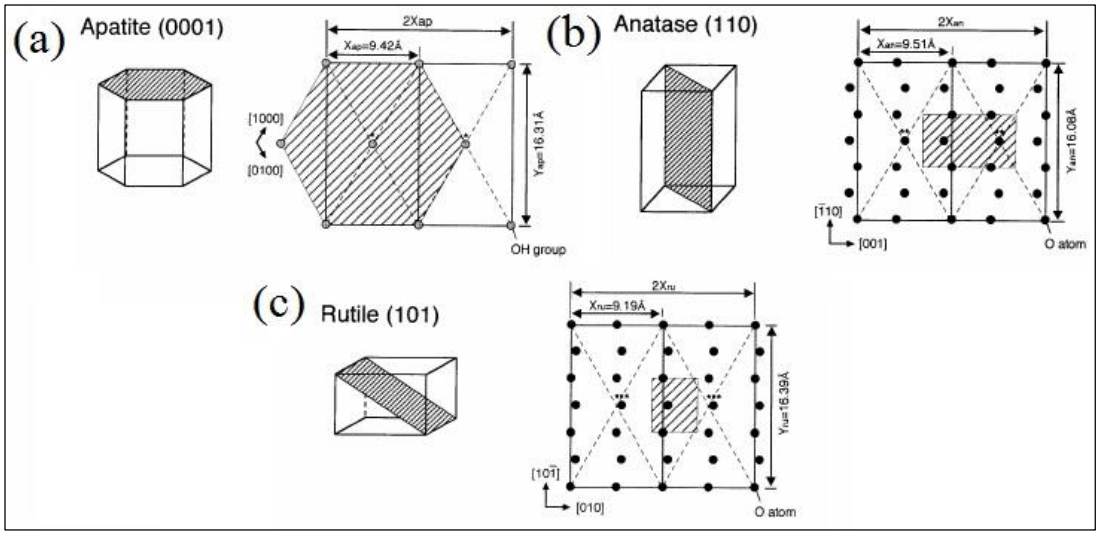

Figure 2.2: Lattice structure matching; (a) HA lattice structure, (b) Anatase (110) lattice matching with HA (0001), (c) Rutile (101) lattice matching with HA (0001) (Uchida *et al.*, 2003)

While *in vitro* assays may generate a quick assessment of cytocompatibility, *in vivo* studies are necessary to fully evaluate new bone growth. A survey of *in vivo* and *in vitro* investigations of bone tissue reactions to anodised titanium implants is listed in Table 2.29. As with *in vitro* analysis, the varied oxide properties not only include thickness, but also morphology, chemical composition, crystallinity, and surface roughness.

2.6.4 Phase Transformation of TiO_2

The Ti-O phase diagram is very rich with many stable phases with a variety of crystal structures (Samsonov, 2013). Figure 2.3 shows the phase diagram of the Ti-O^- and the following is outlined with respect to TiO_2 (Fahmi *et al.*, 1993):

i. Oxygen dissolves up to 30 atom % in the α-Ti phase.

Table 2.28: Parameters and results from studies on of apatite formation ability on TiO_2 in SBF

TiO_2 characterisation	Bioactivity testing	Results/Explanation	References
Treatment: Electrolyte deposition. TiO_2 phase: anatase Nanotube: 11-18 nm	*In vitro*: SBF for 21 days	The matching structure of anatase TiO_2 and apatite may play an important role in the apatite formation ability. Moreover, the cell culture results also indicated that nano-crystalline anatase TiO_2 not only promoted cells differentiation, but also appeared more bioactive while maintaining non-toxicity	(Lin and Yen, 2006)
Treatment: anodic oxidation + heat treatment. TiO_2 phase: anatase + rutile Roughness: 177±0.02 nm	*In vitro*: SBF for 30 days	The surfaces oxidized were fully coated with apatite layer	(Pereira *et al.*, 2014)
Treatment: anodic oxidation. TiO_2 phase: anatase + rutile Roughness: 0.312±0.068 µm Pore size: 100-200 nm	*In vitro*: MEM solution.	TiO_2 with anatase and rutile phase resulted in a higher Ca to P ratio and higher OH stretching	(Song *et al.*, 2009)
Treatment: anodic oxidation. TiO_2 phase: anatase + rutile and rutile Roughness: Pore size: 200 nm	*In vitro*: SBF for 1,3 and 7 days	TiO_2 crystalline (anatase + rutile) and rutile where able to induce apatite. Specially rutile which played an important role in inducing the apatite deposition because of the relationship of lattice matching between rutile and apatite. Surface morphology could also affect apatite deposition	(Cui *et al.*, 2009)
Treatment: anodic oxidation. TiO_2 phase: anatase + rutile and rutile Roughness: Pore size: 200 nm	*In vitro*: SBF for 3 and 6 days	Rutile obtained higher apatite deposition more than anatase or anatase + rutile. The structure of rutile (1 0 1) is matching to the structure of apatite (0 0 0 4). It is reported that the matching structure could be the nuclei for crystal growth.	(Yang *et al.*, 2004a)
Treatment: anodic oxidation. TiO_2 phase: anatase + rutile Roughness: Pore size: 1 µm	*In vitro*: SBF for 3 days	Apatite was able to precipitate on TiO_2 anodised in 0.9M H_2SO_4/0.1M H_3PO_4 for 30 min at 180 V.	(Oh *et al.*, 2008)
Treatment: anodic oxidation. TiO_2 phase: anatase + rutile and rutile Roughness: Pore size: 900 nm	*In vitro*: SBF for 5 days	Ca-rich compounds was able to precipitate on TiO_2 anodised in 1.5 M H_2SO_4/0.3 M H_3PO_4/0.3 M H_2O_2 for 30 min at 180 V.	(Oh *et al.*, 2005)

i. TiO crystallizes in NaCl missing state structure and can be found in a non-stoichiometric form of larger phase width TiO_X ($0.70 \leq x \leq 1.30$).

ii. Rutile is the most stable phase of TiO_2 at normal pressure (5-12 kJ/mol) more stable than anatase (Murray, 1987). The transition from brookite/anatase to rutile at higher temperatures is not reversible (Fahmi *et al.*, 1993).

Table 2.29: Parameters and results from studies of TiO_2 on *in vitro* and *in vivo* studies

TiO_2 characterisation	Bioactivity testing	Results/Explanation	References
Treatment: hydrothermal treatment + heat treatment. TiO_2 phase: anatase Nanotube: 5 - 15 μm	*In vitro*: primary murine alveolar macrophages. *In vivo*: in mice.	This study demonstrates that alteration of anatase TiO_2 nanomaterial into a fibre structure of greater than 15 μm creates a highly toxic particle and initiates an inflammatory response by alveolar macrophages.	(Hamilton *et al.*, 2009)
Treatment: magnetron sputtering + heat treatment. TiO_2 phase: anatase + rutile Roughness: 2.8 – 8.08 μm	*In vitro*: cell culture (CHO-K1)	These results indicate that TiO_2 thin films do not affect mitochondrial function and proliferation of CHO-K1 cells, and back up the use of TiO_2 thin films in biomedical science.	(Cervantes *et al.*, 2016)
Treatment: anodic oxidation. TiO_2 phase: anatase, anatase + rutile Pore size: 0.2-5 μm	*In vitro*: MG63 cells	Anatase and rutile obtained more cell proliferation that anatase. Also proliferation increased with increased pore size	(Ha *et al.*, 2006)
Treatment: anodic oxidation. TiO_2 phase: anatase, anatase + rutile Oxide thickness: 0.2-1 μm Pore size: 1.27-2.10 μm	*In vivo*: Rabbit model	Enhanced bone bonding	(Sul *et al.*, 2002b; Sul *et al.*, 2002c)
Treatment: anodic oxidation. TiO_2 phase: anatase Oxide thickness: ≤ 0.3 μm	*In vivo*: implant in rats'tibia	Exhibited high osteoconductivity more that 40% in bone implant contact ratio R_{B-I} value (in cortical bone)	Yamamoto *et al.*, 2011)
Treatment: anodic oxidation + heat treatment TiO_2 phase: anatase Ra/ μm: ≤ 0.1	*In vivo*: rat's tibiae	Exhibited high osteoconductivity more that 58% in bone implant contact ratio R_{B-I} value (in cortical bone)	(Zuldesmi *et al.*, 2013)

2.6.5 Crystal Structure of TiO_2

Titanium oxide crystallizes in three major different structures:

i. Anatase (crystal unit: tetragonal).

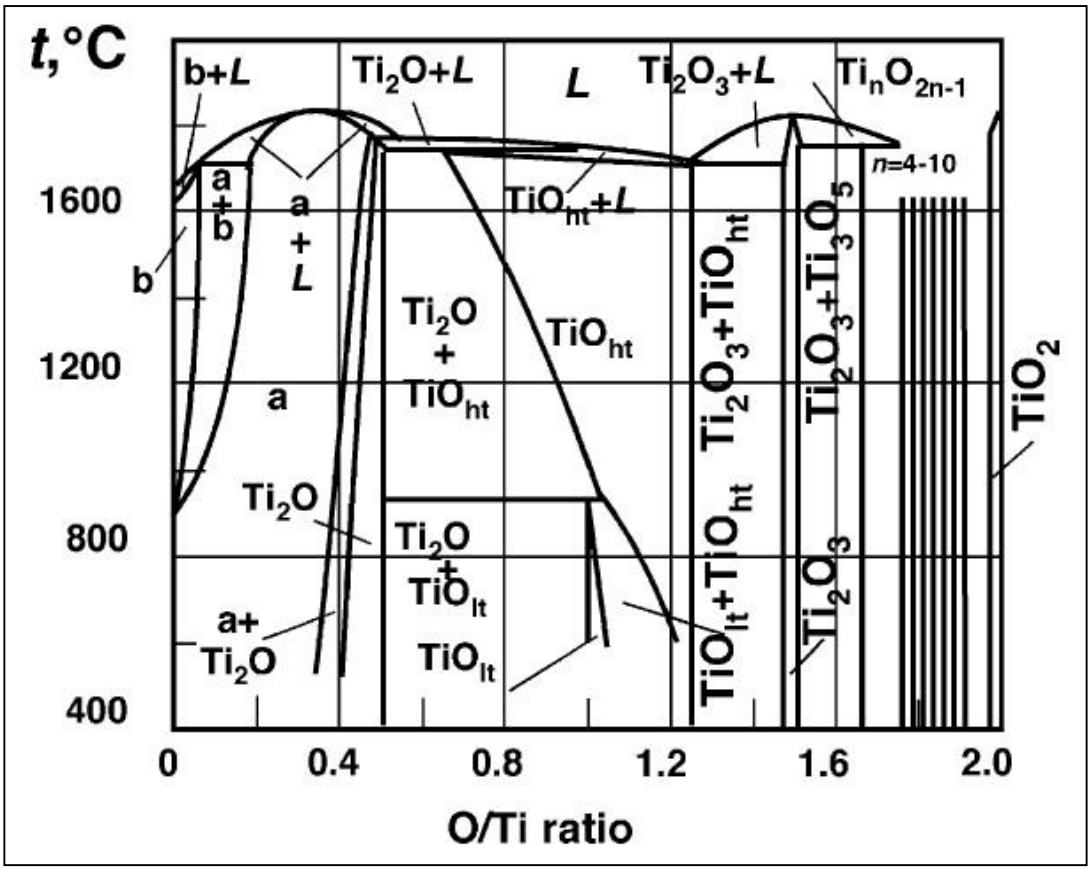

Figure 2.3: Phase diagram of the Ti-O system (Samsonov, 2013)

ii. Rutile (crystal unit: tetragonal).

iii. Brookite (crystal unit: rhombohedral).

Other structures exist as well, for example, Contunite TiO_2 has been synthesized at high pressures and is one of the hardest polycrystalline materials known (Dubrovinsky *et al.,* 2001). However, only rutile and anatase play any role on the applications of TiO_2 as they have been studied with surface science techniques (Diebold, 2003).

2.6.5.1 Anatase

Anatase is the most stable phase for nano-particles below 11 nm (Burnside *et al.,* 1998). Anatase unit cell is shown in Figure 2.4. For anatase and rutile, both of their structure, the basic building block consists of a Ti atom surrounded by six O atoms in a more or less distorted octahedral configuration (Diebold, 2003). Anatase has two low energy surfaces; (101) and (001) as shown in Figure 2.5 (a,b), which is common for natural crystals (Hengerer *et al.,* 2000). The (100) surface as shown in Figure 2.5 (c)

is less common on typical nano-crystals but is observed on rod-like anatase grown hydrothermally under basic conditions (Ramamoorthy *et al.*, 1994). From the tetragonal bulk unit cell of anatase a=b= 3.782 Å, c=9.502 Å as seen in Figure 2.4 has slightly distorted octahedral that are the basic building units. The bond lengths and angles of the octahedrally coordinated Ti atoms are indicated and the stacking of the octahedra in both structures is shown on the right sided (Diebold, 2003).

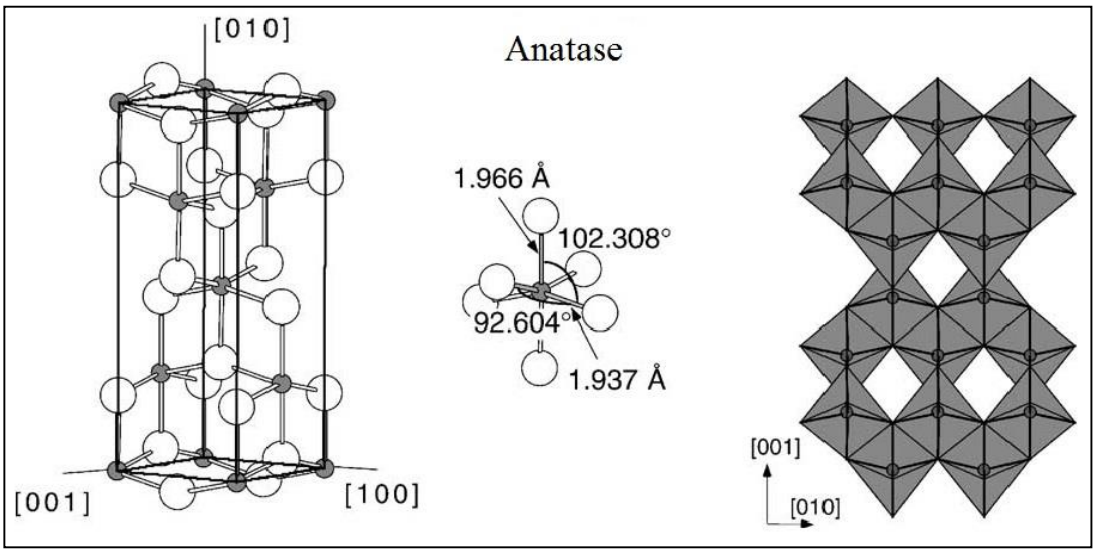

Figure 2.4: Bulk structures of anatase (Diebold, 2003)

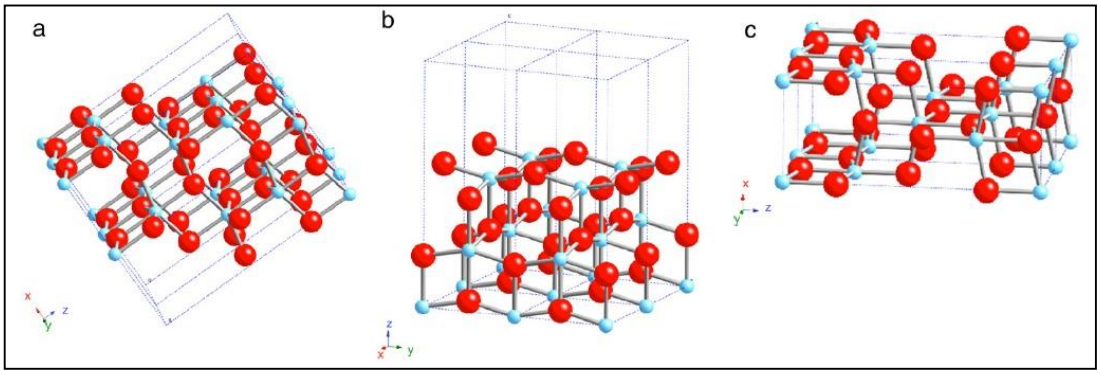

Figure 2.5: Schematic representations of selected low-index faces of anatase: (a) (101); (b) (100); and (C) (001) (Fujishima *et al.*, 2008)

2.6.5.2 Rutile

Rutile is the most stable phase for particles above 35 nm in size (Zhang and Banfield, 1998). Rutile has three main crystal faces, two that are quite low in energy and are thus considered to be important for practical poly-crystalline or powder materials.

These are (110) and (100) (Figure 2.6 a, b). The most thermally stable is (110), and therefore it has been the most studied (Figure 2.6 c) (Ramamoorthy *et al.*, 1994). From Figure 2.7 the tetragonal bulk unit cell of rutile has the dimensions, a=b=4.587 Å, c=2.953 Å. The structure has slightly distorted octahedral that are the basic building units. The bond lengths and angles of the octahedrally coordinated Ti atoms are indicated and the stacking of the octahedra in both structures is shown on the right sided (Diebold, 2003).

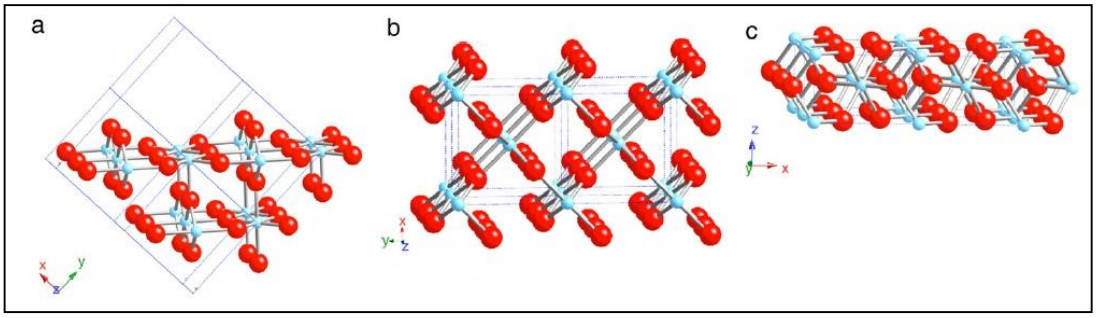

Figure 2.6: Schematic representations of selected low-index faces of rutile: (a) (110); (b) (100); and (C) (001) (Fujishima *et al.*, 2008)

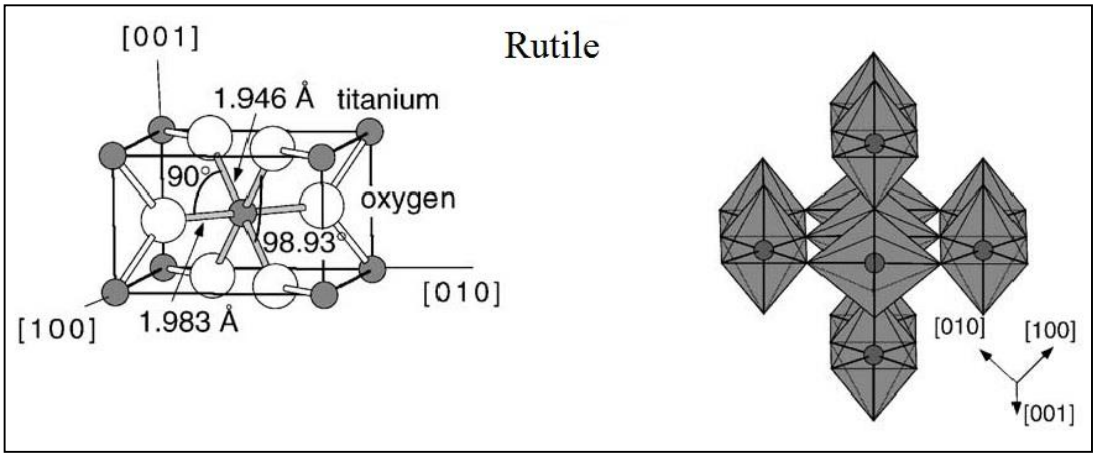

Figure 2.7: Bulk structures of rutile (Diebold, 2003).

2.6.5.3 Brookite

Brookite has been found to be the most stable for nanoparticles in the 11-35 nm range (Burnside *et al.*, 1998). Recently, the brookite phase, which is rarer and more difficult to prepare, has also been studied as a photocatalyst. The order of stability of the crystal faces is (010) < (110) < (100) (Figure 2.8) (Beltrán *et al.*, 2006).

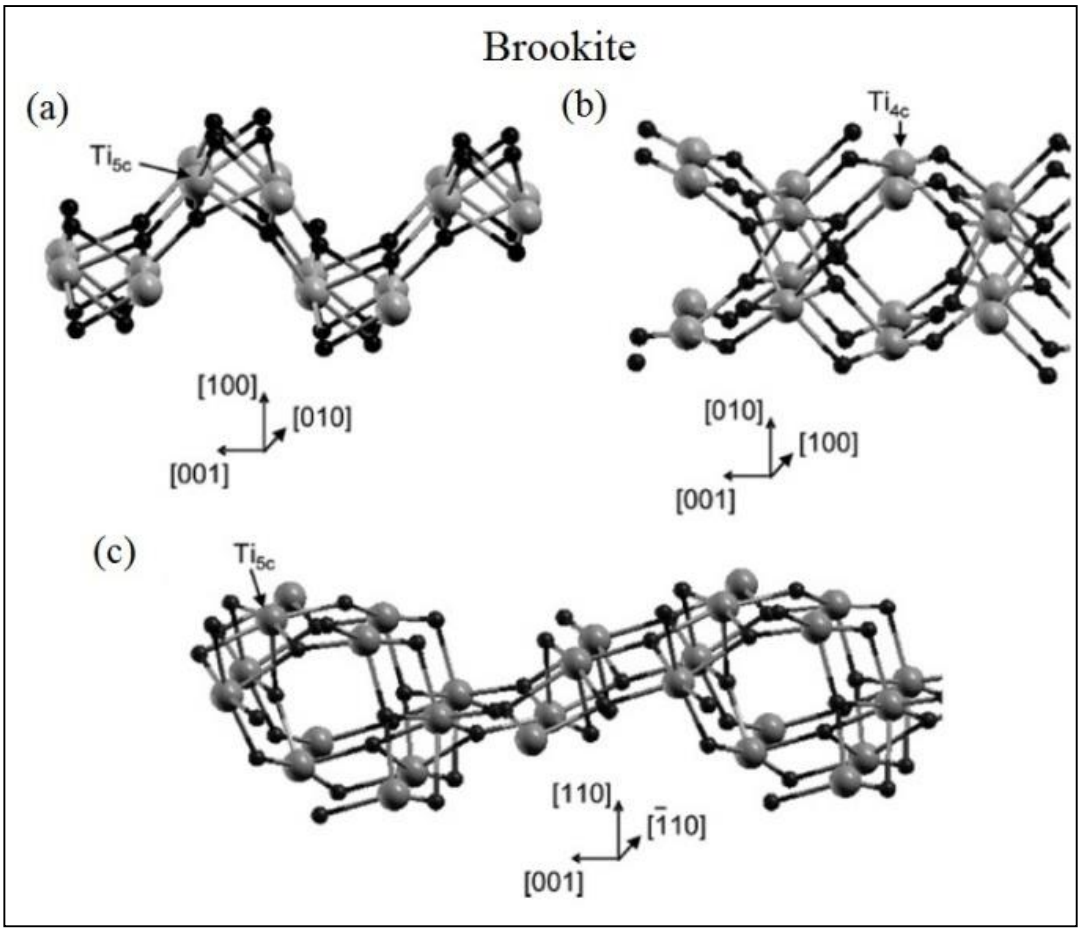

Figure 2.8: Schematic representation of the brookite structure, crystal faces: (a) (100), (b) (010), (c) (110) (Beltrán *et al.*, 2006)

2.7 Properties of TiO_2

Properties of TiO_2 comprise; bulk properties, physical properties, phase properties, photocatalytic properties and colour properties.

2.7.1 Bulk Properties of TiO_2

The bulk properties of TiO_2 will be summarized in Table 2.30.

2.7.2 Physical Properties of TiO_2

In the synthesis of TiO_2 films by various methods, the initial crystalline TiO_2 phase formed is generally anatase (Shin *et al.*, 2005). From a structural perspective, this

could be due to the greater ease of the short-range ordered TiO_6 octahedra in arranging into long-range ordered anatase structure owing to the less-constrained molecular construction of anatase relative to rutile (Matthews, 1976). Alternatively, from a thermodynamic perspective, the more rapid re-crystallization of anatase could be due to the lower surface free energy of this polymorph, despite the lower Gibbs free energy of tile (Ghosh *et al.,* 2003). That is, the higher surface free energy of rutile crystallites may favour the crystallization of anatase.

Table 2.30: Properties of crystal structures of TiO_2

Propertiy	TiO_2		
	Anatase	Rutile	Brookite
Crystal structure	Tetragonal	Tetragonal	Rhombohedral
Atoms per unit cell	4	2	
Lattice parameters (nm)	a=0.3785 c=0.9514	a=0.4594 c=0.29589	a=0.5436 b=0.9166 c=0.5135
Unit cell volume (nm^3)[h]	0.1363	0.0624	-
Molar Mass	[a,b]79.886 g/mol		
Apperance	[d,e,f] White to pale yellow	[d,e,f] Pale brown, yellowish brown, gray	[d,e,g] White to grayish white or yellowish white
Density (g/m^3)	[c] 3830	[c] 4240	[c] 4170
Odor	[a,b]Odorless		
Melting point (°C)	-	[c] 1870	-
Crystal structure	[c] Tetragonal	[c] Tetragonal	[c] Rhombohedral
Solubility in water	[a,b] Insoluble		
Calculated indirect bandgap (eV)	3.23–3.59 345.4–383.9	3.02–3.24 382.7–410.1	
Experimental bandgap (eV) (nm)	~3.2 ~387	~3.0 ~413	
[i] Refractive index n_g n_p	2.5688 2.6584	2.9467 2.6506	2.809 2.677
Solubility in HF	Soluble	Insoluble	-
Solubility in H2O	Insoluble	Insoluble	-
Hardness (Mohs)	5.5–6	6–6.5	5.5–6
Bulk modulus (GPa)	183	206	-
Standard heat capacity, C_p^0 298.15J/(mol °C)	55.52	55.06	-

[a](Wells, 2012), [b](Greenwood and Earnshaw, 2012); [c](Samsonov, 2013); [d](Palache *et al.,* 1954); [e](Deer, Howie and Zussman, 1992), 1962, [f](Howard *et al.,* 1991); [g](Meagher and Lager, 1979); [h](Hanaor and Sorrell, 2011); [i](Samsonov, 2013); [j](Kavan *et al.,* 1996)

It should be noted that it is possible to form rutile under near room temperature conditions (Shin *et al.*, 2005). Hydrothermal methods of synthesis, which can facilitate the precipitation of crystalline TiO_2 directly from a liquid phase, can be controlled to precipitate rutile. Aside from this method, rutile is obtained only through high-temperature treatment. Table 2.31 summarizes the phases that can result from various synthesis methods at room temperature and at elevated temperatures.

Table 2.31: Common synthesis methods of titanium dioxide and resultant phases (Hanaor and Sorrell, 2011)

Synthesis method	Mechanism	Phases formed			
		Amorphous	Anatase	Rutile	Anatase + Rutile
Flame pyrolysis of $TiCl_4$	Combustion of $TiCl_4$ with oxygen; used in industrial processes		✓		✓
Solvothermal/ hydrothermal	Precipitation of TiO_2 from aqueous or organic solution at elevated temperatures		✓	✓	✓
Chemical vapour deposition	Spraying of Ti-bearing solution	✓	✓	✓	✓
Physical vapour deposition	Deposition of evaporated Ti and its subsequent oxidation	✓	✓	✓	✓

Control of the conditions that affect the kinetics to control the anatase to rutile phase transformation is of considerable interest. The generation of the phases of TiO_2 depends significantly on the synthesis parameters, which in turn affect the product. The kinetics of these processes typically is considered in terms of temperature and time. In terms of the former, pure bulk anatase is considered widely to begin to transform irreversibly to rutile in air at 600 ^oC (Li *et al.*, 2005); however, the reported transition temperatures vary in the range 400-1200 ^oC (Zhang *et al.*, 2008) owing to the use of different methods of determining the transition temperatures, raw materials, and processing methods. The anatase to rutile transformation is not instantaneous; it is time dependent because it is reconstructive (Jamieson and Olinger, 1969). Consequently, the kinetics of the phase transformation must be interpreted in terms of all of the factors that influence the requisite temperature-time conditions. These parameters for undoped anatase are:

i. Particle size.

ii. Particle shape (aspect ratio).

iii. Surface area.

iv. Atmosphere.

v. Volume of sample.

vi. Nature of sample container.

vii. Heating rate.

viii. Soaking time.

ix. Impurities (from raw materials and container).

x. Measurement technique.

2.7.3 Phase Differentiation and Quantification of TiO_2 Crystalline

Examination of the kinetics of the anatase to rutile phase transformation may involve assessment of the relative quantities of anatase and rutile following heating in specific conditions of heating rate, temperature, and time in order to examine the effects of parameters such as dopants, particle size, and atmosphere on the resultant phase assemblage. Quantification of phase proportions usually is carried out by x-ray diffraction (XRD) (Ohno *et al.,* 2003). XRD patterns spectra of rutile and anatase powders can be illustrated in Figure 2.9.

Such analyses often are done using the method of Spurr and Myers (Spurr and Myers, 1957), which utilizes the ratio of the rutile (110) peak at 27.355^o 2θ to the anatase (101) peak at 25.176^o 2θ. The ratio of the intensities of these peaks, I_R/I_A, is used in the empirically determined formula in Equation (2.1) to give the weight fractions of anatase and rutile:

$$\frac{W_R}{W_A} = 1.22\frac{I_R}{I_A} - 0.028\infty \qquad (2.1)$$

Despite the number of the above researchers who have utilized this formula in their investigations into the ART, consideration of the relevant issues reveals a number of factors that may affect the accuracy of the results:

i. Preferred orientation: rutile and/or anatase crystallites may be present in preferred orientation owing to morphological and/or sample preparation effects, which may lead to altered XRD relative peak intensities.

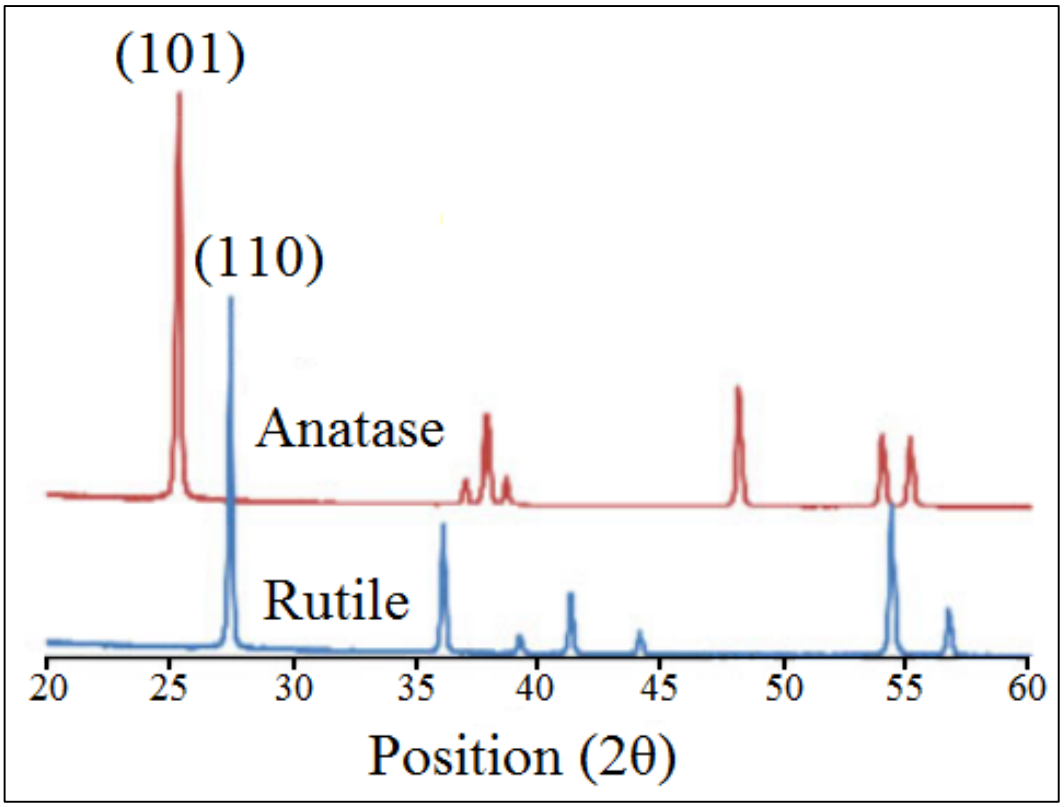

Figure 2.9: XRD patterns spectra of rutile and anatase powders (Hanaor, 2007)

ii. Encapsulation: rutile crystallites may grow as an over-layer of rutile on anatase particles (Bickley *et al.*, 1991) or, alternatively, rutile may form the bulk of the anatase grains, leaving a surface layer of anatase on rutile particles (Zhang *et al.*, 2008), thereby compromising the basis for the intensities of the XRD peaks.

iii. Lattice distortion: the presence of dissolved dopants and/or impurities, especially if differential solubility occurs, may alter the peak heights and areas, thereby altering the relative intensities of the XRD peaks.

iv. The degree of crystallinity: the presence of dopants may increase (nucleation) or decrease (lattice distortion/ stress) the degree of crystallinity, which would alter the consequent peak intensities, particularly if these dopants are preferentially present in one of the phases.

2.7.4 Photocatalytic Properties of TiO_2

2.7.4.1 Photoactivity of TiO_2

The photoactivity of TiO_2 is one of its most attractive properties. The creation of electron-hole pairs through irradiation of light, either in TiO_2 itself, or in adsorbed molecules, and the following chemical or electron transfer reactions are at the heart of TiO_2 based photodevices applied in a range of areas (Fujishima and Honda, 1972). All photoinduced phenomena are activated by an input of super-bandgap energy to the semiconductor TiO_2. Absorption of a photon with enough energy leads to a charge separation due to an electron promotion to the conduction band and a generation of a hole (h^+) in the valence band. The subsequent mode of action of the photogenerated electron-hole pair (e^--h^+), determines which of the phenomena is the dominant process because even if they are intrinsically different processes, they can and in fact take place concomitantly on the same TiO_2 surface.

2.7.4.2 Photocatalysis Phenomena of TiO_2

Photocatalysis is a well-known process and is mostly employed to degrade or transform (into less harmful substances) organic and inorganic compounds and even microorganisms. The recently discovered wettability, termed as (superhydrophilicity) (Fujishima *et al.,* 2008), presents a large range of applications in cleaning and anti-fogging surfaces. The detailed material properties required for enhanced efficiency are different from each other. For enhanced photocatalysis, deep electron traps and high surface acidity are needed to lengthen the lifetime of photoexcited electrons and holes and to ensure better adsorption of organic substances on the surface. Meanwhile, low surface acidity and, most of all, a large quantity of Ti^{3+} is essential for hydrophilic surface conversion. These differences are related to the fact that photocatalysis is more likely to be sensitive to bulk properties, while hydrophilicity can be definite as an interfacial phenomenon (Carp *et al.,* 2004).

Semiconductor electronic structures are characterised by a filled valence band (VB) and an empty conduction band (CB) and can act as sensitizers for light-reduced redox processes. When a photon with an energy of hv matches or exceeds the bandgap

energy E_g of the semiconductor, an electron (e_{CB}^-), is promoted from the valence band, into the conduction band, leaving a hole, (h_{vB}^+), behind. Excited state conduction-band electrons and valence-band holes can react with electron donors and electron acceptors adsorbed on the semiconductor surface or within the surrounding electrical double layer of the charged particles or recombine and dissipate the input energy as heat, get trapped in metastable surface states. The above process in the photocatalysis is illustrated in Figure 2.10.

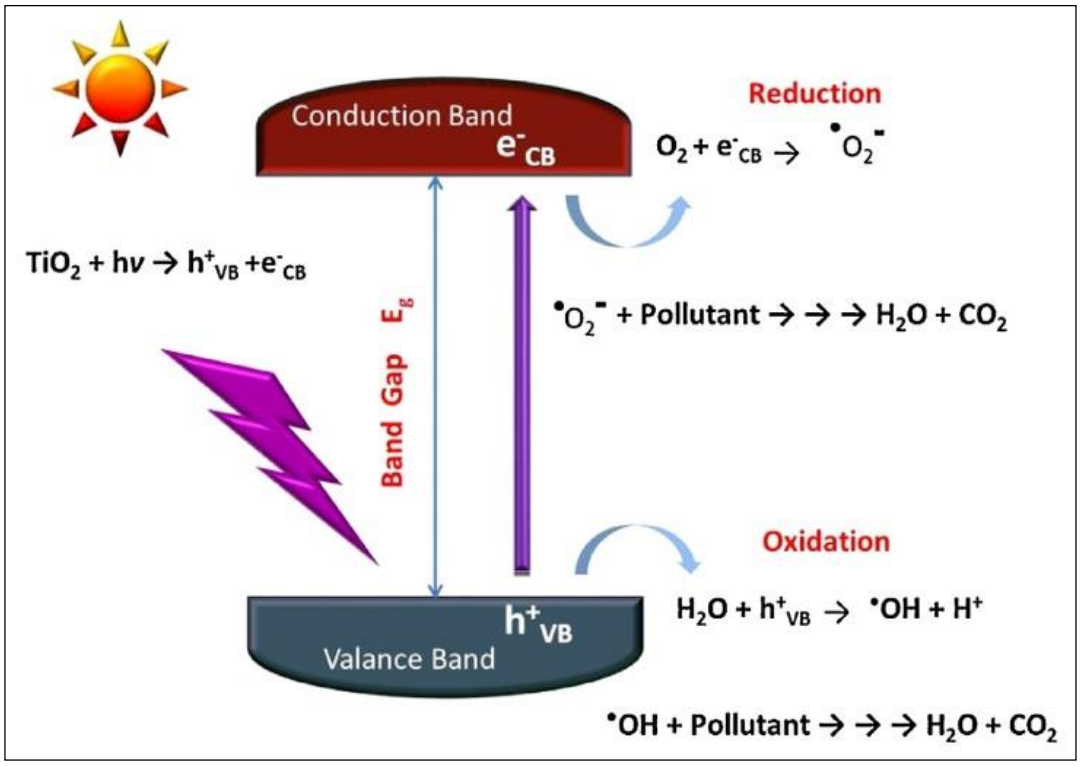

Figure 2.10: Schematic illustration of various processes occurring after photoexcitation of pure TiO_2 with UV light (Banerjee *et al.*, 2015)

For a semiconductor photocatalyst to be efficient, the different interfacial electron processes involving (e_{CB}^-) and (h_{vB}^+) must compete effectively with the major deactivation processes involving ($e_{CB}^- - h_{vB}^+$) recombination, which may occur in the bulk or at the surface (Carp *et al.*, 2004). TiO_2 has a relatively slow rate of charge carrier recombination in comparison with other semiconductors (Zhou *et al.*, 2006), Ideally, a semiconductor photocatalyst should be chemically and biologically inert, photocatalytically stable, easy to produce and to use, efficiently activated by sunlight, able to efficiently catalyze reactions, cheap, and without risks for the environment or humans. TiO_2 is close to being an ideal photocatalyst, displaying almost all the above

properties. The single exception is that it does not absorb visible light (Carp *et al.*, 2004). TiO_2 photocatalysis mechanism can be described as below (Hoffmann *et al.*, 1995):

Charge-carrier generation:

$$TiO_2 + h\nu \rightarrow e^-_{CB} + h^+_{VB} \quad (2.2)$$

Charge-carrier trapping:

$$h^+_{VB} + [-Ti^{4+}OH] \rightarrow [-Ti^{4+}OH^{\bullet+}] \quad (2.3)$$

$$e^-_{CB} + [-Ti^{4+}OH] \rightarrow [-Ti^{3+}OH] \quad (2.4)$$

or

$$e^-_{CB} + Ti^{4+} \rightarrow Ti^{3+} \quad (2.5)$$

Charge-carrier recombination on the surface:

$$e^-_{CB} + [-Ti^{4+}OH^{\bullet+}] \rightarrow Ti^{4+}OH \quad (2.6)$$

$$h^+_{VB} + [-Ti^{3+}OH] \rightarrow Ti^{4+}OH \quad (2.7)$$

Interfacial charge transfer:

$$[-Ti^{4+}OH^{\bullet+}] + R_{ed} \rightarrow [-Ti^{4+}OH] + R^{\bullet+}_{ed} \quad (2.8)$$

$$[-Ti^{3+}OH] + O_x \rightarrow [-Ti^{4+}OH] + O^{\bullet-}_x \quad (2.9)$$

$$Ti^{3+} + O_x \rightarrow Ti^{4+} + O^{\bullet-}_x \quad (2.10)$$

Where [-Ti^{4+}OH] represents OH group of TiO_2, e^-_{CB} is a conduction band electron, h^+_{VB} is a valence-band hole, R_{ed} is an electron donor (i.e. reductant), O_x is an electron acceptor (i.e. oxidant), [-$Ti^{4+}OH^{\bullet+}$] is the surface-trapped VB hole (i.e. surface bound hydroxyl radical), and [-Ti^{3+}OH] is the surface-trapped CB electron. Above reactions may be summarized as follows:

$$(Ox_1)_{ads} + (\mathrm{Re}d_2)_{ads} \xrightarrow{h\nu \geq E_g} \mathrm{Re}d_1 + Ox_2 \qquad (2.11)$$

Depending on whether the sign of the change in Gibbs free energy (ΔG°) of the above reaction is negative or positive, the semiconductor-sensitized reaction may be an example of photocatalysis or photosynthesis, respectively (Bard, 1980).

Both crystal structures, anatase, and rutile, are commonly used as a photocatalyst, with anatase showing a greater photocatalytic activity (Linsebigler *et al.*, 1995) for most reactions. It has been suggested that this increased photoreactivity is due to anatase's slightly higher Fermi level (3.2 eV for anatase and 3.0 eV for rutile), lower capacity to absorb oxygen and a higher degree of hydroxylation (i.e. a number of hydroxyl groups on the surface) (Tanaka *et al.*, 1991). Reactions in which both crystalline phases have the same photoreactivity (Deng *et al.*, 2002) or rutile a higher one (Mills *et al.*, 2003) are also reported. Furthermore, there are also studies which claim that a mixture of anatase (70-75%) and rutile (30-25%) is more active than pure anatase (Ohno *et al.*, 2001). The disagreement of the results may lie in the intervening effect of various coexisting factors, such as specific surface area, pore size distribution, crystal size, and preparation methods, or in the way the activity is expressed (Carp *et al.*, 2004).

2.7.4.3 UV Irradiation

Sunlight is the visible light from the sun. While the solar radiation is the combination of ultraviolet radiation (UV), visible light and the infrared that manages to reach the earth's surface. The difference between each radiation can be distinguished using their wavelength. The ultraviolet radiation (UV) is defined as that portion of the electromagnetic spectrum between x-rays (<100 nm) and visible light (>400 nm and <700 nm), i.e. the wavelength is between 100 nm and 400 nm as obtained in Figure 2.11 (Sutherland, 1997). While Table 2.32 lists the divisions of UV irradiation and their ranges in wavelength and photon energy. From the table, it can be noticed that the wavelength range of (200-280 nm) which is labeled as UVC does not reach the earth's surface because the atmosphere absorbs it. The solar UV, in general, is 95% UVA (315-400 nm) and 5% UVB (280-315 nm) (Young, 2009). However, an exposure

to UVB and UVA radiation is associated with photochemical damage to cellular systems (Youn *et al.*, 2011).

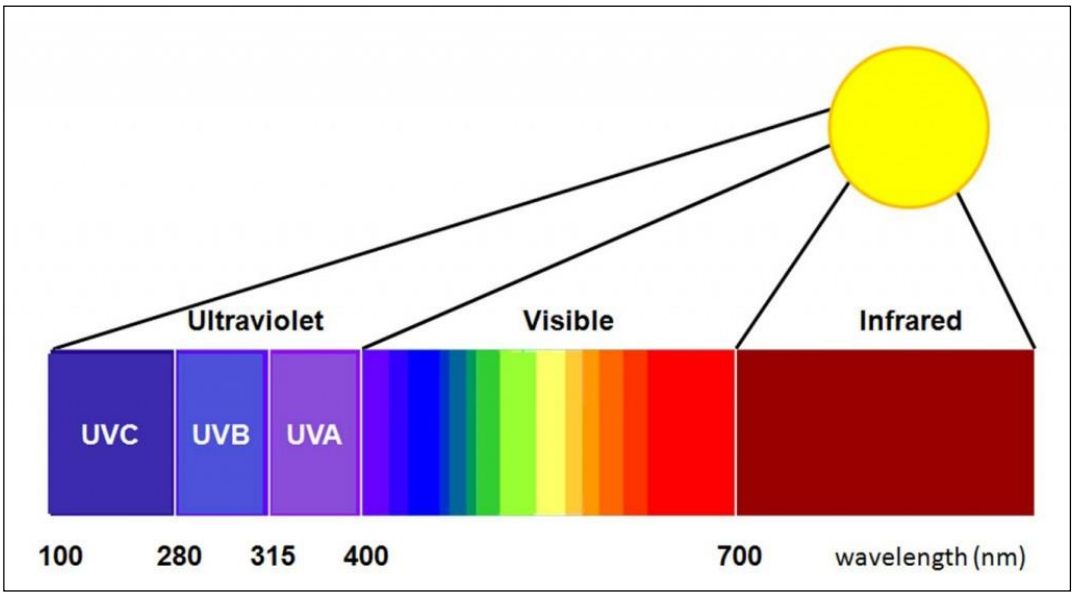

Figure 2.11: Sunlight spectrum analysis (Coolibar, 2011)

Table 2.32: Types of UV irradiation (Dynamics, 2013)

Type	Abbreviation	Wavelength (nm)	Energy/ Photon (eV)
UVA (long wave, or black wave)	UVA	315 mn-400 nm	3.10-3.94 eV
UVB (medium wave)	UVB	280 nm-315 nm	3.94-4.43 eV
UVC (short wave, or germicidal)	UVC	200 nm-280 nm	4.43-12.4 eV
Vacuum Ultraviolet	VUV	100 nm-200 nm	6.20-124 eV

2.7.4.4 Photoinduced Superhydrophilicity of TiO_2

UV illumination of TiO_2 may induce a patchwork of superhydrophilicity (i.e. photoinduced superhydrophilicity or PSH) across the surface that allows both water and oil to spread (Wang *et al.*, 1997). This PSH is accompanied by photocatalytic activity, as both phenomena have a common ground; so the surface contaminants will be either photomineralized or washed away by water. One possible application is self-cleaning windows.

TiO_2 upon exposed to radiation exceeding its bandgap; this radiation normally is in the UV wavelength region (290-380 nm). These electron-hole pairs are formed when an electron is elevated from the valence to the conducting band, leaving behind an electron-hole, as shown in Figure 2.12 (Herrmann, 1999). Where electrons reduce

the Ti^{4+} to Ti^{3+} state and thereby the oxygen atoms will be ejected (creation of oxygen vacancies). Oxygen vacancies will increase the affinity for water molecules and thereby transform the surface hydrophilic (Banerjee *et al.*, 2015). The subsequent dissociative adsorption of water at the site renders it more hydroxylated. An increased amount of chemisorbed -OH leads to an increase of van der Waals forces and hydrogen bonding interactions between H_2O and -OH. Water can easily spread across the surface and hydrophilic properties will be enhanced (Yu and Zhao, 2001; Yu *et al.*, 2001) as shown in Figure 2.13.

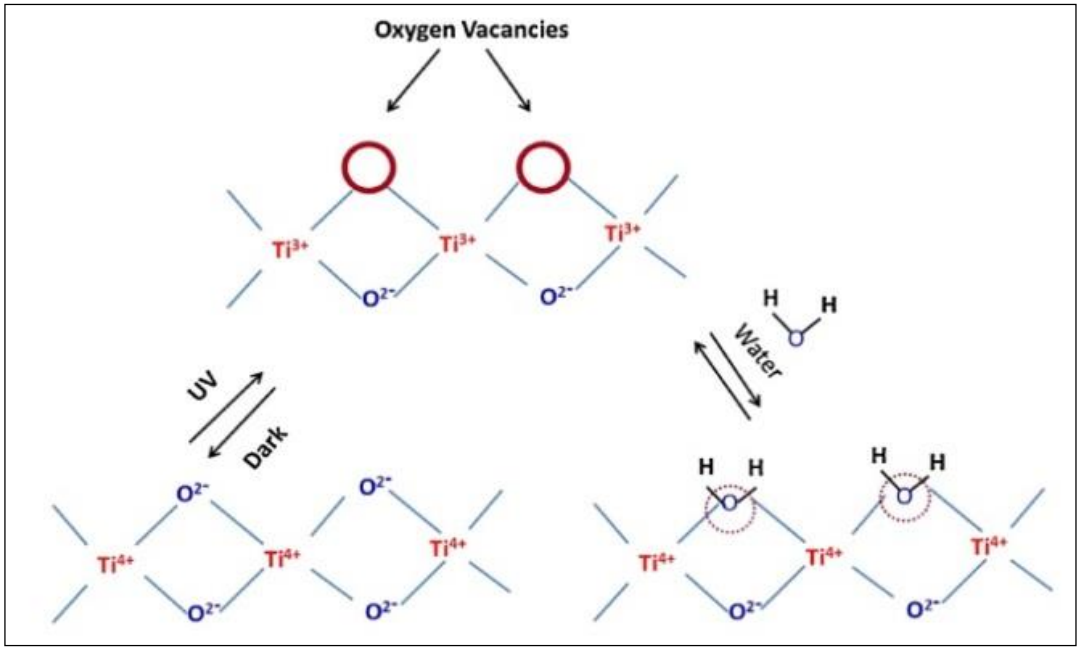

Figure 2.12: Schematic representation of photo-induced hydrophilicity (Banerjee et *al.*, 2015)

Water adsorption does not occur uniformly but produces an amphiphilic surface with alternating hydrophilic and oleophilic regions at the scale of several nanometres (usually <10 nm in size) (Wang *et al.*, 1997). The hydrophilic domains align along the bridging oxygen sites. The reduced sites can be re-oxidized by air and the weakly bound hydroxyl groups reactively desorb (over some time, typically days in the dark) from the surface that returns to a more hydrophobic form. The longer the surface is illuminated with UV light, the smaller the contact angle for water becomes (contact angles close to 0^o mean that water spreads perfectly across the surface). As far as the geometry of the surface is concerned, the hydrophilic properties are known to be enhanced by fine surface roughness (Yu *et al.*, 2002; Yu and Zhao, 2001). PSH

was found to be of primary commercial importance due to the anti-fogging and self-cleaning properties of the deposits (Carp *et al.*, 2004).

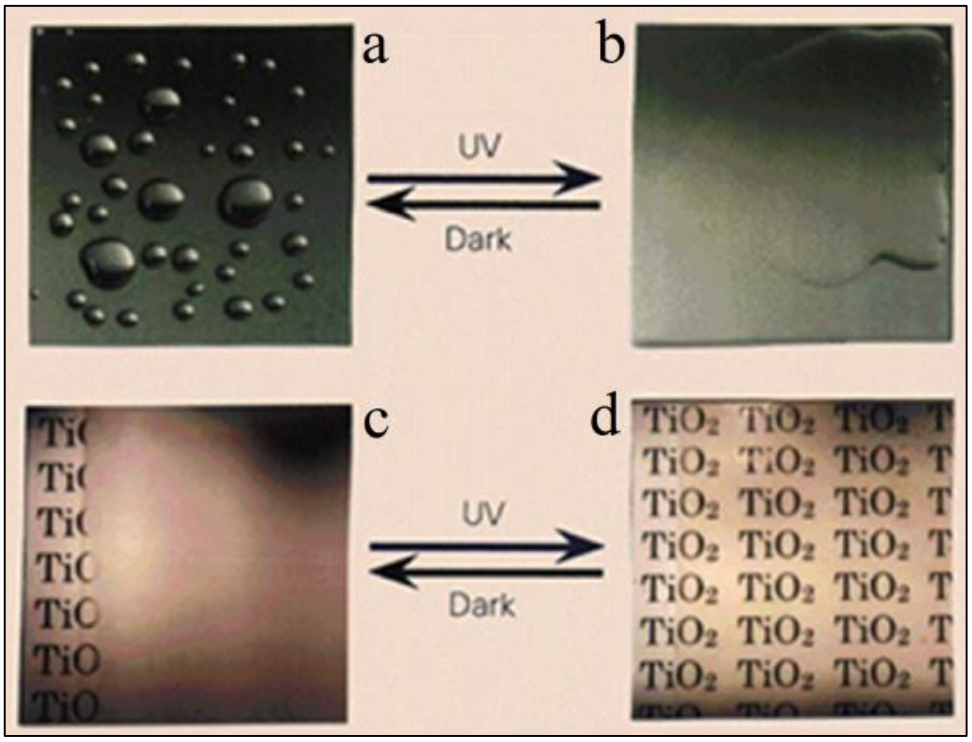

Figure 2.13: Photoinduced wettability switching, where a hydrophobic TiO_2 surface (a) is converted into a superhydrophilic surface (b) upon UV-irradiation, (c) exposure of a hydrophobic TiO_2-coated glass to water vapor results in the formation of fog (small water droplet), (d) antifogging effect induced by UV-illumination (Wang *et al.*, 1997)

2.7.4.5 TiO_2 Crystalline Photoactivity

TiO_2 photocatalytic activity strictly depends on its crystal structure: in fact, both the anatase and the rutile allotropic forms show photocatalytic efficiency, while the amorphous oxide does not. Nevertheless, due to their high bandgap values (rutile 3.0 eV and anatase 3.2 eV), for both phases light radiation absorption and the subsequent photoactivity are established only under UV irradiation (λ<400 nm) (Brunella *et al.*, 2007). An example is shown in Figure 2.14 showing process of decomposition of organic pollutants.

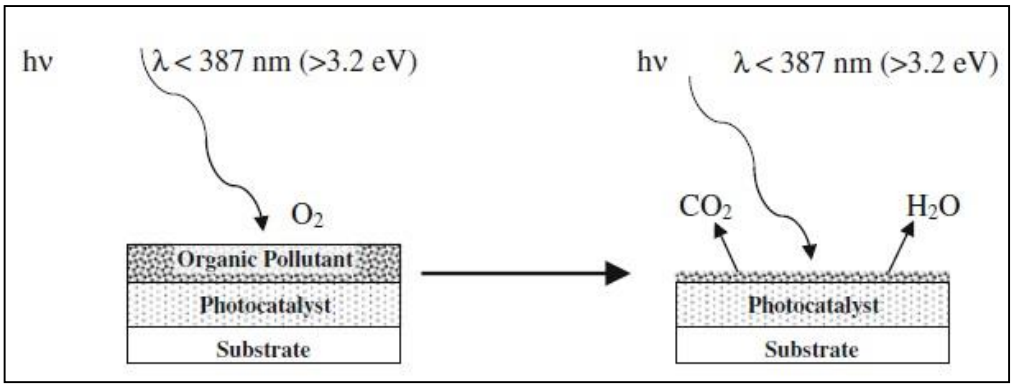

Figure 2.14: Schematic illustration of the photo-oxidation of an organic pollutant on a photocatalyst surface (Hanaor and Sorrell, 2011)

Despite the larger experimental bandgap of anatase compared to rutile, the photocatalytic performance of anatase generally is considered superior to that of the more stable rutile. This is attributed to:

i. A higher density of localized states.

ii. Consequent surface-adsorbed hydroxyl radicals.

iii. Slower charge carrier recombination in anatase relative to rutile (Setiawati and Kawano, 2008), parameters that contribute to improved performance.

Owing to the different crystal structures and associated exposed planes of the two polymorphs, anatase has been reported to have a lower surface enthalpy and lower surface free energy than rutile (Zhang and Banfield, 1998). Hence, it would be expected that the wetting of anatase by water would be less than that of rutile since higher surface free energies generally contribute to hydrophilicity (Rupp *et al.*, 2006).

However, the photoactivity of anatase and rutile have been examined and interpreted by Sclafani and Herrmann (1996) with reference to the densities of surface-adsorbed species (Sclafani and Herrmann, 1996). This study showed that higher levels of radicals adsorbed on the anatase surface give rise to significantly higher photoactivity than rutile. This result was reported to be due to a higher surface area as well as a higher photoactivity per unit of surface area. A similar result was found by Augustynski (1993), who reported that surface-bonded peroxo species on anatase were absent from rutile surfaces (Augustynski, 1993).

In contrast to the widely reported photocatalytic superiority of anatase, several publications have suggested that, in some cases, rutile may be advantageous for certain applications (Ohno *et al.*, 2003).

2.7.4.6 TiO_2 Wettability under UV Irradiation

Control of the wettability of solid surfaces is an important technology in various fields, including printing, adhesion, and coating. Various methods for controlling the wettability of solid surfaces have been reported. One of these methods is light irradiation has also been proposed and has attracted a great attention, owing to its high wettability conversion rate and the ability to produce microscopic patterns of hydrophilic and hydrophobic regions (Kamei and Mitsuhashi, 2000) as described earlier. An amphiphilic and super-hydrophilic TiO_2 surface can be obtained by ultraviolet irradiation (Wang *et al.*, 1998b), which should be beneficial to the bioactivity of TiO_2 surface (Liu *et al.*, 2008). Recently, it was found that ultraviolet (UV) irradiation of TiO_2 materials produces a highly hydrophilic surface, exhibiting 0^o contact angle for water. This phenomenon is considered to be due to structural changes of TiO_2 itself (Wang *et al.*, 1997), which proceed totally differently from the conventional photocatalytic oxidation reactions. This highly hydrophilic surface returns gradually to the initial relatively hydrophobic one in the dark. Table 2.33 summarised the parameters and results from related studies (Miyauchi *et al.*, 2002).

Table 2.33: Studies on the wettability conversion contact angle (CA) on TiO_2 thin films induced by UV irradiation

UV parameters	TiO_2 characterisation	Results/Explanation	References
Power 250 W Wavelength 365 nm Intensity 50 mW/cm^2	100 nm TiO_2 anatase nanoparticle coating	CA Initial 161^o After 10min 20^o After 30min 6^o	(Stepien *et al.*, 2012)
Wavelength 172 nm Intensity 1.0 mW/cm^2	550 nm TiO_2 anatase thin film	CA After 10 min 20^o After 120 min 2.5^o	(Katsumata *et al.*, 2006)
Wavelength 254 nm	10 nm TiO_2 nanoparticle deposition	CA Initial 117.6^o Become 62.5^o	(Li *et al.*, 2013)
Power 10 W Wavelength 365 nm	500 nm TiO_2 anatase thin film	CA Initial 55^o After 60 min 5^o	(Miyauchi *et al.*, 2002)
Wavelength 365 nm	18 µm TiO_2 nanocrystalline thin film	CA Initial 156^o 40 mW/cm^2 after 90 min CA 0^o 30 mW/cm^2 after 120 min CA 0^o 20 mW/cm^2 after 180 min CA 10^o 10 mW/cm^2 after 180 min CA 150^o	(Liang *et al.*, 2012)
Wavelength 365 nm Intensity1.0 mW/cm^2	300 nm TiO_2 anatase nanocrystalline	CA Initial 35^o After 100min 5^o After 140min 25^o After 280min 0^o	(Watanabe *et al.*, 1999)

Figure 2.15 shows a small droplet in equilibrium on a horizontal surface. The degree of wetting (the term wetting is used regardless of the nature of the liquid; hence dry means not that water is absent, but that all liquid is absent) is inversely proportional to the contact angle θ; when $\theta=0^{o}$ corresponds to complete wetting (Young, 1832).

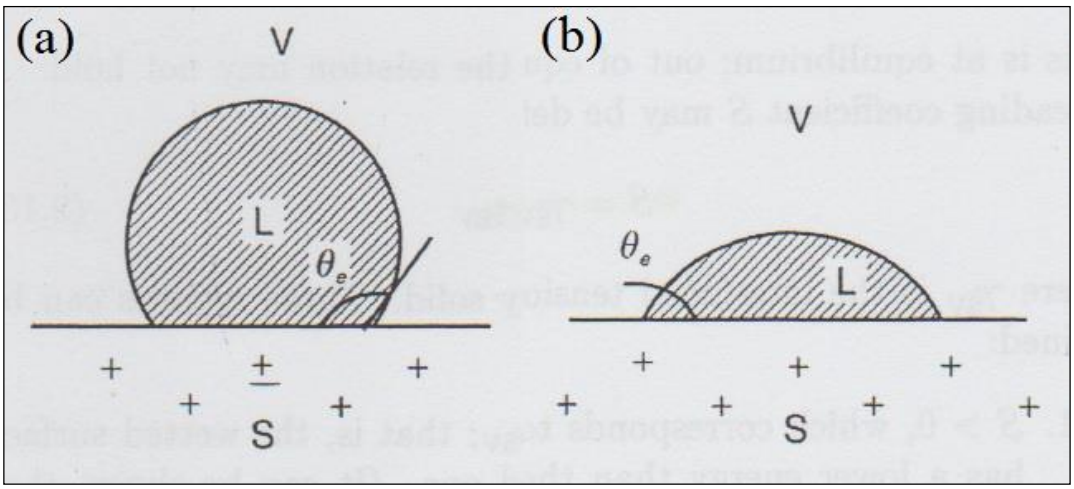

Figure 2.15: Cross section of small droplets of a liquid L sitting at equilibrium on a horizontal surface S in the presence of their vapor V: (a) A relatively hydrophobic surface, and (b) a relatively hydrophilic surface (assuming L=H_2O) (Young, 1832)

2.7.4.7 Bioactivity of TiO_2 under UV Irradiation (*In Vitro* Test)

Reseaches have reported the bioactivity of TiO_2 irradiated by UV in *in vitro* testing. Some have reported UV irradiation prior to *in vitro* in SBF and culture cell, in the air and in the water. Others have reported the irradiation of UV during the *in vitro* testing in SBF. Table 2.34 list *in vitro* studies reporting the bioactivity of TiO_2 under UV irradiation in SBF as illustrated in Figure 2.16 and in cell culture. These reports have concluded an achievement bioactivity enhancement of surface bioactivity of TiO_2 coatings can be induced by UV illumination by means of both *in vitro* and *in vivo* evaluation and the ability of apatite formation on the TiO_2 surface was improved with the increase of UV irradiation time.

2.7.5 Colour Properties of TiO_2

The TiO_2 that spontaneously form on the Ti colour has no colour. The TiO_2 that is formed using anodic oxidation has colourful appearances, depend on the anodization

parameters. It has been reported that the colour interference of the TiO_2 can indicate the thickness of the oxide (Delplancke *et al.*, 1982). Therefore it is of imperative to study the colour properties of TiO_2.

Table 2.34: *In vitro* and *in vivo* studies on TiO_2 thin film induced by UV irradiation

UV parameters	TiO_2 characterisation	UV treatment	*In vitro*	Results/Explanation	References
Power: 500W Wavelength: < 280 nm The lamp was set at a distance of 15 cm from the sample.	0.5g Compacted TiO_2 anatase powder	Prior to *in vitro* test in air for 5 hr at room temperature	4 weeks in 1.5 M SBF	TiO_2 irradiated to UV were able to induce apatite	(Kasuga *et al.*, 2002)
Power: 125W Wavelength: 365 nm	30nm anatase nano-TiO_2 powder formed by plasma spray	Prior to *in vitro* test in air for 24 hr at room temperature	4 weeks in SBF	TiO_2 coating was able to induce apatite under UV	(Liu *et al.*, 2006)
Wavelength: 365 nm	30nm anatase nano-TiO_2 powder formed by plasma spray	Prior to *in vitro* test for 12 hr and 24 hr in air, and during the *in vitro* test 12 hr/day.	2 and 4 weeks in SBF 6 months *in vivo*	Apatite forms more quickly in SBF when irradiated duting the *in vitro* compared to UV prior to *in vitro*. New bones was formed on the UV irradiated TiO_2 coating after implantation for 2 or 6 months.	(Liu *et al.*, 2008)
Wavelength: 365 nm Intensity: 170 mW/cm^2 The lamp was set at a distance of 3.5 cm from the sample.	Anatase TiO_2 gel layer formed by H_2O_2/HCl solution and heat treatment	Prior to *in vitro* test for 1 hr in air and water	1 day in Kokubo's SBF	The UV irradiation in air reduced the number of active sites for apatite nucleation. On the contrary, however, the UV-irradiation in water increased them.	(Uetsuki *et al.*, 2010)
Power: 15 W Intensity: 0.1 mW/cm^2 (360±20nm) Intensity: 2 mW/cm^2 (250±20nm)	200 nm TiO_2 nano layer formed by Sputter coating method	Prior to *in vitro* test for 48 hr	3 and 24 hr in cell culture	UV irradiation has accelerated and augmented the establishment of osteoblast adhesion, associated with upregulated expression of vinculin.	(Iwasa *et al.*, 2010)
Wavelength: 254 nm	TiO_2 formed by dip coating in Sol-gel of Ti6Al4V	Prior to *in vitro* test for 2 hr in water	14 days in SBF	UV irradiation causes the increase of basic Ti-OH groups and the decrease of the water contact angle, so better the apatite-forming ability.	(Guo *et al.*, 2010)

Table 2.34: Continued

UV parameters	TiO_2 characterisation	UV treatment	*In vitro*	Results/Explanation	References
Wavelength: 365 nm	TiO_2 coating formed by chemically treated with 5 M H_2O_2/ 0.1 M HNO_3 aqueous solutions at 353 K for 20 min.	During the *in vitro* test	2 days in SBF	The continuous UV has promoted a much larger number of clusters than the TiO_2 coating formed under in the dark.	(Ueda *et al.*, 2010)
Wavelength: 365 nm	TiO_2 coating formed by MAO in a 0.2 M calcium acetate monohydrate and 0.02 M b-glycerophosphate disodium salt pentahy-drate	Prior to *in vitro* test for 0.5 hr and 2 hr in air	19 days in SBF and 3 days in cell culture	TiO_2 coatings irradiated under UV was able to induce apatite, and not for the not irradiated ones. Significantly greater cell attachment, proliferation obtained under UV irradiated coatings than the coatings that were not irradiated.	(Hans *et al.*, 2008)
Wavelength: 365 nm Intensity: 7 mW/cm^2	TiO_2 formed by gel oxidation	During in vitro test for	1 day in SBF	UV radiation enhanced apatite precipitation with anatase but the effect of rutile was to suppress it	(Abdullah and Sorrell, 2012)

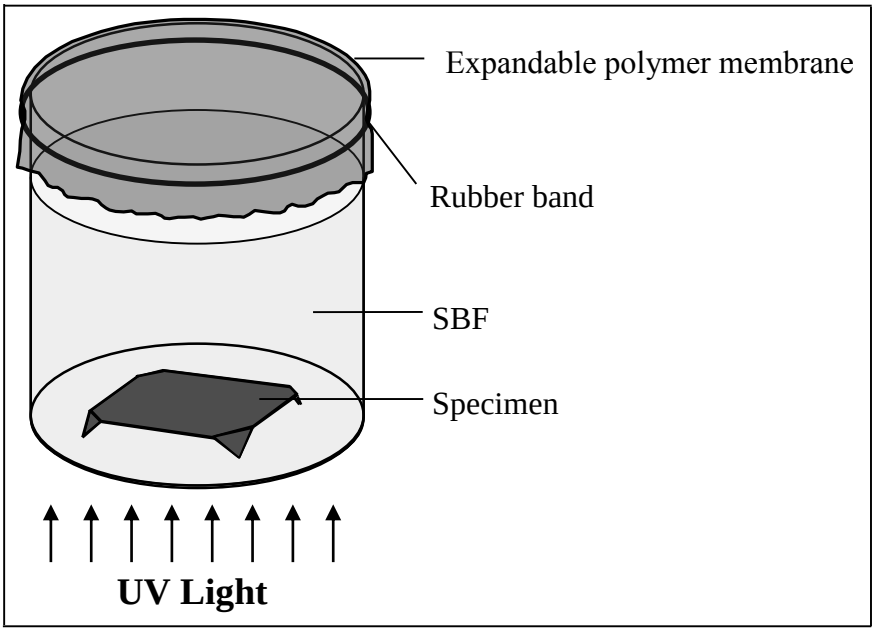

Figure 2.16: Schematic of setup for UV irradiation of specimen during soaking in SBF (Abdullah, 2010)

2.7.5.1 Colour System

Colour is associated with visible light waves (wavelength distributions). Visible light is a very small part of electromagnetic energy; wavelengths within violet (400 nm) and red (700 nm) of the electromagnetic spectrum (Figure 2.17) (Harold, 2001; Vuvlsteker, 2004). The selective absorption of the different amount of wavelengths within violet and red described as the colour of objects. Wavelengths not absorbed are reflected or transmitted by objects and thus visible to observers. The colour measurement for the scientific purpose is based on numerical representations or quantification of three colour response mechanisms in the human eye (Harold, 2001).

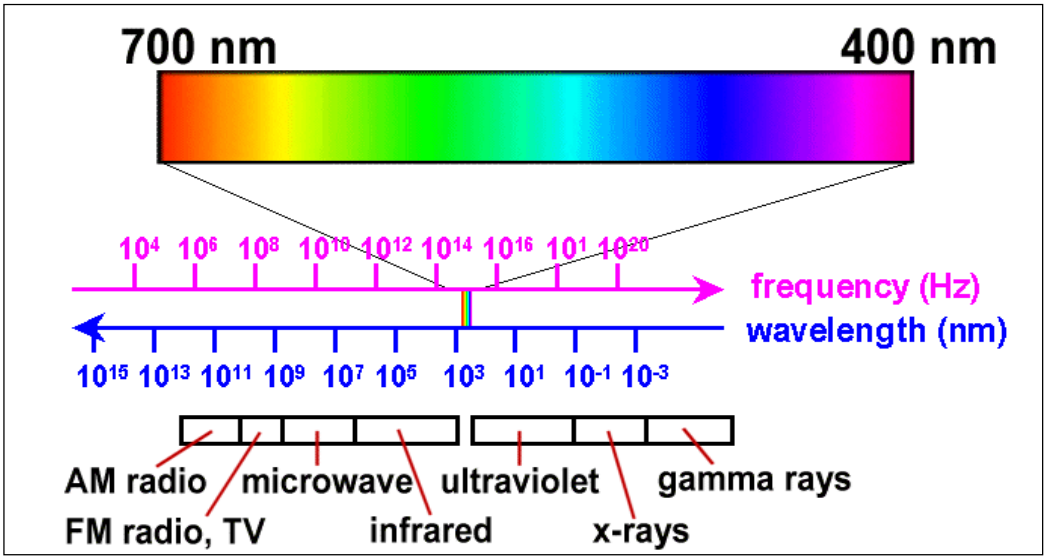

Figure 2.17: Visible light (wavelength, 400-700 nm) as part of electromagnetic energy (Vuvlsteker, 2004)

2.7.5.2 Colour Measurement

Colour measurement by visual is subjective and difficult to correlate the observation of different observer. Scientific colour measurement is based on numerical representation due to difficulty to identify constantly, even for the same observer. Quantitative technique to measure colour are designed to be used as standard measurement.

The opponent-colours (L,a,b-type) colour scale are used in this study to measure the colour of the samples. The L, a, b-type scale originally developed and

refined by Richard S. Hunter between 1942 and 1958. In 1976, the CIE adopted another L, a, b-type scale identified as the CIE 1976 L* a* b* scale ("CIELAB" scale). It is the currently recommended colour scale in almost all domestic and international colour measurement test methods and specifications (Harold, 2001).

The concept of opponent-colours colour scale can be represented on a 3-dimensional axis (Figure 2.18). Opponent colour pairs (red-green and yellow-blue) are positioned on opposite ends of the horizontal axis. The lightness index is positioned on the vertical axis (Busby *et al.*, 1999). The value of the coordinate can be summarized in Table 2.35. The further away a point from the centre (a*,b*) = (0,0), the higher colour saturation. This quantity is measured using chromaticity (amount of colour) (Gils *et al.*, 2004).

$$Chromaticity = \sqrt{a^{*2} + b^{*2}} \tag{2.12}$$

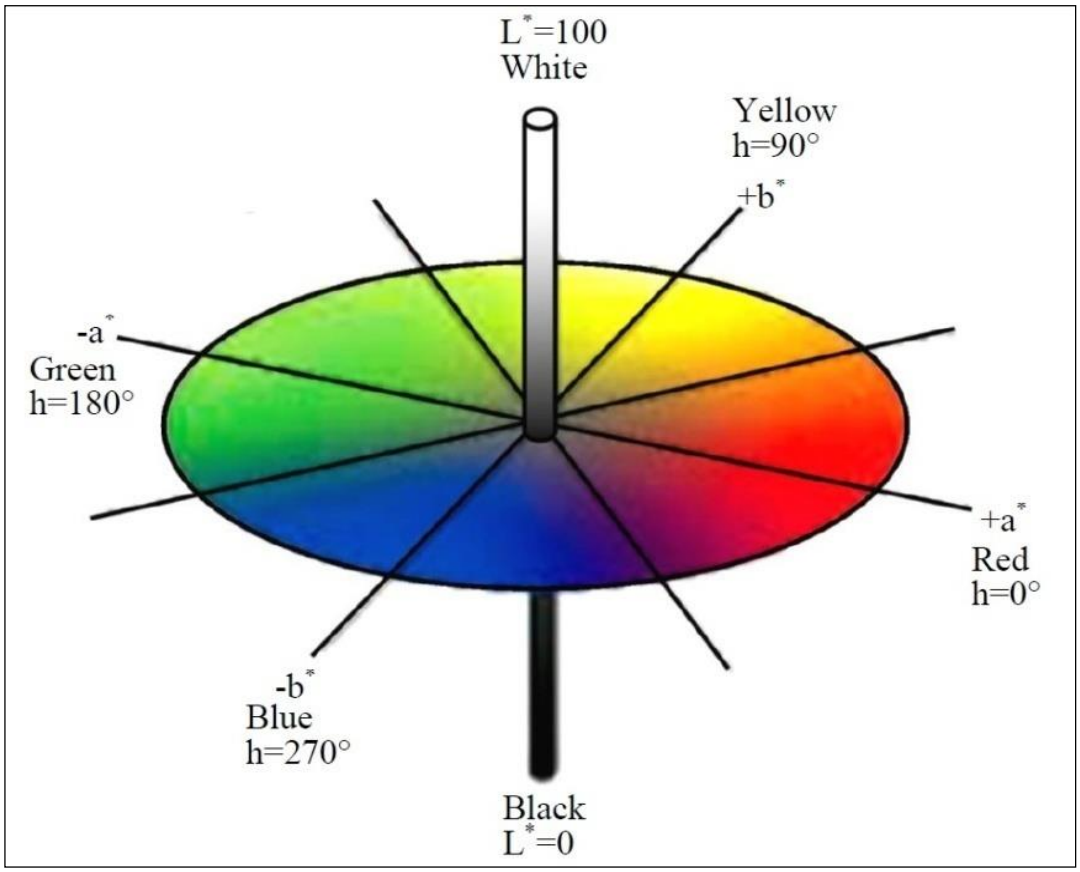

Figure 2.18: CIELAB chromaticities diagram (Harold, 2001)

Table 2.35: The value of the coordinate CIELAB

Colour	Value	Colour	Value
Red	+a*	Green	-a*
Yellow	+b*	Blue	-b*
White	L=100	Black	L=0

2.7.5.3 Ti and TiO_2 Colour

Ti is well known that covered by a passive film TiO_2 with 1.5-10 nm thick that has no colour when exposed to the atmosphere (Sul *et al.*, 2001). The colour of TiO_2 depends on the film thickness. According to multiple-beam interference theory, the colouring results from interference from between the light beams that are reflected from film surface (reflected light ray 1) and film-substrate interface (reflected light ray 2) as shown in Figure 2.19 (Delplancke *et al.*, 1982). From Figure 2.19 the following can be outlined:

i. Initial white light is split into normal and abnormal rays upon entry in the film.
ii. It concludes that two wavelengths of light emerged from the film.
iii. Destructive interference of the two wavelength modified wavelengths of emerged light
iv. The thickness of film determines relative phases of two emergent wavelengths owing to internal reflection.
v. The angle of incidence also affects the proceeding.

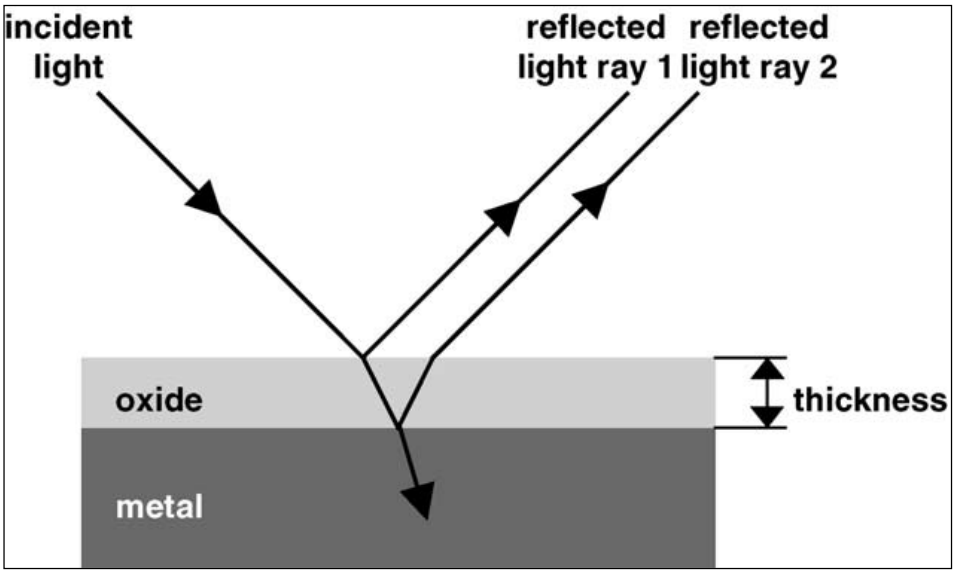

Figure 2.19: Interference between two waves reflected at both surfaces of an oxidised metal (Delplancke *et al.*, 1982; Gils *et al.*, 2004)

2.7.5.4 TiO_2 Colour by Anodic Oxidation

The electrochemical process of Ti anodic oxidation generates TiO_2 on the metal surface, whose thickness can range from 10 nm to some micrometers, depending on the process parameters imposed, such as feeding voltage and an electrolytic solution. The so formed oxide presents different characteristics, such as thickness, colour, density, homogeneity and insulating properties (Diamanti and Pedeferri, 2007).

Traditional anodizing consists of a low voltage anodizing of Ti in an acidic solution to achieve the formation of a thin, amorphous oxide layer, from 10 to a few hundred nm thick, which shows colours that change with its thickness due to interference effects between oxide, metal, and light (Gaul, 1993). The characterisation of these oxides is mainly performed through spectrophotometry, whose output is a reflectance curve that contains information on the oxide thickness: this parameter can be extrapolated through the application of interference principles (Gils *et al.*, 2004). At higher oxide thicknesses the interference effect is lost, together with the surface colour. In some circumstances, oxide crystallization may also occur and impede interference, giving a grey surface as a result (Diamanti *et al.*, 2013). Colouring of the resultant Ti anodic oxide films was the most prominent optical change during galvanostatic anodizing (Sul *et al.*, 2001). Figure 2.20 shows various colours of the anodic oxide film prepared from the clinical implant specimens.

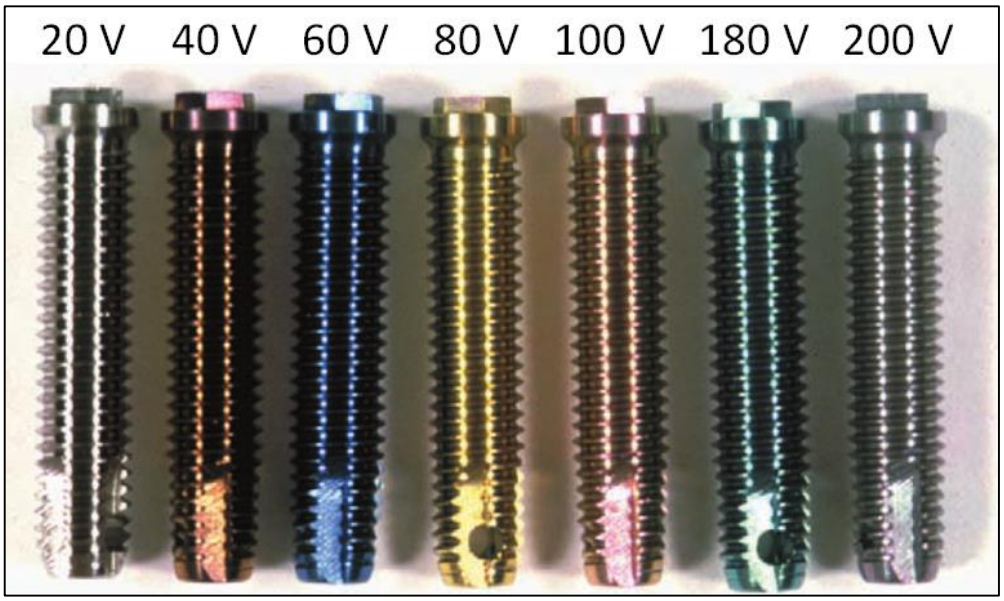

Figure 2.20: Colouring of the clinical Ti implants prepared by anodic oxidation in 0.5 M tartaric acid (Sul *et al.*, 2001)

2.8 Anodic Oxidation

Anodic oxidation is a technique and/or method used to form an oxide layer or on metals substrates such as Al, Ti, Mg, and Zr. It can be used for producing increased oxide thickness (for enhanced corrosion protection and decreased ion release), colouration, and porous coatings (Brunette *et al.,* 2012). It mechanism depends on the reaction of electrodes combined with the electric field which drives the metal and oxide ion to diffuse and form an oxide layer on the anode surface (Liu *et al.,* 2004; Wu *et al.* 2005). Anodization is simple techniques that are useful at low temperature (Xiao *et al.*, 2003).

Many studies have reported the formation of bioactive TiO_2 on Ti (Guo *et al.,* 2010; Song *et al.,* 2009; Uetsuki *et al.,* 2010). Anodization has been successfully used as a surface treatment for orthopaedic implants in the past few decades because it can produce implants with porous, relatively rough, and firmly adherent TiO_2 film. The porous nature of the anodised films enhances the anchorage of the implants to the natural bone (Song *et al.,* 2009). The structural and chemical properties of anodic oxides on Ti can be varied over quite a wide range by controlling the processing parameters, such as anode potential, electrolyte composition, temperature, and current. Different diluted acids (H_2SO_4, H_3PO_4, CH_3COOH, and others) are commonly used electrolytes for anodic oxidation of titanium (Brunette *et al.,* 2012). The anodization set up is schematically shown in Figure 2.21. The Ti and O ions formed are driven through the oxide by the externally applied electric field, leading to the growth of the oxide film. The reactions of oxidation at the anode are as follows (Brunette *et al.,* 2012):
At the Ti/Ti oxide interface:

$$Ti \rightarrow Ti^{2+} + 2e^{-} \tag{2.13}$$

At the Ti oxide/electrolyte interface:

$$2H_2O \rightarrow 2O^{2-} + 4H^{+} \text{ (oxygen ions react with Ti to form oxide)} \tag{2.14}$$

$$2H_2O \rightarrow O_2(gas) + 4H^{+} + 4e^{-} \text{ (O_2 gas evolves)} \tag{2.15}$$

At both interfaces:

$$Ti^{2+} + 2O^{2-} \rightarrow TiO_2 + 2e^- \quad (2.16)$$

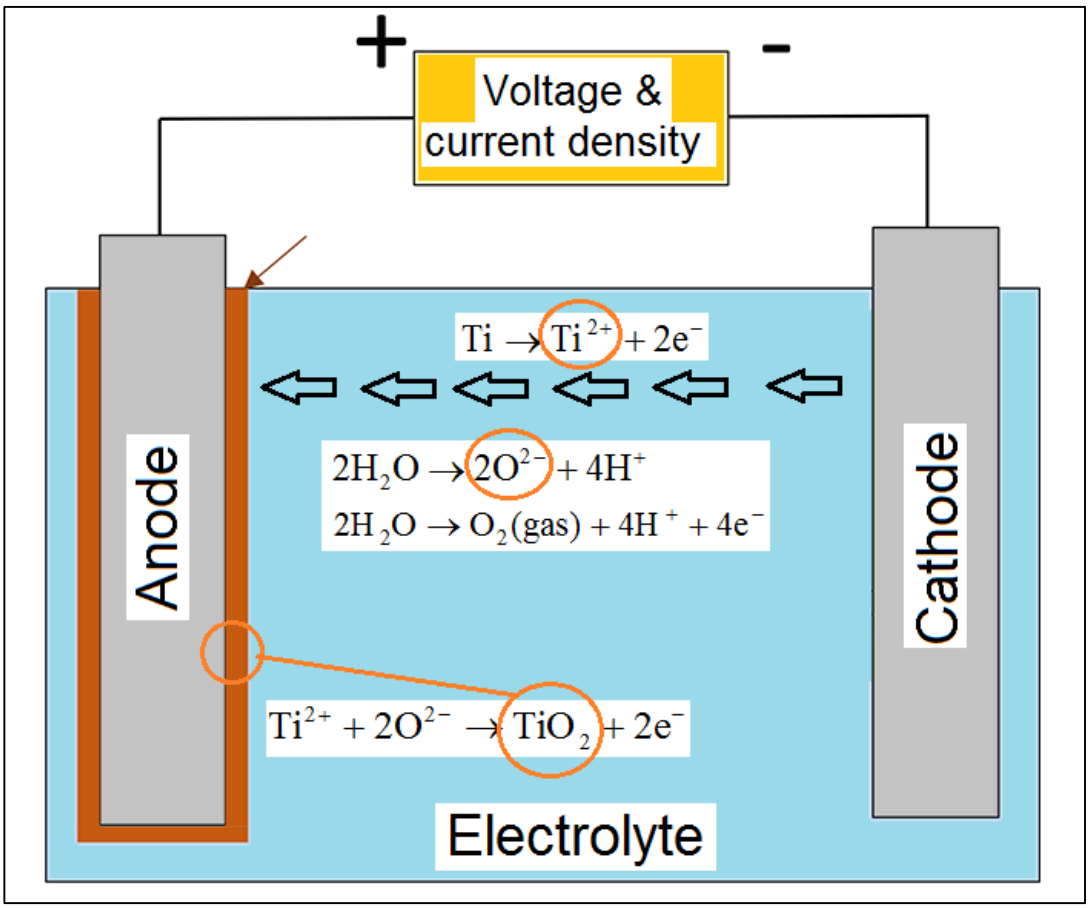

Figure 2.21: Schematic diagram of the anodizing process
(Abdullah and Sorrell, 2007a)

2.8.1 Anodic Oxidation Conditions

The anodic oxidation process can be done either at constant voltage and it is called "poteniostatic" (stage 1) or at constant voltage and constant current (galvanostatic) (stage 2) as seen in Figure 2.22. The timing to move from stage 1 to stage 2 depends on the voltage (V) and current density ($mA.cm^{-2}$) limits. The higher the maximum voltage and the lower maximum the current density, the longer is the time Stage 1.

There are two types of anodic oxidation according to the applied voltage:

i. Below what is called (dielectric breakdown) phenomena as seen in Figure 2.23, the anodic oxide film is relatively thin and usually non-porous using non-fluorine electrolytes (Choi *et al.*, 2004).

ii. If the applied voltage exceeds the dielectric breakdown limit of the oxide, the oxide will no longer be resistive to prevent further current flow and oxide growth, which will lead to more gas revolution and sparking. The anodic oxidation under these conditions is called Micro-Arc Oxidation (MAO) of Ti in electrolyte solutions whose ions would be embedded into the oxide coating, resulting in a microporous structure (Li *et al.*, 2004). The dielectric breakdown voltage is reported to be between 100 V-150 V depending on the electrolyte, current density and other process conditions (Brunette *et al.*, 2012). Table 2.37 shows the anodizing parameters of some MAO studies.

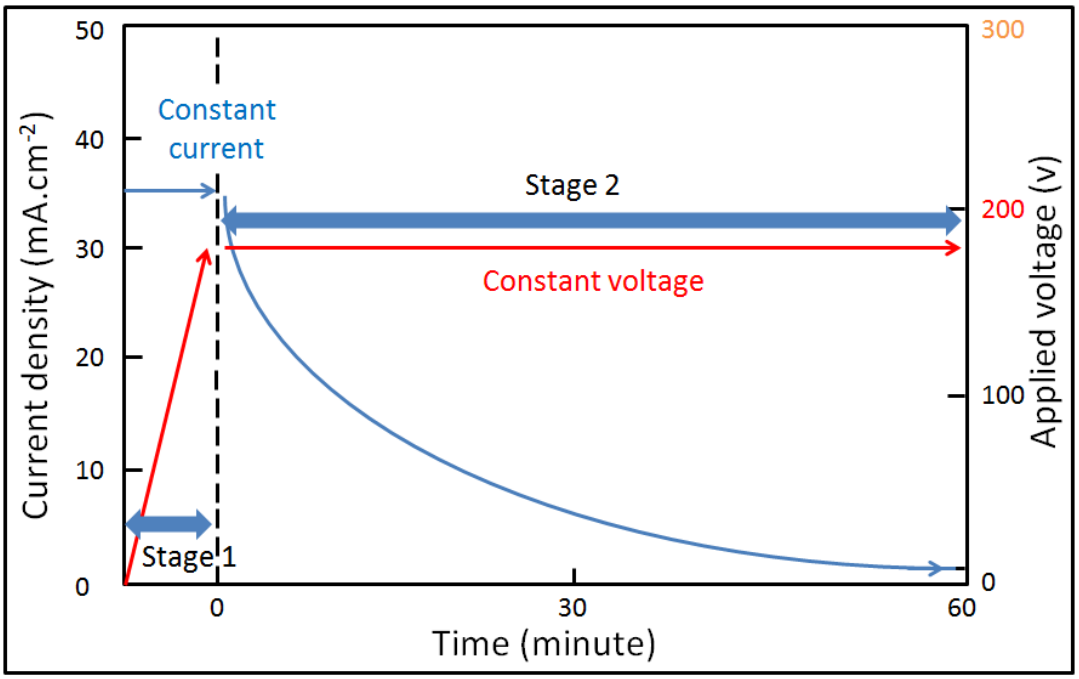

Figure 2.22: Schematic diagram example of anodic oxidation process at 35 mA.cm^{-2} and 180 V for 60 minutes (Oh *et al.*, 2008)

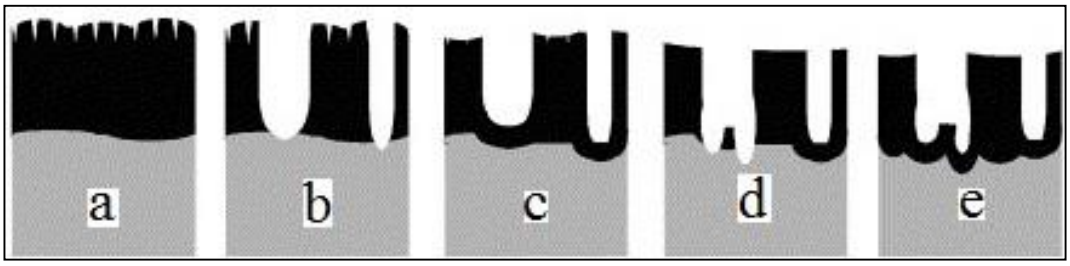

Figure 2.23: Schematic diagram of porous TiO_2 formation above the breakdown potential (a) oxide growth to maximal thickness, (b) burst of oxide by the formation of crystallites (pore formation), (c) immediate repassivation of pore tips, (d) burst of repassivated oxide, and (e) dissolution of the formed oxide and second repassivation (Chio *et al.*, 2004)

Table 2.36: Experimental parameters of some MAO studies

Electrolyte Composition	Molarity	Voltage (current density)	Time (S)	Temperature (°C)	References
Sulfuric acid	1	125	-	-	(Zinger *et al.,* 2003)
	0.5, 1, 3	90, 155, 180	-	-	(Yang *et al.,* 2004a)
Phosphoric acid	1	40-80 (70 A/cm^2)	10-47	17	(Sul *et al.,* 2001)

2.8.2 Anodic Oxidation Growth Rate

As long as the electric field is strong enough to drive the ions through the oxide, a current will flow and the film will continue to grow. This is why the final oxide thickness, d, during anodic oxidation is almost linearly dependent on the applied voltage, U:

$$d = \alpha U \tag{2.17}$$

Where,

α is the growth constant which is usually in the range 1.5 - 2.0 nm V^{-1}, d is the oxide thickness and U is the voltage (Ben-Nissan *et al.,* 2015).

Basically, the anodic film growth is determined by a balance between the oxide film formation rate and the oxide dissolution rate given by the nature of the electrolyte (Sul *et al.,* 2001). Crystallization of TiO_2 is promoted by a low oxidation rate, which allows the growing oxide to rearrange its structure while building up. It is also favoured by high voltages, when a localized breakdown of the oxide takes place in defective points of the oxide itself, leading to structural change (Diamanti *et al.,* 2013).

2.8.3 Corrosion Resistance and Adhesive Strength of TiO_2

The performance of Ti and Ti-based alloys in surgical implant applications can be evaluated with respect to their biocompatibility and capability to withstand the corrosive species involved in fluids within the human body. It is well documented that the excellent corrosion resistance of Ti materials is because of the formation of a dense, protective, and strongly-adhered passive film.

Ti is a highly reactive metal and reacts within microseconds to form oxide layer upon exposure to the atmosphere. Although the standard electrode potential was

reported to range from -1.2 to -2.0 volts for the Ti $\leftrightarrow Ti^{+3}$ electrode reaction, owing to strong chemical affinity for oxygen, it easily produces a compact oxide film, ensuring high corrosion resistance to the metal. This oxide which is primarily TiO_2 forms readily because it has one of the highest heats of reaction known (ΔH=-915 k mol^{-}) (for 298.16 ~ 2000 ^{o}K). It is also quite impenetrable by oxygen (since the atomic diameter of Ti is 0.29 nm, the primary protecting layer is only about 5 to 20 atoms thick). The oxide layer formed adheres strongly to the Ti substrate surface. The average single-bond strength of the TiO_2 to Ti substrate was reported to be about 300 $kcal.mol^{-1}$. Adhesion and adhesive of Ti oxide to the substrate are controlled by oxidation temperature and thickness of the oxide layer as well as the significant influence of the nitrogen on oxidation in air. In addition, adhesion is greater for oxidation in the air than in pure oxygen, suggesting that the influence of nitrogen on the oxidation process is significant. Studies have reported the decreases of adhesion strength as the layer thickness increased. The adhesion strength also decreased with the increased oxidation temperature, despite the increased of oxide plasticity (Oshida and Farzin-Nia, 2009).

Anodization of Ti can produce an increased thick protective TiO_2 layer that can lead to a less ion release in the human body. This relatively thin, non-porous oxide layer under the porous oxide structures is considered to contribute to the improvement of corrosion resistance. However, it was suggested that the implants' mechanical properties could be impaired with increased spark coating thickness. The interface between the anodic oxide layer and the Ti substrate usually does not show any discontinuity (Chiesa *et al.,* 2003). Table 2.38 lists some studies on adhesion strength between the Ti substrate and TiO_2 coating.

Table 2.37: Adhesion strength between the Ti substrate and TiO_2 coating

Treatment	Adhesion strength	References
Ti sparkly anodised in $CaH_2(PO_4)_2$	25 MPa	(Schreckenbach *et al.,* 1999)
Cp-Ti anodised in β-glycerophosphate (β-GP) and calcium acetate (CA)	40 MPa	(Ishizawa and Ogino, 1995)
Plasma-sprayed Ti and zirconia ZrO_2 coated Ti	15-30 MPa	(Yang and Ong, 2003)
MAO of Ti conducted in an electrolyte calcium acetate ($(CH_3COO)_2Ca{\cdot}H_2O$) and monosodium orthophosphate ($NaH_2PO_4{\cdot}2H_2O$).	48.5 N	(Liu *et al.,* 2016)
Ti anodised in ethylene glycol/NH_4F system as electrolyte	58 N	(Zhao *et al.,* 2014)

2.8.4 Anodic Oxidation of Ti in Sulphuric Acid (H_2SO_4)

Anodic oxidation comprises electrode reactions in combination with electric field drove metal and oxygen ion diffusion leading to the formation of an oxide film on the anode surface (Liu *et al.,* 2004). The electrolyte used as a conductive medium in the anodization process. Different diluted acids such as diluted acids, i.e., sulphuric acid (H_2SO_4), phosphorous acid (H_3PO_4) and acetic acid (CH_3COOH) can be used as electrolytes (Liu *et al.,* 2004). The different acidic electrolytes have a different effect on the resulted TiO_2 coating, i.e., microstructure, mineralogical, thickness and colour. The anodization parameters also can influence the properties of the TiO_2, i.e., applied voltage, anodization time, electrolyte concentration, current density and temperature of the electrolyte.

Anodic oxidation of Ti in H_2SO_4 can form crystalline TiO_2 (anatase and rutile) on Ti surface to modify the structure and bioactivity of biomedical Ti (Ikonopisov, 1977). H_2SO_4 is categorised as an electrolyte that provides slow metal dissolution (Yerokhin *et al.,* 1999); therefore the anodic oxide formation rate is much higher than the dissolution rate (Capek *et al.,* 2008). The TiO_2 film with anatase and rutile structure can be formed on the surface of Ti by anodic oxidation in the H_2SO_4 electrolyte. H_2SO_4 is classified as an optimal electrolyte by Diamanti and Pedeferri (2007) when the ultimate aim of anodization is obtaining anatase phase (Diamanti and Pedeferri, 2007). It has been shown that anodised titanium in H_2SO_4 electrolyte forms bone-like apatite on its surface in SBF within 3 days (Kokubo *et al.,* 2003). Kokubo, Kim, and Kawashita, (2003) also reported that Ti-OH groups are the catalyst for the apatite nucleation in the SBF and Ti-OH groups in the anatase structure are the most effective compared to rutile and brookite. Ti with oxide film also forms apatite on its surface *in vivo* which bonds to living bone (Liang *et al.,* 2002).

There are several studies on anodic oxidation in deluted H_2SO_4 electrolyte due to the possibility that the properties of the oxide film could fulfill the requirement for biomaterials (implants in dentistry and orthopaedic). Table 2.39 summarised the parameters and results from these studies.

Table 2.38: Parameters and results from studies on biomaterials applications using deluted H_2SO_4 electrolyte

Parameters	Results/Explanation	References
1 M H_2SO_4 DC power supply 1 min anodizing 90, 155, and 180 V	• > 150 V - Spark discharge • 90 V - Anatase • 155 V - Anatase + rutile • 180 V - Rutile	(Yang *et al.*, 2004)
0.25-2 M H_2SO_4 Current density: 100-1080 $mA.cm^{-2}$ Voltage: 10-150 V	• 90 V - Anatase • 150 V - Anatase + rutile	(Diamanti and Pedeferri, 2007)
1 M H_2SO_4	• <200 V - less rutile formation	(Hitchman *et al.*, 1996)
0.5 M H_2SO_4 Current density: 5 $mA.cm^{-2}$ Voltage: 5-30 V	• 5 V - Amorphous • >10 V - Polycrystalline	(Chang-Ha *et al.*, 1991)
1 M H_2SO_4 Current density: 30 $mA.cm^{-2}$ Voltage: ≤120 V	• >80 V - Spark (polycrystalline) • 120 V - Anatase + rutile	(de Mussy *et al.*, 2003)
1 M H_2SO_4 Voltage: 10, 20, 100, 150 V	• 10 V - Small amount of anatase • 20 V - Porous layer forms	(Jaeggi *et al.*, 2006)
0.5, 1.0, 2.0 M H_2SO_4 Voltage: 100, 150, 180 V	• 100 - 180 V - pore size increased • 180 V (2 M H_2SO_4) - High apatite forming ability	(Xiong *et al.*, 2004)
1.5 H_2SO_4 Current density: 60 $mA.cm^{-2}$ 10 min	• 100 V anatase • 150 V anatase + rutile • 300 V rutile	(Abdullah, 2010)
1.5 H_2SO_4 Current density: 5 $mA.cm^{-2}$ 10 min	• 100 V-150 V anatase	
2 M H_2SO_4 1 min	• 100 V - anatase • 150 V - anatase + rutile • 180 V - rutile	(Cui *et al.*, 2009)
0.1 M H_2SO_4 0.1 $V.S^{-1}$	• 100 V - anatase • 200 V - anatase + rutile	(Yamamoto *et al.*, 2011)

2.8.5 Anodic Oxidation of Ti in Phosphoric Acid (H_3PO_4)

Ti anodised in H_3PO_4 could be possibly used to produce thin and thick anodic films on the surface (Afshar and Vaezi, 2004). Anodic oxidation results in a thickening of the oxide film which may improve the biocompatibility of the anodised implant (Sul *et al.*, 2001). According to Park, 2008 (Park, 2008), H_3PO_4 electrolyte contributes to larger pore sizes on the surface compared to H_2SO_4. H_3PO_4 is categorised as an electrolyte that provides slow metal dissolution (Jaeggi *et al.*, 2005); therefore the anodic oxide can be developed on Ti surface. Jaeggi et al. (2006) explained that H_3PO_4 oxides were slightly thinner than oxides grown in H_2SO_4 under the same conditions. H_3PO_4 electrolyte can results in oxides that are also less crystalline compared to H_2SO_4 at the same applied voltage. An oxide grown under 100 V in H_3PO_4 shows almost the

same Raman signal as an oxide grown under 50 V in H_2SO_4 (Jaeggi *et al.*, 2006). This is all is believed to be due to the slower dissociation rate of H_3PO_4 than H_2SO_4 (Murmson, 2017). This is can cause lower electric field flow to dive ions through the oxide in the electrolyte due to the increased electrolyte density and therefore slower oxide growth. Thus lower oxide thickness, crystallisation, and porosity due to lower breakdown.

Anodic films with different colours can be produced in the deluted H_3PO_4 electrolyte. The colour of the films is indicative of the thickness of the film. The relation between colour and thickness of the oxide depends on the anodization process and the electrolyte (Kuromoto *et al.*, 2007). Sul *et al.* (2001) reported that the electrochemical growth of the oxide on the Ti depends on anodic parameters such as:

i. Concentration of the electrolyte.
ii. Applied current density.
iii. Applied voltage.
iv. Temperature.
v. Agitation speed.
vi. Surface area ratio of cathode to anode.

There are several studies on anodic oxidation in H_3PO_4 electrolyte due to the properties of the oxide film that possibly fulfill the requirements for biomaterials as an implant in dentistry and orthopaedics. Table 2.40 shows the parameters and results from several studies on biomaterial applications.

Acetic acid (CH_3OOH) is considered the weaker acid when compared to H_2SO_4 and H_3PO_4. Previously, acetic acid has been used as the electrolyte in Ti and Ti alloy anodization with the goal of improving corrosion resistance (Milošev *et al.*, 2013), enhancing surface biocompatibility for biomedical uses (Xie *et al.*, 2010), and fabricating TiO_2 nanotube structures in non-aqueous media (Ge *et al.*, 2008).

2.8.6 Anodic Oxidation of Ti in Mixed Acids (H_2SO_4 + H_3PO_4)

These acidic electrolyte mixtures were used in a specific manner to control the surface morphologies, especially with regard to the porosity for a particular application. According to Park *et al.* (2007), anodizing in H_3PO_4 at high voltages produced pores with a large diameter whereas fine pores rapidly developed in H_2SO_4. Mixtures of

H_2SO_4 and/or H_3PO_4 and/or H_2O_2 electrolyte were used to produce the desired properties of biomaterials, such as (Park and Lakes, 2007):

Table 2.39: Summary of studies on biomaterials applications using H_3PO_4 as an electrolyte

Parameters	Results/Explanation	References
1.4 M H_3PO_4 DC power supply 50, 100, 150, 200 and 250 V	•200 V - Spark discharge - Anatase	(Kuromoto *et al.*, 2007)
1.0 M H_3PO_4 DC power supply Current density: 5 mA.cm^{-2} 20, 40, 60, 80 and 100 V	•>100 V - Spark discharge •20-100 V - Anatase + amorphous	(Sul *et al.*, 2001)
1.0 M H_3PO_4 10 - 150 V	•10 V - Anatase starts to form •>150 V - Spark discharge	(Jaeggi *et al.*, 2006)
0.01, 0.05, 0.1 and 0.5 M H_3PO_4 Current density: 9.75 mA.cm^{-2} Heat treatment: 600°C	•Anodised Ti - Amorphous •Anodised + Heat treatment •Anatase	(Afshar and Vaezi, 2004)
0.01 M H_3PO_4 DC power supply Current: 150 mA Time: 90 s	•Film contains phosphorous •Anatase	(Frauchiger *et al.*, 2004)
0.05-0.3 M H_3PO_4 7 mA.cm^{-2}	•263-380 V amorphous + anatase	(Zhu *et al.*, 2002)

i. Micro-porous or nanoporous structure:
   a. Induces the growth of bone tissue into the pores.
   b. Develops strong mechanical interlocking between the implant and the bone tissue.

ii. Biocompatibility of the material:
   a. The biochemical and mechanical properties combine to develop strong bone adhesion.

iii. Chemical composition:
   a. Rapid bone adhesion and a high degree of bone coherence are obtained.

There are several studies on anodic oxidation in mixed solution (H_2SO_4 + H_3PO_4) electrolytes. Table 2.41 summarised the parameters and results from these studies. Table 2.42 obtain the difference between the titanium samples anodised in sulphuric acid H_2SO_4 and phosphoric acid H_3PO_4 in several aspects.

Table 2.40: Parameters and results from studies on biomaterials applications using mixed solution (H_2SO_4 + H_3PO_4) electrolyte

Parameters	Results/Explanation	References
1.5 M H_2SO_4 + 0.3 M H_3PO_4 5 mA.cm^{-2}, 50 min	• 90 and 180 V - anatase	(Abdullah, 2010)
1.5 M H_2SO_4 + 0.3 M H_3PO_4 20 mA.cm^{-2}, 30 min	• 90 and 180 V - anatase	(Abdullah and Sorrell, 2007b)
0.25 M H_2SO_4 + 0.5 M H_3PO_4 80 mA.cm^{-2}, Few minutes	• 100 and 200 V - anatase	(Diamanti *et al.*, 2011)
1.5 M H_2SO_4 + 0.3 M H_3PO_4 30 min	• 180 V - anatase	(Oh *et al.*, 2005)
0.9 M H_2SO_4+0.1 M H_3PO_4 35 mA.cm^{-2}, 30 min	• 180 V – anatase + rutile	(Oh *et al.*, 2008)

Table 2.41: The difference between samples anodised in sulphuric acid H_2SO_4 and phosphoric acid H_3PO_4

H_2SO_4	H_3PO_4	References
Oxide thickness		
Oxidation parameters: 1 M H_2SO_4 ,1 M H_3PO_4 at 5 V/s		(Jackson and Ahmed, 2007; Kern *et al.*, 2005)
Higher than H_3PO_4		
Crystallisation		
More progressed and higher amount of crystalline than H_3PO_4		(Jackson and Ahmed, 2007; Kern *et al.*, 2005)
Breakdown voltage		
0.1 M H_2SO_4 ,0.1 M H_3PO_4		(Abdullah, 2010)
100 V	100 V	
1.5 M H_2SO_4 ,1.5 M H_3PO_4		
150 V	100 V	
1 M H_2SO_4 ,1 M H_3PO_4 at 20 mA.cm^{-2}		(Song *et al.*, 2009)
110 V	200 V	
Pore formation		
1 M H_2SO_4 at 180 V, 1 M H_3PO_4 at 200 V		(Tümmler *et al.*, 2011)
Small pores and rougher surface than H_3PO_4	Bigger pores and lesser surface roughness than H_2SO_4	
1 M H_2SO_4 ,1 M H_3PO_4 at 20 mA.cm^{-2}		(Song *et al.*, 2009)
Smaller surface roughness 100 - 200 nm	Smaller surface roughness 1 µm	
1.5 M H_2SO_4, 0.3 M H_3PO_4		(Abdullah, 2010)
Maximal pore 0.5 µm, smaller pore	Maximal pore 1 µm, bigger pore	

Each testing type has advantages and disadvantages. By understanding the liabilities of the testing types, it offers an insight into the validity of the conclusions arrived by researchers.

2.9 Biological Testing

There are three broad categories of biological testing;

i. *In vitro* testing.

ii. *In vivo* testing.

iii. In silico testing.

2.9.1 *In vivo* Studies

In vivo (Latin synonym: within the living) refers to experimentation using a whole, living organism as opposed to a partial or dead organism. Animal studies and clinical trials are two forms of *in vivo* research. *In vivo* testing is often employed over *in vitro* because it is better suited for observing the overall effects of an experiment on a living subject.

While there are many reasons to believe *in vivo* studies have the potential to offer conclusive insights about the nature of medicine and disease, there is a number of ways that these conclusions can be misleading. For example, a therapy can offer a short-term benefit, but a long-term harm (Kinnings *et al.,* 2009).

2.9.2 In Silico Studies

In silico is an expression which means a testing performed on the computer or via computer simulation expression, which means to characterise biological experiments carried out entirely in a computer.

Although in silico studies represent a relatively new avenue of inquiry, it has begun to be used widely in studies which predict how drugs interact with the body and with pathogens. For example, a 2009 study used software emulations to predict how certain drugs already on the market could treat multiple-drug-resistant and extensively drug-resistant strains of tuberculosis (Kinnings *et al.*, 2009).

2.9.3 *In vitro* Studies

In vitro (Latin synonym for: within the glass) refers to the technique of performing a given procedure in a controlled environment outside of a living organism. Many experiments in cellular biology are conducted outside of organisms or cells. Viruses, which only replicate in living cells, are studied in the laboratory in cell or tissue culture, and many animal virologists refer to such work as being *in vitro* to distinguish it from *in vivo* work in whole animals. One of the abiding weaknesses of *in vitro* experiments is that they fail to replicate the precise cellular conditions of an organism, particularly a microbe. Because of this, the *in vitro* studies may lead to results that do not correspond to the circumstances occurring in a living organism.

Until the last several years, efforts to detect and identify microorganisms in the human body have depended almost exclusively on *in vitro* studies. As a result, many researchers began to assume that chronic diseases were not caused by microbes. The net effect of all this was that the understanding of pathogens in disease was driven by the study of well-known, easy-to-culture microbes–which, as it turns out, represent the vast minority of bacteria in the human body. By one estimate, 99.6% of the species in the human microbiota have not or cannot be characterised through *in vitro* techniques (Relman, 1998).

2.9.3.1 Types of *In vitro* Studies

In vitro studies includes:

i. Isolation.
ii. Growth and identification of cells derived from multicellular organisms in (cell or tissue culture).
iii. Subcellular components (e.g. mitochondria or ribosomes).
iv. Cellular or subcellular extracts (e.g. wheat germ or reticulocyte extracts).
v. Purified molecules such as proteins, DNA, or RNA).
vi. Commercial production of antibiotics and other pharmaceutical products.

2.9.3.2 Types of *In Vitro* Testing

In vitro testing can fall under these categories:

i. Polymerase chain reaction is a method for selective replication of specific DNA and RNA sequences in the test tube.

ii. Protein purification involves the isolation of a specific protein of interest from a complex mixture of proteins, often obtained from homogenized cells or tissues.

iii. *In vitro* fertilization is used to allow spermatozoa to fertilize eggs in a culture dish before implanting the resulting embryo or embryos into the uterus of the prospective mother.

iv. *In vitro* diagnostics refers to a wide range of medical and veterinary laboratory tests that are used to diagnose diseases and monitor the clinical status of patients using samples of blood, cells, or other tissues obtained from a patient (Artursson *et al.,* 2012).

2.9.3.3 Uses of *In Vitro* Testing

In vitro testing has been used to characterise specific adsorption, distribution, metabolism, and excretion processes of drugs or general chemicals inside a living organism; for example, Caco-2 cell experiments can be performed to estimate the absorption of compounds through the lining of the gastrointestinal tract (Artursson *et al.,* 2012). The partitioning of the compounds between organs can be determined to study distribution mechanisms (Gargas *et al.,* 1989). Suspension or plated cultures of primary hepatocytes or hepatocyte-like cell lines (HepG2, HepaRG) can be used to study and quantify metabolism of chemicals (Pelkonen and Turpeinen, 2007). These ADME process parameters can then be integrated into so-called "physiologically based pharmacokinetic models" or PBPK.

2.9.3.4 Advantages and Disadvantages of *In Vitro* Studies

In vitro studies permit a species-specific, simpler, more convenient, and more detailed analysis than can be done with the whole organism. Just as studies in whole animals

more and more replace human trials, so are *in vitro* studies replacing studies in whole animals (Vignais and Vignais, 2010).

The primary disadvantage of *in vitro* experimental studies is that it may be challenging to extrapolate from the results of *in vitro* work back to the biology of the intact organism. Investigators doing *in vitro* work must be careful to avoid over-interpretation of their results, which can lead to erroneous conclusions about organismal and systems biology (Rothman, 2002).

For example, scientists developing a new viral drug to treat an infection with a pathogenic virus (e.g. HIV-1) may find that a candidate drug functions to prevent viral replication in an *in vitro* setting (typically cell culture). However, before this drug is used in the clinic, it must progress through a series of *in vivo* trials to determine if it is safe and effective in intact organisms (typically small animals, primates, and humans in succession). Typically, most candidate drugs that are effective *in vitro* prove to be ineffective *in vivo* because of issues associated with the delivery of the drug to the affected tissues, toxicity towards essential parts of the organism that were not represented in the initial *in vitro* studies, or other issues (De Clercq, 2005).

2.10 Simulation Body Fluid (SBF)

The discovery of bone-bonding glass in the 70s by Hench *et al.* (1971) has opened new possibilities in bioactive implant materials, attracting many research activities and leading to the developments of various commercial products (Hench *et al.,* 1971; Jones, 2015). These bioactive materials can actively form a direct bonding with the surrounding bone, therefore, significantly increasing the implant fixation and the long-term stability.

The rapid development of new potential implant materials presents both scientific and technical challenges for the design of a fast assessment method other than traditional animal experiments for implant evaluation (Zhao *et al.,* 2017). Kokubo *et al.* (1990) proposed an *in vitro* method using an acellular solution with inorganic ion composition and pH similar to biological fluids called simulated body fluid (SBF) to test new implants (Kokubo and Takadama, 2006; Kokubo *et al.,* 1990). The method is based on the observations that a bone-like apatite layer is often found between bioactive implants and the surrounding bone, acting as a key component for

osseointegration (Kokubo, 1990). Therefore, the question of material bioactivity (which hereafter refers to the bone-bonding ability), reduces to the apatite-forming ability of a material *in vivo*. It is further assumed that the apatite-forming behavior *in vivo* can be reproduced using an artificial solution supersaturated with respect to hydroxyapatite (HA) *in vitro*, meaning that a material exhibiting HA deposition in SBF would indicate its bone-bonding ability.

2.10.1 Validation of SBF

In 2007, the testing protocol of this *in vitro* method was standardized by the International Organization for Standardization (ISO 23317) and since then has been widely used to evaluate various implant materials (Kokubo, 2014; Kokubo and Yamaguchi, 2010). Despite the success, the simplifications of using a solution to mimic the body fluid and determining the bioactivity by the apatite-forming ability also have several limitations as follows:

i. The bone bonding/formation process is essentially determined by osteoblasts, the activity of which is regulated by various local factors including both inorganic ions as well as organic growth factors. Although hydroxyapatite is widely used as a coating on implant surfaces to increase the osteoconductivity. The *in vivo* formation of HA would also likely result in enhanced osseointegration (Nishiguchi *et al.*, 2003). It should be noted that the osseointegration is a complex process involving platelet activation, blood clot, recruitment and migration of osteogenic cells (Davies, 2003). Thus other possible mechanisms of bioactivity also exist, which could include bioactivity from specific interactions with osteoblasts/stem cells of biofunctional materials by either releasing certain biomolecules or possessing special surface topographical features (de Oliveira and Nanci, 2004; Kaito *et al.*, 2005). The existence of other possible mechanisms might explain some cases of inconsistency between *in vitro* predictions and *in vivo* results (Zadpoor, 2014).

ii. Assuming the bone-bonding is achieved by the formation of an apatite layer, a qualitative correlation between a material's apatite-forming ability *in vivo* and its bone-bonding strength is still difficult to establish. That is, a higher apatite-forming ability *in vivo* does not necessarily lead to a stronger bonding. This is

due to many other factors determining the final bonding strength including surface mechanical properties (adhesion between the surface porous layer and bulk implant), and surface roughness, which is typically observed to be a critical factor in animal experiments (Nishiguchi *et al.,* 1999).

iii. The major criticism of the method is the lack of organics, especially proteins, which are abundant in human blood plasma (roughly 70 g/L in human blood plasma (Sava *et al.,* 2005) and are well-known to have specific/non-specific adsorption on various surfaces, which could affect the nucleation & growth of apatite in SBF (Bohner and Lemaitre, 2009; Vergaro *et al.,* 2015). In fact, proteins, along with other organic molecules, are also active players in the regulation of the biomineralization processes *in vivo* (Mann *et al.,* 1993). Despite the existence of a number of *in vitro* studies on the effect of proteins, their role as promoters or inhibitors for calcium phosphate nucleation and growth is still unclear.

iv. Also, the current SBF (ISO 23317) uses tris (hydroxymethyl) aminomethane ($(CH_2OH)_3CNH_2$, Tris) to buffer the solution pH, while Tris is not a component of human blood plasma and might have an effect on calcium phosphate nucleation (Jahromi *et al.,* 2013). The human blood is buffered by the equilibrium between carbonates and 5% partial pressure of CO_2 in blood serum (Gamble, 1947). Due to the high structural variability of apatite crystals, the presence of carbonate species in solution will result in carbonate incorporation into the apatite lattice by either substituting the hydroxyl groups (type A) or occupying the phosphate position (type B) (He *et al.,* 2008), as it is the case for apatite in natural bone (Rey *et al.,* 1989). Furthermore, it has also been demonstrated that carbonate complexes could lead to an increased apparent solubility of HA (Pan and Darvell, 2010). Despite being proposed in a review by Bohner and Lemaitre (Bohner and Lemaitre, 2009), unfortunately, so far there have been very limited studies using carbonate-buffered SBFs for implant evaluation (Zhao *et al.,* 2017).

2.10.2 HA Precipitation on Biomaterials

Investigations for inorganic biomaterials have been significantly increased in the past years to replace and repair bone tissue lost from injury or disease (Wu and Chang, 2013). For example, bioactive glasses and ceramics have been intensively investigated for bone tissue engineering because of its good bioactivity to form a chemical bond to natural tissues through an apatite layer (Liu *et al.,* 2015). When a bioactive material is soaked in an SBF (simulated body fluid) solution or dilute phosphate solution, ion-exchanges can take place between the ceramics and SBF solution, then HA layers can form on the surface of materials, which is the common characteristic of a bioactive material (Duta *et al.,* 2013; Liu *et al.,* 2015).

HA has excellent biocompatibility, bioactivity and is similar to the chemical compositions of human hard tissues (50% mass, 70% volume) (Duta *et al.,* 2013) and is recognized as an osteoconductive material. It has been clinically applied in the field of orthopedics and dentistry. HA has an ability to accelerate bone growth and attachment to the surface of implants to improve the fixation and lifetime of the implants (Brzezińska-Miecznik *et al.,* 2015; Dash *et al.,* 2015; Randorn *et al.,* 2015). An important characteristic of a bioactive material is HA layers' precipitation (*in vitro*) on the surface of materials through the ion-exchange between the ceramics and SBF when it is in contact with SBF (simulated body fluid) or dilute phosphate solution. To date, biomaterials modified by HA have been widely investigated to replace and repair bone and dental tissue, for example, titanium (Dash *et al.,* 2015; Prodana *et al.,* 2015), alloy (Bogya *et al.,* 2015), composites (Gheisari *et al.,* 2015), nanomaterials (Wang *et al.,* 2015), glass-ceramic (Ma *et al.,* 2015), ceramic (Dai *et al.,* 2015). Among them, bioactive glasses and glass-ceramics have been intensively investigated because of their excellent ability to react with physiological fluids and to modify the surface, favoring the formation of HA layers that can strongly bond to bone (Qi *et al.,* 2015).

2.10.3 HA Precipitation on TiO_2

TiO_2 crystalline could induce the HA in SBF in dark condition, when anodised in acidic electrolytes (Cui *et al.,* 2009; Oh *et al.,* 2008; Yang *et al.,* 2004a). However, amorphous TiO_2 could not under silimar conditions (Cui *et al.,* 2009). This is due to

the photocatalytic activity of TiO_2 crystalline (Wang *et al.,* 2007) that forms Ti-OH radicals on its surface, which is believed to be responsible for apatite precipitation (Ueda *et al.,* 2010; Uetsuki *et al.,* 2010). TiO_2 crystalline, which is anatase and rutile with bandgap value of 3.20 eV and 3.02 eV can obtain photocatalytic performance (Carp *et al.,* 2004; Diamanti *et al.,* 2011; Mills and Le Hunte, 1997). However, it was reported that higher amount of anatase would enhance the photocatalytic activity (Wang *et al.,* 2007). Moreover, the photocatalytic activity of TiO_2 anatase crystalline could be enhanced by UV irradiation (Masahashi *et al.,* 2008). The mechanism of HA precipitation on TiO_2 in SBF can be illustrated in Figure 2.24 (a,b,c and d). UV was reported to increase the generation of Ti-OH groups on the TiO_2 surface as seen in Figure 2.24 (e,f,g and h) and resulting in superhydrophilic anodised coatings (Han *et al.,* 2008; Masahashi *et al.,* 2008). The UV irradiation results in the generation electron-hole pair on TiO_2 surface as seen in Figure 2.25 (this has also been illustrated in Figure 2.10) and that has resulted in oxygen vacancies and hydroxyl (OH) groups and that is believed to be responsible for the initiate apatite nucleation (Fujishima and Honda, 1972; Fujishima *et al.,* 2008; Kasuga *et al.,* 2002). The chemical reactions of the behaviour of TiO_2 during immersion in SBF are as follows:

$$2Ti^{4+} + O_0 \rightarrow 2Ti^{3+} + \frac{1}{2}O_2 \tag{2.18}$$

$$2Ti^{3+} + H_2O \rightarrow Ti^{4+} - OH + \frac{1}{2}H_2 \tag{2.19}$$

$$Ti^{4+} - OH + OH^- \rightarrow Ti - O^- + H_2O \tag{2.20}$$

$$Ti - O^- + Ca_{2+} + PO_{3-}^4 + OH^- \rightarrow HA \text{ Precipitation} \tag{2.21}$$

The following steps illustrate the difference between the apatite precipitation on TiO_2 when immersed in SBF in dark and under UV irradiation conditions:

i. Oxygen vacancies are most likely created at the two-coordinated bridging sites, resulting in the conversion of the corresponding Ti^{4+} to Ti^{3+} sites as seen in Equation 2.12. Ti^{3+} sites are favourable for dissociating water which is absorbed in the atmosphere (Liu *et al.,* 2006) (Equation 2.13). The resulted in Ti-OH groups on TiO_2 surface react with hydroxyl ions in SBF, which has a

pH of 7.4, and this gives rise to a negatively charged surface with functional Ti-O^- as seen in Equation 2.14 and Figure 2.24 (a) (Liu *et al.*, 2008; Ueda *et al.*, 2009).

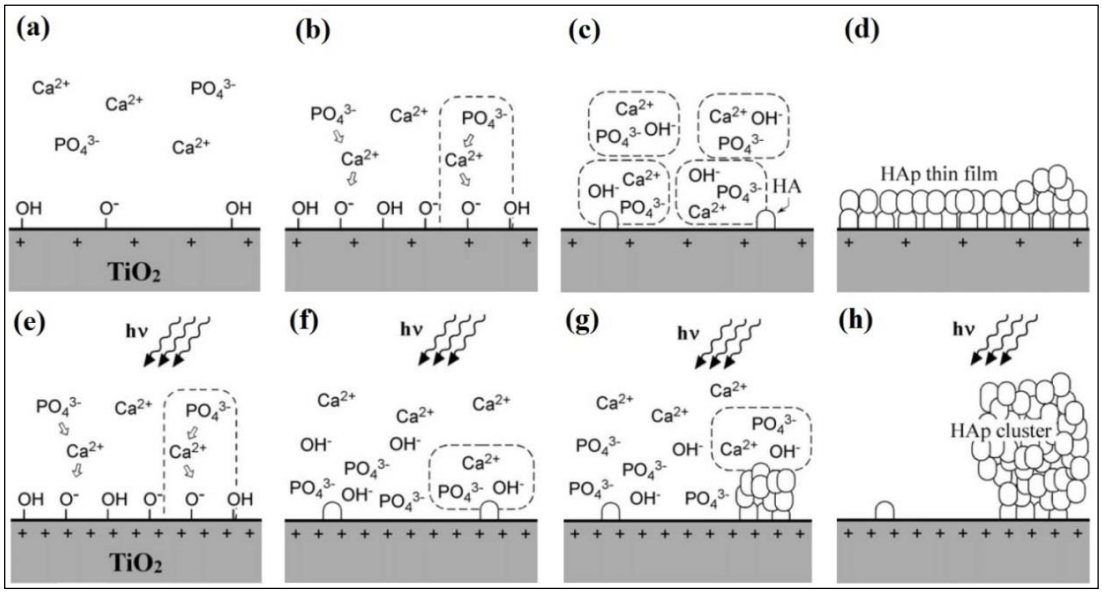

Figure 2.24: The mechanism of HA precipitation on TiO_2 in SBF immersion at dark (a-d) and under UV irradiation (e-h) conditions (Ueda *et al.*, 2009).

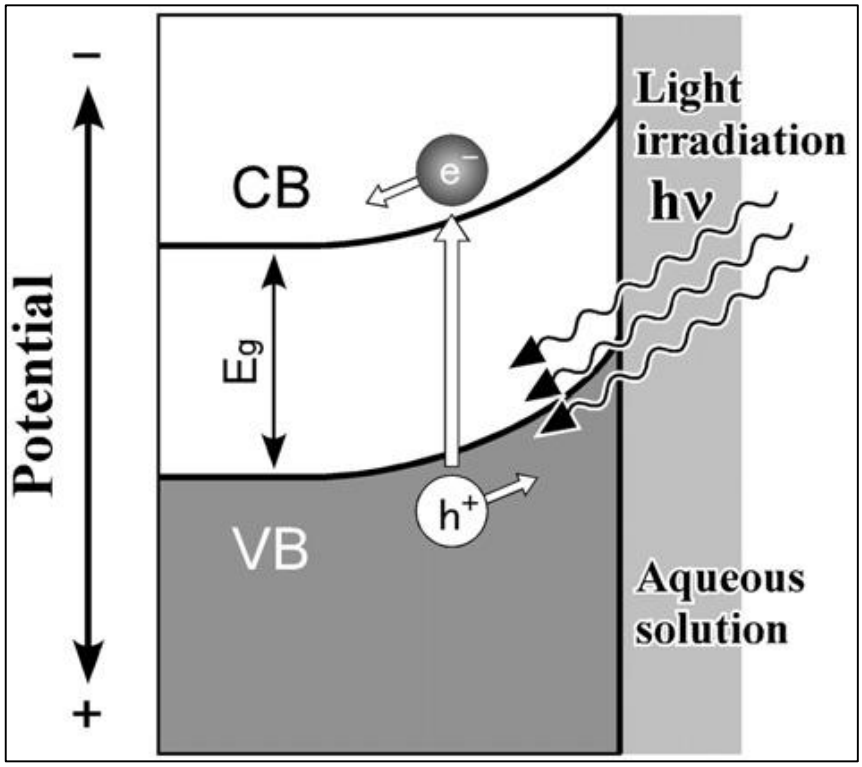

Figure 2.25: Schematic illustration of diffusion potential in an n-type semiconductor immersed in an aqueous solution. The valence and conduction bands are abbreviated as VB and CB, respectively (Ueda *et al.*, 2009)

ii. Oxygen vacancies are most likely created at the two-coordinated bridging sites, resulting in the conversion of the corresponding Ti^{4+} to Ti^{3+} sites as seen in Equation 2.12. Ti^{3+} sites are favourable for dissociating water which is absorbed in the atmosphere (Liu *et al.,* 2006) (Equation 2.13). The resulted in Ti-OH groups on TiO_2 surface react with hydroxyl ions in SBF, which has a pH of 7.4, and this gives rise to a negatively charged surface with functional $Ti\text{-}O^-$ as seen in Equation 2.14 and Figure 2.24 (a) (Liu *et al.,* 2008; Ueda *et al.,* 2009).

iii. The negatively charged surface then attracts calcium (Ca^{2+}) ions in SBF as seen in Figure 2.24 (b) (Fujishima and Honda, 1972; Ueda *et al.,* 2009), forming amorphous calcium titanate (Equation 2.15) (Fujishima and Honda, 1972). As Ca^{2+} build up, positively charge surface take a turn and combine with negative phosphate ions ($PO_3^{4}\_$) in SBF forming amorphous calcium phosphate (Figure 2.24 (c)). Thus, negative and positive ions arrive alternatively at the TiO_2 surface and form an amorphous calcium phosphate layer, which then crystallizes to HA as seen in Figure 2.24 (d) on the surface (Liu *et al.,* 2008; Ueda *et al.,* 2009).

iv. During SBF immersion, Ti-OH and $Ti\text{-}O^-$ formation on TiO_2 surface were speed up by the UV illumination (Han *et al.,* 2008; Liu *et al.,* 2008).

v. The difference between SBF immersion under UV light and the dark condition is the distribution of ions under UV illumination has made TiO_2 surface become more positive as seen in Figure 2.24 (e) due to the up-hill potential gradient, where electron-hole pair that was generated by UV irradiation move to TiO_2 surface. Ca^{2+} ions become less on the surface as seen in Figure 2.24 (f) and only rare Ca^{2+} ions adhered to HA nuclei and resulted in HA cluster coarsen since the precipitation continues at same site Figure 2.24 (g) and (h). HA cluster was obtained when exposing UV light in the SBF immersion because the photogenerated electron pair holes inhibit near to TiO_2 surface prevents Ca^{2+} ions initiating homogeneous HA coating instead of promoting HA cluster (Ueda *et al.,* 2009).

Ti has been wieldy used as a biomaterial for implants due to its biocompatibility properties that is lying on the TiO_2 passive layer. On this study an attempt to investigate on the biocompatibility of TiO_2 by applying anodic oxidation on the Ti, which leads to the growth of TiO_2. TiO_2 crystalline i.e. anatase and rutile were

reported to have good apatite induction, thus good biocompatibility. However, it was also reported that anatase has advantageous photocatalytic properties over rutile. TiO_2 anatase will be investigated due to their advantageous photocatalytic and biocompatibility properties. Anodic oxidation is an effective and simple technique to grow the TiO_2 layer with a controlled thickness. H_2SO_4 and H_3PO_4 electrolytes are the most used electrolytes for anodization of Ti. However, it was reported that H_2SO_4 electrolyte can give higher metal dissolution and higher crystallization than the H_3PO_4 electrolyte. Each electrolyte can give the different TiO_2 appearance, microstructural, elementary, mineralogical, optical and absorption and hydrophilicity properties. Also, a mixture electrolyte of these acids will be used to investigate its effect on TiO_2 properties. An *in vitro* test under the UV is to be conducted to investigate on the TiO_2 biocompatibility using SBF to investigate the effect of the photocatalytic properties of TiO_2 anatase on the apatite formation.

CHAPTER 3

METHODOLOGY

3.1 Introduction

The anodic oxidation of commercially pure titanium (Cp-Ti), the testings on TiO_2, the *in vitro* testing in the dark and under UV has been discussed. Anodization was used to produce titanium oxide (TiO_2) coatings using three medium electrolytes; H_2SO_4 electrolyte (sulfuric acid (H_2SO_4)); H_3PO_4 electrolyte (phosphuric acid (H_3PO_4)) and mixed electrolyte (H_2SO_4 + H_3PO_4). The resulting TiO_2 was tested using X-ray diffraction (XRD), scanning electron microscopy (SEM), energy-dispersive x-ray spectroscopy (EDX), fourier transform infrared spectroscopy (FT-IR) and water contact angle (WCA). *In vitro* test was carried out using simulation body fluid (SBF) medium with and without Ultra-violet irradiation (UV).

3.2 Methodology Flowchart

A flowchart diagram of the work breakdown including experimentation and characterisation is illustrated in Figure 3.1.

3.3 Sample Preparation and Processing

Cp-Ti (grade 2) foils of dimensions 25 mm x 10 mm x 0.05 mm (Figure 3.2 (a)) were wet hand-polished using 1200 grit (~1 μm) abrasive paper (Figure 3.2 (b)), followed by immersion in an ultrasonic bath with ethanol (~6 min), rinsing by dipping in distilled water, and kept drying in air.

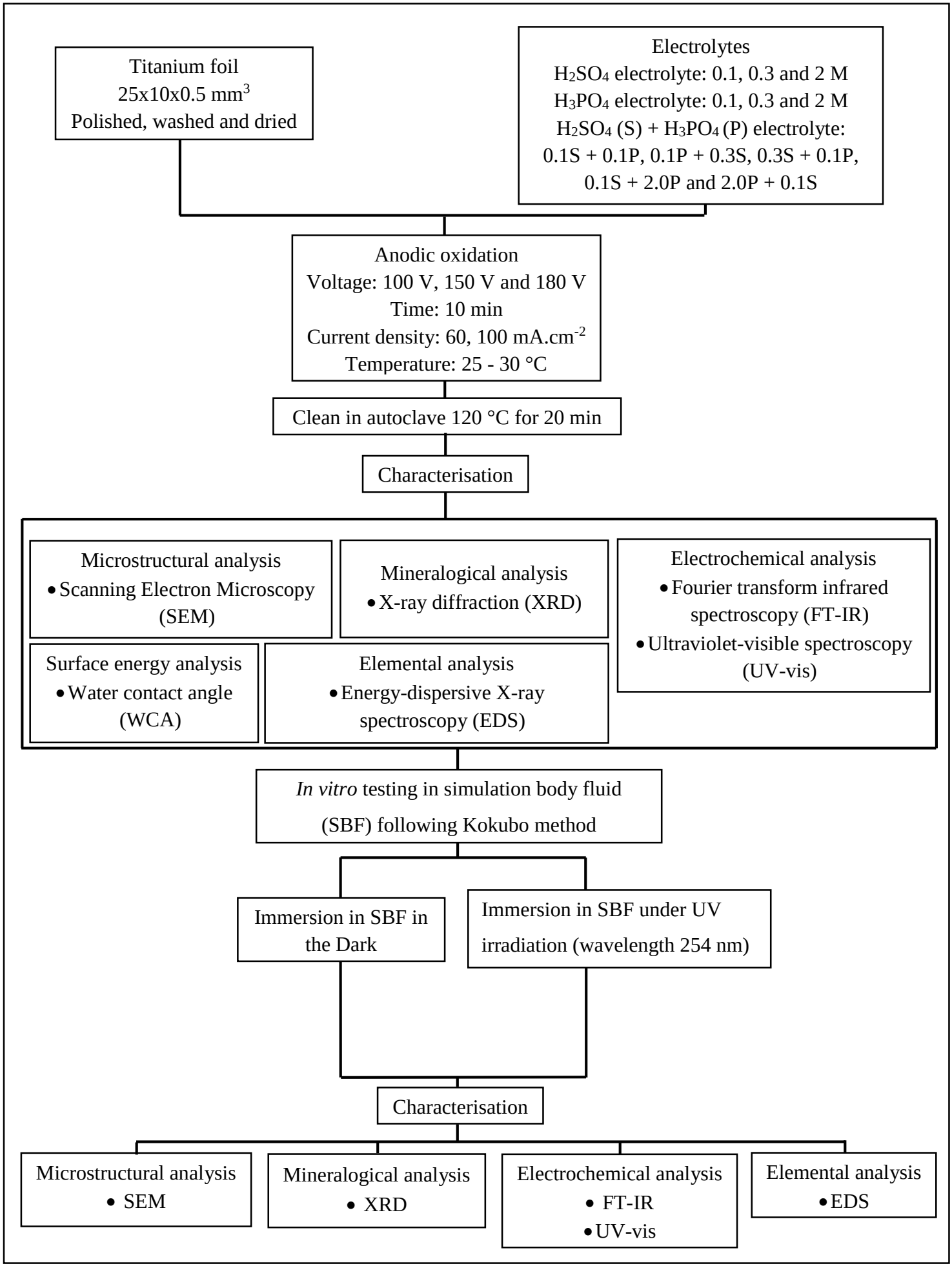

Figure 3.1: Flowchart of the sample preparation, characterisation and testing for this study

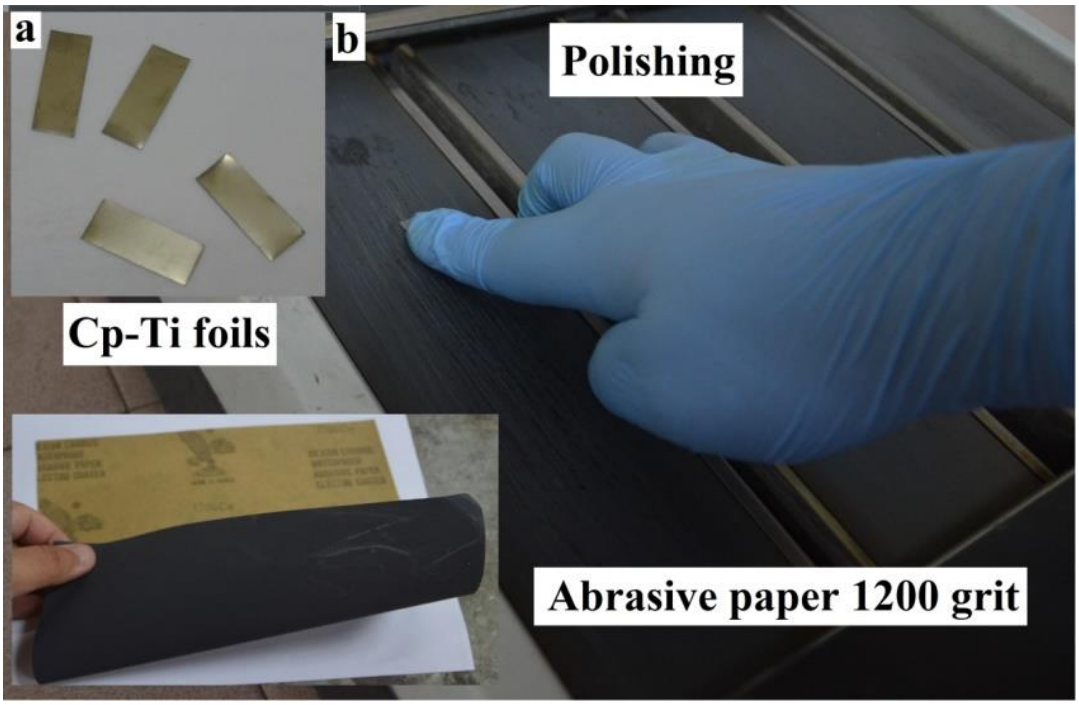

Figure 3.2: (a) Cp-Ti (grade 2) foil of (25 x 10 x 0.05) in mm, (b) Polishing performed using 1200 grit abrasive paper (~1 μm)

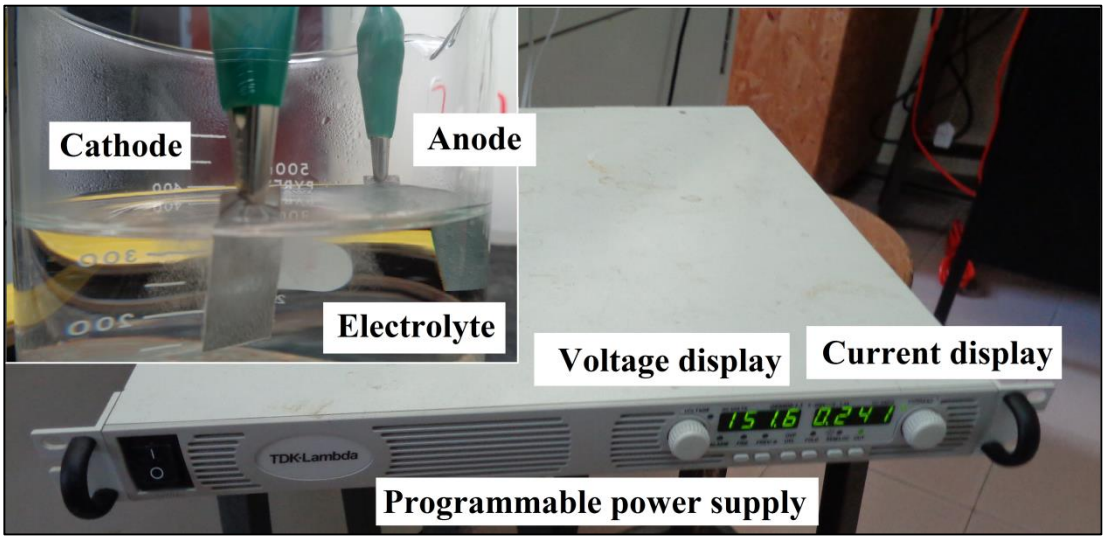

Figure 3.3: Electrochemical process is made using programmable power supply adjustable current density and voltage with Cp-Ti of both cathode and anode ends under medium of electrolyte with specific molarity

Anodic oxidation was done in an electrolyte contained ~0.4 L solutions between 25 °C and 30 °C (Oh *et al.*, 2005). The anode and the cathode were both Cp-Ti (grade 2) foils as illustrated in Figure 3.3. The anodization was done using a programmable power supply (Genesys^{TM} GEN600-1.3 750W) as illustrated in Figure 3.3. The anodised foils were cleaned by distilled water followed by drying in air. After

that, the samples were cleaned in an autoclaving unit at 120 °C for 20 min (Figure 3.4). Investigations with respect to the influence of electrolytes on the oxide formation were made using different solutions.

Figure 3.4: Autoclave unit (*Nklive Nve-50*®)

Electrolyte concentration range, i.e., 0.1 M, 0.3 M and 2.0 M, have been applied in this study for diluted H_2SO_4 and H_3PO_4 electrolytes. This is due to the nature of the acids used. Since H_2SO_4 and H_3PO_4 have contrast in metal dissolution and oxide growth rate (Yerokhin *et al.*, 1999; Jaeggi *et al.*, 2006; Capek *et al.*, 2008). This can result in variation in the TiO_2 properties such as different thickness, porosity and crystalline. This range, i.e., 0.1 M to 2.0 M can give enough evidence of the behavior of each acid on the resulted TiO_2 coatings.

The applied voltage, i.e., 100 V, 150 V and 180 V, and the current density 60 and 100 $mA.cm^{-2}$ were optimized according to the electrolyte concentrations used. It has been reported that the breakdown voltage can reach up to 150 V at 1.5 M H_2SO_4 electrolyte at 60 $mA.cm^{-2}$ (Abdullah, 2010), and up to 200 V at 1.5 M H_3PO_4

electrolyte (Song *et al.*, 2009). It was also reported that the TiO_2 anatase crystalline threshold starts from 100 V for 0.5 M H_2SO_4 electrolyte at 60 $mA.cm^{-2}$ and 100 $mA.cm^{-2}$ (Diamanti and Pedefferi, 2007; Saleh and Abdullah, 2015), while it starts from 200 V for 0.1 M H_3PO_4 electrolyte at 60 $mA.cm^{-2}$ (Saleh and Abdullah, 2016). The anodization time for 10 minutes was enough to allow the maximum voltage to reach (stage 1) when applied for high voltages as described in **Section 2.8.1**. The parameters used from previous studies for the H_2SO_4 electrolyte, H_3PO_4 electrolyte mixture electrolyte (H_2SO_4 + H_3PO_4) were obtained in Table 2.38, Table 2.39 and Table 2.40. While the contrasts between the H_2SO_4 electrolyte and H_3PO_4 electrolyte in term of the parameters used and the resulted TiO_2 were reported in Table 2.41.

UV with a wavelength lower than 400 nm can activate the photoactivity of TiO_2 (Brunella *et al.*, 2007). This has been described in detail in Section 2.7.4.6. Several studies as reported the hydrophilic activity of TiO_2 under UV wavelengths 365 nm and 254 nm as obtained in Table 2.33, also successful apatite formation under these wavelengths as obtained in Table 2.34. In this study, a UV of 254 nm wavelength was used; due to it has a shorter wavelength than UV with 365 nm which therefore can penetrate and get absorbed by the TiO_2 surface and activate the photocatalytic properties. Also according to the UV absorption test, the TiO_2 coatings have obtained a bandgap range between 344 nm and 385 nm. This is has been described in **Section 4.2.5**; **Section 4.3.5**; and **Section 4.4.5**, for The TiO_2 anodised in H_2SO_4, H_3PO_4, and mixed solutions respectively. This can guarantee higher absorption of UV irradiation on all the TiO_2 coatings anodised in the different electrolyte. Therefore, evaluate the photoactivity of TiO_2 in *in vitro* testing.

3.3.1 Sulphuric Acid (H_2SO_4) Electrolyte

The H_2SO_4 electrolyte was prepared by diluting H_2SO_4 (Q-rec, 98 Wt %) in distilled water. To prepare 1000 ml of electrolyte, first add 500 ml of distilled water, then the acid, then add distilled water again to reach 1000 ml. Figure 3.5 obtain a schematic diagram of the dilution preparation method and the amount of acid required for certain molarity targeted. The anodization parameters vary on concentration, current density and applied d.c. voltages as shown in Table 3.1. The parameters values were optimized

according to the discussed in **Section 3.3**. The used test conditions were between 25 °C and 30 °C.

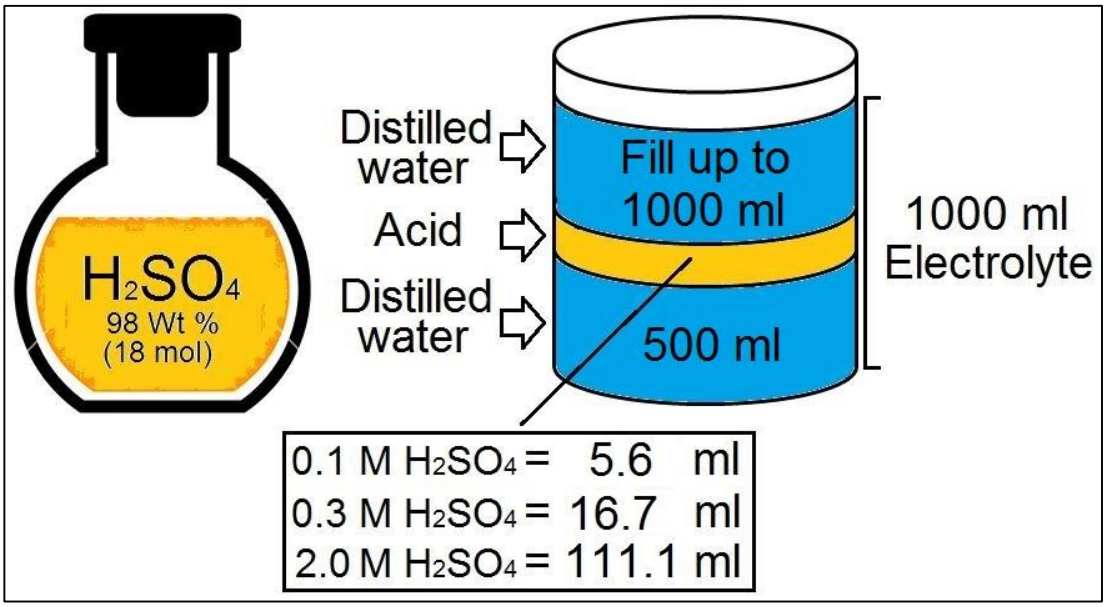

Figure 3.5: Schematic diagram show H_2SO_4 electrolyte preparation

Table 3.1: Parameters used for anodic oxidation in H_2SO_4

Parameter	Value(s)
H_2SO_4 Electrolyte (M)	0.1, 0.3 and 2.0
Temperature (°C)	25-30
d.c. Voltage (V)	100, 150 and 180
Current density ($mA.cm^{-2}$)	60 and 100

3.3.2 Phosphoric Acid (H_3PO_4) Electrolyte

The H_2SO_4 electrolyte was prepared by diluting H_3PO_4 (Bendosen, 85 wt %) in distilled water. To prepare 1000 ml of electrolyte, first add 500 ml of distilled water, then the acid, then add distilled water again to reach 1000 ml. Figure 3.6 obtain a schematic diagram of the dilution preparation method and the amount of acid required for certain molarity targeted. Anodization was carried out under different d.c. voltages and current density between 25 °C and 30 °C. The parameters values were optimized according to the discussed in **Section 3.3**. The parameters are shown in table 3.2.

Table 3.2: Parameters used for anodic oxidation in H_3PO_4

Parameter	Value(s)
Electrolyte (Molar)	0.1, 0.3 and 2.0
Temperature (°C)	25 - 30
d.c. Voltage (V)	100, 150 and 180
Current density ($mA.cm^{-2}$)	60 and 100

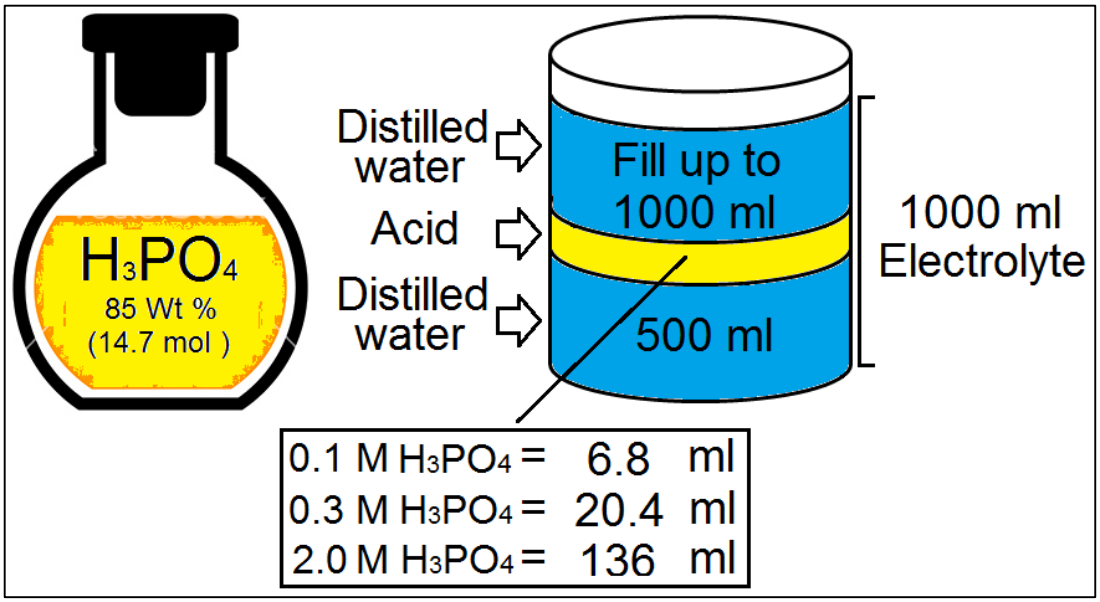

Figure 3.6: Schematic diagram show H_3PO_4 electrolyte preparation

3.3.3 Mixed Electrolyte (H_2SO_4 + H_3PO_4)

The mixed electrolyte is a mixture of H_2SO_4 electrolyte and H_3PO_4 electrolyte. The parameters values were a combination of the values of both acids. The description of the solutions and the associated experimental parameters are shown in Table 3.3. Figure 3.7 obtain a schematic diagram of the dilution preparation method and the amount of acid required for certain molarity targeted.

Table 3.3: Parameters used for anodic oxidation in mixed solution

Electrolyte Composition	Parameter	Value
0.1 M H_3PO_4 + 0.3 M H_2SO_4	Temperature (°C)	25 - 30
0.3 M H_3PO_4 + 0.1 M H_2SO_4	d.c. Voltage (V)	100, 150 and 180
0.1 M H_3PO_4 + 0.1 M H_2SO_4	Current Density ($mA.cm^{-2}$)	60 and 100
2.0 M H_3PO_4 + 0.1 M H_2SO_4		
0.1 M H_3PO_4 + 2.0 M H_2SO_4		

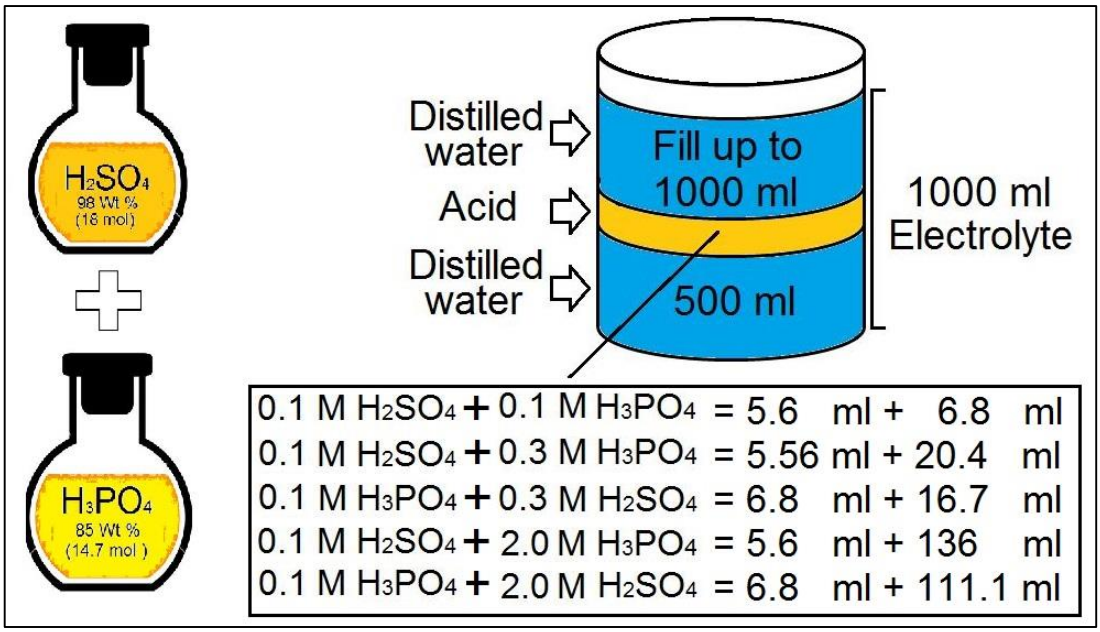

Figure 3.7: Schematic diagram show mixed electrolyte preparation

3.4 *In Vitro* Testing

In vitro test comprised the evaluation of apatite precipitation on TiO_2 coatings by immersion in SBF solution. The bone-bonding ability of a material is often evaluated by examining the ability of apatite to form on its surface in an SBF with ion concentrations nearly equal to those of human blood plasma. The validation of SBF as an *in vitro* is discussed in **Section 2.10.1**.

3.4.1 Sample Preparation and Characterisation of Apatite Formed on TiO_2 Formed in H_2SO_4, H_3PO_4 and Mixed Acids

TiO_2 coatings were cleaned using the autoclave and stored in distilled water. The parameters used in *in vitro* testing were listed in Table 3.4. The coatings were then subjected to *in vitro* testing. They were immersed in SBF (1.5 M) at 36.5 ºC in; the dark using incubator under irradiation of UV mercury lamb (Cole-Parmer®, wavelength 365 nm, 9 W/cm^2) for 6 and 12 days. SBF was prepared according to Kokubo method (Kokubo and Takadama, 2006). The apatite formation characterisation of the coatings was carried out using:

i. Microstructure analysis using scanning electron microscopy (SEM) and elemental analysis using energy dispersive spectrometry (EDS) (**Section 3.5.2**).

ii. Phase mineralogical analysis using x-ray diffraction (XRD) (**Section 3.5.3**).

iii. Absorption analysis using Fourier transform infrared spectroscopy (FT-IR) (**Section 3.5.4**).

Table 3.4: Parameters used for *in vitro* testing in SBF immersion in coatings anodised in H_2SO_4 and H_3PO_4 and mixed electrolytes

Parameters	Value
TiO_2 coatings	H_2SO_4 electrolyte: 0.1 and 2 M H_3PO_4 electrolyte: 0.1 and 2 M H_2SO_4 (S) + H_3PO_4 (P) electrolyte: 0.1 S + 0.1 P, 0.1 S + 2.0 P and 2.0 P + 0.1 S
DC Voltage (V)	150
Current Density ($mA.cm^{-2}$)	100

3.4.2 Simulated Body Fluid (SBF) Preparation

Conventional SBF was prepared for biological tests (*in vitro*) in this study. The amount and procedure used were the same as the recipe of Kokubo and Takadama (2006) as shown in Table 3.5 (Kokubo and Takadama, 2006). The chemical reagents are shown in Figure 3.8 compares conventional SBF having equal concentrations of ions other than C^- and HCO_3^- to blood plasma (Ravaglioli *et al.,* 1992; Xiao *et al.*, 2003).

SBF has prepared step by step according to Kokubo and Takadama (2006) method as follows:

i. ~700 ml of ultra-pure water (distilled water) was poured into a 1000 ml polypropylene beaker and stirred using a magnetic bar at 36.5 ± 0.2 °C.

ii. The reagents were dissolved in water in the order 1-8 as in Table 3.5. Each reagent was completely dissolved before the new reagent added.

iii. The temperature of the solution was set at 36.5 (±1.5 °C). Pure water was added up to 900 ml.

iv. The electrode of the pH meter was inserted before dissolving Tris (9^{th} in the order), and the pH of the solution was 2.0 (±1.0).

v. A small amount of Tris was added until the reagent completely dissolved and pH became constant. After the pH became 7.30 (±0.05), the temperature was maintained at 36.5 (±0.5 °C). Tris was added to raise the pH to 7.45.

vi. 1 M HCl was dropped through a pipette to lower the pH to 7.42 (±0.01).

vii. The remaining Tris and 1 M HCl were poured alternately into the solution to keep the pH within 7.42 - 7.45.

viii. The pH of the solution was adjusted to 7.40 by dropping 1 M HCl dropwise at 36.5 °C.

ix. The solution was transferred to 1000 ml volumetric flask and pure water was added to the marked line after the temperature had cooled down to 20 °C Figure 3.9.

Table 3.5: The order, amounts, weighing containers, purities and formula weights of reagents used for preparing 1000 mL of SBF by (Kokubo and Takadama, 2006)

Order	Reagent	Amount (g)	Container	Purity (%)	Formula weight (g/mol)
1	$NaCl_2$	8.035	Weighing paper	99.5	58.4430
2	$NaHCO_3$	0.355	Weighing paper	99.5	84.0068
3	KCl	0.225	Weighing bottle	99.5	74.5515
4	$K_2HPO_4.3H_2O$	0.231	Weighing bottle	99.0	228.2220
5	$MgCl_2.6H_2O$	0.311	Weighing bottle	98.0	203.3034
6	1.0 M HCl	39 mL	Graduated cylinder	-	-
7	$CaCl_2$	0.292	Weighing bottle	95.0	110.9848
8	Na_2SO_4	0.072	Weighing bottle	99.0	142.0428
9	Tris	6.118	Weighing paper	99.0	121.1356
10	1.0 M HCl	0-5 mL	Syringe	-	-

Tris = Tris-hydroxymethyl aminomethane: $(HOCH_2)_3.CNH_2$

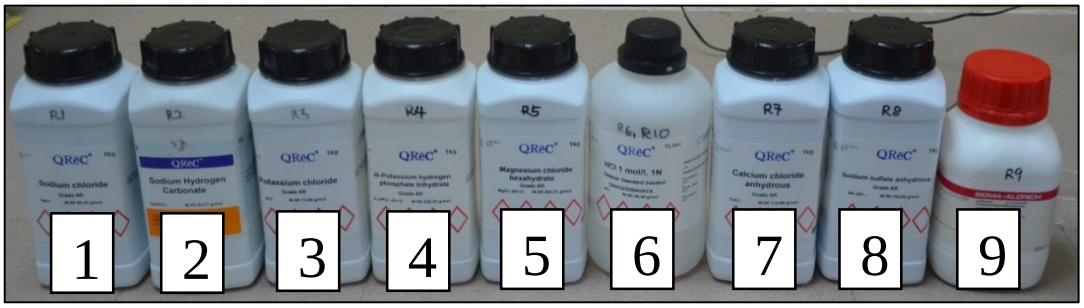

Figure 3.8: Chemical reagents for SBF preparation (Q-rec®): (1) Sodium chloride ($NaCl_2$), (2) Sodium hydrogen carbonate ($NaHCO_3$), (3) Potassium chloride (KCl), (4) di-Potassium hydrogen phosphate trihydrate ($K_2HPO_4.3H_2O$), (5) Magnesium chloride hexahydrate ($MgCl_2.6H_2O$), (6) Hydrochloric acid (1 M), (7) calcium chloride ($CaCl_2$), (8) Sodium sulfate anhydrous (Na_2SO_4), (9) Tris ($C_4H_{11}NO_3$)

3.4.3 Soaking in Simulation Body Fluid (SBF)

Specimen dimensions were measured and the surface area was calculated (with an accuracy of 2 mm^2) for the thin plate. The volume of SBF was calculated for testing using the following Equation 3.1 (Kokubo and Takadama, 2006). According to Kokubo the ratio of sample's surface area to the SBF liquid used is 1:10 as obtained by the following equation.

$$V_s = \frac{S_a}{10} \tag{3.1}$$

Where,

V_s = volume of SBF (ml).

S_a = the apparent surface area of the specimen (mm^2).

Table 3.6: Comparison of nominal ion concentration of SBF to human blood plasma (Kokubo and Takadama, 2006)

Ion	Ion concentration (mM)	
Blood plasma	SBF	
Na^+	142.0	142.0
K^+	5.0	5.0
Mg^{2+}	1.5	1.5
Ca^{2+}	2.5	2.5
Cl^-	103.0	147.8
HCO_3^-	27.0	4.2
HPO_4^{-2}	1.0	1.0
SO_4^{-2}	0.5	0.5
PH	7.2-7.4	7.40

Specimens with dimensions 10 mm × 10 mm × 0.09 mm (Figure 3.10) were used and 22 ml SBF solution is required (as shown in the calculation). For *in vitro* testing, the specimen was soaked in SBF at ~36.5 °C by, covered with expandable polyethylene film (Parafilm®) (Figure 3.11) and placed in an incubator (Incucell MMM Group®) (Figure 3.12).

Calculation of surface area and volume for SBF solution:

S_a = (10 mm × 10 mm × 2) + (10 mm × 0.09 mm × 4) = 103.6 mm^2.

V_s = 102 mm^2/10 = 10.36 ml.

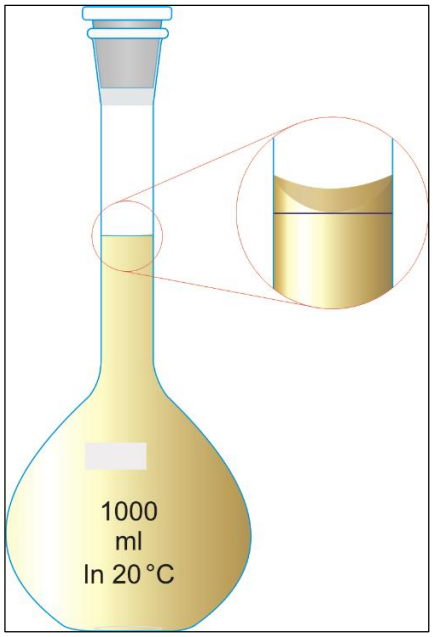

Figure 3.9: SBF in 1000 ml volumetric flask

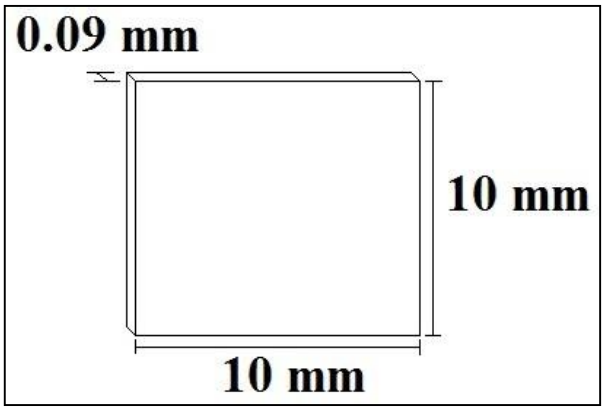

Figure 3.10: Specimen surface area

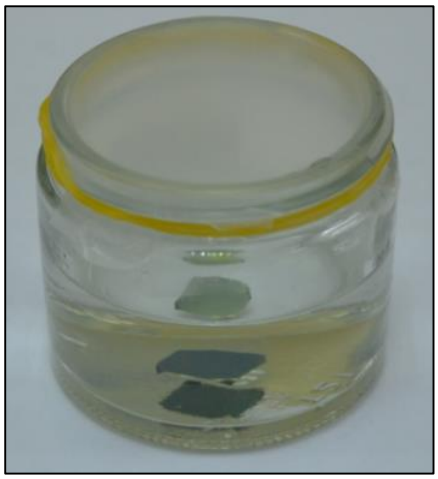

Figure 3.11: Sample immersed in SBF and ready for incubation

Figure 3.12: Incubator for sample preservation at 36.5 °C

3.4.4 Soaking in Simulation Body Fluid (SBF) under Ultraviolet (UV) Light

Multiple studies have reported the irradiation of UV with different wavelengths on TiO_2 coatings formed using dip coating (Guo *et al.,* 2010), chemical treatment (Uetsuki *et al.,* 2010; Iwasa *et al.,* 2010; Ueda *et al.,* 2010), sputtering (Miyauchi *et al.,* 2010), plasma spraying (Liu *et al.,* 2008), gel oxidation (Abdullah and Sorrell, 2012) and Micro-arc oxidation (MAO) (Han *et al.,* 2008). The irradiation was made in air and water prior to immersion in SBF, and it was reported that TiO_2 irradiated in UV in the water has more numbered active sites for apatite nucleation (Uetsuki *et al.,* 2010). Others have reported UV irradiation during the immersion in SBF. These studies have been reported in detail in Table 2.34. They have concluded that UV promoted higher apatite formation ability with increased irradiation time prior to in vitro test in SBF. However, irradiation of UV during the immersion in SBF has promoted an accelerated apatite formation (Ueda *et al.,* 2010). However, no study has reported the UV irradiation in SBF on TiO_2 formed by anodization in diluted H_2SO_4 and H_3PO_4 electrolyte. Therefore, the apatite-forming ability of the TiO_2 coatings that was formed by anodization in diluted H_2SO_4 and H_3PO_4 was tested under UV in SBF. The results were compared with the TiO_2 coatings immersed in SBF in the dark condition to obtain the apatite formation performance under each condition. The specimens were tested by soaking in 22 ml SBF and maintain a temperature of 36.5 ± 0.5 °C and put in the incubator (Figure 3.12) in the dark condition. While the samples were but in a water bath during the continuous exposure of ultraviolet light (Cole-Parmer® UV lamp 230 V / 50-60 Hz, 0.16 Amps) with wavelength 254 nm and intensity 4 W/cm^2. In order to maintain a constant SBF temperature, the lamp was set at a distance of 10 cm from the specimen. Studies have reported the distance is between 3.5 cm (Uetsuki *et al.,* 2010) and 15 cm (Kasuga *et al.,* 2002). The temperature of the water in the water bath was checked frequently to assure the UV temperature hasn't heat it up. The experimental set-up is shown in Figure 3.13.

3.5 Characterisation and Testing of Sample

Multiple characterisations to be used to investigate the properties of the anodised TiO_2 coatings will be discussed as follows.

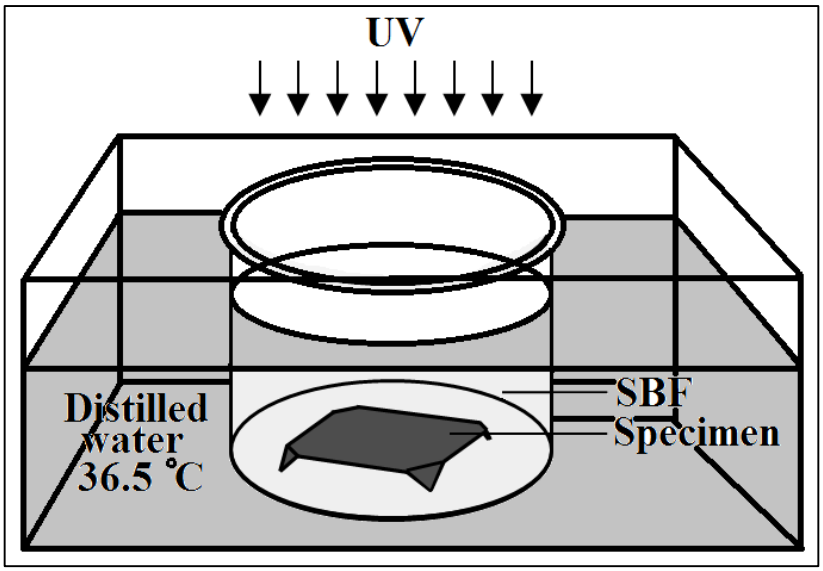

Figure 3.13: Schematic of setup for UV irradiation of specimen during soaking in SBF

3.5.1 Appearance Reflectance (Colour Measurements)

The colours of the titanium oxide films were measured using a Colorimeter (i-Wave WR-10®) as obtained in Figure 3.14 with parameters as follows:

i. Measurement mode: Reflection.

ii. Colour system: L*a*b* system.

iii. Measurement Geometry: Diffuse illumination and 8° viewing.

iv. Illumination Source: Pulsed xenon filtered to approximate D 65.

v. Measurement observer: 10°.

The appearance of titanium oxide coatings was also recorded using digital camera Sony Cypershot® (20.1 Mega Pixels). To compare images' colour was captured using a digital camera, Colour coordinate L*a*b* from colorimeter (Colour Metric Converter online software designed by easyrgb.com, http://www.easyrgb.com /index. php? X=CALC) was used to convert L*a*b* coordinate to digital colour (Table 3.7) (Kim *et al.*, 1996).

3.5.2 Microstructure and Elemental Analysis

The microstructures and the thickness were examined using a Scanning electron microscope (SEM, Hitachi SUI510®) as obtained in Figure 3.15 to characterise surface

morphology and microstructure of the TiO_2 surface. Also SEM was used to detect the TiO_2 coating cross section thickness. Elemental analyses were done using an attached Energy dispersive x-ray spectrometer (EDX) (Horiba Emax X-act®) to identify the ions incorporated into the TiO_2 coating. The operating parameters were as follows:

i. Sample coating: Gold sputtering.

ii. Accelerating voltage: 20 kV.

iii. Imaging: Secondary electron.

iv. Detector: Upper detector.

Figure 3.14: Colourmeter (i-Wave WR-10®)

Table 3.7: The value of the coordinate CIELAB (OIV, 2006)

Colour	Value	Colour	Value
Red	+a*	Green	-a*
Yellow	+b*	Blue	-b*
White	L = 100	Black	L = 0

Figure 3.15: SEM (Hitach SUI510®)

3.5.3 Mineralogical Analysis

X-ray diffraction (XRD, Bruker D8 advance®) as obtained in Figure 3.16 was employed to assess film crystallinity and phase formation. The parameters for x-ray diffraction analyses were as follows:

i. Voltage : 45 kV
ii. Current : 40 mA
iii. Incidence angle : 0.8°
iv. Scanning speed : 0.01° 2θ $^{S-1}$
v. Step size : 0.02° 2θ
vi. Range: 20° – 75° 2θ

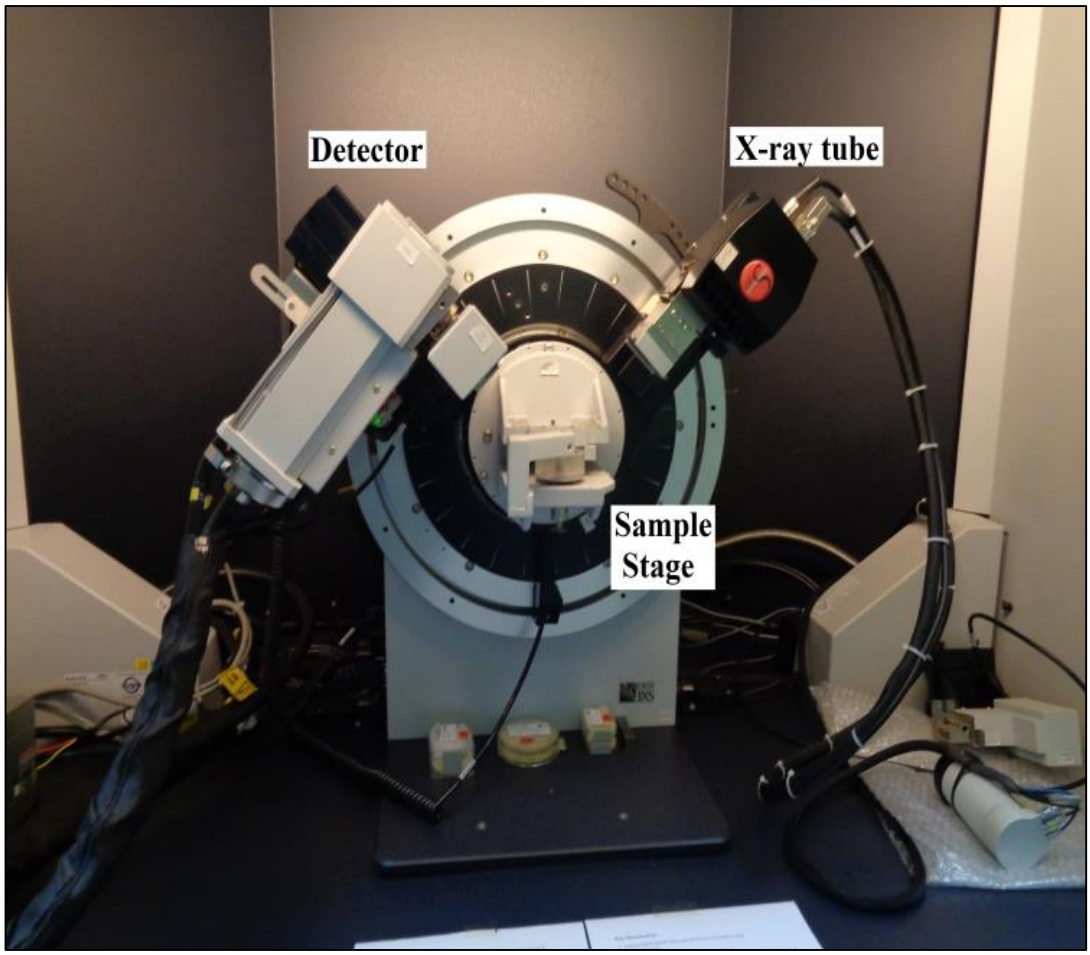

Figure 3.16: XRD Bruker D8 Advance®

3.5.3.1 Phase Crystal Size

The crystal size for a specific crystalline phase of a material can be calculated using the information from the XRD spectrum. The crystal size was calculated for the main orientation peak of the TiO_2 crystalline phases, i.e., anatase and rutile by applying to the following equations:

i. Grain size (D) of the TiO_2 using Debye-Scherrer formula as follows (Weller, 1994):

$$D = \frac{0.9\lambda}{\beta \cos\theta} \tag{4.1}$$

Where;

D is the grain size, (λ = 0.15406 nm) is the x-ray wavelength, θ is the Bragg diffraction angle and β is the full width half maximum (FWHM) of the diffraction peak.

ii. The micro-strain ε is the deformation of an object divided by its ideal length. It is estimated using the equation:

$$\varepsilon = \frac{\beta \cos\theta}{4} \tag{4.3}$$

By fitting the phase mineralogical results, the strain ε and crystal size of the films have been calculated from the (101) for anatase and (110) for rutile diffraction peaks.

3.5.3.2 Crystallisation Percentage

EVA software from BRUKER© has been used to calculate the percent crystallinity of the TiO_2 coating. The crystalline TiO_2, i.e., anatase and rutile percentage can be detected using software analysis by distinguishing the amorphous and crystalline areas within the mineralogical spectrum.

3.5.4 Absorption Analysis

Fourier Transform Infrared Spectroscopy (FT-IR, Perkin-Elmer Spectrum 100®) as shown in Figure 3.17 using Attenuated Total Reflectance (ATR) method was applied to identify the chemical compounds and bonds of the TiO_2 coating. The parameters for x-ray diffraction analyses were as follows:

i. Range: 500-400 cm^{-1}.
ii. No of scans: 32 scans.
iii. Resolution: 4 cm^{-1}.
iv. Fingerprinting Method: ATR.

3.5.5 Bandgap Calculation

The optical bandgap (E_g) of the TiO_2 coating, the acquired diffuse reflectance spectrum from UV-vis has converted to Kubelka-Munk function the following formula (Davis and Mott, 2006):

$$(k * h\nu)^2 = f(h\nu) \tag{4.4}$$

$$k = \frac{(1-R)^2}{2R} \tag{4.5}$$

Where;

h is the Planck's constant, ν is the frequency of vibration, k is the reflectance transformed, E_g is the bandgap, k is the reflectancy (%).

The optical bandgap E_g of the TiO_2 thin films was determined by extrapolation of the linear portion of $(kh\nu)^2$ versus $h\nu$ plots, Here, the unit for $h\nu$ is eV (electron volts), and its relationship to the wavelength λ (nm) become $h\nu = \frac{1239.7}{\lambda}$.

3.5.6 Hydrophilicity Analysis

The hydrophilicity testing was performed using (Ramé-hart Instruments Co.) as obtained in Figure 3.17, by measuring the water contact angle (WCA) of the water drop equal to 4 µL as illustrated in Figure 3.18.

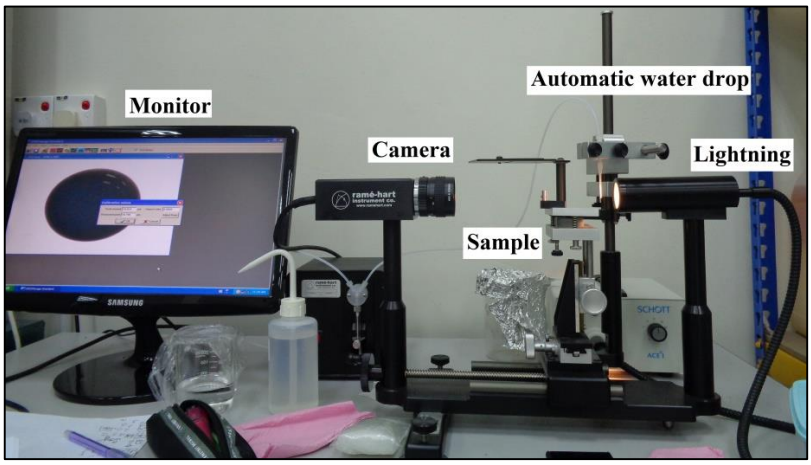

Figure 3.17: WCA tester (Ramé-hart Instruments Co.)

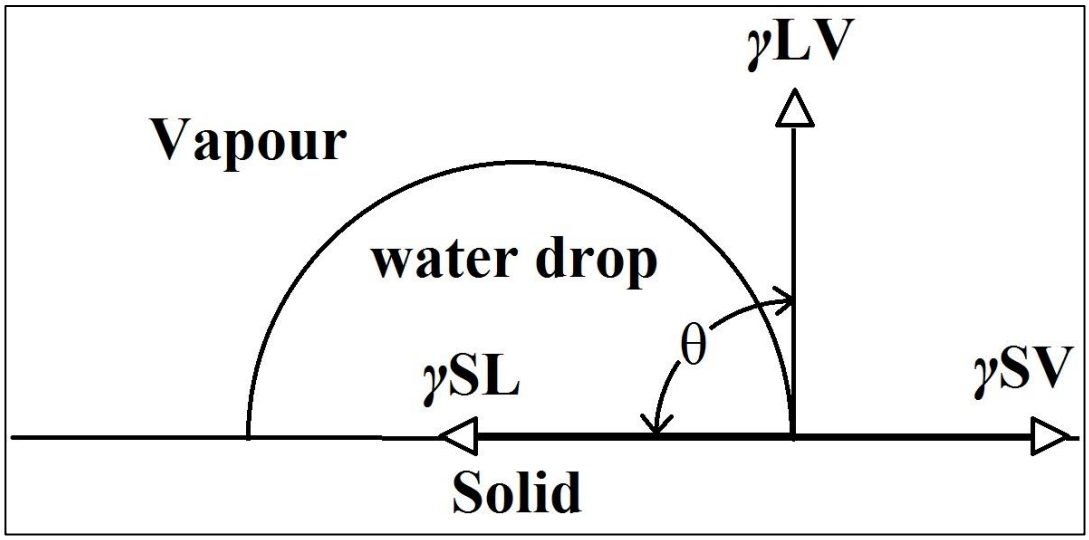

Figure 3.18: Surface energy during water drop contact angle measurments, γ is surface tension, S is soild, V is vapour, L is liquid

CHAPTER 4

ANODISATION OF TITANIUM

4.1 Introduction

Titanium dioxide (TiO_2) produced by anodic oxidation of Titanium (Ti) in different electrolytes to evaluate the microstructural, elementary, mineralogical, optical and absorption and hydrophilicity properties. Three electrolytes were used, sulphuric acid (H_2SO_4) electrolyte, phosphoric acid (H_3PO_4) electrolyte and mixed electrolyte (H_2SO_4 + H_3PO_4) is a mixture of H_2SO_4 and H_3PO_4 acids. Parameters such applied voltage, current density, electrolyte composition and breakdown voltage on the anodised TiO_2 coating was discussed.

4.2 Anodic Oxidation of Ti in Sulphuric Acid (H_2SO_4) Electrolyte

The TiO_2 coatings anodised in a diluted sulphuric acid (H_2SO_4) with different concentration (0.1 M, 0.3 M and 2.0 M) was characterised, i.e., colour, microstructure, morphology, mineralogy and surface energy. The bioactivity of these coatings conducted by *in vitro* test was characterised in Chapter 5.

4.2.1 Colour of Anodised TiO_2 in H_2SO_4 Electrolyte

The visual appearance taken by camera of the TiO_2 coatings anodised in H_2SO_4 electrolyte as a function of applied voltage (V), current density ($mA.cm^{-2}$) and molarity (M) at 10 minutes is shown in Table 4.1. While Table 4.2 has obtained digital colouring for the coatings correspond to Table 4.1 obtain colours using a Colorimeter with

CIELAB coordinates (L*a*b*) and converted to computer colour interface using computer software. The subdivision of these figures is based on visual and mineralogical examination during processing.

Table 4.1: Visual appearance taken by camera of TiO_2 surface colour at a function of applied voltage, current density at 0.1 M, 0.3 M and 2.0 M at 10 min for coatings anodised in H_2SO_4 electrolyte

Voltage (V)	Molarity (M)	Current Density ($mA.cm^{-2}$)	
		60	100
100	0.1	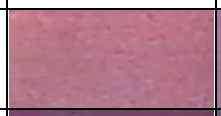	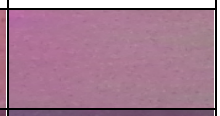
	0.3	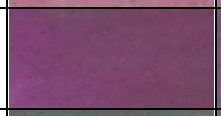	
	2.0	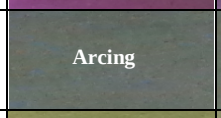 Arcing	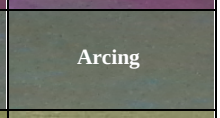 Arcing
150	0.1		
	0.3	 Arcing	 Arcing
	2.0	 Arcing	 Arcing
180	0.1	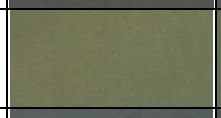	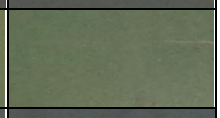
	0.3	 Arcing	 Arcing
	2.0	 Arcing	 Arcing

Arcing; grey interference colour due to breakdown

The present data conclude the following:

i. There is a gradual colour variation as a function of applied voltage and molar concentration. The colours change from bright colours to grey colour with increased molarity and voltage.

ii. The current density has a slight change on the colour interface where the colours become brighter with the increased current density.

iii. The grey colour surface is associated with the oxide film breakdown, where

arcing (spark and discharge), gas bubble and localized melting take place and result in structural change of the oxide surface (Wang *et al.*, 2015). Anodization mechanism has been described in **Section 2.8**.

iv. The Breakdown threshold (arcing) can be obtained starting at 100 V and 2 M.

Table 4.2: CIELAB digital colour generated with colourmeter of TiO_2 surface colour at a function of applied voltage, current density at 0.1 M, 0.3 M and 2.0 M at 10 min for coatings anodised in H_2SO_4 electrolyte

Voltage (V)	Molarity (M)	Current density ($mA.cm^{-2}$)	
		60	100
100	0.1		
	0.3		
	2.0	Arcing	Arcing
150	0.1		
	0.3	Arcing	Arcing
	2.0	Arcing	Arcing
180	0.1		
	0.3	Arcing	Arcing
	2.0	Arcing	Arcing

Arcing; grey colour due to breakdown

The interference that occur between oxide, metal and light which colours the TiO_2 (Gaul, 1993) can be affected by the anodization parameters conditions where the colour varies by changing the current density and the electrolyte concentration (Sul *et al.*, 2001), while the colour changes during anodization are dependent only on anodic film thickness (Yang *et al.*, 2006) which is proportional to the applied voltage (Karambakhsh *et al.*, 2012).

The colour changing due to interference effect is preferred at low anodization voltage where a low thickness of 10 to few hundreds nm thick with amorphous structure of TiO_2 (Gaul, 1993). At higher oxide thickness, the interference effect is lost, alongside the surface colour. Grey colour surface is associated with localized breakdown, where high voltage favoured crystallisation forms, which impede interference effect. Breaking down at different voltage depends on the type and concentration of electrolyte and the current density (Ashraf and Vaezi, 2004; Diamanti *et al.*, 2013).

Previous studies indicated that breakdown occurred at 100 V according to Marchenoir et al. (1980) and at 110 V at 20 $mA.cm^{-2}$ according to Song et al. (2009), when anodizing in 1.0 M (Marchenoir *et al.*, 1980; Song *et al.*, 2009). Arcing is believed to be due to the porous formation on a micron scale as it was discussed in Section 4.2.2. The pores may cause the TiO_2 surface to lose appearance, and results in a gray color surface. This is can be noticed with the increased voltage and molarity as obtained in Table 4.2 and Table 4.3. The light grey that was obtained on the TiO_2 interference that was anodised in 180 V and 2.0 M at 60 and 100 $mA.cm^{-2}$ can be related to the rutile crystalline (more clear at Table 4.3) according to the mineralogical results obtained in Section 4.2.4. Rutile threshold was at 100 V and 2.0 M; It has been reported that anatase to rutile transformation takes place in the range between 400 ºC - 1200 ºC, however, bulk anatase is suggested widely to start transforming to rutile in air at 600 ºC (Li *et al.*, 2005; Hanaor and Sorrell, 2011) and its time-dependent because it is reconstructive (Jamieson and Olinger, 1969).

Previously, Delplancke *et al.* (1982) have described that colour creation is due to the stoichiometric defects in the oxide film composition and/or due to the interference of waves in crystalline layers (Delplancke *et al.*, 1982). However, Van Gils *et al.*, (2004) and Pérez del Pino *et al.*, (2004) specified the main cause of the creation of colour is due to the interference of waves in transition oxide layer of Ti.

Table 4.1 and Table 4.2 obtain a brightness of coatings surfaces at current densities 60 and 100 $mA.cm^{-2}$ respectively. The brightness (L* value) obtained is according to CIELAB coordinates, which is related to colour in Table 4.4. From Table 4.1 and Table 4.2, the brightness at 0.1 M is higher than 0.3 M and 2.0 M when compared at a single voltage. However, 2.0 M is higher than 0.3 M except at 100 V.

It is apparent that molarity has a higher effect than the current density and the voltage with respect to brightness. The high brightness of 0.1 M coatings is due to

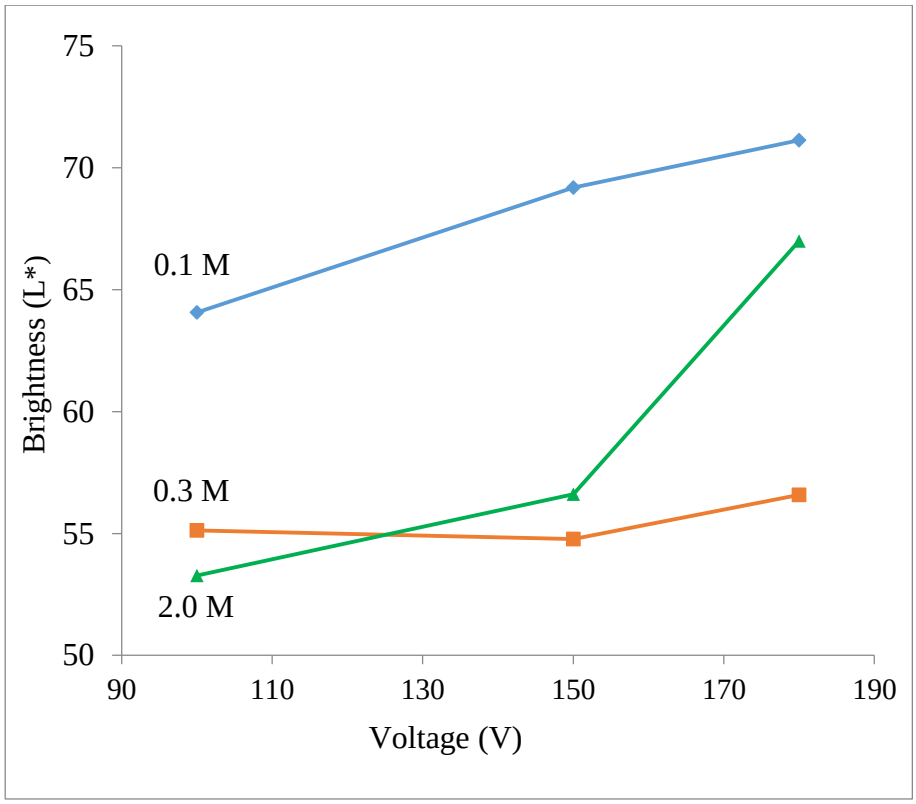

Figure 4.1: TiO_2 surface colour brightness (L*) as a function of applied voltage, at and molar concentration at 60 $mA.cm^{-2}$ in H_2SO_4 electrolyte

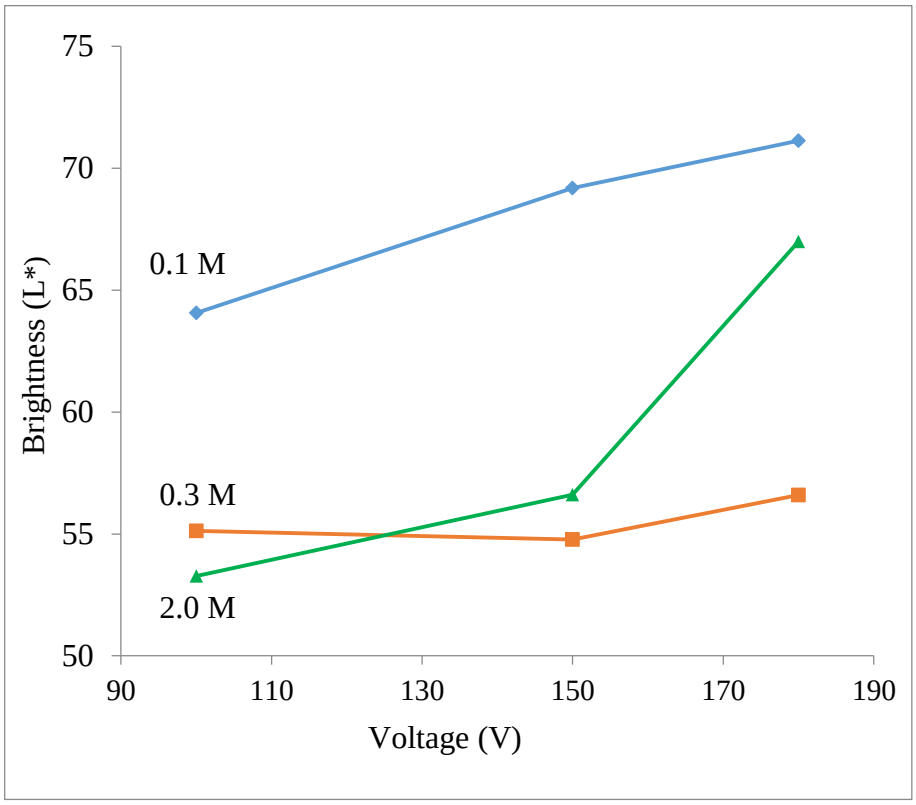

Figure 4.2: TiO_2 surface colour brightness (L*) as a function of applied voltage, at and molar concentration at 100 $mA.cm^{-2}$ in H_2SO_4 electrolyte

the colourful appearance of the TiO_2 coatings that is resulted from the less porous surface. While the low brightness of the coatings at 0.3 M and 2.0 M is due to the grey colour reflectance of their surface that is resulted from the increased porosity due to the breakdown phenomena as described later. At 100 V 0.3 M has brighter interference also due to the less porous surface. The brightness at 2.0 M has increased with the increased voltage due to light grey that has appeared on the TiO_2 surface due to the heavy breakdown which has resulted in a porous surface with rutile formation which will be discussed later.

The colour of the film surfaces in Table 4.2 can be related to the brightness of surfaces (L* value) according to CIELAB coordinates. Harold (2001) defined as brightness as the object's luminous intensity (usually light reflecting or transmitting capability). Where the brightness value is somewhere between 0 (black appearance) and 100 (white appearance) (Harold, 2001).

The anodization parameters i.e., voltage, current density, and molarity have an influence on the TiO_2 coating appearance. The appearance obtained colorful at the lower voltage, current density, and molarity, while the appearance was lost with the increased voltage.

4.2.2 Microstructure of Anodised TiO_2 in H_2SO_4 Electrolyte

Figure 4.3 and Figure 4.4 observe the surface image microstructure of the TiO_2 coatings anodised in H_2SO_4 electrolyte captured using the scanning electron microscope (SEM) at 60 $mA.cm^{-2}$ and 100 $mA.cm^{-2}$ respectively.

It is apparent from both figures that the porosity has increased with the increased molarity and voltage. However, lower current density resulted in a higher porous intensity with smaller pores; this is clear with the increased molar concentration and voltage. For example, the average pore size diameter was 296 nm for the TiO_2 coating anodised at 150 V, 2.0 M and 60 $mA.cm^{-2}$ (Figure 4.3 (i)), while the average pore was 348 nm for the TiO_2 coating anodised at 150 V, 2.0 M and 100 $mA.cm^{-2}$ (Figure 4.4 (i)). However, the average pore size was 727 nm at 150 V, 2.0 M and 60 $mA.cm^{-2}$ (Figure 4.3 (i)), and 484 nm at 100 $mA.cm^{-2}$ (Figure 4.4 (i)). The pore size average was taken for a sample area of 20 μm^2 using Image J software. The highest porous surface among these results was obtained at 180 V and 2.0 M at 60 $mA.cm^{-2}$

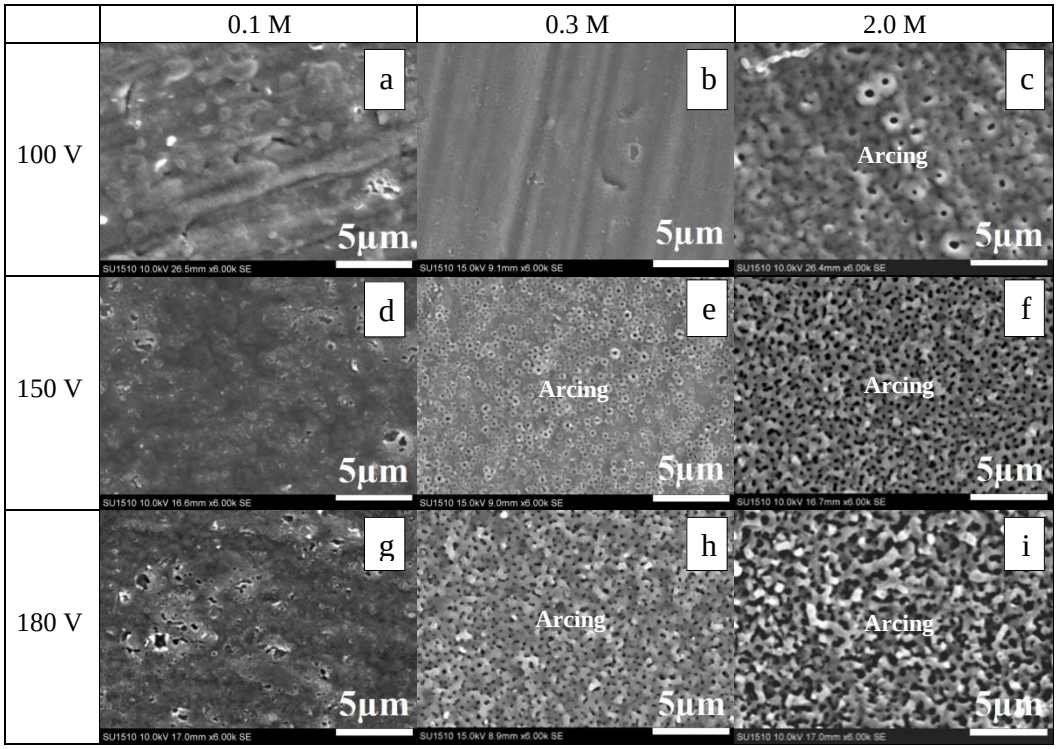

Figure 4.3: Surface microstructure images of TiO_2 coatings anodised in H_2SO_4 electrolyte as a function of applied voltage and molarity at current density of 60 $mA.cm^{-2}$ (Arcing; uniform porosity due to breakdown)

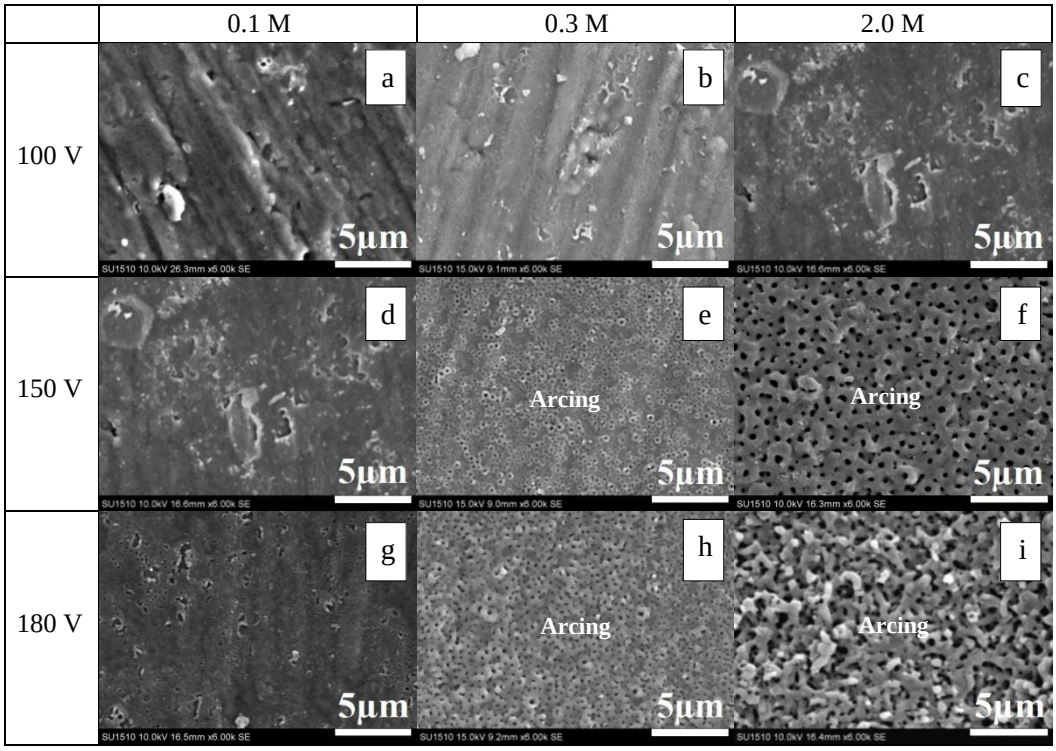

Figure 4.4: Surface microstructure images of TiO_2 coatings anodised in H_2SO_4 electrolyte as a function of applied voltage and molarity at current density of 100 $mA.cm^{-2}$ (Arcing; uniform porosity due to breakdown)

(Figure 4.3 (i)) and 100 $mA.cm^{-2}$ (Figure 4.4 (i)).

Both molar concentration and voltage have a major effect on the surface morphology. The coatings at lower molarity are not uniform, comprising some areas with pores and others without them due to the partial breakdown (Kuromoto *et al.,* 2007). The increased of voltage and molarity results in the higher porous surface due to the local breakdown. This is accompanied by losing appearance and results in a grey color reflectance as discussed in **Section 4.2.1**.

Pore formation is related to the anodization parameters, where the growth behavior of the TiO_2 coating (thickness and topography) depends on the voltage, current density and molar concentration of the electrolyte. Pores are formed due to the dielectric breakdown phenomena at high voltage (Teh *et al.,* 2003), where the oxide reduction, gas evolution (O_2 and H_2) and spark discharge occurs (Narayanan *et al.,* 2014; Wang *et al.,* 2015). It can also be referred to arcing where the uniform porous due to the heavy breakdown of the coating as obtained in Figure 4.3 and Figure 4.4. These results are similar to the results published by Cui *et al.* (2009) and Yang *et al.* (2004a).

Lower current density resulted in an increased breakdown time, which resulted in an increased pores intensity as seen in (c,e,f,h and i) in Figure 4.3 and Figure 4.4. The intense pores rate and heavy breakdown is an indication that the breakdown is higher than the TiO_2 growth rate (Kuromoto *et al.,* 2007). This was caused by two parameters, relatively low current density compared to the voltage applied and increased molarity. The relatively low current density has prolonged the time of the voltage to reach the maximum voltage applied as can be illustrated in Figure 4.5. Where the constant current took 12.5 minutes at 60 $mA.cm^{-2}$ until the voltage has reached the maximum level at 180 V. While it only took 4 min at 100 $mA.cm^{-2}$. The prolonged maximum current flow at 60 $mA.cm^{-2}$ has increased the local breakdown time. This has allowed the maximum allowed current flow to transfer ions to build-up TiO_2 coating and break it down. Also, lower current density means lower ion transition ability to build on an oxide around the breakdown areas. The increased molar concentration resulted in increased coating thickness due to the richer ionic solution that works as good ionic and energy conductor medium. Therefore, an intensive breakdown occurred with the increased voltage. Also, the ability of fast oxide build-up due to the rich ionic solution has caused multiple local breakdowns. This has increased the pores intensity with small pores (compared to coatings at higher current

density) to a level that caused pores overlapped and resulted in sponge-like pores with a larger pore size in Figure 4.3 (f,h and i) and Figure 4.4 (f,h and i).

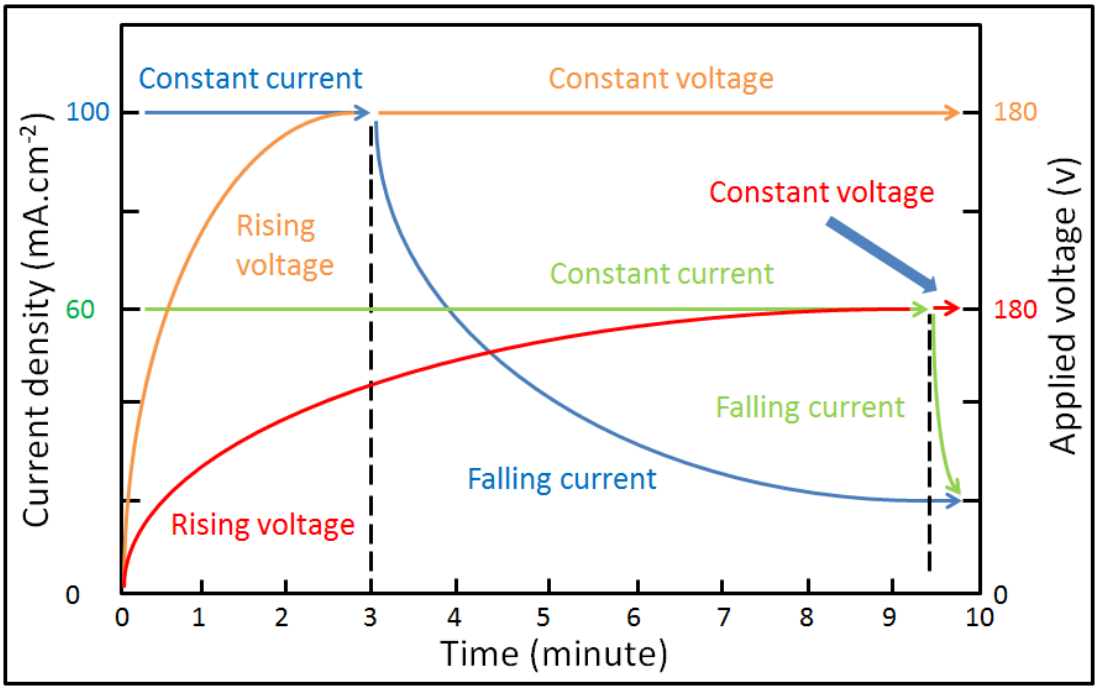

Figure 4.5: Anodization process observes the mechanism of flowed applied voltage (V) and current density (mA.cm^{-2}) through time

The coatings' thicknesses were detected by scanning its cross section. The thicknesses for coatings anodised in 0.1 M and 2.0 M at 100 V and 180 V as a function of current density can be obtained in Figure 4.6. From the figure, it can be noticed that the thickness has increased with the increased voltage, current density, and molarity. However, the thickness at 0.1 M and 180V have decreased. This is can indicate of experimental error and also the lower effect of current density on the thickness formation. The voltage had the highest influence on the coatings with the highest thickness has reached a maximum of 14.5 µm on the coating anodised in 0.1 M at 180 V. While the current density has the lowest effect on the thickness growth, where it has only increased slightly from 60 to 100 mA.cm^{-2} compared to the effect of voltage and molarity. When comparing the thickness growth at the same voltage it can be noticed that thickness of the coatings anodised at 100 V has increased by 19 % with the increased molarity, while it has only increased by 54 % for the coating anodised at 180 V. However, when comparing at the same molarity, the thickness has grown by 42 % for the coatings anodised in 0.1 M wih the incrased voltage, while it has increased

by 67% in 2.0 M. This is can indicate higher influence of the voltage over the molarity on the thickness growth.

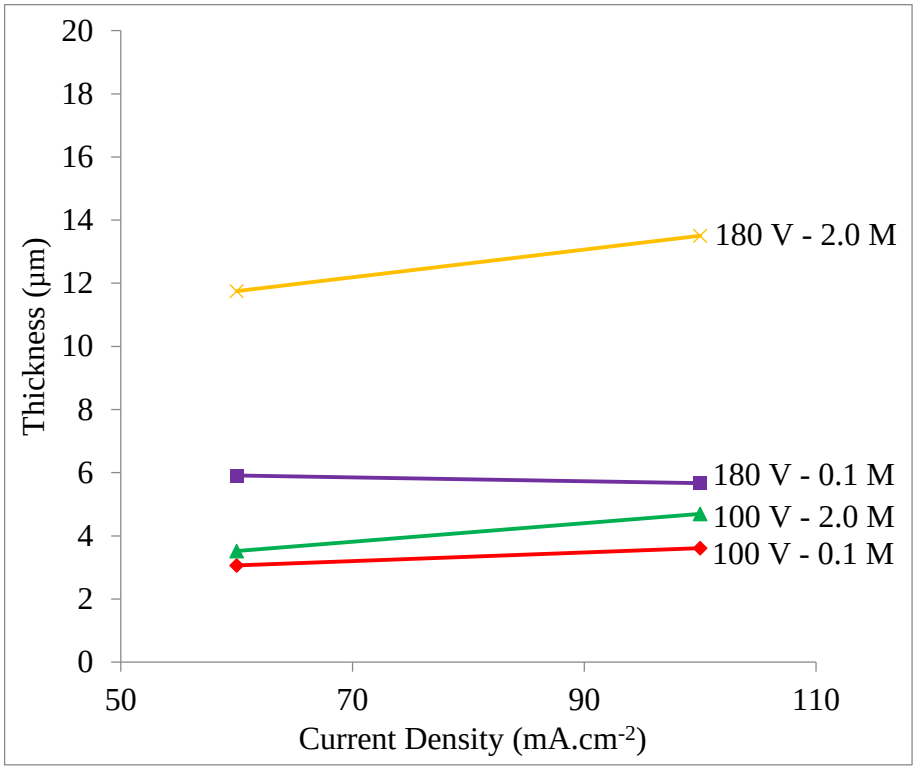

Figure 4.6: Thickness for TiO_2 coatings anodised in H_2SO_4 electrolyte as a function of current density and voltage

The thickness of the TiO_2 coating increased due to the build-up of the TiO_2 with the feed of current density and voltage in the medium of an electrolyte. The anodization process has been explained in **Section 2.8**. Different coating thickness resulted in changed coating surface colour interference (Sul *et al.*, 2001; Diamanti, Del Curto and Pedeferri, 2008). This is can be obtained when relating the colour interference of the TiO_2 coatings as shown in Table 4.1 with the coatings thicknesses as obtained in Figure 4.6. The colour at lower voltage and molarity has obtained colorful interference with higher brightness as obtained for 0.1 M at all voltages and for 0.3 M at 100 V as obtained in Table 4.1 and Table 4.2. It has obtained lower porosity surface as obtained in Figur 4.3 and Figure 4.4 and also lower thickness as obtained in Figure 4.6. While at higher voltage and molarity the coatings obtained lost in appearance colour (grey colour) and lower brightness as obtained in Table 4.1 and Table 4.2 respectively. This is can be due to the increased surface porosity due to the breakdown of the coating with the increased thickness (The relation between porosity

and breakdown phenomena has been explained earlier). This is can be explained where at the beginning of the anodization process, the TiO_2 started build-up which results in increased thickness with a smooth surface and this is can explain the colourful interference. TiO_2 with colourful interference can be obtained at lower anodization parameters, i.e., voltage and molarity, due to the coatings anodised under these parameters have obtained smaller thicknesses that wasn't thick enough to reach the breakdown stage. Where the coating after certain thickness start to breakdown and resulted in a porous structure. This is can be obtained at coatings anodised at higher voltage and molarity. The breakdown phenomena have been explained in **Section 2.8.1** and an illustration of pores formation due to coating breakdown was obtained in Figure 2.23.

The effect of variation of the anodization parameters, i.e., voltage, current density, and molarity, on the TiO_2 coating microstructure and thickness was discussed. The TiO_2 microstructure and thickness was discussed with respect to the results of the TiO_2 appearance.

4.2.3 Elementary of Anodised TiO_2 in H_2SO_4 Electrolyte

Figure 4.7 (a and c) obtain the elements incorporated in the TiO_2 coating anodised in the H_2SO_4 electrolyte for 0.1 M, while Figure 4.7 (b and d) obtain for 2.0 M at 150 V and 100 $mA.cm^{-2}$. From the results, it can be noticed that the sulfur (S) atomic weight in percentage (%) has slightly decreased with the increased electrolyte molarity as obtained in Figure 4.7. This can indicate poor S ions that were incorporated into the coating during the coating build-up. This is somehow got with the nature of the H_2SO_4 which it was reported to obtain a high dissociation constant rate of H_2SO_4 in water (Murmson, 2017). This means that the H_2SO_4 tend to lose concentration all over in water when diluted. This is considering the H_2SO_4 is one of the strongest known acids.

4.2.4 Mineralogy of Anodised TiO_2 in H_2SO_4 Electrolyte

The phase mineralogical patterns of the TiO_2 coatings anodised in the H_2SO_4 electrolyte are illustrated as a function of applied voltage, molarity, and current density. The crystallisation of the TiO_2 coating can be obtained in the phase

	0.1 M	2.0 M
FESEM	a	b
EDX	c	d

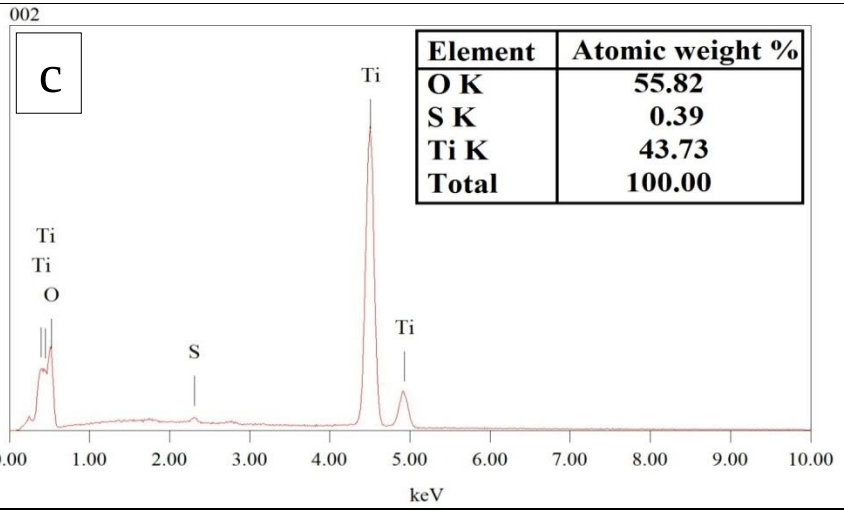

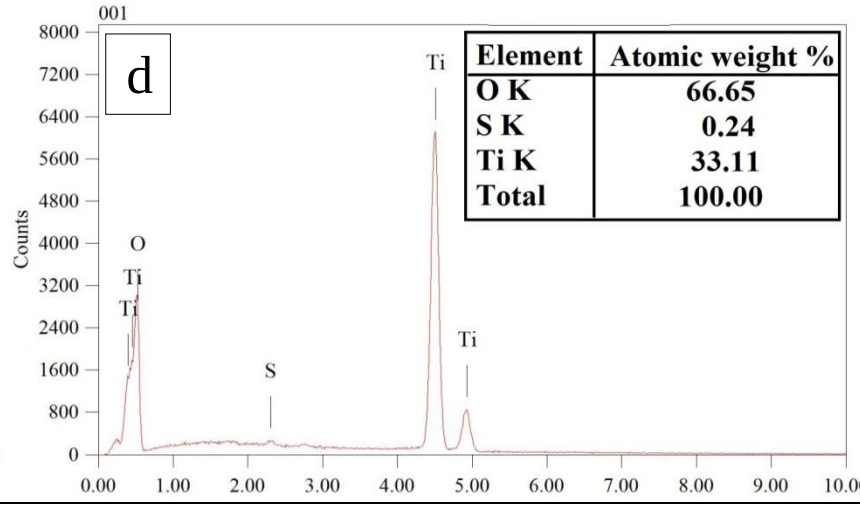

Figure 4.7: Elemental analysis of the coatings anodised in H_2SO_4 electrolyte at 150 V and 100 $mA.cm^{-2}$ for 0.1 M (a and c) and 2.0 M (b and d)

mineralogical patterns in a form of intense peaks (Hanaor, 2007). The TiO_2 coatings anodised at 0.1 M has obtained amorphous and crystalline with low-intensity anatase peaks as seen in Figure 4.8 for the spectrum of the coating that was anodised at 100 V, Figure 4.10 for 150 V and Figure 4.12 for 180 V. It can be noticed that the coatings anodised at 2.0 M has obtained an increased crystallinity, i.e., increased anatase and rutile crystal phases as seen in Figure 4.9 for 100 V, Figure 4.11 150 V and Figure 4.13 for 180 V.

4.2.5 Mineralogy of Anodised TiO_2 in H_2SO_4 Electrolyte

The phase mineralogical patterns of the TiO_2 coatings anodised in the H_2SO_4 electrolyte are illustrated as a function of applied voltage, molarity, and current density. The crystallisation of the TiO_2 coating can be obtained in the phase mineralogical patterns in a form of intense peaks (Hanaor, 2007). The TiO_2 coatings anodised at 0.1 M has obtained amorphous and crystalline with low-intensity anatase peaks as seen in Figure 4.8 for the spectrum of the coating that was anodised at 100 V, Figure 4.10 for 150 V and Figure 4.12 for 180 V. It can be noticed that the coatings anodised at 2.0 M has obtained an increased crystallinity, i.e., increased anatase and rutile crystal phases as seen in Figure 4.9 for 100 V, Figure 4.11 150 V and Figure 4.13 for 180 V.

It is clear from the patterns that the increased molarity, the applied voltage, and the current density have promoted higher crystallisation. This can be obtained where the anatase peak has increased in intensity with the increased voltage at the patterns of the TiO_2 coating that was anodised in 0.1 M. As seen in Figure 4.8 for 100 V, Figure 4.9 for 150 V and Figure 4.12 for 180 V. With the increased molarity to 2.0 M, the crystalline has also increased with the increased voltage, and a phase transformation has appeared; rutile crystalline was obtained starting from 100 V (Figure 4.9) until anatase totally transformed to rutile at 180 V (Figure 4.13).

The crystallinity as obtained in Figure 4.14 has slightly increased with the increased current density from 60 to 100 when compared to the effect of voltage and molarity. This is can be obtained at 100 V and 150 V. However, at 180 V the crystallinity was higher (79 %) for the spectrum that was anodised at 60 $mA.cm^{-2}$, while it obtained a grand descending to (64 %) when elevated to 100 $mA.cm^{-2}$. It was

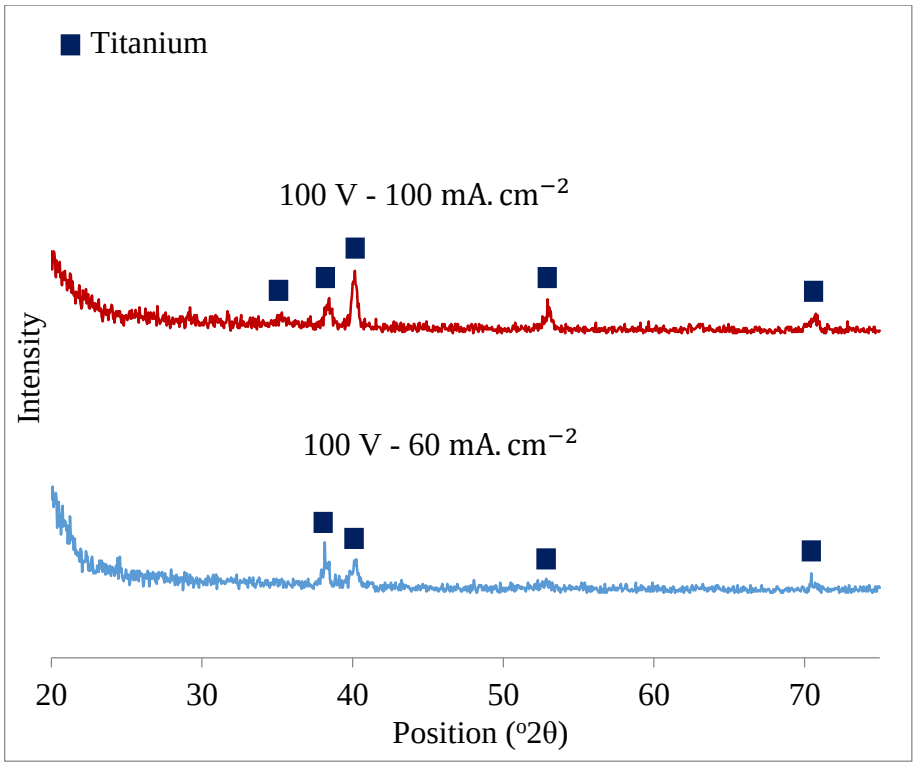

Figure 4.8: Phase mineralogical patterns for 100 V, 60 and 100 mA.cm^{-2} at 0.1 M for coatings anodised in H_2SO_4 electrolyte

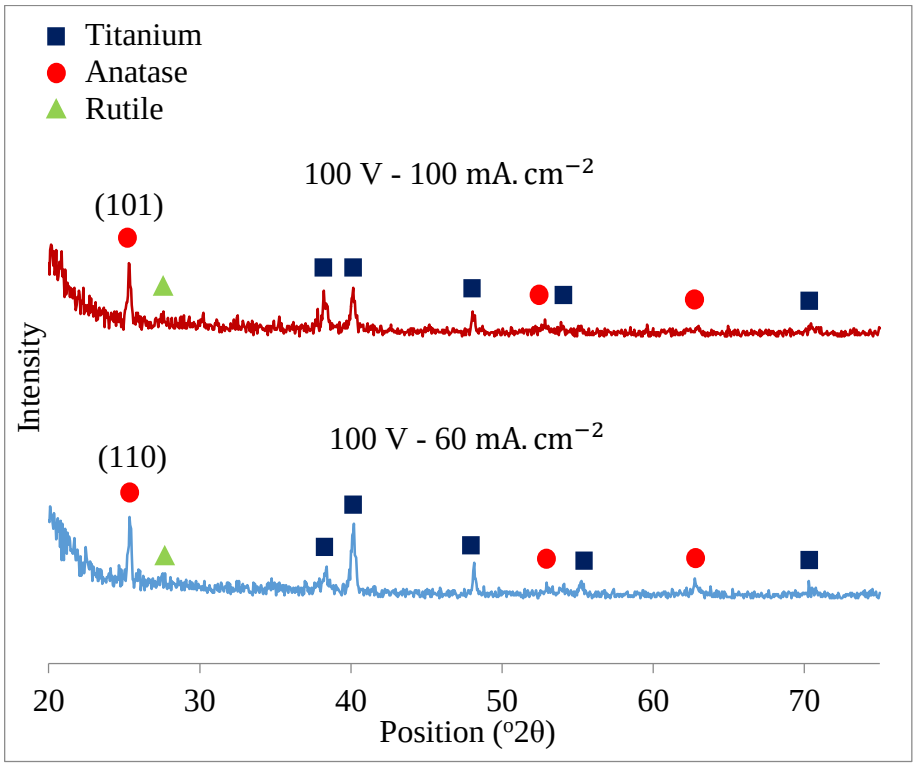

Figure 4.9: Phase mineralogical patterns for 100 V, 60 and 100 mA.cm^{-2} at 2.0 M for coatings anodised in H_2SO_4 electrolyte

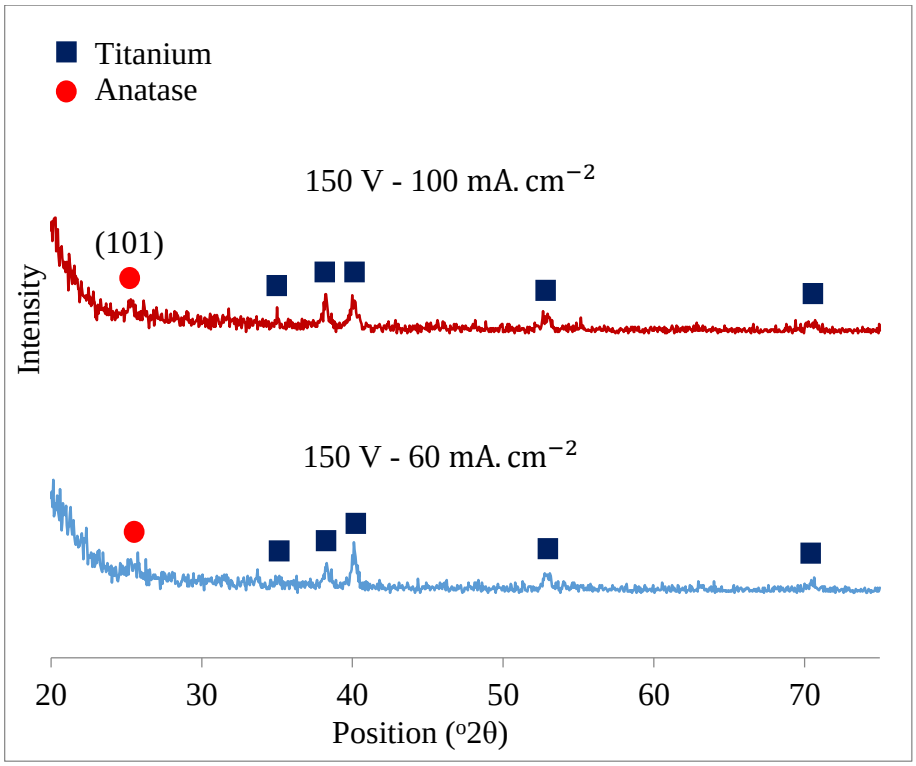

Figure 4.10: Phase mineralogical patterns for 150 V, 60 and 100 mA.cm^{-2} at 0.1 M for coatings anodised in H_2SO_4 electrolyte

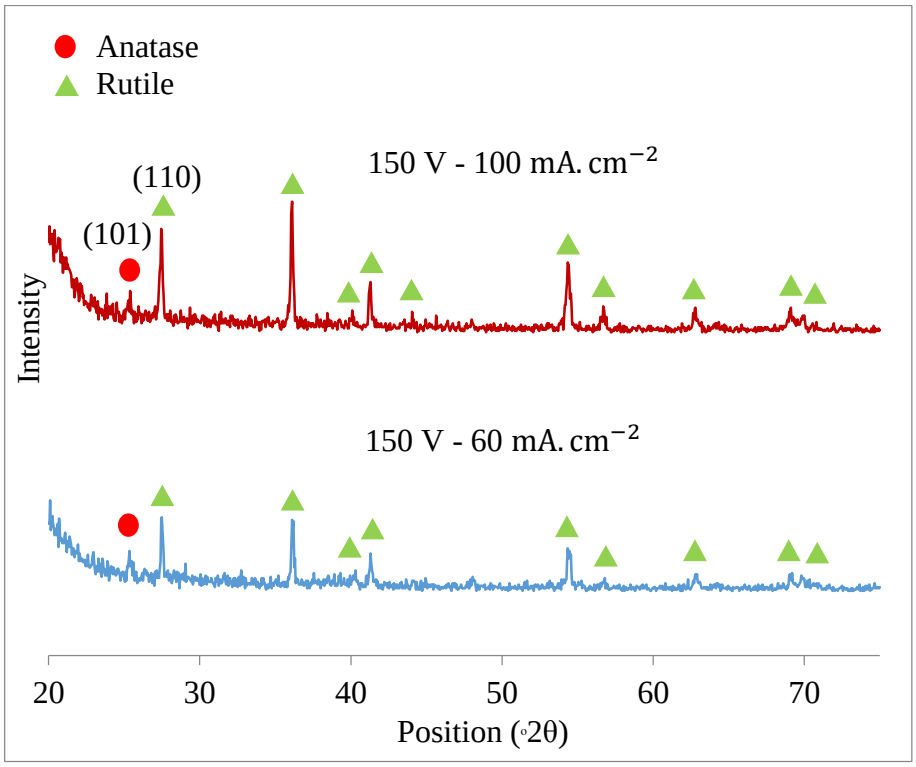

Figure 4.11: Phase mineralogical patterns for for 150 V, 60 and 100 mA.cm^{-2} at 2.0 M coatings anodised in H_2SO_4 electrolyte

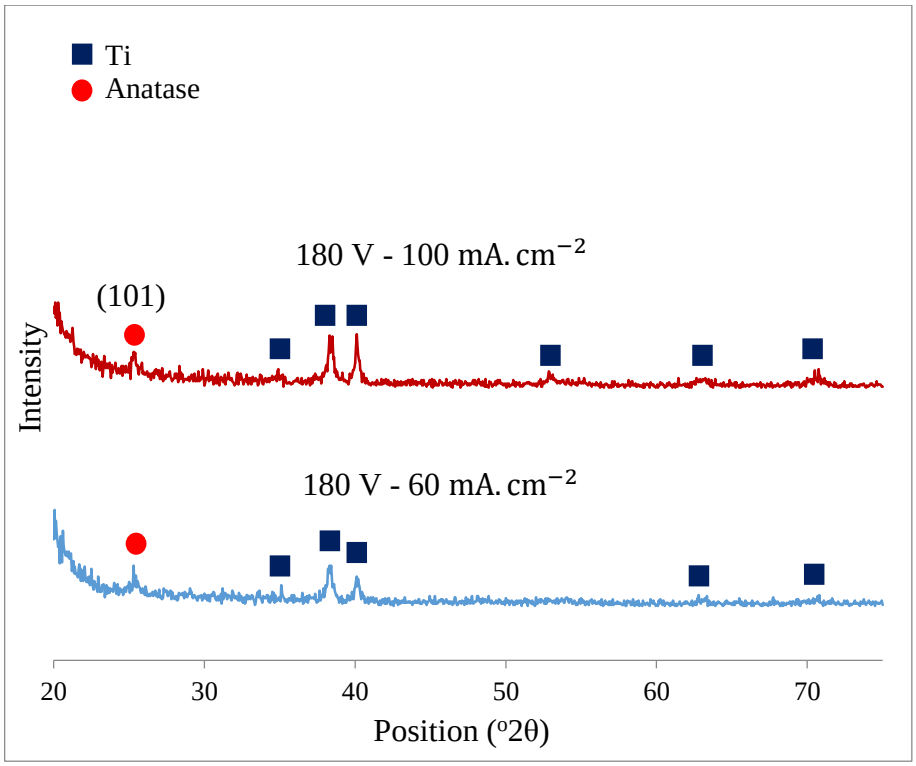

Figure 4.12: Phase mineralogical Patterns for 180 V, 60 and 100 mA.cm^{-2} at 0.1 M for coatings anodised in H_2SO_4 electrolyte

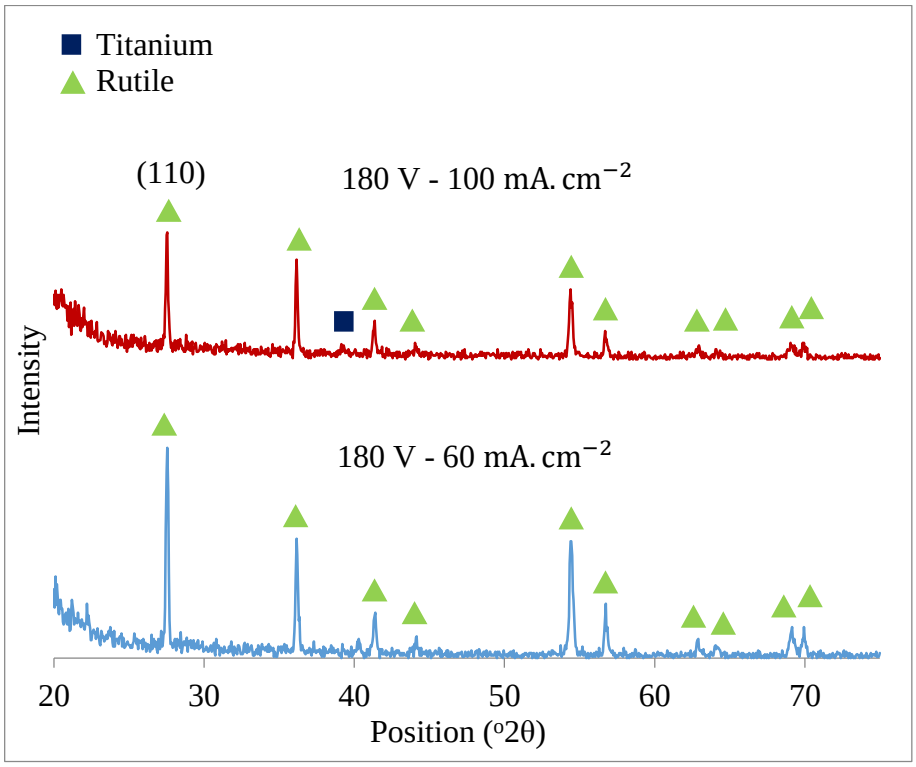

Figure 4.13: Phase mineralogical Patterns for 180 V, 60 and 100 mA.cm^{-2} at 2.0 M for coatings anodised in H_2SO_4 electrolyte

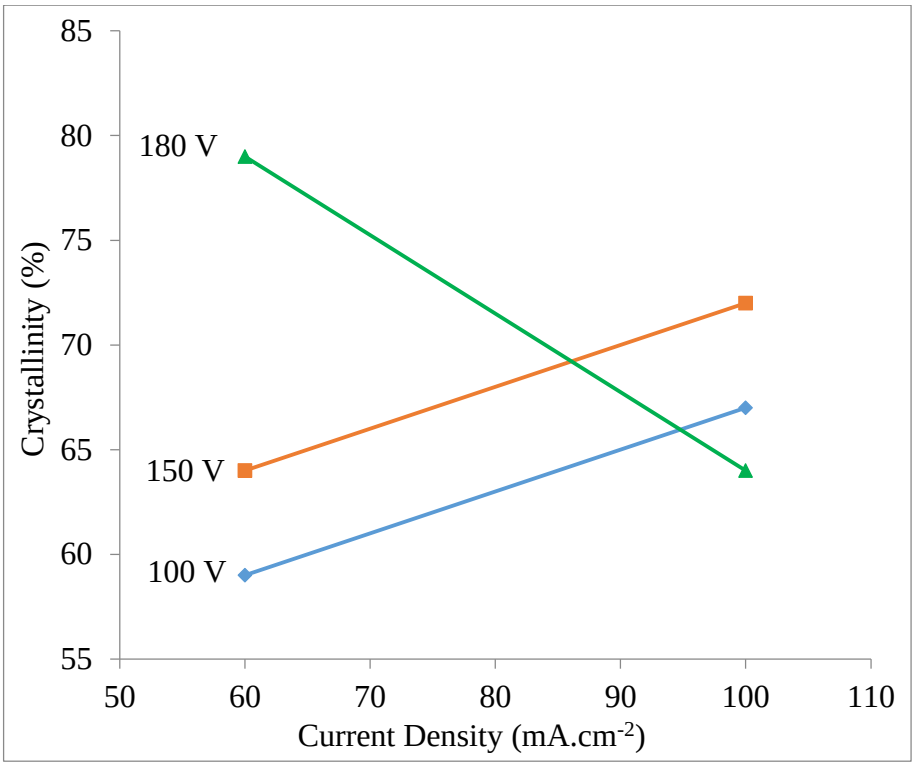

Figure 4.14: Phase mineralogical Patterns crystallinity percent for TiO_2 anodised in 2.0 M H_2SO_4 electrolyte as a function of current density and voltage

interesting to notice that the pattern at 60 mA.cm^{-2} and 180 V as seen in Figure 4.13 (b) did obtain stronger rutile peaks than the pattern at 100 mA.cm^{-2} as seen in Figure 4.13 (a). This can be related to the longer time of local breakdown. This has promoted the coating to reform and produce new layers on the defected areas. Therefore, allow the re-crystallisation of the coating. These results match with the surface microstructure images result from Figure 4.3 and Figure 4.4, where the larger increased porosity caused by the breakdown has promoted higher crystallisation of the coating.

It has been reported that the structure of TiO_2 coating is changed from amorphous to crystalline phase, e.g. anatase, brookite, and rutile, which occurs above critical oxide thickness (Sato, 1971). This crystallographic transformation is closely related to the breakdown, which is dependent on the electrochemical parameters such as the electrolyte concentration (or activity) (El Kader *et al.*, 1981; Yahalom, 1972) and the current density (Leach and Pearson, 1988; Mikula, 1992). The crystallisation has developed after the breakdown. However, there exists some discrepancy about the values of the voltage at which the beginning of the breakdown process and the evolution of the crystallisation begins (Sul *et al.*, 2001; Zhao *et al.*, 2005).

When linking the mineralogical results with the interference colour, it can be noticed that the higher crystallinity that was obtained on the coating anodised at higher molarity has obtained grey colour interference. It was reported that the localized breakdown, where high voltage favoured crystallisation forms, which impede interference effect (Ashraf and Vaezi, 2004; Diamanti *et al.*, 2013). It can also be noticed that the rutile formed at 2.0 M and 180 V as obtained in Figure 4.13 has obtained light grey colour as obtained in Figure 4.3 and Figure 4.4.

Table 4.3: Grain size along (101) direction of TiO_2 anatase crystalline of coatings anodised in H_2SO_4 electrolyte as a function of voltage and current density at 2.0 M.

2.0 M	2 Theta(θ)		Strain (ε)		FWHM		Crystal size (nm)	
Current density ($mA.cm^{-2}$)	60	100	60	100	60	100	60	100
100 V	25.391	25.331	0.041	0.043	0.182	0.192	0.843	0.798
150 V	25.342	25.265	0.016	0.021	0.075	0.095	2.045	1.613
180 V	-	-	-	-	-	-	-	-

Table 4.4: Grain size along (110) direction of TiO_2 rutile crystalline of coatings anodised in H_2SO_4 electrolyte as a function of voltage and current density at 2.0 M.

2.0 M	2 Theta(θ)		Strain (ε)		FWHM		Crystal size (nm)	
Current density ($mA.cm^{-2}$)	60	100	60	100	60	100	60	100
100 V	27.508	27.594	0.031	0.015	0.144	0.069	1.085	2.267
150 V	27.487	27.458	0.036	0.025	0.166	0.116	0.941	1.347
180 V	27.540	27.523	0.042	0.027	0.192	0.126	0.814	1.240

The diffraction peaks from the XRD spectra with scan rate of (1.375 $\frac{2\theta}{\min}$) has obtained a good agreement with those taken from the Joint Committee of Powder Diffraction Standards (JCPDS) card file No. 21-1272 for TiO_2 (anatase) and No. 21-1276 for TiO_2 (rutile) respectively (Li and Zeng, 2011; Pookmanee and Phanichphant, 2009). The crystallinity percentage of the TiO_2 coating has been obtained in Figure 4.14 for the coatings that have been anodised in 2.0 M. The main crystal planes for anatase and rutile crystalline peaks are (101) and (110) respectively. Table 4.3 and Table 4.4 shows the values of crystal size and strain with respect to applied voltage, molarity and current density for anatase (101) and rutile (110) respectively.

By fitting the phase mineralogical results, the strain ε and crystal size of the films have been calculated from the (101) for anatase and (110) for rutile diffraction peaks. The calculated gain size as a function of the applied voltage and the current

density at 2.0 M. FWHM measured broadening of the diffraction line peak at an angle of 2θ and the grain size represents the longitudinal coherence length in the direction perpendicular to the substrate.

It can be noticed from the coatings anodised in Figure 4.9 for 100 V, Figure 4.11 for 150 V and Figure 4.13 for 180 V that the anatase crystalline intensity has decreased and the rutile crystalline intensity has increased with increased voltage. While the current density has increased the intensity of the crystalline peaks. However, at 180 V the rutile crystalline was increased at a lower current density as seen in Figure 4.13. The anatase decreased intensity is associated with increased crystal size with increased voltage. While the rutile increased intensity is associated with decreased crystal size with increased voltage.

The increased anatase crystal size with the increased voltage is associated with the grain growth which indicates the rearranging of the atomic structure (Iida and Ozaki, 1961; Zhang and Reller, 2002). While the crystal size shrinkage of rutile was associated with the crystalline growth, which can indicate decreased grain growth and stabilizing of rutile crystalline. The anatase to rutile transformation is reconstructive, which means that the transformation involves the breaking and reforming of bonds (Batzill, Morales and Diebold, 2006). This is in contrast to a displacive transformation, in which the original bonds are distorted but retained. The reconstructive anatase to rutile transformation involves a contraction of the c-axis and an overall volume contraction of 8% (Shannon and Pask, 1965; Criado and Real, 1983; Rao, Turner and Hoing, 1959). This volume contraction explains the higher density of rutile relative to anatase. The c-axis of anatase appears to be significantly longer than that of rutile only because anatase has more atoms per unit cell than rutile (Hanaor and Sorrell, 2011).

The reduced crystal size with the increased current density for anatase (Table 4.3) at 100 V (Figure 4.9) and at 150 V (Figure 4.11) can be due to the increased peak intensity and narrowing. It has been discussed earlier that the increased peak intensity do agree with the increased crystallinity. However, the increased crystal size with the increased current density for rutile (Table 4.4) indicates that the peaks have lower intensity, thus, lower crystallinity. This is can be seen clearly at 180 V (Figure 4.13), where higher intensity has been obtained at lower current density. The can be related to the breakdown effect as discussed in **Section 4.2.3**. In that case, the oxide was exposed to longer breakdown time as seen in (Figure 4.3 (i)). That has led to oxide

atomic structure to rearrange and promote higher crystalline with the increased breakdown intensity due to the increased breakdown time.

It has been reported that rutile transforms to anatase at a temperature higher than 600 ºC (Li *et al.*, 2005). Therefore, the decreased anatase and increased rutile intensity. Also, is associated with rearranging of atomic structure (Batzill, Morales and Diebold, 2006). When the anatase transforms to rutile, the atomic organisation of the crystal structure of anatase unpacks and rearranging to the crystal structure of rutile. This is associated with crystals expanding (the atoms of crystals expand in distance); grain size increased, with increased anodization temperature. Which leads to the increased crystal size of anatase. At that moment the rutile crystals increased and get packed. This has led to reducing the crystal size with increased intensity. This can explain the decrease of rutile and increase of anatase crystal size with an increased breakdown at lower current density.

The increased voltage has caused to increase in crystalline TiO_2 due to the increased breakdown intensity; the re-build and re-shape of the coating layer have caused an increase in crystalline TiO_2 as it has been explained in **Section 4.2.1** and **Section 4.2.2**. The increased current density has also caused an increase in the crystallinity, however, with lower influence that the voltage. Where the increased flow of build-up rate that caused the increased electron flow at a certain voltage, has cause to increase the amount of crystalline TiO_2. However. It can be noticed that the decreased crystallinity with the increased current density at 180 V has related to the prolonged breakdown time which has caused to increase the crystalline TiO_2 at a lower current of 60 $mA.cm^{-2}$ as has been explained above. This is related to the increased porosity according to the microstructure of the coating as obtained in Figure 4.3 (i) when compared with the coating anodised at 100 $mA.cm^{-2}$ as obtained in Figure 4.4 (i). This has been explained above and in Section 4.2.2. This is can also explain the decreased crystal size of rutile with; the crystalline percent can be assigned to rutile crystalline since anatase has totally transformed to rutile at 180 V as seen in Figure 4.13. The decreased crystal size to 65 % (Table 4.4) with decreased current density can indicate that the rutile has become more stable due to increased breakdown time which has caused an increased in the rearrange time of atoms at 60 $mA.cm^{-2}$. This has caused to increase the anodization temperature and therefore reduce the crystal size. It was reported that the rutile is more stable at an elevated temperature higher than 600

°C (Hanaor and Sorrell, 2011). It has been also concluded from the above discussion that the stability of the crystalline phase is associated with reduced crystal size.

These results confirm that the voltage, current density, and molarity has an influence on the crystallinity of the TiO_2 coatings produced in the H_2SO_4 electrolyte. The crystallinity was highly influenced by the elevated voltage and molarity, where rutile appeared alongside anatase. While the current density had lower influence.

4.2.6 Optics Properties of Anodised TiO_2 in H_2SO_4 Electrolyte

Figure 4.15 and Figure 4.16 observe the bandgap (E_g) of the TiO_2 coatings anodised in the H_2SO_4 electrolyte at 0.1 M and 2.0 M respectively. The parameters were taken at 150 V and 100 $mA.cm^{-2}$. The measured bandgap values were 3.45 eV at 0.1 M and 3.22 eV at 2.0 M.

According to these results, it can be noticed that the bandgap decreased with the increased crystallinity. Generally, the exaction absorption of both coatings is 359.3 nm for 0.1 M and 385 nm for 2.0 M, which is a good condition to conduct the *in vitro* test with the UV irradiation of 254 nm (UVC).

According to phase mineralogical results, the coating produced at 0.1 M have obtained anatase crystalline. However, the bandgap value of intrinsic anatase TiO_2 powder has a bandgap of 3.2 eV. According to the mineralogical analysis, the coatings have obtained low-intensity anatase peak as seen in Figure 4.10. However, the bandgap value of 3.45 eV indicates higher bandgap than the bandgap of anatase. While the coating produced at 2.0 M have obtained a mixture of crystalline; anatase and rutile. It has obtained a bandgap of 3.22 eV. This is also considered higher than the bandgap of intrinsic rutile TiO_2 powder and slightly higher than the bandgap of intrinsic anatase. TiO_2 is considered a semiconductor material that has photocatalytic properties. The bandgap of 3.2 eV for anatase and 3.0 eV for rutile (Carp, Huisman and Reller, 2004). The bandgap is related to the electric conductivity of the materials. The determination of bandgap in materials is important to obtain the basic solid state physics. Bandgap indicates the difference in energy between the top of the valence band filled with electrons and the bottom of the conduction band devoid of electrons (Davis and Mott, 2006). When TiO_2 is exposed to radiation exceeding its bandgap; this radiation normally is in the UV wavelength region (290-380) nm (Hanaor and Sorrell, 2011). A

good linearity was observed at a value equal to 2.0 for the indirect allowed transition. This value was found to give the best fit for these TiO_2 coatings.

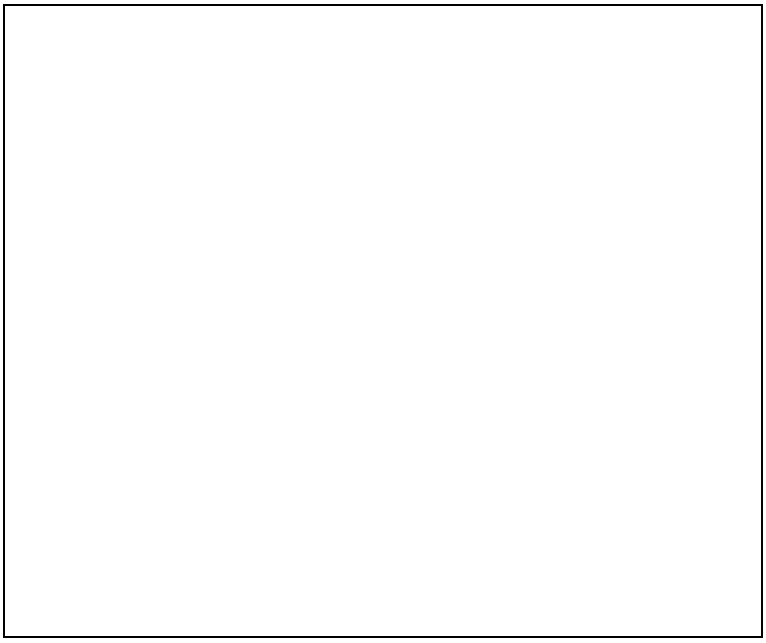

Figure 4.15: Bandgap (Eg) of coatings anodised at 150 V and 100 mA.cm^{-2} at 0.1 M in H_2SO_4 electrolyte

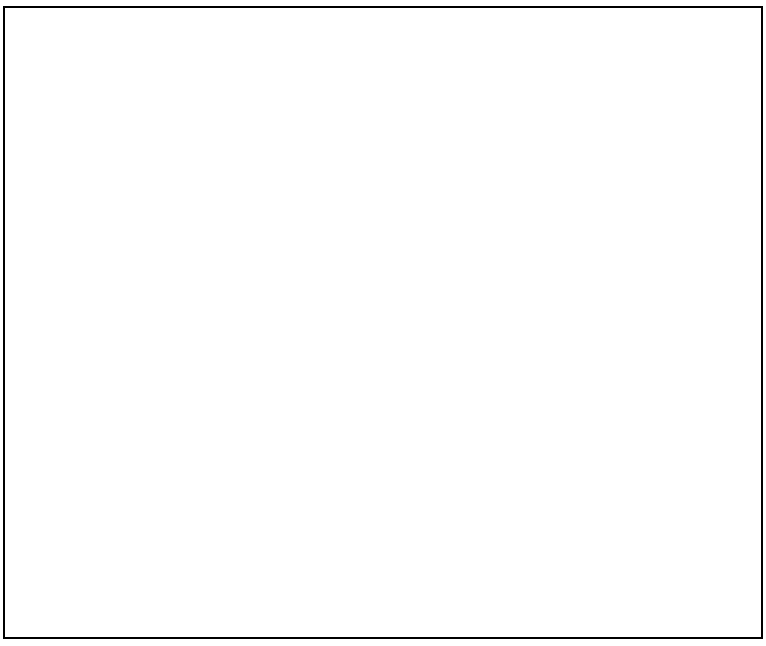

Figure 4.16: Bandgap (Eg) of coatings anodised at 150 V and 100 mA.cm^{-2} at 2.0 M in H_2SO_4 electrolyte

4.2.7 Absorption of Anodised TiO_2 in H_2SO_4 Electrolyte

Absorption analysis was taken for TiO_2 coatings anodised in the H_2SO_4 electrolyte at 0.1 M and 2.0 M at the voltage of 150 V and 100 $mA.cm^{-2}$. The coatings have been irradiated under the UV of 254 nm for 12 hr of in water. It was also reported that the UV can generate the electron pair hole in the TiO_2 due to its photocatalytic ability and results in the formation of oxygen vacancy and hydroxyl (OH) group which is responsible for the initiation of the apatite nucleation (Fujishima and Honda, 1972; Fujishima *et al.,* 2008; Kasuga *et al.,* 2002). The absorption analysis patterns of the coatings anodised in 0.1 M is illustrated in Figure 4.17. While the Figure 4.18 illustrates the absorption analysis of the coatings anodised in 2.0 M.

The absorption patterns for the TiO_2 coatings as shown Figure 4.17 and Figure 4.18 have a presence of Ti-O groups at band 680-800 cm^{-1} (Liu *et al.,* 2008). Sulfone (S=O) that was obtained at the band of 1300-1350 cm^{-1}, carbon dioxide (CO_2) at bands 2440 and 1550 cm^{-1} (Segneanu *et al.,* 2012), water (H_2O) at band 1860 cm^{-1} hydroxyl groups (OH) stretching region 3100-3400 cm^{-1} and Ti-OH groups at band 3635, 3645, 3680, 3750 and 3840 cm^{-1} (Liu *et al.,* 2008).

The $Ti\text{-}O^-$ group at 0.1 M has obtained a strong and a wide stretch and it was maintained the same after UV irradiation as seen in Figure 4.17. The strong $Ti\text{-}O^-$ stretching can indicate that there is an increased formation of distinct atomic defects like Ti^{3+} or Ti^{4+} interstitials, or O^{2-} vacancies (Grujić-Brojčin *et al.,* 2006), While the stretching after the UV irradiation has not significantly increased. This is can be due to an increasing nonstoichiometry of the sample, due to oxygen out-diffusion in a vacuum (Grujić-Brojčin *et al.,* 2006; Šćepanović *et al.,* 2005). Although the apatite was formed higher as was discussed in **Section 5.2.2**. Han et al. 2008 and Liu et al. 2008 have reported that the $Ti\text{-}O^-$ functional groups on TiO_2 (crystalline) can increase upon UV irradiation due to its photocatalysis properties as it was explained in **Section 2.10.3**. The coating anodised in 0.1 M did obtain weak anatase structure according to mineralogical analysis (Figure 4.10). The increased stretching of $Ti\text{-}O^-$ at 2.0 M after UV irradiation as seen in Figure 4.18 can be explained using the same mechanism (The irradiation time for 12 hours was therefore enough to provoke the photocatalytic activity of the coating surface). However, it was not as strong and wide as the stretching at 0.1 M. This is can be related to rutile crystalline along the weak anatase crystalline according to mineralogical analysis as obtained in Figure 4.11. As it was

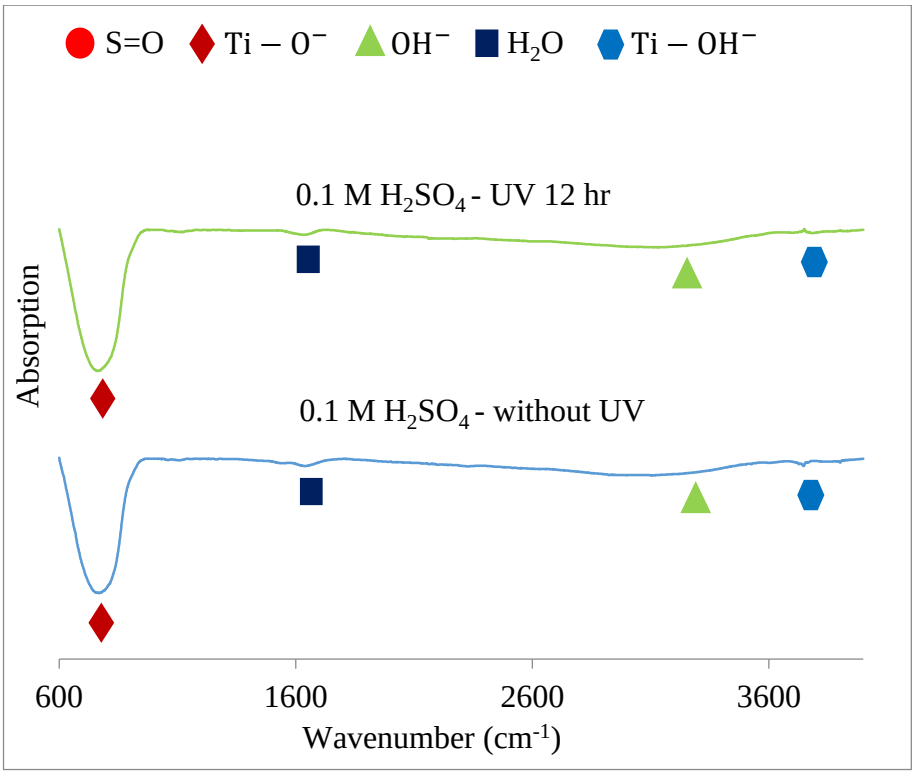

Figure 4.17: Absorption analysis patterns of TiO_2 coatings anodised in 0.1 M H_2SO_4 without treatment and 0.1 M H_2SO_4 after 12 hr of irradiation under UV

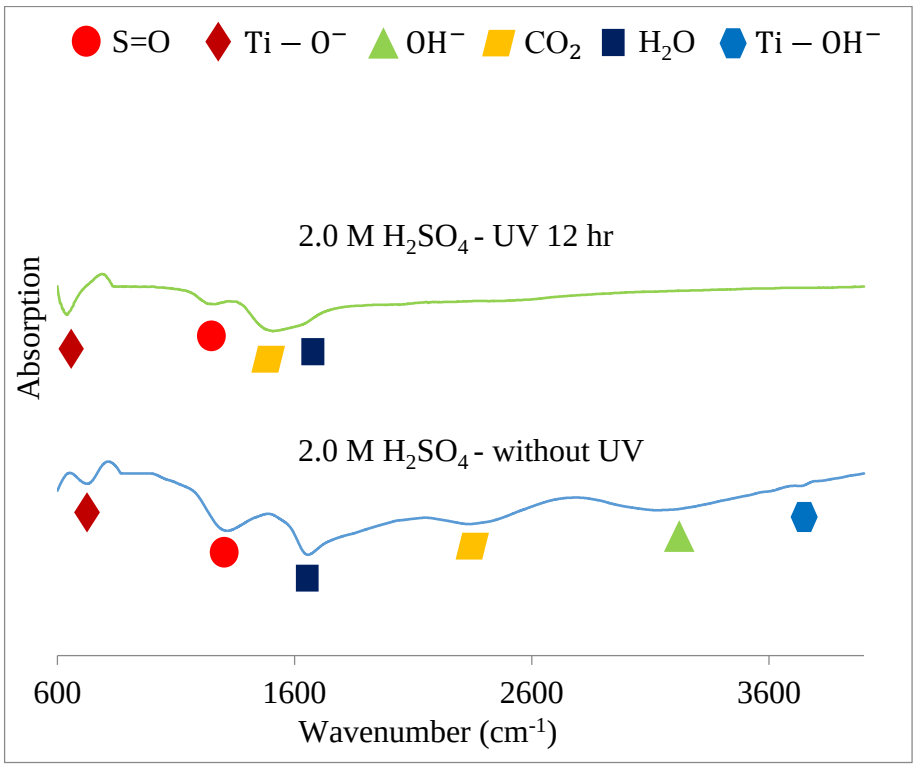

Figure 4.18: Absorption analysis patterns of TiO_2 coatings anodised in; (a) 2.0 M H_2SO_4 without treatment, (b) 2.0 M H_2SO_4 after 12 hr of irradiation under UV

reported that the anatase has higher photocatalytic activity than the rutile (Linsebigler *et al.,* 1995; Wang *et al.,* 2007). Also, the weaker functional groups of Ti-O^- at 2.0 M than the one at 0.1 M can be related to the highly porous structure as obtained in Figure 4.4 (f), while less porosity has appeared at 0.1 M (Figure 4.4 (e)). Also, the weaker functional groups of Ti-O^- at 2.0 M can be due to the appeared sulfone functional group as obtained in the sulfone stretch at 2.0 M (Figure 4.17). While it did not appear at 0.1 M (Figure 4.18). However, the S ions incorporated into the coating has obtained the lower value at 2.0 M that at 0.1 M as obtained in Figure 4.7. The sulfone stretching has become weaker after the UV irradiation. This is can be related to the increased formation of Ti-O^- functional groups have consumed the oxygen bonding that combines with S ions to form sulfone (S=O). This is can also be applied to the OH stretching that was also decreased after UV irradiation (Figure 4.18). The presence of the CO_2 might be resourced from the atmosphere in the form of air bubbles trapped in the coating grooves or from the ethanol during the pretreatment cleaning.

It can be concluded that multiple parameters can be contributed to the strength of the Ti-O^- group stretching at 0.1 M. The lower porosity surface microstructure, low S ionic incorporation, and anatase crystalline of the coating can contribute to the strength of the Ti-O^- group stretching. The strong Ti-O^- stretching on the 0.1 M coating can obtain higher chance to induce apatite in *in vitro* testing (therefore higher bioactivity) in SBF with and without UV. This is due to UV has not increased the Ti-O^- stretching as obtained in Figure 4.17. While for the apatite formation could be increased under the UV at 2.0 M coating.

4.3 Anodic Oxidation of Ti in Phosphuric Acid (H_3PO_4) Electrolyte

The TiO_2 coatings anodised in a diluted sulphuric acid (H_3PO_4) with different concentration (0.1 M, 0.3 M and 2.0 M) was characterised, i.e., colour, microstructure, morphology, mineralogy and surface energy. The bioactivity of these coatings conducted by *in vitro* test was characterised in Chapter 5.

4.3.1 Colour of Anodised TiO_2 in H_3PO_4 Electrolyte

The visual appearance of the TiO_2 coatings anodised in the H_3PO_4 electrolyte as a function of applied voltage (V), current density ($mA.cm^{-2}$) and molarity (M) at 10 minutes is shown in Table 4.5. While Table 4.6 obtain digital colouring for the coatings correspond to Table 4.5 obtained colours using a Colorimeter with CIELAB coordinates (L*a*b*) and converted to computer colour interface using computer software. The subdivision of these figures is based on a visual and mineralogical examination during processing.

The present data conclude the following:

i. There is a gradual colour variation as a function applied voltage and molar concentration. The colours become dimmer with the increased molarity and voltage.

ii. The colour was fluctuating with respect to current density at 2.0 M and 100 V and at 0.1 M and 150 V. Where the colour changed from red to brown and from light blue to light green. However, there was no significant effect on the colour of the other parameters.

iii. The colour has changed from beige and tan at 0.1 M and 0.3 M to red and brown at 2.0 M and 100 V. While at 150 V it has changed from green and bluish green to at 0.1 M and 0.3 M to reddish brown at 2.0 M. At 180 V the colour has changed from light violet at 0.1 M and heavy violet at 0.3 M to grey at 180 V.

iv. The colour has changed from beige and tan at 0.1 M and 0.3 M to red and brown at 2.0 M and 100 V. While at 150 V it has changed from green and bluish green to at 0.1 M and 0.3 M to reddish brown at 2.0 M. At 180 V the colour has changed from light violet at 0.1 M and heavy violet at 0.3 M to grey at 180 V.

v. The grey colour resulted at 180 V and 2.0 M, could be related to the breakdown voltage of the coatings. This is to be obtained later when surface microstructure and mineralogical results to be discussed.

Table 4.5: Visual appearance taken by camera of TiO_2 surface colour at a function of applied voltage, current density at 0.1 M, 0.3 M and 2.0 M at 10 min for coatings anodised in H_3PO_4 electrolyte

Voltage (V)	Mole (M)	Current Density ($mA.cm^{-2}$)	
		60	100
100	0.1	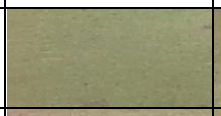	
	0.3		
	2.0		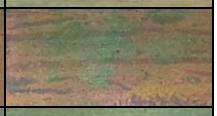
150	0.1		
	0.3	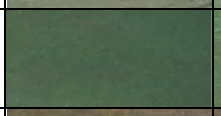	
	2.0		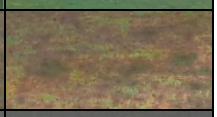
180	0.1	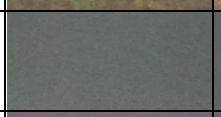	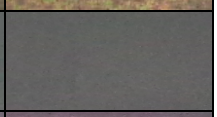
	0.3	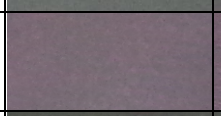	
	2.0	Arcing	Arcing

Arcing; grey interference colour due to breakdown.

Figure 4.19 and Figure 4.20 has obtained the brightness of coatings surfaces. The brightness (L* value) obtained is according to CIELAB coordinates, which is related to colour in Table 4.6. From Figure 4.19 and Figure 4.20, the behaviour of the graphs can be considered irregular and can conclude the following:

i. The brightness has decreased with the increased voltage at both current densities (60 and 100).
ii. The brightness followed linear correlation with respect to molar concentration.
iii. Where the brightness for each molarity has followed simultaneously linear downward flow at all the current density.
iv. 0.1 M has a higher brightness that 0.3 M, and 0.3 M has higher brightness than 2.0 M.

v. It is apparent that molarity has a higher efficiency than the current density with respect to brightness.

Table 4.6: CIELAB digital colour generated with colourmeter of TiO_2 surface colour at a function of applied voltage, current density at 0.1 M, 0.3 M and 2.0 M at 10 min for coatings anodised in H_3PO_4 electrolyte

Voltage (V)	Mole (M)	Current Density ($mA.cm^{-2}$)	
		60	100
100	0.1		
	0.3		
	2.0		
150	0.1		
	0.3		
	2.0		
180	0.1		
	0.3		
	2.0	Arcing	Arcing

Arcing; grey interference colour due to breakdown

An exception from all the above are the coatings anodised at 0.1 M and 0.3 M at current density of 60 $mA.cm^{-2}$ and 150 V as obtained in Table 4.6 and Figure 4.20; the colour reflectance at 0.1 M had lower brightness than the one at 0.3 M. This is can be due to the increased porosity at 0.1 M that at 0.3 M as was obtained in **Section 4.3.2** in Figure 4.21. The lower brightness with the increased time can be due to the increased breakdown as explained in **Section 4.2.1**, that results in increased porosity as was obtained in **Section 4.3.2.**

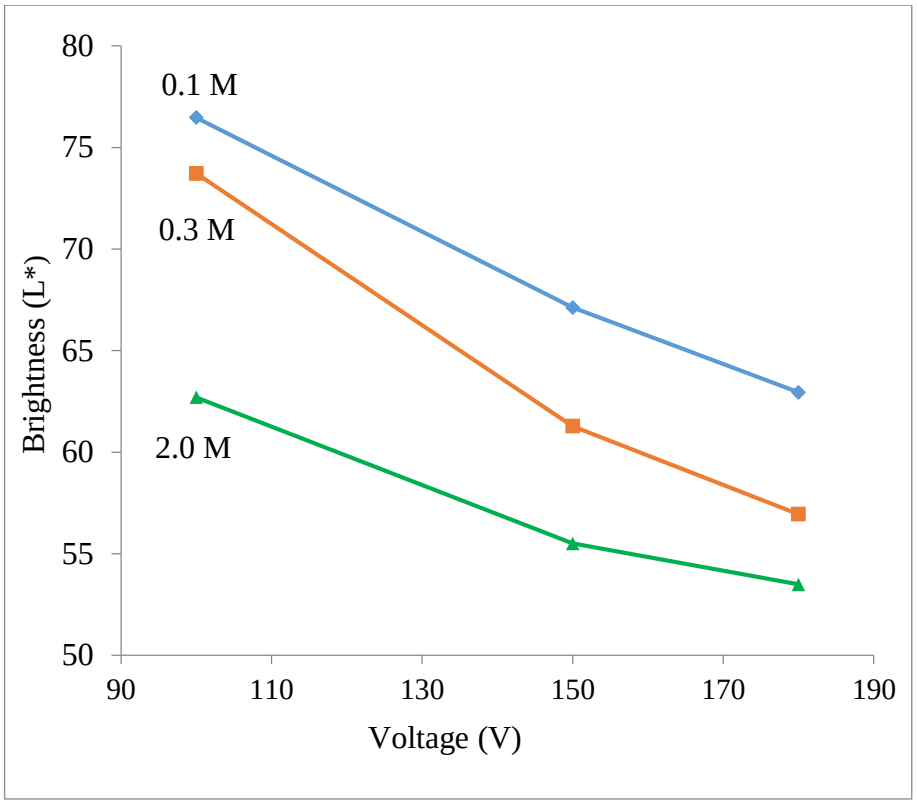

Figure 4.19: TiO_2 surface colour brightness (L*) at a function of applied voltage, at and molar concentration at 60 $mA.cm^{-2}$ for coatings anodised in H_3PO_4 electrolyte.

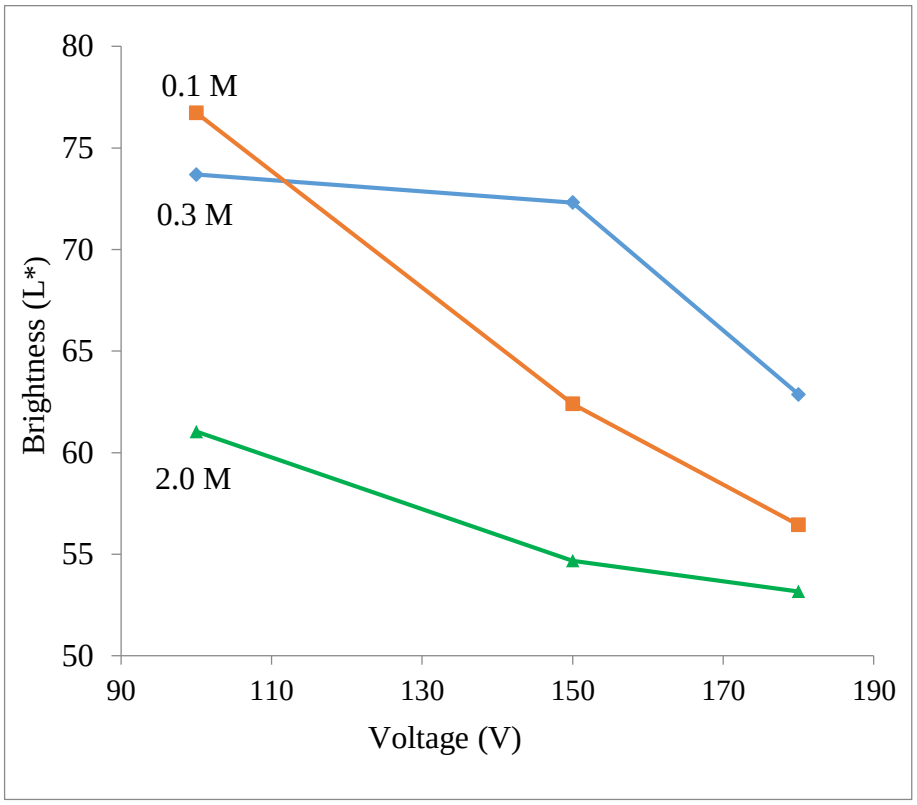

Figure 4.20: TiO_2 surface colour brightness (L*) at a function of applied voltage, at and molar concentration at 100 $mA.cm^{-2}$ for coatings anodised in H_3PO_4 electrolyte.

The brightness of H_3PO_4 electrolyte coatings has obtained higher brightness than the ones anodised in H_2SO_4 electrolyte as obtained in **Section 4.2.1**. This can be related to the breakdown phenomenon of the coatings anodised in H_2SO_4 electrolyte, where the increased breakdown intensity on the coatings anodised in H_2SO_4 electrolyte have cause to increase the porosity on the coatings surface and therefore losing the appearance colour which results in grey colur on the surface (Ashraf and Vaezi, 2004; Diamanti *et al.,* 2013). This has been explained in **Section 4.2.1**.

The anodization parameters i.e., voltage, current density, and molarity have influenced the TiO_2 coating appearance. The appearance obtained colorful at the lower voltage, current density, and molarity. While the appearance was lost with the increased voltage. However, the effect of breakdown seemed to have lower effect than the apprearance of the coatings anodised in H_2SO_4 electrolyte.

4.3.2 Microstructure of Anodised TiO_2 in H_3PO_4 Electrolyte

Figure 4.21 and Figure 4.22 observe the surface image microstructure captured for the coatings anodised in the H_3PO_4 electrolyte at 60 mA.cm^{-2} and 100 mA.cm^{-2} respectively.

It is apparent that the porosity has increased with the increased molarity, voltage and current density. Pores have reached their maximum size at the voltage of 180, 2 M and 100 mA.cm^{-2} (Figure 4.22 (g)) with pore size of 942.4 nm and 707.8 nm at 180 V and 60 mA.cm^{-2} (Figure 4.21 (i)). The pore size takes volcano orifice like shape. The pore formation can be related to the localized breakdown (arcing) of the coating (Teh *et al.,* 2003). The pore size average was taken for a sample area of 20 µm^2 using Image J software.

When comparing the surface microstructure images results in their colour interference, it can be noticed that the higher the porosity the dimmer the colour. The coatings at 180 V and 2.0 M as obtained at 60 mA.cm^{-2} (Figure 4.21 (i)) and 100 mA.cm^{-2} (Figure 4.22 (i)) has the largest pores among the other coatings and this is can be related to the corresponding grey interference colour as obtained in Table 4.5.

All the coatings have obtained nonuniform porosity except the coating that was anodised at 180 V, 2.0 M and 100 mA.cm^{-2} (Figure 4.22). This can relate to the nonuniform color reflectance within the same coating as obtained in Table 4.5. This

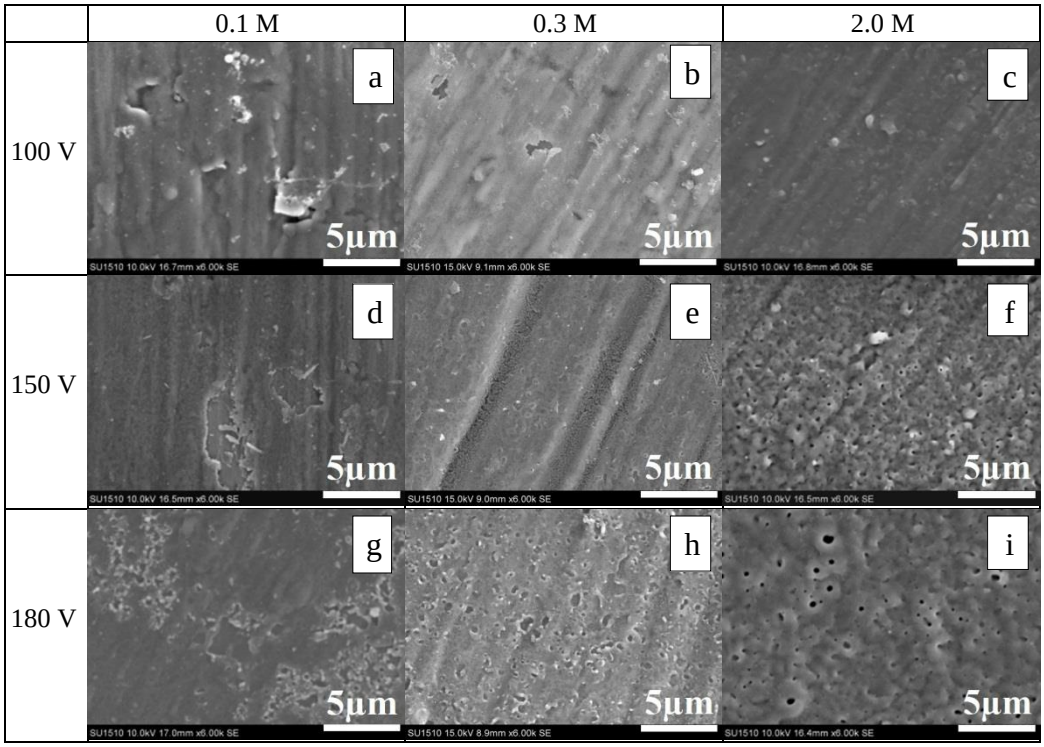

Figure 4.21: Surface microstructure images of TiO_2 anodised in H_3PO_4 electrolyte as a function of applied voltage and molarity at current density of 60 $mA.cm^{-2}$ (Arcing; uniform porosity due to breakdown)

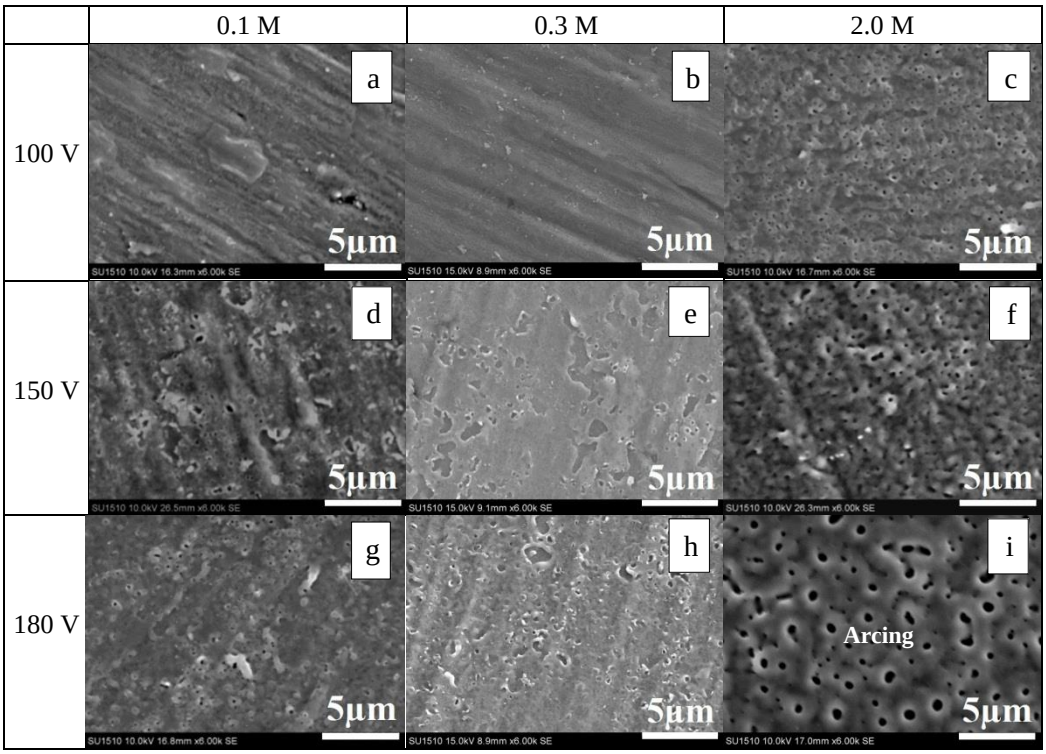

Figure 4.22: Surface microstructure images of TiO_2 anodised in H_3PO_4 electrolyte as a function of applied voltage and molarity at current density of 100 $mA.cm^{-2}$ (Arcing; uniform porosity due to breakdown)

can be obtained clearly at 100 V and 150 V, while the interference of the coatings at 180 V have obtained uniform colour. This can indicate that these coatings were not fully breakdowned were some areas were smooth and others were heavily porous. This is can be related to the nature of the anodization acid. Where it was reported that H_3PO_4 electrolyte contributes to larger pore sizes on the surface compared to the H_2SO_4 electrolyte (Park, 2008). However. H_3PO_4 is categorised as an electrolyte that provides slow metal dissolution (Jaeggi *et al.,* 2005) as explained in **Section 2.8.5**; therefore lesser anodic oxide can be developed on Ti surface due to the lesser electrons transfer from the cathode to the anode (the mechanism of anodization was explained in explained in **Section 2.8**). Thus, thinner coatings where build on H_3PO_4 electrolyte than the coatings grown in the H_2SO_4 electrolyte under the same conditions. The H_3PO_4 electrolyte coatings were reported to favour less crystalline compared to the ones anodised in the H_2SO_4 electrolyte at the same applied voltage (Jaeggi *et al.,* 2006). That can be related to the lower breakdown intensity results in lower porosity on the H_3PO_4 electrolyte coatings when compared to the ones anodised in the H_2SO_4 electrolyte under the same conditions as obtained in **Section 4.2.2**. Where it was reported that higher breakdown intensity results in a higher porosity and therefore crystalline TiO_2 (Ashraf and Vaezi, 2004; Diamanti *et al.,* 2013). This is has been explained in **Section 4.2.1**. It can be also seen in the crystalline TiO_2 that was obtained in **Section 4.2.4** for the H_2SO_4 electrolyte coatings compared to the H_3PO_4 electrolyte ones as was obtained in **Section 4.3.4**.

The coatings' thicknesses were detected by scanning its cross section. The thicknesses for coatings anodised in 0.1 M and 2.0 M at 100 V and 180 V as a function of current density can be obtained in Figure 4.23. From the figure, it can be noticed that the thickness has increased with the increased voltage, current density, and molarity. However, the thickness at 2.0 M and 100V have decreased. This is can indicate of experimental error and also the lower effect of current density on the thickness. The voltage had the highest influence on the coatings with the highest thickness has reached a maximum of 3.71 µm on the coating anodised in 0.1 M at 180 V. When compared to the effect of voltage and molarity on the thickness growth. It can be noticed that thickness at the same voltage of the coatings anodised at 100 V has increased by 29 % with the increased molarity, while it has only increased by 45 % for the coating anodised at 180 V. However, when comparing at the same molarity, the thickness has grown by 58 % for the coatings anodised in 0.1 M with the increased

voltage, while it has increased by 67% in 2.0 M. This is can indicate higher influence of the voltage over the molarity on the thickness growth.

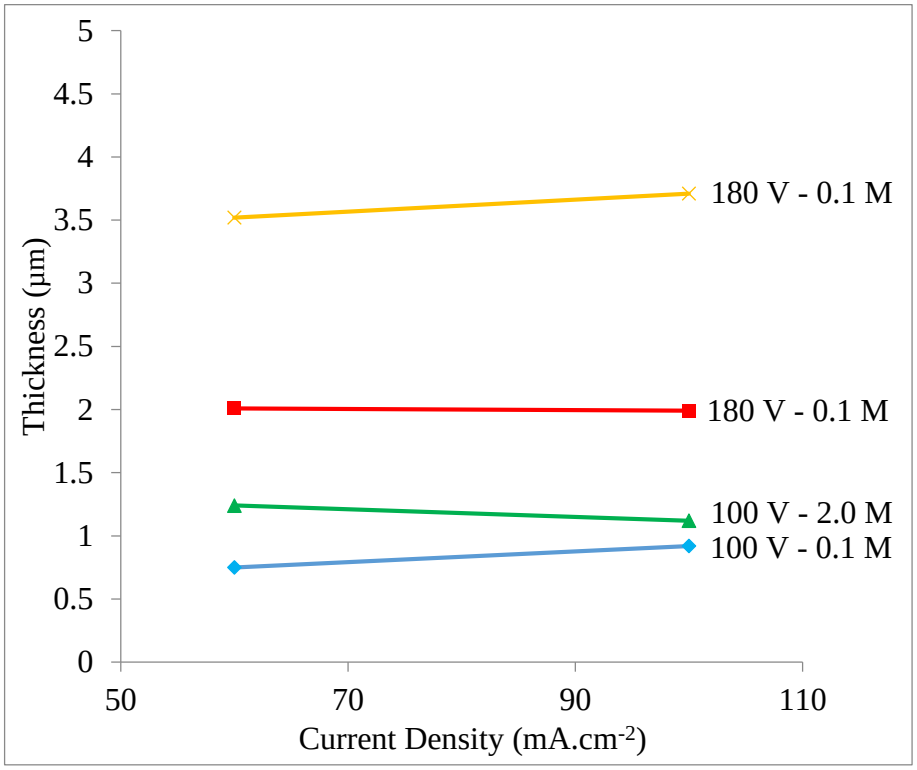

Figure 4.23: Thickness for TiO_2 coatings anodised in H_3PO_4 electrolyte as a function of current density and voltage

The thicknesses of the coatings anodised in the H_3PO_4 electrolyte was much lower than the coatings anodised in the H_2SO_4 electrolyte. Where the coatings have obtained 70 % lower thicknesses. Similar results were obtained by Sul et al. (2011) and Abdullah (2010). Abdullah has concluded that different thicknesses of TiO_2 coatings are a function of the nature of the electrolyte (Abdullah, 2010). This is believed to be due to the slower dissociation rate of H_3PO_4 than H_2SO_4 (Murmson, 2017). As a result, a lower electric field driving the ions through the oxide (Liu et al., 2004), and therefore, lower coating formation. The surface colour interference as obtained in Table 4.5 were more colourful, i.e., smoother surface, and has obtained higher brightness as obtained in Table 4.6 than the coatings anodised in the H_2SO_4 electrolyte. This is can also confirm the lower TiO_2 coating formation in the H_3PO_4 electrolyte. Where the smoother and brighter coating surfaces that were obtained by thinner coatings that obtained lower breakdown intensity as confirmed on the coatings' microstructure porosity in Figure 4.21 and Figure 4.22 when compared to the porosity

of the coatings anodised in the H_2SO_4 electrolyte. The relationship between the coating appearance, microstructure and thickness were discussed in detail in Section 4.2.1.

The effect of variation of the anodization parameters, i.e., voltage, current density, and molarity, on the TiO_2 coating microstructure and thickness was discussed. The TiO_2 microstructure and thickness were discussed with respect to the results of the TiO_2 appearance.

4.3.3 Elementary of Anodised TiO_2 in H_3PO_4 Electrolyte

Figure 4.24 (a and c) obtain the elements incorporated in the coating anodised in the H_3PO_4 electrolyte for 0.1 M and Figure 4.24 (b and d) obtain for 2.0 M at 150 V and 100 $mA.cm^{-2}$. From the results, it can be noticed that the phosphorous (P) atomic weight in percentage (%) has increased with the increased electrolyte molarity as obtained in Figure 4.24. This is due to the increased P ions that were incorporated into elemental analysis pattern has increased with the increased molarity. A similar results has been reported by Jaeggi et al. (2006). H_2SO_4 has a 320 million times more dissociation rate than the H_3PO_4 in water, the loss of concentration of H_3PO_4 in water is so minimal that it can be ignored altogether (Murmson, 2017). The very low dissociation of H_3PO_4 is due to the strength of the phosphate ion and the weak alkaline properties of water, which make the H_3PO_4, conserve its concentration in water. Therefore, consequently, the concentrated P ions can be heavily incorporated into the coating build-up.

4.3.4 Mineralogy of Anodised TiO_2 in H_3PO_4 Electrolyte

The phase mineralogical patterns of the TiO_2 coatings anodised in the H_3PO_4 electrolyte are illustrated as a function of applied voltage, current density. From the figures, apparently, there are no crystalline peaks. On the contrary to mineralogical patterns of the coatings produced in the H_2SO_4 electrolyte, where the increased porosity on the later caused by breakdown promotes higher crystallisation of the coating.

It has been reported that coatings produced in the H_3PO_4 electrolyte are less crystalline compared to H_2SO_4 electrolyte coatings under same applied voltage (Jaeggi

	0.1 M	2.0 M
FESEM	a	b
EDX	c	d

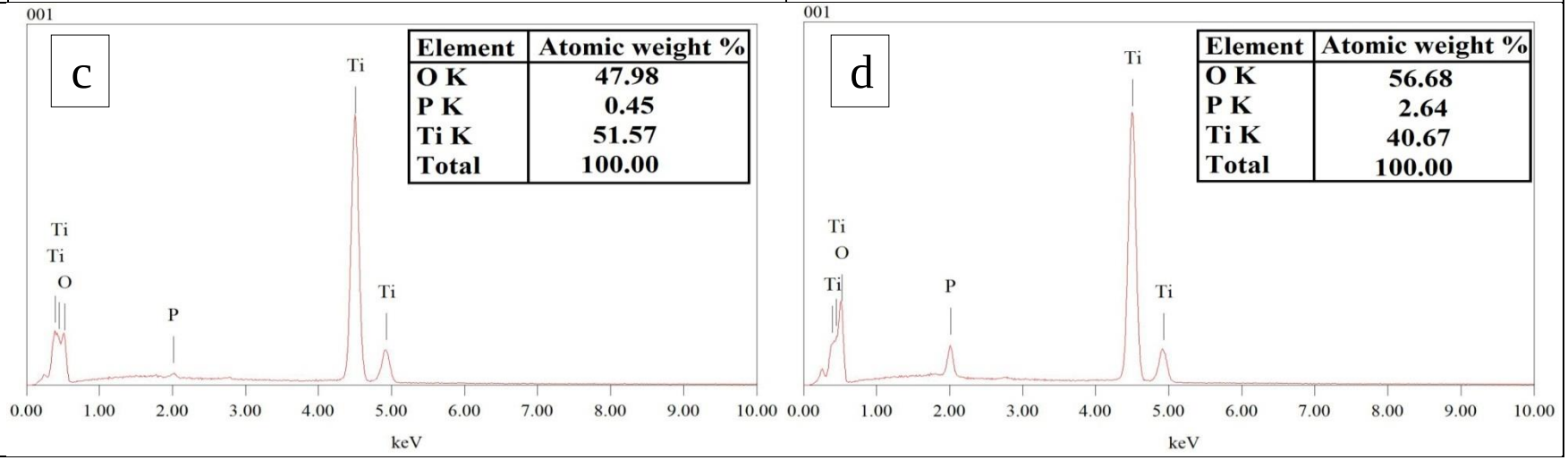

Figure 4.24: Elemental analysis of the coatings anodised in H_2SO_4 electrolyte at 150 V and 100 mA.cm^{-2} for 0.1 M (a and c) and 2.0 M (b and d)

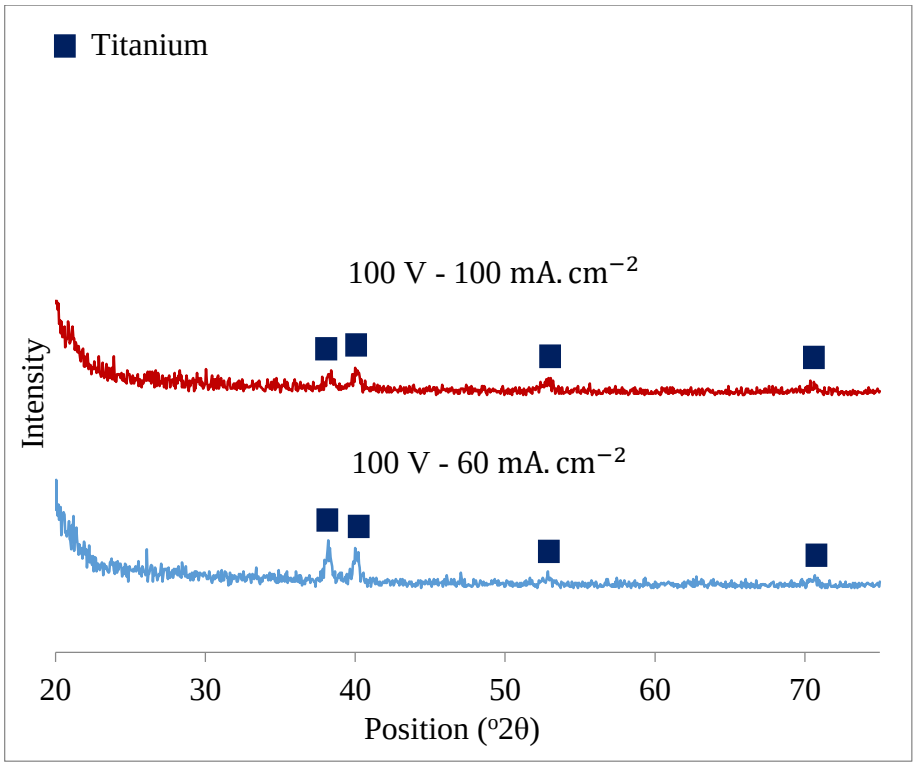

Figure 4.25: Phase mineralogical Patterns for 100 V, 60 and 100 mA.cm^{-2} at 0.1 M for coatings anodised in H_3PO_4 electrolyte

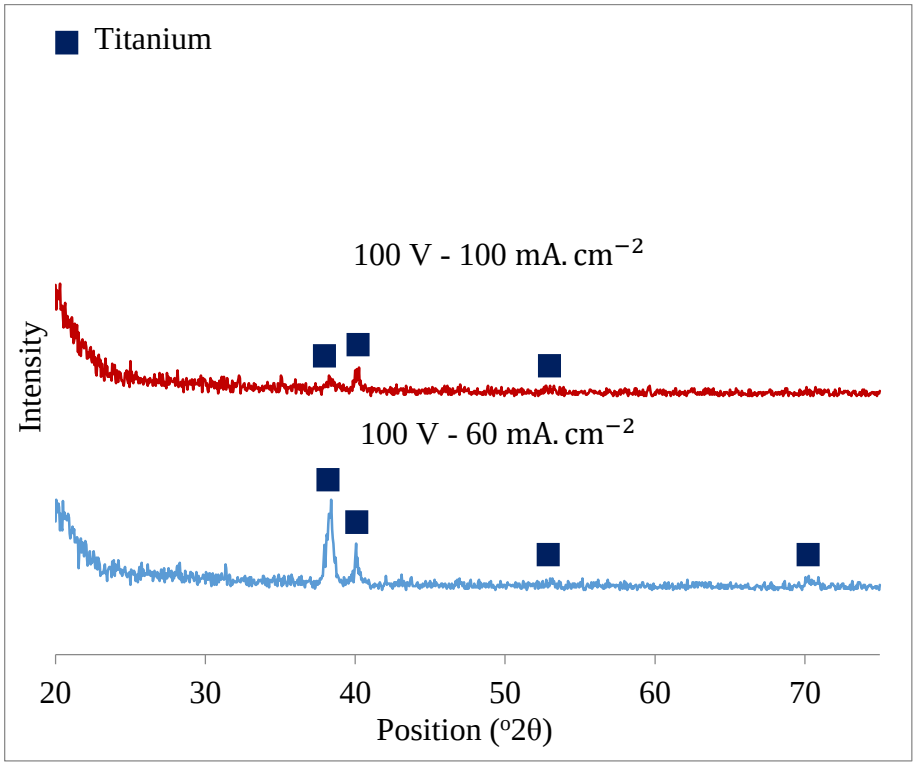

Figure 4.26: Phase mineralogical Patterns for 100 V, 60 and 100 mA.cm^{-2} at 2.0 M for coatings anodised in H_3PO_4 electrolyte

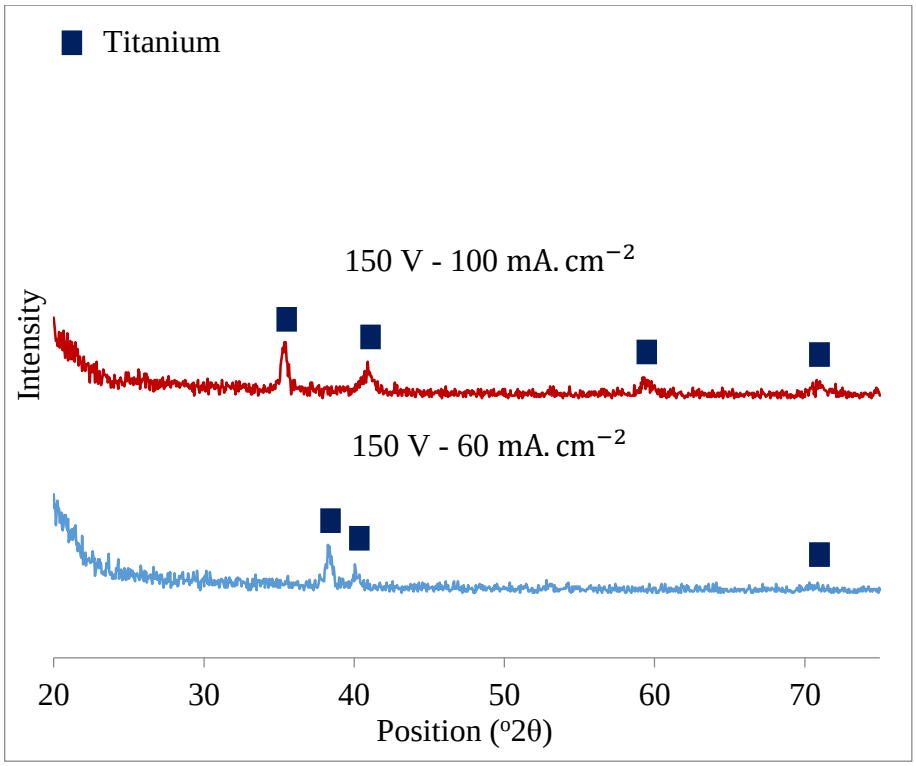

Figure 4.27: Phase mineralogical Patterns for 150 V, 60 and 100 mA.cm^{-2} at 0.1 M for coatings anodised in H_3PO_4 electrolyte

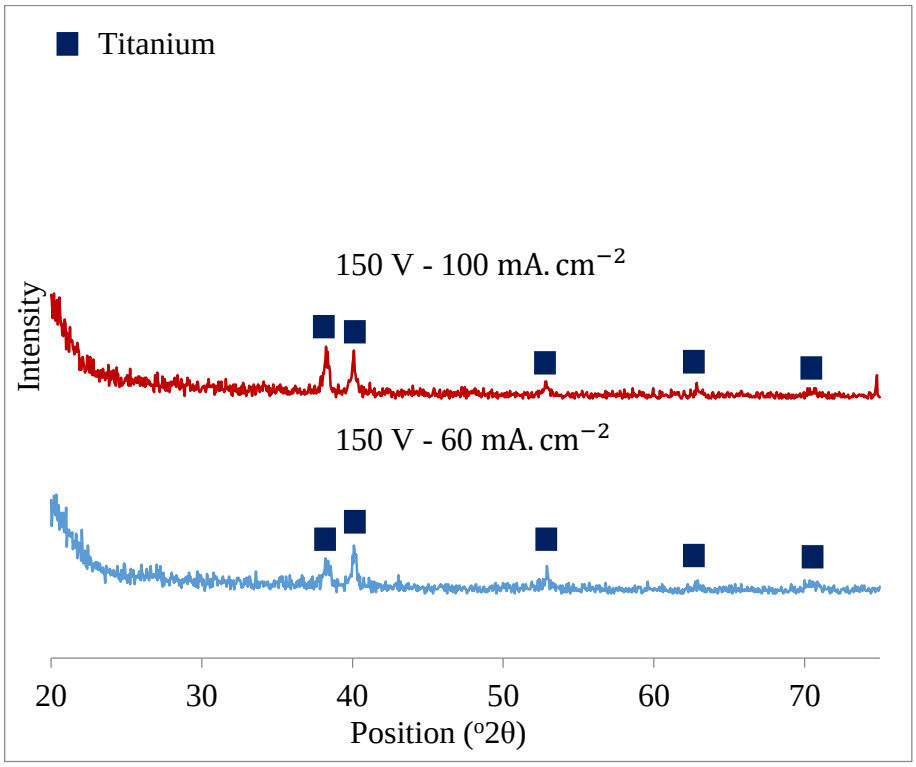

Figure 4.28: Phase mineralogical Patterns for 150 V, 60 and 100 mA.cm^{-2} at 2.0 M for coatings anodised in H_3PO_4 electrolyte

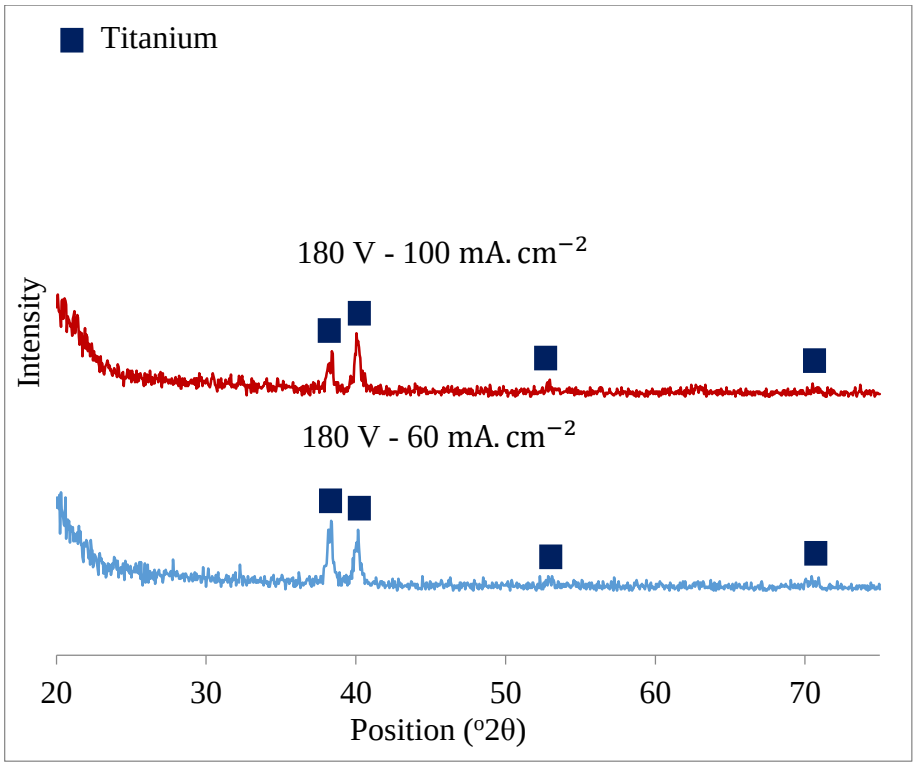

Figure 4.29: Phase mineralogical Patterns for 180 V, 60 and 100 mA.cm^{-2} at 0.1 M for coatings anodised in H_3PO_4 electrolyte

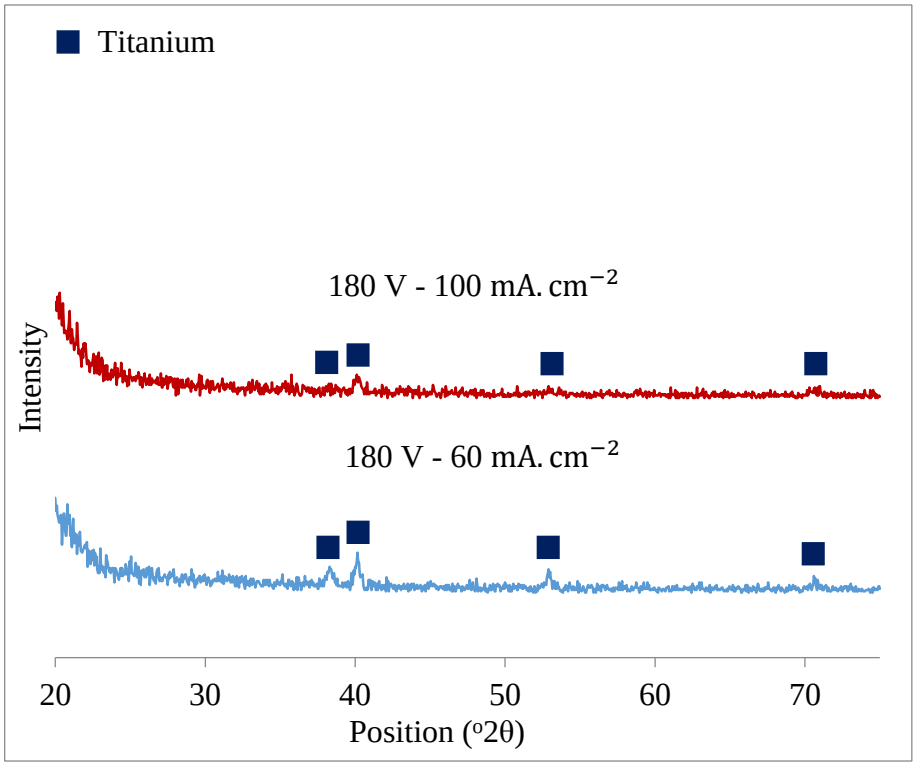

Figure 4.30: Phase mineralogical Patterns for 180 V, 60 and 100 mA.cm^{-2} at 2.0 M for coatings anodised in H_3PO_4 electrolyte

et al., 2005) as explained in **Section 4.3.2**. Song *et al.* (2009) have reported that the amorphous TiO_2 produced using H_3PO_4 electrolyte is due to the lower pore density on their coating surfaces when compared to the H_2SO_4 electrolyte coatings. This can be related to the slower dissolution of H_3PO_4 in the electrolyte compared to the H_2SO_4 as discussed in **Section 4.3.2**. This can lead to the lower ability of the local breakdown on the coating surface. It has already been known that the crystallographic transformation and development is closely related to the breakdown of the coating surface (El Kader *et al.*, 1981; Sul *et al.*, 2001; Zhao *et al.*, 2005).

From these results, it can be concluded that the coatings anodised in the H_3PO_4 electrolyte are unable to produce crystalline TiO_2 under the used anodization parameters compared to the crystallinity that was obtained in coatings anodised in the H_2SO_4 electrolyte.

4.3.5 Optics of Anodised TiO_2 in H_3PO_4 Electrolyte

Figure 4.31 and Figure 4.32 observe the exaction absorption of TiO_2 coating anodised in the H_3PO_4 electrolyte for 0.1 M and 2.0 M respectively. The parameters were taken at 150 V and 100 $mA.cm^{-2}$. The bandgap (E_g) values were 3.28 eV (378 nm) for 0.1 M and 3.57 eV (347.2 nm) for 2.0 M. This is a good condition to conduct the *in vitro* test with the UV irradiation of 254 nm (UVC).

According to the phase mineralogical results, all the coating produced in H_3PO_4 electrolyte have obtained amorphous results. It is known that the bandgap value of the intrinsic crystalline TiO_2 powder is 3.2 eV for anatase and 3.02 eV for rutile. The values of the bandgap that has been obtained are higher than the values of the intrinsic TiO_2 crystalline. When comparing these values with the values obtained from the H_2SO_4 electrolyte. The bandgap values have obtained dissimilarity. Where the bandgap values at 0.1 M from H_2SO_4 electrolyte (Figure 4.15) was higher than the bandgap value from H_3PO_4 electrolyte (Figure 4.31). In contrast, the bandgap from H_2SO_4 electrolyte at 2.0 M (Figure 4.16) was lower than the bandgap obtained in the H_3PO_4 electrolyte (Figure 4.32). Not to mention that the coatings from H_2SO_4 electrolyte have obtained TiO_2 crystallinity.

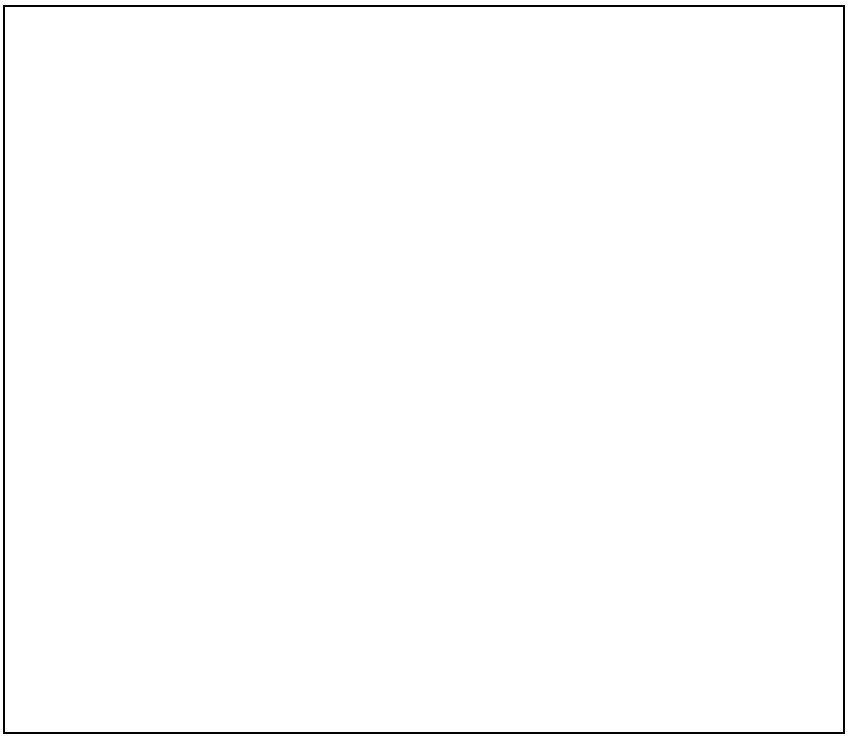

Figure 4.31: Bandgap (Eg) of coatings anodised at 150 V and 100 mA.cm^{-2} at 0.1 M in H_3PO_4 electrolyte

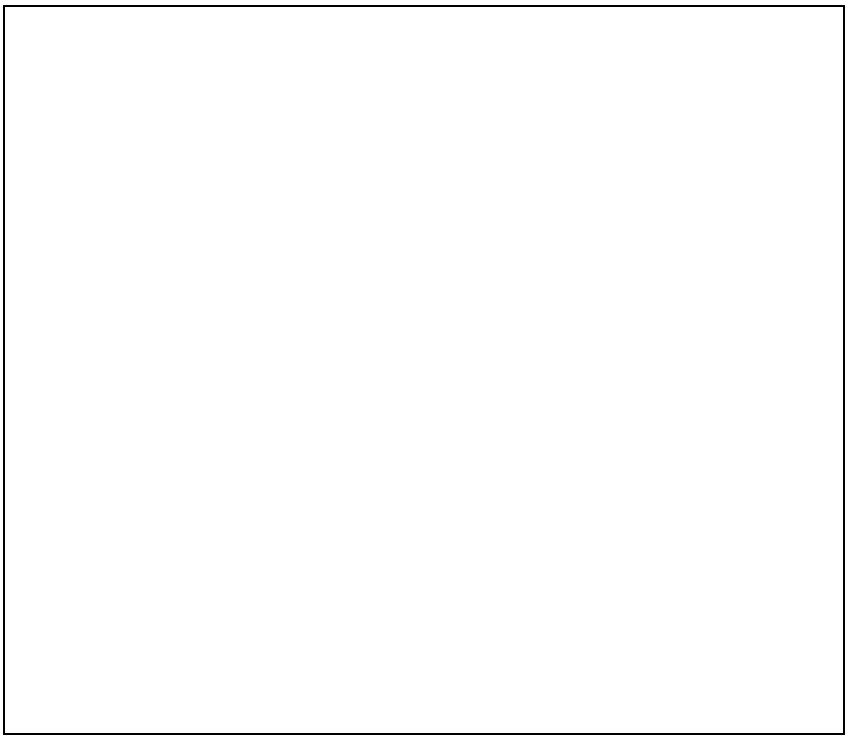

Figure 4.32: Bandgap (Eg) of coatings anodised at 150 V and 100 mA.cm^{-2} at 2.0 M in H_3PO_4 electrolyte

4.3.6 Absorption of Anodised TiO_2 in H_3PO_4 Electrolyte

Absorption analysis was taken for TiO_2 coatings anodised in the H_3PO_4 electrolyte for 0.1 M and 2.0 M at 150 V and 100 $mA.cm^{-2}$. The coatings have been irradiated under the UV of 254 nm for 12 hours of in water. The absorption analysis patterns of the coatings anodised in 0.1 M illustrated in Figure 4.33. While Figure 4.34 illustrates the absorption analysis of the coatings anodised in 2.0 M.

The absorption pattern has shown a presence of $Ti\text{-}O^-$ groups at band 680-800 cm^{-1} (Liu *et al.,* 2008), Phosphine (P-H) was obtained at band of 950-1200 cm^{-1} (Segneanu *et al.,* 2012), water (H_2O) at band 1860 cm^{-1}, Hydroxyl groups (OH) stretching region 3100-3400 cm^{-1} and Ti-OH groups at band 3635, 3645, 3680, 3750 and 3840 cm^{-1} (Liu *et al.,* 2008).

The $Ti\text{-}O^-$ group stretching was obtained at 0.1 M (Figure 4.33) and 2.0 M (Figure 4.34) and it was stronger at 0.1 M. The $Ti\text{-}O^-$ stretching has increased after the UV irradiation. Phosphine stretching was also obtained at 0.1 M and 2.0 M and it was stronger at 2.0 M. The OH, H_2O, and Ti-OH had a smaller stretching on 0.1 M and 2.0 M spectra.

The strong $Ti\text{-}O^-$ functional groups can indicate that there is an increased formation of distinct atomic defects like Ti^{3+} or Ti^{4+} interstitials, or O^{2-} vacancies (Grujić-Brojčin *et al.,* 2006). The strong phosphine's functional groups obtained in 2.0 M can be related to the intense P ions as obtained in Figure 4.24 (d). The stronger phosphine functional groups with increased molarity from 0.1 M as seen in Figure 4.33 to 2.0 M as seen in Figure 4.34 do agree with the increased P intensity according to the coating elemental analysis as discussed in **Section 4.3.3**.

The coatings that were anodised at both electrolytes; H_2SO_4 and H_3PO_4 have obtained a stronger $Ti\text{-}O^-$ functional groups at 0.1 M. as obtained in Figure 4.17 and Figure 4.33 respectively. This is can be related to the less acidic ions incorporated into the coatings; S and P as obtained in Figure 4.7 (d) and Figure 4.24 (d). Also, could be related to the lower porosity than the coatings anodised at 2.0 M as obtained in Figure 4.4 and Figure 4.22. However, the increased $Ti\text{-}O^-$ functional groups on the H_2SO_4 electrolyte coatings at 0.1 M can be related to the anatase crystalline, thus the photocatalytic activity of the crystalline TiO_2 (Wang *et al.,* 2007) as obtained in Figure 4.10 compared to the amorphous structure obtained on 0.1 M in the H_3PO_4 electrolyte (Figure 4.27). While the lower $Ti\text{-}O^-$ functional groups that were obtained at 2.0 M for

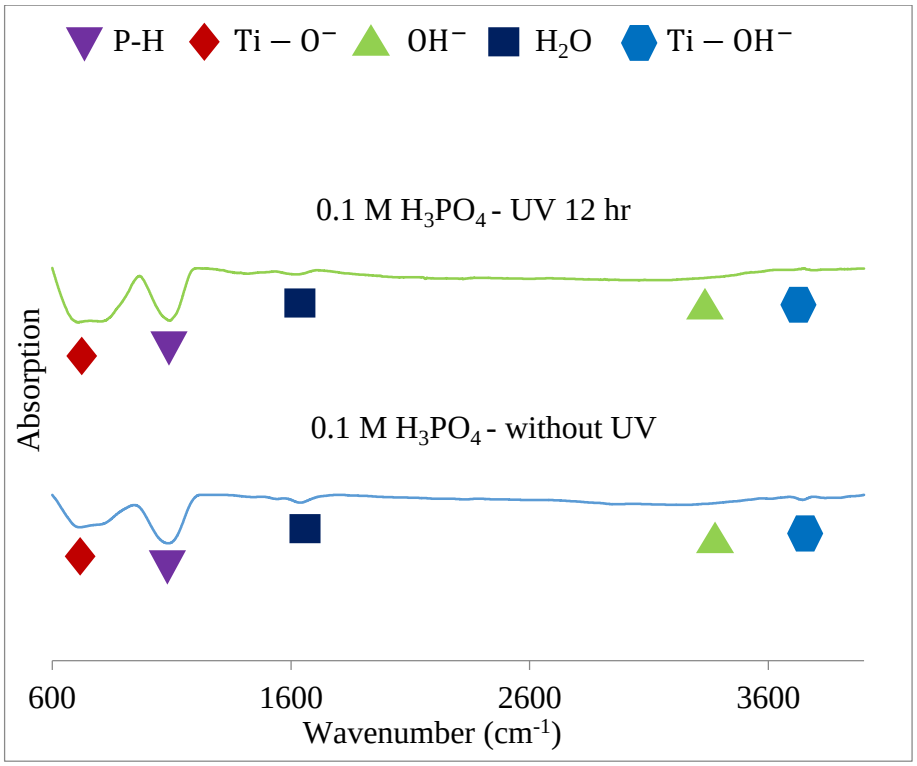

Figure 4.33: Absorption analysis patterns of TiO_2 coatings anodised in; (a) 0.1 M H_3PO_4 without treatment, (b) 0.1 M H_3PO_4 after 12 hr of irradiation under UV

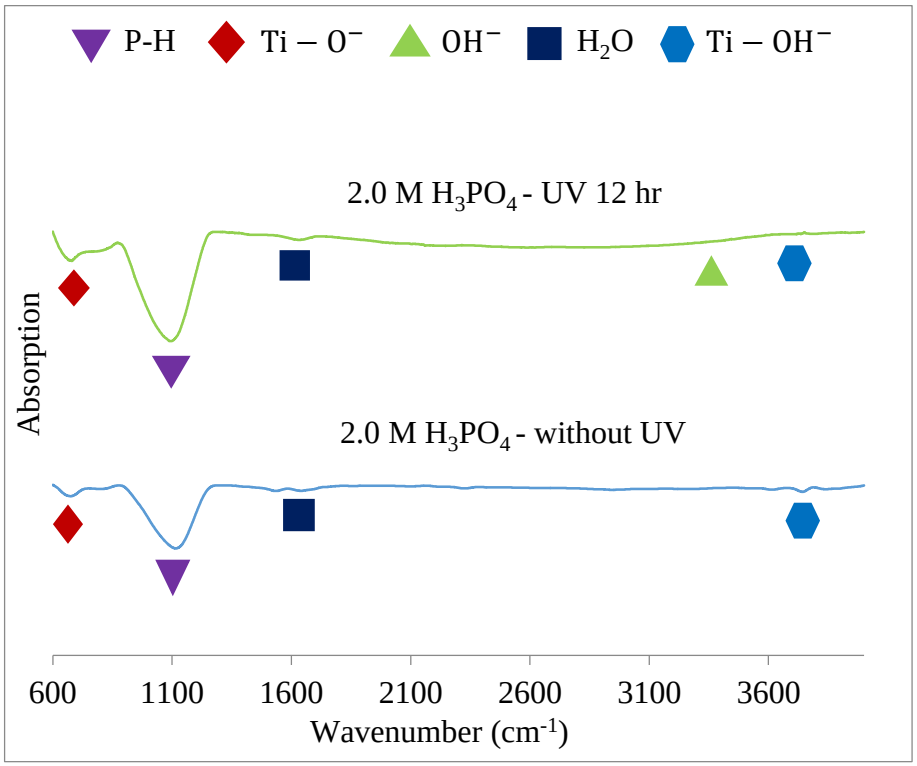

Figure 4.34: Absorption analysis patterns of TiO_2 coatings anodised in; (a) 2.0 M H_3PO_4 without treatment, (b) 2.0 M H_3PO_4 after 12 hr of irradiation under UV

the coatings that were anodised at both electrolytes can be related to the increased porosity on their coating surface as obtained in Figure 4.4 (f) and Figure 4.22 (f). Also can be related to the increased acidic ions functional groups; S=O and P-H as obtained in Figure 4.18 and Figure 4.34 respectively. Where S=O can consume the oxygen atomic bonding as described in **Section 4.2.6** and P-H can reflect on the increased P ions incorporation on the coating surface as obtained in Figure 4.24 (d). However, the effect of the P ions on the formation of $Ti\text{-}O^-$ is not clear. The crystallinity appears to have no effect on the formation of the $Ti\text{-}O^-$ functional groups. Where the coatings that were anodised at both electrolytes at 2.0 M have obtained similar $Ti\text{-}O^-$ functional groups strength, however, the H_2SO_4 coatings have obtained crystalline mainly rutile as obtained in Figure 4.11 and the H_3PO_4 coatings have obtained an amorphous structure as obtained in Figure 4.28.

The stronger $Ti\text{-}O^-$ functional groups on the 0.1 M coating than at 2.0 M can obtain higher chance to induce apatite in SBF and increased with UV. However, the stronger functional groups on the 0.1 M coating that were anodised in H_2SO_4 were expected to induce much apatite formation in *in vitro* testing in SBF, thus higher bioactivity.

4.4 Anodic Oxidation of Ti in Mixture of Sulphuric acid (H_2SO_4) and Phosphoric acid (H_3PO_4) Electrolyte

The TiO_2 coatings anodised in a mixture of dilute sulphuric acid (H_2SO_4) + phosphoric acid (H_3PO_4) electrolyte will be characterised. Colour, microstructure, morphology, mineralogy, and surface energy of the coatings will be discussed to later evaluate the *in vitro* bioactivity of these coatings produced under mixed electrolyte parameters.

4.4.1 Colour of Anodised TiO_2 in Mixed Electrolyte

The visual appearance of the TiO_2 coatings as a function of applied voltage (V), current density ($mA.cm^{-2}$) and molarity (M) at 10 minutes is shown in Table 4.7. While Table 4.8 obtain digital colouring for the coatings correspond to Table 4.7. Table 4.8 obtain colours using colorimeter with CIELAB coordinates (L*a*b*) and converted to computer colour interface using computer software. The subdivision of these figures

Table 4.7: Visual appearance taken by camera of TiO_2 surface colour at a function of applied voltage, current density at molarity at 10 min for coatings anodised in mixed electrolyte

Voltage (V)	Mole (M)	Current Density ($mA.cm^2$)	
		60	100
100	0.1 S + 0.1 P	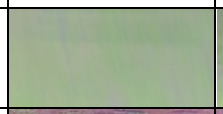	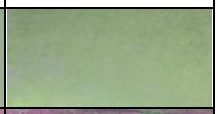
	0.1 S + 0.3 P	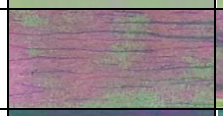	
	0.3 S + 0.1 P		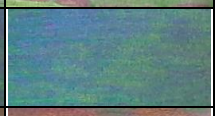
	0.1 S + 2.0 P		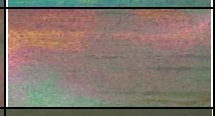
	2.0 S + 0.1 P	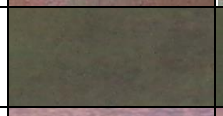	
150	0.1 S + 0.1 P		
	0.1 S + 0.3 P		
	0.3 S + 0.1 P	Arcing	Arcing
	0.1 S + 2.0 P		
	2.0 S + 0.1 P	Arcing	Arcing
180	0.1 S + 0.1 P		
	0.1 S + 0.3 P	Arcing	Arcing
	0.3 S + 0.1 P	Arcing	Arcing
	0.1 S + 2.0 P	Arcing	Arcing
	2.0 S + 0.1 P	Arcing	Arcing

S; H_2SO_4, P; H_3PO_4, Arcing; grey interference colour due to breakdown

Table 4.8: CIELAB digital colour generated with colourmeter of TiO_2 surface colour at a function of applied voltage, current density and molarity at 10 min for coatings anodised in mixed electrolyte

Voltage (V)	Mole (M)	Current Density ($mA.cm^2$)	
		60	100
100	0.1 S + 0.1 P		
	0.1 S + 0.3 P		
	0.3 S + 0.1 P		
	0.1 S + 2.0 P		
	2.0 S + 0.1 P		
150	0.1 S + 0.1 P		
	0.1 S + 0.3 P		
	0.3 S + 0.1 P	Arcing	Arcing
	0.1 S + 2.0 P		
	2.0 S + 0.1 P	Arcing	Arcing
180	0.1 S + 0.1 P		
	0.1 S + 0.3 P	Arcing	Arcing
	0.3 S + 0.1 P	Arcing	Arcing
	0.1 S + 2.0 P	Arcing	Arcing
	2.0 S + 0.1 P	Arcing	Arcing

S; H_2SO_4, P; H_3PO_4, Arcing; grey interference colour due to breakdown

is based on a visual and mineralogical examination during processing.

The present data conclude the following:

i. There is a gradual colour variation as a function applied voltage and molar concentration. The colours change from bright colours to grey colour with increased molarity and voltage.

ii. It is apparent that colour is turning darker with increased H_2SO_4 molarity than increased H_3PO_4. At 180 V the colour is grey for all the interfaces with an increased molarity of both solutions.

iii. The colour brightness with respect to current density is fluctuating. Alternately the brightness takes advantage between 60 $mA.cm^{-2}$ and 100 $mA.cm^{-2}$ at all voltages. However, the brightness at 2.0 S + 0.1 P at 180 V has taken attention with higher brightness (light grey) at 100 $mA.cm^{-2}$ than 60 $mA.cm^{-2}$.

iv. The grey colour resulted at 180 V and 150 V, could be related to the breakdown voltage of the coatings (arcing). This is to be obtained later when surface microstructure and mineralogical results to be discussed.

Figure 4.33 and Figure 4.34 obtain the brightness of coatings surfaces. The brightness (L* value) obtained is according to CIELAB coordinates, which is related to colour in Table 4.8. From Figure 4.35 and Figure 4.36, the behaviour of the graphs can be considered irregular and can conclude the following:

i. The brightness has decreased with the increased voltage at both current densities (60 and 100). Only the brightness at 2.0 S + 0.1 P was out the course with the increased brightness that the other interfaces with increased voltage.

ii. At 100 V the brightness has decreased with increased molarity. Especially with increased H_2SO_4 concentration. At 180 V the brightness values for all interfaces are close to each other with grey colour interference. Except for 2.0 S + 0.1 P, this has high brightness with light grey interference.

iii. The decreased brightness with increased voltage could be related to breakdown voltage which leads to impede interference. This phenomenon has been explained in **Section 4.2.2**.

The anodization parameters i.e., voltage, current density, and molarity have influenced the TiO_2 coating appearance. The appearance obtained colorful at the lower voltage, current density, and molarity, while the appearance was lost with the increased voltage. The loose of appearance was obtained to be higher at the coatings anodised in the mixed electrolyte with increased H_2SO_4 molarity with the increased voltage due

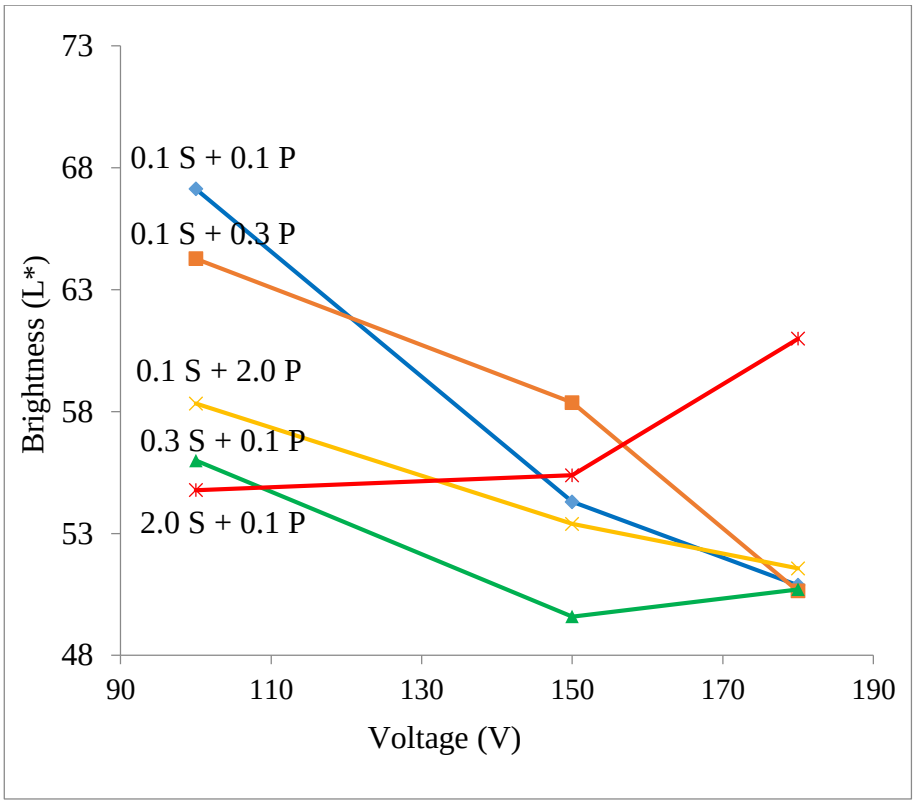

Figure 4.35: TiO_2 surface colour brightness (L*) at a function of applied voltage, at and molar concentration at 60 $mA.cm^{-2}$ for coatings anodised in mixed electrolyte

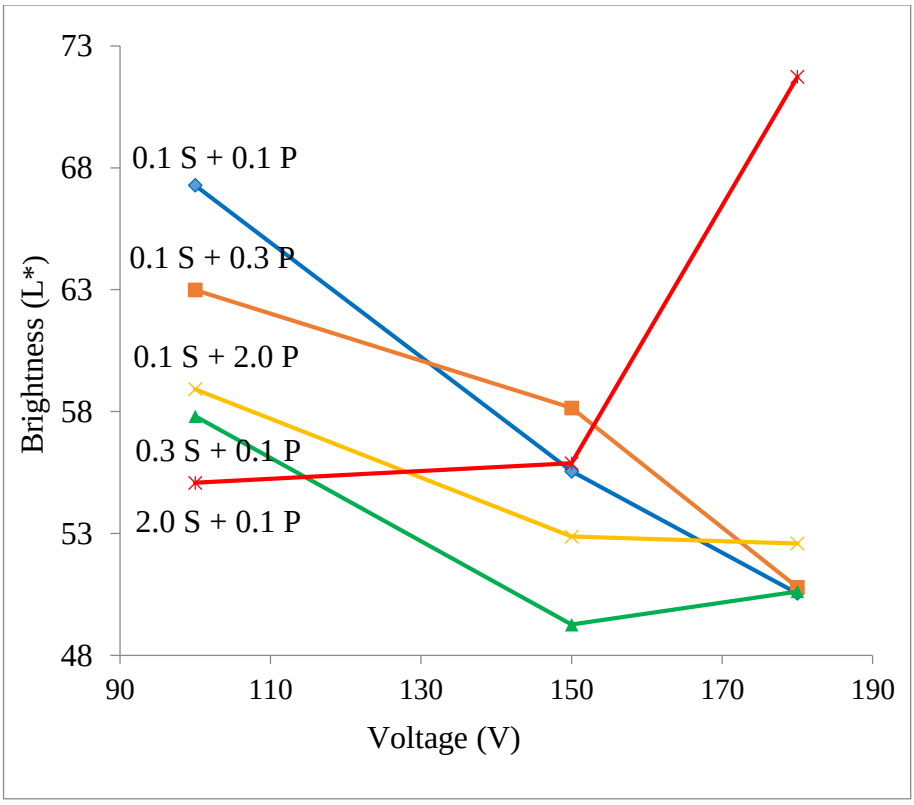

Figure 4.36: TiO_2 surface colour brightness (L*) at a function of applied voltage, at and molar concentration at 100 $mA.cm^{-2}$ for coatings anodised in mixed electrolyte

to the increased breakdown intensity. While the coatings anodised in the mixed electrolyte with increased H_3PO_4 molarity had more colourful and brighter appearance due to the lower breakdown effect at the elevated voltage. This is has been caused by the lower metal dissolution that was caused by H_3PO_4.

4.4.2 Microstructure of Anodised TiO_2 in Mixed Electrolyte

Figure 4.37 and Figure 4.38 observe the surface image microstructure captured for the coatings anodised in mixture electrolyte at 60 $mA.cm^{-2}$ and 100 $mA.cm^{-2}$ respectively. The coating anodised in 0.1 M H_2SO_4 + 0.1 M H_3PO_4, i.e., 0.1 S + 0.1 P; 0.1 M H_2SO_4 + 0.3 M H_3PO_4, i.e., 0.1 S + 0.3 P; 0.3 M H_2SO_4 + 0.1 M H_3PO_4, i.e., 0.3 S + 0.1 P; 0.1 M H_2SO_4 + 2.0 M H_3PO_4, i.e., 0.1 S + 2.0 P; 2.0 M H_2SO_4 + 0.1 M H_3PO_4, i.e., 2.0 S + 0.1 P.

Generally, higher voltage resulted in bigger pores, especially with increased molarity. While non-porous surface coatings can be seen at low molarity and low voltage. The pores take volcano-like shape or donut-like shape at higher voltages (150 V and 180 V), when H_2SO_4 concentration has increased to 0.3 M. And when increased to 2.0 M it takes grooves-like shape density is higher at coatings anodised in higher H_2SO_4 concentration than at higher H_3PO_4. Also higher H_3PO_4 concentration the pores take volcano-like shape. However, at 2.0 M at 180 V (Figure 4.37 (m) and Figure 4.38 (m)) the pores take flat shape. At higher current density, the porosity and pore size has increased with increased H_3PO_4 molarity and voltage. When molarity reaches 2.0 M at 180 V, the pore size mean increased from 519.2 nm at 60 $mA.cm^{-2}$ (Figure 4.37 (m)) to 627.2 nm at 100 $mA.cm^{-2}$ (Figure 4.38 (m)). However, the porosity and pore size is higher at lower current density with increased H_2SO_4 concentration. This is clear at 2.0 M at 150 V and 180 V. Where the pore mean size has decreased from 1105.4 nm at 60 $mA.cm^{-2}$ (Figure 4.37 (n)) to 979.5 nm at 100 $mA.cm^{-2}$ (Figure 4.38 (n)). The pore formation as discussed in **Section 4.2.3** and **Section 4.3.3** can be related to the local breakdown of the coating. The coatings anodised at higher H_2SO_4 have obtained higher breakdown concentration. The breakdown at lower current density was higher. This can be due to the lower amount of current density (60) to push the voltage to reach its maximum. This has led to longer breakdown time. Therefore, overlapping pores due to increased porosity which led to bigger pores at lower current density.

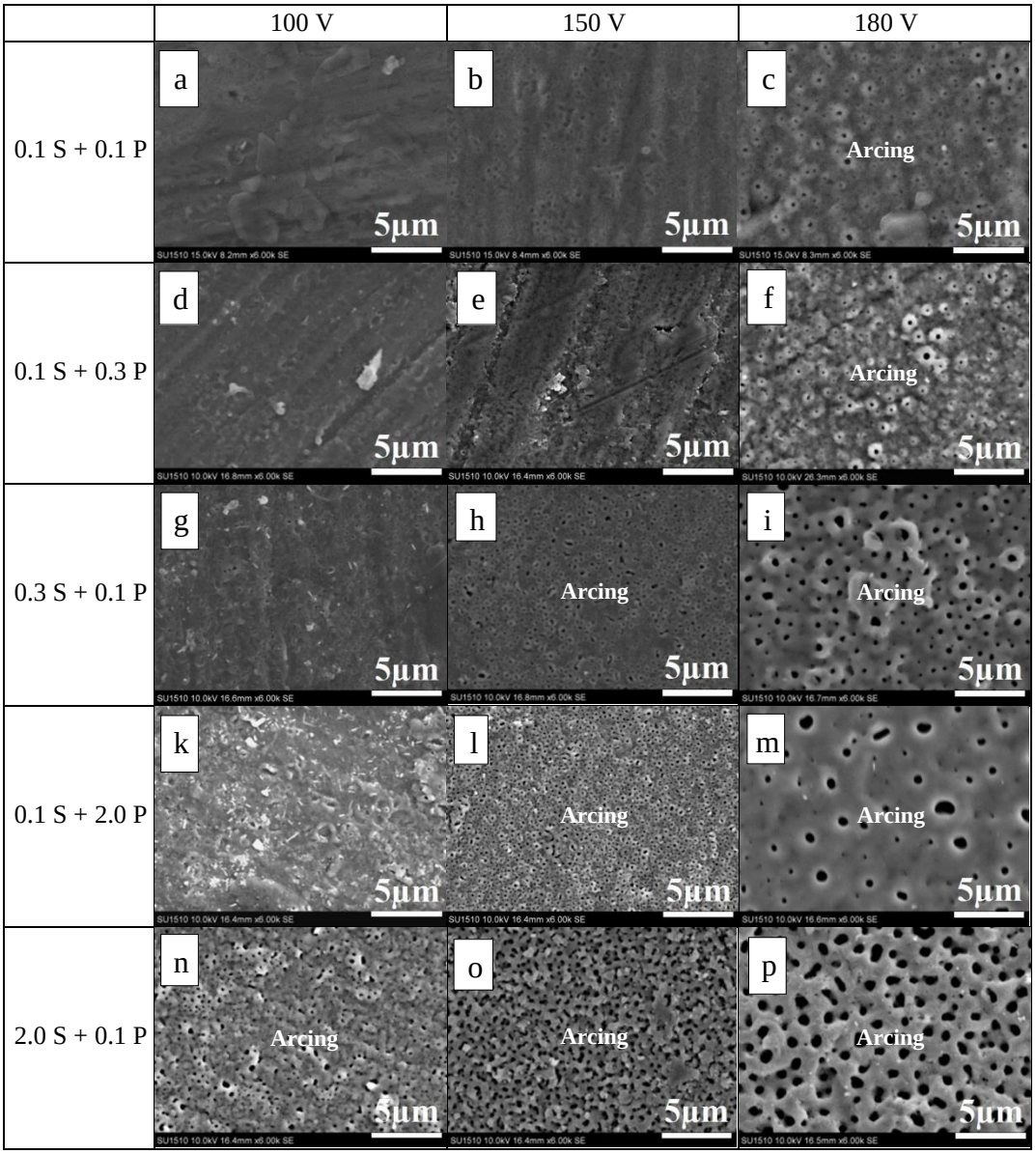

Figure 4.37: Surface microstructure images of TiO_2 coatings anodised in mixed electrolyte as a function of applied voltage and molarity at current density of 60 $mA.cm^{-2}$ (Arcing; uniform porosity due to breakdown)

By comparing the pore size at 180 V between surface coatings produced at higher H_2SO_4 molarity (2.0 S + 0.1 P) and higher H_3PO_4 molarity (0.1 S + 2.0 P). The pore size average and statistics were taken for a sample area of 20 μm^2 using Image J software. Pore size for coating produced in (2.0 S + 0.1 P) has bigger pore size by 53% over coating produced in (0.1 S + 2.0 P) at 60 $mA.cm^{-2}$. While the size advanced by 36% at 100 $mA.cm^{-2}$. While the size advances by 36% at 100 $mA.cm^{-2}$. In general, pore size for coatings produced in mixed electrolyte (2.0 S + 0.1 P) has 34 % at 60 $mA.cm^{-2}$ and 18.3 % at 100 $mA.cm^{-2}$ higher pore size over H_2SO_4 electrolyte (2 M

H_2SO_4). However, pore size for coatings produced in mixed electrolyte (2.0 P + 0.1 S) has 26.6 % at 60 mA.cm^{-2} and 33.4 % at 100 mA.cm^{-2} lower pore size than in H_3PO_4 electrolyte (2.0 M H_3PO_4).

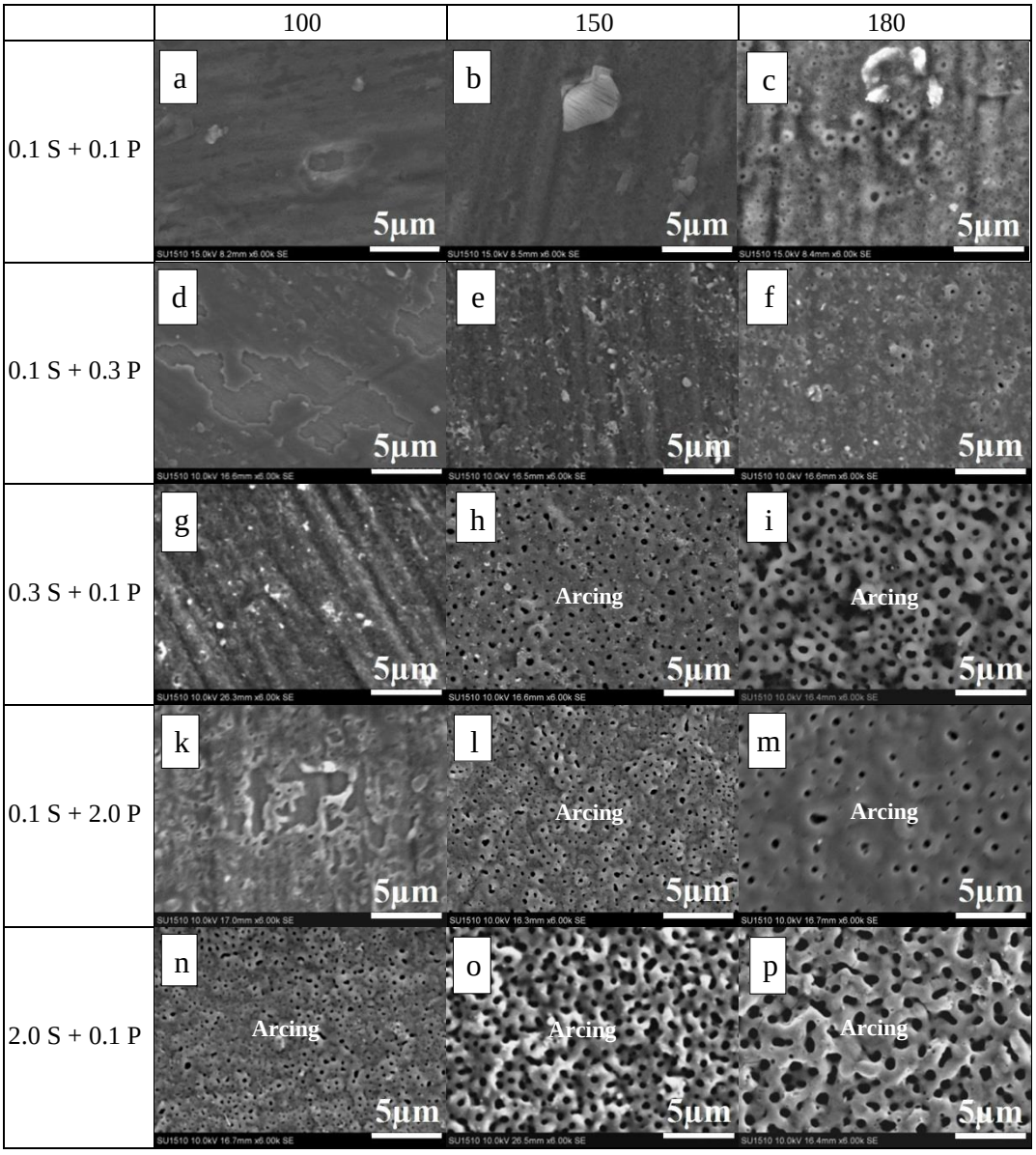

Figure 4.38: Surface microstructure images of TiO_2 coatings anodised in mixed electrolyte as a function of applied voltage and molarity at current density of 100 mA.cm^{-2} (Arcing; uniform porosity due to breakdown)

According to these statistics, it can be concluded that H_2SO_4 results in lower pore size, unlike H_3PO_4. When H_2SO_4 is added to H_3PO_4 it tends to lower the pore size and vice versa. This was obvious when coating produced in (2.0 S + 0.1 P) was progressed by over 50% larger pore size than coatings produced in (0.1 S + 2.0 P) at a current density of 60. The larger pore size at 60 mA.cm^{-2} than at 100 mA.cm^{-2} can be

related to breakdown phenomenon which led to bigger size pores. This phenomenon has been explained in **Section 4.2.3**. The same explanation can be applied when compared between mixed electrolyte (2.0 S + 0.1 P) and H_2SO_4 electrolyte (2.0 M H_2SO_4). Also between mixed electrolyte (0.1 S + 2.0 P) and H_3PO_4 electrolyte (2.0 M H_3PO_4.

By refereeing to the colour results, it can be noticed that the larger the pores the dimmer the colour due to the increased of breakdown (arcing). The coatings with higher molar concentration at 180 V have obtained higher porosity, which corresponds to the grey colour interference as seen in Table 4.7 and Table 4.8.

The coatings' thicknesses were detected by scanning its cross section. The thicknesses for coatings anodised in for 0.1 S + 0.1 P, 0.1 S + 2.0 P and 2.0 S + 0.1 P at 100 V and 180 V as a function of current density can be obtained in Figure 4.39. From the figure, it can be noticed that the thickness has increased with the increased voltage, current density, and molarity. It can be noticed that voltage had the highest influence on the coatings with the thickness has reached a maximum of 17.46 µm on the coating anodised in 2.0 S + 0.1 P at 180 V. While the current density has the lowest effect on the thickness. The thicknesses of the coatings anodised in 2.0 S + 0.1 P were the highest. Where the average of the thicknesses anodised in 2.0 S + 0.1 P was higher by 59 % when compared to the thicknesses of the coatings anodised in 0.1 S + 0.1 P. While the thicknesses of the coatings anodised in 0.1 S + 2.0 P were higher by only 17 %. However, when compared the coating growth anodised under same molarity with respect to voltage increased. The thickness has the highest coating growth on the coatings anodised in 0.1 S + 2.0 P, where the thickness has increased by 56 % with the increased voltage from 100 V to 180 V, while it was 53 % for 2.0 S + 0.1 P and only 34 % for 0.1 S + 0.1 P. Moreover, when compared the thicknesses under the same voltage with respect to the changed molarity, the coatings anodised in 0.1 S + 2.0 P has obtained 7 % decreased thickness at 100 V when compared to the thickness of the coatings anodised in 0.1 S + 0.1 P, while the thickness was increased by 49 % for 2.0 S + 0.1 P. When compared at 180 V, a 28 % thickness increased for 0.1 S + 2.0 P and 63 % for 2.0 S + 0.1 P. This is can indicate the higher effect of voltage molarity on the TiO_2 thickness growth.

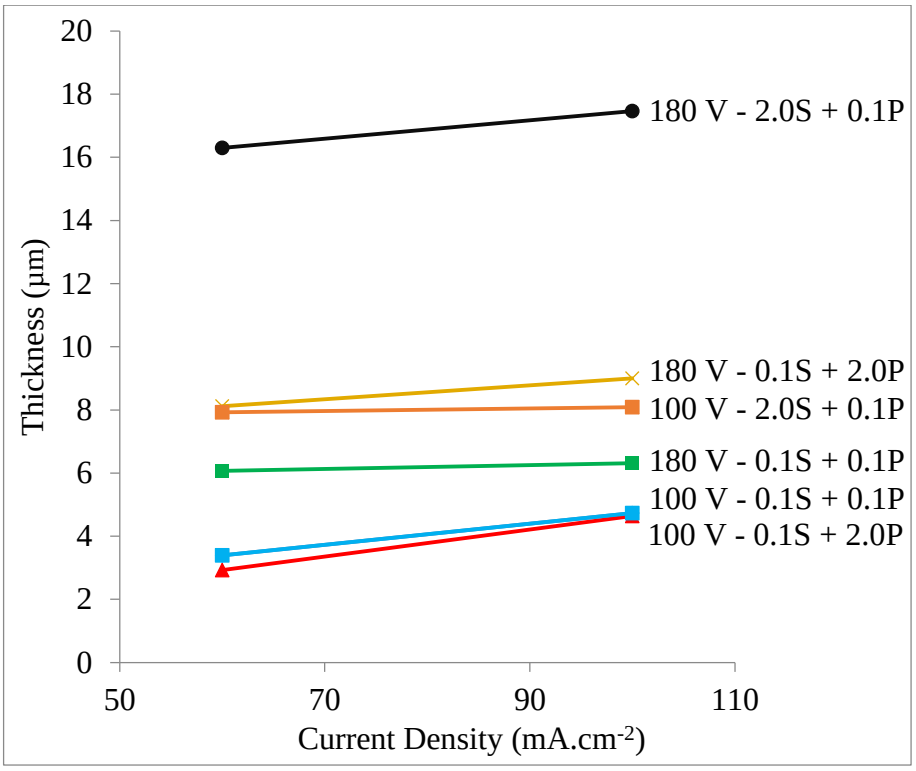

Figure 4.39: Thickness for TiO_2 coatings anodised in mixed electrolyte as a function of current density and voltage

The higher thickness of the coatings anodised at higher H_2SO_4 molarity can be related to higher dissociation rate in the electrolyte medium (Murmson, 2017). Comparatively the lower dissociation rate of the H_3PO_4 has proved to result in lower thickness formation. Also when relating the resulted thickness with the surface appearance as obtained in Table 4.7 and surface brightness in Table 4.8, it was clear that the coatings anodised in higher H_2SO_4 molarity have obtained thicker coatings and lower brightness. The coatings thicknesses have reached the breakdown level and resulted in increased porosity in Figure 4.37 and 4.38. This is believed to be due to the increased TiO_2 build-up, i.e., thickness, have caused an electric pressure due to the increased electric resistance and therefore the TiO_2 started to breakdown. This is has been explained in **Section 4.2.1**. While the thinner coatings that were anodised at higher H_3PO_4 have obtained higher brightness coating surfaces. This is can indicate to the smoother coatings surfaces that weren't thick enough to reach the breakdown level. This is was explained in **Section 3.3.2**. The thicknesses of the coatings anodised in mixed have obtained to be higher than the ones anodised in H_2SO_4 and H_3PO_4 electrolytes. This is can be related to the nature of the mixed electrolytes themselves. Similar results were obtained by Abdullah (2010).

4.4.3 Elementary of Anodised TiO_2 in Mixed Electrolyte

Figure 4.40 obtain the elements incorporated in the coating anodised in mixed electrolyte at 0.1 M H_2SO_4 + 0.1 M H_3PO_4, i.e., 0.1 S + 2.0 P, 0.1 M H_2SO_4 + 2.0 M H_3PO_4, i.e., 0.1 S + 2.0 P and 2.0 M H_2SO_4 + 0.1 M H_3PO_4, i.e., 2.0 S + 0.1 P at 150 V and 100 $mA.cm^{-2}$. The elements testing have been conducting for the TiO_2 coatings that was conducted for the *in vitro* testing.

From the results, it can be noticed that the phosphorous (P) atomic weight in percentage (%) is higher than the sulphur (S) on all the coatings. This means that the P has higher ions incorporation on the coating build-up over the S ions even on the coatings anodised in the electrolytes with level and higher H_2SO_4 mixture molarity. This is again due to the higher dissociation rate of H_2SO_4 than the H_3PO_4 in water as explained in **Section 4.2.4** and **Section 4.3.4**.

4.4.4 Mineralogy of Anodised TiO_2 in Mixed Electrolyte

The phase mineralogical patterns of the TiO_2 coatings are illustrated as a function of applied voltage, current density for 0.1 H_2SO_4 + 0.1 H_3PO_4, i.e., 0.1 S + 0.1 P, 0.1 H_2SO_4 + 2.0 H_3PO_4 i.e., 0.1 S + 2.0 P and 2.0 H_2SO_4 + 0.1 H_3PO_4 i.e., 2.0 S + 0.1 P. The mineralogy testing have been conducting for the TiO_2 coatings that were conducted for the *in vitro* testing.

It is apparent there were no crystalline peaks at the coatings produced at 0.1 S + 0.1 P as seen in Figure 4.41 for 100 V, Figure 4.42 for 150 V and Figure 4.43 for 180 V and at 0.1 S + 2.0 P as seen in Figure 4.44 for 100 V, Figure 4.45 for 150 V and Figure 4.46 for 180 V. While TiO_2 crystalline, i.e., anatase and rutile, was obtained at 2.0 S + 0.1 P as seen in Figure 4.47 for 100 V, Figure 4.48 150 V and Figure 4.49 for 180 V. The crystallinity percentage of the TiO_2 coating has been obtained in Figure 4.50 for the coatings that have been anodised in 0.1 P + 2.0 S. The crystallisation of the TiO_2 coating can be obtained in the phase mineralogical patterns in a form of intense peaks (Hanaor, 2007). The coatings produced in 2.0 S + 0.1 P have obtained an increased anatase crystalline with increased voltage and current density. Anatase crystalline peaks can be obtained at 100 V. A stronger anatase peaks can be obtained at 150 V. Rutile threshold alongside a stronger anatase peaks can be obtained at 180

	0.1 S + 0.1 P	0.1 S + 2.0 P	2.0 S + 0.1 P
FESEM	a	b	c
EDX	d	e	f

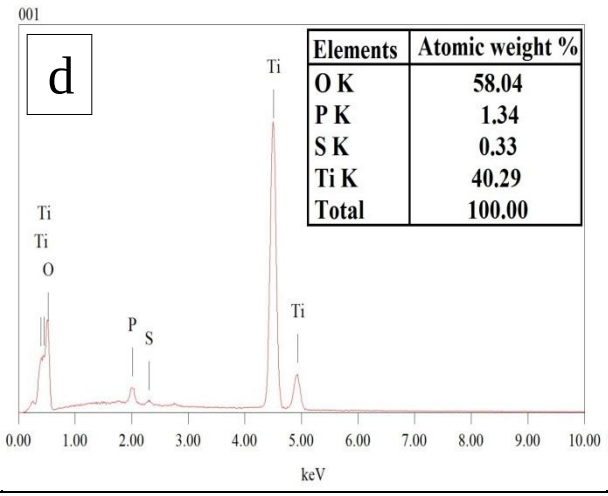

Elements	Atomic weight %
O K	58.04
P K	1.34
S K	0.33
Ti K	40.29
Total	100.00

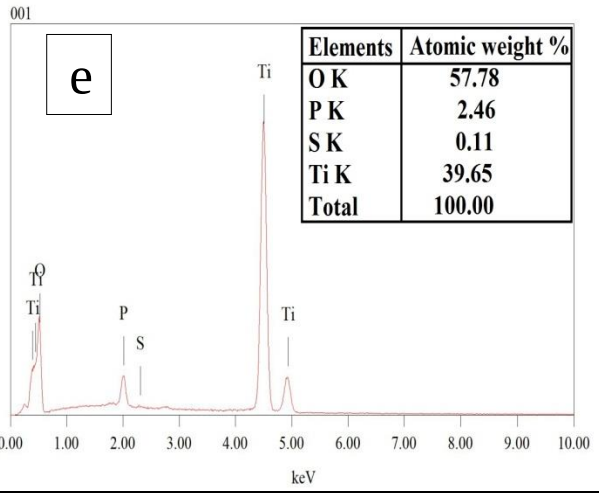

Elements	Atomic weight %
O K	57.78
P K	2.46
S K	0.11
Ti K	39.65
Total	100.00

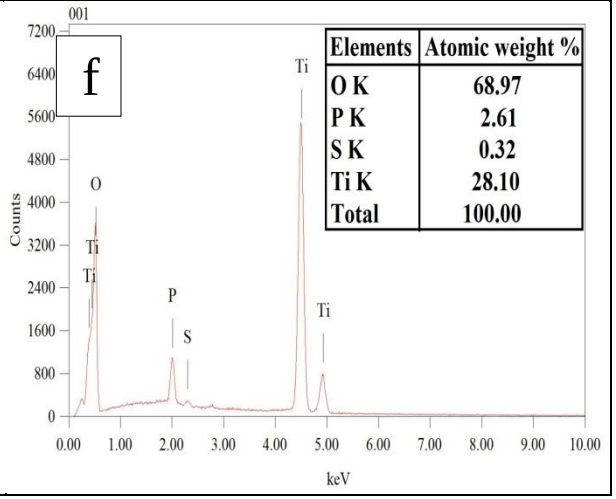

Elements	Atomic weight %
O K	68.97
P K	2.61
S K	0.32
Ti K	28.10
Total	100.00

Figure 4.40: Elemental analysis of the coatings anodised in mixed electrolyte at 150 V and 100 mA.cm^{-}

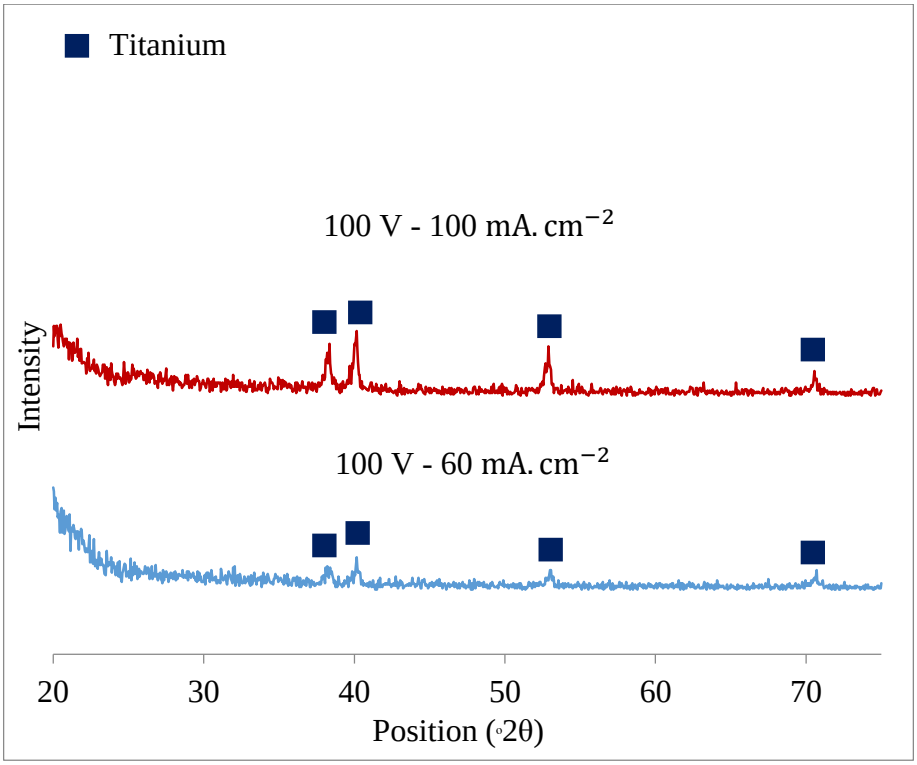

Figure 4.41: Phase mineralogical Patterns for 100 V, 60 and 100 mA.cm^{-2} at 0.1 S + 0.1 P

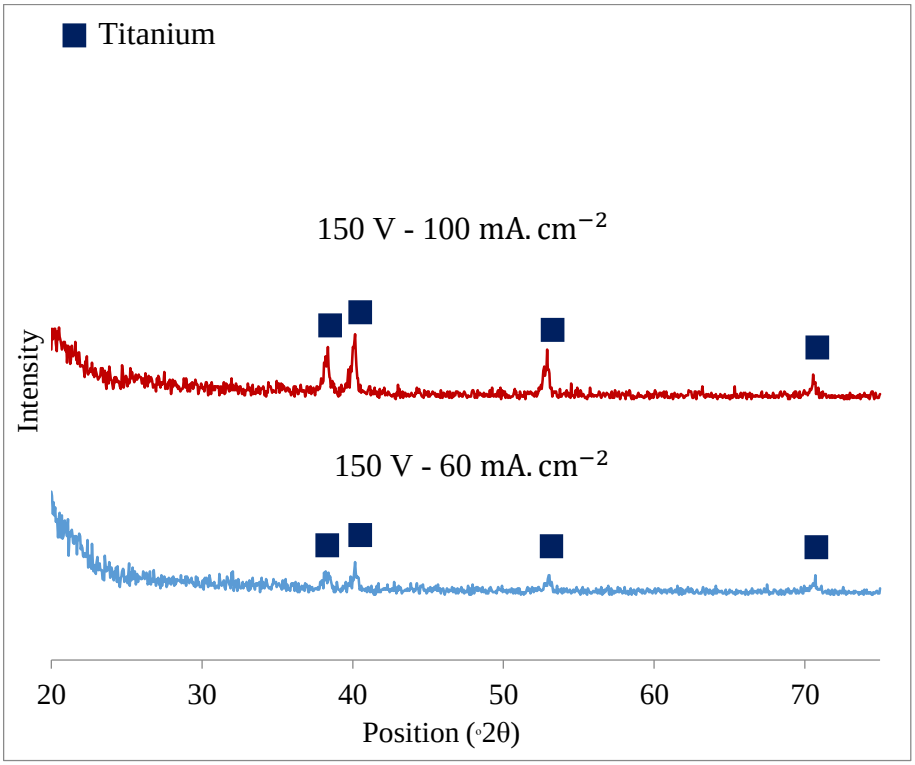

Figure 4.42: Phase mineralogical Patterns for 150 V, 60 and 100 mA.cm^{-2} at 0.1 S + 0.1 P

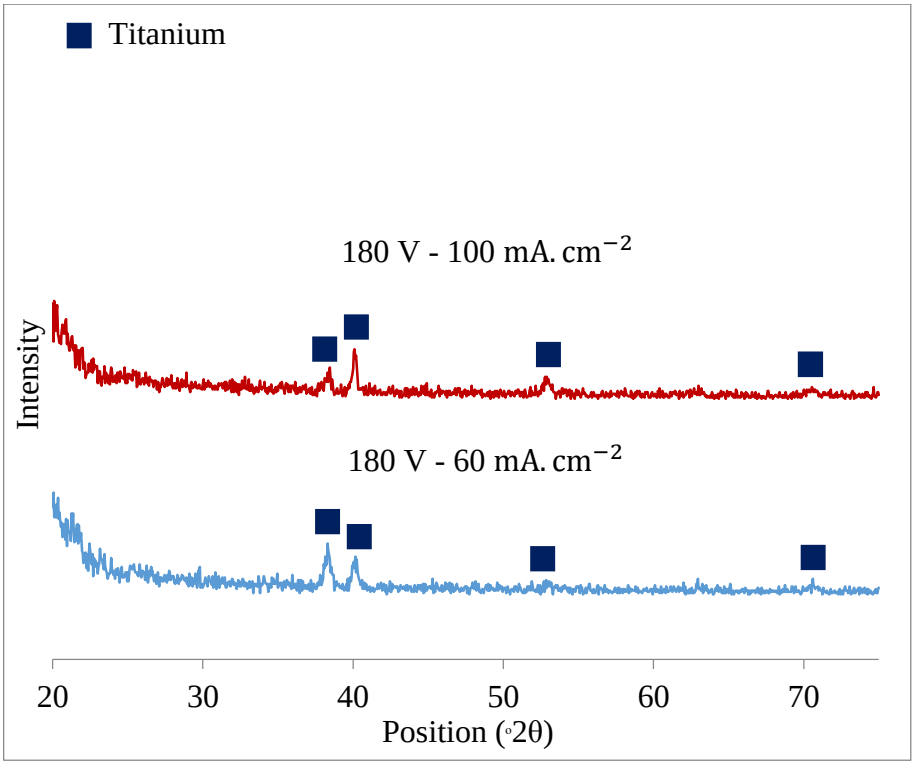

Figure 4.43: Phase mineralogical Patterns for 180 V, 60 and 100 mA.cm^{-2} at 0.1 S + 0.1 P

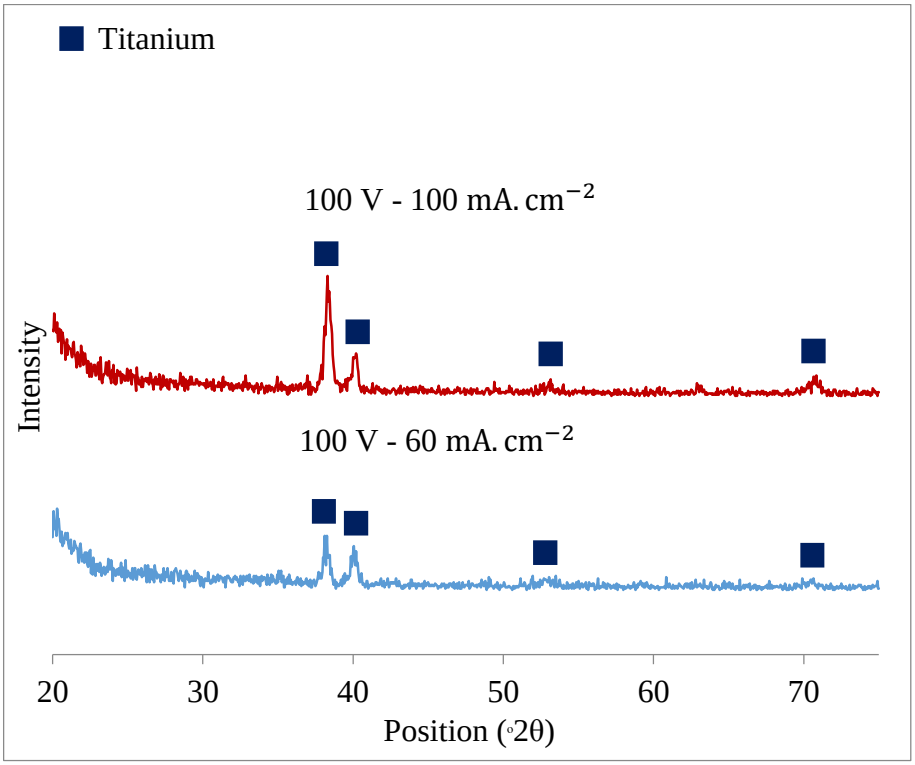

Figure 4.44: Phase mineralogical Patterns for 100 V, 60 and 100 mA.cm^{-2} at 0.1 S + 2.0 P

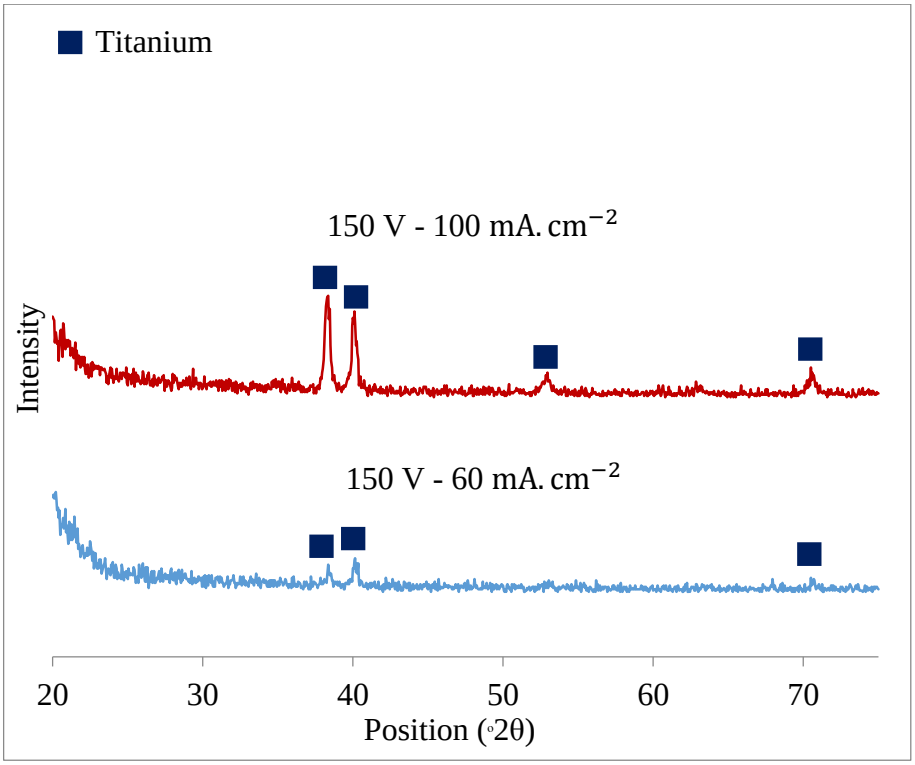

Figure 4.45: Phase mineralogical Patterns for 150 V, 60 and 100 mA.cm^{-2} at 0.1 S + 2.0 P

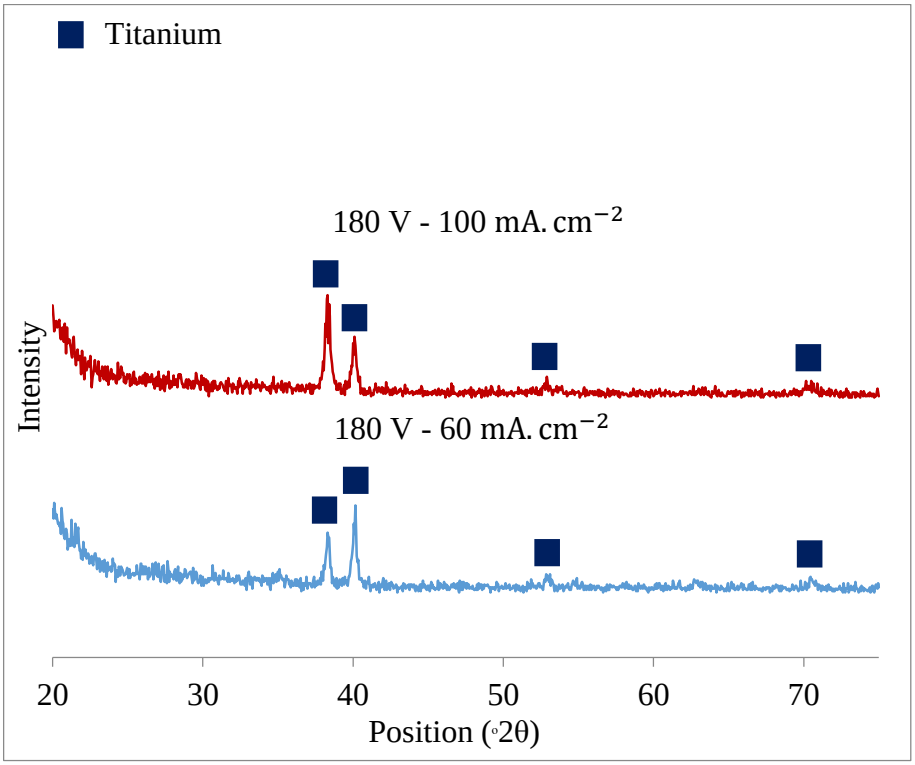

Figure 4.46: Phase mineralogical Patterns for 180 V, 60 and 100 mA.cm^{-2} at 0.1 S + 2.0 P

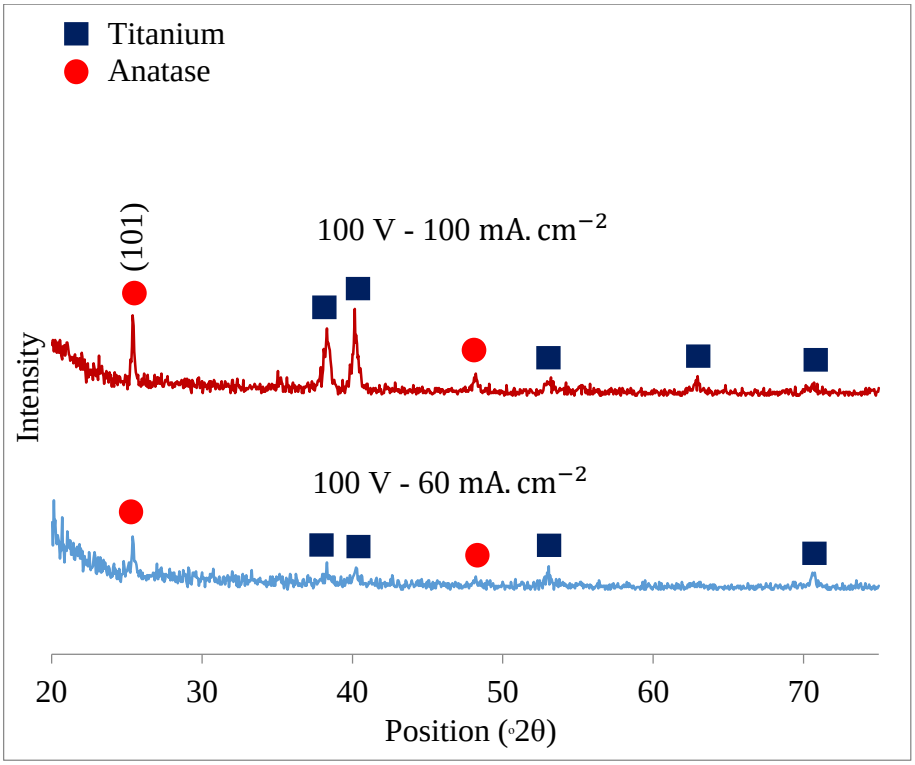

Figure 4.47: Phase mineralogical Patterns for 100 V, 60 and 100 mA.cm^{-2} at 2.0 S + 0.1 P

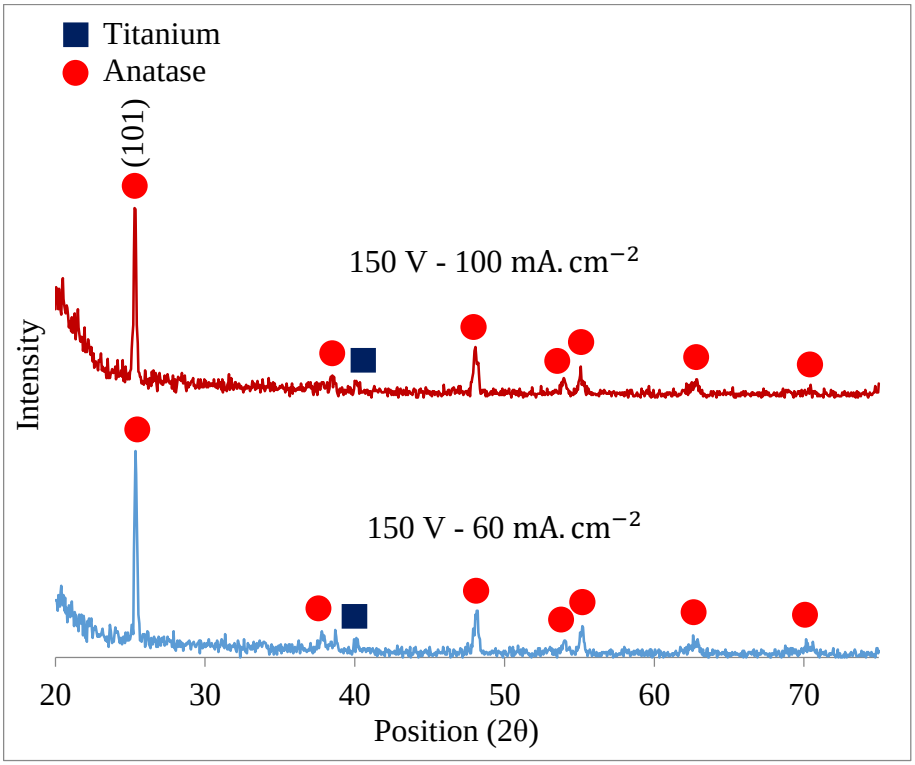

Figure 4.48: Phase mineralogical Patterns for 150 V, 60 and 100 mA.cm^{-2} at 2.0 S + 0.1 P

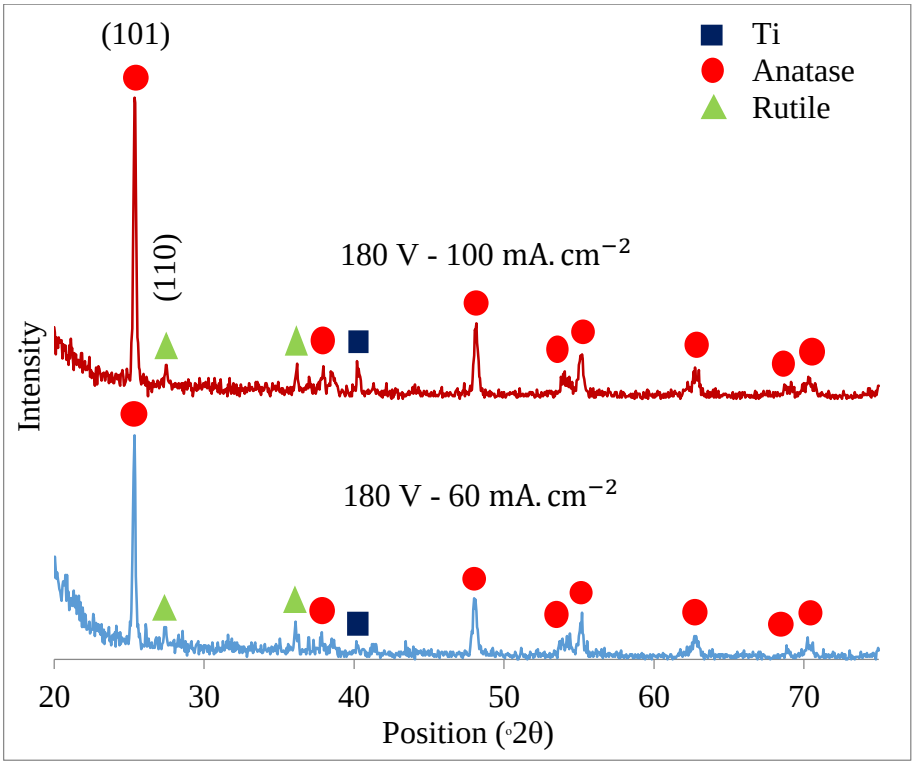

Figure 4.49: Phase mineralogical Patterns for 180 V, 60 and 100 mA.cm^{-2} at 2.0 S + 0.1 P

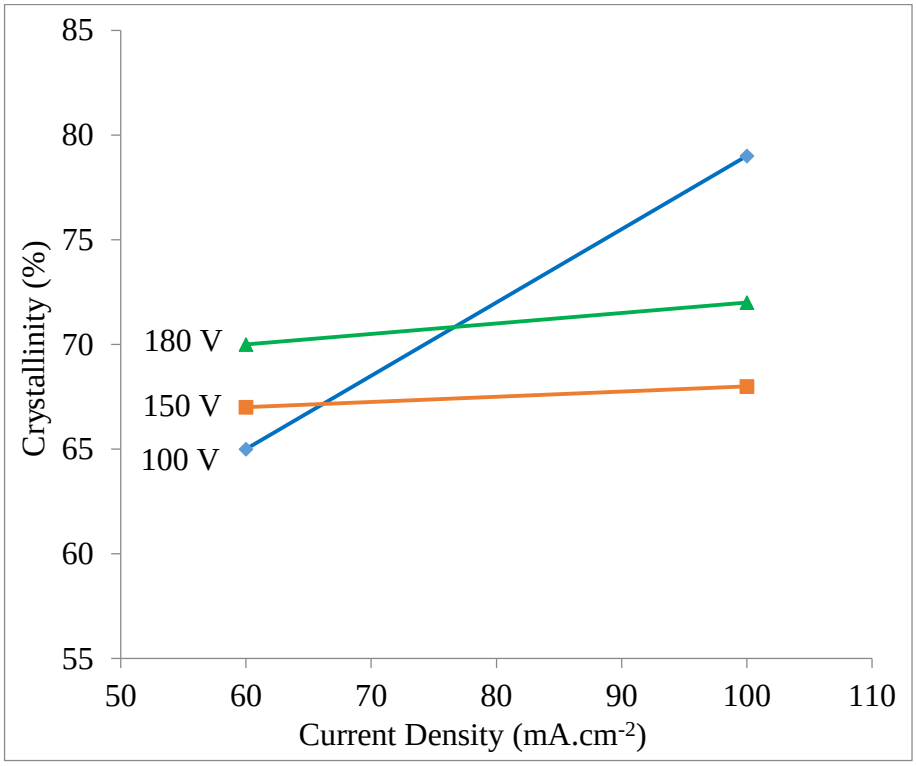

Figure 4.50: Phase mineralogical Patterns crystallinity percent for TiO_2 anodised in 2.0 M H_2SO_4 electrolyte as a function of current density and voltage

V with ratio 1 to 10 respectively. Higher anatase crystalline was obtained at 100 V with the increased current density. This is can be obtained with 17.7 % higher crystallinity with the increased current density compared to only 1.5 % at 150 V as illustrated in Figure 4.50. The crystallinity was measured for the whole spectrum and only TiO_2 anatase crystalline was obtained at 100 V and 150 V. Therefore, the crystallinity will count for the anatase on those spectra. While anatase and rutile were obtained at 180 V.

From these results, it can be concluded that H_2SO_4 has promoted higher crystallinity, while H_3PO_4 has obstructed it. This is clear when comparing the crystallinity between H_2SO_4 electrolyte, H_3PO_4 electrolyte, and mixed electrolyte. This can be obtained where higher anatase intensity was obtained with the increased voltage at 0.1 M H_2SO_4 electrolyte for the coating anodised in H_2SO_4 and at elevated molarity to 2.0 M the anatase has transformed to rutile as obtained in **Section 4.2.5**. However, the H_3PO_4 electrolyte for the coatings anodised in H_3PO_4 has not promoted any crystallinity. The coatings anodised in mixed acids did not promote higher crystallinity with the increased voltage (**Section 4.3.5**). This can be obtained where no rutile was obtained at the elevated voltage or at higher molarity, and anatase was only obtained at 2.0 S + 0.1 P with increased voltage as seen in Figure 4.47 at 100 V, Figure 4.48 at 150 V and Figure 4.49 at 180 V.

The amorphous structure obtained on the coatings anodised in 0.1 S + 0.1 P and 0.1 S + 2.0 P can be related to the slower dissolution of H_3PO_4 in the electrolyte compared to the stronger H_2SO_4. This is has been discussed in **Section 4.3.4.** While the increased H_2SO_4 molarity at the coatings anodised in 2.0 S + 0.1 P has promoted a crystalline coating.

The amorphous favoured TiO_2 structure that was build using H_3PO_4 electrolyte as discussed in **Section 4.3.4** can clearly affect the TiO_2 crystallinity when mixed H_3PO_4 electrolyte with the highly favoured crystalline electrolyte H_2SO_4 as discussed in **Section 4.2.4**. This is can be clearly obtained on the coatings anodised in 2.0 S + 0.1 P. Where higher crystallinity can be obtained (anatase and rutile) at Figure 4.8 and Figure 4.10 and the anatase has transformed completely to rutile at 180 V at Figure 4.12.

The amorphous structured coatings produced in (0.1 S + 0.1 P) has obtained bright colour at all voltages. While the grey colour that corresponds to the coatings produced in (2.0 S + 0.1 P) at 150 V and 180 V is associated with the crystalline

structure. However, the arsenic colour that corresponds to the coatings produced (0.1 S + 2.0 P) at 180 V is associated with the amorphous structure. It has already been reported that losing colour interference with increased voltage is associated with increased oxide breakdown and thickness. This has been explained in **Section 4.2.2**. According to the microstructure results, the higher the porosity resulted from the coating breakdown the lower the colour brightness. However, there was no direct or clear relationship between the crystallography and the colour interference of the coatings. Also according to these results, it can be concluded that the crystallinity depends on nature and concentration of the electrolyte, the current density, and the applied voltage.

Table 4.9 and Table 4.10 shows the values of the crystal size and strain for anatase (101) and rutile (110) with respect to the applied voltage, molarity, and current density. They show a good agreement with those taken from the Joint Committee of Powder Diffraction Standards (JCPDS) card file No. 21-1272 for TiO_2 (anatase) and No. 21-1276 for TiO_2 (rutile) respectively (Li and Zeng, 2011; Pookmanee and Phanichphant, 2009).

Table 4.9: Grain size along (101) direction of TiO_2 anatase crystalline of coatings anodised in mixed electrolyte as a function of voltage and current density at 2.0 M

0.1 P + 2.0 S	2 Theta(θ)		Strain (ε)		FWHM		Crystal size (nm)	
Current density ($mA.cm^{-2}$)	60	100	60	100	60	100	60	100
100 V	25.409	25.421	0.025	0.032	0.113	0.143	1.358	1.073
150 V	25.365	25.305	0.044	0.038	0.197	0.170	0.778	0.902
180 V	25.340	25.376	0.043	0.047	0.194	0.212	0.790	0.723

Table 4.10: Grain size along (110) direction of TiO_2 rutile crystalline of coatings anodised in mixed electrolyte as a function of voltage and current density at 2.0 M

0.1 P + 2.0 S	2 Theta (θ)		Strain (ε)		FWHM		Crytal size (nm)	
Current density ($mA.cm^{-2}$)	60	100	60	100	60	100	60	100
100 V	-	-	-	-	-	-	-	-
150 V	-	-	-	-	-	-	-	-
180 V	27.403	27.471	0.042	0.039	0.192	0.178	0.813	0.877

By fitting the phase mineralogical results, the strain ε and grain size of the films have been calculated from the (101) and (110) diffraction peaks. The calculated gain size as a function of applied voltage and current density at 0.1 P + 2.0 S. As the crystalline peak of anatase increased with the increased voltage and current density for

the spectra of the coatings anodised in 0.1 P + 2.0 S, the crystallinity also increased (Figure 4.50). This is accompanied with a decreased crystal size as obtained in table 4.9 for anatase main crystalline peak. At 100 V the anatase has increased faster with the increased current density (Figure 4.47) as mentioned earlier when compared with the spectra of the other voltages, i.e., 150 V (Figure 4.48) and 180 V (Figure 4.49). The increased in crystalline percent by 17.7 % as can be obtained in Figure 4.50 has accompanied with a 21% decrease in crystal size (Table 4.9) with increased current density. While the crystallinity has only increased by 1.5 % at 150 V and 2.8 % at 180 V. However, the crystal size has increased by 13.7% at 150 V. This is can be obtained in Figure 4.48 where the anatase main peak intensity was higher at 60 $mA.cm^{-2}$. While the crystal size of the rutile has increased with the increased current density at 180 V.

The growth of anatase is accompanied by decrease in the crystal size. This is can indicate the stabilization of anatase with the peak growth. Also at the transformation threshold to rutile at 180 V (Figure 4.49). This is in contrast to the advanced transformation level, where the grain gowth take place as been obtained by the spectra of the coatings anodised at 2.0 H_2SO_4. Where the anatase crystal size increased and the rutile's has increased due phase transformation. This is has been described in **Section 4.2.4**. The increased crystal size of anatase at 150 V as obtained in Table 4.9 is due to the decreased peak intensity with the increased current density. This is can be due to experimental error occurred, or might be due to contamination in the Ti sample. It was supposed to obtain an increased peak intensity with the increased current density. However, the crystallinity has increased, although the decreased crystal size. A smiliar issue occurred to rutile crystalline at 180 V, where the increased crystal size by 7.3 % as obtained in Table 4.10. However, it can be neglectible since the rutile has only obtained a threshold peak at one voltage (180 V) at it not enough to give the behaviour activity of rutile. It can also be noticed that the rutile thres hold crystal size much smaller than the anatase's threshold at 100 V. This is can be due to the reconstructive anatase to rutile transformation involves a contraction of the c-axis and an overall volume contraction of 8% (Shannon and Pask, 1965; Criado and Real, 1983; Rao, Turner and Honig, 1959). This volume contraction explains the higher density of rutile relative to anatase. The c-axis of anatase appears to be significantly longer than that of rutile only because anatase has more atoms per unit cell than rutile (Hanaor and Sorrell, 2011).

These results confirm that the voltage, current density and molarity influence on the crystalline formation of the growth of TiO_2 coatings produced in mixed electrolyte. H_2SO_4 promoted crystallinity, while H_3PO_4 obstructed it. Only the coatings anodised in mixed electrolyte with higher H_2SO_4 molarity were able to promote TiO_2 crystalline.

4.4.5 Optics of Anodised TiO_2 in Mixed Electrolyte

Figure 4.51 and Figure 4.52 observe the bandgap (E_g) of the TiO_2 coatings anodised in 0.1 M H_2SO_4 + 2.0 M H_3PO_4, i.e., 0.1 S + 0.1 P and in 2.0 M H_2SO_4 + 0.1 M H_3PO_4, i.e., 2.0 S + 0.1 P respectively. The parameters are taken for 150 V and 100 mA.cm^{-2}. From the results, the following can be described:

The $(k*hv)^2$ versus hv plots are shown in Figure 4.51 and Figure 4.52. They correspond to the measured bandgap values of 3.60 eV at 0.1 S + 2.0 P and 3.39 eV at 2.0 S + 0.1 P respectively.

According to phase mineralogical results, the coating produced at 0.1 S + 2.0 P have obtained the amorphous structure. It has obtained higher bandgap values than the bandgap of the intrinsic TiO_2 crystalline powder. While the coatings produced at 2.0 S + 0.1 P have obtained anatase intensity, however, balance value of 3.39 eV, which is higher bandgap than the bandgap of anatase (3.2 eV).

The increased of the bandgap values of amorphous than the bandgap value of crystalline coatings is unknown. It has been reported that the mechanism of the hole conductivity at a level much higher than the edge of the valence band is still a mystery (Pham and Wang, 2015). The exaction absorption of these coatings is 344.3 nm for 0.1 S + 2.0 P and 365.7 nm for 2.0 S + 0.1 P. This means that these coatings are in a good condition to conduct the *in vitro* test with the UV irradiation of 254 nm (UVC). This is due to their higher excitation wavelength than 254 nm of the UV lamp.

4.4.6 Absorption of Anodised TiO_2 in Mixed Electrolyte

The absorption analysis patterns of the coatings anodised in 0.1 H_2SO_4 + 0.1 H_3PO_4, i.e., 0.1 S + 0.1 P, 0.1 H_2SO_4 + 2.0 H_3PO_4 i.e., 0.1 S + 2.0 P and 2.0 H_2SO_4 + 0.1 H_3PO_4 i.e., 2.0 S + 0.1 P. at 150 V and 100 mA.cm^{-2} as illustrated in Figure 4.53,

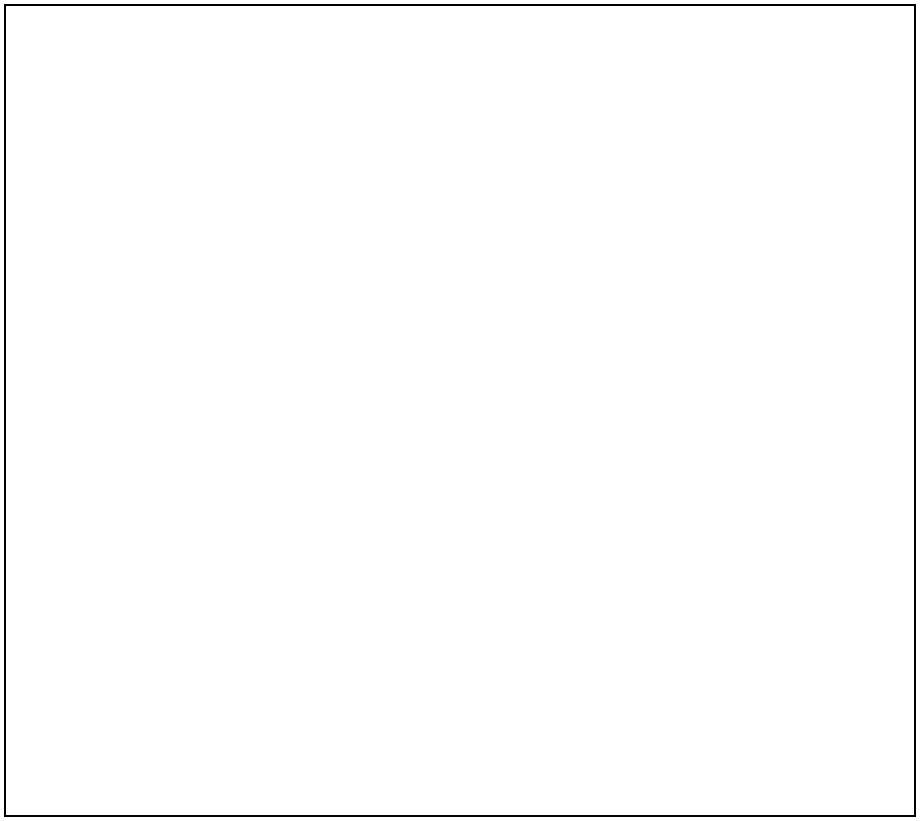

Figure 4.51: Bandgap (Eg) of coatings at 0.1 S + 2.0 P anodised at 150 V and 100 mA.cm^{-2}

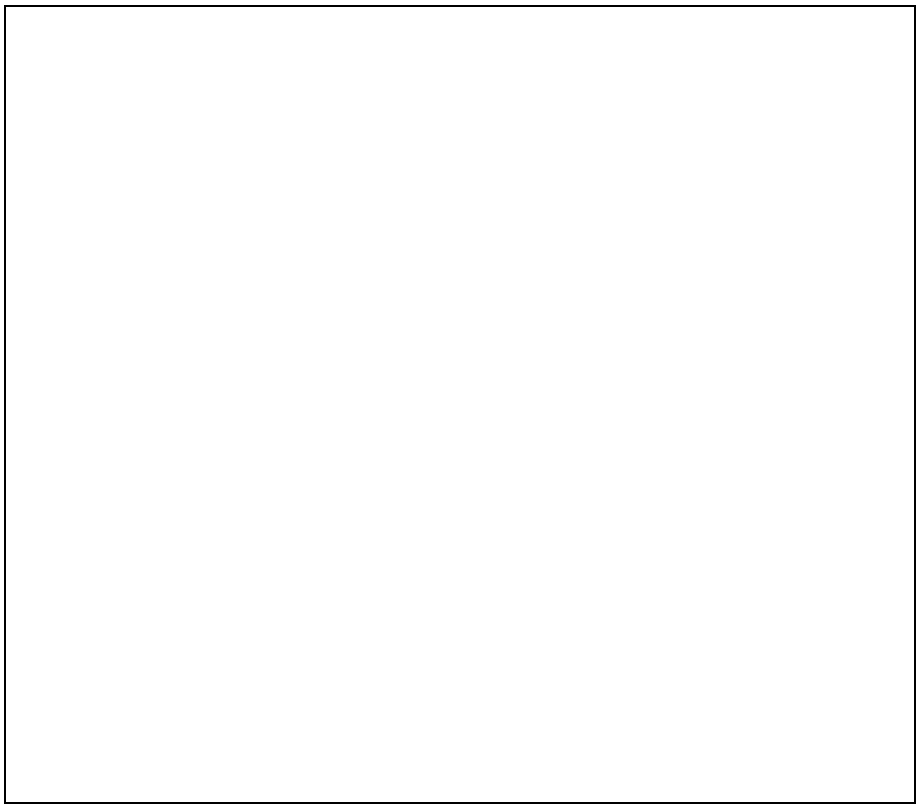

Figure 4.52: Bandgap (Eg) of coatings anodised at 150 V and 100 mA.cm^{-2} for 2.0 S + 0.1 P

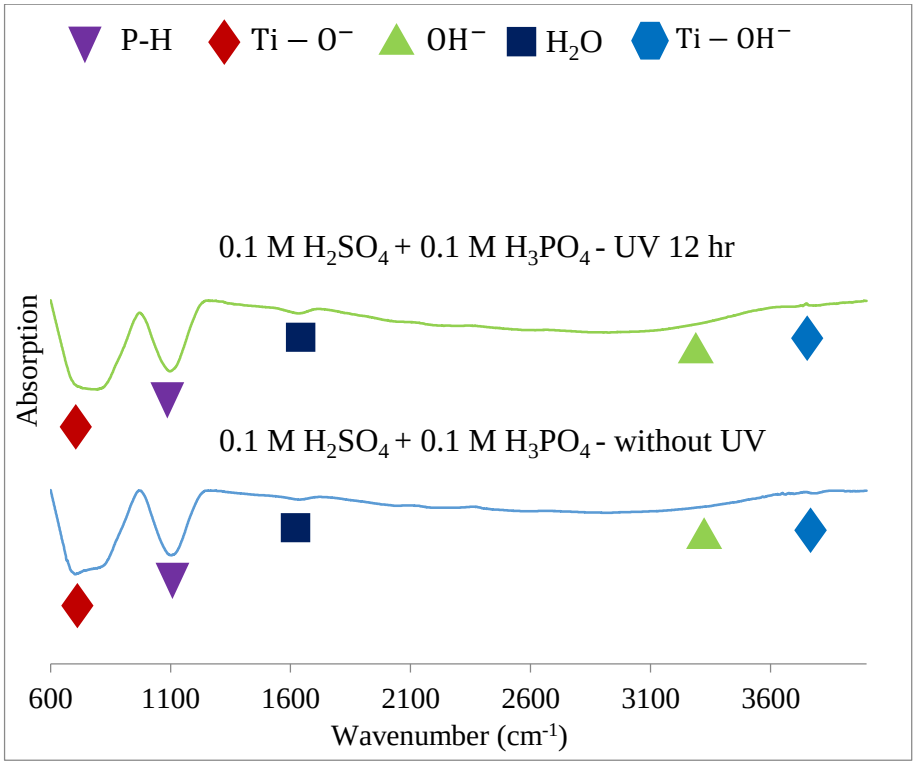

Figure 4.53: Absorption analysis patterns of TiO_2 coatings anodised in; (a) 0.1 S + 0.1 P without treatment, (b) 0.1 S + 0.1 P after 12 hr of UV irradiation

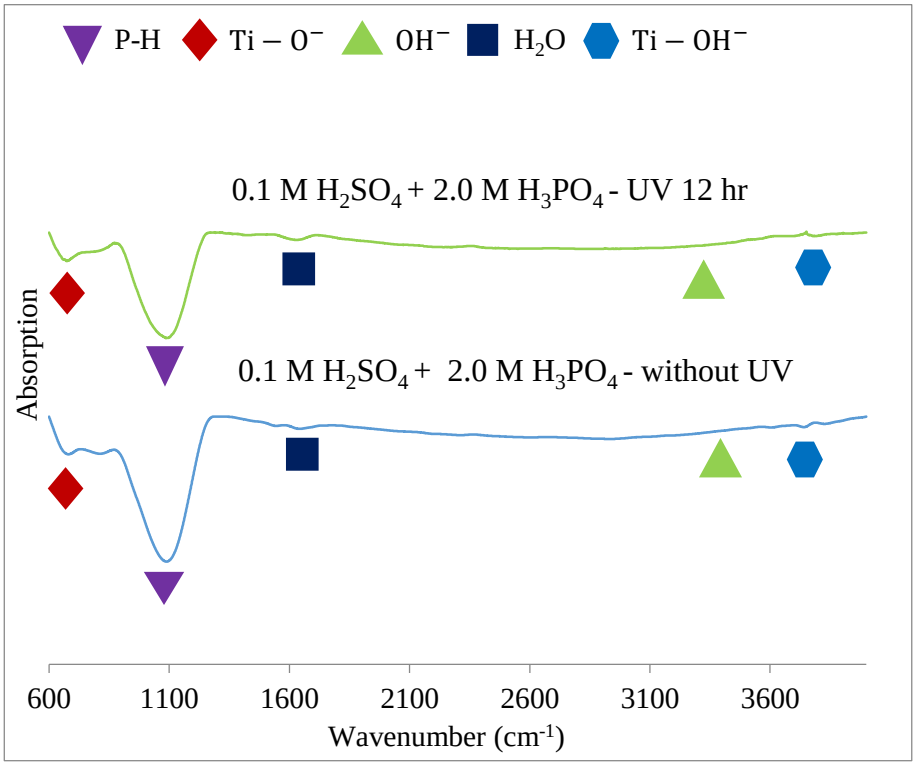

Figure 4.54: Absorption analysis patterns of TiO_2 coatings anodised in; (a) 0.1 S + 2.0 P without treatment, (b) 0.1 S + 2.0 P after 12 hr of UV irradiation

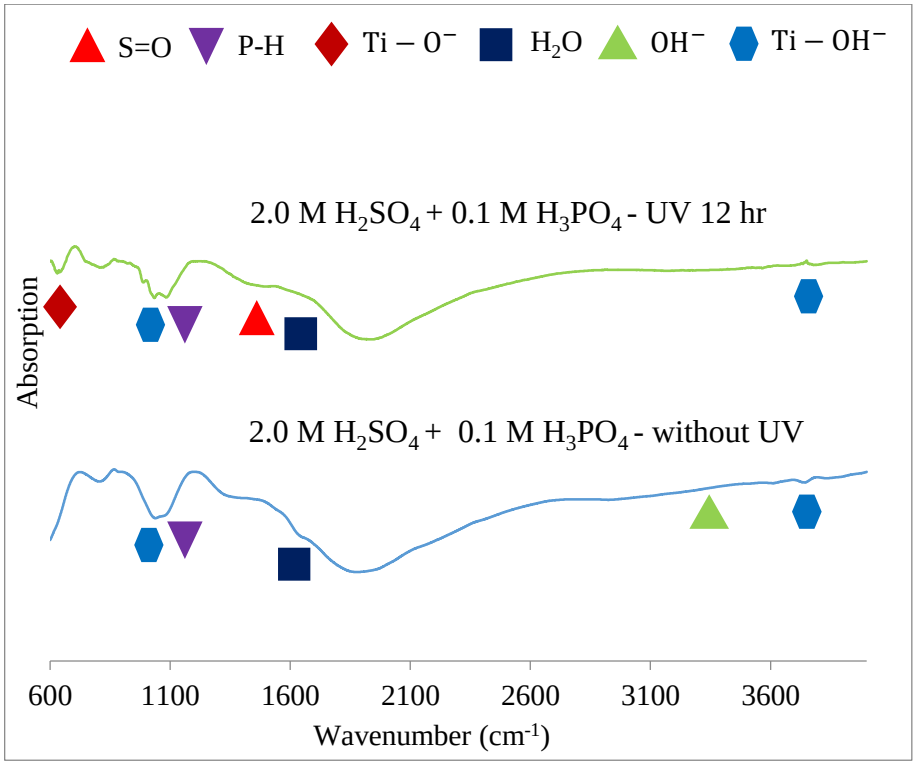

Figure 4.55: Absorption analysis patterns of TiO_2 coatings anodised in; (a) 2.0 S + 0.1 P without treatment, (b) 2.0 S + 0.1 P after 12 hr of irradiation UV

Figure 4.54 and Figure 4.55 respectively before and after 12 hours of UV irradiation of 254 nm in the water.

Absorption pattern have a presence of Ti-O groups at band 600-800 cm^{-1} (Liu *et al.*, 2008), sulfone (S=O) that was obtained at the band of 1300-1350 cm^{-1}, phosphine (P-H) was obtained at band of 950-1200 cm^{-1} (Segneanu *et al.*, 2012), water (H_2O) at band 1860

cm^{-1}, hydroxyl groups (OH) stretching region 3100-3400 cm^{-1} and Ti-OH groups at band 3635, 3645, 3680, 3750 and 3840 cm^{-1} (Liu *et al.*, 2008).

It is apparent from the figures that the phosphine has appeared on all the patterns. The sulfone has appeared only on the pattern of the coating anodised in 2.0 S + 0.1 P as seen in Figure 4.55. The Ti-O^- stretching has increased with the UV treatment. The Ti-OH have not changed after the treatment around the band 3635-3840 cm^{-1} on all the patterns, however, the Ti-OH stretching at around 1000 cm^{-1} has sharpened at only in 2.0 S + 0.1 P (Figure 4.55).

The presence of only the phosphine at the coating patterns can be related to the remaining acid on the coatings that have resulted from the anodization process. It can also be noticed that the phosphine stretching has increased with the increased H_3PO_4

concentration as obtained from Figure 4.53 to Figure 4.54. This can be related to the lower dissociation constant of H_3PO_4 than H_2SO_4 (Murmson, 2017). Therefore, some of the remaining acidic compounds still exist on the coating even after cleaning. Also, the remaining acid inside the grooves of the porous coating as seen in Figure 4.38 (m) of the coating pores and P ions incorporated within the coating can be counted according to the elemental analysis as obtained in Figure 4.40. Although the H_2SO_4 has higher dissociation rate than the H_3PO_4, the presence of the sulfone on the pattern of the coating anodised in 2.0 S + 0.1 P can be due to the increased H_2SO_4 concentration which have caused the remaining acid to stick on the coating surface and inside the pores grooves of the porous coating as seen in Figure 4.38 (p). It can be noticed that the $Ti\text{-}O^-$ presence has a little increase in all the coating patterns after the UV treatment. However, the original pattern at 0.1 S + 0.1 P had the strongest $Ti\text{-}O^-$ stretching as seen in Figure 4.53.

When comparing with the results from H_2SO_4 electrolyte and H_3PO_4 electrolyte, it can be noticed that the strongest $Ti\text{-}O^-$ stretching has been obtained on the less porous coating anodised in lower molarity electrolyte when compared with the coating produced in higher molarity as obtained in Figure 4.38 (b) for the coating anodised in 0.1 S + 0.1 P, 0.1 M at H_2SO_4 electrolyte (Figure 4.4 (d)) and 0.1 M at H_3PO_4 electrolyte (Figure 4.22 (d)).

Also, these coatings have a common of minimal S and/or P ions incorporation when compared with the coating produced in higher molarity. This can be obtained in Figure 4.7 (a and c) at 0.1 M in H_2SO_4 electrolyte, Figure 4.24 (a and c) at 0.1 M in the H_3PO_4 electrolyte and Figure 4.40 (a and d) for 0.1 S + 0.1 P in the mixed electrolyte.

The anatase crystalline coatings could also be related to the stronger $Ti\text{-}O^-$ as obtained in 0.1 M in the H_2SO_4 electrolyte and in 2.0 S + 0.1 P in the mixed electrolyte. The coating produced in 0.1 M at H_2SO_4 electrolyte with anatase structured coating (Figure 4.10) has obtained stronger $Ti\text{-}O^-$ stretching (Figure 4.17) than the coating produced at 2.0 M (Figure 4.18) that obtained anatase and rutile with ratio 1 to 3 respectively (Figure 4.11). The coating that was anodised in 2.0 S + 0.1 P with anatase crystalline (Figure 4.48) has obtained strong Ti-OH stretching at the band of 1000 cm^{-1} (Figure 4.55). This is due to the photocatalytic activity of the TiO_2 crystalline (Wang *et al.*, 2007). This Ti-OH group has obtained multiple stretching around the band 1000 cm^{-1} after the UV irradiation. This is due to the greater photocatalytic activity of the

anatase over rutile (Linsebigler *et al.*, 1995). It is has been reported that the TiO_2 anatase crystalline display a photocatalytic activity under the UV, results in a formation of hydroxide groups (Ueda *et al.*, 2010). These hydroxyl groups interact with the OH^- in the SBF liquid and give rise to the negatively charged surface with functional $Ti\text{-}O^-$. This is has been explained in detailed in **Section 2.10.3** (Liu *et al.*, 2008; Ueda *et al.*, 2009).

However, it can be noticed as a conclusion that the coating crystallinity was not the domain influence of the strength of the $Ti\text{-}O^-$ group. All the coatings that obtained high $Ti\text{-}O^-$ group stretching have obtained lower porous surface microstructure along with lower acidic incorporated ions (S and/or P). This is clear with the coating anodised in 0.1 M in the H_2SO_4 electrolyte, where low surface porosity as obtained in Figure 4.4 (d), low S incorporated ions was obtained in Figure 4.7 (a and c) and strong $Ti\text{-}O^-$ group stretching was obtained in Figure 4.17. The coating anodised in 0.1 M in H_3PO_4 electrolyte has also obtained low surface porosity as obtained in Figure 4.22 (d), low P ions intensity as seen in Figure 4.24 (a and c) and strong $Ti\text{-}O^-$ stretching group as obtained in Figure 4.33. Last, the coating anodised in 0.1 S + 0.1 P has contained low porosity as in Figure 4.38 (b) and low S and P ions intensity as in Figure 4.40 (a and d) and the strong $Ti\text{-}O^-$ stretching as in Figure 4.53. These parameters can take the domain influence of the $Ti\text{-}O^-$ group stretching that is responsible for the apatite precipitation (Ueda *et al.*, 2010; Uetsuki *et al.*, 2010).

The stronger $Ti\text{-}O^-$ functional groups that were obtained on the mixed acids electrolyte with lower molarity can obtain higher chance to induce apatite in SBF due to apatite nucleation was induced by those groups. Furthermore, these groups were expected to increase with UV irradiation and therefore resulted in higher apatite formation. Highest hydrophilicty was obtained on the coating that obtained Ti-OH functional groups that was obtained on the coating that was anodised in the mixed electrolyte. It was also expected to form higher apatite formation due to it reaction with the OH^- in the SBF results in $Ti\text{-}O^-$ groups on the surface.

4.5 Hydrophilicity of Anodised TiO_2

The water contact angle testing (WCA) was taken for the TiO_2 coatings produced at 150 V and 100 $mA.cm^{-2}$ in the H_2SO_4 electrolyte, H_3PO_4 electrolyte, and mixed

electrolyte. The water contact angle as obtained in Figure 4.56 was taken to test the hydrophilicity of the coatings. While the Table 4.11 list their water contact angle and surface energy values.

It can be noticed from the results that the TiO_2 anodised in mixed electrolyte has obtained a lower surface contact angle than the coatings anodised in the H_2SO_4 electrolyte and H_3PO_4 electrolyte, therefore, higher hydrophilicity (Young, 1832). The TiO_2 coating anodised in 2.0 M H_3PO_4 + 0.1 M H_2SO_4 has produced the highest hydrophilicity among the other coatings.

It has been reported that the anatase containing coatings show higher hydrophilic surface than the rutile containing oxides (Das *et al.,* 2007). However, Yamamoto et al., (2012a) have attributed the increased hydrophilicity to the presence and/or absence of OH groups and hydrocarbons on the surface rather than the anatase crystalline (Yamamoto *et al.,* 2012a). It has also been reported that the surface roughness and morphology can also affect the wettability (Das *et al.*, 2007). Moreover, it was found that the incorporated P ions within the Ti oxide can contribute to the surface hydrophilicity (Park *et al.,* 2009). Also, Yamamoto *et al.* (2012b) have reported that the TiO_2 coatings anodised in H_2SO_4 and H_3PO_4 have obtained higher hydrophilicity among the other coatings anodised in common known acidic, neutral and alkaline electrolytes. According to these studies, the TiO_2 crystalline, the Ti-OH groups, the surface roughness and the P ions can influence the surface hydrophilicity of the coating.

The higher hydrophilicity of the coatings anodised in the H_3PO_4 electrolyte that in the H_2SO_4 electrolyte can be related to P ions incorporated within the coating. However, the higher hydrophilicity of the coatings anodised in the mixed electrolyte that H_2SO_4 electrolyte and H_3PO_4 electrolyte unknown. The incorporation of S and P ions in the same coating has somehow influenced the hydrophilicity of the TiO_2 coating. This is due that the coatings anodised in mixed electrolyte have obtained similar properties with the coatings anodised in the H_3PO_4 electrolyte, where both electrolytes have obtained the amorphous structure, various porosity, and low Ti-OH functional groups.

The coating anodised in 2.0 M H_2SO_4 + 0.1 M H_2SO_4 has obtained a strong Ti-OH at the stretching band of 1000 cm^{-1} (Figure 4.52), strong anatase crystalline (Figure 4.45), higher porous surface (Figure 4.36 (o)) and the P ions incorporated within the coating (Figure 4.37 (c and f)). However, the anatase contained coating that was

obtained in 0.1 M (Figure 4.9) and 2.0 M (Figure 4.10) in H_2SO_4 electrolyte hasn't contributed to the hydrophilicity of the coating. This is clearly where the amorphous structured coatings at H_3PO_4 electrolyte have obtained higher hydrophilicity. Also, the coatings have obtained various microstructures at each electrolyte.

Table 4.11: Water contact angles and surface energies with the TiO_2 coating surface

No	Samples	Contact angle	Surface energy (mJ/m^2)
1	As-polished	57.68 ± 0.00º	49.23 ± 0.00
2	0.1 H_2SO_4	65.94 ± 0.01	44.22 ± 0.01
3	0.1 H_3PO_4	51.90 ± 0.01º	52.66 ± 0.01
4	2.0 H_2SO_4	58.74 ± 0.01º	48.60 ± 0.01
5	2.0 H_3PO_4	50.22 ± 0.02º	53.64 ± 0.01
6	0.1 H_2SO_4 + 0.1 H_3PO_4	43.81 ± 0.01º	57.28 ± 0.01
7	0.1 H_2SO_4 + 2.0 H_3PO_4	34.44 ± 0.01º	62.29 ± 0.01
8	2.0 H_2SO_4 + 0.1 H_3PO_4	17.04 ± 0.04º	69.79 ± 0.01

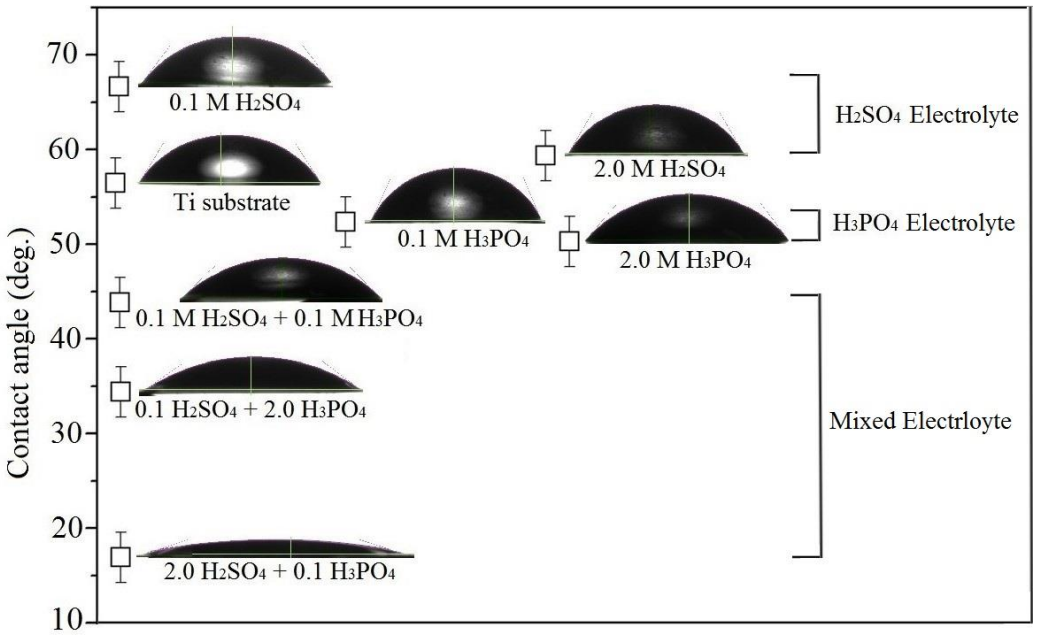

Figure 4.56: Surface energy analysis on the TiO_2 coating surface

4.6 Summary

TiO_2 coatings anodised in different acidic electrolytes, i.e., H_2SO_4 electrolyte, H_3PO_4 electrolyte and mixture electrolyte (H_2SO_4 + H_3PO_4) have undergone several testings, i.e., appearance, microstructure, mineralogy, elements, optical, chemical absorption, to study their characteristics and optimize the samples selection for *in vitro* testing under UV irradiation. Table 4.12 summarize the significant findings from these testings in comparison.

Table 4.12: A signifincant findings discussed comparatively between the TiO_2 coatings in individuals and mixed electrolyte.

Characterisation	TiO_2 coatings anodised in H_2SO_4 electrolyte	TiO_2 coatings anodised in H_3PO_4 electrolyte	TiO_2 coatings anodised in mixture electrolyte
Appearance	Higher loose of appearance with the increased voltage due to higher breakdown intensity	Lower loose of appearance with the increased voltage due to lower breakdown intensity	Higher loose of appearance with the increased voltage at electrolyte with the increased H_2SO_4 concentration
Microstructure	Smaller pores with sponge-like shaped pores and higher thickness than the coatings anodised in the H_3PO_4 electrolyte.	Larger pores with volcano orifice like shaped pores, however, a less porous density that the coatings anodised in the H_2SO_4 electrolyte.	A mixture between sponge-like and volcano orifice like shaped pores. Obtained higher thickness that the coatings anodised in H_2SO_4 and H_3PO_4.
Elementary	S ions intensity hasn't obtained significant increase with the increased molar concentration	P ions intensity has increased significantly with the increased molar concentration	P ions has obtained higher intensity at all coatings.
Mineralogy	Crystalline TiO_2, i.e., anatase and rutile were obtained.	No crystallinity was obtained; only amorphous structure.	The H_3PO_4 electrolyte has suppressed crystalline formation, therefore only crystalline TiO_2 mostly anatase has appeared at the coatings anodised in a mixed electrolyte with higher H_2SO_4 molarity.
Optical	Coatings have obtained a minimum excitation absorption of ≈ 360 nm, which is suitable for the coatings to get excited under 254 nm UV irradiation in *in vitro*.	Coatings have obtained a minimum excitation absorption of ≈ 248 nm, which is suitable for the coatings to get excited under 254 nm UV irradiation in *in vitro*.	Coatings have obtained a minimum excitation absorption of ≈ 345 nm, which is suitable for the coatings to get excited under 254 nm UV irradiation in *in vitro*.
Absorption	Stronger $Ti\text{-}O^-$ functional groups were obtained at the coating anodised at lower molarity and it has not increased under UV.	Stronger $Ti\text{-}O^-$ functional groups were obtained at the coating anodised at lower molarity, however with less strength than the coating anodised in the H_2SO_4 electrolyte and it increased under UV.	Stronger $Ti\text{-}O^-$ functional groups were obtained at the coating anodised at lower molarity and it has increased under UV. Ti-OH functional groups have been obtained at the coating anodised in the mixed electrolyte with higher H_2SO_4 molarity and increased under UV.
In vitro expectations	Higher apatite expected to form under UV and on the coatings with higher porosity, hydrophilicity, thickness and stronger $Ti\text{-}O^-$ functional groups.		

CHAPTER 5

IN VITRO ASSESSMENT

5.1 Introduction

TiO_2 was subjected to *in vitro* testing to assess the bioactivity of TiO_2 surface anodised in different medium electrolytes. The bioactivity assessment of the TiO_2 coating was tested using *in vitro* testing in simulation body fluid (SBF) in dark and under UV irradiation to mimic the reactions that may occur with the human bone-like cells layer. The effect of microstructure, mineralogical structure, absorption analysis and hydrophilicity of the TiO_2 surface was considered in the assessment.

5.2 Apatite Formation Evaluation on TiO_2 Coatings Anodised in Sulphuric Acid (H_2SO_4) Electrolyte

The TiO_2 coatings anodised in the H_2SO_4 electrolyte for 0.1 M and 2.0 M at 150 V and 100 $mA.cm^{-2}$ was subjected to *in vitro* test using SBF in dark and under UV irradiation. Microstructure, morphology, mineralogy, and surface energy of the coatings were discussed.

5.2.1 Microstructure of Apatite Formed on TiO_2 Anodised in H_2SO_4 Electrolyte

Figure 5.1 and Figure 5.2 obtain the surface image microstructure captured of the coatings anodised in the H_2SO_4 electrolyte for 0.1 M and 2.0 M at 150 V and 100 $mA.cm^{-2}$ immersed in the SBF in dark and under the UV irradiation condition respectively, while Table 5.1 obtained the apatite-forming ability

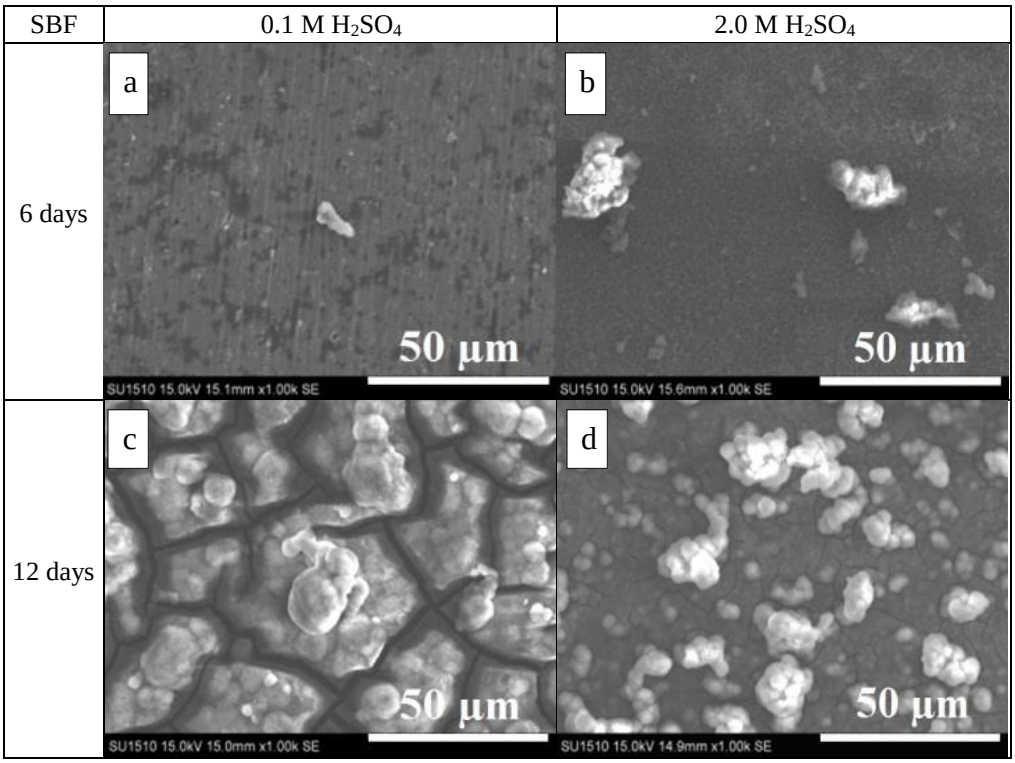

Figure 5.1: Surface microstructure images of coatings produced in H_2SO_4 electrolytes (0.1 M and 2.0 M) at 150 V and 100 mA.cm^{-2} immersed in SBF in the dark for 6 and 12 days

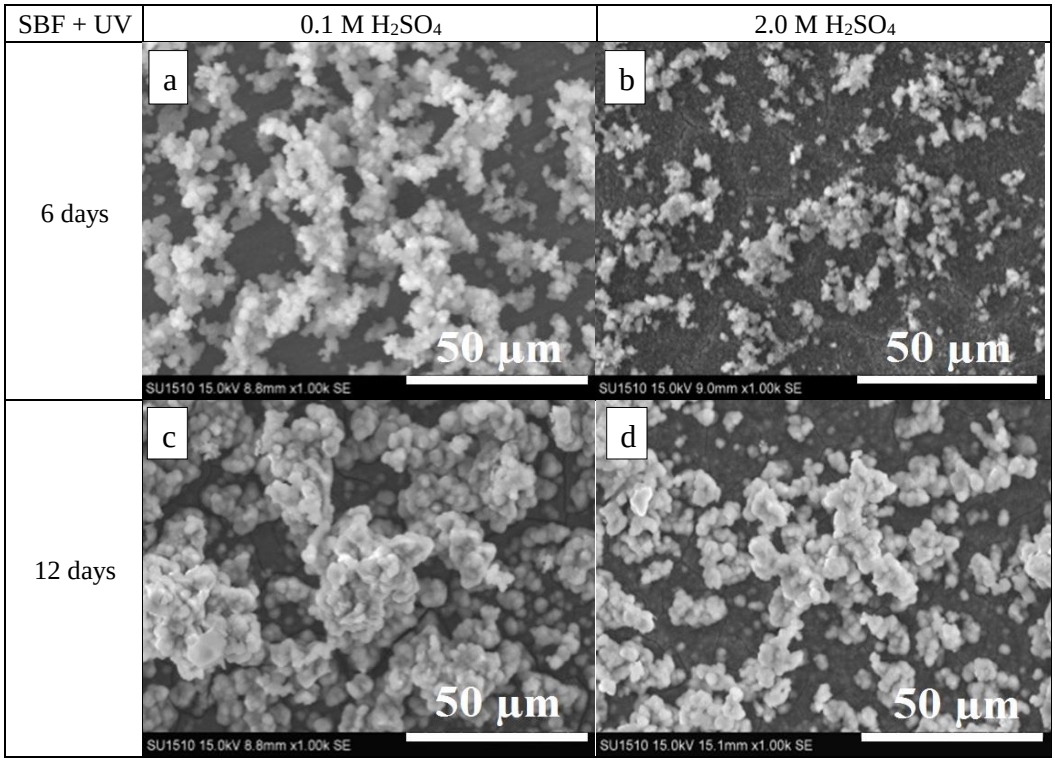

Figure 5.2: Surface microstructure images of coatings produced in H_2SO_4 electrolytes (0.1 M and 2.0 M) at 150 V and 100 mA.cm^{-2} immersed in SBF under UV for 6 and 12 days

Table 5.1: The apatite forming ability of the coatings anodised in H_2SO_4 electrolyte immersed in the dark and under the UV as a function of electrolyte molarity

In vitro treatment	SBF		SBF + UV	
H_2SO_4 electrolyte molarity	0.1 M	2.0 M	0.1 M	2.0 M
6 days	+	++	++++	+++
12 days	+++++	+++	+++++	++++

of the coatings immersed in the dark and under the UV as a function of electrolyte molarity.

The apatite has increased with increased immersion time in SBF in the dark and under the UV as obtained in Figure 5.1 and Figure 5.2. This is can be related to the increased nucleation of HA particles on the TiO_2 surface as obtained in Figure 2.24. Also, higher apatite formation was obtained at coatings produced at lower anodization molar concentration as obtained in Figure 5.1 (a and c) for 0.1 M and Figure 5.2 (a and c) for 2.0 M. This is can be due to the strong Ti-O^- functional group stretching obtained in Figure 4.17 for 0.1 M. Also it can be due to the lower surface microstructure porosity than for 2.0 M as obtain in Figure 4.4 (d). This was clear for coatings immersed at dark and under UV (Figure 5.1 and Figure 5.2). It is also clear that apatite formed under UV has progressed apatite deposition than apatite formed in the dark. This can be seen at coatings after 6 days of incubation as obtained in Figure 5.2. This is can be reasonable with the increased Ti-O^- stretching for 2.0 M after the UV irradiation as obtained in Figure 4.18. However, for 0.1 M the UV irradiation has not caused a significant increased in Ti-O^- functional groups. This is can be due to the increasing nonstoichiometry of the sample, due to oxygen out-diffusion in a vacuum (Grujić-Brojčin *et al.,* 2006; Šćepanović *et al.,* 2005). This is has been explained in detail in **Section 4.2.6**.

It can be also noted that from the beginning until day 6 the apatite was precipitated more at coatings produced at 2.0 M (Figure 5.1 (b)) than at 0.1 M (Figure 5.1 (a)) in the dark condition. This is can be related to higher surface porosity on the coating surface for 2.0 M than for 0.1 M as obtained in Figure 4.4 (f). A similar results by Yang et al. (2004) and Cui et al. (2009) an increase in apatite formation was obtained at the coatings with higher porosity, thickness, and molar concentration after 3 days and 7 days respectively in SBF in the dark. While from day 6 to day 12 the apatite precipitation has suddenly accelerated on the coating produced at 0.1 M and resulted in a surface covered apatite. However, the apatite at 2.0 M did cover only

certain parts in the dark condition. This is can be due to the stronger Ti-O^- functional groups obtained has accelerated the apatite growth on the coating surface of 0.1 M. As for the apatite precipitated under UV, a regular progression was obtained after 6 days and after 12 days at 0.1 M as obtained in Figure 5.2 (a and c). This is can be explained as the UV provoked the photocatalysis activity of the coatings surface and increased the apatite growth, where the microstructure effect can be minimized when the coatings applied for UV.

The apatite of coatings incubated in the dark has obtained separated deposited apatite pieces grown on the surface. This is apparent for coating incubated for 6 days as seen in Figure 5.1 (a and b) and Figure 5.2 (a and b). While the apatite of coatings incubated for 12 days has grown in a form of spherical agglomerates as seen in Figure 5.1 (c and d) and Figure 5.2 (c and d). As for the apatite grown under UV, it can be seen that the apatite has been formed in a shape of clusters and agglomerates in a perpendicular direction to the coating surface. This is due to the increased positive charged surface that is caused by the UV that caused the Ca^{2+} to get repulsed from the surface and therefore the Ca^{2+} ions build join the negative phosphate ions (PO_{3-}^{4}) and OH^- ions to build the particles away from surface and above each other and thus form clusters (Ueda *et al.*, 2009). This is has been explained in detail in **Section 2.10.3**.

The resulted apatite formation match with the mechanism of HA precipitation on TiO_2 in the dark and under the UV as explained in **Section 2.10.3**. The progressed apatite appeared on the coating that has been incubated for 6 days under the UV (Figure 5.2 (a and b)) than of the coatings incubated in the dark (Figure 5.1 (a and b) is due to the apatite formation was speeding up by UV (Han *et al.*, 2008; Liu *et al.*, 2008).

Abdullah and Sorrell (2007) have reported that the existence of phosphorus, calcium, or oxygen on anodised coating indicates that HA has grown on it and the bone bioactivity of a material can be predicted from the apatite formation in SBF (Abdullah and Sorrell, 2007).

5.2.2 Elements of the Apatite Formation on TiO_2 Anodised in H_2SO_4 Electrolyte

Figure 5.3 and Figure 5.4 show the Ca to P ratio for the apatite precipitated on the coatings anodised in the H_2SO_4 electrolyte for 0.1 M and 2.0 M at 150V and 100

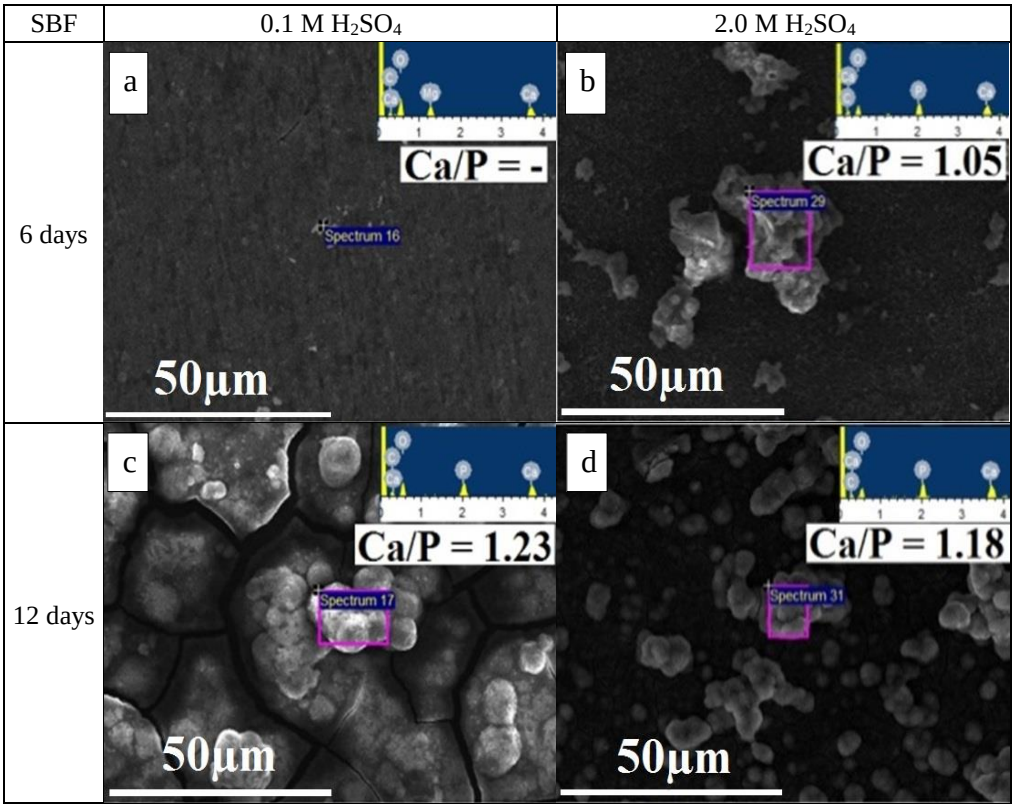

Figure 5.3: Ca to P ratio of coatings produced in H_2SO_4 electrolytes (0.1 M and 2.0 M) at 150 V and 100 mA.cm^{-2} immersed in SBF in the dark for 6 and 12 days

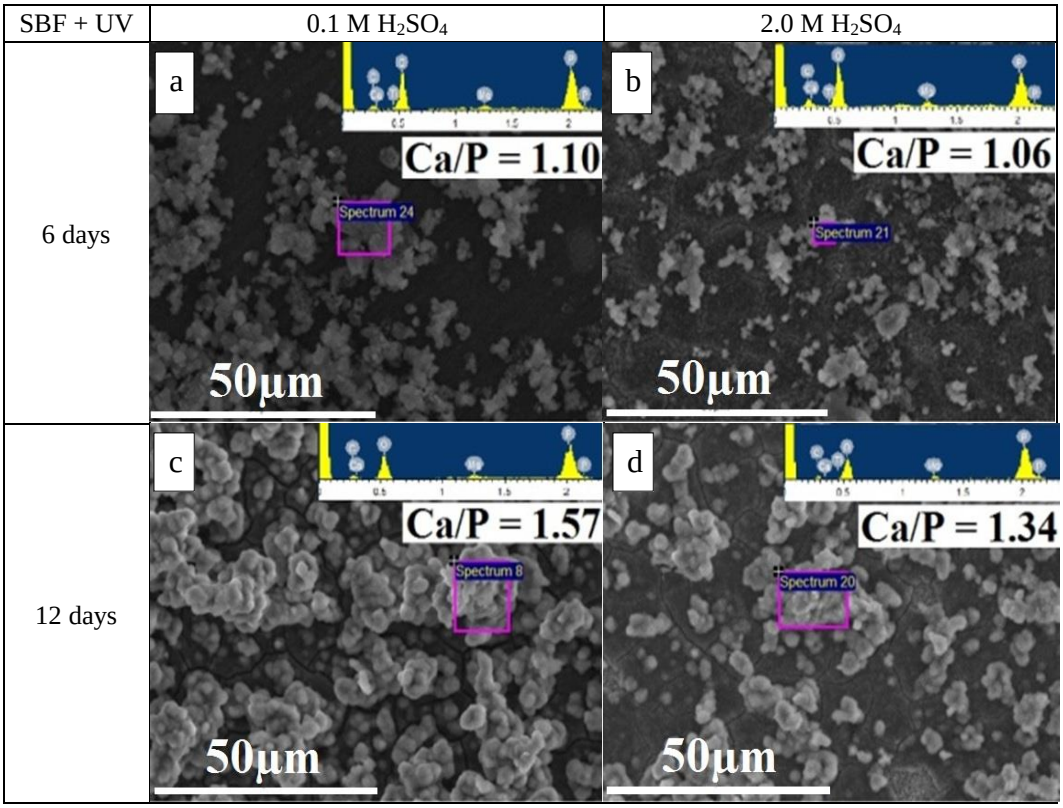

Figure 5.4: Ca to P ratio of coatings produced in H_2SO_4 electrolytes (0.1 M and 2.0 M) at 150 V and 100 mA.cm^{-2} immersed in SBF under UV for 6 and 12 days

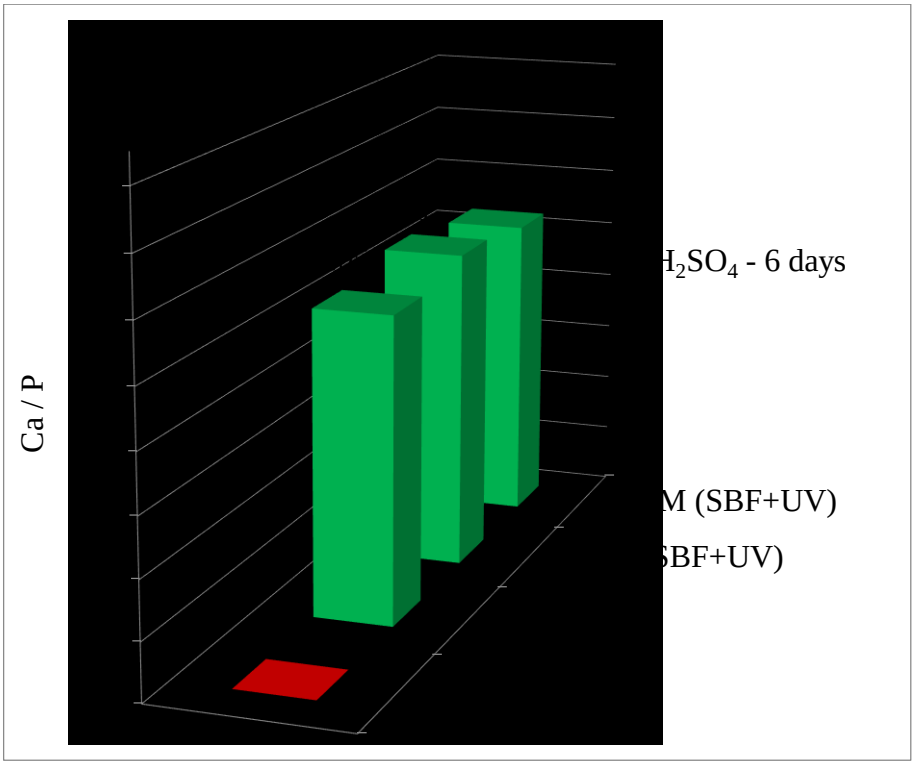

Figure 5.5: Bar chart of Ca to P ratio of coatings produced in H_2SO_4 electrolyte at 150 V and 100 mA.cm^{-2} immersed for 6 days in SBF in the dark and under UV

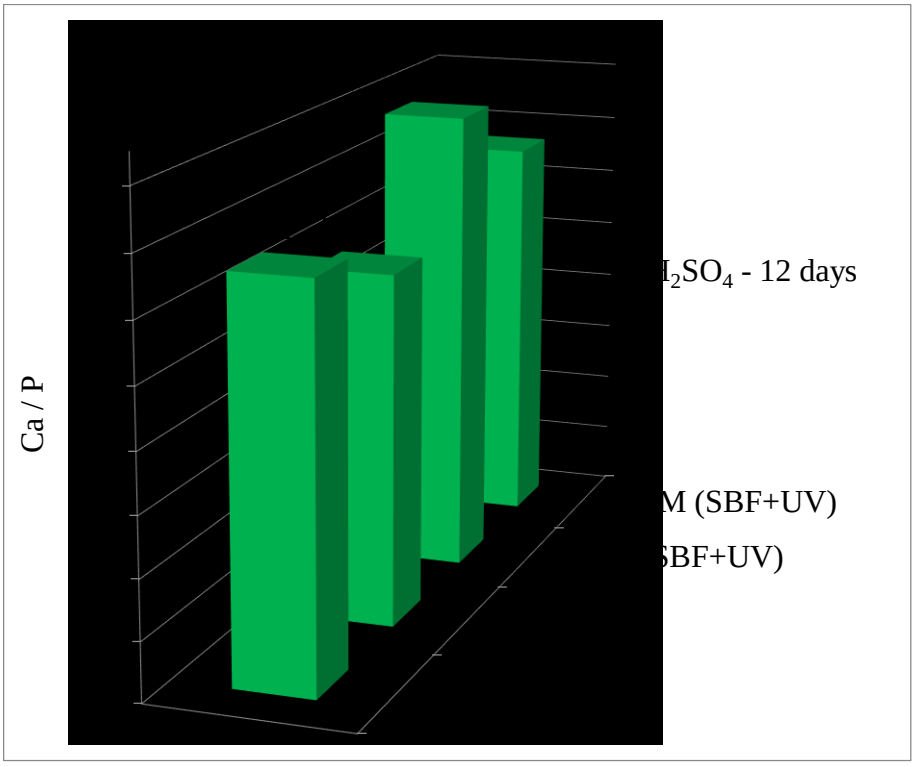

Figure 5.6: Bar chart of Ca to P ratio of coatings produced in H_2SO_4 electrolyte at 150 V and 100 mA.cm^{-2} immersed for 12 days in SBF in the dark and under UV

$mA.cm^{-2}$ in the dark and under the UV respectively. While Figure 5.5 and Figure 5.6 obtain the bar chart to compare the Ca to P ratio of the apatite formed in SBF in the dark and under UV.

The coatings anodised at 0.1 M incubated in the dark (Figure 5.3 (a)) did not obtain calcium phosphates precipitation after 6 days of incubation, where P was not detected after incubated in the dark. Generally, the ratio of Ca to P has increased with the increased incubation time at both incubation conditions. It can be noticed from the results that only the apatite formed on the coating anodised in 0.1 M after 12 days under UV did match the ratio of the calcium-deficient HA (Ca/P = 1.5-1.67). This ratio has been reported by Ramesh et al. (2007) and Zyman et al. (2013). The apatite that was formed on the other coatings didn't obtain the ratio of HA. This can indicate that the apatite precipitated on the coating is amorphous calcium phosphates. However, the elemental analysis was taken for a partial area equal to approximately 225 μm^2 out of the whole coating area which is equal of 10000 μm^2. This might not indicate the exact Ca to P ratio of the whole coating area.

5.2.3 Mineralogy of the Apatite Formation on TiO_2 Anodised in H_2SO_4 electrolyte

Figure 5.7 and Figure 5.8 obtain the mineralogical patterns of the coatings anodised in the H_2SO_4 electrolyte for 0.1 M and 2.0 M respectively at 150 V and 100 $mA.cm^{-2}$ immersed in the SBF in dark for 6 and 12 days. Figure 5.9 and Figure 5.10 obtain the mineralogical patterns of the coatings immersed under the UV for 0.1 M and 2.0 M respectively. The phase mineralogical analysis has confirmed the formation of the crystalline apatite HA (JCPDS card #00-055-0592) on the coatings that obtained crystalline peaks with orientations (002) and (211).

All the coatings have obtained a crystalline apatite peaks after 12 days of incubation in the dark and under the UV. The patterns that didn't obtain crystalline peaks have an amorphous apatite as obtained in Figure 5.8 (a), which corresponds to the apatite formed in the dark on the coating anodised in 2.0 M, and in Figure 5.10 (b), which corresponds to the apatite formed under the UV on the 2.0 M coating. The coating anodised in 0.1 M didn't obtain any apatite as obtained in Figure 5.7 (b), this can be obtained on the corresponding microstructure surface image Figure 5.1 (a) and

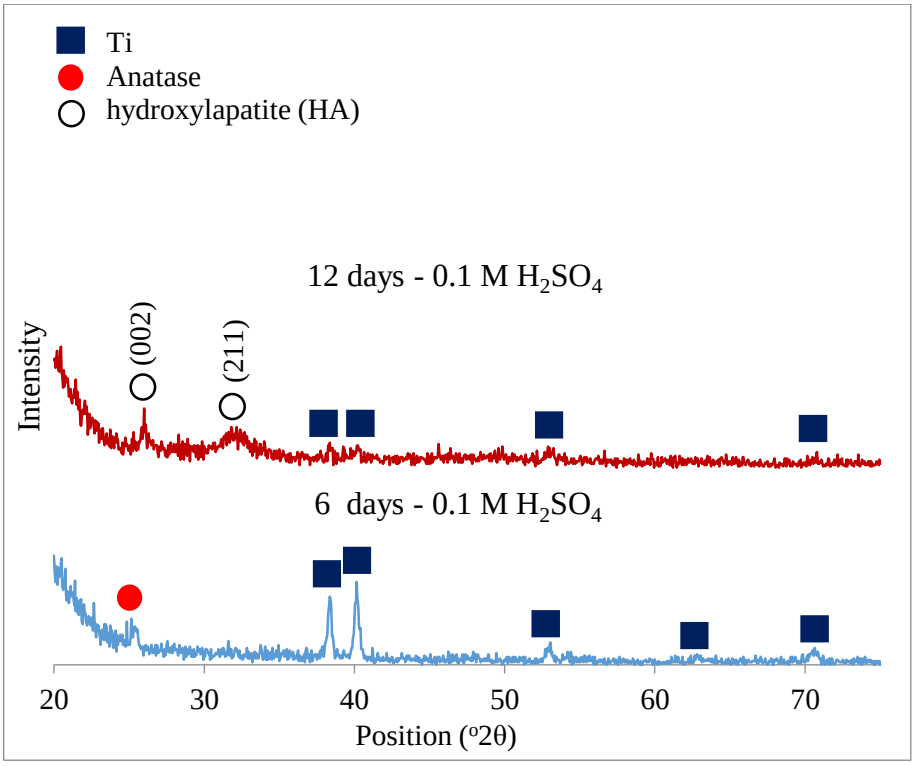

Figure 5.7: Phase mineralogical Patterns for apatite precipitation in SBF for 6 and 12 days in the dark for coatings anodised at 150 V and 100 mA.cm^{-2} in 0.1 M H_2SO_4 electrolyte

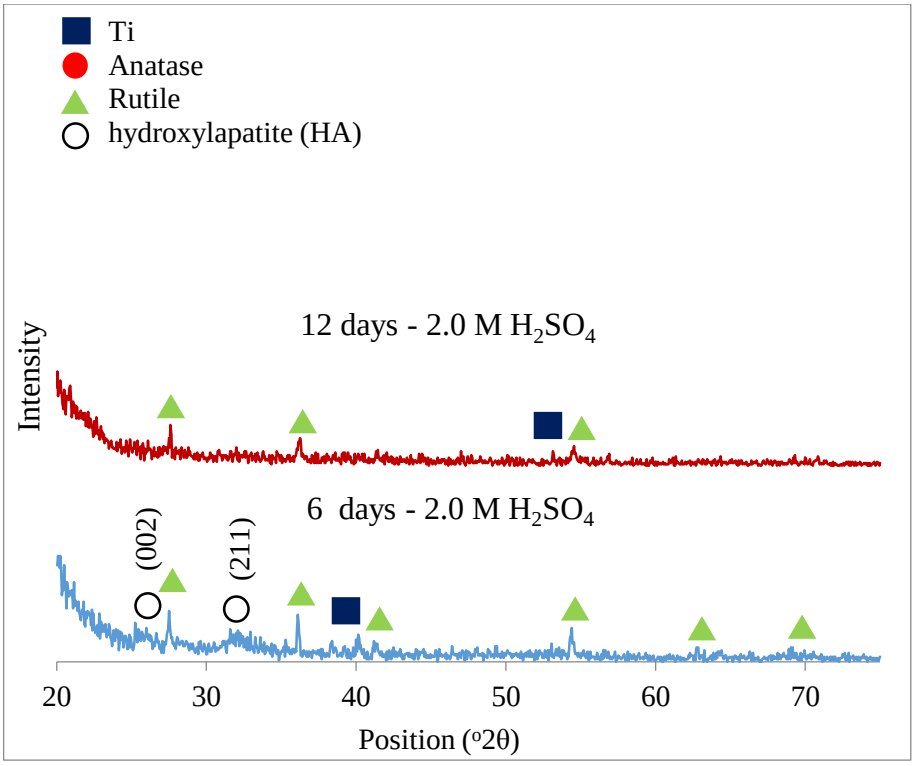

Figure 5.8: Phase mineralogical Patterns for apatite precipitation in SBF for 6 and 12 days in the dark for coatings anodised at 150 V and 100 mA.cm^{-2} in 2.0 M H_2SO_4 electrolyte

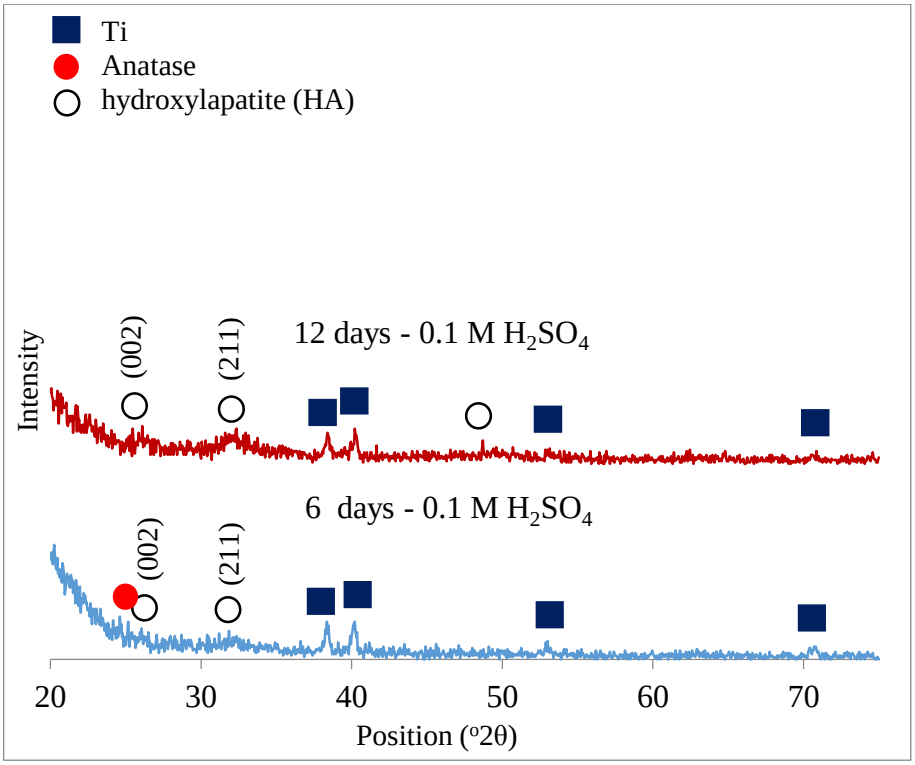

Figure 5.9: Phase mineralogical Patterns for apatite precipitation in SBF for 6 and 12 days under UV for coatings anodised at 150 V and 100 mA.cm^{-2} in 0.1 M H_2SO_4 electrolyte

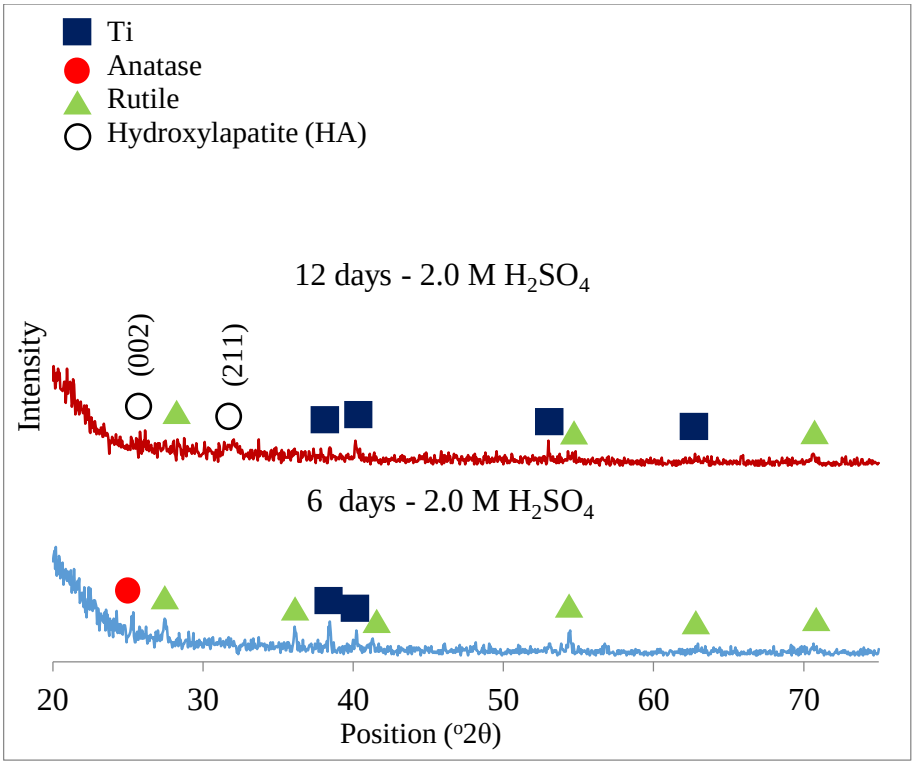

Figure 5.10: Phase mineralogical Patterns for apatite precipitation in SBF for 6 and 12 days under UV for coatings anodised at 150 V and 100 mA.cm^{-2} in 2.0 M H_2SO_4 electrolyte

elemental analysis where no P was found on the precipitation (Figure 5.3 (a)).

The increased peak strength with the increased incubation time can be an indication of the increased HA crystallinity. However, most patterns do not obtain significant clear peaks. This can be an indication that the coatings in general obtained low crystallinity along with the amorphous HA.

It can be noticed that the UV irradiation has promoted an early apatite formation on both coatings at 0.1 M and 2.0 M and early crystallization at 0.1 M. This is clearly where the coatings incubated for 6 days under the UV has obtained crystalline apatite at 0.1 M (Figure 5.9 (b)) and amorphous apatite at 2.0 M (Figure 5.10 (b)). Their corresponding apatite that was formed in the dark has obtained no apatite at 0.1 M after 6 days of incubation in the dark (Figure 5.7 (b)), and crystalline has been obtained at 2.0 M (Figure 5.8 (b)). The coatings after 12 days of incubated under the UV has obtained crystalline apatite on 0.1 M (Figure 5.9 (a)) and 2.0 M (Figure 5.10 (a)), with calcium-deficient HA with ratio of Ca to P equal to 1.57 as obtained at 0.1 M on Figure 5.4 (c) and Figure 5.6. While their corresponding apatite that formed in the dark at 0.1 M did obtain lower Ca to P ratio (Figure 5.3 (c)), however, it did obtain high crystalline peaks (Figure 5.7 (a)). While for the apatite formed at 2.0 M has obtained amorphous apatite (Figure 5.8 (a)).

In general, higher apatite crystalline precipitated in SBF in the dark and under the UV after 12 days was obtained on the coatings anodised in 0.1 M. The apatite that formed in SBF the dark condition has no external catalyst or stimulator, which can be an indication of coating ability strength to induce apatite. The apatite that
obtained on the 0.1 M that formed in the dark has obtained the same or slightly higher crystallinity than the crystalline apatite that formed under the UV irradiation. This can indicate the strength of apatite induction ability of the coatings anodised in 0.1 M in the H_2SO_4 electrolyte.

The microstructure image results in Figure 5.1 and Figure 5.2 are in a positive matching with the mineralogical results as obtained in Figure 5.7, Figure 5.8, Figure 5.9 and Figure 5.10. It can be obtained that the increased apatite formed according to the microstructure images has obtained an increase in the HA crystalline according to the mineralogical patterns. An exception is for the patterns of the apatite precipitation in the SBF in the dark for the coatings anodised in 2.0 M (Figure 5.8 (a)). This can indicate that the grown apatite on that coating according to the mineralogical pattern is still an amorphous HA. However, it has been reported that with the growth of the

apatite on TiO_2, the structure change from amorphous to crystalline on the surface (Liu *et al.,* 2008; Ueda *et al.,* 2009).

In comparison between the mineralogical patterns of the coating mineralogy for the coating anodised in 0.1 M and in 2.0 M with the apatite formed mineralogy. It can be noticed that higher apatite crystalline was obtained on the coating anodised in 0.1 M that has obtained anatase crystalline structure as seen in Figure 4.10 (a). This can be seen on the apatite that was formed in the dark (Figure 5.7 (a)) and the apatite formed under the UV (Figure 5.9 (a)) that obtained the Ca to P ratio of calcium-deficient HA. This can be related to the higher photocatalytic activity of the anatase has been reported by Wang *et al.* (2007). It has also been reported that the photocatalytic activity of the anatase crystalline could be enhanced by the UV irradiation (Masahashi *et al.,* 2008). The coating that contains a mixture of anatase and rutile crystalline (2.0 M) has also obtained a crystalline apatite under the UV after 12 days (Figure 5.10 (a)), while it has obtained an amorphous apatite in the dark (Figure 5.8 (a)).

It was reported that the Ti-OH groups react with the hydroxyl ions in the SBF to produce a negatively charged surface with the functional group $Ti\text{-}O^-$. The UV was also reported to increase the formation of Ti-OH (Han *et al.,* 2008; Liu *et al.,* 2008). The higher apatite crystalline that was formed on 0.1 M can be related to the strong and stable Ti-O that was obtained by the absorption analysis (Figure 5.16). However, the Ti-O was less strong on the coating that was anodised in 2.0 M even after the UV irradiation (Figure 5.17), and this can be related to the less apatite formation and crystallization.

The dominant apatite crystalline at 0.1 M at both conditions (Figure 5.7 (a) and Figure 5.9 (a)) that is corresponding to the highest apatite as obtained in Figure 5.1 (a) and Figure 5.2 (a) might be related to several factors. The coating crystalline might not be the key factor in the difference in the apatite formation and crystallization. This is due to the difference in the surface morphology between the coatings, where the coating at 0.1 M (Figure 4.4 (d)) had less porosity and less roughness than of the coating produced in 2.0 M (Figure 4.4 (f)) as discussed in **Section 5.2.2**. Also, the difference in the solute ions concentration that was included in the coatings due to the different molarity of the electrolytes might take an effect.

5.2.4 Absorption of the Apatite Formation on TiO_2 in Anodised in H_2SO_4 Electrolyte

Figure 5.11 and Figure 5.12 obtain the absorption analysis patterns of the coatings anodised in H_2SO_4 electrolyte for 0.1 M and 2.0 M at 150 V and 100 mA.cm^{-2} immersed in the SBF in dark. While Figure 5.13 and Figure 5.14 obtain the absorption analysis of the coatings immersed in the SBF under the UV for 0.1 M and 2.0 M respectively.

The absorption patterns have obtained the appearance of intense stretching of phosphate group PO_4^{-3} at 1000 cm^{-1} and bending modes of the apatite structure (Kannan *et al.*, 2006; Kuriakose *et al.*, 2004; Liu *et al.*, 2003), along with weak OH stretching region at 1620 cm^{-1} which it was attributed to the bending mode of H_2O (Balamurugan *et al.*, 2006; Ma *et al.*, 2006) and the broad stretching at 3100-3400 cm^{-1} can be assigned for the adsorbed water on HA microstructures (Jokanovic *et al.*, 2006; Panda *et al.*, 2003) on all the precipitated apatite. The phosphate stretching has increased with the increased in the incubation time in SBF in the dark and under UV. While the phosphate stretching is higher for the apatite precipitated under UV as obtained in Figure 5.13 and Figure 5.14 than the apatite formed in the dark (Figure 5.11 and Figure 5.12). The presence of the carbonate group CO_3^{-2} stretching band at 1470 cm^{-1} might be due to the carbonate ions in the synthesized HA particles originated from the atmospheric CO_2 during the analysis (Kumar *et al.*, 2004; Ma, 2012).

The absorption analysis can provide a supporting evidence for the formation of HA on the anodised coatings (May *et al.*, 2016). The higher phosphate absorbed of the apatite formed under the UV as seen Figure 5.13 and Figure 5.14 with the apatite formed in the dark (Figure 5.11 and Figure 5.12), indicates that the apatite was denser when formed under the UV than the apatite formed in the dark.

This is clear when relating to the mineralogical results in **Section 5.2.4**. It can be noticed that the higher apatite density is in agreement with the stronger crystalline peak with increased incubation time. Except for the coating anodised in 2.0 M as seen in Figure 5.8 (a), where the higher apatite density has obtained an amorphous structure as obtained in the mineralogical pattern. Although a higher apatite density was obtained on the patterns of apatite precipitated under the UV. However, the mineralogical results did not obtain a significant crystalline difference between the

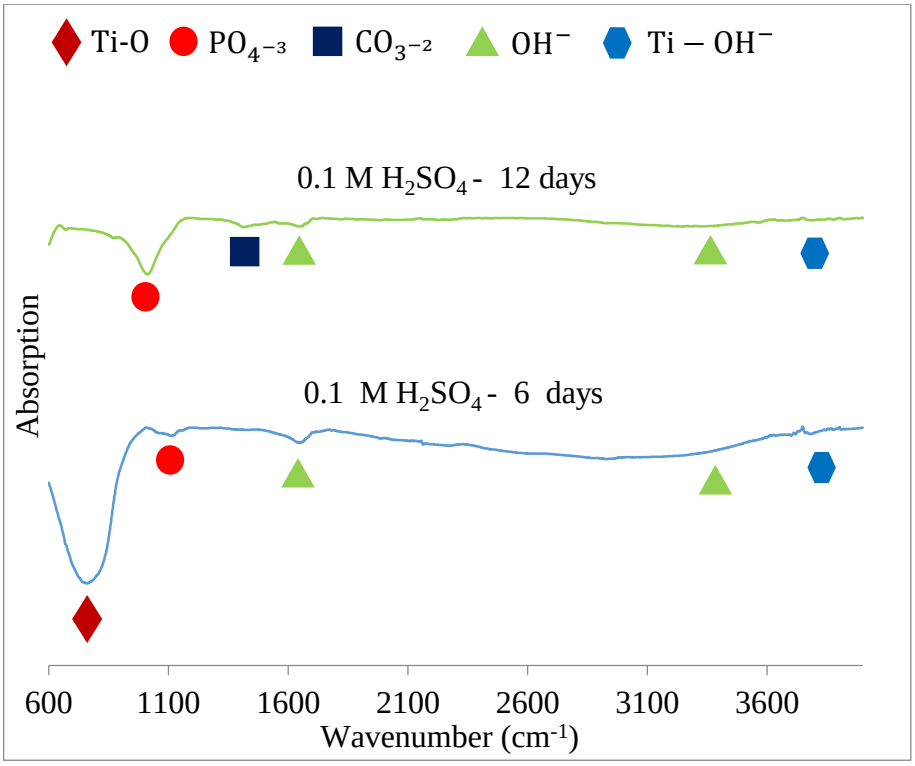

Figure 5.11: Absorption analysis patterns for apatite precipitation in SBF for 6 and 12 days in the dark for coatings anodised at 150 V and 100 mA.cm^{-2} in 0.1 M H_2SO_4 electrolyte

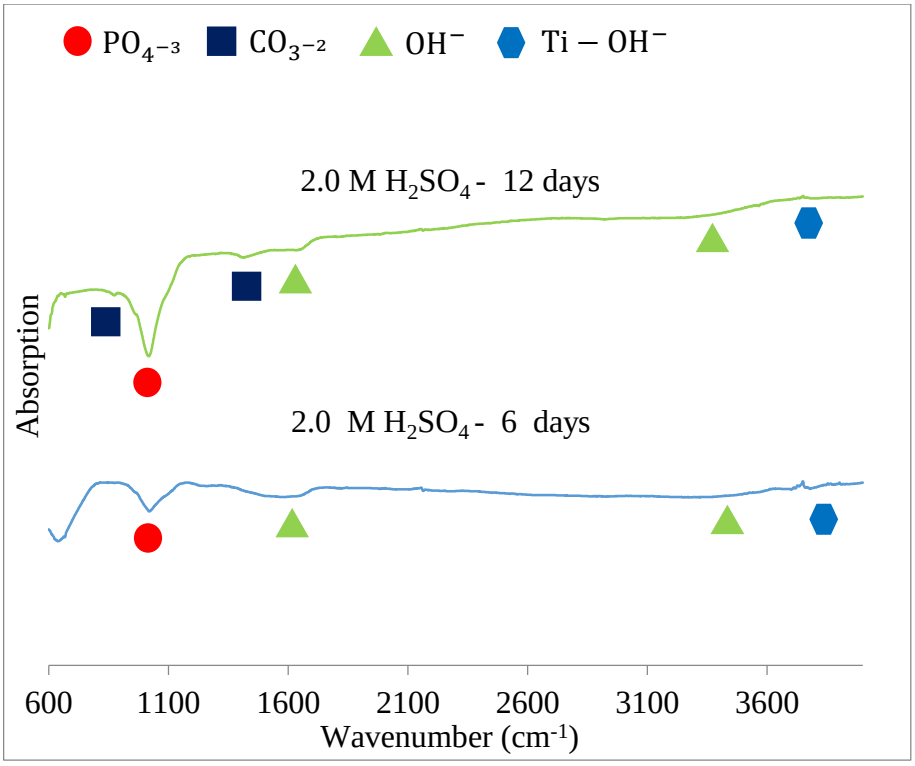

Figure 5.12: Absorption analysis patterns for apatite precipitation in SBF for 6 and 12 days in the dark for coatings anodised at 150 V and 100 mA.cm^{-2} in 2.0 M H_2SO_4 electrolyte

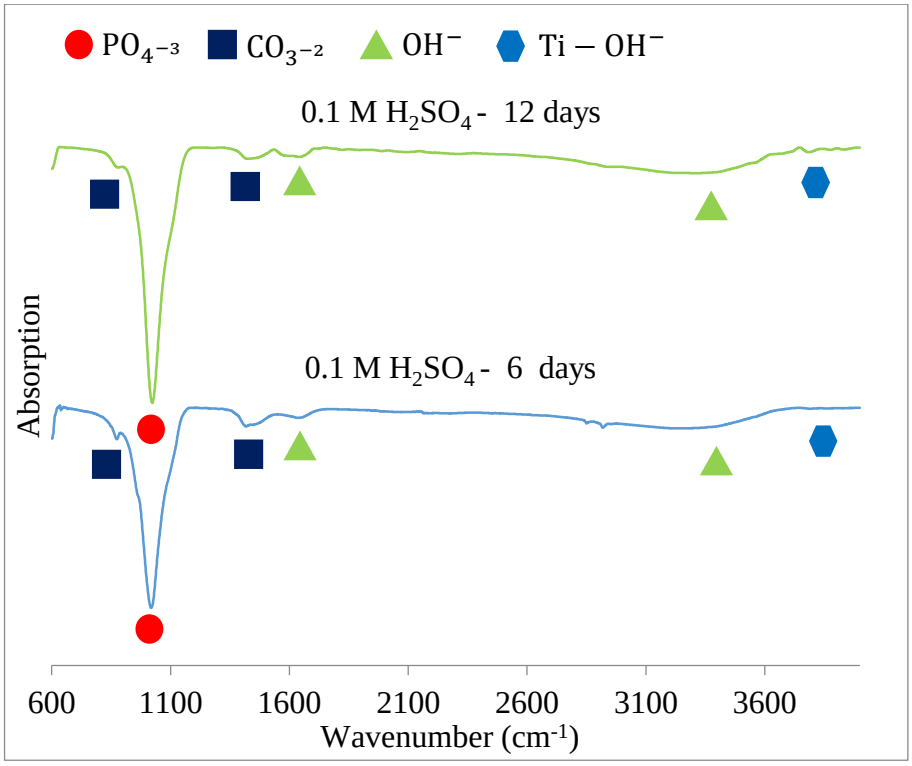

Figure 5.13: Absorption analysis patterns for apatite precipitation in SBF for 6 and 12 days under UV for coatings anodised at 150 V and 100 mA.cm^{-2} in 0.1 M H_2SO_4 electrolyte

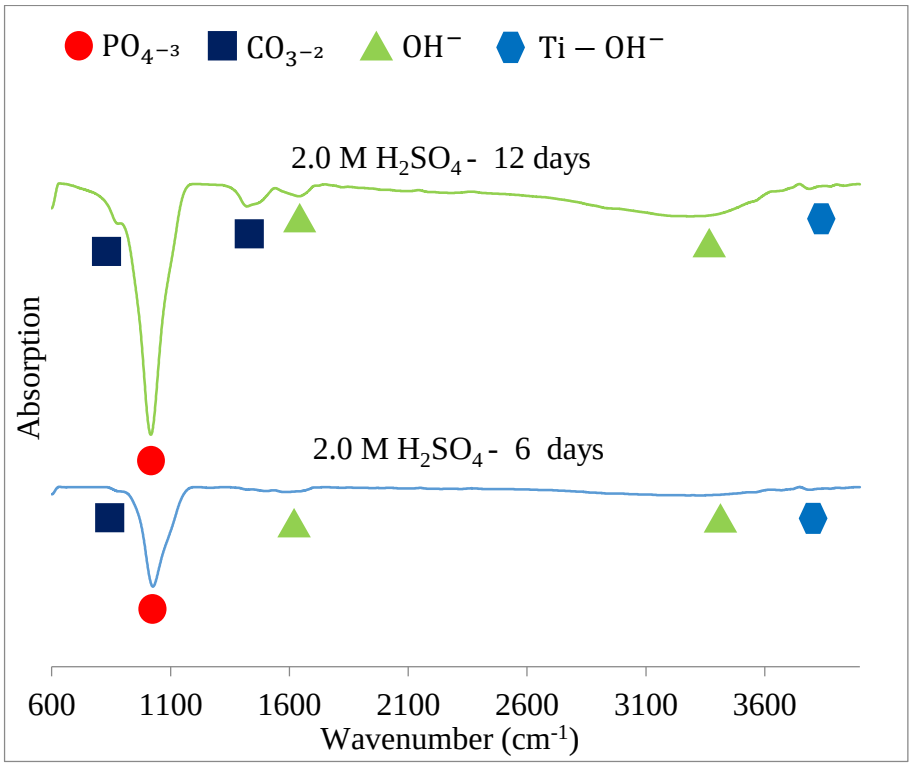

Figure 5.14: Absorption analysis patterns for apatite precipitation in SBF for 6 and 12 days under UV for coatings anodised at 150 V and 100 mA.cm^{-2} in 2.0 M H_2SO_4 electrolyte

patterns of the apatite precipitated under the UV in Figure 5.9 and Figure 5.10 and the patterns of the apatite precipitated in the dark in Figure 5.7 and Figure 5.8. This can be explained that higher apatite density on the coating produced under the UV, although the crystallinity obtained to be similar. This can conclude that the apatite formed under the UV promotes little crystalline structure when compared with the apatite density of the coating produced in the dark.

There is a clear relationship between the absorption analysis and the microstructure images obtained in **Section 5.2.2**, where the apatite density was higher with the increased apatite precipitation. It appears that the cluster apatite formation that formed on the coatings produced under the UV (Figure 5.9 and Figure 5.10) has obtained a higher apatite density over the spherical-like apatite coatings that produced in the dark (Figure 5.7 and Figure 5.8). It is also worth mentioning that the absorption pattern that was obtained in Figure 5.11, that correspond to the apatite formed on the coatings anodised in 0.1 M after 6 days of incubation in the dark, has obtained a very weak stretching; thus low density, which correspond to the small pieces of apatite formed as obtained in Figure 5.1 (a).

5.3 Apatite Formation Evaluation on TiO_2 Coatings Anodised in Phosphoric Acid (H_3PO_4) Electrolyte

The TiO_2 coatings anodised in the H_3PO_4 electrolyte for 0.1 M and 2.0 M at 150 V and 100 $mA.cm^{-2}$ was subjected to *in vitro* test using SBF in dark and under UV irradiation. Microstructure, morphology, mineralogy, and surface energy of the coatings will be discussed.

5.3.1 Microstructure of Apatite Formed on TiO_2 Anodised in H_3PO_4 Electrolyte

Figure 5.15 and Figure 5.16 show the surface image microstructure captured of the coatings anodised in H_3PO_4 electrolyte for 0.1 M and 2.0 M at 150 V and 100 $mA.cm^{-2}$ immersed in SBF in dark and under the UV respectively. Table 5.2 obtained the apatite-forming ability of the coating immersed in the dark and under the UV as a function of electrolyte molarity.

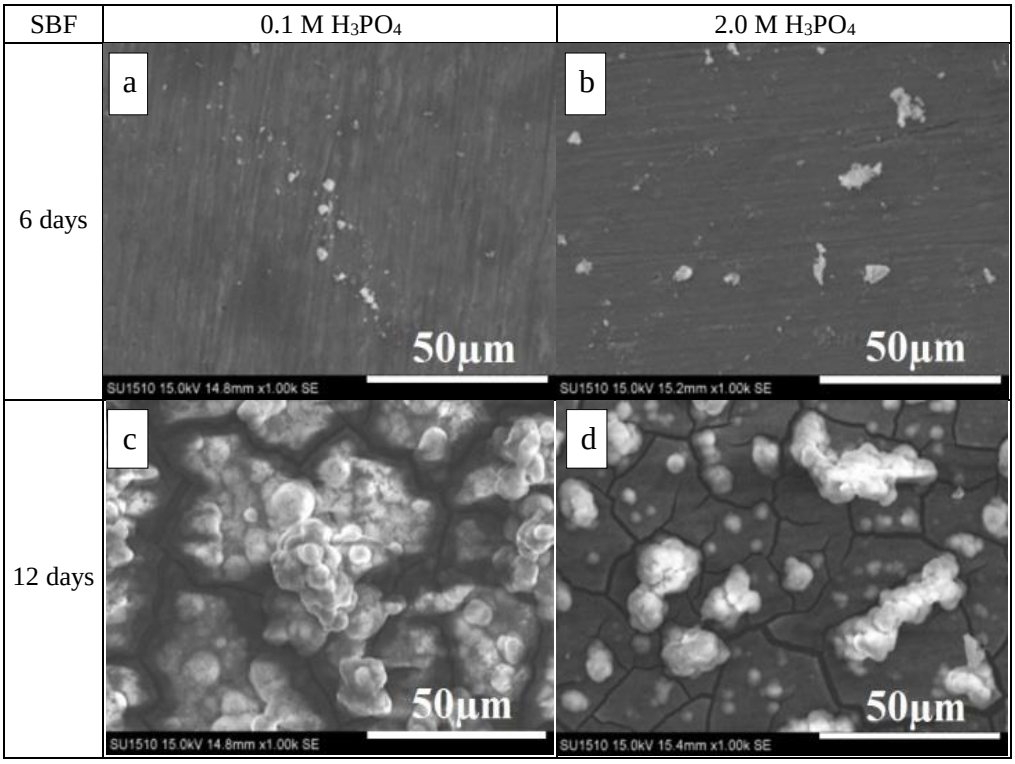

Figure 5.15: Surface microstructure images of the coatings produced in H_3PO_4 electrolytes (0.1 M and 2.0 M) at 150 V and 100 mA.cm^{-2} immersed in SBF in the dark for 6 and 12 days

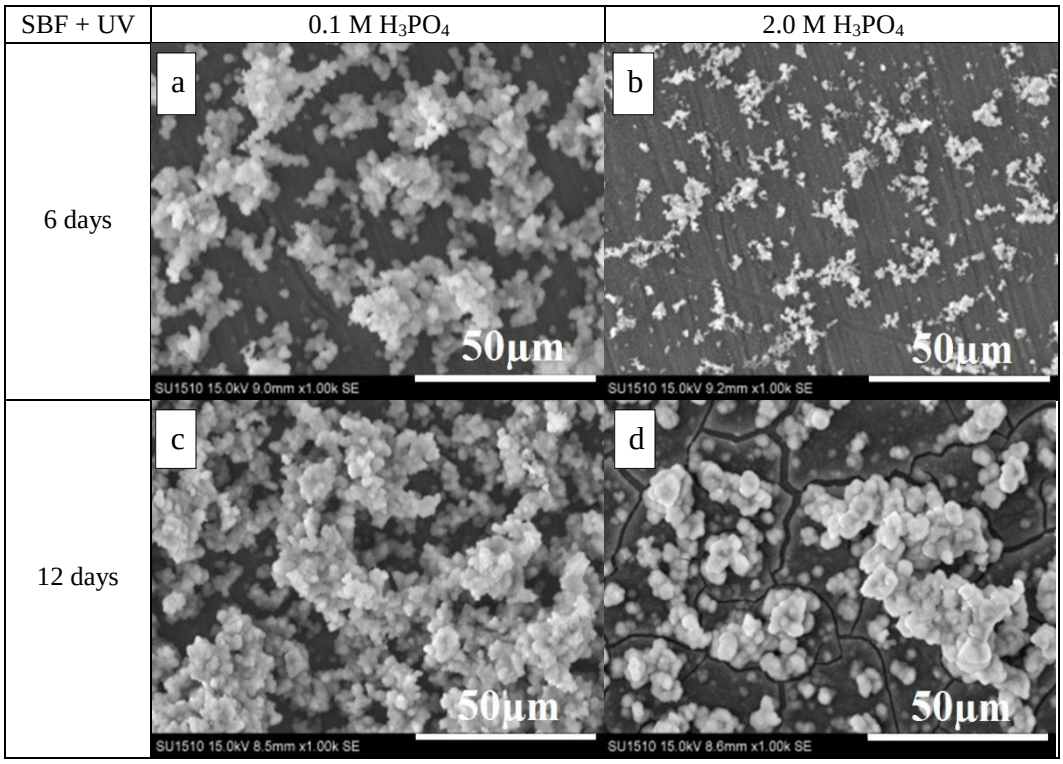

Figure 5.16: Surface microstructure images of the coatings produced in H_3PO_4 electrolytes (0.1 M and 2.0 M) at 150 V and 100 mA.cm^{-2} immersed in SBF under UV for 6 and 12 days

Table 5.2: The apatite forming ability of the coatings anodised in H_3PO_4 electrolyte immersed in the dark and under the UV as a function of electrolyte molarity

In vitro treatment	SBF		SBF + UV	
H_2SO_4 electrolyte molarity	0.1 M	2.0 M	0.1 M	2.0 M
6 days	+	+	++++	+++
12 days	+++++	+++	+++++	++++

The apatite has increased with the increased immersion time in SBF. Also, higher apatite formation was obtained at coatings produced at lower anodization molar concentration. This can be seen on the apatite after 12 days of incubation in the dark as seen in Figure 5.15, while the apatite formed under UV have obtained to be progressed after 6 days and after 12 days as seen in Figure 5.16. The apatite produced in the dark grows in a small pieces shape after 6 days of incubation as seen in Figure 5.15 (a and b). While it became agglomerates in spheres like shapes and cover all over the floor after 12 days of incubation as seen on coating produced in 0.1 M as seen in Figure 5.15 (c). However, the apatite produced under UV takes clusters like shape and agglomerates in a perpendicular direction to the coating floor after 6 and 12 days of incubation as seen in Figure 5.16 (a,b,c and d). Although, the highest apatite formed on 0.1 M after 12 days did not cover 100 % the floor, where voids can be seen in Figure 5.16 (c).

The resulted in apatite formation have similar aspects with the apatite formed in the coatings anodised in H_2SO_4, as explained in **Section 5.2.1**. The $Ti\text{-}O^-$ is believed to have progressed the formation of apatite on the coating that was anodised in 0.1 M H_3PO_4 than at 2.0 M H_3PO_4. This is apparent after 12 days of incubation in the dark as obtained in Figure 5.15 (c), and for 6 and 12 days under UV Figure 5.16 (a and c). The apatite has obtained similarly with that obtained on the coating anodised in 0.1 M H_2SO_4 in the dark and under the UV as obtained in Figure 5.1 and Figure 5.2. However, the $Ti\text{-}O^-$ functional group stretching at 0.1 M H_3PO_4 (Figure 4.33) wasn't as strong as the stretching that was obtained for 0.1 M H_2SO_4 (Figure 4.17), even after the UV irradiation. The advantages of apatite formed in the dark condition at 0.1 M H_3PO_4 can be due to the lower microstructure porosity (Figure 4.22 (d)) and to the higher $Ti\text{-}O^-$ (Figure 4.33) than at 2.0 M H_3PO_4, similar that was obtained for 0.1 M H_2SO_4 (Figure 4.4 (d)) when compared with the apatite formed at 2.0 M H_2SO_4. While the apatite that was formed at 2.0 M H_3PO_4 have obtained lower porosity (Figure 4.22 (f)) than at 2.0 M H_2SO_4 (Figure 4.4 (d)). This is might be the reason for the lower apatite formation

in the dark condition (Figure 5.15 (b and d)) when compared with the coating formed at 2.0 M H_2SO_4 (Figure 5.1 (b and d)). However, the apatite formed under the UV was similar with that formed at 2.0 M H_2SO_4 (Figure 5.2 (b and d)), and this is might be due to the higher efficiency of the Ti-O^- functional groups that was provoked with the UV, and has obtained similar stretching (Figure 4.34) with that at 2.0 M H_2SO_4 (Figure 4.18).

5.3.2 Elements of the Apatite Formation on TiO_2 Anodised in H_3PO_4 Electrolyte

Figure 5.17 and Figure 5.18 obtain the Ca to P ratio for the apatite formation precipitated in the H_3PO_4 electrolyte for 0.1 M and 2.0 M at 150 V and 100 $mA.cm^{-2}$ in the dark and under the UV respectively. While Figure 5.19 and Figure 5.20 obtain the bar chart to compare the Ca to P ratio of the apatite formed in SBF in the dark and under UV.

According to the elemental analysis, the coatings anodised at 0.1 M incubated in SBF in the dark (Figure 5.17 (a)) did not obtain calcium phosphates precipitation after 6 days of incubation. Where there was neither P nor Ca were detected on the coating. In general, the ratio of Ca to P has increased with the increase of incubation time at the apatite obtained in the dark as seen in Figure 5.17. While the apatite obtained under the UV has obtained the same ratio with the increased in incubation time as seen in Figure 5.18.

It can be noticed from the results that the precipitation ratio did not match the ratio of stoichiometric HA (Ca/P = 1.67) of human bone nor the ratio of calcium-deficient HA (Ca/P = 1.5 - 1.67) as reported by Ramesh et al. (2007) and Zyman et al. (2013). This can indicate that the apatite precipitated on the coating is amorphous calcium phosphates.

However, it has to be noticed that the lower ratio obtained in the apatite formed under the UV comparing to the apatite formed in the dark has no clear reason. While it is worth noticing that the closer intensity of the P to the S might not be related to the content of the apatite. The phosphate ions incorporated within the coating must be taken into the account. Where higher P ions intensity can be detected especially on the coatings anodised in 2.0 M.

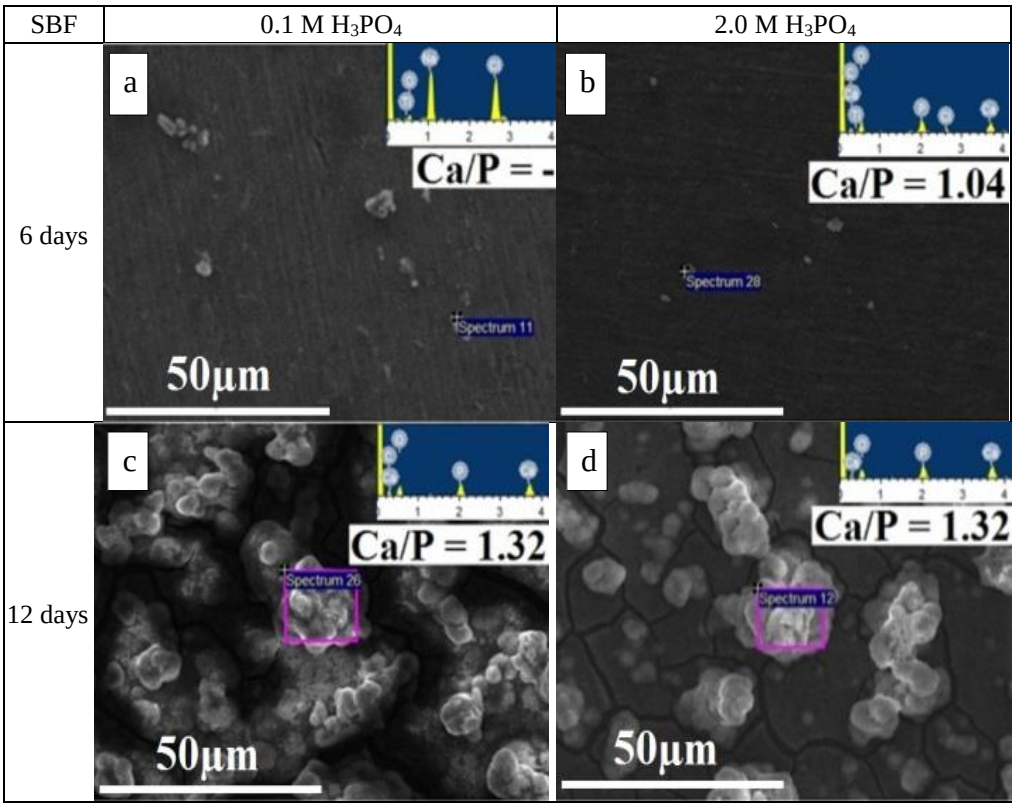

Figure 5.17: Ca to P ratio of the coatings produced in H_3PO_4 electrolytes (0.1 M and 2.0 M) at 150 V and 100 mA.cm^{-2} immersed in SBF in the dark for 6 and 12 days

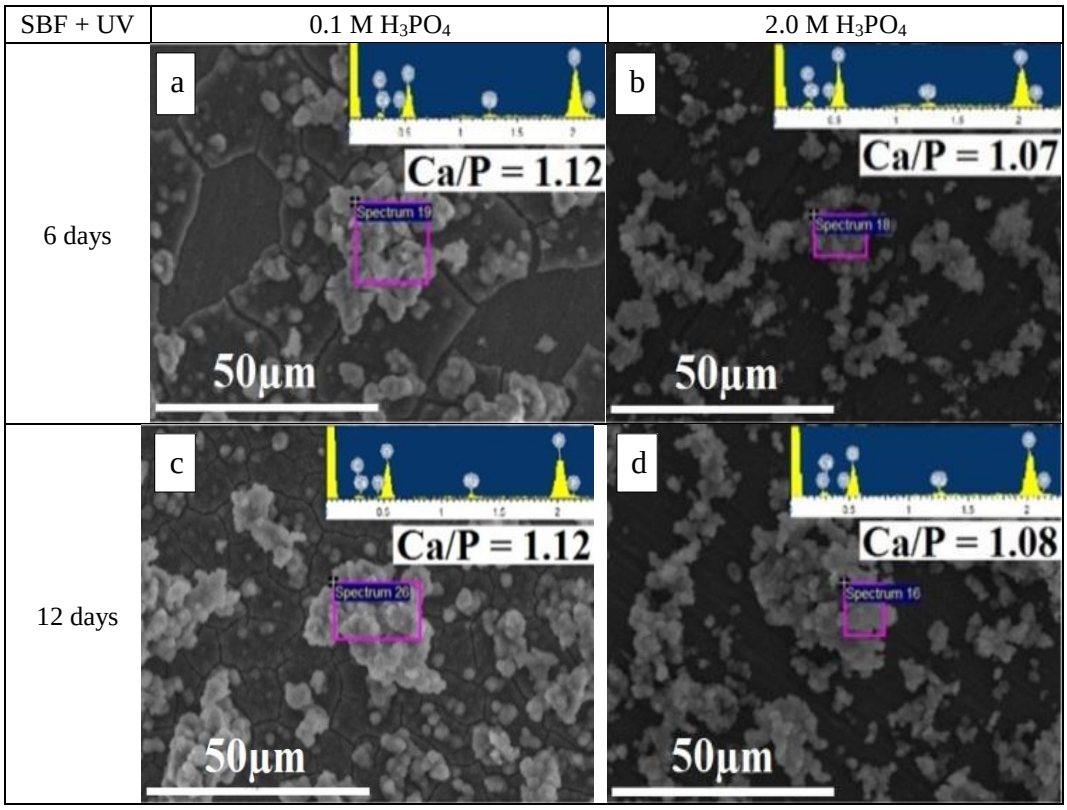

Figure 5.18: Ca to P ratio of coatings produced in H_3PO_4 electrolytes (0.1 M and 2.0 M) at 150 V and 100 mA.cm^{-2} immersed in SBF under UV for 6 and 12 days

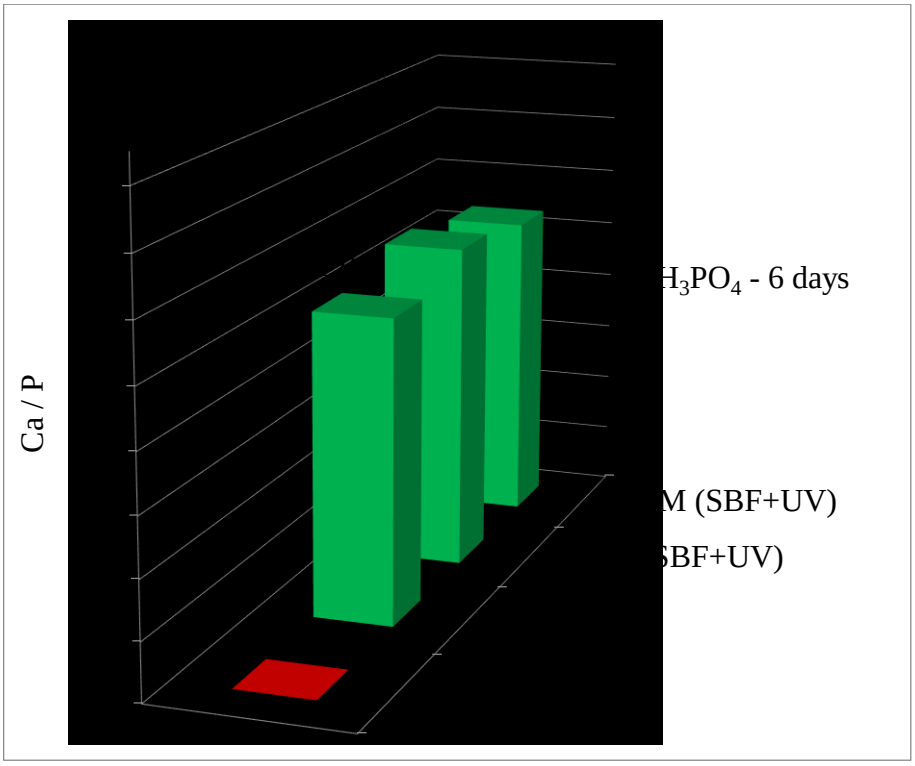

Figure 5.19: Bar chart of Ca to P ratio of coatings produced in H_3PO_4 electrolyte at 150 V and 100 mA.cm^{-2} immersed for 6 days in SBF in the dark and under UV

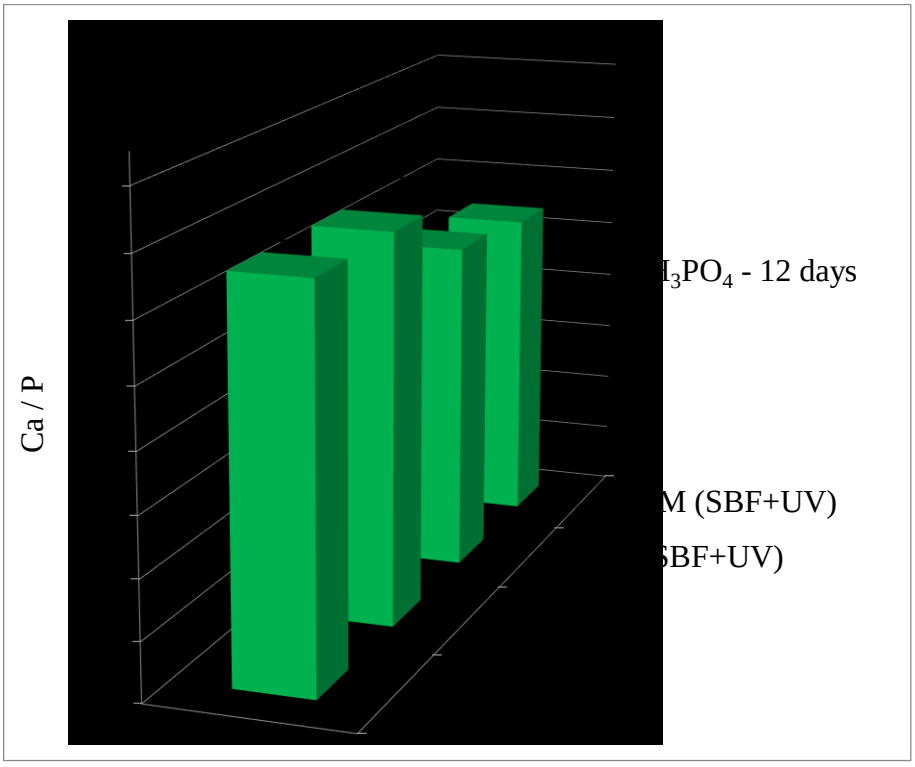

Figure 5.20: Bar chart of Ca to P ratio of coatings produced in H_3PO_4 electrolyte at 150 V and 100 mA.cm^{-2} immersed for 12 days in SBF in the dark and under UV

When comparing with the Ca to P ratio of the apatite formed on the coatings anodised in the H_2SO_4 electrolyte. It can be noticed that H_3PO_4 electrolyte did not obtain the Ca to P ratio of HA apatite even after the UV irradiation. This can be advantageous for the H_2SO_4 electrolyte, where the coating did obtain HA ratio at 0.1 M after 12 days of incubation in SBF under UV as seen in Figure 5.4 (c). Also, the H_2SO_4 electrolyte has obtained higher Ca to P ratio after incubation in SBF under UV. However, not for the apatite after incubated in the dark, where the ratio was higher on H_3PO_4 electrolyte (Figure 5.17 (a and b)) than in H_2SO_4 electrolyte (Figure 5.18 (a and b)).

This indicates that the coatings anodised in H_3PO_4 electrolyte had a higher potential to buildup HA on the coating incubated in the dark. However, the lower ratio of the apatite formed under the UV in the H_3PO_4 electrolyte can be related to the increase in the P ions concentration on the coating. This can have affected the ratio of Ca to P, or due to these ions have been affected by the UV to build an amorphous apatite. Song *et al.* (2009) have concluded that H_2SO_4 electrolyte did obtain a higher ratio that H_3PO_4 electrolyte after 3 days of incubation in MEM solution. While Cui *et al.* (2009) did not obtain any apatite formation ability on H_3PO_4 electrolyte even after 7 days in SBF.

5.3.3 Mineralogy of the Apatite Formation on TiO_2 Anodised in H_3PO_4 electrolyte

Figure 5.21 and Figure 5.22 obtain the mineralogical patterns of the coatings anodised in 0.1 M and 2.0 M respectively at 150 V and 100 $mA.cm^{-2}$ immersed in SBF in the dark for 6 and 12 days. While Figure 5.23 and Figure 5.24 obtain for the coatings immersed under the UV for 0.1 M and 2.0 M respectively.

The patterns as obtained in Figure 5.21 and Figure 5.22 correspond to the coatings incubated in SBF in the dark, while the patterns as obtained in Figure 5.23 and Figure 5.24 to correspond to the coatings incubated in SBF under the UV irradiation. The phase mineralogical analysis has confirmed the formation of the crystalline apatite HA (JCPDS card #00-055-0592) on all the crystalline coatings, except the coating anodised in 2.0 M that was incubated in the dark and under the UV, where they have obtained HA (JCPDS card #00-055-0592) and HA (JCPDS card #00-

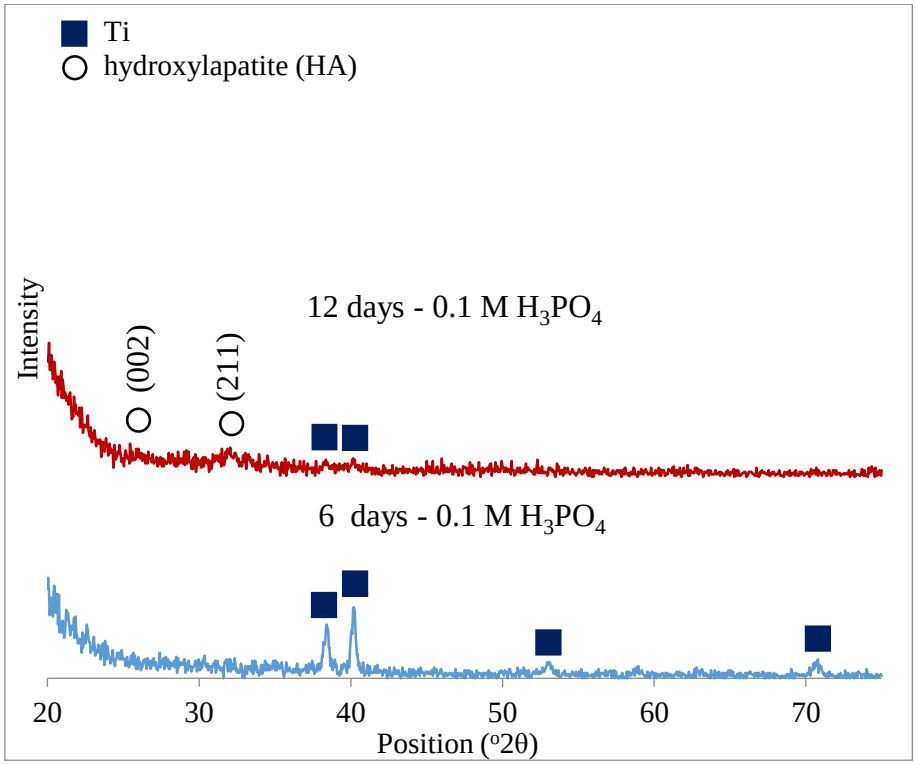

Figure 5.21: Phase mineralogical patterns for apatite precipitation in SBF for 6 and 12 days the dark for coatings anodised at 150 V and 100 mA.cm^{-2} in 0.1 M H_3PO_4 electrolyte

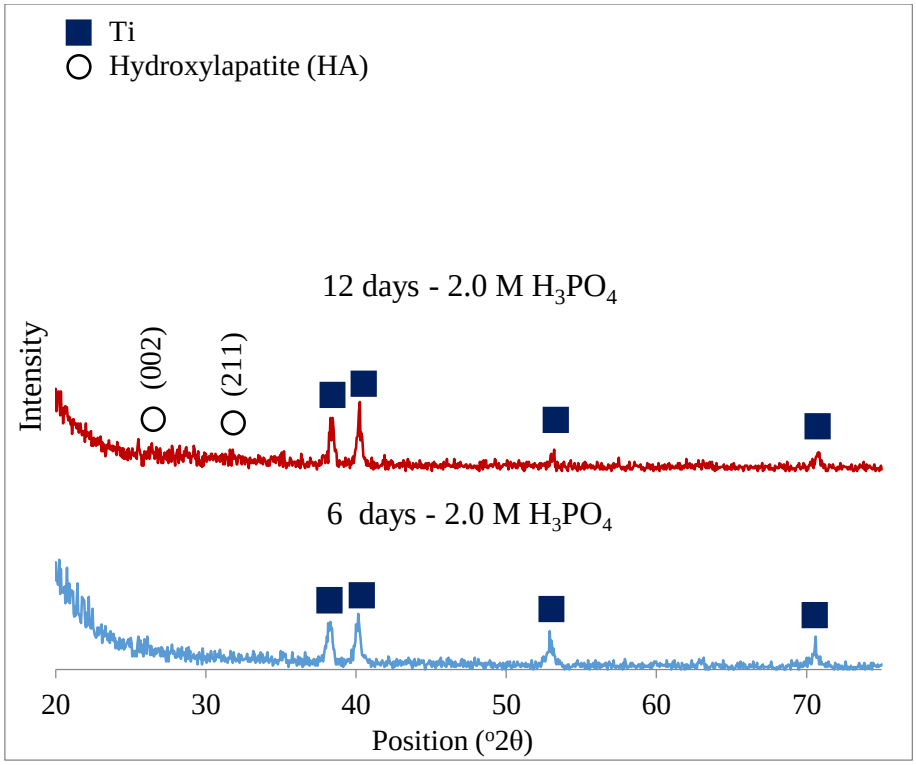

Figure 5.22: Phase mineralogical patterns for apatite precipitation in SBF for 6 and 12 days in the dark for coatings anodised at 150 V and 100 mA.cm^{-2} in 2.0 M H_3PO_4 electrolyte

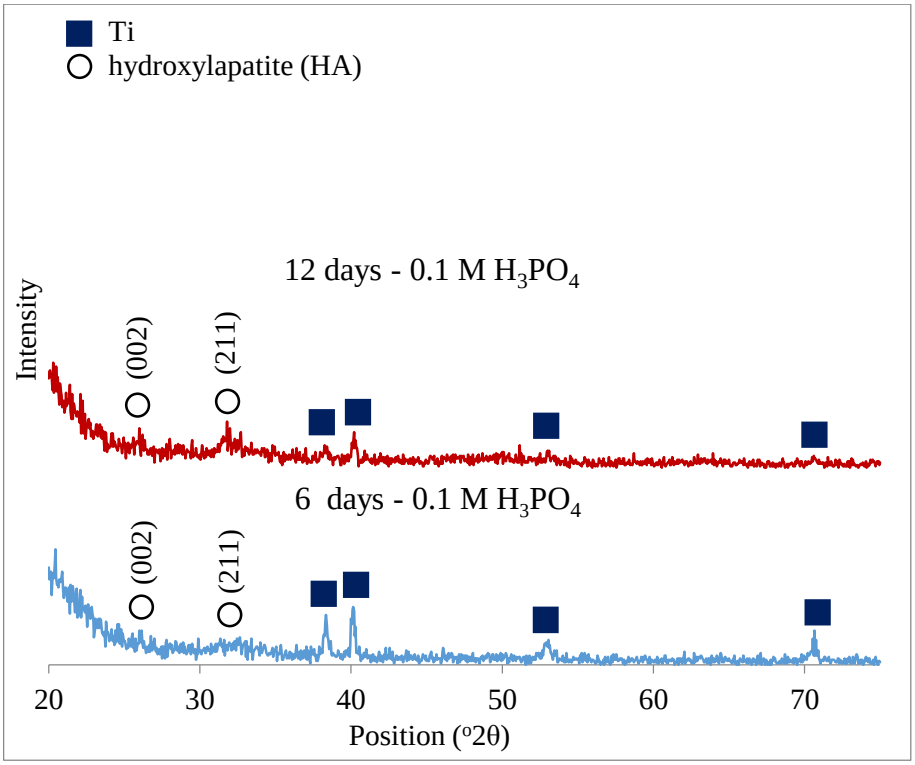

Figure 5.23: Phase mineralogical patterns for apatite precipitation in SBF for 6 and 12 days under UV for coatings anodised at 150 V and 100 mA.cm^{-2} in 0.1 M H_3PO_4 electrolyte

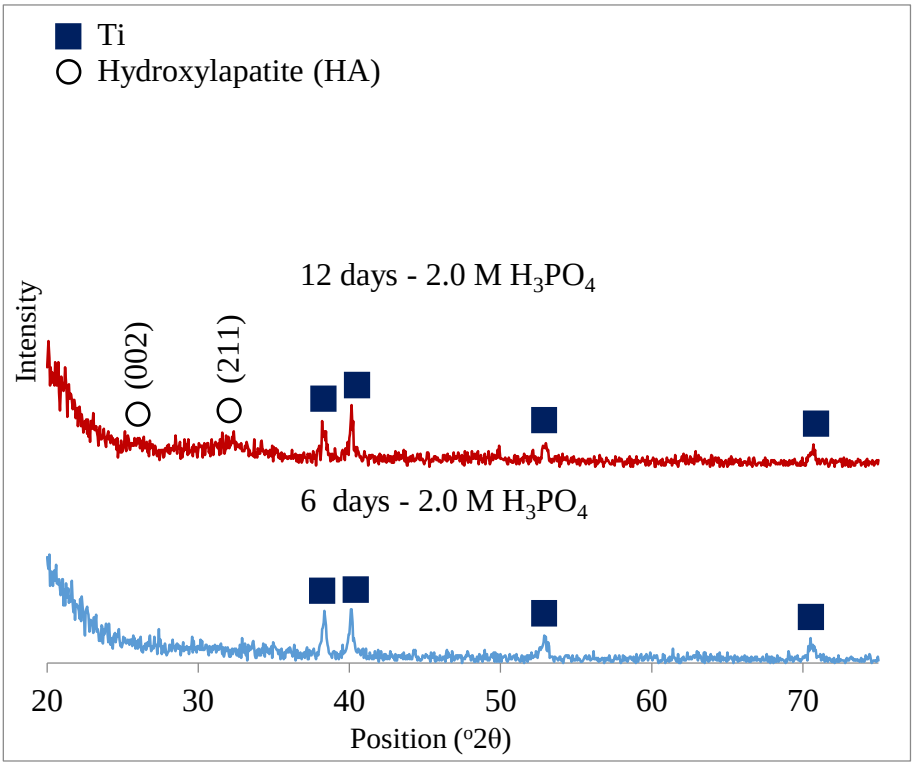

Figure 5.24: Phase mineralogical patterns for apatite precipitation in SBF for 6 and 12 days under UV for coatings anodised at 150 V and 100 mA.cm^{-2} in 2.0 M H_3PO_4 electrolyte

073-6113) respectively. All the crystalline coatings have that obtained crystalline peaks with orientations (002) and (211).

All the coatings have obtained crystalline apatite peaks after 12 days of incubation in the dark and under the UV. However, the crystalline peaks of the apatite formed under the UV as seen in Figure 5.21 (a) for 0.1 M and Figure 5.22 (a) for 2.0 M were higher than the ones formed in the dark as obtained in Figure 5.23 (a) for 0.1 M and Figure 5.24 (a) for 2.0 M. The patterns that didn't obtain crystalline peaks have an amorphous apatite in the apatite formed at 2.0 M for 6 days in the dark (Figure 5.22 (b)) and their corresponding apatite formed under the UV (Figure 5.24 (b)). While the remaining coating anodised in 0.1 M has obtained no apatite (Figure 5.21 (b)). this has been cleared by the elemental analysis, where the small precipitations on the coating have obtained no Ca or P (Figure 5.21 (a)).

It can be noticed that the apatite mineralogy has obtained the same results with the ones in H_2SO_4 electrolyte, where the UV irradiation has promoted an earlier apatite formation on both coatings at 0.1 M and 2.0 M and earlier crystallization at 0.1 M. However, unlike H_2SO_4 electrolyte the crystalline apatite formed under the UV (Figure 5.21 and Figure 5.22) has obtained an increased intensity than the apatite formed in the dark (Figure 5.23 and Figure 5.24). In general, the coatings anodised in 0.1 M have obtained higher apatite crystalline than the coating anodised in 2.0 M.

The apatite that formed in the dark (Figure 5.21 and Figure 5.22) has no external catalyst or stimulator, which can be an indication of the coating ability strength to induce apatite. While the increased crystalline apatite (Figure 5.23 and Figure 5.24) that corresponds to the higher apatite formed under the UV (Figure 5.16) can indicate that the UV has stimulated higher apatite formation and crystallization. This phenomenon can be related to the mechanism as explained in **Section 2.10.3**.

The microstructure image results in Figure 5.15 for the apatite formed in the dark and in Figure 5.16 for the apatite formed under the UV are in a positive matching with the mineralogical results as obtained in Figure 5.7 and Figure 5.8 for the apatite formed in the dark, and for Figure 5.9 and Figure 5.10 for the ones formed under the UV. It can be noticed that the increased apatite formed according to the microstructure images has obtained an increase in the apatite crystalline according to the mineralogical patterns. This can be obtained in the apatite formed under the UV has obtained an increased precipitation and crystallization than the apatite formed in the

dark. It has been reported that with the growth of the apatite on TiO_2, the structure change from amorphous to crystalline on the surface (Liu *et al.*, 2008; Ueda *et al.*, 2009).

In a comparison between the mineralogical results of the apatite formed on the coatings anodised in the H_3PO_4 electrolyte with their corresponding in the H_2SO_4 electrolyte. It can be noticed that the crystalline apatite formed under the UV in H_2SO_4 electrolyte has almost the same crystalline intensity with their corresponding in the H_3PO_4 electrolyte. While the coatings anodised in H_2SO_4 electrolyte has obtained a progressed apatite crystalline over their corresponding in the H_3PO_4 electrolyte in the dark. This can be obtained after 12 days of incubation on 0.1 M (Figure 5.7 (a)) and on 2.0 M (Figure 5.8 (a)) after 6 days. This can give an advantage of apatite crystallinity formed on H_2SO_4 electrolyte over H_3PO_4 electrolyte.

The crystalline coatings that were on the coatings anodised in the H_2SO_4 electrolyte (Figure 4.10 (a) and Figure 4.11 (a)) has been given an advantage regarding the apatite crystalline over the amorphous coatings of H_3PO_4 electrolyte (Figure 4.27 (a) and Figure 4.28 (a)). This can be obtained at the coatings incubated in the dark has obtained higher apatite crystalline in the H_2SO_4 electrolyte (Figure 5.7 and Figure 5.8). The crystalline apatite of the coatings under the UV on both coatings has obtained to be the same. This is due to the apatite induction has been forced by the UV irradiation. Moreover, the crystalline has obtained to be higher on the coatings anodised in 0.1 M at both electrolytes in the dark (Figure 5.7 and Figure 5.21) and under the UV (Figure 5.8 and Figure 5.22). It can be noticed that the coatings anodised at 0.1 M at both electrolytes have obtained stronger $Ti\text{-}O^-$ group stretching as obtained in Figure 4.17 for H_2SO_4 electrolyte and in Figure 4.34 for the H_3PO_4 electrolyte.

In general, it can be concluded that there are several factors that can affect the apatite formation and crystallization between the H_2SO_4 electrolyte and H_3PO_4 electrolyte. The higher apatite formation and crystallization in the dark and under the UV conditions were obtained on the coatings that obtained lower microstructure surface porosity, higher $Ti\text{-}O^-$ functional groups and the lower acidic incorporated ions on the coatings surface. All of these factors have been obtained on the coatings that were anodised in 0.1 M in both electrolytes. Moreover, the anatase crystalline advantage compared to the amorphous and the stronger and stable $Ti\text{-}O^-$ groups of the coating anodised in 0.1 M can be related to the apatite formation and crystallization of H_2SO_4 electrolyte over the coating anodised in the H_3PO_4 electrolyte.

5.3.4 Absorption of the Apatite Formation on TiO_2 in Anodised in H_3PO_4 Electrolyte

Figure 5.25 and Figure 5.26 obtain the absorption analysis patterns of the coatings anodised in 0.1 M and 2.0 M respectively immersed in SBF in the dark. While Figure 5.27 and Figure 5.28 obtain for the coatings immersed under the UV irradiation for 0.1 M and 2.0 M respectively.

The phosphate stretching has increased with the increased incubation time in the SBF in the dark (Figure 5.25 and Figure 5.26) and under the UV (Figure 5.27 and Figure 5.28). The phosphate stretching was higher for the apatite precipitated under the UV (as obtained in Figure 5.27 and Figure 5.28) than the apatite formed in the dark as seen in Figure 5.25 and Figure 5.26. It can also be noticed that the phosphate stretching of the apatite formed in the SBF in the dark had the same intensity for the coatings produced in 0.1 M (Figure 5.25) and 2.0 M (Figure 5.26). However, the phosphate for the apatite formed under the UV was higher on 0.1 M (Figure 5.27) and at its highest intensity after 12 days of incubation as seen in Figure 5.27 (a).

The phosphate intensity can indicate the apatite density on the coating (Mary *et al.*, 2016). It can be noticed that the higher apatite density does agree with the high crystalline peaks in **Section 5.3.4** as obtained on the apatite incubated in SBF after 12 days as obtained in Figure 5.21 (a), Figure 5.22 (a), Figure 5.23 (a) and Figure 5.24 (a).

The higher apatite density according to the absorption analysis was obtained of the apatite precipitated under the UV, and it in on an agreement with the mineralogical results that has slightly higher crystalline peaks on the patterns of apatite precipitated under the UV Figure 5.8 and Figure 5.10. Therefore, this can confirm that the UV promotes higher crystalline structure with the increased apatite density. However, the results in H_2SO_4 electrolyte did not obtain an increased crystalline intensity with the increased in the apatite density under UV as discussed in **Section 5.2.5.**

There is a clear relation with the microstructure images in **Section 5.3.2**, where the higher apatite density does agree with the higher apatite precipitation. These results have obtained to be similar to results in the H_2SO_4 electrolyte. However, the phosphate stretching of the apatite produced in the dark, especially after 6 days in SBF have obtained to be stronger in H_3PO_4 electrolyte than in H_2SO_4 electrolyte (Figure 5.25 and Figure 5.26), although the apatite obtained was very little according to the

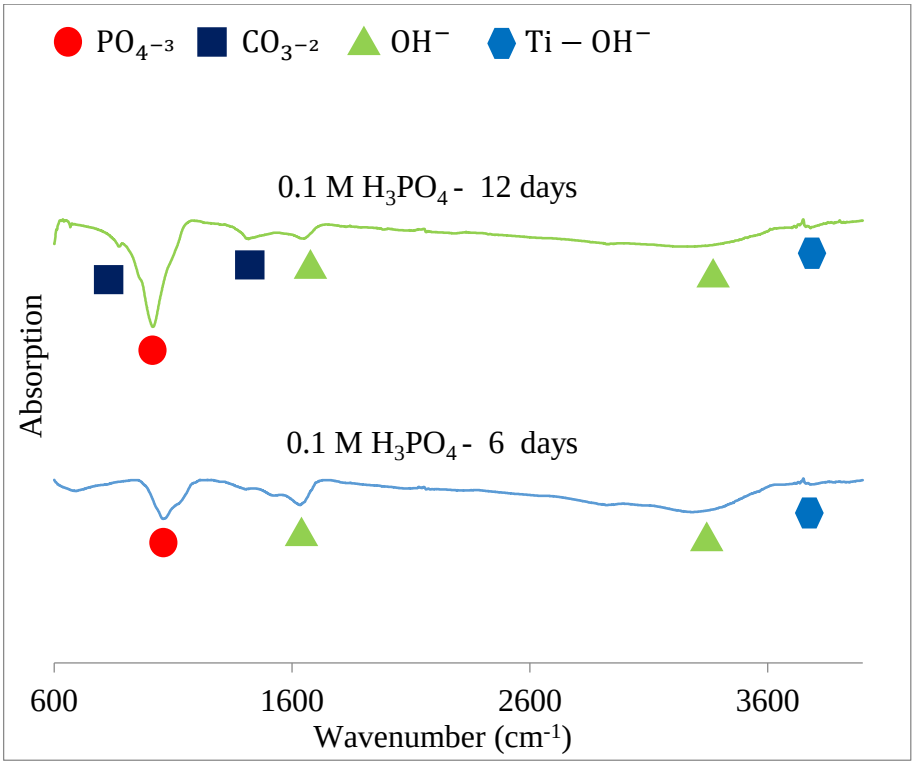

Figure 5.25: Absorption analysis patterns for apatite precipitation in SBF for 6 and 12 days in the dark for coatings anodised at 150 V and 100 mA.cm^{-2} in 0.1 M H_2SO_4 electrolyte

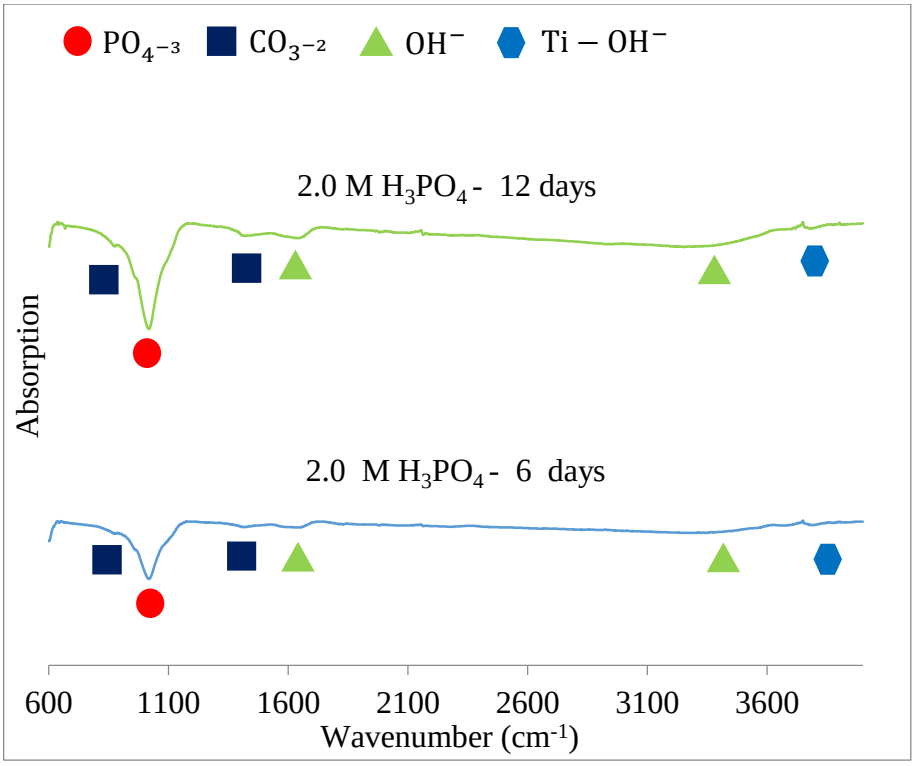

Figure 5.26: Absorption analysis patterns for apatite precipitation in SBF for 6 and 12 days in the dark for coatings anodised at 150 V and 100 mA.cm^{-2} in 2.0 M H_2SO_4 electrolyte

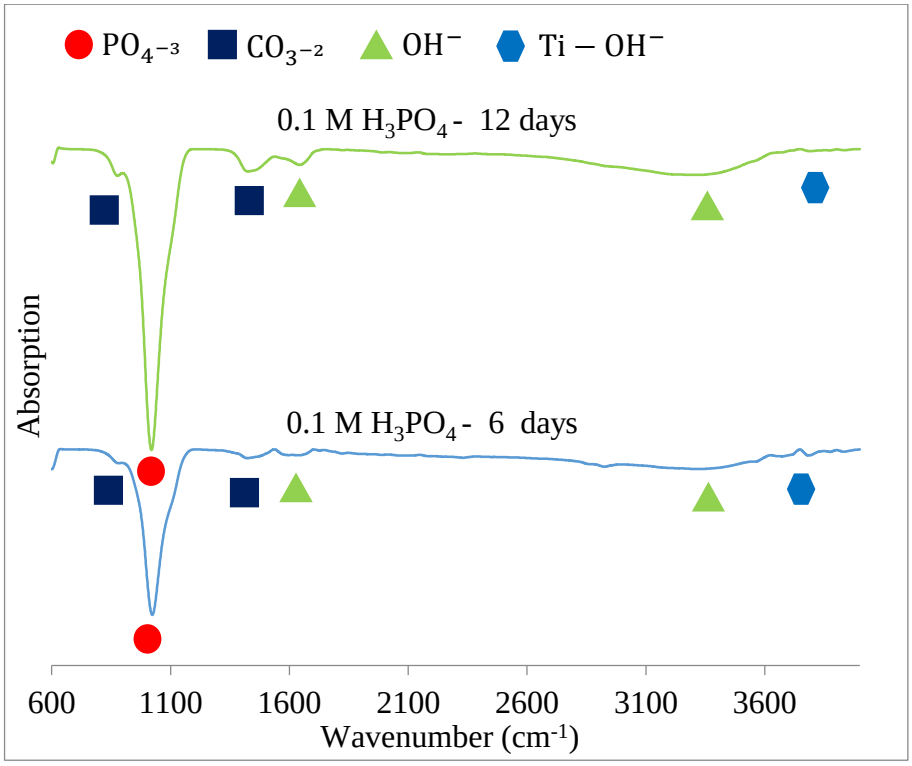

Figure 5.27: Absorption analysis Patterns for apatite precipitation in SBF for 6 and 12 days under UV for coatings anodised at 150 V and 100 $mA.cm^{-2}$ in 0.1 M H_2SO_4 electrolyte

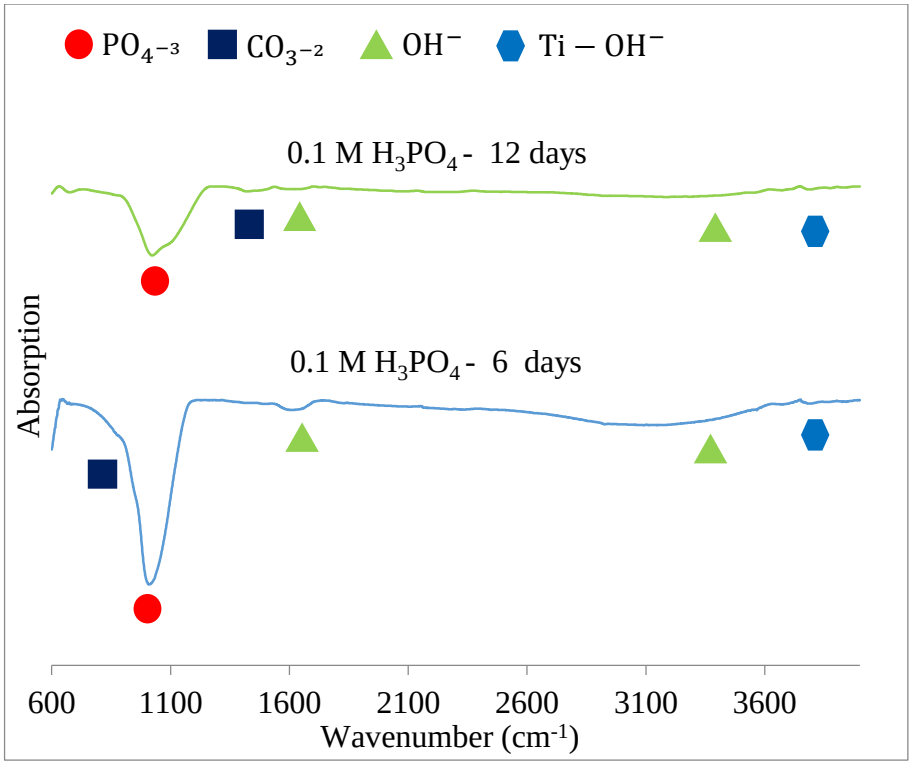

Figure 5.28: Absorption analysis Patterns for apatite precipitation in SBF for 6 and 12 days under UV for coatings anodised at 150 V and 100 $mA.cm^{-2}$ in 2.0 M H_2SO_4 electrolyte

microstructure images (Figure 5.15 (a and b)) when compared with H_2SO_4 electrolyte. This can be related to the P ions that was incorporated into the coating has affected the intensity pattern.

Both electrolytes have obtained a common advantageous apatite formation on the coating anodised in 0.1 M. The coating at 0.1 M have obtained higher apatite formation according to the microstructure images at H_2SO_4 electrolyte and H_3PO_4 electrolyte, a progressed HA crystalline as obtained in the mineralogical analysis, the ratio of crystalline HA after 12 days in SBF as obtained in Figure 5.7 (c) and Figure 5.21 (c) for H_2SO_4 electrolyte and H_3PO_4 electrolyte respectively. Also, the higher apatite density according to the absorption analysis after incubated in SBF under the UV for 12 days as obtained in Figure 5.11 and Figure 5.25 respectively. Also the apatite formed on the coating anodised in 0.1 M as obtained in Figure 5.1 (a and c) and Figure 5.15 (a and c) respectively, after incubated in SBF in the dark condition have obtained a progressed results over their corresponding apatite formed in 2.0 M (Figure 5.1 (b and d) and Figure 5.15 (b and d)). Incubation for 12 days was enough to distinguish the advantageous of apatite formed on 0.1 M coating over the coating anodised in 2.0 M on H_2SO_4 and H_3PO_4 electrolytes.

5.4 Apatite Formation Evaluation on TiO_2 Coatings Anodised in Mixture of Sulphuric acid (H_2SO_4) and Phosphoric acid (H_3PO_4) Electrolyte

The TiO_2 coatings in mixed electrolyte were subjected to *in vitro* test using SBF in the dark and under the UV. Microstructure, morphology, mineralogy, and surface energy of the coatings will be discussed.

5.4.1 Microstructure of Apatite Formed on TiO_2 Anodised in Mixed Electrolyte

Figure 5.29 and Figure 5.30 obtain the surface image microstructure of the coating anodised in mixed electrolyte captured of the coatings immersed in SBF in the dark and under the UV respectively. Table 5.3 obtained the apatite-forming ability of the coating immersed in the dark and under the UV as a function of electrolyte molarity.
In the dark condition, the coating anodised in 2.0 M H_2SO_4 + 0.1 M H_3PO_4 has obtained the highest apatite formation as shown in Figure 5.29 (c and f). While the

lowest formation was obtained on the coating that was anodised in 0.1 M H_2SO_4 + 2.0 M H_3PO_4. Both the coatings anodised in 0.1 M H_2SO_4 + 0.1 M H_3PO_4 and in 2.0 M H_2SO_4 + 0.1 M H_3PO_4 have obtained a full floor covered apatite as obtained in Figure 5.29 (d and f). It can be noticed that the higher apatite formation at 2.0 M H_2SO_4 + 0.1 M H_3PO_4 is believed to be related to Ti-OH functional groups according to the absorption analysis obtained in Figure 4.55. The Ti-OH was reported to interact with the OH^- in SBF to form Ti-O^- radiacals that is responsible for apatite nucleation (Ueda *et al.*, 2010; Uetsuki *et al.*, 2010). This is considered advantage when compared to the coating anodised in 2.0 M H_2SO_4 electrolyte only that didn't obtain similar apatite formation ability. Although it has obtained porous structure with smaller pores (Figure 4.4 (h)) and weak Ti-O^- functional groups (Figure 4.18). Also considered advantageous over the coating anodised in 0.1 M H_3PO_4 that didn't obtain similar apatite ability although it has obtained stronger Ti-O^- functional groups (Figure 4.33). This is can be got something to do with the mixed acidic ions, i.e., S and P, incorporated on the coating anodised in 2.0 M H_2SO_4 + 0.1 M H_3PO_4 (Figure 4.40 (f)). That has promoted atomic order, i.e., strong anatase crystalline (Figure 4.48) that promote higher apatite formation. Also has promoted higher porosity with larger porous than the other coatings with sponge-like shape porous as obtained in Figure 4.38 (o). This comparison can also be applied to the coating anodised in 0.1 M H_2SO_4 + 0.1 M H_3PO_4 with the coating andozied in 0.1 M H_2SO_4 and in 0.1 M H_3PO_4. Where at 0.1 M H_2SO_4 + 0.1 M H_3PO_4 has obtained higher apatite formation ability (Figure 5.30 (a and d)). Although it hasn't obtained advantageous crystalline structure (Figure 4.42), not stronger Ti-O functional groups (Figure 4.53) than the ones formed at 0.1 M H_2SO_4 (Figure 4.17). This advantageous apatite formation ability at 0.1 M H_2SO_4 + 0.1 M H_3PO_4 can also be related to the mixed acidic ions incorporated into the coating (Figure 4.40 (d)). However, the lower porosity of the coating (Figure 4.4 (d)) might also be related to the increased apatite formation.

Table 5.3: The apatite forming ability of the coatings anodised in mixed electrolyte immersed in the dark and under the UV as a function of electrolyte molarity

In vitro treatment	SBF			SBF + UV		
H_2SO_4 electrolyte molarity	0.1 S + 0.1 P	0.1 S + 2.0 P	2.0 S + 0.1 P	0.1 S + 0.1 P	0.1 S + 2.0 P	2.0 S + 0.1 P
6 days	++	+	++	++	+++	++++
12 days	+++++	++	+++++	++++	++++	++++

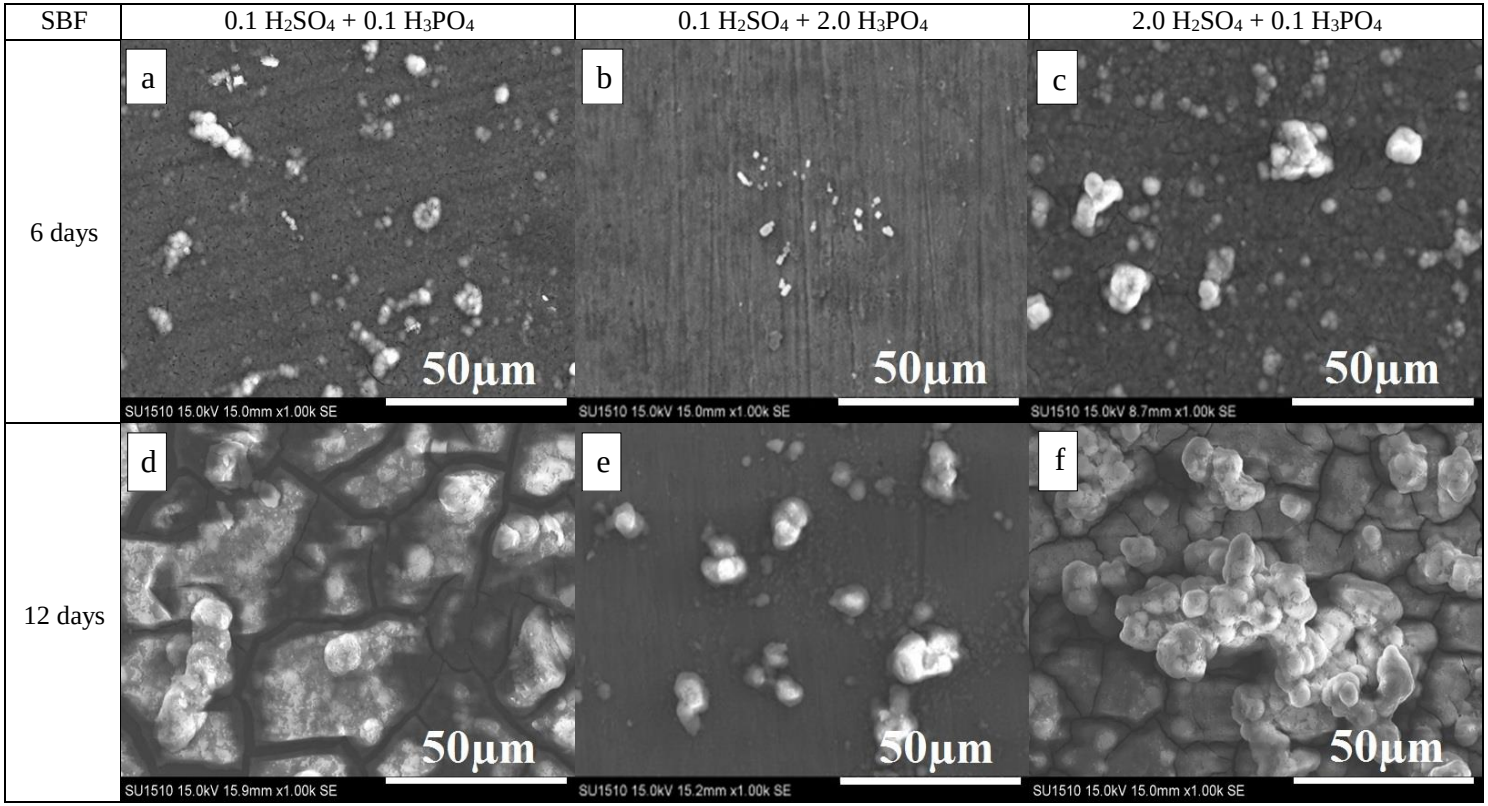

Figure 5.29: Surface microstructure images of the coatings produced in mixed electrolytes at 150 V and 100 mA.cm^{-2} immersed in SBF for 6 and 12 days in the dark for 6 and 12 days

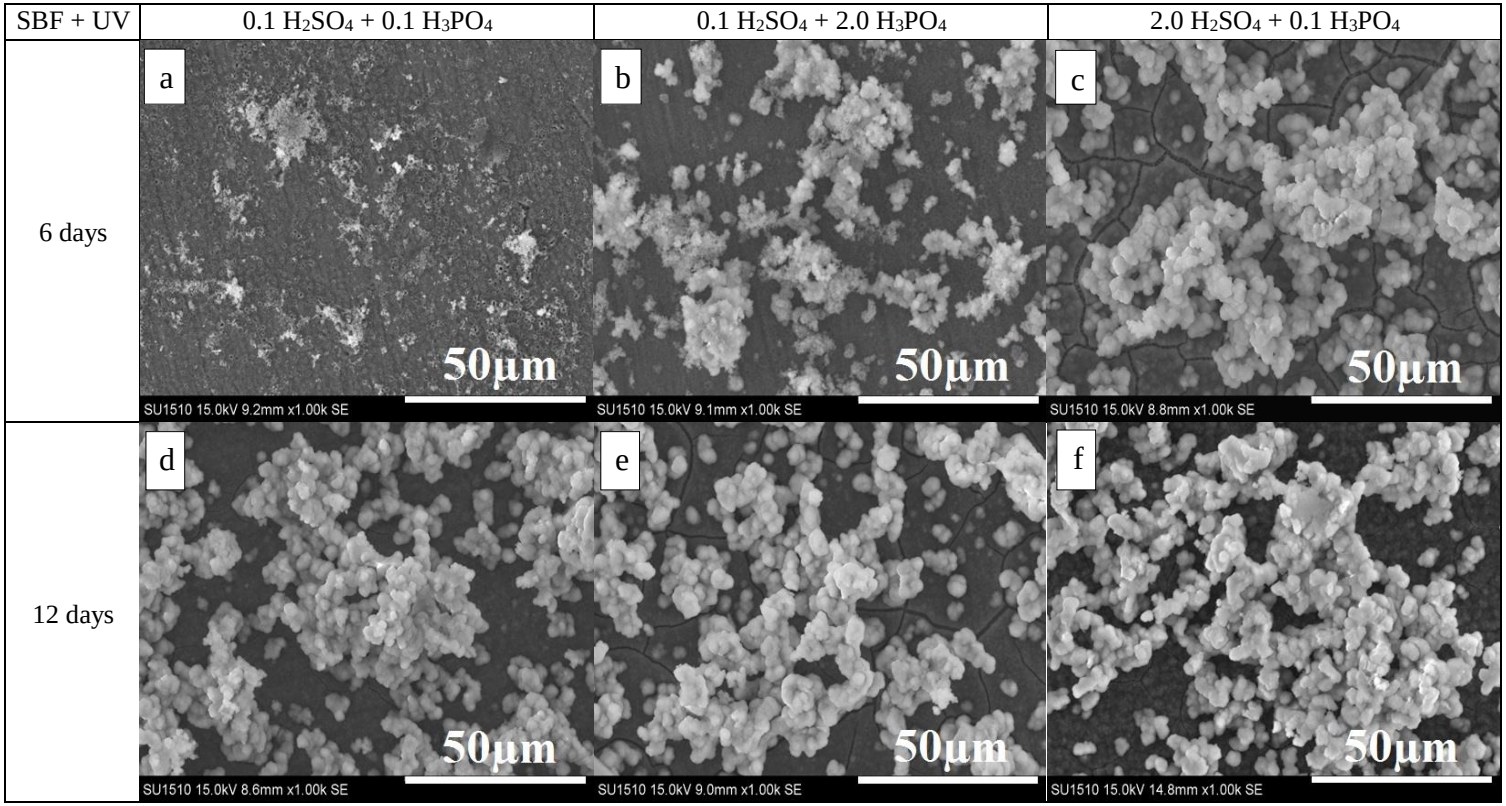

Figure 5.30: Surface microstructure images of the coatings produced in mixed electrolytes at 150 V and 100 mA.cm^{-2} immersed in SBF for 6 and 12 days under the UV for 6 and 12 days

While the coating anodised in 2.0 M H_3PO_4 + 0.1 M H_2SO_4 has obtained the lowest apatite formation after 6 and 12 days as obtained in Figure 5.29 (b and e). This is can be related to the increased P ions that were incorporated into the TiO_2 coating according to the elemental analysis obtained in Figure 4.40 (e). The concentrated P ions can somehow obstruct the formation of functional groups on the coating surface. The apatite formed under the UV has also resulted in higher apatite formed at an earlier time (6 days) at 0.1 M H_3PO_4 + 2.0 M H_2SO_4 (Figure 5.30 (c)), while the apatite was formed equally after 12 days of incubation (Figure 5.30 (d,e and f)). However, the apatite formed at 0.1 M H_3PO_4 + 0.1 M H_2SO_4 has obtained the lowest apatite formation at the earlier time of incubation (6 days) (Figure 5.30 (a)). The change in the apatite formation can be explained as the UV provoked the photocatalysis activity of the coatings surface and increased the apatite growth, where the microstructure effect can be minimized when the coatings applied for UV. This is can be obtained clearly at 2.0 M H_3PO_4 + 0.1 M H_2SO_4. Where it has obtained higher apatite formed under the UV (Figure 5.30 (b and e)) than the apatite formed in the dark (Figure 5.29 (b and e)). However, it didn't obtain strong Ti-O^- stretching (Figure 4.54). The higher porosity, coating thickness, mixed acidic ions within the coatings, TiO_2 anatase crystalline, hydrophilicity and Ti-OH functional groups that was obtained at 2.0 M H_3PO_4 + 0.1 M H_2SO_4 is believed to cause the higher apatite formation. It has been reported that osseointegration is better led by higher surface roughness, higher wettability and increased number and size of micro-pores (Das *et al.*, 2007; Zhu *et al.*, 2004).

5.4.2 Elements of the Apatite Formation on TiO_2 Anodised in Mixed Electrolyte

Figure 5.31 and Figure 5.32 obtain Ca to P ratio for apatite formation precipitated in the dark and under the UV respectively. While Figure 5.33 and Figure 5.34 obtain the bar chart to compare the Ca to P ratio of the apatite formed in SBF in the dark and under UV.

It can be noticed that the Ca to P ratio has increased with the increased incubation time in the dark and under the UV conditions. However, the ratio values fluctuate and cannot distinguish that which condition has higher ratio values. None of the coatings has obtained the Ca to P ratio of the stoichiometric HA (Ca/P = 1.67) of

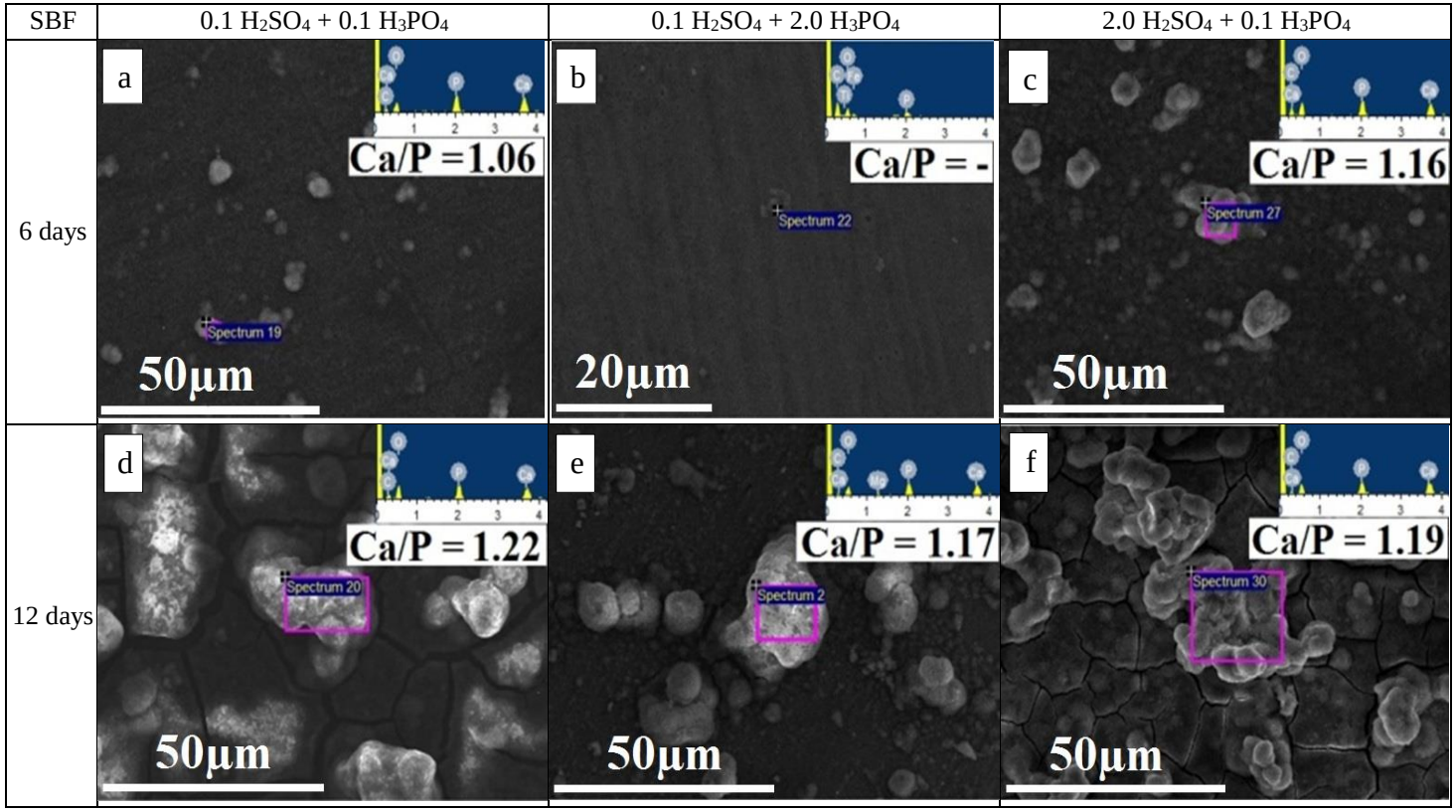

Figure 5.31: Ca to P ratio of the coatings produced in mixed electrolyte at 150 V and 100 mA.cm^{-2} immersed in SBF in the dark for 6 and 12 days

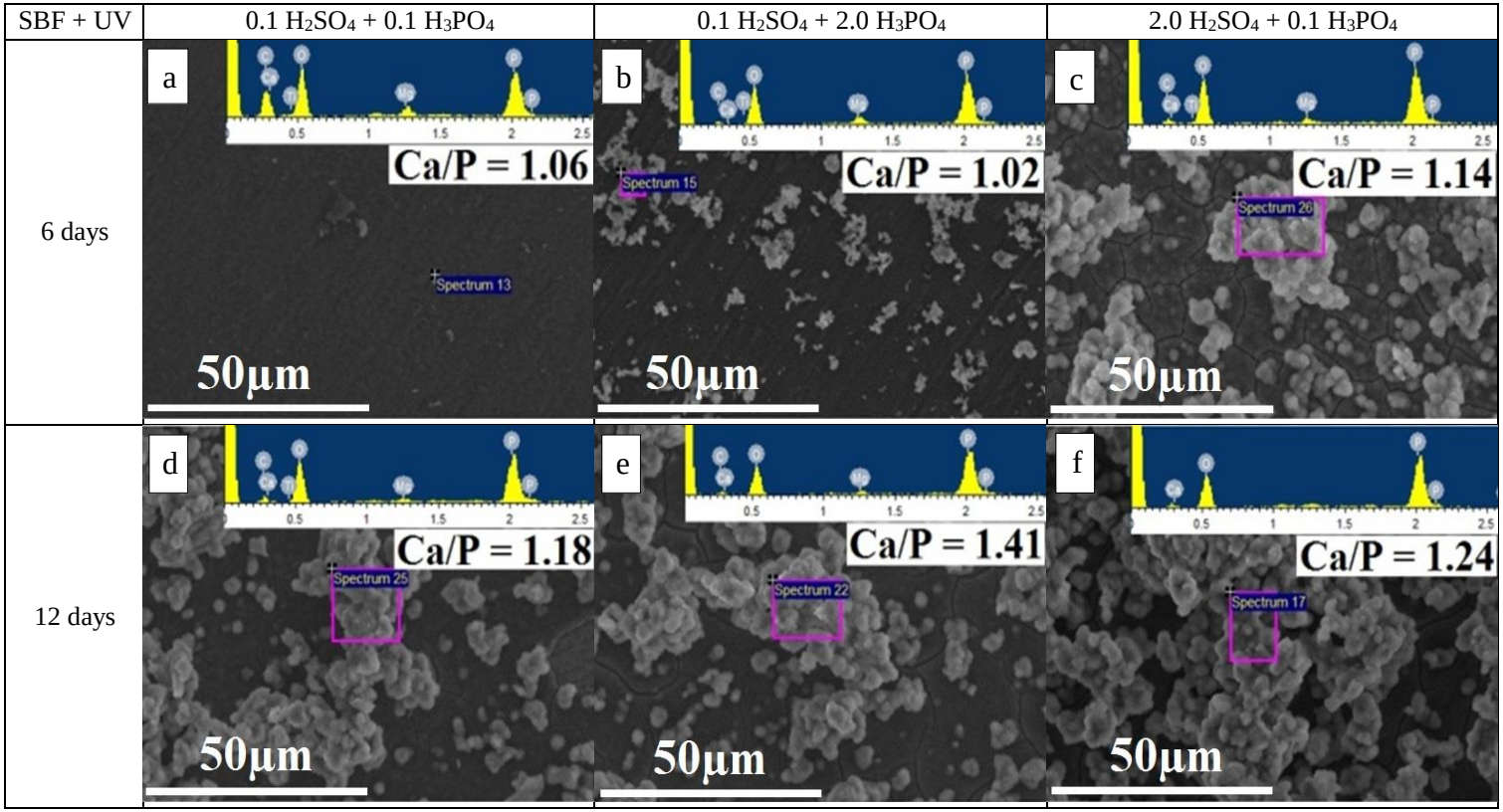

Figure 5.32: Ca to P ratio of coatings produced in mixed electrolyte at 150 V and 100 mA.cm^{-2} immersed in SBF under UV for 6 and 12 days

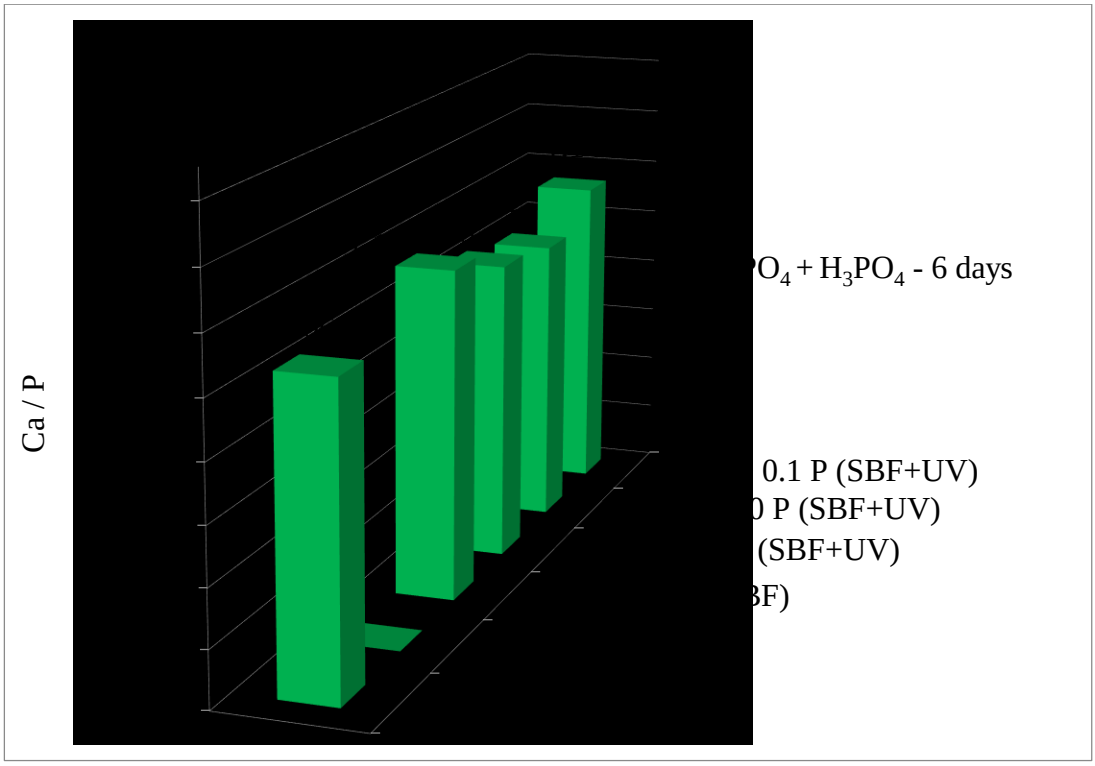

Figure 5.33: Bar chart of Ca to P ratio of coatings produced in mixed electrolyte at 150 V and 100 mA.cm^{-2} immersed for 6 days in SBF in the dark and under UV

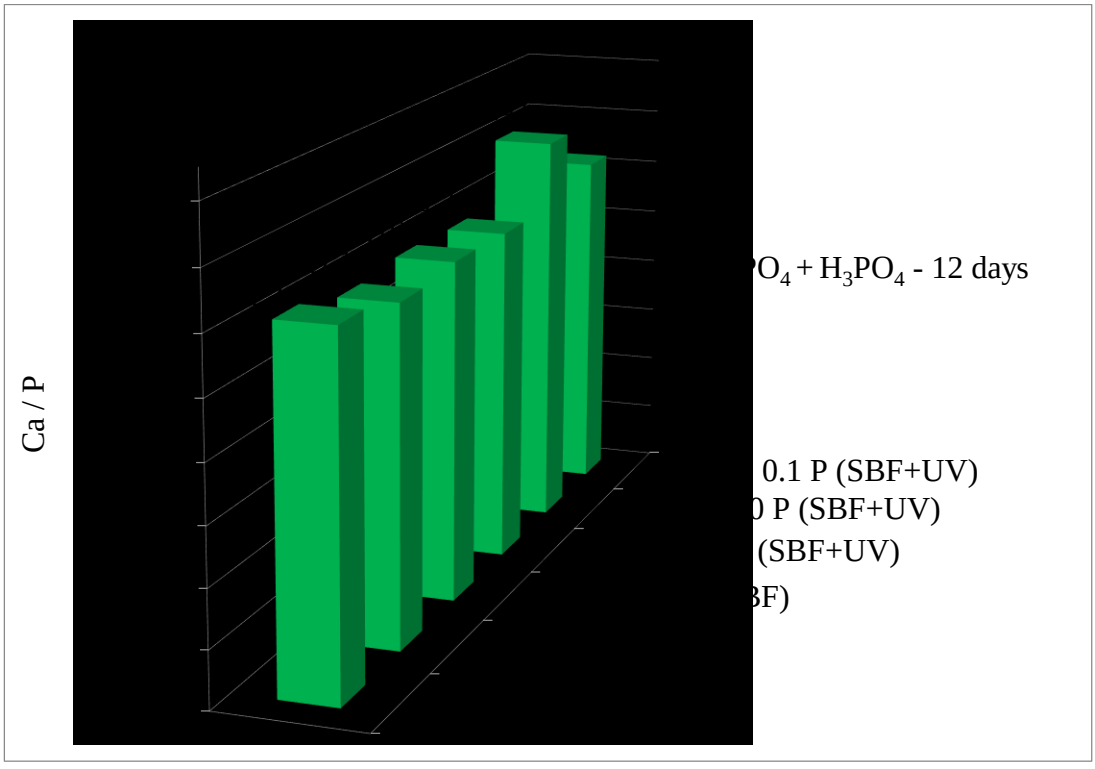

Figure 5.34: Bar chart of Ca to P ratio of coatings produced in mixed electrolyte at 150 V and 100 mA.cm^{-2} immersed for 12 days in SBF in the dark and under UV

neither human bone nor the ratio of calcium-deficient HA (Ca/P = 1.5 - 1.67) (Ramesh *et al.*, 2007; Zyman *et al.*, 2013). This can indicate that the apatite precipitated on the coating is amorphous calcium phosphates.

However, these coatings have not obtained higher apatite precipitation after 6 days of incubation as obtained in Figure 5.1 (c) and Figure 5.15 (c) respectively. These coatings have obtained single incorporated ions on their coating. As the coating anodised in 0.1 M H_2SO_4 has obtained S ions (Figure 4.7 (c)) and P ions incorporated on 0.1 M H_3PO_4 (Figure 4.24 (c)). While the coating anodised in 0.1 M H_3PO_4 + 0.1 M H_2SO_4 has obtained S and P ions incorporated within the coatings as obtained in Figure 4.40 (d). This mixed ions incorporated, higher hydrophilicty, higher coating thickness can be behind the higher apatite formed at an earlier stage (Figure 5.29 (a)), compared to the apatite formed at 0.1 M H_2SO_4 (Figure 5.1 (a)) and 0.1 M H_3PO_4 (Figure 5.15 (a)).

5.4.3 Mineralogy of the Apatite Formation on TiO_2 Anodised in Mixed Electrolyte

Figure 5.35, Figure 5.36 and Figure 5.37 obtain the mineralogical patterns of coatings anodised in 0.1 M H_2SO_4 + 0.1 M H_3PO_4, 0.1 M H_2SO_4 + 2.0 M H_3PO_4 and 2.0 M H_2SO_4 + 0.1 M H_3PO_4 respectively immersed in SBF in dark for 6 and 12 days. Figure 5.38, Figure 5.39 and Figure 5.40 obtain the mineralogical patterns of coatings immersed under the UV.

The patterns as obtained in Figure 5.35, Figure 5.36 and Figure 5.37 correspond to the coatings incubated in SBF in the dark, while the patterns as obtained in Figure 5.38, Figure 5.39 and Figure 5.40 correspond to the coatings incubated in SBF under the UV irradiation. The phase mineralogical analysis has confirmed the formation of the crystalline apatite HA (JCPDS card #00-055-0592) on all the crystalline coatings, except the coating anodised in 0.1 M H_3PO_4 + 2.0 M H_2SO_4 that was incubated in the dark and under the UV, where they have obtained HA (JCPDS card #00-024-0033) All the crystalline coatings have that obtained crystalline peaks with orientations (002) and (211).

All the coatings have obtained crystalline apatite peaks in the dark and under the UV after 12 days, while the crystalline apatite at an earlier time has only been

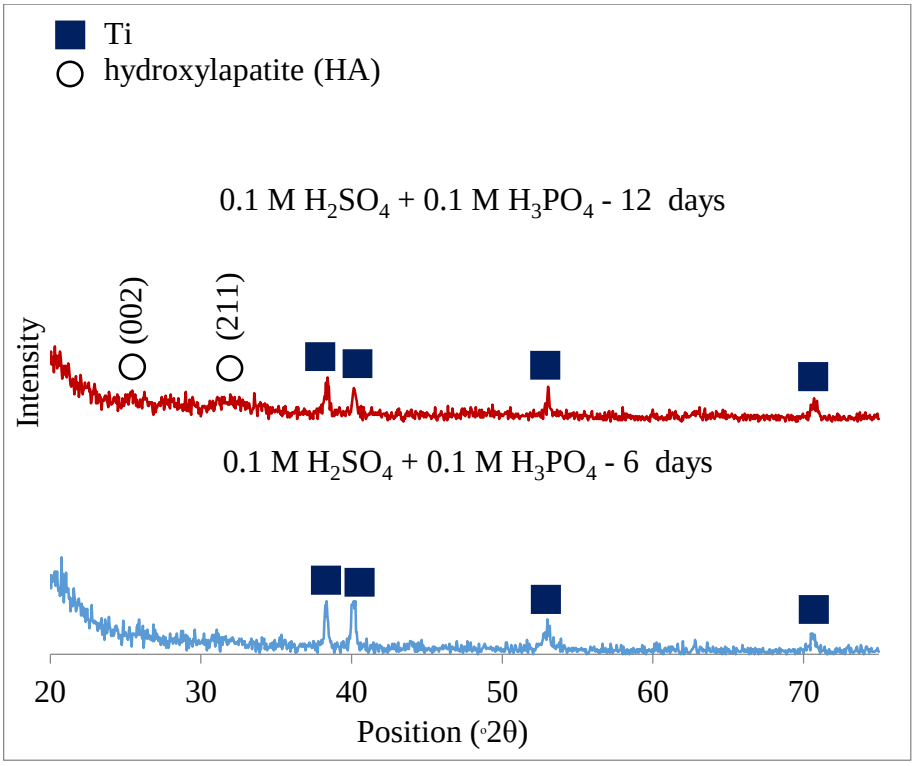

Figure 5.35: Phase mineralogical patterns for apatite precipitation in SBF for 6 and 12 days in the dark for coatings anodised at 150 V and 100 mA.cm^{-2} in 0.1 M H_2SO_4 + 0.1 M H_3PO_4 electrolyte

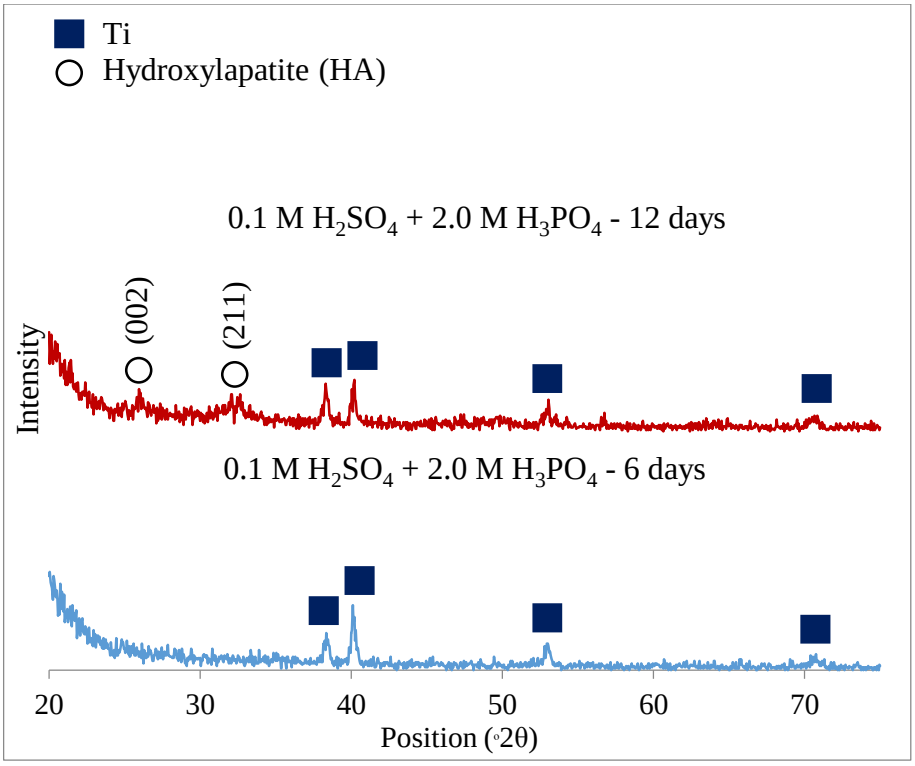

Figure 5.36: Phase mineralogical Patterns for apatite precipitation in SBF for 6 and 12 days in the dark for coatings anodised at 150 V and 100 mA.cm^{-2} in 0.1 M H_2SO_4 + 2.0 M H_3PO_4 electrolyte

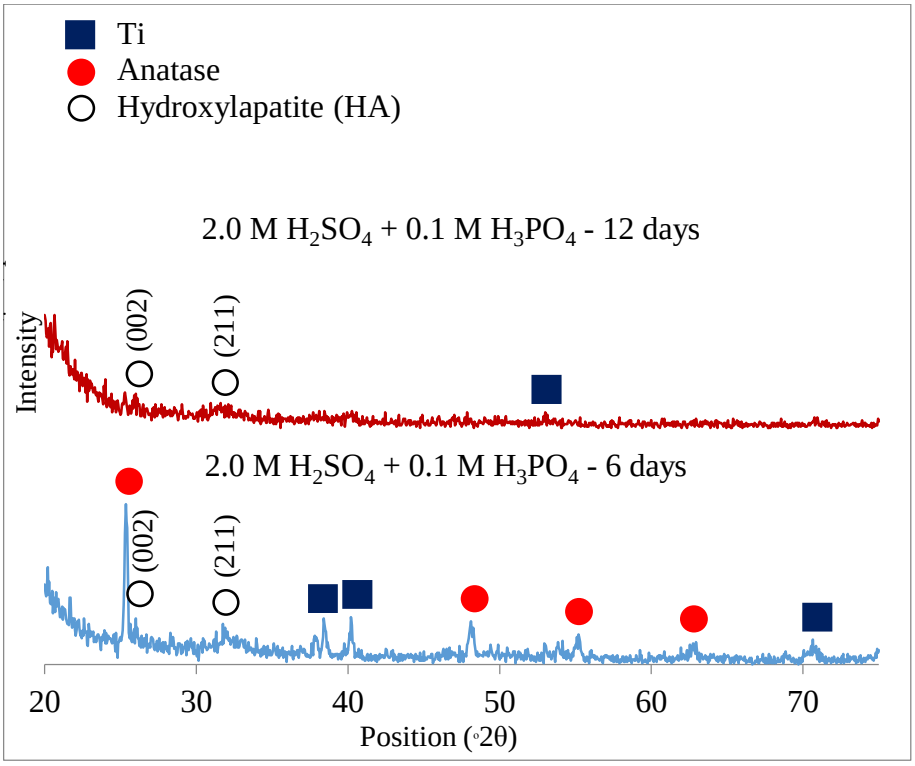

Figure 5.37: Phase mineralogical Patterns for apatite precipitation in SBF for 6 and 12 days in the dark for coatings anodised at 150 V and 100 mA.cm^{-2} in 2.0 M H_2SO_4 + 0.1 M H_3PO_4 electrolyte

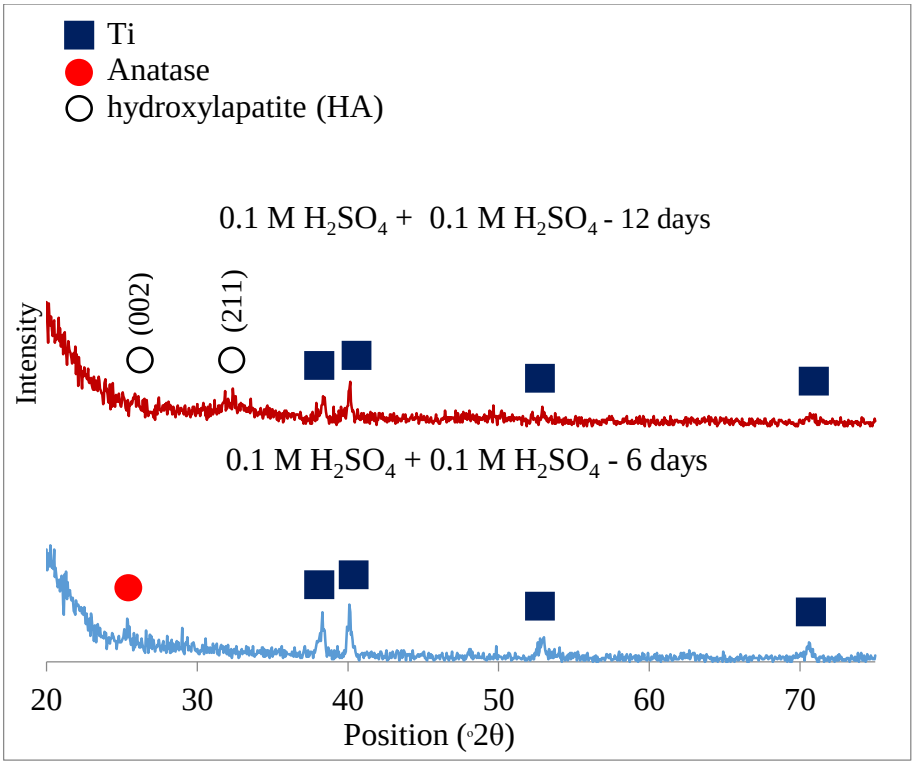

Figure 5.38: Phase mineralogical Patterns for apatite precipitation in SBF for 6 and 12 days under UV for coatings anodised at 150 V and 100 mA.cm^{-2} in 0.1 M H_2SO_4 + 0.1 M H_3PO_4 electrolyte

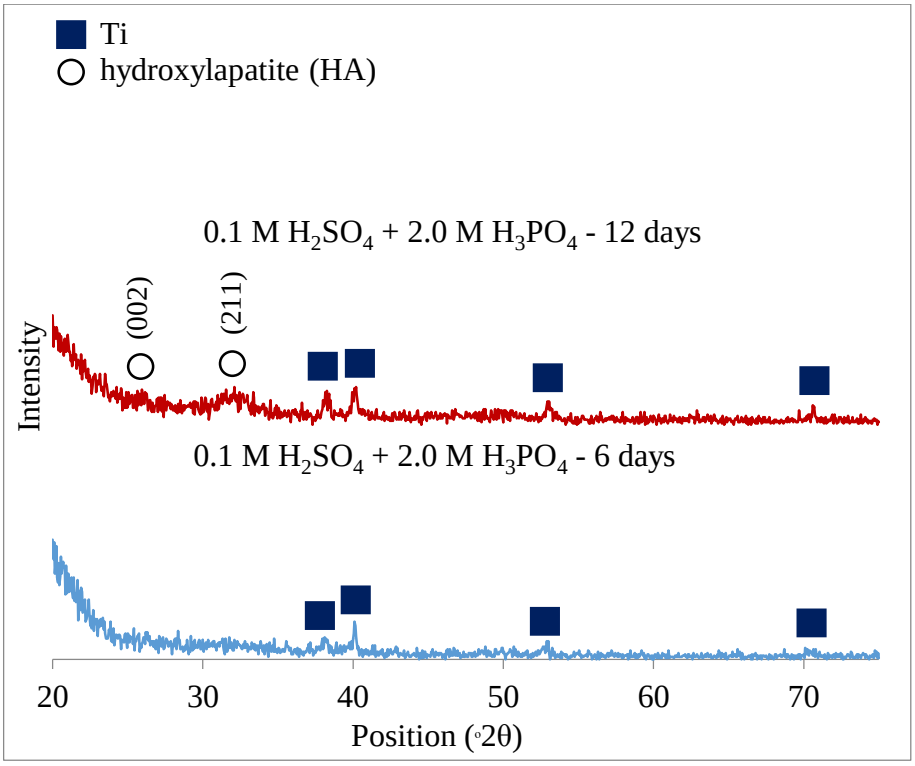

Figure 5.39: Phase mineralogical Patterns for apatite precipitation in SBF for 6 and 12 days under UV for coatings anodised at 150 V and 100 mA.cm^{-2} in 0.1 M H_2SO_4 + 2.0 M H_3PO_4 electrolyte

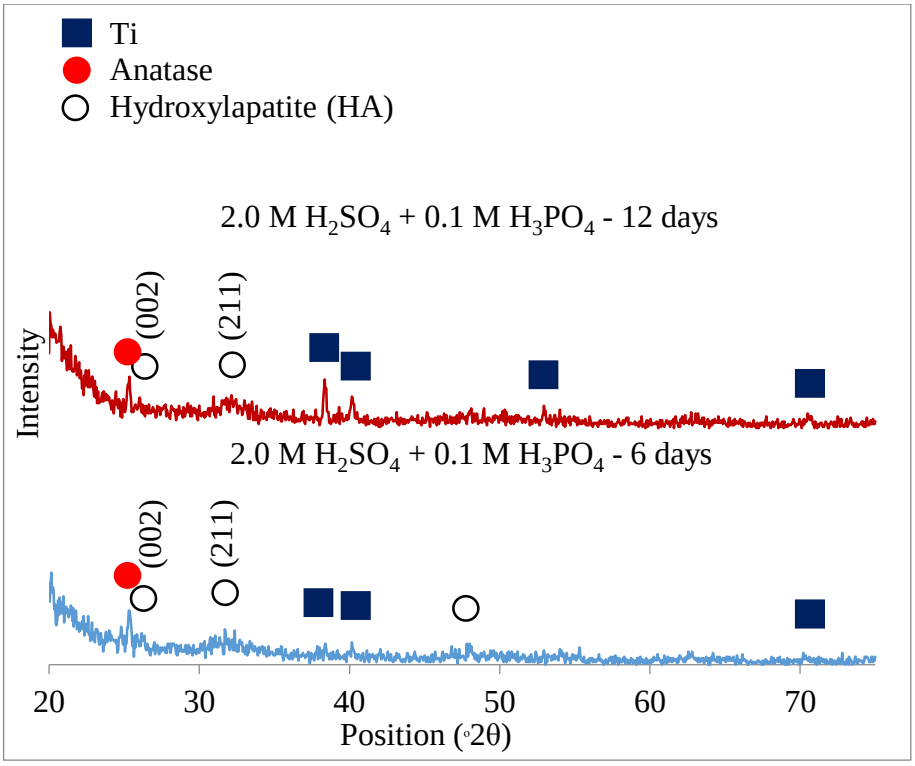

Figure 5.40: Phase mineralogical Patterns for apatite precipitation in SBF for 6 and 12 days under UV for coatings anodised at 150 V and 100 mA.cm^{-2} in 2.0 M H_2SO_4 + 0.1 M H_3PO_4 electrolyte

obtained by the coating anodised in 2.0 M H_2SO_4 + 0.1 M H_3PO_4. The coating anodised in 0.1 M H_2SO_4 + 2.0 M H_3PO_4 has obtained no apatite according to the elemental analysis obtained in Figure 5.31 (b), where Ca was not detected on the precipitation. There is no significant difference in the crystalline peak intensity between the apatite formed in the dark and the apatite formed under the UV. Also between the apatite formed in the different coatings incubated in the same condition.

When relating between the apatite crystallinity and the apatite surface microstructure images as obtained in Figure 5.29 and Figure 5.30, it can be noticed that the coatings anodised in 2.0 M H_2SO_4 + 0.1 M H_3PO_4 have obtained, in general, the highest apatite formation among the other coatings in the dark (Figure 5.29 (c and f)) and under the UV (Figure 5.30 (c and f)), after 6 and 12 days of incubation time. This can be related the that it was the only coating to obtain a crystalline apatite after 6 and 12 days as obtained in Figure 5.37 and Figure 5.40 for the apatite formed in the dark and under the UV respectively.

When comparing the coating crystallinity and the apatite formed in the different condition, it can be noticed that the crystalline coating has promoted higher crystallization. This can be seen on the anatase structured coating that was anodised in 2.0 M H_2SO_4 + 0.1 M H_3PO_4 (Figure 4.48) that has obtained crystalline apatite after 6 and 12 days of incubation in the different conditions. While the other coatings have obtained amorphous coating structure as obtained in Figure 4.42 for 0.1 M H_2SO_4 + 0.1 M H_3PO_4 and in Figure 4.45 for 0.1 M H_2SO_4 + 2.0 M H_3PO_4. These coatings have obtained crystalline apatite only after 12 days of incubation at both conditions.

According to the absorption results, it can be noticed that the Ti-O^- group stretching as obtained in **Section 4.4.7** has not affected the apatite crystalline intensity. However, it has affected the apatite formation ability according to the surface microstructure image. This can be obtained where the increased Ti-O^- has obtained an increased apatite formation. This can be obtained when compared between the coatings anodised in 0.1 M H_2SO_4 + 0.1 M H_3PO_4 (Figure 5.29 (a and d)) and in 0.1 M H_2SO_4 + 2.0 M H_3PO_4 (Figure 5.39 (b and e)). Where the Ti-O^- was observed to be stronger at 0.1 M H_2SO_4 + 0.1 M H_3PO_4 even before the UV irradiation (Figure 4.53) when compared with the coating obtained on 0.1 M H_2SO_4 + 2.0 M H_3PO_4 (Figure 4.54). While the coating anodised in 2.0 M H_2SO_4 + 0.1 M H_3PO_4 that obtained the highest apatite formation and earlier apatite crystallization has obtained a weaker Ti-O^- stretching only after the UV irradiation (Figure 4.55). However, it has obtained strong

Ti-OH stretching that hasn't obtained on the other coatings. This can be related to the coating's advantageous apatite formation and crystallization. This is due to the photocatalytic activity of the TiO_2 crystalline (Wang *et al.,* 2007) that forms Ti-OH radicals on its surface, which is believed to be responsible for apatite precipitation (Ueda *et al.,* 2010; Uetsuki *et al.,* 2010). It was also found to be increased with the UV irradiation (Han *et al.,* 2008; Liu *et al.,* 2008).

When compared the results from mixed electrolyte with the results from the H_2SO_4 electrolyte and H_3PO_4 electrolyte, it can be concluded that the coating anodised in 2.0 M H_2SO_4 + 0.1 M H_3PO_4 has obtained the highest apatite crystalline and formation performance. This can be obtained on the crystalline apatite that was obtained after 6 days of incubation in the dark (Figure 5.37) and under the UV (Figure 5.40) that were not obtained on any other coating. Also, the apatite formation that has obtained in the dark (Figure 5.29 (c and f)) and under the UV (Figure 5.30 (c and f)) were higher than the other coatings. However, the Ti-O^- group stretching obtained on the 2.0 M H_2SO_4 + 0.1 M H_3PO_4 (Figure 4.55) has been obtained only after the UV irradiation. Nonetheless, it was noticed that the coating has obtained an increased strong Ti-OH with the UV irradiation under water at band 1000 cm^{-1}.

It can be concluded that there are several factors which influence the apatite formation and crystallization between H_2SO_4 electrolyte, H_3PO_4 electrolyte, and mixed electrolyte. The higher apatite formation and crystallization in the dark and under the UV conditions were obtained on the coatings anodised in 0.1 M H_2SO_4 in the H_2SO_4 electrolyte and 0.1 M H_3PO_4 on H_3PO_4 electrolyte. While the coating anodised in 2.0 M H_2SO_4 + 0.1 M H_3PO_4 on mixed electrolyte has obtained the highest apatite formation and crystallization especially at earlier incubation time. These coatings have a different surface microstructure, where they have obtained different porosity and roughness. Also, they have obtained the different intensity of acidic incorporated ions on the coating according to the elemental analysis. The coatings anodised in 0.1 M H_2SO_4 and 2.0 M H_2SO_4 + 0.1 M H_3PO_4 has obtained anatase with increased intensity to the later, while the coating anodised in 0.1 M H_3PO_4 has obtained an amorphous structure.

All of the three coatings have obtained Ti-O^- functional group stretching, however, in a different level. The strong and stable Ti-O^- stretching at 0.1 M H_2SO_4 could be related to the higher apatite formation and crystallization along with the coating crystallinity advantage (anatase) over the weaker Ti-O^- that was obtained on

0.1 M H_3PO_4. The Ti-O^- stretching at 2.0 M H_2SO_4 + 0.1 M H_3PO_4 was only obtained after the UV irradiation in the water and it was not as strong as in the 0.1 M H_2SO_4 and 0.1 M H_3PO_4, however, it has obtained a strong Ti-OH functional group at the band 1000 cm^{-1}. The advantage of the apatite formation and crystallization on the coating anodised in 2.0 M H_2SO_4 + 0.1 M H_3PO_4 can be related to the strong anatase crystalline, higher porous coating and thickness, higher hydrophilicity, Ti-OH functional group and acidic incorporated ions; S and P. From the above discussion, it can be concluded that the Ti-O^- and Ti-OH functional groups, hydrophilicity and the S and P mixture ions incorporation can influence the apatite formation and crystallization.

5.4.4 Absorption of the Apatite Formation on TiO_2 in Anodised in Mixed Electrolyte

Figure 5.41, Figure 5.42 and Figure 5.43 obtain the absorption analysis patterns of the coatings anodised in 0.1 M H_2SO_4 + 0.1 M H_3PO_4, 0.1 M H_2SO_4 + 2.0 M H_3PO_4 and 2.0 M H_2SO_4 + 0.1 M H_3PO_4 respectively immersed in the SBF in the dark. While Figure 5.44, Figure 5.45 and Figure 5.46 obtain the absorption analysis of the coatings immersed under the UV irradiation.

The phosphate stretching has increased with the increased incubation time in SBF in the dark and under the UV, and it was higher for the apatite precipitated under the UV than the apatite formed in the dark. The phosphate intensity can indicate the apatite density on the coating (Mary *et al.*, 2016). The apatite density can be related to amount of the apatite formation as obtained in Figure 5.29 and Figure 5.30 according to the surface microstructure. This can be obtained on the higher apatite density with the increased incubation time. Also, the coatings incubated under the UV, where the higher phosphate stretching can indicate of the higher apatite density than the apatite formed in the dark.

The coatings anodised in 0.1 M H_2SO_4 + 2.0 M H_3PO_4 have obtained no apatite after 6 days (Figure 5.29 (b)) and the lowest apatite formation after 12 days (Figure 5.29 (d)) of incubation in the dark. However, it has obtained the same phosphate intensity after 6 days of incubation in the dark as obtained in Figure 5.42, with the corresponding pattern for the apatite formed on 0.1 M H_2SO_4 + 0.1 M H_3PO_4

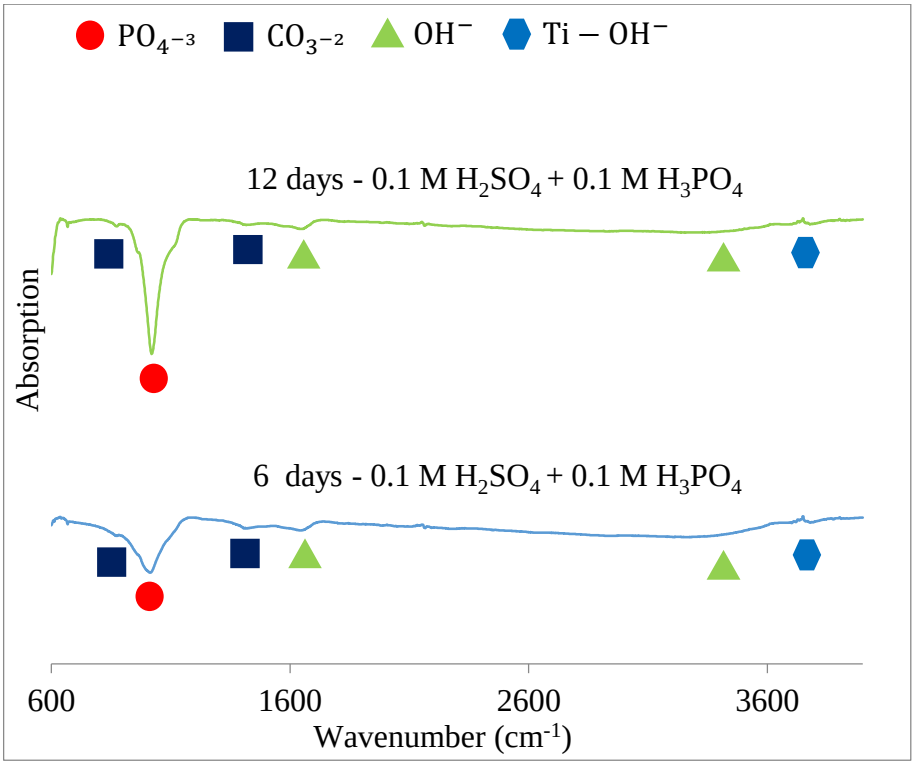

Figure 5.41: Absorption analysis patterns for apatite precipitation in SBF for 6 and 12 days in the dark for coatings anodised at 150 V and 100 mA.cm^{-2} in 0.1 M H_2SO_4 + 0.1 M H_3PO_4 electrolyte

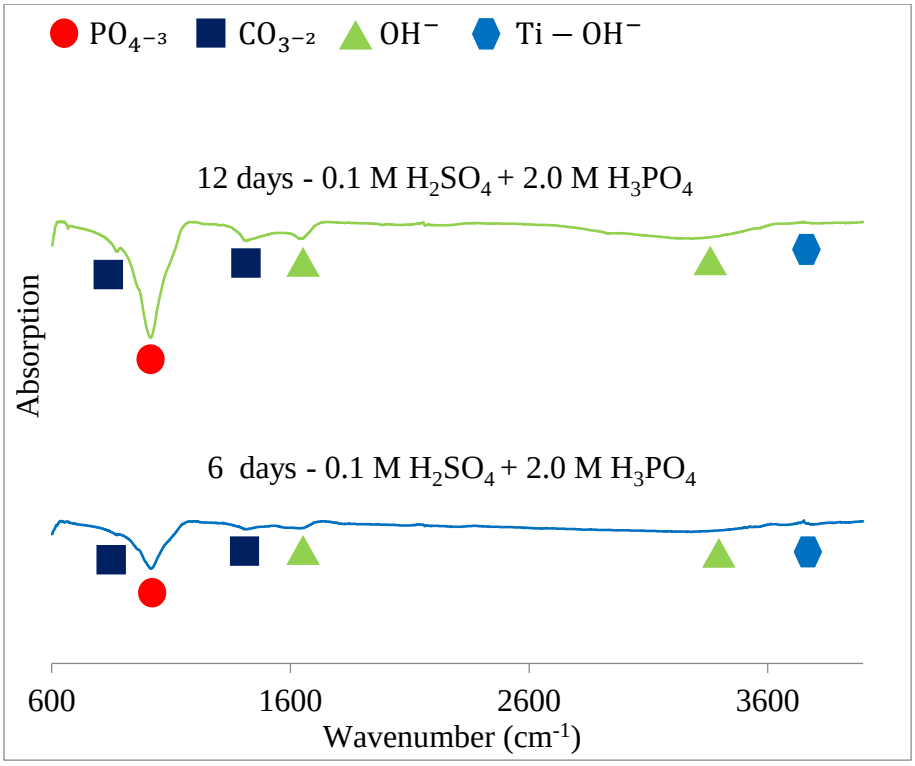

Figure 5.42: Absorption analysis patterns for apatite precipitation in SBF for 6 and 12 days in the dark for coatings anodised at 150 V and 100 mA.cm^{-2} in 0.1 M H_2SO_4 + 2.0 M H_3PO_4 electrolyte

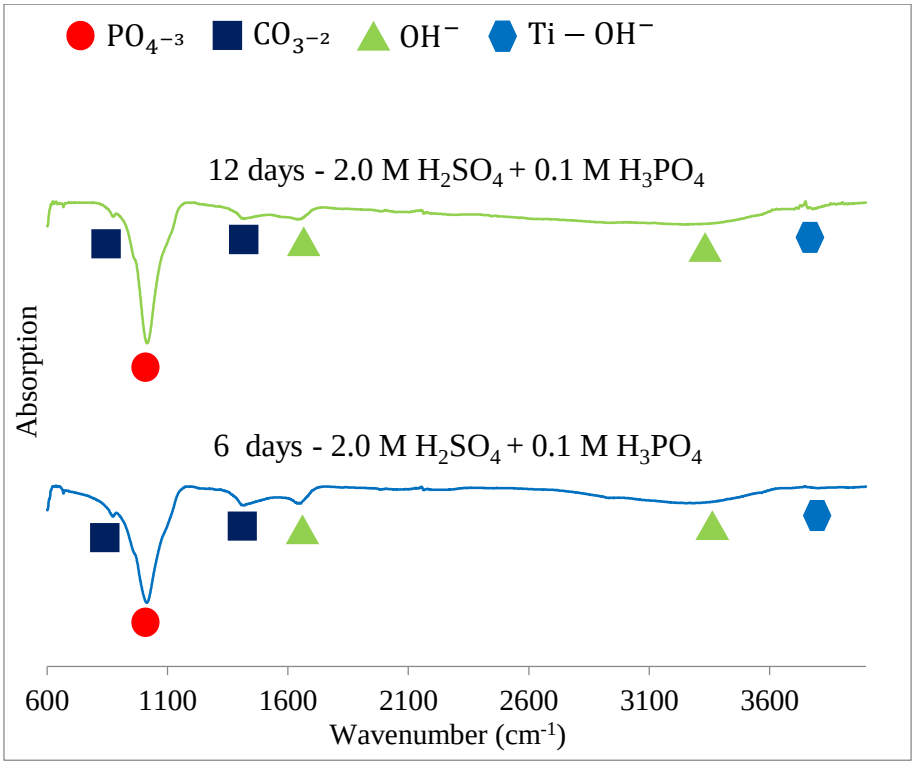

Figure 5.43: Absorption analysis patterns for apatite precipitation in SBF for 6 and 12 days in the dark for coatings anodised at 150 V and 100 mA.cm^{-2} in 2.0 M H_2SO_4 + 0.1 M H_3PO_4 electrolyte

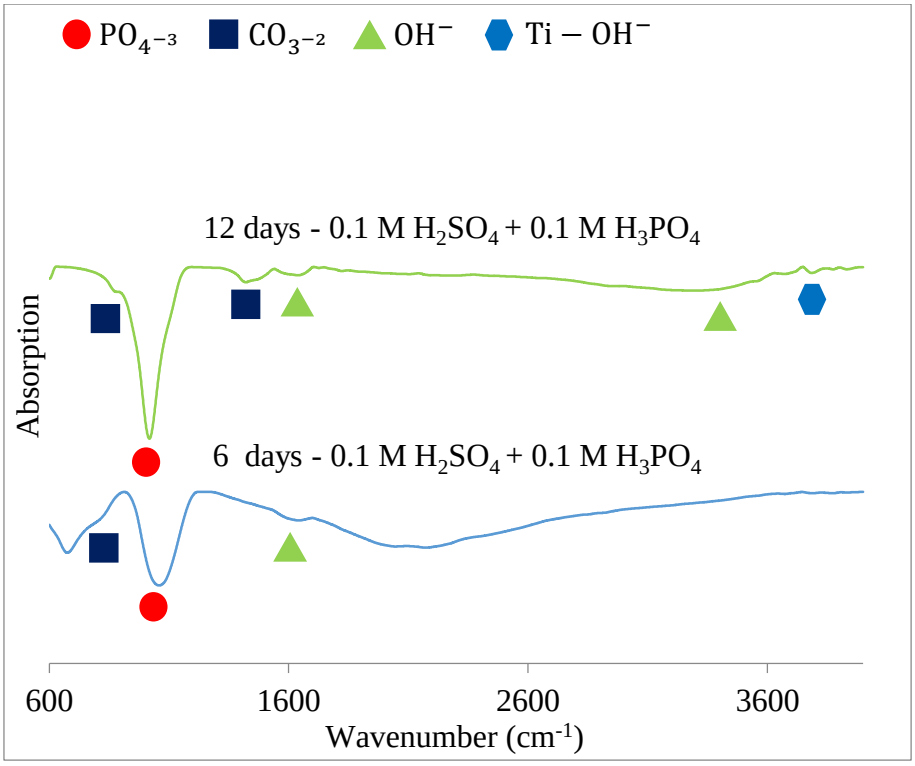

Figure 5.44: Absorption analysis Patterns for apatite precipitation in SBF for 6 and 12 days under UV for coatings anodised at 150 V and 100 mA.cm^{-2} in 0.1 M H_2SO_4 + 0.1 M H_3PO_4 electrolyte

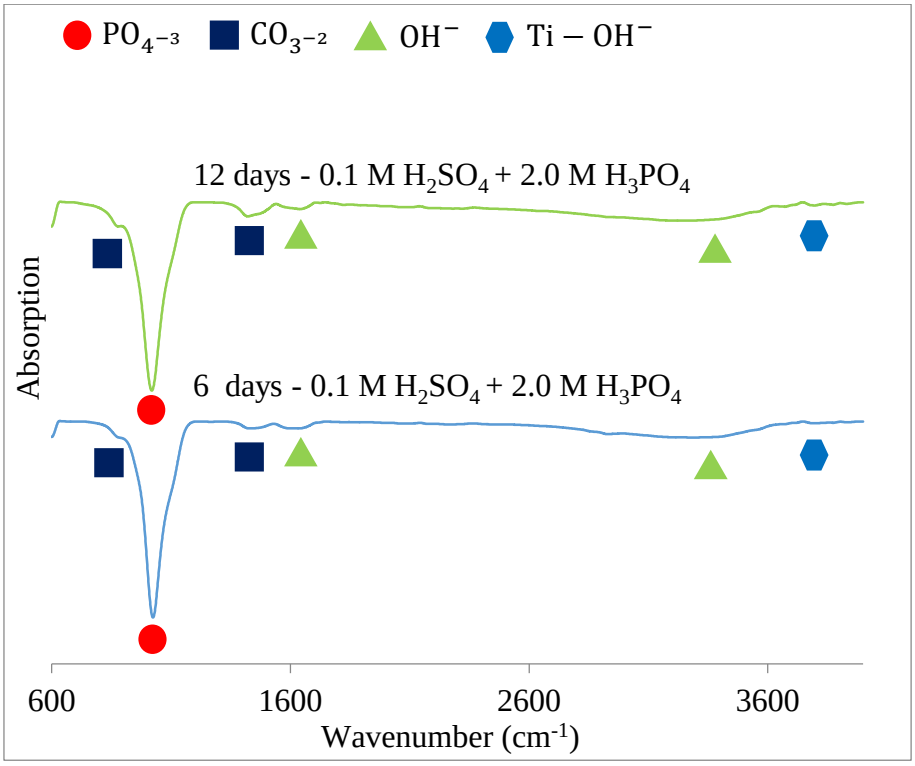

Figure 5.45: Absorption analysis Patterns for apatite precipitation in SBF for 6 and 12 days under UV for coatings anodised at 150 V and 100 mA.cm^{-2} in 0.1 M H_2SO_4 + 2.0 M H_3PO_4 electrolyte

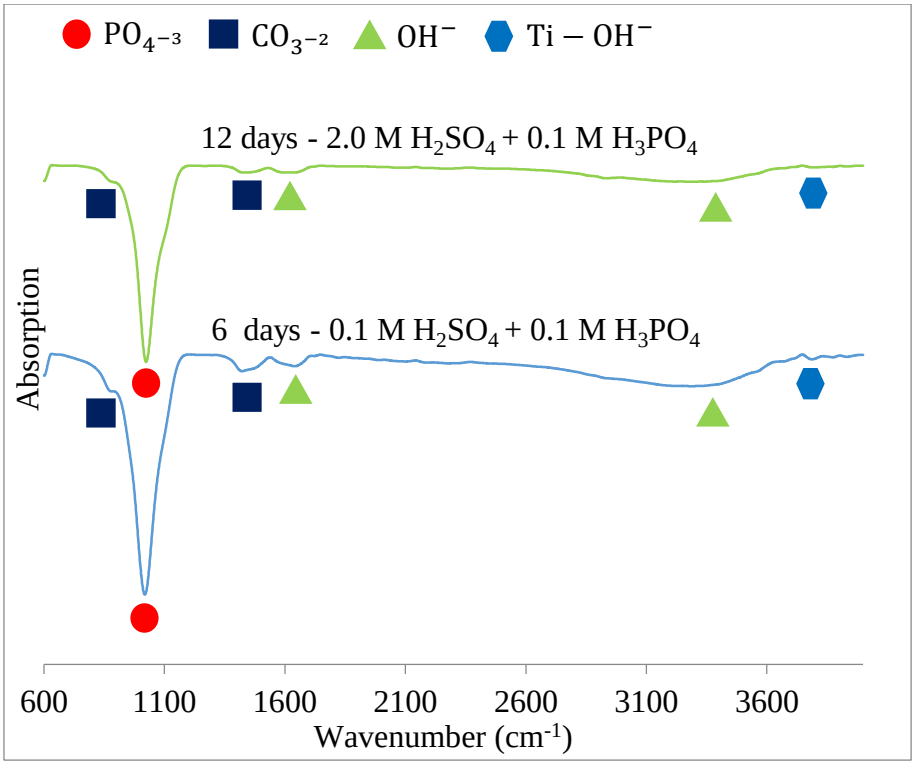

Figure 5.46: Absorption analysis patterns for apatite precipitation in SBF for 6 and 12 days in the UV for coatings anodised at 150 V and 100 mA.cm^{-2} in 2.0 M H_2SO_4 + 0.1 M H_3PO_4 electrolyte

(Figure 5.41). Also the same phosphate intensity after 12 days of incubation in the dark as obtained in 0.1 M H_2SO_4 + 2.0 M H_3PO_4 (Figure 5.42) with the corresponding pattern for the apatite formed on 0.1 M H_2SO_4 + 0.1 M H_3PO_4 (Figure 5.41) and on 2.0 M H_2SO_4 + 0.1 M H_3PO_4 (Figure 5.43) This can be related to the detection of the higher intensity of the P ions that were incorporated into the coating (Park *et al.*, 2009) as obtained in Figure 4.40. This can also be applied to the pattern that corresponds to the apatite formed under the UV as obtained in Figure 5.45. Where the high phosphate intensity that was obtained on the pattern for the apatite that was incubated for 6 days (Figure 5.45) obtained the same level with their corresponding in 2.0 M H_2SO_4 + 0.1 M H_3PO_4 (Figure 5.46), although it has obtained lower apatite formation according to Figure 5.30 (b).

The higher apatite density according to the higher phosphate stretching that was obtained in 2.0 M H_2SO_4 + 0.1 M H_3PO_4 after 6 days of incubation in the dark as seen in Figure 5.43 and under the UV Figure 5.46 do agree with the corresponding higher apatite formed according to the surface microstructure image in Figure 5.29 (c) and in Figure 5.30 (c). Also, do correspond with the crystalline apatite that was obtained in Figure 5.37 (b) and Figure 5.40 (b). The higher apatite density according to the higher phosphate stretching on the 2.0 M H_2SO_4 + 0.1 M H_3PO_4 can be related to the increased porosity and thickness on the coating surface as obtained in Figure 4.38 (o), strong anatase crystalline (Figure 4.48), mixed ions incorporation (Figure 4.40), higher hydrophilicity (Figure 4.56) and strong Ti-OH functional groups (Figure 4.55).

5.5 Summary

TiO_2 coatings anodised in different acidic electrolytes, i.e., H_2SO_4 electrolyte, H_3PO_4 electrolyte and mixture electrolyte (H_2SO_4 + H_3PO_4) have undergone *in vitro* testing. The coatings have been incubated in SBF in the dark and under the UV for 6 and 12 days. Afterward, the coatings have been characteristically examined, i.e., microstructure, mineralogy, elements and chemical absorption, to study the apatite formation on these coatings. Table 5.4 summarize the significant findings from these testings comparatively.

Table 5.4: *In vitro* results characterised comparatively between the TiO_2 coatings in individuals and mixed electrolyte.

Characterisation	Apatite formed on H_2SO_4 electrloyte	Apatite formed on H_3PO_4 electrloyte	Apatite formed on H_2SO_4 + H_3PO_4
Microstructure	Increased apatite was formed with the increased incubation time and under UV and on the coatings anodised in lower molarity and it is believed is due to the strong Ti-O^- functional groups.	Increased apatite was formed with the increased incubation time and under UV and on the coatings anodised in lower molarity and it is believed is due to the strong Ti-O^- functional groups. However, it wasn't as strong as the apatite formed the coating anodised in H_2SO_4.electrloyte with lower molarity	Increased apatite was formed with the increased incubation time and under UV and on the coatings anodised in an electrolyte with increased H_2SO_4 concentration. It is believed is due to the strong Ti-OH functional groups.
Elementary	The Ca to P ratio was obtained higher for the apatite formed under UV with lower molarity has obtained calcium-deficient HA.	The Ca to P ratio was obtained higher for the apatite formed under UV with no HA ratio.	The Ca to P ratio was obtained higher for the apatite formed under UV with no HA ratio.
Mineralogy	Apatite crystalline increased with the increased incubation time and under UV for the coatings anodised at lower molarity.	Apatite crystalline increased with the increased incubation time and under UV for the coatings anodised at lower molarity.	Apatite crystalline increased with the increased incubation time and under UV. Higher apatite crystalline was obtained on the coatings anodised in an electrolyte with increased H_2SO_4 concentration. In the dark and under the UV.
Absorption	Increased apatite density with the increased time and UV. Increased density was obtained for the coatings anodised in lower molarity.	Increased apatite density with the increased time and UV. Increased density was obtained for the coatings anodised in lower molarity.	Increased apatite density with the increased time and UV. Increased density was obtained for the coatings anodised in an electrolyte with increased H_2SO_4 concentration.
In vitro findings	Higher apatite was formed on the TiO_2 coatings anodised in a single acid electrolyte with lower acidic build-in ions, lower porous microstructure and with stronger Ti-O^- functional groups. Highest apatite was formed on the coatings anodised in mixed electrolyte that obtained strong Ti-OH groups, higher porosity and coating thickness and higher wettability and obtained mixed acidic ions build-in within the coating. In general, it was found that the Ti-O^- and Ti-OH functional groups, hydrophilicity and the S and P mixture ions incorporation can influence the apatite formation and crystallization.		

CHAPTER 6

CONCLUSION AND RECOMMENDATIONS

6.1 Conclusion

It was found that the porosity increase with the increased anodization parameters, i.e., voltage, current density, and molarity. However, the voltage and molarity had the higher influence. The porosity took sponge-like shape pores on the TiO_2 coatings anodised in the H_2SO_4 electrolyte. While it took volcano-like orifice shape on the coatings anodised in the H_3PO_4 electrolyte. The increased porosity can indicate the increased breakdown of the coatings surface and results in loss of interference colour. The TiO_2 coatings anodised in H_2SO_4 electrolyte has obtained an increased breakdown when compared with the coatings anodised in the H_3PO_4 electrolyte. Also, H_2SO_4 has promoted crystallisation, i.e., anatase and rutile, while the H_3PO_4 promoted amorphous structure due to the slower dissociation of H_3PO_4. The TiO_2 coatings anodised at mixed electrolyte has obtained the highest coating thickness and higher surface hydrophilicty.

According to the *in vitro* results, the UV irradiation has promoted higher apatite precipitation than the apatite incubated in the dark condition. Higher apatite was formed on the TiO_2 coatings with higher $Ti\text{-}O^-$ functional groups. The UV has increased the photocatalysis properties of TiO_2 and increased the $Ti\text{-}O^-$ and Ti-OH on the coating surface, and resulted in induction of higher apatite formation ability. The highest apatite formation ability was formed on the thickest coatings with the highest porosity, strong TiO_2 anatase crystalline, highest hydrophilicity, obtain mixed acidic ions build-in within the coating and obtained Ti-OH functional groups. In general, it can be concluded that $Ti\text{-}O^-$ and Ti-OH functional groups, hydrophilicity and S and P

mixture ions incorporation can influence the apatite formation and crystallization. **Section 6.1.1** and **Section 6.1.2** list in details the findings for the TiO_2 coatings characterisatrion and *in vitro* results respectively.

6.1.1 Anodic Oxidation

i. TiO_2 coating microstructure:
   a. The porosity increased with the increased voltage, current density, and molarity.
   b. The breakdown can occur with the increased voltage and molarity.
   c. The increased porosity on the coatings is accompanied with the loss of the interference colour and resulted in a grey colour.
   d. The H_2SO_4 electrolyte has obtained higher porosity with smaller pore size and higher coating thickness, while H_3PO_4 electrolyte has obtained the lower porosity with larger pore size.
   e. The coatings anodised in mixed electrolyte has obtained thicker TiO_2 coatings than the coatings anodised in H_2SO_4 and H_3PO_4 electrolytes.

ii. TiO_2 coating mineralogy:
   a. The H_2SO_4 electrolyte promotes TiO_2 coating crystallinity, while the H_3PO_4 electrolyte promotes amorphous structure. At mixed electrolyte, the addition of H_3PO_4 to H_2SO_4 was slower the TiO_2 coating crystallization.
   b. The crystalline increase with the increased voltage, current density, and molarity.
   c. The breakdown voltage can increase the crystallinity at lower current density due to the prolonged voltage increase, which allows for TiO_2 coating recrystallisation.

iii. TiO_2 coating elements:
   a. Phosphate ions (P) intensity obtained higher into the TiO_2 coatings compared to sulphur ions (S).
   b. The ions incorporation into the coatings has increased with the increased voltage.

iv. TiO_2 coating optical:

a. The coatings' bandgap was fluctuating, where the anatase and rutile crystalline coatings have obtained higher bandgap values that the values of the intrinsic TiO_2 crystalline.

v. TiO_2 coating absorption:
   a. Higher Ti-O^- functional groups are promoted by the TiO_2 coatings anodised in lower porous microstructure and lower acidic ions incorporation.
   b. Strong anatase crystalline promotes strong Ti-OH functional group.

vi. TiO_2 coating hydrophilicity:
   a. The coatings with P incorporated ions has obtained higher wettability than the S ioned coatings, also the coatings with mixed incorporated ions has obtained much higher wettability.
   b. The coating that obtained Ti-OH functional group, higher coating surface porosity and coating thickness, strong TiO_2 anatase crystalline, mixed acidic ions incorporated within the coating and obtained the highest hydrophilicity.

6.1.2 *In Vitro* Testing

i. Apatite microstructure:
   a. Higher apatite was formed on the TiO_2 coatings with lower porosity in the H_2SO_4 electrolyte and H_3PO_4 electrolyte, while in mixed electrolyte higher apatite was formed on the increased porous coating.
   b. Higher apatite was formed on the TiO_2 coatings immersed in SBF under the UV than the coating immersed in SBF in the dark especially at earlier exposure time.
   c. The TiO_2 coating crystallinity has no direct relation with the apatite formation growth.

ii. Apatite elements:
   a. All the coatings have not obtained the bone-like apatite ratio of 1.65.

iii. Apatite mineralogy:
   a. The TiO_2 coating crystallinity has no direct relation with the apatite crystallization.

b. The UV irradiation has forced for early apatite crystallization.

iv. Apatite absorption:

a. Higher apatite density was obtained on the coatings formed by the UV irradiation.

b. Ti-O^- functional groups have contributed to the increased apatite formation and crystallization for H_2SO_4 electrolyte and H_3PO_4 electrolyte. While the coating that obtained Ti-OH functional groups, highest porosity and coating thickness, strong TiO_2 anatase crystalline, S and P mixture ions incorporation within the coating and highest hydrophilicity has contributed to higher apatite formation and crystallization ability. In general, it was found that Ti-O^- and Ti-OH functional groups, hydrophilicity and S and P mixture ions incorporation can influence the apatite formation and crystallization.

6.2 Recommendations

The following may suggest further investigations on the apatite formation improvement on the TiO_2.coatings:

i. A focused study on the effect of the acidic ions mixture (i.e. sulfur and phosphorus) that is incorporated into the TiO_2 coating on the apatite formation in the SBF.

ii. A study of the effect of the UV irradiation effect on the apatite formation under different SBF molarity (e.g. 1M and 2 M).

iii. A focused study on the effect of the TiO_2 anatase crystalline on the OH functional group.

iv. A focused study on the effect of the UV irradiation on the OH functional group, and their effect on the apatite formation.

REFERENCES

Abdullah, H. Z. (2010). *Titanium Surface Modification by Oxidation for Biomedical Application*. University of New South Wales: Ph.D. Thesis.

Abdullah, H. Z., & Sorrell, C. C. (2007). Preparation and characterisation of TiO_2 thick Films fabricated by anodic oxidation. in materials science forum. *Trans Tech Publications*, 561, pp. 2159-2162.

Abdullah, H. Z., & Sorrell, C. C. (2007). TiO_2 thick films by anodic oxidation. *Journal of the Australasian Ceramic Society*, 43(2), pp. 125-130.

Abdullah, H. Z., & Sorrell, C. C. (2012). Gel oxidation of titanium and effect of UV irradiation on precipitation of hydroxyapatite from simulated body fluid. in Advanced Materials Research. *Trans Tech Publications*, 488, pp. 1229-1237.

Åberg, J., Eriksson, O., Spens, E., Nordblom, J., Mattsson, P., Sjödahl, J & Engqvist, H. (2012). Calcium sulfate spinal cord scaffold: a study on degradation and fibroblast growth factor 1 loading and release. *Journal of Biomaterials Applications*, 26(6), pp. 667-685.

Acero, J., Calderon, J., Salmeron, J. I., Verdaguer, J. J., Concejo, C., & Somacarrera, M. L. (1999). The behaviour of titanium as a biomaterial: microscopy study of plates and surrounding tissues in facial osteosynthesis. *Journal of cranio-maxillo-facial surgery*, 27(2), pp. 117-123.

Afshar, A., & Vaezi, M. R. (2004). Evaluation of electrical breakdown of anodic films on titanium in phosphate-base solutions. *Surface and Coatings Technology*, 186(3), pp. 398-404.

Agrawal, C. M. (1998). Reconstructing the human body using biomaterials. *Jom*, 50(1), pp. 31-35.

Allouni, Z. E., Cimpan, M. R., Høl, P. J., Skodvin, T., & Gjerdet, N. R. (2009). Agglomeration and sedimentation of TiO_2 nanoparticles in cell culture medium. *Colloids and Surfaces B: Biointerfaces*, 68(1), pp. 83-87.

Ambrosio, L. (Ed.). (2017). *Biomedical Composites*. 2nd ed UK: Woodhead Publishing.

Ambrosio, L., De Santis, R., & Nicolais, L. (1998). Composite hydrogels for implants. Proceedings of the Institution of Mechanical Engineers, *Part H: Journal of Engineering in Medicine*, 212(2), pp. 93-99.

American Society for Testing and Materials (ASTM). (2013a). *Standard Specification for Unalloyed Titanium for Surgical Implant Applications*. Philadelphia, PA: F67-13.

American Society for Testing and Materials (ASTM). (2013b). *Standard Specification for Wrought Titanium-6 Aluminium-4 Vanadium ELI (Extra Low Interstitial) Alloy for Surgical Implant Applications*. Philadelphia, PA: F136 - 08.

Angelova, N., & Hunkeler, D. (1999). Rationalizing the design of polymeric biomaterials. *Trends in Biotechnology*, 17(10), pp. 409-421.

AnthonyáSpackman, R. (1996). Photoelectrochemical study of titanium dioxide films prepared by anodisation of titanium metal in sulfuric acid. *Journal of the Chemical Society, Faraday Transactions*, 92(20), pp. 4049-4052.

Artursson, P., Palm, K., & Luthman, K. (2012). Caco-2 monolayers in experimental and theoretical predictions of drug transport. *Advanced Drug Delivery Reviews*, 64, pp. 280-289.

Augustynski, J. (1993). The role of the surface intermediates in the photoelectrochemical behaviour of anatase and rutile TiO_2. *Electrochimica Acta*, 38(1), pp. 43-46.

Balamurugan, A., Michel, J., Faure, J., Benhayoune, H., Wortham, L., Sockalingum, G., & Balossier, G. (2006). Synthesis and structural analysis of sol gel derived stoichiometric monophasic hydroxyapatite. *Ceramics-Silikaty*, 50(1), pp. 27-31.

Banerjee, S., Dionysiou, D. D., & Pillai, S. C. (2015). Self-cleaning applications of TiO_2 by photo-induced hydrophilicity and photocatalysis. *Applied Catalysis B: Environmental*, 176, pp. 396-428.

Banfield, J. (1998). Thermodynamic analysis of phase stability of nanocrystalline titania. *Journal of Materials Chemistry*, 8(9), pp. 2073-2076.

Bard, A. J. (1980). Photoelectrochemistry. *Science*, 207(4427), pp. 139-144.

Batzill, M., Morales, E. H., & Diebold, U. (2006). Influence of nitrogen doping on the defect formation and surface properties of TiO_2 rutile and anatase. *Physical Review Letters*, 96(2), pp. 026103.

Beltran, A., Gracia, L., & Andres, J. (2006). Density functional theory study of the brookite surfaces and phase transitions between natural titania polymorphs. *The Journal of Physical Chemistry B*, 110(46), pp. 23417 - 23423.

Ben-Nissan, B., Choi, A. H., Roest, R., Latella, B. A., & Bendavid, A. (2015). Adhesion of Hydroxyapatite on Titanium Medical Implants. in *Hydroxyapatite (Hap) for Biomedical Applications*. pp. 21-51.

Bergallo, C. (2000). Friction and wear of medical implants and prosthetic devices. *Revista Chilena de Infectología*, 17, 97-91.

Berger-Keller, N., Bertrand, G., Filiatre, C., Meunier, C., & Coddet, C. (2003). Microstructure of plasma-sprayed titania coatings deposited from spray-dried powder. *Surface and Coatings Technology*, 168(2-3), pp. 281-290.

Bickley, R. I., Gonzalez-Carreno, T., Lees, J. S., Palmisano, L., & Tilley, R. J. (1991). A structural investigation of titanium dioxide photocatalysts. *Journal of Solid State Chemistry*, 92(1), pp. 178 - 190.

Bigelow, P. (2010). How to Make Standard Solutions for Chemistry.

Binnig, G., Quate, C. F., & Gerber, C. (1986). Atomic force microscope. Physical Review Letters, pp, 56(9). 930.

Black, J. (2005). *Biological Performance of Materials: Fundamentals of Biocompatibility*. Roca Raton, FL: CRC Press.

Bogya, E. S., Károly, Z., & Barabás, R. (2015). Atmospheric plasma sprayed silica-hydroxyapatite coatings on magnesium alloy substrates. *Ceramics International*, 41(4), pp. 6005-6012.

Bohner, M., & Lemaitre, J. (2009). Can bioactivity be tested *in vitro* with SBF solution?. *Biomaterials*, 30(12), pp. 2175-2179.

BomBač, D., Brojan, M., Fajfar, P., Kosel, F., & Turk, R. (2007). Review of materials in medical applications pregled materialov v medicinskih aplikacijah. *RMZ-Materials and Geoenvironment*, 54(4), pp. 471-499.

Bonfield, W., Grynpas, M. D., Tully, A. E., Bowman, J., & Abram, J. (1981). Hydroxyapatite reinforced polyethylene-a mechanically compatible implant material for bone replacement. *Biomaterials*, 2(3), pp. 185-186.

Bos, R. R., Boering, G., Rozema, F. R., & Leenslag, J. W. (1987). Resorbable poly (L-lactide) plates and screws for the fixation of zygomatic fractures. *Journal of Oral and Maxillofacial Surgery*, 45(9), pp. 751-753.

Bragg, W. L. (2014). The diffraction of X-rays by crystals. *Zeitschrift Für Physikalische Chemie*, 228(10-12), pp. 957-968.

Brunella, M. F., Diamanti, M. V., Pedeferri, M. P., Di Fonzo, F., Casari, C. S., & Bassi, A. L. (2007). Photocatalytic behavior of different titanium dioxide layers. *Thin Solid Films*, 515(16), pp. 6309 - 6313.

Brunette, D. M., Tengvall, P., Textor, M., & Thomsen, P. (Eds.). (2012). Titanium in Medicine: Material Science, Surface Science, Engineering, Biological Responses and Medical Applications. Berlin: Springer Science and Business Media.

Brzezińska-Miecznik, J., Haberko, K., Sitarz, M., Bućko, M. M., & Macherzyńska, B. (2015). Hydroxyapatite from animal bones-extraction and properties. *Ceramics International*, 41(3), pp. 4841-4846.

Burnside, S. D., Shklover, V., Barbé, C., Comte, P., Arendse, F., Brooks, K., & Grätzel, M. (1998). Self-organization of TiO_2 nanoparticles in thin films. *Chemistry of Materials*, 10(9), pp. 2419-2425.

Busby, F., Hughes, K. R., & Hyun, K. S. (1999). Colour Measurement Techniques for Rapid Determination of Residence Time Distributions. in *ANTEC 99, Society of Plastics Engineers Annual Technical Papers*. New York City: ANTEC. (1). pp. 230-234.

Capek, D., Gigandet, M. P., Masmoudi, M., Wery, M., & Banakh, O. (2008). Long-time anodisation of titanium in sulphuric acid. *Surface and Coatings Technology*, 202(8), pp. 1379-1384.

Carp, O., Huisman, C. L., & Reller, A. (2004). Photoinduced reactivity of titanium dioxide. *Progress in solid state chemistry*, 32(1-2), pp. 33-177.

Cerruti, M. G. (2004). Characterisation of bioactive glasses. Effect of the immersion in solutions that simulate body fluids. *International Journal of Innovative Research in Science and Engineering*.

Cervantes, B., López-Huerta, F., Vega, R., Hernández-Torres, J., García-González, L., Salceda, E., & Soto, E. (2016). Cytotoxicity evaluation of anatase and rutile TiO_2 thin films on CHO-K1 cells *in vitro*. *Materials*, 9(8), pp. 619.

Chang-Ha, K., Su-Il, P., & Eung-Jo, L. (1991). Donor distribution over anodically passivating crystalline and amorphous TiO_2 films. *Materials Letters*, 10(7-8), pp. 387-391.

Chen, X., & Mao, S. S. (2007). Titanium dioxide nanomaterials: synthesis, properties, modifications, and applications. *Chemical Reviews*, 107(7), pp. 2891-2959.

Cheng, Y., & Hu, C. (1999). *MOSFET Modeling and BSIM3 User's Guide*. US: Springer Science and Business Media.

Chien, C. S., Chiao, C. L., Hong, T. F., Han, T. J., & Kuo, T. Y. (2009). Synthesis and Characterisation of TiO_2 + HA Coatings on Ti-6Al-4V Substrates by Nd-YAG Laser Cladding. in *13th International Conference on Biomedical Engineering*. Berlin, Heidelberg: Springer. pp. 1401-1404.

Chiesa, R., Sandrini, E., Santin, M., Rondelli, G., & Cigada, A. (2003). Osteointegration of titanium and its alloys by anodic spark deposition and other electrochemical techniques: a review. *Journal of Applied Biomaterials and Biomechanics*, 1(2), pp. 91-107.

Choi, J., Wehrpohn, R. B., Lee, J., & Gösele, U. (2004). Anodization of nanoimprinted titanium: a comparison with formation of porous alumina. *Electrochimica Acta*, 49(16), pp. 2645-2652.

Chu, P. K. (2013). Surface engineering and modification of biomaterials. *Thin Solid Films*, 528, pp. 93-105.

Commandeur, S., Van Beusekom, H. M., & Van Der Giessen, W. J. (2006). Polymers, Drug Release, and Drug-Eluting Stents. *Journal of Interventional Cardiology*, 19(6), pp. 500-506.

Coolibar (2014). *It's all in the Fabric-Coolibar SUNTECT*. 2011. Retrieved 23 May 2014 from http://blog.coolibar.com/coolibar-suntect/

Criado, J., & Real, C. (1983). Mechanism of the inhibiting effect of phosphate on the anatase→ rutile transformation induced by thermal and mechanical treatment of TiO_2. *Journal of the Chemical Society, Faraday Transactions 1: Physical Chemistry in Condensed Phases*, 79(12), pp. 2765-2771.

Cui, X., Kim, H. M., Kawashita, M., Wang, L., Xiong, T., Kokubo, T., & Nakamura, T. (2009). Preparation of bioactive titania films on titanium metal via anodic oxidation. *Dental Materials*, 25(1), pp. 80-86.

Currey, J. D. (1998). Mechanical properties of vertebrate hard tissues. *Proceedings of the Institution of Mechanical Engineers, Part H: Journal of Engineering in Medicine*, 212(6), pp. 399-411.

Dai, Y., Liu, H., Liu, B., Wang, Z., Li, Y., & Zhou, G. (2015). Porous β-Ca_2SiO_4 ceramic scaffolds for bone tissue engineering: *In vitro* and *in vivo* characterisation. *Ceramics International*, 41(4), pp. 5894-5902.

Damore, A., Pompo, A., Netti, P., Masi, E., & Nicolais, L. (1993). Non-linear viscoelastic behavior of poly-ether-ether-ketone (PEEK) and PEEK-based composites. *Journal of Reinforced Plastics and Composites*, 12(3), pp. 327-340.

Das, K., Bose, S., & Bandyopadhyay, A. (2007). Surface modifications and cell–materials interactions with anodised Ti. Acta Biomaterialia, 3(4), pp. 573-585.

Dash, S. R., Sarkar, R., & Bhattacharyya, S. (2015). Gel casting of hydroxyapatite with naphthalene as pore former. *Ceramics International*, 41(3), pp. 3775-3790.

Davidson, J. A., & Georgette, F. S. (1987). State of the art materials for orthopedic prosthetic devices. *Society of Manufacturing Engineers*, pp. 87-122.

Davidson, J. A., Mishra, A. K., Kovacs, P., & Poggie, R. A. (1994). New surface-hardened, low-modulus, corrosion-resistant Ti-13Nb-13Zr alloy for total hip arthroplasty. *Bio-medical materials and engineering*, 4(3), pp. 231-243.

Davis, E. A., & Mott, N. (1970). Conduction in non-crystalline systems V. Conductivity, optical absorption and photoconductivity in amorphous semiconductors. *Philosophical Magazine*, 22(179), pp. 0903 - 0922.

Davis, J. R. (Ed.). (2006). *Handbook of Materials for Medical Devices*. Materials Park, OH: ASM international.

De Clercq, E. (2005). Recent highlights in the development of new antiviral drugs. *Current Opinion in Microbiology*, 8(5), pp. 552-560.

de Mussy, J. P. G., Langelaan, G., Decerf, J., & Delplancke, J. L. (2003). TEM and X-ray diffraction investigation of the structural characteristics of the microporous oxide film formed on polycrystalline Ti. *Scripta Materialia*, 48(1), pp. 23-29.

de Oliveira, P. T., & Nanci, A. (2004). Nanotexturing of titanium-based surfaces upregulates expression of bone sialoprotein and osteopontin by cultured osteogenic cells. *Biomaterials*, 25(3), pp. 403-413.

De Sena, L. A., Rocha, N. C. C., Andrade, M. C., & Soares, G. A. (2003). Bioactivity assessment of titanium sheets electrochemically coated with thick oxide film. *Surface and Coatings Technology*, 166(2-3), pp. 254-258.

Deer, W. A., Howie, R. A., & Zussman, J. (1992). *An Introduction to the Rock-Forming Minerals*. Hong Kong: Longman Scientific and Technical. 696.

Del Pino, A. P., Fernández-Pradas, J. M., Serra, P., & Morenza, J. L. (2004). Coloring of titanium through laser oxidation: comparative study with anodizing. *Surface and Coatings Technology*, 187(1), pp. 106-112.

Deligianni, D. D., Katsala, N., Ladas, S., Sotiropoulou, D., Amedee, J., & Missirlis, Y. F. (2001). Effect of surface roughness of the titanium alloy Ti-6Al-4V on human bone marrow cell response and on protein adsorption. *Biomaterials*, 22(11), pp. 1241-1251.

Delplancke, J. L., Degrez, M., Fontana, A., & Winand, R. (1982). Self-colour anodizing of titanium. *Surface Technology*, 16(2), pp. 153-162.

Deng, X., Yue, Y., & Gao, Z. (2002). Gas-phase photo-oxidation of organic compounds over nanosized TiO_2 photocatalysts by various preparations. *Applied Catalysis B: Environmental*, 39(2), pp. 135-147.

Diamanti, M. V., & Pedeferri, M. P. (2007). Effect of anodic oxidation parameters on the titanium oxides formation. *Corrosion Science*, 49(2), pp. 939-948.

Diamanti, M. V., Del Curto, B., & Pedeferri, M. (2008). Interference colors of thin oxide layers on titanium. *Color Research and Application*, 33(3), 221-228.

Diamanti, M. V., Ormellese, M., Marin, E., Lanzutti, A., Mele, A., & Pedeferri, M. P. (2011). Anodic titanium oxide as immobilized photocatalyst in UV or visible light devices. *Journal of Hazardous Materials*, 186(2-3), pp. 2103-2109.

Diamanti, M. V., Spreafico, F. C., & Pedeferri, M. P. (2013). Production of anodic TiO_2 nanofilms and their characterisation. *Physics Procedia*, 40, pp. 30-37.

Diebold, U. (2003). The surface science of titanium dioxide. *Surface Science Reports*, 48(5-8), pp. 53-229.

Ding, X. Z., Liu, X. H., & He, Y. Z. (1996). Grain size dependence of anatase-to-rutile structural transformation in gel-derived nanocrystalline titania powders. *Journal of Materials Science Letters*, 15(20), pp. 1789-1791.

Dubrovinsky, L. S., Dubrovinskaia, N. A., Swamy, V., Muscat, J., Harrison, N. M., Ahuja, R., & Johansson, B. (2001). Materials science: The hardest known oxide. *Nature*, 410(6829), pp. 653.

Duta, L., Oktar, F. N., Stan, G. E., Popescu-Pelin, G., Serban, N., Luculescu, C., & Mihailescu, I. N. (2013). Novel doped hydroxyapatite thin films obtained by pulsed laser deposition. *Applied Surface Science*, 265, pp. 41-49.

Dynamics, L. (2013). *Types of UV and Visible Light*. Retrieved 23 May 2014. From http://blog.coolibar.com/coolibar-suntect/

El Kader, J. A., El Wahab, F. A., El Shayeb, H. A., & Khedr, M. G. A. (1981). Oxide film thickening on titanium in aqueous solutions in relation to anion type and concentration. *British Corrosion Journal*, 16(2), pp. 111-114.

Elias, C. N., Lima, J. H. C., Valiev, R., & Meyers, M. A. (2008). Biomedical applications of titanium and its alloys. *Jom*, 60(3), pp. 46-49.

Fahmi, A., Minot, C., Silvi, B., & Causa, M. (1993). Theoretical analysis of the structures of titanium dioxide crystals. *Physical Review B*, 47(18), pp. 11717.

Feenstra, L. (2018). Medical Use of Calcium Phosphate Ceramics. in *Bioceramics Calcium Phosphate*. CRC Press. pp. 131-141.

Feng, B., Chen, J. Y., Qi, S. K., He, L., Zhao, J. Z., & Zhang, X. D. (2002). Characterisation of surface oxide films on titanium and bioactivity. *Journal of materials science: Materials in Medicine*, 13(5), pp. 457-464.

Fernandez, A., Lassaletta, G., Jimenez, V. M., Justo, A., Gonzalez-Elipe, A. R., Herrmann, J. M., & Ait-Ichou, Y. (1995). Preparation and characterisation of TiO_2 photocatalysts supported on various rigid supports (glass, quartz and stainless steel). Comparative studies of photocatalytic activity in water purification. *Applied Catalysis B: Environmental*, 7(1-2), pp. 49-63.

Finklea, H. O. (1988). *Semiconductor Electrodes*. Netherlands: International Nuclear Information System. (21)10.

Förch, R., Schönherr, H., & Jenkins, A. T. A. (Eds.). (2009). Surface Design: Applications in *Bioscience and Nanotechnology*. John Wiley & Sons.

Ford, W. E., & Dana, E. S. (1991). A textbook of Mineralogy. 4nd ed. US: John Whiley & Sons.

Frauchiger, V. M., Schlottig, F., Gasser, B., & Textor, M. (2004). Anodic plasma-chemical treatment of CP titanium surfaces for biomedical applications. *Biomaterials*, 25(4), pp. 593-606.

Fujishima, A. Kohayakawa, K and Honda, K. Hydrogen production under sunlight with an electrochemical photocell. *Journal of the Electrochemical Society*. 1975. 122(11): 1487.

Fujishima, A. Zhang, X and Tryk, D. (2008). TiO_2 photocatalysis and related surface phenomena. *Surface Science Reports*, 63(12), pp. 515.

Fujishima, A., & Honda, K. (1972). Electrochemical photolysis of water at a semiconductor electrode. *Nature*, 238(5358), pp. 37.

Fujishima, A., Rao, T. N., & Tryk, D. A. (2000). Titanium dioxide photocatalysis. *Journal of Photochemistry and Photobiology C: Photochemistry Reviews*, 1(1), pp. 1-21.

Gamble, J. L. (1947). *Chemical Anatomy, Physiology and Pathology of Extracellular Fluid: A Lecture Syllabus*. UK: Harvard University Press.

Gao, Y., Masuda, Y., Peng, Z., Yonezawa, T., & Koumoto, K. (2003). Room temperature deposition of a TiO_2 thin film from aqueous peroxotitanate solution. *Journal of Materials Chemistry*, 13(3), pp. 608-613.

Gargas, M. L., Burgess, R. J., Voisard, D. E., Cason, G. H., & Andersen, M. E. (1989). Partition coefficients of low-molecular-weight volatile chemicals in various liquids and tissues. *Toxicology and Applied Pharmacology*, 98(1), pp. 87-99.

Gaul, E. (1993). Coloring titanium and related metals by electrochemical oxidation. *Journal of Chemical Education*, 70(3), pp. 176.

Ge, R., Fu, W., Yang, H., Zhang, Y., Zhao, W., Liu, Z., & Zou, G. (2008). Fabrication and characterisation of highly-ordered titania nanotubes via electrochemical anodization. *Materials Letters*, 62(17-18), pp. 2688-2691.

Geetha, M., Singh, A. K., Asokamani, R., & Gogia, A. K. (2009). Ti based biomaterials, the ultimate choice for orthopaedic implants–a review. *Progress in Materials Science*, 54(3), pp. 397-425.

Gheisari, H., Karamian, E., & Abdellahi, M. (2015). A novel hydroxyapatite–hardystonite nanocomposite ceramic. *Ceramics International*, 41(4), pp. 5967-5975.

Ghosh, T. B., Dhabal, S., & Datta, A. K. (2003). On crystallite size dependence of phase stability of nanocrystalline TiO_2. *Journal of Applied Physics*, 94(7), pp. 4577-4582.

Giordano, C., Saino, E., Rimondini, L., Pedeferri, M. P., Visai, L., Cigada, A., & Chiesa, R. (2011). Electrochemically induced anatase inhibits bacterial colonization on Titanium Grade 2 and Ti6Al4V alloy for dental and orthopedic devices. *Colloids and Surfaces B: Biointerfaces*, 88(2), pp. 648-655.

Goldstein, J. I., Newbury, D. E., Michael, J. R., Ritchie, N. W., Scott, J. H. J., & Joy, D. C. (2017). *Scanning Electron Microscopy and X-Ray Microanalysis*. 3rd ed. Springer.

Goossens, A., Maloney, E. L., & Schoonman, J. (1998). Gas-Phase synthesis of nanostructured anatase TiO_2. *Chemical Vapor Deposition*, 4(3), pp. 109-114.

Greenwood, N. N., & Earnshaw, A. (2012). *Chemistry of the Elements*. 2nd ed. Elsevier.

Grujić-Brojčin, M., Šćepanović, M., Dohčević-Mitrović, Z., & Popović, Z. V. (2006). Infrared study of nonstoichiometric anatase TiO_2 nanopowders. *Science of Sintering*, 38(2), pp. 183-189.

Guillemot, F., Prima, F., Bareille, R., Gordin, D., Gloriant, T., Porté-Durrieu, M. C., & Baquey, C. (2004). Design of new titanium alloys for orthopaedic applications. *Medical and Biological Engineering and Computing*, 42(1), pp, 137-141.

Guo, Y. P., Tang, H. X., Zhou, Y., Jia, D. C., Ning, C. Q., & Guo, Y. J. (2010). Effects of mesoporous structure and UV irradiation on *in vitro* bioactivity of titania coatings. *Applied Surface Science*, 256(16), 4945-4952.

Ha, H. S., Kim, C. W., Lim, Y. J., & Kim, M. J. (2006). Surface characteristics of anodic oxidized titanium according to the pore size. *Journal of Korean Academic Prosthodontics*, 44(3), pp. 200.

Hamilton, R. F., Wu, N., Porter, D., Buford, M., Wolfarth, M., & Holian, A. (2009). Particle length-dependent titanium dioxide nanomaterials toxicity and bioactivity. *Particle and Fibre Toxicology*, 6(1), pp. 35.

Han, Y., Chen, D., Sun, J., Zhang, Y., & Xu, K. (2008). UV-enhanced bioactivity and cell response of micro-arc oxidized titania coatings. *Acta Biomaterialia*, 4(5), pp. 1518-1529.

Hanaor, D. (2007). PhD Thesis. UNSW: School of Materials Science and Engineering.

Hanaor, D. A., & Sorrell, C. C. (2011). Review of the anatase to rutile phase transformation. *Journal of Materials Science*, 46(4), 855-874.

Harold, R. M. (2001). An introduction to appearance analysis. *Gatfworld*, 13(3), pp. 5-12.

Hayashi, K., Matsuguchi, N., Uenoyama, K., Kanemaru, T., & Sugioka, Y. (1989). Evaluation of metal implants coated with several types of ceramics as

biomaterials. *Journal of Biomedical Materials Research Part A*, 23(11), pp. 1247-1259.

Hayashi, K., Matsuguchi, N., Uenoyama, K., Kanemaru, T., & Sugioka, Y. (1989). Evaluation of metal implants coated with several types of ceramics as biomaterials. *Journal of Biomedical Materials Research Part A*, 23(11), pp. 1247-1259.

He, Q. J., Huang, Z. L., Cheng, X. K., & Yu, J. (2008). Thermal stability of porous A-type carbonated hydroxyapatite spheres. *Materials Letters*, 62(3), pp. 539-542.

Hench, L. L. (1991a). Bioceramics: from concept to clinic. *Journal of the American Ceramic Society*, 74(7), pp. 1487-1510.

Hench, L. L. (1991b). Molecular design of bioactive glasses and ceramics for implants. *Ceramics: Towards the 21st Century Ceram Soc of Japan*, pp. 519-34.

Hench, L. L. (Ed.). (2013). *An Introduction to Bioceramics*. Singapore: World Scientific Publishing Company.

Hench, L. L., Splinter, R. J., Allen, W. C., & Greenlee, T. K. (1971). Bonding mechanisms at the interface of ceramic prosthetic materials. *Journal of Biomedical Materials Research Part A*, 5(6), pp. 117-141.

Heness, G. L., & Ben-Nissan, B. (2004). Innovative bioceramics. *Materials Forum*, 27, pp. 104-114.

Hengerer, R., Bolliger, B., Erbudak, M., & Grätzel, M. (2000). Structure and stability of the anatase TiO_2 (101) and (001) surfaces. *Surface Science*, 460(1-3), pp. 162-169.

Herman, H. (1988). Plasma spray deposition processes. *MRS Bulletin*, 13(12), pp. 60-67.

Herrmann, J.-M. (1999). Heterogeneous photocatalysis: fundamentals and applications to the removal of various types of aqueous pollutants. *Catalysis Today*, 53(1): pp. 115.

Hoffmann, M. R., Martin, S. T., Choi, W., & Bahnemann, D. W. (1995). Environmental applications of semiconductor photocatalysis. *Chemical Reviews*, 95(1), pp. 69-96.

Hollinger, J. O. (Ed.). (2011). *An Introduction to Biomaterials*. Boca Raton, FL: CRC press.

Howard, C. J., Sabine, T. M., & Dickson, F. (1991). Structural and thermal parameters for rutile and anatase. *Acta Crystallographica Section B: Structural Science*, 47(4), pp. 462-468.

Huang, H., Winchester, K. J., Suvorova, A., Lawn, B. R., Liu, Y., Hu, X. Z., & Faraone, L. (2006). Effect of deposition conditions on mechanical properties of low-temperature PECVD silicon nitride films. *Materials Science and Engineering: A*, 435, pp. 453-459.

Iida, Y., & Ozaki, S. (1961). Grain growth and phase transformation of titanium oxide during calcination. *Journal of the American Ceramic Society*, 44(3), pp. 120-127.

Ikonopisov, S. (1977). Theory of electrical breakdown during formation of barrier anodic films. *Electrochimica Acta*, 22(10), pp. 1077-1082.

Imam, M. A., Fraker, A. C., Harris, J. S., & Gilmore, C. M. (1983). Influence of heat treatment on the fatigue lives of Ti-6Al-4V and Ti-4.5 Al-5Mo-1.5 CR. in Titanium Alloys in Surgical Implants, ASTM International.

Ishizawa, H., & Ogino, M. (1995). Characterisation of thin hydroxyapatite layers formed on anodic titanium oxide films containing Ca and P by hydrothermal treatment. Journal of Biomedical Materials Research Part A, 29(9), pp. 1071-1079.

Iwasa, F., Hori, N., Ueno, T., Minamikawa, H., Yamada, M., & Ogawa, T. (2010). Enhancement of osteoblast adhesion to UV-photofunctionalized titanium via an electrostatic mechanism. Biomaterials, 31(10), pp. 2717-2727.

Izman, S., Abdul-Kadir, M. R., Anwar, M., Nazim, E. M., Rosliza, R., Shah, A., & Hassan, M. A. (2012). Surface modification techniques for biomedical grade of titanium alloys: oxidation, carburization and ion implantation processes. in *Titanium Alloys-Towards Achieving Enhanced Properties for Diversified Applications*, London: InTech. 9, pp. 201-228.

Jackson, M. J., & Ahmed, W. (Eds.). (2007). *Surface Engineered Surgical Tools and Medical Devices*. US: Springer Science and Business Media.

Jaeggi, C., Kern, P., Michler, J., Patscheider, J., Tharian, J., & Munnik, F. (2006). Film formation and characterisation of anodic oxides on titanium for biomedical applications. *Surface and Interface Analysis*, 38(4), pp. 182-185.

Jaeggi, C., Kern, P., Michler, J., Zehnder, T., & Siegenthaler, H. (2005). Anodic thin films on titanium used as masks for surface micropatterning of biomedical devices. *Surface and Coatings Technology*, 200(5-6), pp. 1913-1919.

Jahromi, M. T., Yao, G., & Cerruti, M. (2013). The importance of amino acid interactions in the crystallization of hydroxyapatite. *Journal of the Royal Society Interface*, 10(80), pp. 20120906.

Jamieson, J. C., & Olinger, B. (1969). Pressure-temperature studies of anatase, brookite, and TiO_2: a discussion. *American Mineralogist*, 54(9-10), pp. 1477.

Jimmy, C. Y., Yu, J., Tang, H. Y., & Zhang, L. (2002). Effect of surface microstructure on the photoinduced hydrophilicity of porous TiO_2 thin films. *Journal of Materials Chemistry*, 12(1), pp. 81-85.

Johansson, C. B. (1991). *On Tissue Reactions to Metal Implants*. University of Göteborg. Dental Implants.

Jokanović, V., Izvonar, D., Dramićanin, M. D., Jokanović, B., Živojinović, V., Marković, D., & Dačić, B. (2006). Hydrothermal synthesis and nanostructure of carbonated calcium hydroxyapatite. *Journal of Materials Science: Materials in Medicine*, 17(6), pp. 539-546.

Jones, J. R. (2015). Reprint of: Review of bioactive glass: From Hench to hybrids. *Acta Biomaterialia*, 23, pp. S53-S82.

Jordan, D. R., Brownstein, S., Gilberg, S., Coupal, D., Kim, S., & Mawn, L. (2002). Hydroxyapatite and calcium phophate coatings on aluminium oxide orbital implants. *Canadian Journal of Ophthalmology*, 37(1), pp. 7-13.

Kaito, T., Myoui, A., Takaoka, K., Saito, N., Nishikawa, M., Tamai, N., & Yoshikawa, H. (2005). Potentiation of the activity of bone morphogenetic protein-2 in bone regeneration by a PLA–PEG/hydroxyapatite composite. *Biomaterials*, 26(1), pp. 73-79.

Kalita, S. J., Bhardwaj, A., & Bhatt, H. A. (2007). Nanocrystalline calcium phosphate ceramics in biomedical engineering. *Materials Science and Engineering: C*, 27(3), 441-449.

Kamei, M., & Mitsuhashi, T. (2000). Hydrophobic drawings on hydrophilic surfaces of single crystalline titanium dioxide: surface wettability control by mechanochemical treatment. *Surface Science*, 463(1), pp. L609-L612.

Kannan, S., Lemos, A. F., & Ferreira, J. M. F. (2006). Synthesis and mechanical performance of biological-like hydroxyapatites. *Chemistry of Materials*, 18(8), pp. 2181-2186.

Karambakhsh, A., Afshar, A., & Malekinejad, P. (2012). Corrosion resistance and color properties of anodised Ti-6Al-4V. *Journal of Materials Engineering and Performance*, 21(1), pp. 121-127.

Kasuga, T., Kondo, H., & Nogami, M. (2002). Apatite formation on TiO_2 in simulated body fluid. *Journal of Crystal Growth*, 235(1-4), pp. 235-240.

Katsumata, K. I., Nakajima, A., Shiota, T., Yoshida, N., Watanabe, T., Kameshima, Y., & Okada, K. (2006). Photoinduced surface roughness variation in polycrystalline TiO_2 thin films. *Journal of Photochemistry and Photobiology A: Chemistry*, 180(1-2), pp. 75-79.

Kavan, L., Grätzel, M., Gilbert, S. E., Klemenz, C., & Scheel, H. J. (1996). Electrochemical and photoelectrochemical investigation of single-crystal anatase. *Journal of the American Chemical Society*, 118(28), pp. 6716-6723.

Kern, P., Michler, J., & Jäggi, C. H. (2005). Anodic titanium oxides grown in sulphuric and phosphoric acid electrolytes. *European Cells and Materials*. 5(10): pp. STE5.

Keshmiri, M., & Troczynski, T. (2003). Apatite formation on TiO_2 anatase microspheres. *Journal of Non-Crystalline Solids*, 324(3), pp. 289-294.

Khan, W., Kapoor, M., & Kumar, N. (2007). Covalent attachment of proteins to functionalized polypyrrole-coated metallic surfaces for improved biocompatibility. *Acta Biomaterialia*, 3(4), pp. 541-549.

Kim, H. M. (2003). Ceramic bioactivity and related biomimetic strategy. *Current Opinion in Solid State and Materials Science*, 7(4-5), pp. 289-299.

Kim, H. M., Miyaji, F., Kokubo, T., & Nakamura, T. (1996). Preparation of bioactive Ti and its alloys via simple chemical surface treatment. *Journal of Biomedical Materials Research: An Official Journal of the Society for Biomaterials and the Japanese Society for Biomaterials*, 32(3), pp. 409-417.

Kim, H. M., Miyaji, F., Kokubo, T., & Nakamura, T. (1997). Effect of heat treatment on apatite-forming ability of Ti metal induced by alkali treatment. *Journal of Materials Science: Materials in Medicine*, 8(6), pp. 341-347.

Kim, H. M., Miyaji, F., Kokubo, T., Nishiguchi, S., & Nakamura, T. (1999). Graded surface structure of bioactive titanium prepared by chemical treatment.

Journal of Biomedical Materials Research: An Official Journal of The Society for Biomaterials, *The Japanese Society for Biomaterials, and The Australian Society for Biomaterials*, 45(2), pp. 100-107.

Kinnings, S. L., Liu, N., Buchmeier, N., Tonge, P. J., Xie, L., & Bourne, P. E. (2009). Drug discovery using chemical systems biology: repositioning the safe medicine Comtan to treat multi-drug and extensively drug resistant tuberculosis. *PLoS Computational Biology*, 5(7), pp. e1000423.

Kobayakawa, K., Sato, C., Sato, Y., & Fujishima, A. (1998). Continuous-flow photoreactor packed with titanium dioxide immobilized on large silica gel beads to decompose oxalic acid in excess water. *Journal of Photochemistry and Photobiology A: Chemistry*, 118(1), pp. 65-69.

Kokubo, T. (1990). Surface chemistry of bioactive glass-ceramics. *Journal of Non-Crystalline Solids*, 120(1-3), pp. 138-151.

Kokubo, T. (1991). Recent progress in glass-based materials for biomedical applications. *Journal of the Ceramic Society of Japan*, 99(1154), pp. 965-973.

Kokubo, T. (2014). *Implants for Surgery-In Vitro Evaluation for Apatite-Forming Ability of Implant Materials*. ISO 23317.

Kokubo, T., & Takadama, H. (2006). How useful is SBF in predicting *in vivo* bone bioactivity?. *Biomaterials*, 27(15), pp. 2907-2915.

Kokubo, T., & Yamaguchi, S. (2009). Novel bioactive titanate layers formed on Ti metal and its alloys by chemical treatments. *Materials*, 3(1), pp. 48-63.

Kokubo, T., Kim, H. M., & Kawashita, M. (2003). Novel bioactive materials with different mechanical properties. *Biomaterials*, 24(13), pp. 2161-2175.

Kokubo, T., Kushitani, H., Sakka, S., Kitsugi, T., & Yamamuro, T. (1990). Solutions able to reproduce *in vivo* surface-structure changes in bioactive glass-ceramic A-W3. *Journal of Biomedical Materials Research Part A*, 24(6), pp. 721-734.

Kraft, L., & Hermansson, L. (2003). *Dimension Stable Binding Agent Systems for Dental. Application*. U.S. Patent 6,620,232.

Kumar, R., Prakash, K. H., Cheang, P., & Khor, K. A. (2004). Temperature driven morphological changes of chemically precipitated hydroxyapatite nanoparticles. *Langmuir*, 20(13), pp. 5196-5200.

Kumar, S., Narayanan, T. S., Raman, S. G. S., & Seshadri, S. K. (2010). Thermal oxidation of Ti6Al4V alloy: Microstructural and electrochemical characterisation. *Materials Chemistry and Physics*, 119(1-2), pp. 337-346.

Kuriakose, T. A., Kalkura, S. N., Palanichamy, M., Arivuoli, D., Dierks, K., Bocelli, G., & Betzel, C. (2004). Synthesis of stoichiometric nano crystalline hydroxyapatite by ethanol-based sol–gel technique at low temperature. *Journal of Crystal Growth*, 263(1-4), pp. 517-523.

Kuromoto, N. K., Simão, R. A., & Soares, G. A. (2007). Titanium oxide films produced on commercially pure titanium by anodic oxidation with different voltages. *Materials Characterisation*, 58(2), pp. 114-121.

Kutz, M. (2003). Standard handbook of biomedical engineering and design. McGraw-Hill.

Langer, R., & Peppas, N. A. (2003). Advances in biomaterials, drug delivery, and bionanotechnology. *AIChE Journal*, 49(12), pp. 2990-3006.

Lausmaa, J., & Linder, L. (1988). Surface spectroscopic characterisation of titanium implants after separation from plastic-embedded tissue. Biomaterials, 9(3), pp. 277-280.

Leach, J. S. L., & Pearson, B. R. (1988). Crystallization in anodic oxide films. *Corrosion Science*, 28(1), pp. 43-56.

Leconte, J., Markovits, A., Skalli, M. K., Minot, C., & Belmajdoub, A. (2002). Periodic ab initio study of the hydrogenated rutile TiO_2 (1 1 0) surface. *Surface Science*, 497(1-3), pp. 194-204.

Lee, H. B. (1989). Application of Synthetic Polymers in Implants. in Seagusa, L., Higashimura, T., & Abe, A. (Eds.). *Frontiers of Macromolecular Sciences.* Oxford: Blackwell Scientific Publications. pp. 579-584.

LeGeros, R. Z. (1988). Calcium phosphate materials in restorative dentistry: a review. *Advances in Dental Research*, 2(1), pp. 164-180.

Li, G., Li, L., Boerio-Goates, J., & Woodfield, B. F. (2005). High purity anatase TiO_2 nanocrystals: near room-temperature synthesis, grain growth kinetics, and surface hydration chemistry. *Journal of the American Chemical Society*, 127(24), pp. 8659-8666.

Li, L. H., Kong, Y. M., Kim, H. W., Kim, Y. W., Kim, H. E., Heo, S. J., & Koak, J. Y. (2004). Improved biological performance of Ti implants due to surface modification by micro-arc oxidation. *Biomaterials*, 25(14), pp. 2867-2875.

Li, P., & Ducheyne, P. (1998). Quasi-biological apatite film induced by titanium in a simulated body fluid. *Journal of Biomedical Materials Research: An Official Journal of The Society for Biomaterials, The Japanese Society for*

Biomaterials, and the Australian Society for Biomaterials, 41(3), pp. 341-348.

Li, P., Kangasniemi, I., Groot, K., & Kokubo, T. (1994). Bonelike Hydroxyapatite Induction by a Gel-Derived Titania on a Titanium Substrate. *Journal of the American Ceramic Society*, 77(5), pp. 1307-1312.

Li, P., Kangasniemi, I., Groot, K., & Kokubo, T. (1994). Bonelike Hydroxyapatite Induction by a Gel-Derived Titania on a Titanium Substrate. *Journal of the American Ceramic Society*, 77(5), pp. 1307-1312.

Li, W., Guo, T., Meng, T., Huang, Y., Li, X., Yan, W., & Li, X. (2013). Enhanced reversible wettability conversion of micro-nano hierarchical TiO_2/SiO_2 composite films under UV irradiation. *Applied Surface Science*, 283, pp. 12-18.

Liang, B., Fujibayashi, S., Tamura, J., Neo, M., Kim, H. M., Uchida, M., & Nakamura, T. (2003). Bone-bonding ability of anodic oxidized titanium. in Key Engineering Materials. *Trans Tech Publications*. 240, pp. 923-926.

Liang, Q., Chen, Y., Fan, Y., Hu, Y., Wu, Y., Zhao, Z., & Meng, Q. (2012). Tailoring the wettability of nanocrystalline TiO_2 films. *Applied Surface Science*, 258(7), pp. 2266-2269.

Lin, C. M., & Yen, S. K. (2006). Biomimetic growth of apatite on electrolytic TiO_2 coatings in simulated body fluid. *Materials Science and Engineering: C*, 26(1), pp. 54-64.

Lindberg, F., Heinrichs, J., Ericson, F., Thomsen, P., & Engqvist, H. (2008). Hydroxylapatite growth on single-crystal rutile substrates. *Biomaterials*, 29(23), pp. 3317-3323.

Linsebigler, A. L., Lu, G., & Yates Jr, J. T. (1995). Photocatalysis on TiO_2 surfaces: principles, mechanisms, and selected results. *Chemical reviews*, 95(3), pp. 735-758.

Liu, J., Ye, X., Wang, H., Zhu, M., Wang, B., & Yan, H. (2003). The influence of pH and temperature on the morphology of hydroxyapatite synthesized by hydrothermal method. *Ceramics International*, 29(6), pp. 629-633.

Liu, Q., Matinlinna, J. P., Chen, Z., Ning, C., Ni, G., Pan, H., & Darvell, B. W. (2015). Effect of thermal treatment on carbonated hydroxyapatite: Morphology, composition, crystal characteristics and solubility. *Ceramics International*, 41(5), pp. 6149-6157.

Liu, S., Li, B., Liang, C., Wang, H., & Qiao, Z. (2016). Formation mechanism and adhesive strength of a hydroxyapatite/TiO_2 composite coating on a titanium surface prepared by micro-arc oxidation. *Applied Surface Science*, 362, pp. 109-114.

Liu, X. Y., Zhao, X. B., Ding, C. X., & Chu, P. K. (2006). Light-induced Bioactive TiO_2 Surface. *Applied Physics Letters*. 2006. (88): 13905.

Liu, X., Chu, P. K., & Ding, C. (2004). Surface modification of titanium, titanium alloys, and related materials for biomedical applications. *Materials Science and Engineering: R: Reports*, 47(3-4), 49-121.

Liu, X., Zhao, X., Li, B., Cao, C., Dong, Y., Ding, C., & Chu, P. K. (2008). UV-irradiation-induced bioactivity on TiO_2 coatings with nanostructural surface. *Acta Biomaterialia*, 4(3), 544-552.

Long, M., & Rack, H. J. (1998). Titanium alloys in total joint replacement-a materials science perspective. *Biomaterials*, 19(18), 1621-1639.

Ma, J., Ge, X., Pelate, N., & Lei, S. (2015). Numerical investigation of two-dimensional thermally assisted ductile regime milling of nanocrystalline hydroxyapatite bioceramic material. *Ceramics International*, 41(3), pp. 3409-3419.

Ma, M. G. (2012). Hierarchically nanostructured hydroxyapatite: hydrothermal synthesis, morphology control, growth mechanism, and biological activity. *International Journal of Nanomedicine*, 7, pp. 1781.

Mann, S., Archibald, D. D., Didymus, J. M., Douglas, T., Heywood, B. R., Meldrum, F. C., & Reeves, N. J. (1993). Crystallization at inorganic-organic interfaces: biominerals and biomimetic synthesis. *Science*, 261(5126), pp. 1286-1292.

Mao, C., Li, H., Cui, F., Ma, C., & Feng, Q. (1999). Oriented growth of phosphates on polycrystalline titanium in a process mimicking biomineralization. *Journal of Crystal Growth*, 206(4), pp. 308-321.

Marchenoir, J. C., Loup, J. P., & Masson, J. (1980). Étude des couches poreuses formées par oxydation anodique du titane sous fortes tensions. *Thin Solid Films*, 66(3), pp. 357-369.

Mary, I. R., Sonia, S., Viji, S., Mangalaraj, D., Viswanathan, C., & Ponpandian, N. (2016). Novel multiform morphologies of hydroxyapatite: Synthesis and growth mechanism. *Applied Surface Science*, 361, pp. 25-32.

Masahashi, N., Semboshi, S., Ohtsu, N., & Oku, M. (2008). Microstructure and superhydrophilicity of anodic TiO_2 films on pure titanium. *Thin Solid Films*, 516(21), pp. 7488-7496.

Matthews, A. (1976). The crystallization of anatase and rutile from amorphous titanium dioxide under hydrothermal conditions. *American Mineralogist*, 61(5-6), pp. 419-424.

Mattie, D. R., & Bajpai, P. K. (1988). Analysis of the biocompatibility of ALCAP ceramics in rat femurs. *Journal of Biomedical Materials Research Part A*, 22(12), pp. 1101-1126.

Meagher, E. P., & Lager, G. A. (1979). Polyhedral thermal expansion in the TiO_2 polymorphs; refinement of the crystal structures of rutile and brookite at high temperature. *The Canadian Mineralogist*, 17(1), pp. 77-85.

Mehta, R. (2015). Powder metallurgy processing for low-cost titanium. Materials World Magazine. IOM^3. Retrieved June 5, 2018, from http://www.iom3.org/materials-world-magazine/news/2008/jul/01/powder-metallurgy-processing-lowcost-titanium

Messer, R. L., Lockwood, P. E., Wataha, J. C., Lewis, J. B., Norris, S., & Bouillaguet, S. (2003). *In vitro* cytotoxicity of traditional versus contemporary dental ceramics. *Journal of Prosthetic Dentistry*, 90(5), pp. 452-458.

Metzger, A. (1976). Polyethylene terephthalate and the pillar™ palatal implant: its historical usage and durability in medical applications. *Biomedical Engineering*, 11(9), pp. 301-306.

Mihov, D., & Katerska, B. (2010). Some biocompatible materials used in medical practice. *Trakia Journal of Sciences*, 8(2), pp. 119-125.

Mikula, M., Blecha, J., & Čeppan, M. (1992). Photoelectrochemical properties of anodic TiO_2 layers prepared by various current densities. *Journal of the Electrochemical Society*, 139(12), pp. 3470-3474.

Milella, E., Cosentino, F., Licciulli, A., & Massaro, C. (2001). Preparation and characterisation of titania/hydroxyapatite composite coatings obtained by sol-gel process. *Biomaterials*, 22(11), pp. 1425-1431.

Mills, A., & Le Hunte, S. (1997). An overview of semiconductor photocatalysis. *Journal of photochemistry and photobiology A: Chemistry*, 108(1), pp. 1-35.

Mills, A., Lee, S. K., & Lepre, A. (2003). Photodecomposition of ozone sensitised by a film of titanium dioxide on glass. *Journal of Photochemistry and Photobiology A: Chemistry*, 155(1-3), pp. 199-205.

Milošev, I., Blejan, D., Varvara, S., & Muresan, L. M. (2013). Effect of anodic oxidation on the corrosion behavior of Ti-based materials in simulated physiological solution. *Journal of Applied Electrochemistry*, 43(7), pp.645-658.

Miyata, T., Tsukada, S., & Minami, T. (2006). Preparation of anatase TiO_2 thin films by vacuum arc plasma evaporation. *Thin Solid Films*, 496(1), pp. 136-140.

Miyauchi, M., Kieda, N., Hishita, S., Mitsuhashi, T., Nakajima, A., Watanabe, T., & Hashimoto, K. (2002). Reversible wettability control of TiO_2 surface by light irradiation. *Surface Science*, 511(1-3), pp. 401-407.

Miyauchi, T., Yamada, M., Yamamoto, A., Iwasa, F., Suzawa, T., Kamijo, R., & Ogawa, T. (2010). The enhanced characteristics of osteoblast adhesion to photofunctionalized nanoscale TiO_2 layers on biomaterials surfaces. *Biomaterials*, 31(14), pp. 3827-3839.

Mor, G. K., Varghese, O. K., Paulose, M., Shankar, K., & Grimes, C. A. (2006). A review on highly ordered, vertically oriented TiO_2 nanotube arrays: Fabrication, material properties, and solar energy applications. Solar Energy *Materials and Solar Cells*, 90(14), pp. 2011-2075.

Morejón-Alonso, L., Santos, L. A., & García Carrodeguas, R. (2009). Influence of mixing liquid on the properties of calcium aluminate cement. in Key Engineering Materials. *Trans Tech Publications*. 396. pp. 241-244.

Murmson (2017). *Use of Sulfuric Acid and Phosphoric Acid in Titration*. Retrieved June 29, 2017, from http://sciencing.com/use-sulfuric-acid-phosphoric-acid-titration-9632.html

Murray, J. L. (1987). Phase diagrams of binary titanium alloys. *ASM international*, 340-345.

Nan, H., Ping, Y., Xuan, C., Yongxang, L., Xiaolan, Z., Guangjun, C., & Tingfei, X. (1998). Blood compatibility of amorphous titanium oxide films synthesized by ion beam enhanced deposition. *Biomaterials*, 19(7-9), 771-776.

Narayan, R. (Ed.). (2009). *Biomedical Materials*. US: Springer Science and Business Media.

Narayanan, T. S., Park, I. S., & Lee, M. H. (2014). Strategies to improve the corrosion resistance of microarc oxidation (MAO) coated magnesium alloys for degradable implants: prospects and challenges. *Progress in Materials Science*, 60, pp. 1-71.

Negishi, N., Iyoda, T., Hashimoto, K., & Fujishima, A. (1995). Preparation of transparent TiO_2 thin film photocatalyst and its photocatalytic activity. *Chemistry letters*, 24(9), pp. 841-842.

Niinomi, M. (2003). Recent research and development in titanium alloys for biomedical applications and healthcare goods. *Science and Technology of Advanced Materials*, 4(5), pp. 445.

Niinomi, M. (2008a). Mechanical biocompatibilities of titanium alloys for biomedical applications. *Journal of the Mechanical Behavior of Biomedical Materials*, 1(1), pp. 30-42.

Niinomi, M. (2008b). Biologically and mechanically biocompatible titanium alloys. *Materials Transactions*, 49(10), pp. 2170-2178.

Niinomi, M., Hanawa, T., & Narushima, T. (2005). Japanese research and development on metallic biomedical, dental, and healthcare materials. *JOM*, 57(4), pp. 18-24.

Nishiguchi, S., Fujibayashi, S., Kim, H. M., Kokubo, T., & Nakamura, T. (2003). Biology of alkali-and heat-treated titanium implants. *Journal of Biomedical Materials Research Part A*, 67(1), pp. 26-35.

Nishiguchi, S., Nakamura, T., Kobayashi, M., Kim, H. M., Miyaji, F., & Kokubo, T. (1999). The effect of heat treatment on bone-bonding ability of alkali-treated titanium. *Biomaterials*, 20(5), pp. 491-500.

Nordström, E. G., & Sánchez Muñoz, O. L. (2001). Physics of bone bonding mechanism of different surface bioactive ceramic materials *in vitro* and *in vivo*. *Bio-medical Materials and Engineering*, 11(3), pp. 221-231.

Oh, H. J., Lee, J. H., Jeong, Y., Kim, Y. J., & Chi, C. S. (2005). Microstructural characterisation of biomedical titanium oxide film fabricated by electrochemical method. *Surface and Coatings Technology*, 198(1-3), pp. 247-252.

Oh, H. J., Lee, J. H., Kim, Y. J., Suh, S. J., Lee, J. H., & Chi, C. S. (2008). Surface characteristics of porous anodic TiO_2 layer for biomedical applications. *Materials Chemistry and Physics*, 109(1), pp. 10-14.

Ohno, T., Sarukawa, K., Tokieda, K., & Matsumura, M. (2001). Morphology of a TiO_2 photocatalyst (Degussa, P-25) consisting of anatase and rutile crystalline phases. *Journal of Catalysis*, 203(1), pp. 82-86.

Ohno, T., Tokieda, K., Higashida, S., & Matsumura, M. (2003). Synergism between rutile and anatase TiO_2 particles in photocatalytic oxidation of naphthalene. *Applied Catalysis A: General*, 244(2), pp. 383-391.

OIV (2006). *Determination of chromatic characteristics according to CIELab. Compendium of International Methods of Analysis of Wines and Musts*. Retrieved June 5, 2018, from http://www.oiv.int/oiv/info/enmethodesinternationalesvin

Oldani, C., & Dominguez, A. (2012). Titanium as a Biomaterial for Implants. in *Recent Advances in Arthroplasty*. London: InTech, 9, pp. 149-162.

Oliva, A., Salerno, A., Locardi, B., Riccio, V., Della Ragione, F., Iardino, P., & Zappia, V. (1998). Behaviour of human osteoblasts cultured on bioactive glass coatings. *Biomaterials*, 19(11-12), pp. 1019-1025.

Oshida, Y., & Farzin-Nia, F. (2009). Response of Ti–Ni Alloys for Dental Biomaterials to Conditions in The Mouth. in *Shape Memory Alloys for Biomedical Applications*, pp. 101-149.

Palache, C., Berman, H., & Frondel, C. (1952). Dana's System of Mineralogy. *Geologiska Föreningen i Stockholm Förhandlingar*, 74(2), pp. 218-219.

Pan, H., & Darvell, B. W. (2010). Effect of carbonate on hydroxyapatite solubility. *Crystal Growth & Design*, 10(2), pp. 845-850.

Panda, R. N., Hsieh, M. F., Chung, R. J., & Chin, T. S. (2003). FTIR, XRD, SEM and solid state NMR investigations of carbonate-containing hydroxyapatite nano-particles synthesized by hydroxide-gel technique. *Journal of Physics and Chemistry of Solids*, 64(2), pp. 193-199.

Park, J. W., Jang, J. H., Lee, C. S., & Hanawa, T. (2009). Osteoconductivity of hydrophilic microstructured titanium implants with phosphate ion chemistry. *Acta Biomaterialia*, 5(6), pp. 2311-2321.

Park, J., & Lakes, R. S. (2007). Biomaterials: An Introduction. US: Springer Science & Business Media.

Park, S. J. (2008). Chemical observation of anodic TiO_2 for biomaterial application. *Metals and Materials International*, 14(4), pp. 449.

Park, T. E., Choe, H. C., & Brantley, W. A. (2013). Bioactivity evaluation of porous TiO_2 surface formed on titanium in mixed electrolyte by spark anodization. *Surface and Coatings Technology*, 235, pp. 706-713.

Pelkonen, O., & Turpeinen, M. (2007). *In vitro-in vivo* extrapolation of hepatic clearance: biological tools, scaling factors, model assumptions and correct concentrations. *Xenobiotica*, 37(10-11), pp. 1066-1089.

Pereira, B. L., Tummler, P., Marino, C. E., Soares, P. C., & Kuromoto, N. K. (2014). Titanium bioactivity surfaces obtained by chemical/electrochemical treatments. Matéria (Rio de Janeiro), 19(1), pp. 16-23.

Pham, H. H., & Wang, L. W. (2015). Oxygen vacancy and hole conduction in amorphous TiO_2. *Physical Chemistry Chemical Physics*, 17(1), pp. 541-550.

Pookmanee, P., & Phanichphant, S. (2009). Titanium dioxide powder prepared by a sol-gel method. *Journal of Ceramic Processing Research*, 10(2), pp. 167-170.

Prodana, M., Duta, M., Ionita, D., Bojin, D., Stan, M. S., Dinischiotu, A., & Demetrescu, I. (2015). A new complex ceramic coating with carbon nanotubes, hydroxyapatite and TiO_2 nanotubes on Ti surface for biomedical applications. *Ceramics International*, 41(5), pp. 6318-6325.

Qi, S., Huang, Y., Lin, Q., Cheng, H., & Seo, H. J. (2015). A bioactive Ca2SiB2O7 ceramics and *in vitro* hydroxyapatite mineralization ability in SBF. *Ceramics International*, 41(9), pp. 12011-12019.

Rack, H. J., & Qazi, J. I. (2006). Titanium alloys for biomedical applications. *Materials Science and Engineering: C*, 26(8), pp. 1269-1277.

Ramakrishna, S., Mayer, J., Wintermantel, E., & Leong, K. W. (2001). Biomedical applications of polymer-composite materials: a review. *Composites Science and Technology*, 61(9), pp. 1189-1224.

Ramamoorthy, M., Vanderbilt, D., & King-Smith, R. D. (1994). First-principles calculations of the energetics of stoichiometric TiO_2 surfaces. *Physical Review B*, 49(23), pp. 16721.

Ramesh, S., Tan, C. Y., Hamdi, M., Sopyan, I., & Teng, W. D. (2007). The influence of Ca/P ratio on the properties of hydroxyapatite bioceramics. in *International Conference on Smart Materials and Nanotechnology in Engineering. International Society for Optics and Photonics*. 6423, pp. 64233A.

Randorn, C., Kanta, A., Yaemsunthorn, K., & Rujijanakul, G. (2015). Fabrication of dense biocompatible hydroxyapatite ceramics with high hardness using a

peroxide-based route: a potential process for scaling up. *Ceramics International*, 41(4), pp. 5594-5599.

Rao, C. N. R., Turner, A., & Honig, J. M. (1959). Some observations concerning the effect of impurities on the anatase-rutile transition. *Journal of Physics and Chemistry of Solids*, 11(1-2), pp. 173-175.

Rao, S., Ushida, T., Tateishi, T., Okazaki, Y., & Asao, S. (1996). Effect of Ti, Al, and V ions on the relative growth rate of fibroblasts (L929) and osteoblasts (MC3T3-E1) cells. *Bio-medical materials and engineering*, 6(2), pp. 79-86.

Ratner, B. D. (2001). A Perspective on Titanium Biocompatibility. in *Titanium in Medicine*. Berlin, Heidelberg: Springer. pp. 1-12.

Ravaglioli, A., & Krajewski, A. (2012). *Bioceramics: Materials Properties·Applications*. US: Springer Science and Business Media.

Relman, D. A. (1998). Detection and identification of previously unrecognized microbial pathogens. *Emerging Infectious Diseases*, 4(3), pp. 382.

Rey, C., Collins, B., Goehl, T., Dickson, I. R., & Glimcher, M. J. (1989). The carbonate environment in bone mineral: a resolution-enhanced Fourier transform infrared spectroscopy study. *Calcified Tissue International*, 45(3), pp. 157-164.

Rothman, S. S. (2002). *Lessons from the Living Cell: The Culture Of Science And The Limits Of Reductionism*, New York: McGraw-Hill.

Rupp, F., Scheideler, L., Olshanska, N., De Wild, M., Wieland, M., & Geis-Gerstorfer, J. (2006). Enhancing surface free energy and hydrophilicity through chemical modification of microstructured titanium implant surfaces. *Journal of Biomedical Materials Research Part A*, 76(2), pp. 323-334.

Sakai, H., Baba, R., Hashimoto, K., Kubota, Y., & Fujishima, A. (1995). Selective killing of a single cancerous T24 cell with TiO_2 semiconducting microelectrode under irradiation. *Chemistry Letters*, 24(3), 185-186.

Saleh, S. S., & Abdullah, H. Z. (2015). Optimization and Characterisation of Anatase Formed on Anodised Titanium in Sulfuric Acid. in Advanced Materials Research. *Trans Tech Publications*. 1125, pp. 479-483.

Saleh, S. S., & Abdullah, H. Z. (2016). Optimization and Characterisation of Anatase Formed on Anodised Titanium in Phosphoric Acid. in Materials Science Forum. *Trans Tech Publications*. 840, pp. 240-244.

Samsonov, G. V. (2013). *The Oxide Handbook*. US: Springer Science and Business Media.

Samuneva, B., Kozhukharov, V., Trapalis, C., & Kranold, R. (1993). Sol-gel processing of titanium-containing thin coatings. *Journal of Materials Science*, 28(9), pp. 2353-2360.

Sarmiento, A. U. G. U. S. T. O., Zych, G. A., Latta, L. L., & Tarr, R. R. (1979). Clinical experiences with a titanium alloy total hip prosthesis: a posterior approach. *Clinical Orthopaedics and Related Research*, (144), pp. 166-173.

Sato, N. (1971). A theory for breakdown of anodic oxide films on metals. *Electrochimica Acta*, 16(10), pp. 1683-1692.

Sava, L., Pillai, S., More, U., & Sontakke, A. (2005). Serum calcium measurement: total versus free (ionized) calcium. *Indian Journal of Clinical Biochemistry*, 20(2), pp. 158-161.

Šćepanović, M., Dohčević-Mitrović, Z., Hinić, I., Grujić-Brojčin, M., Stanišić, G., & Popović, Z. V. (2005). Photoluminescence of laser-synthesized anatase titanium dioxide nanopowders. in *Materials Science Forum*. Trans Tech Publications. 494, pp. 265-270.

Scholz, M. S., Blanchfield, J. P., Bloom, L. D., Coburn, B. H., Elkington, M., Fuller, J. D., & Trevarthen, J. A. (2011). The use of composite materials in modern orthopaedic medicine and prosthetic devices: A review. *Composites Science and Technology*, 71(16), pp. 1791-1803.

Schreckenbach, J. P., Marx, G., Schlottig, F. E. A., Textor, M., & Spencer, N. D. (1999). Characterisation of anodic spark-converted titanium surfaces for biomedical applications. *Journal of Materials Science: Materials in Medicine*, 10(8), pp. 453-457.

Schwartz, Z., Kieswetter, K., Dean, D. D., & Boyan, B. D. (1997). Underlying mechanisms at the bone-surface interface during regeneration. *Journal of Periodontal Research*, 32(1), pp. 166-171.

Sclafani, A., & Herrmann, J. M. (1996). Comparison of the photoelectronic and photocatalytic activities of various anatase and rutile forms of titania in pure liquid organic phases and in aqueous solutions. *The Journal of Physical Chemistry*, 100(32), pp. 13655-13661.

Segneanu, A. E., Gozescu, I., Dabici, A., Sfirloaga, P., & Szabadai, Z. (2012). Organic Compounds FT-IR Spectroscopy. in *Macro To Nano Spectroscopy*. London: InTech.

Setiawati, E., & Kawano, K. (2008). Stabilization of anatase phase in the rare earth; Eu and Sm ion doped nanoparticle TiO_2. *Journal of Alloys and Compounds*, 451(1-2), pp. 293-296.

Setiawati, E., Kawano, K., Tsuboi, T., & Seo, H. J. (2008). Studies on thermal migration of Eu ion doped into TiO_2 nanoparticles. *Japanese Journal of Applied Physics*, 47(6R), pp. 4651.

Shannon, R. D., & Pask, J. A. (1965). Kinetics of the Anatase-Rutile Transformation. *Journal of the American Ceramic Society*, 48(8), pp. 391-398.

Shin, H., Jung, H. S., Hong, K. S., & Lee, J. K. (2005). Crystal phase evolution of TiO_2 nanoparticles with reaction time in acidic solutions studied via freeze-drying method. *Journal of Solid State Chemistry*, 178(1), pp. 15-21.

Silver, F. H., & Christiansen, D. L. (1999). Introduction to Structure and Properties of Polymers, Metals, and Ceramics. in *Biomaterials Science and Biocompatibility*. Springer: New York, NY. pp. 87-120.

Smith, S. J., Stevens, R., Liu, S., Li, G., Navrotsky, A., Boerio-Goates, J., & Woodfield, B. F. (2009). Heat capacities and thermodynamic functions of TiO_2 anatase and rutile: Analysis of phase stability. *American Mineralogist*, 94(2-3), pp. 236-243.

Song, H. J., Park, S. H., Jeong, S. H., & Park, Y. J. (2009). Surface characteristics and bioactivity of oxide films formed by anodic spark oxidation on titanium in different electrolytes. *Journal of Materials Processing Technology*, 209(2), pp. 864-870.

Spivak, J. M., Ricci, J. L., Blumenthal, N. C., & Alexander, H. (1990). A new canine model to evaluate the biological response of intramedullary bone to implant materials and surfaces. *Journal of Biomedical Materials Research Part A*, 24(9), pp. 1121-1149.

Spurr, R. A., & Myers, H. (1957). Quantitative analysis of anatase-rutile mixtures with an X-ray diffractometer. *Analytical Chemistry*, 29(5), pp. 760-762.

Steinemann, S. G. (1980). Corrosion of surgical implants *in vivo* and *in vitro* tests in evaluation of biomaterials. *Advances in Biomaterials*, 1, pp. 1-34.

Stepien, M., Saarinen, J. J., Teisala, H., Tuominen, M., Aromaa, M., Kuusipalo, J., & Toivakka, M. (2012). Surface chemical analysis of photocatalytic wettability conversion of TiO_2 nanoparticle coating. *Surface and Coatings Technology*, 208, pp. 73-79.

Sul, Y. T., Johansson, C. B., Jeong, Y., & Albrektsson, T. (2001). The electrochemical oxide growth behaviour on titanium in acid and alkaline electrolytes. *Medical Engineering and Physics*, 23(5), pp. 329-346.

Sul, Y. T., Johansson, C. B., Jeong, Y., Wennerberg, A., & Albrektsson, T. (2002b). Resonance frequency and removal torque analysis of implants with turned and anodised surface oxides. *Clinical Oral Implants Research*, 13(3), pp. 252-259.

Sul, Y. T., Johansson, C. B., Kang, Y., Jeon, D. G., & Albrektsson, T. (2002d). Bone reactions to oxidized titanium implants with electrochemical anion sulphuric acid and phosphoric acid incorporation. *Clinical implant dentistry and related research*, 4(2), pp. 78-87.

Sul, Y. T., Johansson, C. B., Petronis, S., Krozer, A., Jeong, Y., Wennerberg, A., & Albrektsson, T. (2002a). Characteristics of the surface oxides on turned and electrochemically oxidized pure titanium implants up to dielectric breakdown: the oxide thickness, micropore configurations, surface roughness, crystal structure and chemical composition. *Biomaterials*, 23(2), pp. 491-501.

Sul, Y. T., Johansson, C. B., Röser, K., & Albrektsson, T. (2002c). Qualitative and quantitative observations of bone tissue reactions to anodised implants. *Biomaterials*, 23(8), pp. 1809-1817.

Sumita, T., Yamaki, T., Yamamoto, S., & Miyashita, A. (2002). Photo-induced surface charge separation of highly oriented TiO_2 anatase and rutile thin films. *Applied Surface Science*, 200(1-4), pp. 21-26.

Sutherland, B. (1997). Ultraviolet Radiation Hazards to Humans. in Hardy, K. Meltz, M and Glickman, R (Eds.). *Nonionizing Radiation: An Overview of the Physics and Biology*. Madison: Medical Physics Publishing.

Svetina, M., Ciacchi, L. C., Sbaizero, O., Meriani, S., & De Vita, A. (2001). Deposition of calcium ions on rutile (110): a first-principles investigation. *Acta Materialia*, 49(12), pp. 2169-2177.

Takami, K., Adachi, T., Nakajima, A., Hashimoto, K., & Watanabe, T. (2002). Inorganic-organic functionally-graded films: The role of intermediate layers between TiO_2 coatings and polymer substrates. *Surface Coatings International Part B: Coatings Transactions*, 85(2), pp. 155-158.

Tanaka, K., Capule, M. F., & Hisanaga, T. (1991). Effect of crystallinity of TiO_2 on its photocatalytic action. *Chemical Physics Letters*, 187(1-2), pp. 73-76.

Teh, T. H., Berkani, A., Mato, S., Skeldon, P., Thompson, G. E., Habazaki, H., & Shimizu, K. (2003). Initial stages of plasma electrolytic oxidation of titanium. *Corrosion Science*, 45(12), pp. 2757-2768.

Thamaraiselvi, T., & Rajeswari, S. (2004). Biological evaluation of bioceramic materials-a review. *Carbon*, 24(31), pp. 172.

Thomas, M. V., & Puleo, D. A. (2009). Calcium sulfate: properties and clinical applications. *Journal of Biomedical Materials Research Part B: Applied Biomaterials*, 88(2), pp. 597-610.

Thomsen, P., Eriksson, A. S., & Olsson, R. (1986). Morphological Studies on Titanium Implants Inserted in Rabbit Knee-Joints. *Biomaterials and Clinical Applications*, pp. 87-92.

Tian, H., Tang, Z., Zhuang, X., Chen, X., & Jing, X. (2012). Biodegradable synthetic polymers: preparation, functionalization and biomedical application. *Progress in Polymer Science*, 37(2), pp. 237-280.

Tümmler, P., Pereira, B. L., Lepienski, C. M., Kuromoto, N. K., de Souza, P. R., & Soares, P. (2011). Bioactive films on titanium surface obtained by anodic oxidation in sulphuric and phosphuric Acid. in: *21st Brazilian Congress of Mechanical Engineering*. Natal, RN: Brazil. pp. 24-28.

Uchida, M., Kim, H. M., Kokubo, T., & Nakamura, T. (2001). Apatite-Forming Ability of Sodium-Containing Titania Gels in a Simulated Body Fluid. *Journal of the American Ceramic Society*, 84(12), pp. 2969-2974.

Uchida, M., Kim, H. M., Kokubo, T., Fujibayashi, S., & Nakamura, T. (2002). Effect of water treatment on the apatite-forming ability of NaOH-treated titanium metal. *Journal of Biomedical Materials Research Part A*, 63(5), pp. 522-530.

Uchida, M., Kim, H. M., Kokubo, T., Fujibayashi, S., & Nakamura, T. (2003). Structural dependence of apatite formation on titania gels in a simulated body fluid. *Journal of Biomedical Materials Research Part A*, 64(1), pp. 164-170.

Ueda, M., Kinoshita, T., Ikeda, M., & Ogawa, M. (2009). Photo-induced formation of hydroxyapatite on TiO_2 synthesized by a chemical-hydrothermal treatment. *Materials Science and Engineering: C*, 29(7), pp. 2246-2249.

Ueda, M., Sai, H., Ikeda, M., & Ogawa, M. (2010). Formation of hydroxyapatite on titanium oxides in simulated body fluid under UV irradiation. in Materials Science Forum. *Trans Tech Publications*. 654, pp. 2257-2260.

Uetsuki, K., Kaneda, H., Shirosaki, Y., Hayakawa, S., & Osaka, A. (2010). Effects of UV-irradiation on *in vitro* apatite-forming ability of TiO_2 layers. *Materials Science and Engineering: B*, 173(1-3), pp. 213-215.

Vallet-Regí, M. (2001). Ceramics for medical applications. Journal of the Chemical Society, *Dalton Transactions*, (2), pp. 97-108.

Van Gils, S., Mast, P., Stijns, E., & Terryn, H. (2004). Colour properties of barrier anodic oxide films on aluminium and titanium studied with total reflectance and spectroscopic ellipsometry. *Surface and Coatings Technology*, 185(2-3), pp. 303-310.

Van Noort, R. (1987). Titanium: the implant material of today. *Journal of Materials Science*, 22(11), pp. 3801-3811.

Venkatraman, S., Boey, F., & Lao, L. L. (2008). Implanted cardiovascular polymers: Natural, synthetic and bio-inspired. *Progress in Polymer Science*, 33(9), pp. 853-874.

Vergaro, V., Carlucci, C., Cascione, M., Lorusso, C., Conciauro, F., Scremin, B. F., & Ciccarella, G. (2015). Interaction between human serum albumin and different anatase TiO_2 nanoparticles: A nano-bio interface study. *Nanomaterials and Nanotechnology*, 5, 30.

Viceconti, M., Muccini, R., Bernakiewicz, M., Baleani, M., & Cristofolini, L. (2000). Large-sliding contact elements accurately predict levels of bone–implant micromotion relevant to osseointegration. *Journal of biomechanics*, 33(12), pp. 1611-1618.

Vignais, P. V., & Vignais, P. M. (2010). Discovering Life, Manufacturing Life: How The Experimental Method Shaped Life Sciences. US: Springer Science and Business Media.

von Laue, M. (1915). *Concerning the Detection of X-Ray Interferences*. Nobel lecture, 13.

von Recum, A. F. (1994). Biomaterials: Educational Goals. in *Annual Biomaterials Society Meeting*.

Vuvlsteker, P. (2004) *Colour Topics in Computer Graphics. Visible Spectrum*. Retrieved 6 June 2014, from http://escience.anu.edu.au/lecture/cg/ Colour/ HSV_HLS.en.html

Wang, H., Wang, T., & Xu, P. (1998). Effects of substrate temperature on the microstructure and photocatalytic reactivity of TiO_2 films. *Journal of Materials Science: Materials in Electronics*, 9(5), pp. 327-330.

Wang, M. C., Chen, H. T., Shih, W. J., Chang, H. F., Hon, M. H., & Hung, I. M. (2015). Crystalline size, microstructure and biocompatibility of hydroxyapatite nanopowders by hydrolysis of calcium hydrogen phosphate dehydrate (DCPD). *Ceramics International*, 41(2), pp. 2999-3008.

Wang, R., Hashimoto, K., Fujishima, A., Chikuni, M., Kojima, E., Kitamura, A., & Watanabe, T. (1998). Photogeneration of highly amphiphilic TiO_2 surfaces. *Advanced Materials*, 10(2), pp. 135-138.

Wang, R., Hashimoto, K., Fujishima, A., Chikuni, M., Kojima, E., Kitamura, A., & Watanabe, T. (1997). Light-induced amphiphilic surfaces. *Nature*, 388(6641), pp. 431.

Wang, Y., Yu, H., Chen, C., & Zhao, Z. (2015). Review of the biocompatibility of micro-arc oxidation coated titanium alloys. *Materials and Design*, 85, pp. 640-652.

Watanabe, T., Nakajima, A., Wang, R., Minabe, M., Koizumi, S., Fujishima, A., & Hashimoto, K. (1999). Photocatalytic activity and photoinduced hydrophilicity of titanium dioxide coated glass. *Thin solid films*, 351(1-2), pp. 260-263.

Wei, W., Jie, T., Tao, W., & Ling, W. A. N. G. (2007). Photocatalytic activity of porous TiO_2 films prepared by anodic oxidation. *Rare Metals*, 26(2), pp. 136-141.

Weir, A., Westerhoff, P., Fabricius, L., Hristovski, K., & Von Goetz, N. (2012). Titanium dioxide nanoparticles in food and personal care products. Environmental Science and Technology, 46(4), pp. 2242-2250.

Weller, M. T. (1994). *Inorganic Materials Chemistry*. UK: Oxford University Press.

Wells, A. F. (2012). *Structural Inorganic Chemistry*. UK: Oxford university press.

Williams, D. (1990). An introduction to medical and dental materials. Concise Encyclopedia of Medical and Dental Materials. In: W. D (Ed.). *Pergamon Press and The MIT Press*.

Williams, D. F. (2008). On the mechanisms of biocompatibility. *Biomaterials*, 29(20), pp. 2941-2953.

Wong, J. Y., & Bronzino, J. D. (2007). *Biomaterials*. Boca Raton, FL: CRC Press.

Wong, J. Y., Bronzino, J. D., & Peterson, D. R. (2013). *Biomaterials: Principles and Practices*. Boca Raton, FL: CRC Press.

Wu, C., & Chang, J. (2013). A review of bioactive silicate ceramics. *Biomedical materials*, 8(3), pp. 032001.

Wu, H., Lu, X., Long, B., Wang, X., Wang, J., & Jin, Z. (2005). The effects of cathodic and anodic voltages on the characteristics of porous nanocrystalline titania coatings fabricated by microarc oxidation. *Materials Letters*, 59(2-3), pp. 370-375.

Wu, K. R., Ting, C. H., Liu, W. C., Lin, C. H., & Wu, J. K. (2006). Successive deposition of layered titanium oxide/indium tin oxide films on unheated substrates by twin direct current magnetron sputtering. *Thin Solid Films*, 500(1-2), pp. 110-116.

Xia, W., Lindahl, C., Lausmaa, J., & Engqvist, H. (2011). Biomimetic hydroxyapatite deposition on titanium oxide surfaces for biomedical application. in *Advances in Biomimetics*. InTech. 20, pp. 429-452.

Xia, W., Lindahl, C., Lausmaa, J., Borchardt, P., Ballo, A., Thomsen, P., & Engqvist, H. (2010). Biomineralized strontium-substituted apatite/titanium dioxide coating on titanium surfaces. *Acta Biomaterialia*, 6(4), pp. 1591-1600.

Xiao, F., Tsuru, K., Hayakawa, S., & Osaka, A. (2003). *In vitro* apatite deposition on titania film derived from chemical treatment of Ti substrates with an oxysulfate solution containing hydrogen peroxide at low temperature. *Thin Solid Films*, 441(1-2), pp. 271-276.

Xie, L., Yin, G., Yan, D., Liao, X., Huang, Z., Yao, Y., & Liu, Y. (2010). Structure, morphology and fibroblasts adhesion of surface-porous titanium via anodic oxidation. *Journal of Materials Science: Materials in Medicine*, 21(1), pp. 259-266.

Xiong, T. Y., Cui, X. Y., Kim, H. M., Masakazu, K., Kokubo, T., Wu, J., & Nakamura, T. (2004). Effect of surface morphology and crystal structure on bioactivity

of titania films formed on titanium metal via anodic oxidation in sulfuric acid solution. in Key Engineering Materials. *Trans Tech Publications*. 254, pp. 375-378.

Yahalom, J. (1972). The role of the film/electrolyte interface in anodic breakdown. *Journal of The Electrochemical Society*, 119(8), pp. C231.

Yamamoto, A., Honma, R., Sumita, M., & Hanawa, T. (2004). Cytotoxicity evaluation of ceramic particles of different sizes and shapes. *Journal of Biomedical Materials Research Part A*, 68(2), 244-256.

Yamamoto, D., Iida, T., Arii, K., Kuroda, K., Ichino, R., Okido, M., & Seki, A. (2012b). Surface hydrophilicity and osteoconductivity of anodised Ti in aqueous solutions with various solute ions. *Materials Transactions*, 53(11), pp. 1956-1961.

Yamamoto, D., Kawai, I., Kuroda, K., Ichino, R., Okido, M., & Seki, A. (2011). Osteoconductivity of anodised titanium with controlled micron-level surface roughness. *Materials Transactions*, 52(8), 1650-1654.

Yamamoto, D., Kawai, I., Kuroda, K., Ichino, R., Okido, M., & Seki, A. (2012a). Osteoconductivity and hydrophilicity of TiO_2 coatings on Ti substrates prepared by different oxidizing processes. *Bioinorganic chemistry and applications*. pp. 1-7.

Yamamuro, T. (1989). Patterns of osteogenesis in relation to various biomaterials. Journal of Japanese Society for Biomaterials, 7, pp. 19-23.

Yang, B. C., Gan, L., Li, Z. S., Huang, Y., Qu, Y., & Zhang, X. D. (2007). Preparation of bioactive tantalum metal via anodic oxidation treatment. *Key Engineering Materials*. 330, pp. 637-640.

Yang, B., Uchida, M., Kim, H. M., Zhang, X., & Kokubo, T. (2004a). Preparation of bioactive titanium metal via anodic oxidation treatment. *Biomaterials*, 25(6), pp. 1003-1010.

Yang, C. L., Chen, F. L., & Chen, S. W. (2006). Anodization of the dental arch wires. Materials Chemistry and Physics, 100(2-3), pp. 268-274.

Yang, M. C., Yang, T. S., & Wong, M. S. (2004). Nitrogen-doped titanium oxide films as visible light photocatalyst by vapor deposition. *Thin Solid Films*, 469, pp. 1-5.

Yang, Y., & Ong, J. L. (2003). Bond strength, compositional, and structural properties of hydroxyapatite coating on Ti, ZrO_2-coated Ti, and TPS-coated Ti substrate. *Journal of Biomedical Materials Research Part A*, 64(3), pp. 509-516.

Yerokhin, A. L., Nie, X., Leyland, A., Matthews, A., & Dowey, S. J. (1999). Plasma electrolysis for surface engineering. *Surface and Coatings Technology*, 122(2-3), pp. 73-93.

Yin, Z. F., Wu, L., Yang, H. G., & Su, Y. H. (2013). Recent progress in biomedical applications of titanium dioxide. *Physical Chemistry Chemical Physics*, 15(14), pp. 4844-4858.

Yoruç, A. B. H., & Şener, B. C. (2012). Biomaterials. In: Kara, S (Ed.). *A Roadmap of Biomedical Engineers and Milestones*. London: InTech, pp. 67-114.

Youn, H. Y., McCanna, D. J., Sivak, J. G., & Jones, L. W. (2011). *In vitro* ultraviolet-induced damage in human corneal, lens, and retinal pigment epithelial cells. *Molecular Vision*, 17, 237.

Young, C. (2009). Solar ultraviolet radiation and skin cancer. *Occupational Medicine*, 59(2), pp. 82-88.

Young, T. (1832). An essay on the cohesion of fluids. In Abstracts of the Papers Printed in the Philosophical Transactions of the Royal Society of London, *The Royal Society*, 1, pp. 171-172.

Yu, J., & Zhao, X. (2001). Effect of surface microstructure on the super-hydrophilic property of the sol-gel derived porous TiO_2 thin films. *Journal of Materials Science Letters*, 20(7), pp. 671-673.

Yu, J., Zhao, X., Zhao, Q., & Wang, G. (2001). Preparation and characterisation of super-hydrophilic porous TiO_2 coating films. *Materials Chemistry and Physics*, 68(1-3), pp. 253-259.

Zadpoor, A. A. (2014). Relationship between in vitro apatite-forming ability measured using simulated body fluid and *in vivo* bioactivity of biomaterials. *Materials Science and Engineering: C*, 35, pp. 134-143.

Zeman, P., & Takabayashi, S. (2002). Self-cleaning and antifogging effects of TiO_2 films prepared by radio frequency magnetron sputtering. Journal of Vacuum Science & Technology A: Vacuum, *Surfaces, and Films*, 20(2), pp. 388-393.

Zhang, J., Xu, Q., Feng, Z., Li, M., & Li, C. (2008). Importance of the relationship between surface phases and photocatalytic activity of TiO_2. *Angewandte Chemie International Edition*, 47(9), pp. 1766-1769.

Zhang, M., & Matinlinna, J. P. (2012). E-glass fiber reinforced composites in dental applications. *Silicon*, 4(1), pp. 73-78.

Zhang, Y. H., & Reller, A. (2002). Phase transformation and grain growth of doped nanosized titania. *Materials Science and Engineering: C*, 19(1-2), pp. 323-326.

Zhao, J., Wang, X., Chen, R., & Li, L. (2005). Fabrication of titanium oxide nanotube arrays by anodic oxidation. *Solid State Communications*, 134(10), pp. 705-710.

Zhao, M., Li, J., Li, Y., Wang, J., Zuo, Y., Jiang, J., & Wang, H. (2014). Gradient control of the adhesive force between Ti/TiO_2 nanotubular arrays fabricated by anodization. *Scientific Reports*, 4, pp. 7178.

Zhao, W., Lemaître, J., & Bowen, P. (2017). A comparative study of simulated body fluids in the presence of proteins. *Acta Biomaterialia*, 53, pp. 506-514.

Zhou, M., Yu, J., & Cheng, B. (2006). Effects of Fe-doping on the photocatalytic activity of mesoporous TiO_2 powders prepared by an ultrasonic method. *Journal of Hazardous Materials*, 137(3), pp. 1838-1847.

Zhu, X., Kim, K., Ong, J. L., & Jeong, Y. (2002). Surface analysis of anodic oxide films containing phosphorus on titanium. *International Journal of Oral and Maxillofacial Implants*, 17(3).

Zinger, O., Chauvy, P. F., & Landolt, D. (2003). Scale-resolved electrochemical surface structuring of titanium for biological applications. *Journal of The Electrochemical Society*, 150(11), pp. B495-B503.

Zisman, W. A. (1964). Relation of the equilibrium contact angle to liquid and solid constitution. In: Fowkes, F. M (Ed.). *Contact Angle, Wettability, and Adhesion*. Washington D.C: American Chemical society. pp. 43.

Zuldesmi, M., Waki, A., Kuroda, K., & Okido, M. (2013). High osteoconductive surface of pure titanium by hydrothermal treatment. *Journal of Biomaterials and Nanobiotechnology*, 4(03), pp. 284.

Zyman, Z. Z., Rokhmistrov, D. V., & Loza, K. I. (2013). Determination of the Ca/P ratio in calcium phosphates during the precipitation of hydroxyapatite using X-ray diffractometry. *Processing and Application of Ceramics*, 7(2), pp. 93-95.

APPENDICES

APPENDIX A

Digital Reflectance Colour Taken By Colormeter

Digital interference colour of the coatings anodised in 0.1 M H_2SO_4

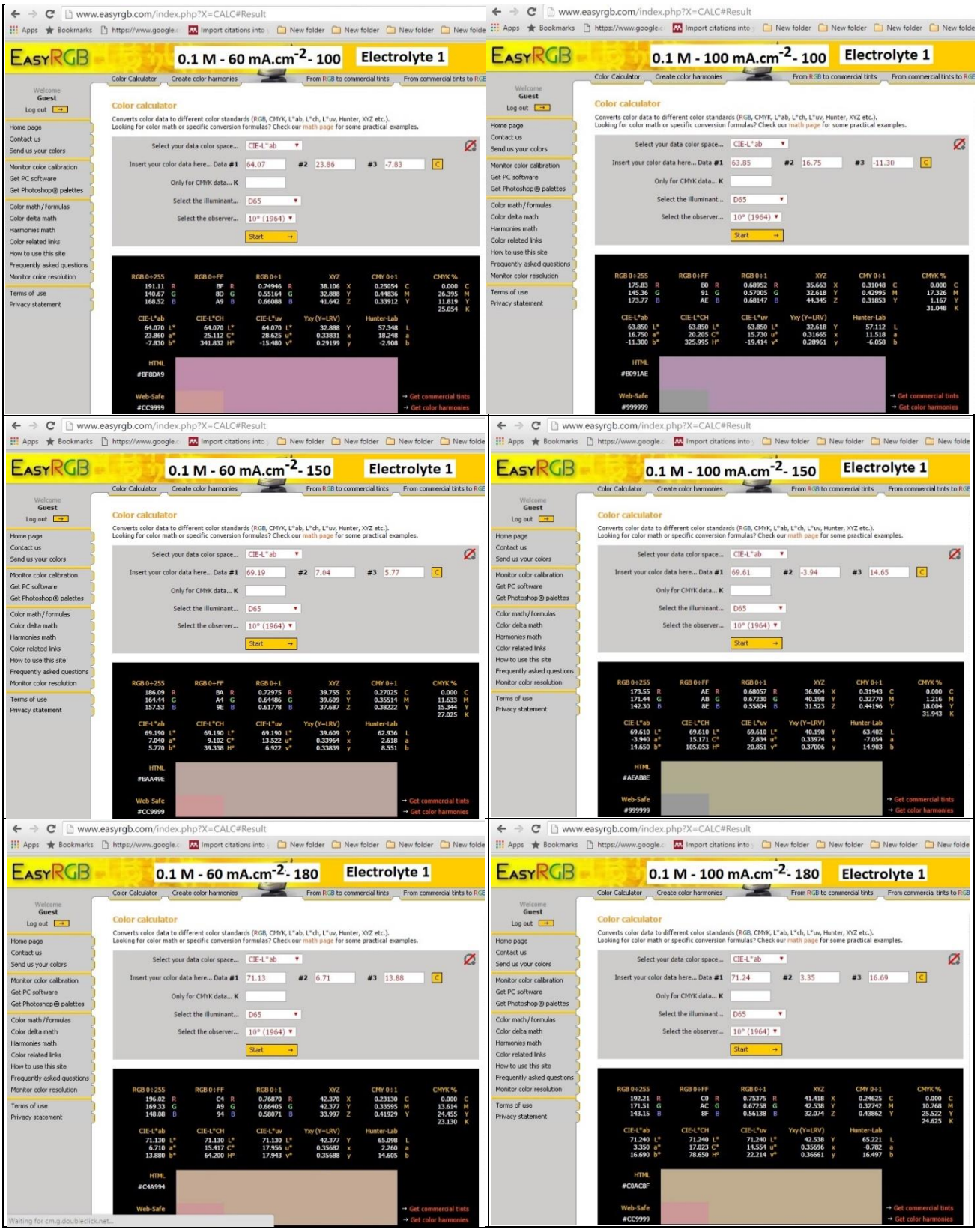

APPENDIX B

Elemental Results Taken By Energy Dispersive X-Ray Spectroscopy (EDX)

Digital interference colour of the coatings anodised in 0.1 M H_2SO_4 at 150 V and 100 mA.cm^{-2}

View000

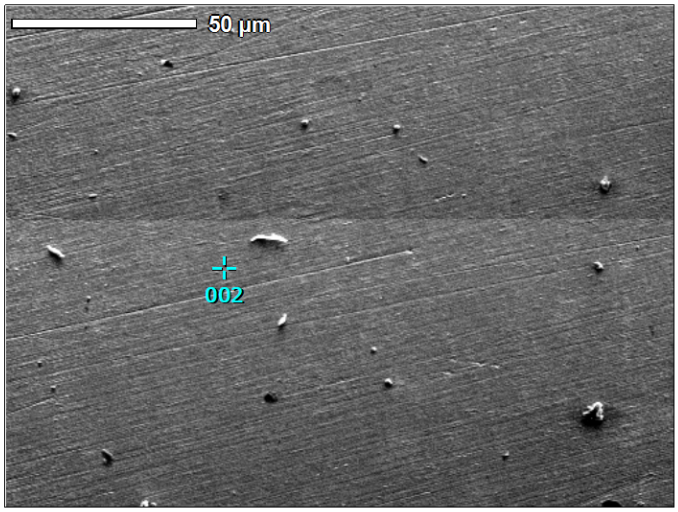


```
---------------------------
Title        : IMG1
---------------------------
Instrument   : 6380(LA)
Volt         : 15.00 kV
Mag          : x 700
Date         : 2016/08/15
Pixel        : 512 x 384
---------------------------
```

002

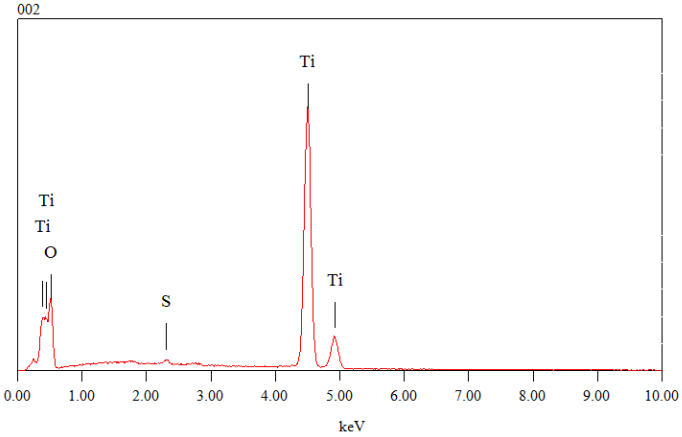


```
Acquisition Parameter
Instrument    : 6380(LA)
Acc. Voltage : 15.0 kV
Probe Current: 1.00000 nA
PHA mode      : T3
Real Time     : 114.14 sec
Live Time     : 100.00 sec
Dead Time     : 12 %
Counting Rate: 2449 cps
Energy Range :  0 - 20 keV
```

ZAF Method Standardless Quantitative Analysis
Fitting Coefficient : 0.2928

Element	(keV)	mass%	Error%	At%	Compound	mass%	Cation	K
O K	0.525	29.77	0.58	55.86				12.1093
S K	2.307	0.42	0.15	0.39				0.5704
Ti K	4.508	69.81	0.42	43.75				87.3203
Total		100.00		100.00				

Digital interference colour of the apatite formed in the coating anodised in 0.1 M H_2SO_4 at 150 V and 100 mA.cm^{-2} in the dark for 6 days

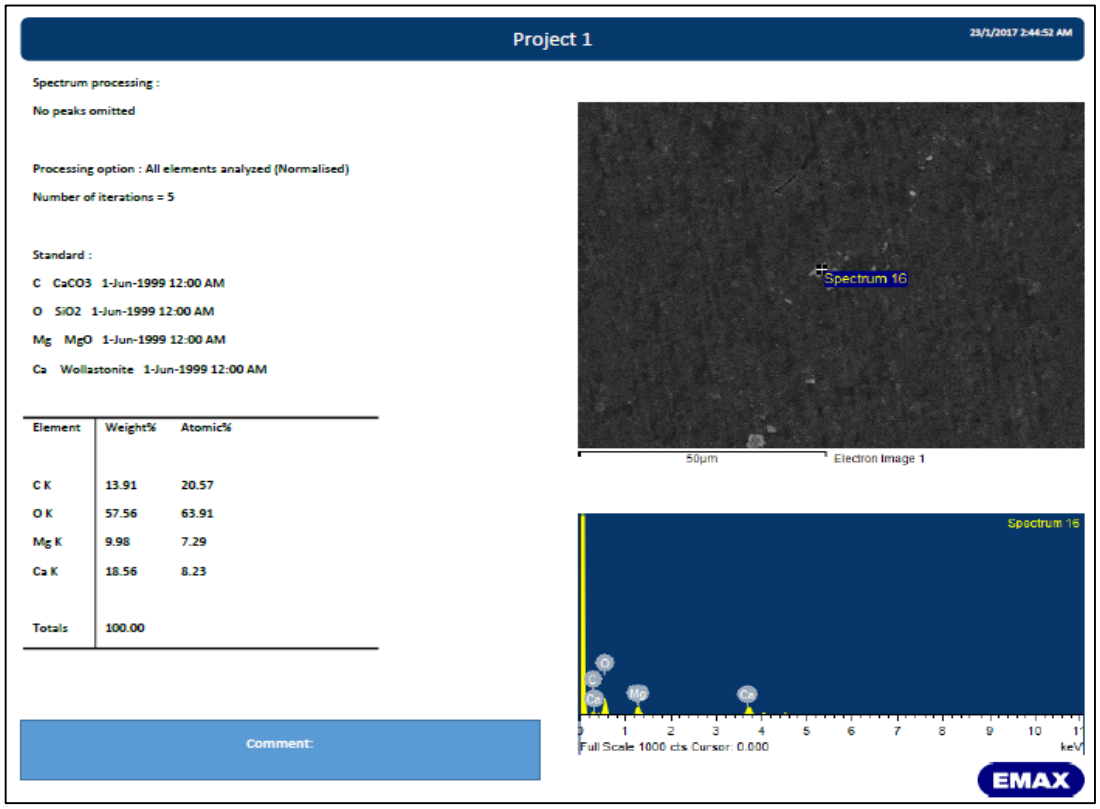

Digital interference colour of the apatite formed in the coating anodised in 0.1 M H_2SO_4 at 150 V and 100 mA.cm^{-2} in the dark for 12 days

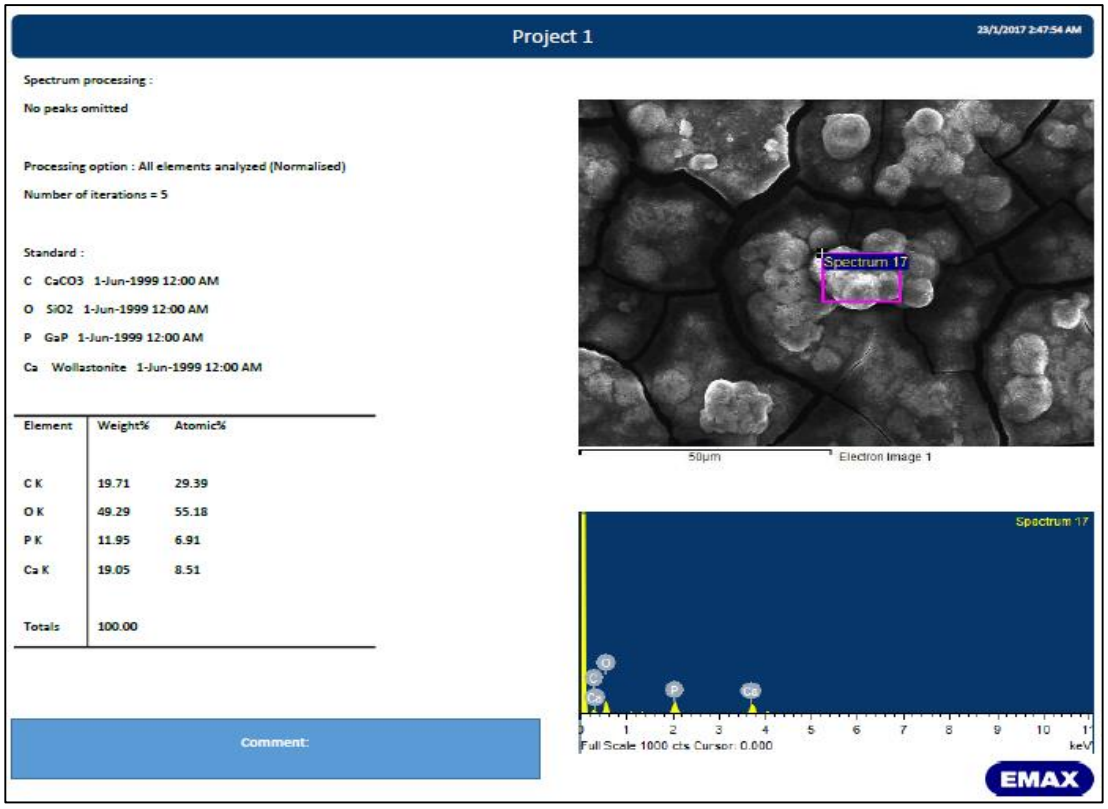

APPENDIX C

Thickness measurement by sample cross section using microstructure image

Cross-section of the coatings anodised in 0.1 M H_2SO_4 at 150 V at 100 V and 60 $mA.cm^{-2}$

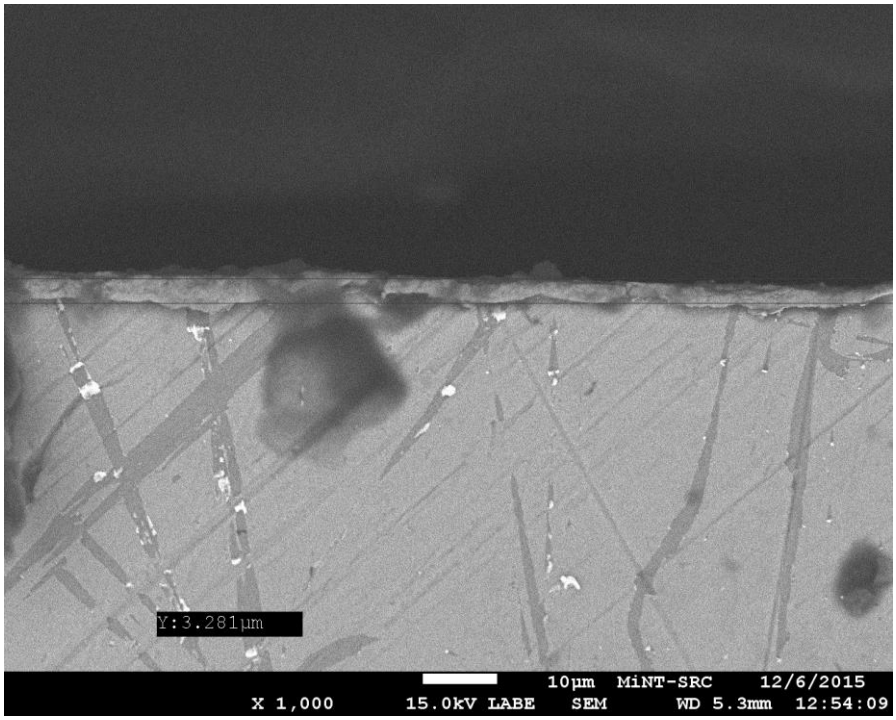

Cross-section of the coatings anodised in 0.1 M H_2SO_4 at 150 V at 100 V and 100 $mA.cm^{-2}$

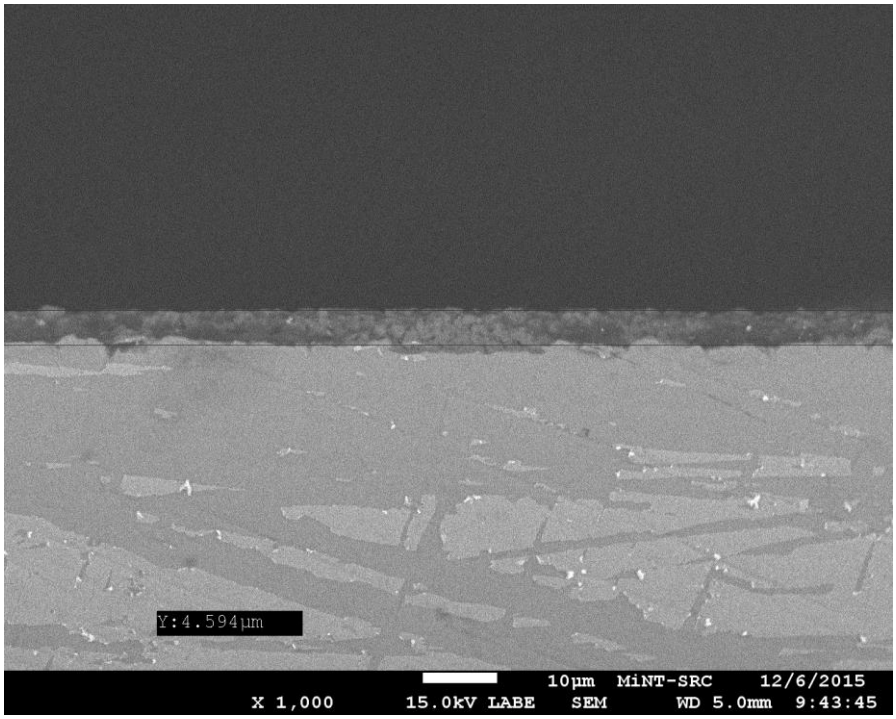

APPENDIX D

Mineralogical Analysis Taken By X-Ray Diffraction (XRD)

Mineralogical pattern of the TiO_2 coating anodised in 0.1 M H_2SO_4 at 150 V and 100 $mA.cm^{-2}$

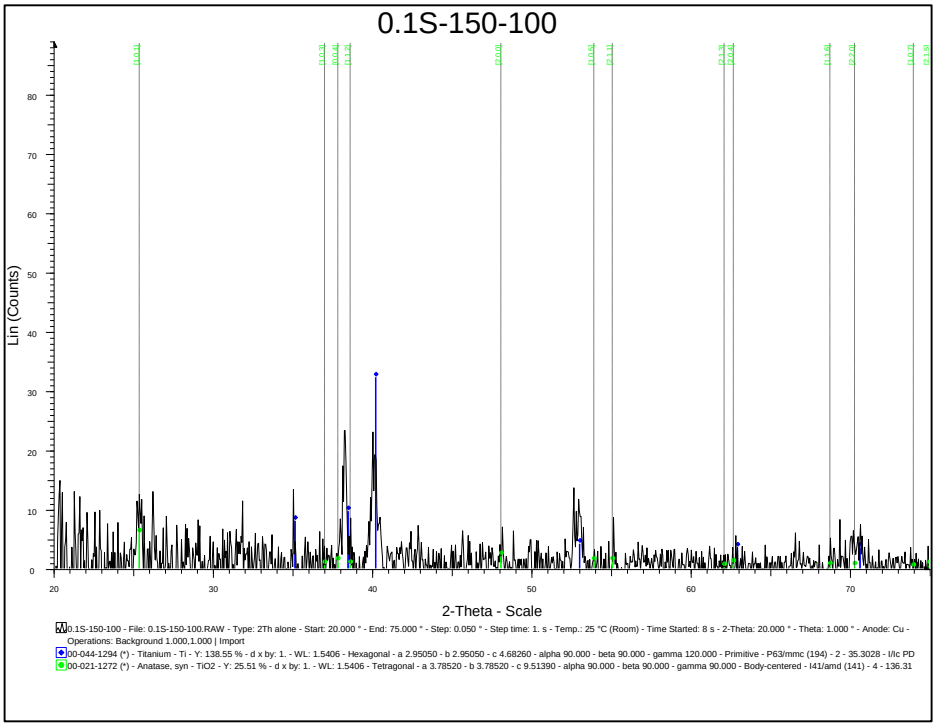

Mineralogical pattern of the TiO_2 coating anodised in 2.0 M H_2SO_4 at 150 V and 100 $mA.cm^{-2}$

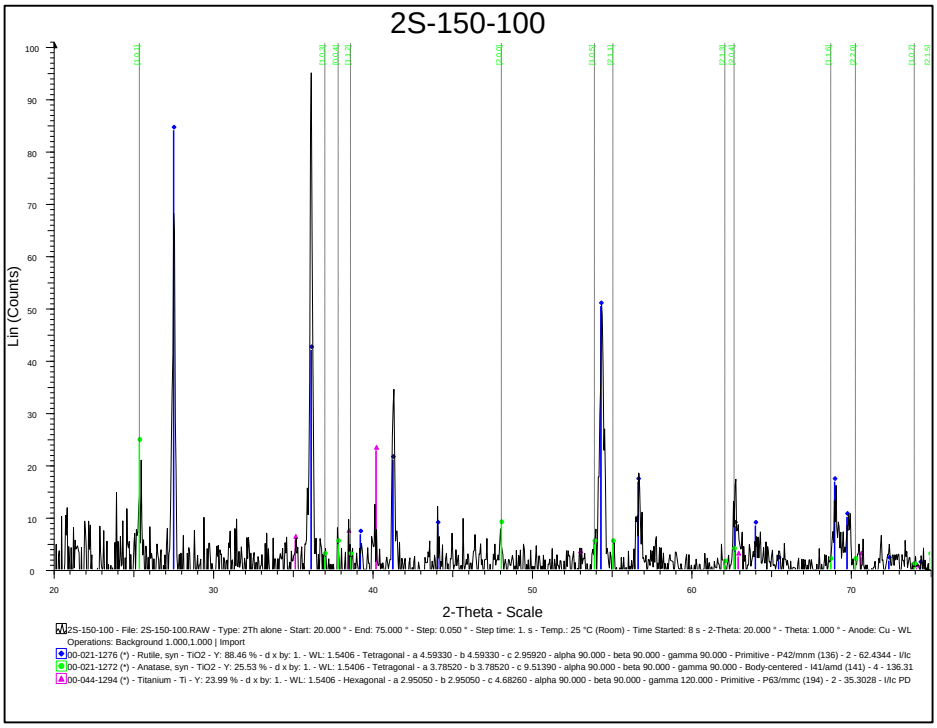

APPENDIX E

Hydrophilicity Taken By Water Contact Angle (WCA) Tester

Hydrophilicity test of the coating anodised in 0.1 M H_2SO_4 at 150 V and 100 $mA.cm^{-2}$

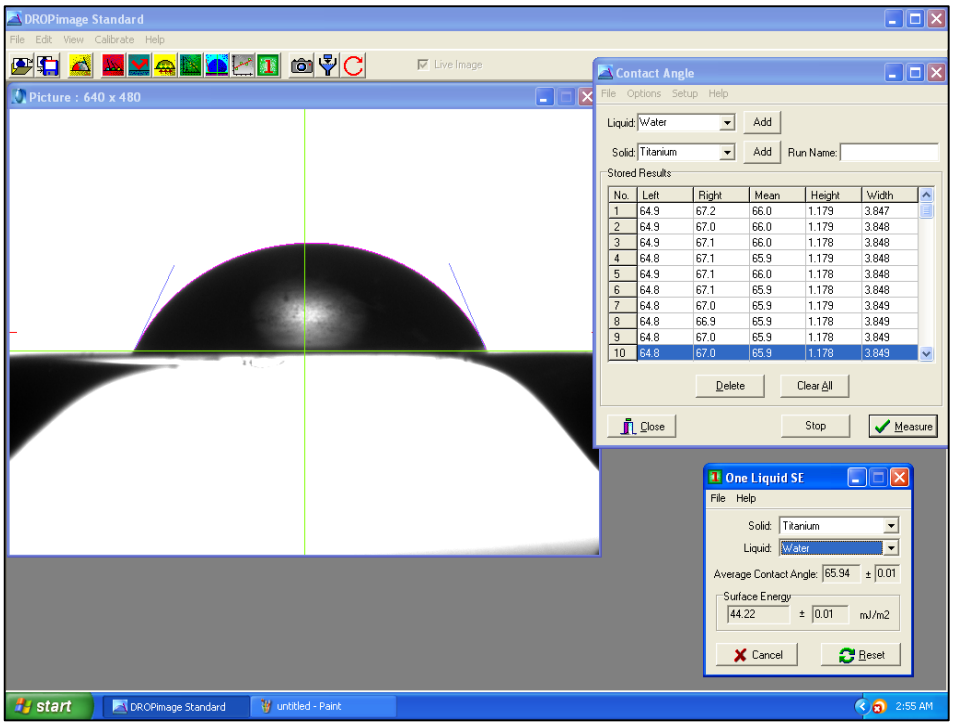

Hydrophilicity test of the coating anodised in 2.0 M H_2SO_4 at 150 V and 100 $mA.cm^{-2}$

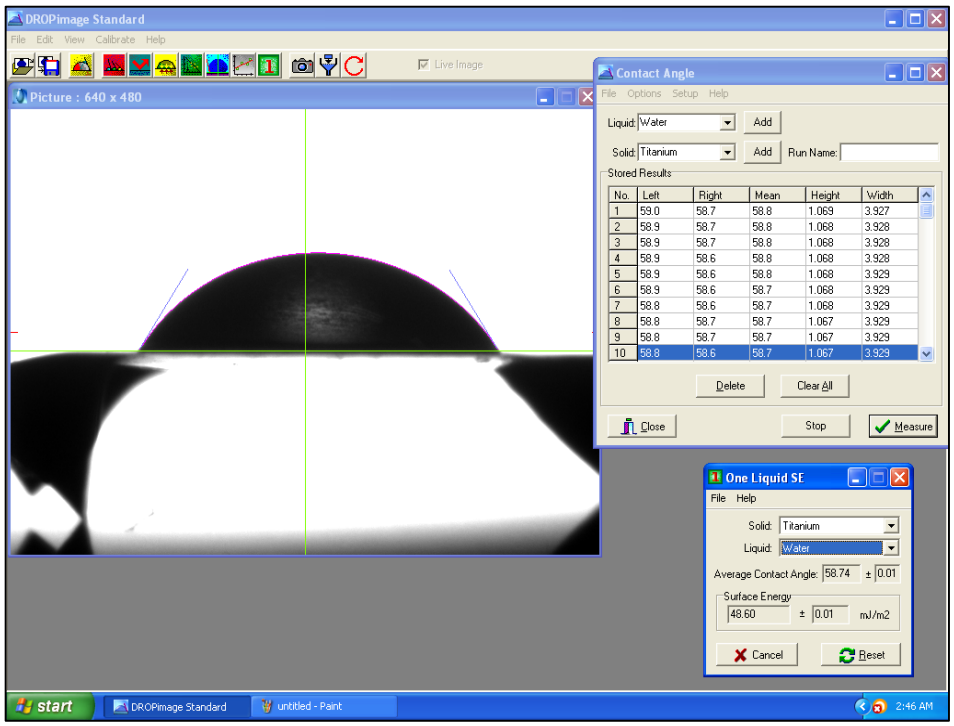

APPENDIX F

Pore Size Measurement Using Image J

Porosity measurement of the TiO_2 coating anodised in 2.0 M H_2SO_4 at 180 V and 100 mA.cm^{-2}

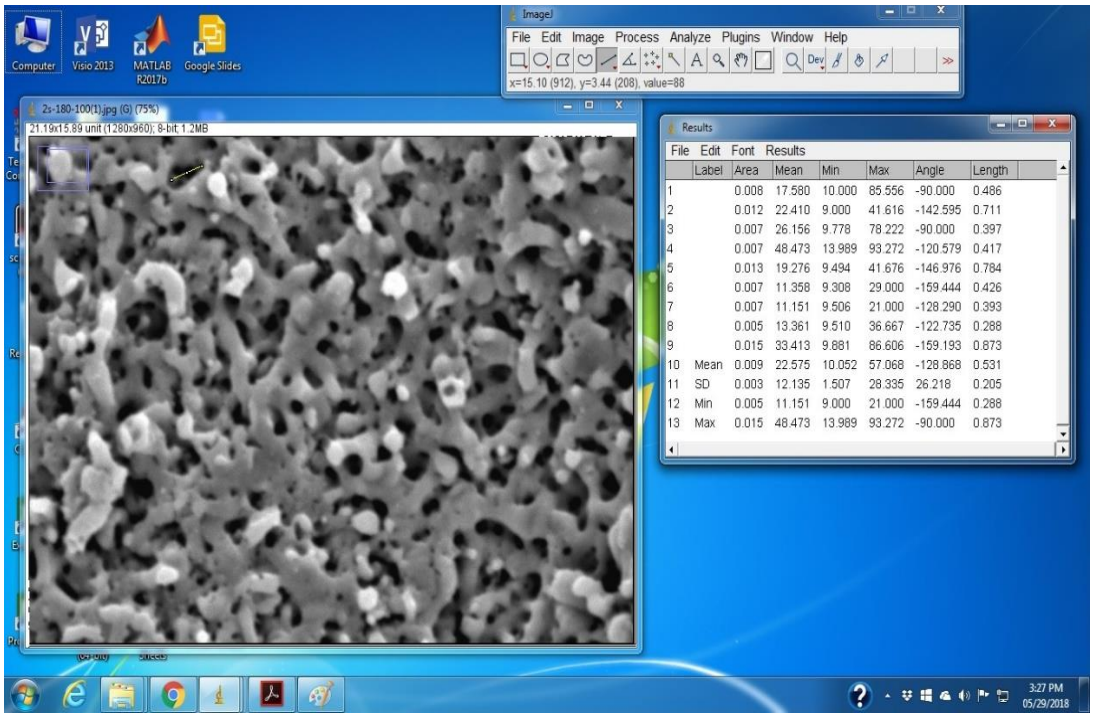

Porosity measurement of the TiO_2 coating anodised in 2.0 M H_3PO_4 at 180 V and 100 mA.cm^{-2}

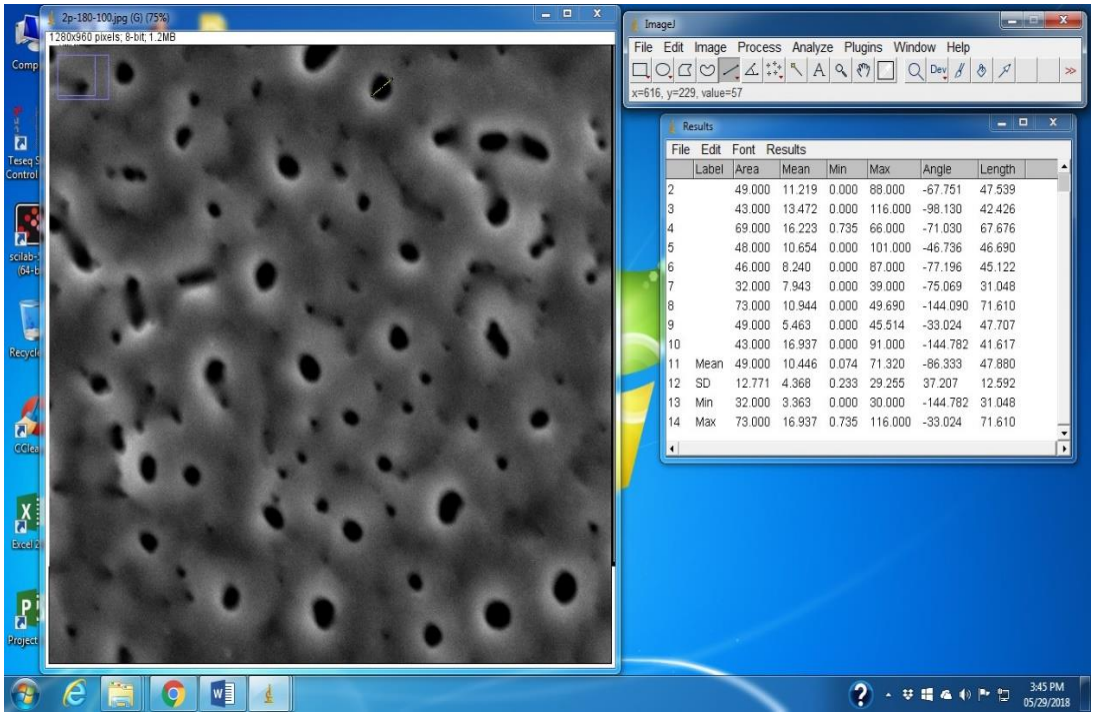

LIST OF PUBLICATIONS

Saleh, S.S., Sorrell, C.C., & Abdullah, H.Z. (2015). The anatase formation on anodised titanium in sulphuric acid. *Advanced Materials Research*, 1087, pp. 334-339.

Saleh, S.S., & Abdullah, H.Z. (2015). Optimization and characterisation of anatase formed on aodized titanium in sulphuric acid. *Advanced Materials Research*, 1125, pp. 479-483.

Saleh, S.S., & Abdullah, H.Z. (2015). Optimization and characterisation of anatase formed on anodised titanium in phosphoric acid. *Materials Science Forum*, 840, pp. 240-244.

Saleh, S.S., & Abdullah, H.Z. (2016). Optimization and characterisation of anatase formed on anodised titaniumin mixed acids. *ARPN Journal of Engineering and Applied Sciences*, 11(16), pp. 9809-9804.

Saleh, S.S., Yunus, M.R.M., & Abdullah, H.Z. (2018). Effect of UV irradiation on apatite deposition on anodised tio_2 coating formed under mixed acid solution. *International Journal of Current Science, Engineering & Technology*, AMCT 2017 Malaysia, pp. 88-94.

VITA

The author was born on April 6, 1987, in Benghazi, Libya. He went to Benghazi University to pursue his degree at the University of Benghazi, Libya (the University of Garyounis previously), and graduated with the B.Eng. in Industrial and Manufacturing Engineering in 2010. Upon graduation, he pursued further studies at the postgraduate school at Universiti Tun Hussein Onn Malaysia. Where he studies Masters by coursework in Mechanical Engineering at Department of Materials Engineering and Design at the Faculty of Mechanical and Manufacturing Engineering. After that, he pursued his Ph.D. at the same Department in Biomedical Engineering field. During his post-graduate studies, he participated in four conferences and published 6 papers.